



University of  
**Salford**  
MANCHESTER

**Sireetorn Kuharat, BEng (Hons), MSc (Salford)**

**School of Science, Engineering and Environment (SEE)**  
**Department of Aeronautical and Mechanical Engineering**  
***Multi-Physical Engineering Sciences Group (MPESG)***

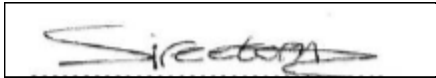
**“Numerical study of nanofluid-based direct absorber solar collector systems with metallic/carbon nanoparticles, multiple geometries and multi-mode heat transfer”**

**Miss Sireetorn Kuharat, BEng (Hons) MSc**  
**@00336603**

**Submitted in Partial fulfilment of the Requirements for the Degree of**  
**Doctor of Philosophy, March 2021**

## DECLARATION

I, Sireetorn Kuharat, declare that this thesis is my original work, and no portion of the work referred to in this report has been submitted in support of an application for another degree or qualification of this or any other university, or other institution of learning.

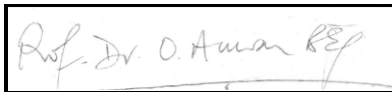


22/3/2021

.....  
**Signature**

.....  
**Date**

*Miss Sireetorn Kuharat*



22/3/2021

.....  
**Approved by**  
**Prof. Dr. Anwar Béq (Supervisor)**

.....  
**Date**



22/3/2021

.....  
**Approved by**  
**Mr. Ali Kadir (Co-Supervisor)**

.....  
**Date**

## **Acknowledgements**

This PhD thesis contains seven of my publications which took over three years of research to accomplish. However, this wonderful research would not be possible without great support and guidance. I would like to express my sincere gratitude to my supervisor Prof. Dr. Anwar Bég for his valuable knowledge, encouragement and generosity which made my journey through my PhD at Salford University very enjoyable and hugely rewarding.

I would also like to thank all my co-supervisors (Mr. Ali Kadir, Dr. Walid Jouri) and technicians (Mr. Alan Mappin and Mr. David Connor) for all the guidance, knowledge and laboratory support.

I am also grateful to the Amelia Earhart fellowship received through the Zonta International Group. This provided immense support towards my PhD tuition fee and conferences.

Also, I would like to thank you my mother (Dr. Rapin Chuchen), my father (Mr. Viwat Kuharat) and my Stepdad (Mr. Andrew Dare) for all the love and financial support. Thanks to Mr. Armghan Zubair for being a great companion though out my PhD. Thanks to all my friends and family in the UK and Thailand for their love and support during a stressful time.



# Abstract

Nanofluids are complex colloidal suspensions comprising nanoparticles (metallic or carbon based or both) suspended in a base fluid (e.g. water). The resulting suspension provides demonstrably greater thermal performance than base fluids on their own without the agglomeration or sedimentation effects associated with larger (micron-sized) particles. The substantial elevation in thermal conductivity achieved with nanoparticles has made nanofluids very attractive for numerous energy applications including solar collectors. Solar energy is a clean, renewable source available and is essential for all life to exist on earth. Current technology which harvests solar energy with heat transfer fluids (HTFs) e.g., Direct Absorber Solar Collectors (DASCs), Flat Plat Solar Collector (FPCs), Parabolic Trough Solar Collector (PTSCs) etc, still requires continuous improvement in achieving higher efficiencies and greater sustainability. Nanotechnology has emerged as a significant area in recent years and features the use of sophisticated “green” nanomaterials embedded in conventional engineering materials. In this PhD a range of different DASC geometries are explored (annular, trapezoidal, prismatic, quadrilateral, biomimetic channel etc) with a variety of real nanofluids (water-based with metallic nanoparticles such as silver, copper, gold, zinc, titanium etc or carbon based e.g. diamond, graphite etc). Viscous incompressible laminar flows using Newtonian fluid models (Navier-Stokes equations) with *thermal convection and radiative heat transfer* are considered both with and without thermal buoyancy. Several thermal radiative flux models are deployed to mimic solar radiation effects such as the Rosseland model, P1 Traugott model, Chandrasekhar discrete ordinates model (DOM). ANSYS FLUENT and MAPLE symbolic software are used as the numerical tools to solve the relevant boundary value problems. Generally, the Tiwari-Das nanoscale model is used although the Buongiorno two-component nanofluid model (with thermophoresis and Brownian motion) has also been deployed.

Extensive visualizations of streamline and isotherms are computed. Validation with alternative numerical methods and experimental studies is also included. Comprehensive appraisal of the relative performance of different nanofluids is evaluated. Generally, non-magnetic nanoparticles are studied although for the biomimetic channel (solar pump) case magnetic nanoparticles are addressed. The simulations show the significant improvement in thermal conductivities (and thermal efficiency) achieved with different types of geometry and nanoparticle type. Aspect ratio and inclination effects are also considered for some DASC cases. Extensive physical interpretation of thermofluid characteristics is provided. Where possible key dimensionless scaling parameters (Rayleigh number, Nusselt number, Prandtl number, Rosseland number etc) are utilized. The analyses reported herein constitute significant novel developments in solar collector nanofluid dynamics and many chapters have been published in leading international journals and conferences. The results have furnished good guidance for solar designers to assist in the selection of different geometries, nanoparticle types and volume fraction (percentage doping) for larger scale deployment in the future. Furthermore, some pathways for extending the current simulations to e.g. non-Newtonian nanofluid physics, turbulence etc are also outlined.

# Table of Contents

Chapter 1	Introduction.....	1
1.1	Motivation.....	1
1.2	Aims.....	1
1.3	Objectives.....	3
1.4	Literature review.....	4
1.4-1	Solar Energy and Solar collectors.....	4
1.4-2	Nanofluids.....	4
1.5	CFD Models developed.....	7
1.5-1	Two-dimensional models of nanofluid DASCs.....	7
1.5-2	Three-dimensional models of nanofluid DASCs.....	16
Chapter 2	Theoretical and Numerical Methodology.....	43
	Abstract.....	43
2.1-1	Solar Collector Classification.....	43
2.1-2	Nanofluids.....	49
2.2	Analytical Approach.....	53
2.2-1	Viscous flow.....	54
2.2-2	Tiwari-Das volume fraction nanofluid model.....	55
2.2-3	Other Nanoscale Models for Nanofluids.....	57
2.2-4	Buongiorno nanoscale model.....	58

2.2-5	Magnetic nanoparticles .....	62
2.2-6	Magnetohydrodynamics.....	63
2.2-7	Natural Convection and Dimensionless Numbers .....	65
2.2-8	Forced Convection and Dimensionless Numbers .....	69
2.2-9	Magnetic Nanoparticles .....	71
2.2-10	Direct absorption solar collector with magnetic nanofluid: CFD model and parametric analysis.....	72
2.2-11	Radiation Models .....	72
2.3	Numerical Aspects .....	82
2.3-1	ANSYS FLUENT .....	82
2.3-2	Maple numerical quadrature .....	89
Chapter 3	Natural Convection of Nanofluids Inside a Two-dimensional Quadrilateral Solar Enclosure with Copper, Silver and Titania Metallic nanoparticles and multiple radiative transfer models.....	93
	Abstract.....	93
a.	Introduction and Mathematical Model.....	94
3.1	Grid Sensitivity Analysis .....	99
3.2	Validation with Published Studies .....	100
3.3	Results and Discussion.....	101
3.4	Conclusions.....	124
Chapter 4	Diamond and Zinc Nanoparticles Performance in A Water-Based Trapezium Direct Absorber Solar Collector .....	127

Abstract.....	127
4.1 Mathematical Model .....	128
4.2 Grid Sensitivity Analysis .....	131
4.3 Results and Discussion.....	133
4.4 Conclusions .....	147
Chapter 5 Three-dimensional tilted prismatic solar enclosure with aspect ratio and volume fraction effects .....	149
Abstract.....	149
5.1 Computational Mathematical Model.....	149
5.2 Grid Sensitivity Analysis .....	152
5.3 Validation with Published Studies .....	153
5.4 Results and Discussion.....	155
5.5 Conclusions .....	166
Chapter 6 Computational Fluid Dynamics Simulation of a Nanofluid-Based Annular Solar Collector with Different Metallic Nano-Particles.....	169
6.1 Abstract .....	169
6.2 Computational Mathematical Model.....	169
6.3 Grid Sensitivity Analysis .....	171
6.4 Results and Discussion.....	172
6.5 Conclusions .....	193

Chapter 7	Numerical simulation of forced convection-radiation transfer in a flat plate prismatic 3-d solar collector with inlet/outlet conditions, metallic/carbon nanoparticles and the Chandrasekhar discrete ordinates method. ....	195
7.1	Introduction .....	195
7.2	Mathematical Model .....	196
7.3	Grid Sensitivity Analysis .....	200
7.4	Validation with Published Studies .....	201
7.5	Results and Discussion.....	203
7.2.1	Parametric analysis of varies volume fractions of nanofluid (CuO water based nanofluid and Graphite water based nanofluid).....	211
7.2.2	Parametric analysis of varies mass flow rates of CuO water based nanofluid and Graphite water based nanofluid. ....	214
7.6	Conclusions .....	218
Chapter 8	Modelling a magnetic nanofluid-based hybrid magneto-biomimetic deformable nano-collector with Buongiorno’s two-component nanoscale model .....	220
	Abstract.....	220
8.1	Mathematical formulation .....	221
8.2	Validation with maple17 .....	228
8.3	Numerical evaluation of results and discussion .....	229
8.3-1	Pumping characteristics .....	241
8.3-2	Axial Velocity distribution .....	246
8.3-3	Temperature and Nanoparticle volume fraction distributions .....	249

8.3-4	Trapping phenomena .....	251
8.3-5	Further Validation with Published Literature .....	252
8.4	Concluding remarks .....	253
Chapter 9	Conclusions, Recommendations and Future Research Directions .....	258
9.1	CONCLUSIONS .....	259
9.1-1	Natural Convection and Inclination Effects.....	259
9.1-2	Solar Collector Enclosure Geometrical Effects .....	260
9.1-3	Forced Convection Effects.....	261
9.1-4	Radiative Heat Transfer aspects.....	262
9.1-5	Magnetic metallic nanoparticles .....	263
9.1-6	Future pathways .....	264
9.1-7	Extension to Non-Newtonian nanofluid systems.....	265
9.1-8	Extension to bioconvection in solar nanofluid collectors .....	267
9.1-9	Extension to include turbulence effects .....	268
9.1-10	Extension to more refined nanopowder coatings/carbon nanotube coatings ..	269
References.....		269
Appendix .....		307

## Nomenclature

Abbreviations	
<i>AR</i>	Aspect Ratio
CNTs	Carbon Nanotubes
CFD	Computational Fluid Dynamics
DAPTCs	Direct Absorption Parabolic Trough Collectors
DASCs	Direct Absorption Solar Collectors
DOM	Chandrasekhar Discrete Ordinates Method
FEA	Finite Element Analysis
FPCs	Flat Plat Solar Collectors
HTF	Heat Transfer Fluids
LDV	Laser Doppler Velocimetry
PTSCs	Parabolic Trough Solar Collector
PV	Photovoltaic Solar Collectors
PVT	Photovoltaic Thermal Hybrid Solar Collector
RTE	Radiative Transfer Equation
S2S	Surface-to-Surface
SIMPLE	Semi-Implicit Method for Pressure-Linked Equations
SWCNT	Single-Walled Carbon Nanotube

Greek letters	
$\alpha_m$	Thermal diffusivity ( $m^2/s$ )
$\alpha$	Tilt angle (degrees)
$\beta$	Coefficient of volume expansion ( $1/K$ )



$\eta$	Solar collector efficiency (-)
$\Gamma$	Relaxation angular frequency (Rad/s)
$\phi$	Volume fraction (-)
$\mu$	Dynamic viscosity (kg/m.s)
$\nu$	Kinematic viscosity of fluid (m <sup>2</sup> /s)
$\rho$	Density (kg/m <sup>3</sup> )
$\sigma_s$	Scattering coefficient (m <sup>-1</sup> )
$\sigma$	Stefan-Boltzmann constant (5.669×10 <sup>-8</sup> W/m <sup>2</sup> K <sup>4</sup> )

Roman Notations	
$A$	Collector area (m <sup>2</sup> )
$a$	absorption coefficient (m <sup>-1</sup> )
$C_p$	Specific heat capacity (J/Kg.K)
$G$	Solar irradiance (W/m <sup>2</sup> )
$g$	Gravitational acceleration (m/s <sup>2</sup> )
$Ha$	Hartmann magnetic Number
$h$	Convective Heat Transfer Coefficient (W/m <sup>2</sup> K)
$I$	radiation intensity (W/m <sup>2</sup> )
$k$	Thermal conductivity (w/m.K)
$L$	Length of the enclosure (m)
$Nu$	Nusselt number (-)
$\overline{Nu}$	Average Nusselt number (-)
$n$	refractive index (-)
$Ra$	Rayleigh number (-)

$T$	Temperature (K)
$V$	Volume of fluid (m <sup>3</sup> )
$q$	Heat flux (W/m <sup>2</sup> )
$Q_c$	Thermal conduction flux (W/m <sup>2</sup> )
$Q_{rad}$	Radiative flux term (W/m <sup>2</sup> )
$q''_{w\ CFD}$	Heat flux rate computed in ANSYS FLUENT (W/m <sup>2</sup> )
$u$	Velocity in x-direction (m/s)
$v$	Velocity in y-direction (m/s)
$w$	Velocity in z-direction (m/s)
$W$	Solar collector width (m)
$x, y, z$	Global Cartesian coordinates (m)

Subscripts and Superscripts	
$nf$	Nanofluid
$f$	Based fluid
$s$	Nanoparticle
$\infty$	Bulk

## List of Figures

FIGURE 2-1 CLASSIFICATION OF VARIOUS SOLAR COLLECTORS	44
FIGURE 2-2 SOLAR ENERGY CONVERSION TO THERMAL ENERGY	45
FIGURE 2-3 A) SURFACE VS B) DIRECT SURFACE ABSORPTION-BASED-	46
FIGURE 2-4 FLAT PLATE SOLAR COLLECTOR	46
FIGURE 2-5 CPC (A) FLAT ONE-SIDED ABSORBER, (B) FLAT BIFACIAL ABSORBERS, (C) WEDGE-SHAPED ABSORBER, (D) TUBULAR ABSORBER	47
FIGURE 2-6 TUBULAR DASC SYSTEM (BÉG, ET AL., 2020)	48
FIGURE 2-7 ANNULAR TILTED COMPOSITE DASC SYSTEM (KUHARAT, 2019)	48
FIGURE 2-8 EVACUATED TUBE ANNULAR DASC SYSTEM (KUHARAT, 2019)	48
FIGURE 2-9 CORRUGATED (WAVY) DASC SYSTEM (KUHARAT, 2019)	49
FIGURE 2-10 SERPENTINE DASC SYSTEM (KUHARAT, 2019)	49
FIGURE 2-11 APPLICATIONS OF NANOFLUIDS IN ENGINEERING	50
FIGURE 2-12 NANOPARTICLE TYPES	51
FIGURE 2-13 SHAPES OF NANOPARTICLES	51
FIGURE 2-14 TYPES OF NANOPARTICLES	52
FIGURE 2-15 ORGANIC NANOPARTICLES	52
FIGURE 2-16 SEM IMAGE OF SILVER NANOPARTICLES- STUDIED IN CHAPTER 3	52
FIGURE 2-17 NANOPARTICLE SYNTHESIS METHODS - CLASSIFICATION	53
FIGURE 2-18 NANOPARTICLE SYNTHESIS METHODS - TYPES	53
FIGURE 2-19 NATURAL CONVECTION	66
FIGURE 2-20 FORCED CONVECTION	69
FIGURE 2-21 APPLICATIONS OF MAGNETIC NANOPARTICLES	72
FIGURE 2-22 RADIATIVE HEAT TRANSFER PROCESS	75
FIGURE 2-23 TREATMENT FOR OPAQUE WALLS	78
FIGURE 2-24 TREATMENT AT SEMI-TRANSPARENT WALLS	80
FIGURE 2-25 BEAM WIDTH AND DIRECTION FOR EXTERNAL IRRADIATION BEAM	81

FIGURE 2-26 CFD ANSYS FLUENT METHODOLOGY FOR SOLVING NANOFLUID DASC ENCLOSURE BOUNDARY VALUE PROBLEM	83
FIGURE 2-27 VALIDATION METHODOLOGY DIAGRAM	84
FIGURE 2-28 METHODOLOGY OF SIMPLE METHOD	86
FIGURE 2-29 ANSYS FLUENT EXPLAINED IN FURTHER DETAIL	87
FIGURE 3.1 DIRECT ABSORBER SOLAR NANOFLUID COLLECTOR ENCLOSURE GEOMETRY	95
FIGURE 3.2: GRIND SENSITIVITY ANALYSIS	100
FIGURE 3.3 FINITE VOLUME RESULTS FOR STREAMLINE AND ISOTHERM PLOTS FOR COPPER-WATER NANOFLUID, WITH A RAYLEIGH NUMBER OF $10^3$ , VOLUME FRACTION OF 0.01 (ABU-NADA & OZTOP, 2009)	101
FIGURE 3.4 ANSYS FLUENT STREAMLINE AND ISOTHERM PLOTS FOR COPPER-WATER NANOFLUID, WITH A RAYLEIGH NUMBER OF $10^3$ , VOLUME FRACTION OF 0.01	101
FIGURE 3.5 ISOTHERMS FOR SILVER-WATER NANOFLUID, $RA = 10^4$ , ROSSELAND FLUX MODEL WITH $\Phi = 0.01$ .	102
FIGURE 3.6 ISOTHERMS FOR SILVER-WATER NANOFLUID, $RA = 10^4$ , NO RADIATIVE FLUX WITH $\Phi = 0.01$ .	102
FIGURE 3.7 ISOTHERMS FOR SILVER-WATER NANOFLUID, $RA = 10^4$ , P1 RADIATIVE FLUX WITH $\Phi = 0.01$ .	103
FIGURE 3.8 STREAMLINE DISTRIBUTIONS FOR SILVER-WATER NANOFLUID, $RA = 10^4$ , P1 FLUX MODEL WITH $\Phi = 0.01$ .	104
FIGURE 3.9 STREAMLINE DISTRIBUTIONS FOR SILVER-WATER NANOFLUID, $RA = 10^4$ , ROSSELAND FLUX WITH $\Phi = 0.01$ .	105
FIGURE 3.10 ISOTHERMS FOR SILVER-WATER NANOFLUID, $RA = 10^5$ , P1 RADIATIVE FLUX WITH $\Phi = 0.04$ .	106
FIGURE 3.11 ISOTHERMS FOR SILVER-WATER NANOFLUID, $RA = 10^5$ , NO RADIATIVE FLUX WITH $\Phi = 0.04$	106
FIGURE 3.12 STREAMLINE DISTRIBUTIONS FOR SILVER-WATER NANOFLUID, $RA = 10^5$ , P1 RADIATIVE FLUX WITH $\Phi = 0.04$	107

FIGURE 3.13 STREAMLINE DISTRIBUTIONS FOR SILVER-WATER NANOFLUID, $RA = 10^5$ , NO RADIATIVE FLUX WITH $\Phi = 0.04$ .	107
FIGURE 3.14 ISOTHERMS FOR SILVER-WATER NANOFLUID, $RA = 10^6$ , P1 RADIATIVE FLUX WITH $\Phi = 0.04$ .	109
FIGURE 3.15 ISOTHERMS FOR SILVER-WATER NANOFLUID, $RA = 10^6$ , NO RADIATIVE FLUX WITH $\Phi = 0.04$ .	110
FIGURE 3.16 STREAMLINE DISTRIBUTIONS FOR SILVER-WATER NANOFLUID, $RA = 10^6$ , P1 RADIATIVE FLUX WITH $\Phi = 0.04$ .	110
FIGURE 3.17 STREAMLINE DISTRIBUTIONS FOR SILVER-WATER NANOFLUID, $RA = 10^6$ , NO RADIATIVE FLUX WITH $\Phi = 0.04$ .	111
FIGURE 3.18 NUSSELT NUMBERS ALONG HOT WALL FOR SILVER-WATER NANOFLUID, P1 FLUX WITH $\Phi = 0.04$ FOR DIFFERENT RAYLEIGH NUMBERS	113
FIGURE 3.19 NUSSELT NUMBERS FOR DIFFERENT NANOFLUIDS, P1 FLUX WITH $\Phi = 0.04$ , $RA = 10^4$ .	114
FIGURE 3.20 NUSSELT NUMBERS FOR DIFFERENT NANOFLUIDS, P1 FLUX WITH $\Phi = 0.04$ , $RA = 10^5$	114
FIGURE 3.21 NUSSELT NUMBERS FOR DIFFERENT NANOFLUIDS, P1 FLUX WITH $\Phi = 0.04$ , $RA = 10^6$ .	115
FIGURE 3.22 ISOTHERMS FOR TITANIUM OXIDE-WATER NANOFLUID, P1 FLUX WITH $\Phi = 0.04$ , $RA = 10^5$ AND ABSORPTION COEFFICIENT OF 0.2 FOR ASPECT RATIO $AR = 4$ .	117
FIGURE 3.23 STREAMLINES FOR TITANIUM OXIDE-WATER NANOFLUID, P1 FLUX WITH $\Phi = 0.04$ , $RA = 10^5$ AND ABSORPTION COEFFICIENT OF 0.2 FOR ASPECT RATIO $AR = 4$ .	117
FIGURE 3.24 ISOTHERMS FOR TITANIUM OXIDE-WATER NANOFLUID, P1 FLUX WITH $\Phi = 0.04$ , $RA = 10^5$ AND ABSORPTION COEFFICIENT OF 0.2 FOR ASPECT RATIO $AR = 2$	118
FIGURE 3.25 STREAMLINES FOR TITANIUM OXIDE-WATER NANOFLUID, P1 FLUX WITH $\Phi = 0.04$ , $RA = 10^5$ AND ABSORPTION COEFFICIENT OF 0.2 FOR ASPECT RATIO $AR = 2$ .	118
FIGURE 3.26 ISOTHERMS FOR TITANIUM OXIDE-WATER NANOFLUID, P1 FLUX WITH $\Phi = 0.04$ , $RA = 10^5$ AND ABSORPTION COEFFICIENT OF 0.2 FOR ASPECT RATIO $AR = 4/3$ .	119
FIGURE 3.27 STREAMLINES FOR TITANIUM OXIDE-WATER NANOFLUID, P1 FLUX WITH $\Phi = 0.04$ , $RA = 10^5$ AND ABSORPTION COEFFICIENT OF 0.2 FOR ASPECT RATIO $AR = 4/3$ .	119

FIGURE 3.28 ISOTHERMS FOR TITANIUM OXIDE-WATER NANOFLUID, P1 FLUX WITH $\Phi = 0.04$ , $RA = 10^5$ AND ABSORPTION COEFFICIENT OF 0.2 FOR ASPECT RATIO $AR = 1$ (SQUARE CAVITY).	120
FIGURE 3.29 STREAMLINES FOR TITANIUM OXIDE-WATER NANOFLUID, P1 FLUX WITH $\Phi = 0.04$ , $RA = 10^5$ AND ABSORPTION COEFFICIENT OF 0.2 FOR ASPECT RATIO $AR = 1$ (SQUARE CAVITY).	120
FIGURE 3.30 ISOTHERMS FOR TITANIUM OXIDE-WATER NANOFLUID, P1 FLUX WITH $\Phi = 0.04$ , $RA = 10^5$ AND ABSORPTION COEFFICIENT OF 0.2 FOR ASPECT RATIO $AR = 0.5$ (SHALLOW CAVITY).	121
FIGURE 3.31 STREAMLINES FOR TITANIUM OXIDE-WATER NANOFLUID, P1 FLUX WITH $\Phi = 0.04$ , $RA = 10^5$ AND ABSORPTION COEFFICIENT OF 0.2 FOR ASPECT RATIO $AR = 0.5$ (SHALLOW CAVITY).	121
FIGURE 3.32 NUSSELT NUMBERS ALONG HOT WALL FOR TITANIUM OXIDE-WATER NANOFLUID, P1 FLUX WITH $\Phi = 0.04$ , $RA = 10^5$ WITH DIFFERENT ENCLOSURE ASPECT RATIOS ( $AR$	123
FIGURE 4.1 TRAPEZIUM WATER NANOFLUID DIRECT ABSORBER SOLAR COLLECTOR	128
FIGURE 4.2 GRID REFINEMENT TEST	131
FIGURE 4.3 FINAL MESH DESIGN FOR NANOFLUID DASC	132
FIGURE 4.4 COMPARISON OF ANSYS FLUENT AND FEM SOLUTION OF (NATARAJAN, ET AL., 2008).	132
FIGURE 4.5 DIAMOND-WATER BASED NANOFLUID WITH VOLUME FACTION $\Phi = 0.02$ , <i>angle</i> $\phi = -10^\circ$	134
FIGURE 4.6 DIAMOND-WATER BASED NANOFLUID WITH VOLUME FACTION $\Phi = 0.02$ , <i>angle</i> $\phi = 0^\circ$	135
FIGURE 4.7 DIAMOND-WATER BASED NANOFLUID WITH VOLUME FACTION $\Phi = 0.02$ , <i>angle</i> $\phi = 10^\circ$	136
FIGURE 4.8 DIAMOND-WATER BASED NANOFLUID WITH VOLUME FACTION $\Phi = 0.02$ , <i>angle</i> $\phi = 20^\circ$	137
FIGURE 4.9 DIAMOND-WATER BASED NANOFLUID WITH VOLUME FACTION $\Phi = 0.02$ , <i>angle</i> $\phi = 30^\circ$	138
FIGURE 4.10 TOTAL HEAT FLUX VS RAYLEIGH NUMBER	139
FIGURE 4.11 SURFACE HEAT TRANSFER COEF. VS RAYLEIGH NUMBER	139
FIGURE 4.12 AVERAGE NUSSELT NUMBER VS RAYLEIGH NUMBER	140
FIGURE 4.13 LOCAL NUSSELT NUMBER	141

FIGURE 4.14 DIAMOND NANOFUID IN TRAPEZIUM WITH 30 DEGREE SLOPE AT RAYLEIGH NUMBER $10^3$ WITH DIFFERENT VOLUME FRACTION	141
FIGURE 4.15 ZINC NANOFUID IN TRAPEZIUM WITH 30 DEGREE SLOPE AT RAYLEIGH NUMBER $10^3$ AT DIFFERENT VOLUME FRACTION	142
FIGURE 4.16 HEAT TRANSFER COEFFICIENT VERSUS S VOLUME FRACTIONS	143
FIGURE 5.1 3-DIMENSIONAL SOLAR NANOFUID ABSORBER PRISMATIC GEOMETRY	150
FIGURE 5.2 FINITE VOLUME ANSYS FLUENT GRID INDEPENDENCE STUDY	153
FIGURE 5.3 ANSYS 3-D MESH FOR NANOFUID PRISMATIC COLLECTOR	153
FIGURE 5.4 BENCHMARK CASE FOR VALIDATION WITH LBM RESULTS OF (WANG, ET AL., 2018).	154
FIGURE 5.5 PRESENT ANSYS FLUENT STREAMLINE AND ISOTHERM RESULTS	155
FIGURE 5.6 COMPARISON OF ANSYS FLUENT SOLUTION (x) AND LBM RESULTS (-) OF (WANG, ET AL., 2018)	155
FIGURE 5.7 3-D FULL BODY TEMPERATURE CONTOURS FOR GOLD-WATER NANOFUID, WITH $\phi = 5\%$ , AR =2 AND RA = $10^5$ FOR INCLINATION ( $\alpha$ ) = 0 DEGREES (VERTICAL ORIENTATION).	156
FIGURE 5.8 3-D FULL BODY TEMPERATURE CONTOURS FOR GOLD-WATER NANOFUID, WITH $\phi = 5\%$ , AR =2 AND RA = $10^5$ FOR INCLINATION ( $\alpha$ ) = 10 DEGREES (WEAK TILT ORIENTATION).	156
FIGURE 5.9 3-D FULL BODY TEMPERATURE CONTOURS FOR GOLD-WATER NANOFUID, WITH $\phi = 5\%$ , AR =2 AND RA = $10^5$ FOR INCLINATION ( $\alpha$ ) = 30 DEGREES.	156
FIGURE 5.10 3-D FULL BODY TEMPERATURE CONTOURS FOR GOLD-WATER NANOFUID, WITH $\phi = 5\%$ , AR =2 AND RA = $10^5$ FOR INCLINATION ( $\alpha$ ) = 45 DEGREES.	156
FIGURE 5.11 3-D FULL BODY TEMPERATURE CONTOURS FOR GOLD-WATER NANOFUID, WITH $\phi = 5\%$ , AR =2 AND RA = $10^5$ FOR INCLINATION ( $\alpha$ ) = 60 DEGREES.	157
FIGURE 5.12 3-D FULL BODY TEMPERATURE CONTOURS FOR GOLD-WATER NANOFUID, WITH $\alpha = 30$ DEGREES, AR =2 AND RA = $10^5$ FOR GOLD VOLUME FRACTION ( $\phi$ ) = 5%.	158
FIGURE 5.13 3-D FULL BODY TEMPERATURE CONTOURS FOR GOLD-WATER NANOFUID, WITH $\alpha = 30$ DEGREES, AR =2 AND RA = $10^5$ FOR GOLD VOLUME FRACTION ( $\phi$ ) = 8%.	158

FIGURE 5.14 3-D FULL BODY TEMPERATURE CONTOURS FOR GOLD-WATER NANOFLUID, WITH $\alpha = 30$ DEGREES, $RA = 10^6$ AND GOLD VOLUME FRACTION ( $\phi$ ) = 5% FOR $AR = 1$ (CUBICAL ENCLOSURE).	159
FIGURE 5.15 3-D FULL BODY TEMPERATURE CONTOURS FOR GOLD-WATER NANOFLUID, WITH $\alpha = 30$ DEGREES, $RA = 10^6$ AND GOLD VOLUME FRACTION ( $\phi$ ) = 5% FOR $AR = 2$ .	159
FIGURE 5.16 3-D FULL BODY TEMPERATURE CONTOURS FOR GOLD-WATER NANOFLUID, WITH $\alpha = 30$ DEGREES, $RA = 10^6$ AND GOLD VOLUME FRACTION ( $\phi$ ) = 5% FOR $AR = 4$ (SLENDER ENCLOSURE).	160
FIGURE 5.17 3-D FULL BODY TEMPERATURE CONTOURS FOR GOLD-WATER NANOFLUID, WITH $\alpha = 30$ DEGREES, $AR = 2$ AND GOLD VOLUME FRACTION ( $\phi$ ) = 5% FOR $RA = 10^3$ .	161
FIGURE 5.18 3-D FULL BODY TEMPERATURE CONTOURS FOR GOLD-WATER NANOFLUID, WITH $\alpha = 30$ DEGREES, $AR = 2$ AND GOLD VOLUME FRACTION ( $\phi$ ) = 5% FOR $RA = 10^4$ .	161
FIGURE 5.19 3-D FULL BODY TEMPERATURE CONTOURS FOR GOLD-WATER NANOFLUID, WITH $\alpha = 30$ DEGREES, $AR = 2$ AND GOLD VOLUME FRACTION ( $\phi$ ) = 5% FOR $RA = 10^5$ .	161
FIGURE 5.20 3-D FULL BODY TEMPERATURE CONTOURS FOR GOLD-WATER NANOFLUID, WITH $\alpha = 30$ DEGREES, $AR = 2$ AND GOLD VOLUME FRACTION ( $\phi$ ) = 5% FOR $RA = 10^6$ .	161
FIGURE 5.21 3-D FULL BODY TEMPERATURE CONTOURS FOR GOLD-WATER NANOFLUID, WITH $\alpha = 30$ DEGREES, $AR = 2$ AND GOLD VOLUME FRACTION ( $\phi$ ) = 5% FOR $RA = 10^7$ .	162
FIGURE 5.22 AVERAGE NUSSELT NUMBER VERSUS VOLUME FRACTION ( $\phi$ )	163
FIGURE 5.23 AVERAGE NUSSELT NUMBER VERSUS ENCLOSURE INCLINATION ANGLE ( $\alpha$ )	163
FIGURE 5.24 AVERAGE NUSSELT NUMBER VERSUS ENCLOSURE ASPECT RATIO	163
FIGURE 5.25 AVERAGE NUSSELT NUMBER VERSUS RAYLEIGH NUMBER ( $RA$ )	164
FIGURE 6.1 GEOMETRICAL AND PHYSICAL MODEL FOR ANNULAR NANOFLUID SOLAR COLLECTOR	170
FIGURE 6.2 ANSYS FLUENT 3-DIMENSIONAL MESH OF SOLAR CONFIGURATION (MESH DENSITY NODES: 479188, ELEMENTS: 443970)	171
FIGURE 6.3 ANSYS FLUENT GRID INDEPENDENCE STUDY	172
FIGURE 6.4 TEMPERATURE CONTOUR FOR CUO NANOFLUID, $\phi = 0.01$	173
FIGURE 6.5 TEMPERATURE CONTOUR CROSS-SECTIONS FOR CUO NANOFLUID, $\phi = 0.01$	174
FIGURE 6.6 VELOCITY CONTOURS FOR CUO NANOFLUID, $\phi = 0.01$	174



FIGURE 6.7 PRESSURE CONTOURS FOR CUO NANOFUID, $\Phi = 0.01$	175
FIGURE 6.8 TEMPERATURE CONTOUR FOR CUO NANOFUID, $\Phi = 0.05$	175
FIGURE 6.9 TEMPERATURE CONTOUR CROSS SECTIONS FOR CUO NANOFUID, $\Phi = 0.05$	176
FIGURE 6.10 VELOCITY CONTOURS FOR CUO NANOFUID, $\Phi = 0.05$	176
FIGURE 6.11 PRESSURE CONTOURS FOR CUO NANOFUID, $\Phi = 0.05$	177
FIGURE 6.12 TEMPERATURE CONTOUR FOR CUO NANOFUID, $\Phi = 0.1$	177
FIGURE 6.13 TEMPERATURE CONTOUR CROSS SECTIONS FOR CUO NANOFUID, $\Phi = 0.1$	178
FIGURE 6.14 VELOCITY CONTOURS FOR CUO NANOFUID, $\Phi = 0.1$	178
FIGURE 6.15 PRESSURE CONTOURS FOR CUO NANOFUID, $\Phi = 0.1$	179
FIGURE 6.16 TEMPERATURE CONTOUR FOR AL <sub>2</sub> O <sub>3</sub> NANOFUID, $\Phi = 0.01$	179
FIGURE 6.17 TEMPERATURE CONTOUR CROSS SECTIONS FOR AL <sub>2</sub> O <sub>3</sub> NANOFUID, $\Phi = 0.01$	180
FIGURE 6.18 VELOCITY CONTOURS FOR AL <sub>2</sub> O <sub>3</sub> NANOFUID, $\Phi = 0.01$	180
FIGURE 6.19 PRESSURE CONTOURS FOR AL <sub>2</sub> O <sub>3</sub> NANOFUID, $\Phi = 0.01$	181
FIGURE 6.20 TEMPERATURE CONTOURS FOR AL <sub>2</sub> O <sub>3</sub> NANOFUID, $\Phi = 0.05$	181
FIGURE 6.21 TEMPERATURE CONTOUR CROSS SECTIONS FOR AL <sub>2</sub> O <sub>3</sub> NANOFUID, $\Phi = 0.05$	182
FIGURE 6.22 VELOCITY CONTOURS FOR AL <sub>2</sub> O <sub>3</sub> NANOFUID, $\Phi = 0.05$	182
FIGURE 6.23 PRESSURE CONTOURS FOR AL <sub>2</sub> O <sub>3</sub> NANOFUID, $\Phi = 0.05$	183
FIGURE 6.24 TEMPERATURE CONTOURS FOR AL <sub>2</sub> O <sub>3</sub> NANOFUID, $\Phi = 0.1$	183
FIGURE 6.25 TEMPERATURE CONTOUR CROSS SECTIONS FOR AL <sub>2</sub> O <sub>3</sub> NANOFUID, $\Phi = 0.1$	184
FIGURE 6.26 VELOCITY CONTOURS FOR AL <sub>2</sub> O <sub>3</sub> NANOFUID, $\Phi = 0.1$	184
FIGURE 6.27 TEMPERATURE CONTOURS FOR TIO <sub>2</sub> NANOFUID, $\Phi = 0.01$	184
FIGURE 6.28 TEMPERATURE CONTOUR CROSS SECTIONS FOR TIO <sub>2</sub> NANOFUID, $\Phi = 0.01$	185
FIGURE 6.29 VELOCITY CONTOURS FOR TIO <sub>2</sub> NANOFUID, $\Phi = 0.01$	185
FIGURE 6.30 PRESSURE CONTOURS FOR TIO <sub>2</sub> NANOFUID, $\Phi = 0.01$	185
FIGURE 6.31 TEMPERATURE CONTOURS FOR TIO <sub>2</sub> NANOFUID, $\Phi = 0.05$	186
FIGURE 6.32 TEMPERATURE CONTOURS CROSS SECTIONS FOR TIO <sub>2</sub> NANOFUID, $\Phi = 0.05$	186
FIGURE 6.33 VELOCITY CONTOURS FOR TIO <sub>2</sub> NANOFUID, $\Phi = 0.05$	187

FIGURE 6.34 PRESSURE CONTOURS FOR TIO <sub>2</sub> NANOFLUID, $\Phi = 0.05$	187
FIGURE 6.35 TEMPERATURE CONTOURS FOR TIO <sub>2</sub> NANOFLUID, $\Phi = 0.1$	188
FIGURE 6.36 TEMPERATURE CONTOUR CROSS SECTIONS FOR TIO <sub>2</sub> NANOFLUID, $\Phi = 0.1$	188
FIGURE 6.37 VELOCITY CONTOURS FOR TIO <sub>2</sub> NANOFLUID, $\Phi = 0.1$	189
FIGURE 6.38 PRESSURE CONTOURS FOR TIO <sub>2</sub> NANOFLUID, $\Phi = 0.1$	189
FIGURE 6.39 RESIDUAL ITERATIONS FOR ANSYS FLUENT SIMULATION (TIO <sub>2</sub> NANOFLUID, $\Phi = 0.1$ )	190
FIGURE 7.1 DIRECT ABSORBER SOLAR NANOFLUID COLLECTOR	197
FIGURE 7.2: GRIND SENSITIVITY ANALYSIS	200
FIGURE 7.3 INFRARED IMAGE DEMONSTRATING RAPID TEMPERATURE INCREASE (BLUE: COOLEST AND PINK: WARMEST) (OTANICAR, ET AL., 2010)	202
FIGURE 7.4 ANSYS FLUENT TEMPERATURE CONTOUR PLOT FOR GRAPHITE-WATER BASED NANOFLUID (BLUE: COOLEST AND RED: WARMEST).	202
FIGURE 7.5 COMPARISON OF MODELLING AND EXPERIMENTAL RESULTS OF GRAPHITE- WATER BASED NANOFLUID.	203
FIGURE 7.6 TEMPERATURE CONTOUR OF WATER BASED SOLAR COLLECTOR.	204
FIGURE 7.7 TEMPERATURE CONTOUR OF 4 TYPES OF NANOFLUIDS AT 0.04 PERCENTAGE VOLUME FRACTION	205
FIGURE 7.8 TEMPERATURE CONTOUR OF 3 TYPES OF NANOFLUIDS AT 0.04 PERCENTAGE VOLUME FRACTION	205
FIGURE 7.9 LOCAL SURFACE NUSSELT NUMBER OF VARIOUS NANOFLUIDS WITH 0.004 PERCENTAGE VOLUME FRACTION	207
FIGURE 7.10 AVERAGE NUSSELT NUMBER OF VARIOUS NANOFLUIDS WITH 0.004 PERCENTAGE VOLUME FRACTION	209
FIGURE 7.11 SOLAR COLLECTOR EFFICIENCY WITH VARIOUS NANOFLUIDS	210
FIGURE 7.12 TEMPERATURE CONTOUR OF CUO- WATER BASED NANOFLUIDS AT VARIOUS PERCENTAGE VOLUME FRACTIONS.	212
FIGURE 7.13 TEMPERATURE CONTOUR OF GRAPHITE - WATER BASED NANOFLUIDS AT VARIOUS PERCENTAGE VOLUME FRACTIONS.	213

FIGURE 7.14 SOLAR COLLECTOR EFFICIENCY VS VOLUME FRACTION (CUO-WATER BASED NANOFLUID)	213
FIGURE 7.15 AVERAGE NUSSELT NUMBER VS VOLUME FRACTION (CUO-WATER BASED NANOFLUID)	213
FIGURE 7.16 TEMPERATURE CONTOUR OF CUO-WATER BASED NANOFLUID (0.001 %V) WITH VARIOUS MASS FLOWRATES.	214
FIGURE 7.17 VELOCITY STREAMLINES OF CUO-WATER BASED NANOFLUID (0.001 %V) WITH VARIOUS MASS FLOWRATES.	215
FIGURE 7.18 TEMPERATURE CONTOUR OF GRAPHITE-WATER BASED NANOFLUID (0.001 %V) WITH VARIOUS MASS FLOWRATES.	215
FIGURE 7.19 VELOCITY STREAMLINES OF GRAPHITE-WATER BASED NANOFLUID (0.001 %V) WITH VARIOUS MASS FLOWRATES.	216
FIGURE 7.20 SOLAR COLLECTOR EFFICIENCY VS MASS FLOW RATES	217
FIGURE 8.1 SCHEMATIC DIAGRAM OF THE SOLAR MAGNETIC NANOFLUID PERISTALTIC PUMP COLLECTOR (ASYMMETRIC CHANNEL).	223
FIGURE 8.2 PRESSURE RISE PROFILE WITH VARIATION IN (A) A, (B) M, (C) K, (D) RN, (E) B AND (F) BR.	232
FIGURE 8.3 AXIAL VELOCITY DISTRIBUTIONS (AXIAL VELOCITY VS. TRANSVERSE COORDINATE) FOR (A) M, (B) RN, (C) PR, (D) K, (E) B, (F) A.	235
FIGURE 8.4 TEMPERATURE AND NANOPARTICLE VOLUME FRACTION PROFILES WITH VARIATION IN (A)B, (B) NT, (C) PR, (D) RN	237
FIGURE 8.5 STREAM LINES AT $A=0.3, B=0.2, PR=0.7, RN=0.5, B=0.5, NB=0.5, NT=0.5, M=1, D=1.1, BR=3, \Theta=2, K=0.2, \Phi=\pi/4, GR=2, PR=2, NT=1$ , FOR (A) $A=0$ , (B) $A=0.1$ .	238
FIGURE 8.6 STREAM LINES AT $A=0.3, B=0.2, PR=0.7, RN=0.5, A=0, NB=0.5, NT=0.5, M=1, D=1.1, BR=3, \Theta=2, K=0.2, \Phi=\pi/4, GR=2, PR=2, NT=1$ , FOR (A) $B=0$ (B) $B=0.5$ .	239
FIGURE 8.7 STREAM LINES AT $A=0.3, B=0.2, PR=0.7, RN=0.5, A=0, NB=0.5, NT=0.5, B=0.25, D=1.1, BR=3, \Theta=2, K=0.2, \Phi=\pi/4, GR=2, PR=2, NT=1$ , FOR (A) $M=0$ , (B) $M=1$ .	240
FIGURE 8.8 COMPARISON RESULT OF STREAM FUNCTION VERSUS TRANSVERSE AXIS.	241

FIGURE 9.1 METALLIC NANOPARTICLES CONSIDERED IN PHD	267
FIGURE 9.2 RANGE OF ROBUST NON-NEWTONIAN MODELS AVAILABLE FOR NANOFUIDS	265
FIGURE 9.3 SOLAR DAYLIGHT TRACKING	269
FIGURE 9.4 CNT FOR NANOFUID COLLECTORS - COURTESY MIT ENERGY INSTITUTE, USA.	270

# **Chapter 1 Introduction**

## **1.1 Motivation**

Solar energy is a clean, renewable source available anywhere in the world and is essential for all life to exist on earth. In addition to providing earthly sustenance, solar energy is an effective means of providing green, sustainable energy to technological societies via electrical power. However current technology which harvests solar energy with heat transfer fluids (HTFs) e.g., Direct Absorber Solar Collectors (DASCs), Flat Plat Solar Collector (FPCs), Parabolic Trough Solar Collector (PTSCs) etc, still requires continuous improvement in achieving higher efficiencies and greater sustainability. Nanotechnology has emerged as a significant area in recent years and features the use of sophisticated “green” nanomaterials embedded in conventional engineering materials. One sub-set of nanomaterials is nanofluids which are colloidal suspensions of base fluids doped with metallic nanoparticles (silver, copper, gold, zinc, titanium etc) to improve the overall thermal conductivity of the working fluid and, hence enhance significantly thermal efficiency of the solar collector.

## **1.2 Aims**

The main aim of this research is to investigate the impact of different types of nanoparticles (metallic) combined with water base fluid with a view to improving thermal efficiency in solar collectors.

Therefore, this PhD explores the application of nanofluids in different solar collector geometries to improve heat transfer rates and therefore efficiency. This is achieved by

improving existing mathematical and computational models to refine substantially current understanding of many key fluid dynamic phenomena inherent to the successful design and performance of such systems i.e. natural convection, forced convection, mixed convection, coupled radiative heat transfer models (i.e., Rosseland, P1, S2S and Chandrasekhar discrete ordinates model-DOM), different combinations of metallic nanoparticles (e.g. copper, zinc, diamond, alumina, titania etc), advanced nanoscale volume fraction models in ANSYS FLUENT, dimensionless scaling parameters (Rayleigh number, Nusselt number, Prandtl number etc). Geometric considerations explored include solar collector inclination, prismatic, trapezium, annular, tubular, quadrilateral and other configurations. ANSYS FLUENT finite volume simulations are conducted and all analyses are benchmarked with either published experimental data or alternative numerical studies from the literature.

## 1.3 Objectives

1. To produce more accurate and refined simulations of 2D/3D solar collector systems (DASC, FSC, PTSC) with nanofluids to achieve enhanced thermal efficiency.
2. To validate where possible the simulations with previous experiment studies.
3. To study natural convection, forced convection, mixed convection and coupled conduction-convection-radiation in solar collector systems.
4. To extend the current state of knowledge of solar collector heat transfer to new geometries (square, rectangle, trapezoid, cube, cuboid, cylindrical and annulus) for water-based nanofluids doped with metallic nanoparticles.
5. To apply the Tiwari-Das nanoscale volume fraction model in ANSYS FLUENT CFD software and to simulate the steady-state laminar enclosure flows whilst incorporating aspects of objectives i) and iii) above.
6. To utilize different radiative heat transfer models (Rosseland, P Traugot differential, Chandrasekhar discrete ordinates model DOM, Solar daylight tracking model, all in ANSYS FLUENT)
7. To carefully study experiments from the literature for solar collectors with different nanoparticles (e.g., Titanium oxide, Copper oxide, Aluminium and Silver) for benchmarking ANSYS simulations.
8. To compare different metallic (non-magnetic and magnetic) and carbon nanoparticle performance in a variety of thermal solar collector geometrical designs.
9. To produce high-quality journal papers, conference presentations and book chapters.

## **1.4 Literature review**

### **1.4-1 Solar Energy and Solar collectors**

Motivated by cleaner and more sustainable energy resources in the 21st century, engineers have intensified efforts in studying and developing more efficient renewable energy designs. While many different options exist, solar energy remains the most promising owing to the vast quantities of heat received daily in many parts of the world. The current energy utilization globally is a fraction of the total solar radiation reaching the earth as noted by (Kalogirou, 2013). Solar collector design continues to undergo refinements and is being implemented on large scales in many continents. Solar thermal collectors are one of the popular types of solar collector technology that are mostly used in residential and industrial applications such as domestic water heating, heating of swimming pools, space heating. It is can also be considered legendary based on the type of heat transfer fluids (HTF), e.g., water, non-freezing liquid, air, or heat transfer fluid (Nagarajan, et al., 2014). To receiver a higher solar energy, the HTF should have a high heat transfer rate which can be done in many ways. One approach is to enhance the fluid thermophysical properties and this can be done by using nanofluid as a working fluid instant of normal working fluid. As nanofluids increase the heat transfer rate of the base fluids (Xuan & Roetzel, 2000). Addition of small amount of high thermal conductivity solid nanoparticles in base fluid increases the thermal conductivity, thus increasing the heat transfer rate.

### **1.4-2 Nanofluids**

Nanofluids were introduced by (Choi & Eastman, 1995) as a mechanism for enhancing thermal properties of engineering fluids such as water, air, and oil. A nanofluid comprises a colloidal mixture of a small quantity of conducting nanoparticles suspended in a base fluid, such as



water. Nanofluids have been shown to exhibit high, non-linear, and anomalous thermal conductivity, compared to the base fluid and to achieve significant elevations in heat transfer rates in either free (natural) or forced convection. Nanofluid dynamics involve four scales: the molecular scale, the microscale, the macroscale and the mega-scale and an interaction is known to take place between these scales. Diverse types of nanofluids can be synthesized by combining different nanoparticles (e.g., metallic oxides, silicon carbides, carbon nanotubes) with different base fluids. An elaborate description of the numerous manufacturing methods developed for robust and stable nanofluid suspensions has been provided in (Das, et al., 2007). Engineers have explored many applications of nanofluids which have aimed at manipulating the structure and distribution of nanoparticles to modify macroscopic properties of the nanofluid such as its thermal conductivity. Recent examples of the implementation of nanofluids in energy and other applications include automobile radiator systems (Oliveira & Bandarra Filho, 2014) (Silver nanoparticles dispersed in distilled water), drilling muds (Bég, et al., 2018) (titanium oxide and aluminium oxides in bentonite base fluid), IC cycle marine gas turbine intercoolers (copper and alumina nano-particles in air) (Zhao, et al., 2015), separation and purification of biological molecules and cells (Salata, 2004) (gold nanoparticles), pharmaco-dynamics (Ali, et al., 2015) (silver and gold nano-particles) and PEM fuel cells (RafiqulIslam, et al., 2016). Another key area of interest for nanofluids is solar engineering. Recently green Titanium oxide nanoparticles have been considered for deployment in parabolic trough solar collectors (Okonkwo, et al., 2018) and magnetic iron oxide nanoparticles have been studied for solar pumping systems (Prakash, et al., 2019). Among the many systems available for modern solar energy, direct absorption solar collectors (DASCs), compared to conventional collectors, have been found to be simpler and often more efficient since owing to the absence of an absorber plate, thermal resistance is reduced to the

path of energy absorption. Direct absorption solar collectors, although employed for many decades in for example water heating however have traditionally yielded low thermal efficiency due to the limited absorption properties of the working fluid (air or water). However, with recent developments in nanofluid technologies, doping of conventional solar collector fluids with metallic nanoparticles has shown that significant improvements in working liquid thermophysical properties (e.g. thermal conductivity) and radiative absorption properties are achievable in direct absorption solar collectors (Moghadam, et al., 2017) (Bait & Si-Ameur, 2018) (Otanicar, et al., 2010). (Karami, et al., 2018) observed substantial thermal enhancement with silver-water nanofluids in field tests of direct solar absorbers. (Tyagi, et al., 2009) studied the performance of water-aluminium nanofluid in a DASC observing that the presence of nanoparticles increases the absorption of incident radiation by more than nine times over that of pure water and nanofluids achieve at least a ten percent better efficiency than conventional water-based flat-plate collectors. (Gorji & Ranjbar, 2017) described experiments on a nanofluid-based direct absorption solar collector (DASC) using graphite, magnetite and silver nanoparticles dispersed in de-ionized water. They observed that magnetite dispersions attained the highest thermal and exergy efficiencies; followed by graphite and silver nanofluids, respectively. (Godson, et al., 2010) reviewed characteristics of nanofluids relevant to solar and other renewable energy systems including increase in surface volume ratio, Brownian motion, thermophoresis, thermal conductivity enhancement and also surveyed in some detail, a variety of computational and experimental investigations on forced and free convective heat transfer. (Bozorgan & Shafahi, 2015) reviewed number of studies on design of direct absorber solar thermal systems using nanofluids for working at optimum conditions.

## **1.5 CFD Models developed**

In the next sections we will consider literature pertinent to all the special models developed in Chapter 3-7. These feature different dimensionality of the models e. g. 2-D, 3-D, axisymmetric (quasi-3-D), various nanoparticles (metallic and/or carbon-based), geometries, types of convection mode, radiative heat transfer models, mesh designs and orientations of the solar collector. First, we address the 2-D models and then the more complex 3-D models. This pathway proved to be very successful in the work conducted since 2-D models established the confidence to simulate more realistic scenarios. Each of the **5 models (ANSYS FLUENT simulations)** produced has its own chapter and includes experimental verification and also mesh independence testing and benchmarking with other numerical codes (e. g. finite element method) depending on the literature of relevance. Furthermore, each of these 5 chapters were further organized and edited into comprehensive journal papers or book chapters, of which all have now been published. Additionally, several conference papers were also produced using supplementary results generated in these chapters. All publications produced are listed at the end of this chapter, and also include supplementary works conducted in parallel in nanofluid solar systems engineering.

### **1.5-1 Two-dimensional models of nanofluid DASCs**

During Year 1 and part of Year 2 of this PhD program, two comprehensive models of 2-dimensional solar enclosure transport phenomena were produced.

#### **1.5-1.1 Two-dimensional solar enclosure with radiative heat transfer, aspect ratio and volume fraction effects**

An important application of nanofluids in energy engineering is the area of direct absorber solar collectors (DASCs) (Duffie, et al., 2017). These feature a working fluid which traps solar

radiation in an enclosure and circulates the heat for subsequent use in a variety of technologies including electricity generation, domestic heating etc. To better predict the performance of such solar absorbers, mathematical and numerical simulation of enclosure convection flows has become an indispensable tool. Many excellent studies have appeared in the past three decades considering a diverse range of solar collector designs and working fluids. Such investigations generally feature Navier-Stokes viscous flow models with an energy equation including thermal buoyancy (and other) effects. Where a fundamental configuration of relevance to DASC is the rectangular enclosure. (Kosti, et al., 2013) employed a finite element method to simulate buoyancy-driven laminar incompressible flow in a two-dimensional tilted rectangular enclosure for the case of copper–water nanofluid with constant heat flux at the left vertical wall and convective boundary condition on the other three walls. They observed that with greater Rayleigh number and inclination angle there is a sizeable elevation in average Nusselt number and that has Nusselt number is highest with low aspect ratio. (Öğüt, 2009) used the polynomial differential quadrature (PDQ) method to analyse the free convection heat transfer of water-based nanofluids in an inclined square enclosure where the left vertical side is heated with constant heat flux (with a heat source at the centre), the right side is cooled, and adiabatic conditions are enforced on the other sides. They considered five metallic nanoparticles, copper, silver, copper oxide, aluminium oxide, and Titanium oxide. They showed that average heat transfer decreases is depressed with greater heat source length and lower inclination angles but enhanced with both particle volume fraction and Rayleigh number increase. (Arani, et al., 2017) used the finite volume method with a SIMPLER algorithm to simulate the coupled heat and mass transfer in mixed convection of temperature-dependent alumina-water nanofluid in a lid-driven square enclosure. They computed solutions for the case where the temperature and concentration of the left wall are higher than those of the right wall, while the two other walls

are adiabatic and impermeable. They considered the influence of Richardson number, buoyancy ratio, nanoparticle volume fractions (up to 4%) and observed that with an increment in nanoparticle volume fraction (at high Richardson numbers) there is a depression in average Nusselt number, whereas the opposite effect is induced at low Richardson numbers. They also found that for buoyancy-assisted flow, higher average Nusselt or Sherwood numbers are achieved and that heat lines are closer for nanofluid than pure water base fluid indicating superior convective heat transfer by nanofluids. (Yu, et al., 2018) employed the Buongiorno nanoscale model and a wavelet homotropy analysis code to analyse the laminar mixed convection flow in an inclined lid-driven nanofluid enclosure flow featuring internal heat generation with sinusoidally heated sidewalls of the enclosure are sinusoidally heated and upper and lower insulated walls. They noted significant modification in heat transfer characteristics and flow behaviour with Grashof number, Brownian motion, thermophoresis, enclosure the inclination and amplitude ratios of temperature and concentration. (Ahmed & Eslamian, 2015) deployed a two-phase lattice Boltzmann computational solver and the Buongiorno nanoscale model to study the laminar natural convection in differentially heated inclined and bottom-heated square enclosure, observing that thermophoresis exerts a major influence on heat transfer augmentation and that heat transfer rate is minimized with bottom heating whereas it is maximized by a unique inclination angle which influences the Rayleigh number. The Tiwari-Das model is an alternative nanoscale formulation to the Buongiorno model (Tiwari & Das, 2007). It does not feature a separate nano-particle species conservation equation but instead modifies the key properties of the doped nanofluid (thermal conductivity, density and viscosity) and allows different types of nano-particle material to be modelled via more realistic empirical correlations which are formulated in terms of the nano-particle concentration (volume fraction). In this regard it is a much more useful approach for real solar

energy direct absorber systems. (Sheremet, et al., 2015) used a second-order accurate finite difference method to investigate computationally the free convection in a square enclosure containing a nanofluid-saturated porous medium for the case of copper and aluminium nanoparticles

The above studies were confined to thermal convection heat transfer and did not consider radiative heat transfer. In the design of real solar collectors however thermal radiation is a critical consideration. Radiative properties and models must be employed to capture the contribution of solar radiative flux. (Sharaf, et al., 2018) have shown that water-based nanofluids achieve stronger radiation absorption than alternative nanofluids in solar collectors. They have also shown that above a critical nanoparticle volume fraction value, the solar collector performance is no longer significantly influenced. Even with powerful numerical methods (such as those available in ANSYS FLUENT finite volume software), it remains very challenging to simulate the solve the general integro-differential radiative transfer equation (RTE) and this is further complicated when coupled to natural convection. Algebraic flux model approximations are therefore popular in computational studies of combined radiation and convection flows. These include the Rosseland diffusion flux model, P1 flux model, Schuster-Schwartzchild two-flux model and Hamaker six-flux model. For example, in solar collector nanofluid coating simulations, (Mehmood, et al., 2018) recently employed the Rosseland flux model and observed a dramatic increase in heat transfer characteristics in nanofluids when radiation is included. Alternative approaches for modelling radiative effects include Rayleigh scattering. Recently (Sharaf, et al., 2018) studied coupled radiative transfer and convection in a nanofluid-based, direct absorption solar collector (DASC) using a Rayleigh scattering approximation for the optical properties of the nanofluid. They showed that DASC performance is significantly influenced by spectral distribution of the extinction coefficient of

the nanoparticles and that. the use of a blackbody incident spectrum over-predicts the thermal enhancement performance overestimations for certain types of nanoparticle suspensions (e.g., silver) more than others (e.g., graphite). They also observed that much higher nanoparticle volume fraction results in less substantial increases in the efficiency of the collector with incident radiation. (Lee, et al., 2012) used a Monte Carlo algorithm and finite element analysis to computationally investigate the performance of a direct solar thermal collector using localized surface plasmon of metallic nanoparticles suspended in water. They studied the case of a direct solar thermal collector with four types of gold nano-shell particles blended in the aquatic solution and observed that blended plasmonic nanofluids can significantly enhance the solar collector efficiency by 70% with an extremely low particle concentration (0.05% particle volume fraction) by dramatically increasing radiative absorption.

Aspect ratio effects in nanofluid solar collectors have been considered by several researchers in recent years and these may involve either the enclosure geometry or the nanoparticles themselves or both. (Bouhaleb & Abbassi, 2014) simulated natural convection in inclined cavity filled with CuO-water nanofluid heated from one side and cooled from the ceiling using a finite volume method based on the SIMPLER algorithm. They observed that the impact of Rayleigh number on heat transfer is reduced for a shallow enclosure (aspect ratio less than unity) whereas the influence of aspect ratio is stronger when the enclosure is tall (aspect ratio greater than unity) and the Rayleigh number is high. They also found that as Rayleigh number is elevated, a significant compression of isotherms arises towards the hot wall and the cold upper boundary with the majority of the enclosure being occupied by warmer fluid, leading to an expansion of the single circulation cells, flow distortion and the emergence of boundary layers. (Trodi & Benhamza, 2017) also used a finite volume method to compute heat and flow characteristics in differentially heated square enclosures filled with  $\text{Al}_2\text{O}_3$ -water nanofluid also

considering the influence of shapes and aspect ratios of nanoparticles, Rayleigh number and volume fraction. They demonstrated that increasing both nanofluid volume fraction and Rayleigh number boosts the heat transfer rate and that oblate and prolate spheroid shaped nanoparticles achieve the best overall heat transfer. (Wong, et al., 2007) used COMSOL finite element software to investigate the effects of mass fraction concentration of nanoparticles (10 and 25%), enclosure aspect ratio and inclination on natural convection in water-based alumina nanofluid in rectangular enclosures. They also utilized a non-invasive method (ultrasound thermometry) to measure the temperature distribution. They found that multi-cellular enclosure regime is modified to a boundary layer regime at a Rayleigh number of about 10million for an aspect ratio of 2.625 and at 200million when the aspect ratio is 1.0, for different concentrations of nanofluid. They also noted that instability in the core region is computed and observed at a Rayleigh number of about 12 million and aspect ratio equal to 2.625. (Qi, et al., 2017) used a two-phase lattice Boltzmann model to simulate the natural convection heat transfer in horizontal rectangle enclosures containing Ag-Ga nanofluid (at different nanoparticle volume fractions of 1%, 3%, 5%) and different Rayleigh numbers (100 and 100,000). They also studied Nusselt number ratio enhancements for two geometries of the enclosures (aspect ratios are 2 and 4) noting that the flatter horizontal rectangular enclosure (aspect ratio of 4) has a higher Nusselt number. They also showed that Nusselt number increases with the decreasing nanoparticle radius and that Brownian force and drag force are influenced by enclosure aspect ratio.

From the literature quoted, the critical requirements and necessity for simulating accurately and carefully natural convection in a nanofluid direct absorber (DASC) has been emphasized. A computational fluid dynamic simulations of steady state nanofluid natural convection in a two-dimensional enclosure is conducted as a first stage of the research is presented in chapter



3. Incompressible, laminar, Newtonian viscous flow is considered with radiative heat transfer. Validation with earlier simulations by (Abu-Nada & Oztop, 2009) is also included for the copper-water nanofluid and vertical enclosure (non-inclined) case. Isotherm and streamline distributions are presented for the influence of different solar radiative flux models, Rayleigh number, types of metallic nanoparticle (silver, titanium oxide and copper), aspect ratio (ratio of base to height of the solar collector geometry) and nano-particle volume fractions. Interesting thermal and hydrodynamic features are computed with extensive physical interpretation.

#### **1.5-1.2 Finite volume numerical analysis of diamond and zinc nanoparticles performance in a water-based trapezium direct absorber solar collector with buoyancy effects**

From the first quadrilateral (square) model described before, which addressed 2D natural convection in DASC, a further geometry and different nanoparticle combination was explored. The objective was to further establish the modifications in heat transfer rates (and thermal efficiency) of the solar collector with a novel geometry and different types of nanoparticles in aqueous base fluid. An alternative geometry which has been increasingly deployed in commercial solar systems is the *trapezium*. This has been found to achieve easier implementation in orientation towards the sun and large-scale manufacturing (Kumar, 2004). Engineers have therefore explored the implementation of a variety of nanofluids in both 2-dimensional trapezium and 3-dimensional trapezoidal enclosures in recent years. (Job, et al., 2017) employed a mixed finite element method with polynomial pressure projection stabilization to compute the transient magnetic free convection flows of alumina ( $Al_2O_3$ )-water and single-walled carbon nanotube (SWCNT)-water nanofluids within a symmetrical wavy trapezoidal enclosure. They considered the case wherein the wavy lower boundary is instantaneously elevated raised to a constant hot temperature with the upper boundary sustained

as thermally insulated. (Akbarzadeh & Fardi, 2018) utilized the finite volume method and the Patankar SIMPLER algorithm to investigate the free convection of nanofluids with variable properties inside two- and three-dimensional channels with trapezoidal cross sections. They observed that with stronger thermal buoyancy (i.e., higher Rayleigh number) heat transfer rates are enhanced in both geometries. They further showed that Nusselt number is reduced with an increase in the nanoparticle volume fraction from zero to 2% whereas it is subsequently elevated for nanoparticle volume fraction greater than 2% in the two-dimensional case. They also showed that greater inclination of the channel trapezoidal cross section walls boosts the heat transfer rate.

Whereas most studies of solar nanofluids have considered metallic nanoparticles (copper, aluminium etc) or carbon nanotubes (CNTs) suspended in water base fluid, relatively few have addressed diamond-water nanofluids. Diamond, a natural allotrope of carbon has impressive thermal, mechanical, and electrical properties (Mashali, et al., 2019). Nano-diamond-nanofluid systems have therefore also attracted interest very recently owing to their potential in achieving a stable and consistent increase in thermal conductivity (Tyler, et al., 2006). (Sani, et al., 2018) presented experimental results light-intensity dependent optical properties of graphite/nano-diamond suspensions in ethylene glycol for direct absorption solar collectors and solar vapor generation. (Branson, et al., 2013) used de-aggregation of oxidized ultra-dispersed diamond (UDD) in dimethylsulfoxide to study the thermal performance of nano-diamond (ND)-poly(glycidol) polymer brush: ethylene glycol (EG) nanofluids, observing that a 12% thermal conductivity enhancement is achieved with a 0.9 volume fraction. Many other laboratory-based studies on viscosity and thermal property modification achieved with diamond nanofluids have been reported including (Mashali, et al., 2020), (Kumar, et al., 2019), (Chin, et al., 2018) and (Syam Sundar, et al., 2016). Quite recently several computational analyses of diamond

nanofluids have also appeared in the scientific literature. (Izadi, et al., 2018) presented finite element solutions for natural convection of different nanofluids (water-copper, water-diamond and water–silicon dioxide nanofluids) inside a porous medium annular cylindrical enclosure using the Buongiorno model was utilized to track the nanoparticles concentration. They observed that water-diamond achieves the highest heat transfer rates whereas water–silicon dioxide produces the lowest. (Jang & Choi, 2006) investigated theoretically the cooling performance of a microchannel heat sink with 6 nm copper-in-water and 2 nm diamond-in-water nanofluids.

Another promising metallic material which can be deployed in nanofluids is zinc which has excellent anti-corrosion properties and is only a moderately reactive metal making it useful for solar collector nanofluids. It is also the fourth most abundant metal employed in industry after iron, aluminium, and copper. It has been studied both in its pure form and oxide form for nanofluid deployment in solar energy systems. Important studies in this regard include (Wang, et al., 2018) (zinc oxide oil based nanofluids for DASCs), (Radkar, et al., 2019) (ZnO water nanofluid in helical copper tube heat exchangers in which 18.6% elevation in Nusselt numbers was achieved for 0.25 vol% of ZnO nanoparticles), (Ali, et al., 2015) (zinc oxide water nanofluid automobile radiators), (Zhang, et al., 2007) (Zhang, et al., 2008) (anti-bacterial and sterilization medical applications), (Khatak, et al., 2015) (electronic cooling), (Lee, et al., 2012) (thermal enhancement) and (Yu, et al., 2009) (viscosity measurements of zinc water/ethylene glycol nanofluids).

A computational fluid dynamics analysis of steady state incompressible thermal convection in a two-dimensional trapezium solar collector geometry is conducted to evaluate the relative performance of both carbon-based (i.e., diamond) and metal-based (i.e., zinc) nanoparticles

which is elaborated at length in chapter 4. The Tiwari-Das formulation is implemented to compute viscosity, thermal conductivity and heat capacity properties for diamond-water and zinc-water nanofluids at different volume fractions. The finite volume code (ANSYS FLUENT ver. 19.1) (ANSYS, Inc, 2018) is deployed. Laminar Newtonian flow is examined. The SIMPLE solver is utilized, and residual iterations utilized for convergence monitoring. Mesh independence is included. Verification with the penalty finite element computations of (Natarajan, et al., 2008) for the case of a Newtonian viscous fluid (zero volume fraction) is also conducted and excellent correlation achieved. Isotherm, streamline and local Nusselt number plots are presented for different volume fractions, sloping wall inclinations (both negative and positive slopes are considered) and Rayleigh numbers.

### **1.5-2 Three-dimensional models of nanofluid DASCs**

During Year 2 and part of Year 3 of this PhD program, three further comprehensive models of 3-dimensional solar enclosure transport phenomena were produced. These built successfully on the earlier 2-D simulations, which were reported in the Interim Report (November 2018, Dr Martin Burby was the Internal Assessor) and also partially in the internal Evaluation (November 2019, Dr. G.P. Enyi and Dr A. J. Abbas were the Internal Assessors). The justification for these simulations was based on extensive literature reviews to identify aspects that had never been examined before and which were particularly beneficial and feasible in real life solar engineering implementation, globally. The foundational literature for each of these three 3-dimensional models is now given in the next three sub-sections.

#### **1.5-2.1 Three-dimensional tilted prismatic solar enclosure with aspect ratio and volume fraction effects**

Natural convection in three dimensional enclosures is also a major area of interest in solar engineering, in the design of actual field direct absorber solar collectors (DASCs). It has been

studied extensively both from a theoretical and computational perspective and experimentally with a focus on visualization. Many studies including (Hiller, et al., 1992) have identified the complex spiral vortex structures generated in three-dimensional flows under buoyancy effects. While experimental studies have been important, since the advent of more powerful computer resources and commercial field solvers, numerical simulation has increasingly become a major area of activity since it provides a relatively inexpensive and less time-consuming methodology for predicting such flows. Numerical simulation also provides a good compliment to experimental investigations since the data from the latter can be used as important benchmark cases for validation of computational codes. Many different computational methodologies are available now in this regard including molecular dynamics, Lattice Boltzmann methods, finite element techniques and finite difference or finite volume solvers (Ferziger, 2001). (Mallinson & De Vahl Davis, 1997) were among the first researchers to investigate 3-dimensional natural convection in a box-like enclosure. They employed a finite element method and identified that at intermediate Rayleigh numbers a strong convective motion is mobilized due to the inertial interaction of the rotating flow with the stationary walls together with a contribution arising from buoyancy forces generated by longitudinal temperature gradients. They also showed that with stronger thermal buoyancy (higher Rayleigh numbers), there is an emergence of multiple longitudinal flows develop which are controlled by aspect ratios, Prandtl number and Rayleigh number. (Fusegi, et al., 1991) used a three-dimensional finite-difference method to analyse natural convection flows of air flow in a differentially heated cubical box with isothermal vertical sidewalls at different temperatures and the remaining vertical walls (end walls) being thermally insulated. They considered both adiabatic and perfectly conducting wall boundary conditions and observed enhanced heat transfer in the latter case. (Sharma, et al., 2013) employed the PHOENICS solver to investigate the three-dimensional thermosyphon flow in

an unglazed solar flat plate collector and computed mass flow rates in the collector loop for a range of solar heat flux inputs. (Li, et al., 2016) applied a multiple-relaxation-time model (MRT) and lattice Boltzmann method (LBM) solver to analyse the three-dimensional cubic natural convection for a solar cell at various Rayleigh numbers. They considered a variety of thermal boundary conditions including adiabatic and linear temperature variations. (Campos, et al., 2019) conducted photothermal conversion experiments on water-based nanofluids doped with spherical gold, silver, and copper nanoparticles, non-spherical silver nanoparticles, layered graphene oxides and hybrid graphene oxide/silver hybrid structures, for direct absorption solar collectors under 1000 Watts of solar radiation flux. They observed that gold and copper nanofluids achieved the best thermal efficiencies. (Mallah, et al., 2018) investigated the deployment of silver plasmonic nanofluids (which feature localized surface plasmon resonance phenomenon to enhance the extinction efficiency of the plasmonic nanoparticle several times at the resonance wavelength) in direct absorber solar collectors. They showed that silver nanoparticles exhibit a high intensity of the localized surface plasmon, which may be precisely adjusted via shape, size and aspect ratio of nanoparticles to perform within the broadband 350–1200 nm. They further showed via computational simulation that nanofluids composed of blended Ag nano-morphologies achieve a significant improvement in absorbance over the entire solar spectrum and elevate efficiency of the direct solar collector to in excess of 85% even at low volume fractions. Further investigations of nanofluid-based solar collectors have been communicated by (Farhana, et al., 2019) (who have reviewed multiple metallic hybrid types), (Jin, et al., 2019) who have identified exceptional photothermal conversion efficiencies of gold and silver nano-particles, (Gimeno-Furio, et al., 2019) who have explored oil-based carbon “black” nanofluids in various solar receiver geometries including prisms, annular and parabolic troughs, (Shah & Ali, 2019) (copper oxide nanofluids), (Dehaj &

Mohiabadi, 2019) (magnesium oxide nanofluids for heat pipe solar systems) and (Bellos, et al., 2018) (alumina and titania-water nanofluids for solar concentrators). (Khanafar & Vafai, 2018) presented a succinct review of many aspects of solar nanofluid technology including solar stills, photovoltaic/thermal systems, doping methods, cost-benefit analysis and sustainability. (Zayed, et al., 2019) addressed flat plate solar collector nanofluid performance considering a variety of metal, metal oxides, semiconductor crystalized oxides, and carbon based nanofluids as the absorbing media and noting that copper oxide achieves the best efficiency whereas carbon based nanofluids achieved both superior energy and exergy efficiencies. (Mehmood, et al., 2019) investigated the manufacturing flows of solar copper oxide-doped nano-polymer coatings for photo-voltaic applications, noting their superiority in durability, anticorrosion and thermal efficiency. (Dugaria, et al., 2018) studied computationally the thermal performance of aqueous nanofluids containing suspensions of single wall carbon nano-horns (SWCNHs) as volumetric absorbing media in a concentrating direct absorption parabolic trough solar collector. They presented extensive solutions of the coupled energy balance and radiative heat transfer equations for a participating medium and elaborated in detail the variation in heat transfer rates, thermal absorption, and penetration distance of the concentrated solar radiation inside the nanofluid volume. Other interesting studies of nanofluid solar absorbers have been communicated by (Zhang, et al., 2018) (for solar-powered distillation systems), (Zeiny, et al., 2018) (for large scale solar evaporation projects), (Bait & Si-Ameur, 2018) for combined thermal and mass diffusion in metallic nanofluid solar still designs and (Mehrali, et al., 2018) for graphene/silver plasmonic nanofluid solar thermal conversion.

The above studies did not consider the *tilt* of the solar collector enclosure. To optimize the capture of solar energy by collectors, they are frequently orientated at a specific angle i.e., tilted upwards. To produce more realistic predictions of heat transfer rates, mathematical models

need to incorporate *inclination of the direct absorber collector*. Several researchers have explored the influence of inclination on thermo-fluid characteristics in solar absorbers, *although not for gold nanofluids*. (Esfandiary, et al., 2016) used the two-phase mixture Buongiorno nanoscale model and a finite volume method to analyse the influence of inclination angle on natural convective heat transfer and fluid flow in an enclosure filled with Al<sub>2</sub>O<sub>3</sub>–water nanofluid. They considered inclination angles from zero to 60 degrees and Rayleigh numbers up to 10 million with a maximum volume fraction of 3%. They noted that maximum Nusselt number is attained with a 30 degrees tilt angle. (Motlagh & Soltanipour, 2017) studied computationally the natural convection of alumina–water nanofluid inside a tilted square enclosure with non-homogenous two-phase Buongiorno's model and the Patankar SIMPLE algorithm. They identified that at high Rayleigh numbers the average Nusselt number at the walls is elevated initially but thereafter suppressed with inclination angle whereas heat transfer enhancement percent continuously increases with increasing inclination angle. They also computed that at any title angle and at low Rayleigh numbers, the particle distribution is non-uniform whereas a more homogenous distribution is achieved at high Rayleigh numbers (strong thermal buoyancy). (Ghachem, et al., 2015) used a control volume algorithm and a vorticity-vector potential formulation to simulate the combined natural convection and radiation in an inclined solar thermal collector containing a gray medium.

Finite volume computational fluid dynamic simulations of steady-state nanofluid natural convection in a three-dimensional enclosure (as a model of a flat plate collector) containing gold-water nanofluid is therefore conducted and discussed in chapter 5. Incompressible, laminar, Newtonian viscous flow is considered with natural convection. The ANSYS FLUENT finite volume code (version 19.1) (Baek, et al., 2014) is employed. The Tiwari-Das volume fraction nanofluid model is used and spherical, homogeneously distributed gold nanoparticles



are considered. The superior optical and thermo-physical properties of gold nanoparticles (relative to other metallic nanomaterials) have been shown to achieve superior thermal conductivity, suspension stability and long-term performance in the field which are all key factors required to enhance solar energy absorption and conversion. In this regard, the deployment of gold nanoparticles in 3-D numerical simulations in a tilted prismatic enclosure constitutes a new direction in solar absorber research and the novelty of the present work. Extensive visualizations of streamline and isotherm distributions for a range of gold nanoparticle volume fraction, geometrical aspect ratio, Rayleigh number and enclosure tile angle are provided. Heat flux and Nusselt number profiles are also computed. Validation with earlier simulations is also included (Wang, et al., 2018). Intricate vortex and thermal field structures are identified. The significant benefit of *tilting* enclosures and scaling gravity (and therefore buoyancy) effects is shown. The computations and interpretation furnish useful *and novel* insight into more realistic performance of direct absorber nanofluid solar collector designs and provide critical guidance on achieving optimal specifications for aspect ratio, nanoparticle volume fraction and orientation.

#### **1.5-2.2 Computational fluid dynamics simulation of a nanofluid-based *annular* solar collector with different metallic nanoparticles.**

There are several published articles related to investigation of convective heat transfer of nanofluids, although the vast majority are based on experimental works. (Fotukian & Nasr, 2010) experimentally investigated turbulent heat transfer and pressure drop of Al<sub>2</sub>O<sub>3</sub> - water nanofluid in a circular tube. The results showed that as increasing volume fraction of nanoparticle from 0.03% to 0.135%, there is not much effect on enhancement of the heat transfer. Additionally, the pressure drop was higher than a base fluid. (Kayhani, et al., 2012) conducted a similar experiment, investigated turbulent convective heat transfer of Al<sub>2</sub>O<sub>3</sub>/water (40nm size) nanofluid inside uniformly heated horizontal tube. At nanoparticle volume fraction

of 2.0%, Nusselt number increased by 22% at Reynolds number of 13500. (Zeinali, et al., 2007) experimentally investigated laminar convective heat transfer of  $\text{Al}_2\text{O}_3$  nanofluid through a circular tube with constant wall temperature. The results show that heat transfer coefficient of nanofluids increases with nanofluid volume fraction as well as the Peclet number. (Ho, et al., 2010) experimentally investigated the forced convective cooling performance of a copper Microchannel heat sink with  $\text{Al}_2\text{O}_3$ /water nanofluid as the coolant, Reynolds number ranging 226 to 1676. Results showed that the nanofluid-cooled heat sink have significantly higher average heat transfer coefficient and thereby lower thermal resistance, friction factor was found slightly increased. (Azari, et al., 2013) investigated laminar convective heat transfer of three different types water-based nanofluids which are  $\text{Al}_2\text{O}_3$ ,  $\text{TiO}_2$  and  $\text{SiO}_2$  though a circular tube.  $\text{Al}_2\text{O}_3$  and  $\text{TiO}_2$  water based nanofluids increased heat transfer coefficient substantially, an average of 16% and 8.2% increase in heat transfer coefficient were observed with the average of 28% and 15% penalty in pressure drop for  $\text{Al}_2\text{O}_3$  and  $\text{TiO}_2$  nanofluids. While the  $\text{SiO}_2$  nanofluids showed the opposite behaviour. (Azari, et al., 2014) presented both experimental and Computational Fluid Dynamics (CFD) investigations of the laminar convective heat transfer coefficient of  $\text{Al}_2\text{O}_3$ /water nanofluids in a circular tube under uniform and constant heat flux on the wall. Their results showed that the thermal performance of nanofluids is higher than that of the base fluid and the heat transfer enhancement increases with the particle volume concentration and Reynolds number. Additionally, the simulation results demonstrated that the two-phase model prediction and experimental data match significantly and that the model can be employed with confidence for the prediction of any type of nanofluid. (Hatwar & Kriplani, 2016) studied heat transfer characteristics of water based nanofluid of  $\text{Al}_2\text{O}_3$  and  $\text{CuO}$  flowing through a uniform heat flux horizontal circular tube at Reynolds number range of 2800 to 5000 via experimental. The heat transfer coefficient of  $\text{CuO}$ /water nanofluid is higher than that of

Al<sub>2</sub>O<sub>3</sub> nanofluid for the same concentration and same Reynolds number. Results indicated that heat transfer coefficient of CuO/water nanofluid is higher than Al<sub>2</sub>O<sub>3</sub> nanofluid for the same concentration and same Reynolds number. At volume fraction of 0.1%, the percentage increase in heat transfer coefficient was 40% for CuO and 22.2% for Al<sub>2</sub>O<sub>3</sub> as compared to water. The pressure drops via using nanofluids was unnoticeable. There are several published articles related to the investigation of nanofluids on thermal efficiency enhancement of parabolic trough solar collector (PTC) most of them are based on experimental and computational fluid analysis. (Subramani, et al., 2017) reported from the experiment that the thermal efficiency of PTC could be enhanced by 8.54% if the maximum volume fraction of 0.5% vol% of Al<sub>2</sub>O<sub>3</sub>/water was used. Similar experiment was conducted by (Siva Reddy, et al., 2015) , where they examined the effect of Al<sub>2</sub>O<sub>3</sub>/water nanofluid up to 0.06 vol.% on the thermal efficiency of PTC and resulted in maximum efficiency enhancement due to the nanofluid application of 28.95%. (Chaudhari, et al., 2015) experimentally investigated on the effect of 1% volumetric concentration of Al<sub>2</sub>O<sub>3</sub>/water nanofluid in the thermal characteristic enhancement of PTC which reported a maximum increase in Nusselt number of 32%. (Bretado de los Rios, et al., 2018) reported from his experiment that using 3% volumetric concentration of Al<sub>2</sub>O<sub>3</sub> in PTC can enhance the thermal efficiency by approximately 28% compared to water as a base flow at incident angles varying from 20–30. (Menbari, et al., 2016) experimentally and numerically studied the effect of CuO/water nanofluid on thermal efficiency and temperature distribution in direct absorption parabolic trough collectors for a different range of volume fractions. The thermal efficiency of the collector increases by 18% to 52%, when using 0.002–0.008 vol. % CuO nanoparticles, compared to the base fluid case. (Subramani, et al., 2018) examined the effect of TiO<sub>2</sub>/water nanofluid at different volume fractions of 0.05%–0.5% on PTC thermal performance. They reported that at 4 kg/min mass flow rate both convection heat transfer and

thermal efficiency of PTC could be enhanced by 22.76% and 8.66%. employed finite difference method to calculate the efficiency of parabolic shaped solar collector with used water based-  $\text{Al}_2\text{O}_3$  nanofluid (0.05% vol. conc.). The solar collector performance is improved by 6.7% in comparison to conventional working fluid. (Khullar & Tyagi, 2010) evaluated the possible application of different types of nanofluids in parabolic concentrating solar collector using experiments and CFD analysis. The nanofluids considered  $\text{SiO}_2\text{-H}_2\text{O}$  (DI) and  $\text{CuO-H}_2\text{O}$  (DI) of 0.01% volume concentration are used where the flow rates of the fluids are 40 LPH and 80 LPH. Results indicated that at the flow rate of 80 LPH with 0.01 volume concentration,  $\text{SiO}_2\text{-H}_2\text{O}$ (DI) and  $\text{CuO-H}_2\text{O}$ (DI) have improved solar collector efficiency around 7.15% and 8.42%, respectively. However, at flow rate of 40 LPH shows slightly lower improvement in efficiency of collector of about 6.68% and 7.64% for  $\text{SiO}_2\text{-H}_2\text{O}$  (DI) nanofluid and  $\text{CuO-H}_2\text{O}$  (DI) respectively. (Kundan Guide Lal, 2014) studied the effect of  $\text{Al}_2\text{O}_3$  and  $\text{CuO}$  water based nanofluids on PTC thermal performance and found that  $\text{CuO/water}$  nanofluid gave the highest thermal enhancement followed by  $\text{Al}_2\text{O}_3$  and water. Via using 0.05 vol.% of  $\text{CuO}$  gave the maximum overall thermal efficiency of 15.25% which lead to approximately 44% increase in efficiency compared to pure water. (Sekhar, et al., 2017) investigated the effect of  $\text{CeO}_2$  (Cerium oxide),  $\text{Al}_2\text{O}_3$ , and  $\text{TiO}_2$  with water based nanofluid performance used in PTC and found that  $\text{CeO}_2\text{/water}$  nanofluid had highest thermal efficiency enhancement by 27% at 3 percent vol.%. (Marefati, et al., 2018) experimentally investigated the effect of  $\text{Al}_2\text{O}_3$ ,  $\text{CuO}$ , and  $\text{SiC}$  mixed with water at 1–5 vol. % on the thermal and optical performance of the PTC at four different locations in Iran (Tehran, Yazd, Shiraz and Tabriz). Shiraz was found to have the highest thermal efficiency result to install the PTC. They also mentioned that the application of  $\text{CuO/water}$  nanofluid enhances the convection heat transfer by approximately 33% compared with water itself. Hence, as expected,  $\text{CuO/water}$  nanofluid is the best option for

thermal efficiency enhancement. (Khullar, et al., 2013) studied aluminium based nanofluid with Therminal VP-1 base fluid in concentrating parabolic solar collector (CPSC) via theoretical & experimental calculations. When compared to conventional concentric parabolic solar collectors, an increase in 5 to 10% of thermal efficiency was observed. (Rehan, et al., 2018) examined the effect of  $\text{Al}_2\text{O}_3$  and  $\text{Fe}_2\text{O}_3$  water-based nanoparticle with weight fraction between 0.2%-0.3% on thermal efficiency of the PTC in winter. At the flow rate of 2L/m and 0.3 wt. %,  $\text{Al}_2\text{O}_3$ /water and  $\text{Fe}_2\text{O}_3$ /water nanofluids enhance the thermal efficiency by 13% and 11%, respectively. (Alsaady, et al., 2018) conducted an experimental study on Ferrofluids (magnetic nanofluid) with 0.05% volume fraction with and without magnetic field presence. They found that if a magnetic field is applied, the thermal efficiency can be enhanced up to 25% compared to conventional PTC. (Paul & Morshed, 2013) carried out experimental analysis of Nanoparticle Enhanced Ionic Liquids (NEILS) in solar collectors and found that thermal conductivity was enhanced around 5% depending on the base fluid and ionic concentration. The heat capacity of nanofluid using  $\text{Al}_2\text{O}_3$  nano particles was enhanced by 23% and 26% for nanofluids using silica nano particles and similarly 20% enhancement in convective heat transfer capacity was also observed.

From literature reviews and simulations conducted in chapter 3, 4 and 5 it is shown that nanofluids work well for DASCS. To produce a geometrically simpler but still 3-D model of a solar collector, the tubular geometry or annulus is ideal. It is manufactured often in practical systems e.g. Schott glass, Germany. It also provides a simpler simulation than fully 3-D models since only two coordinates are essentially required (axisymmetric - *radial and longitudinal coordinates*). Annular solar collectors comprising an inner tube containing pure water and an annular region containing metal-water nanofluid is therefore very advantageous for certain solar designs and is therefore simulated in **Chapter 6** with ANSYS FLUENT. Three different

metallic nanoparticles (copper oxide, aluminium oxide and titanium oxide nanoparticles) are examined. Via the Tiwari-Das model the thermal conductivity, specific heat capacity and viscosity for each metal-water nanofluid suspension is calculated as a function of solid nanoparticle volume fraction. Radiative heat transfer is also incorporated using the ANSYS solar flux and Rosseland radiative models.

### **1.5-2.3 Numerical simulation of forced convection-radiation transfer in a flat plate prismatic 3-D solar collector with inlet/outlet conditions.**

The energy associated with solar light consists of about 40% visible, 8% ultraviolet (UV), and 52% infrared radiation (Sokolik, 2008). (Matino & Maccari, 2015) showed that optical properties enable useful thermal energy to be extracted in the available infrared region. Solar collectors may also utilize the energy in the visible region in this way and engineers can tune fluids to absorb the energy in the infrared as well as the visible region. As a result, most of the solar spectrum can be utilized and solar absorption efficiency will also increase. In recent years solar engineers have explored many technologies to achieve a sustained improvement in thermal performance of solar collectors. These have included improved coatings and also working fluids in combinations with different geometries. An important development in this regard has been *nanofluids*. These have been described in detail in previous chapters and constitute colloidal suspensions of metallic or carbon-based nanoparticles in conventional working (base) fluids. The resulting mixture demonstrates enhanced thermal conductivity and modified viscosity properties. Radiative properties of nanofluids are particularly critical in solar collector direct absorber collectors. Absorption characteristics of nanofluids are one of the main parameters used to estimate their energy-capturing ability. In general, the absorption coefficient increases with an increase in the volume fraction. The absorption of metal-based nanofluids has been investigated extensively in recent years by varying the path depth, type of base fluid, particle size, and volume fraction. These studies have shown that the absorption

coefficient of metal-based nanofluids is found to be *linearly proportional* to the volume fraction. (Saidur, et al., 2012) studied the effect of metal aluminium-water based nanofluid in direct absorber solar collectors (DASCs) via the investigation of the extinction coefficient of the fluid with various nanoparticle sizes and volume fractions. They found that the extinction coefficient is linearly proportional to volume fraction. The improvement is promising within 1.0% volume fraction and the nanofluid is almost opaque to light waves. (Said, et al., 2014) studied the optical properties of metal oxide  $\text{Al}_2\text{O}_3$  and  $\text{TiO}_2$  distilled water-based nanofluids with different volume concentrations experimentally. They considered two volume concentrations of 0.1% to 0.3% v/v for the optical properties and found that the extinction coefficient and refractive index of  $\text{TiO}_2$  nanofluids are higher than  $\text{Al}_2\text{O}_3$  nanofluids in the visible region of light for all concentrations. However, aluminium oxide achieved greater stability, although its optical enhancement was lower than that of titanium, whereas titanium was less stable. (Otanicar, et al., 2010) conducted an experimental and numerical study of nanofluid-based direct absorption solar collectors, where the nanoparticles considered were non-metallic (carbon nanotubes, graphite) and metallic (silver). These nanofluids demonstrated an initial rapid increase in efficiency with volume fraction, followed by a levelling in efficiency as volume fraction continued to increase. The efficiency improvement was elevated by 5% in solar thermal collectors by utilizing nanofluids as the absorption medium. (Bardsgard, et al., 2020) simulated a rectangular DASC with incident light on the top surface using an Eulerian-Eulerian two-phase model and validated against the experiment of (Otanicar, et al., 2010) and reported that the optimum volume fraction of particles for enhancing efficiency was obtained for 0.3 wt.%, and a decrease in efficiency was observed for 0.5 wt.%. The optimum configuration of the considered collector attained a highest total efficiency of 87%. (Taylor, et al., 2011) compared model predictions to spectroscopic measurements of extinction

coefficients of nanofluids with particle diameters less than 100 nm over wavelengths that are feasible for solar energy (0.25 to 2.5  $\mu\text{m}$ ). Their study revealed that the approximation works well with water-based nanofluids containing graphite nanoparticles, but less well with metallic nanoparticles and/or oil-based fluids. For the materials used, over 95% of incoming sunlight can be absorbed (in a nanofluid thickness  $\geq 10$  cm) with extremely low nanoparticle volume fractions - less than  $1 \times 10^{-5}$ , or 10 parts per million. Thus, nanofluids could be used to absorb sunlight with a negligible increase in viscosity and/or density. The literature generally shows that nanofluids with high absorption coefficients can improve the efficiency of the DASC, however many researchers have focused solely on radiation but have not included the effects of convection. This study will investigate the efficiency of direct absorption solar collectors with three different water based nanofluids, which are metallic (copper, copper oxide, silver), non-metallic (graphite) and various mass flow rates (0.005, 0.01 and 0.015 kg/s).

Critical to more accurate appraisal of the DASC nanofluid performance is the interaction of thermal radiation with thermal convection which can be achieved via computational fluid dynamics field codes e. g. ANSYS FLUENT. Later in this PhD thesis I will explore various algebraic flux radiative models. These include Rosseland's diffusion flux approximation (Kuharat, et al., 2019) (Chapter 3), the Traugott P1 differential flux approximation (chapter 4 and 5) (Kuharat, et al., 2020) and many other methodologies e.g. Monte Carlo method (Lataillade, et al., 2002) all of which approximate the solution of the formidable radiative transfer equation (RTE), as explained in Chapter 2. Extensive details of all these and other models are given in the monumental treatise by the Indian American astrophysicist, Chandrasekhar (Chandrasekhar, 1960) and the more recent monograph by Modest (Modest 1993). A more comprehensive model which works more accurately in high participative media and presents a good directional accuracy for radiative heat flux is the *Chandrasekhar discrete*



*ordinates model* (DOM). Extensive mathematical details have been given on DOM in Chapter 2. This model has received some attention in modern coupled convective-radiative CFD studies. (Gómez, et al., 2012) studied a solar radiation porous medium fluid absorber with CFD and dispersed particle techniques and benchmarked their computations with experimental data. They deployed the DOM approach for radiation and modified the original model for multiphase media where the temperatures and radiative properties of the different phases could be correctly predicted and found good agreement with experimental results. (Moreno, et al., 2019) developed an adaptive quadrature, to improve the Discrete Ordinate Method (DOM) in parallel and cone-shaped radiation sources using the OpenFOAM finite element code. They refined the conventional DOM model which is restricted to isotropic emission, diffuse phenomena, and non-scattering media, to consider volumetric and superficial absorption, isotropic and anisotropic scattering (with user-defined phase functions), diffuse and specular reflection, diffuse and parallel transmission, and three types of superficial emission sources, i.e., isotropic, cone-shaped, and parallel. They also generalized the DOM algorithm to cater for the grey mode or with wavelength bands, demonstrating that adaptive quadrature improves the view angle and light direction of emission source computational accuracy relative to conventional DOM simulations and enhances accuracy of the simulation of non-isotropic sources in for example solar collector systems. (Laria, et al., 2011) investigated the combined radiative and natural convection heat transfer in a square cavity under normal room conditions for a participating medium using the finite volume method and the discrete ordinates method (DOM) for radiative transfer in absorbing-emitting media. They considered Rayleigh numbers from 100 to 1 million and optical thickness in a broad range from 0 to 100 and found that the DOM radiative model predicts a sweep behavior on the isotherms, streamlines and velocity distributions of the cavity along the optical thickness and a reverse behavior on maximum stream function and convective

Nusselt number at different Rayleigh numbers. (Rightley, 1989) studied the multi-dimensional radiative transfer in a free-falling particle cloud direct absorption solar central receiver using the discrete ordinates approximation to simulate the spectral equation of transfer (EOT) as a partial differential equation. They showed that the discrete ordinates model provides good estimates of the radiant intensity, the heat flux and the temperature distributions for ordinate sets above  $S^{-4}$  (12-flux approximation) for both black and gray cases. They also measured extinction coefficient, curtain porosities, transmitted fluxes and the exit temperatures and using a Fredholm integral boundary condition, observed that DOM achieves quite accurate flux distributions with a significant improvement from the 12- to the 24-flux model and provides an improved approach for modelling full scale solar receivers. Other interesting studies featuring the DOM radiative approach have been communicated by (Fiveland, 1982) on axisymmetric solar enclosure radiation, (Fiveland, 1984) on rectangular solar enclosure radiative transport, (Myneni *et al.* 1988) on DOM scattering source effects and Risner *et al.* (1985) on solar ray tracking.

As noted earlier, flat plate solar collectors are very popular in modern solar engineering. Many interesting CFD studies of such systems have been conducted in recent years both for conventional and also nanofluids and with/without radiative heat transfer effects. Mohammed *et al.* (2008) investigated the water-based flat plate solar energy collector with water flow is simulated and analyzed using CFD-ACE software. They included solar irradiation and mixed convection and radiation heat transfer between tube surface, glass cover, side walls, and insulating base of the collector also examining the mixed convective heat transfer in the circulating water inside the tube and conduction between the base and tube material. They found good correlation of the CFD simulations for outlet temperature with experimental results for both circulating and stationary water cases (Farhana, *et al.*, 2018) simulated the turbulent

convection flow of both nanofluids and hybrid nanofluids flowing through inside header and riser tube of flat plate solar collector, for (Al<sub>2</sub>O<sub>3</sub>, TiO<sub>2</sub>, ZnO)-water unitary nanofluids and hybrid (Al<sub>2</sub>O<sub>3</sub>+TiO<sub>2</sub>, TiO<sub>2</sub>+ZnO, ZnO + Al<sub>2</sub>O<sub>3</sub>) hybrid nanofluids based on a single-phase viscous formulation. They studied the effects of different combinations of header tubes and riser tubes and computed a maximum dynamic pressure increased for both nanofluid and hybrid nanofluid of about 48% and 16% respectively. (Vetter, et al., 2018) used the STAR CCM+ computational fluid dynamics to compute the convective flow in a transparent flat plate solar collector with gross area of 2.1 m<sup>2</sup> with the absorber coated in aluminum sheet with copper pipes and a harp flow pattern with eight riser pipes. (Gertzos & Caouris, 2007) simulated the 3-D thermofluid dynamics in a flat plate integrated recirculating collector storage device, with ANSYS FLUENT software, comparing their computations with a Plexiglas transparent solar device using a laser doppler velocity (LDV) system, observing that the outlet temperature of the service water is significantly higher. (Vasudeva Karanth & Corneli, 2017) investigated numerically the flow in solar water heaters constructed with absorber tubes of different sizes and shapes. They showed that a circular cross section tube of the collector has a flattened out contact surface with that of the absorber plate providing significantly better thermal performance in terms of Nusselt number. Indeed, ANSYS FLUENT (finite volume method for pressure-velocity coupling) has emerged as a very popular computational approach for modern solar collector coupled nanofluid heat transfer and fluid flow analysis. (Shahi, et al., 2011) used the ANSYS FLUENT SIMPLE algorithm to compute the, entropy generation due to natural convection of a copper-water nanofluid in an enclosure with a protruded heat source. They investigated the impact of Rayleigh number, nanoparticle solid concentration and heat source location on entropy generation, noting that the maximum Nusselt number and minimum entropy generation correspond to the case of heat source located at the base horizontal wall.

(Mahmoodi & Sebdani, 2012) used ANSYS FLUENT to study free convection heat transfer of Cu–water nanofluid inside a square cavity with adiabatic square bodies positioned at the center, noting that for all Rayleigh numbers with the exception of  $10,000$ , the average Nusselt number is elevated with a boost in nanoparticle volume fraction of the nanoparticles. They also showed that at low Rayleigh numbers ( $10^3$  and  $10^4$ ) (i. e. weak thermal buoyancy scenarios), Nusselt numbers are suppressed with larger adiabatic square body increases whereas the opposite effect is induced at high Rayleigh numbers. Further studies include (Chatterjee, et al., 2014) who considered mixed convective transport of Cu-H<sub>2</sub>O nanofluid in a differentially heated and lid-driven square enclosure containing a spinning inner circular cylinder with top and bottom walls maintained as isothermal at different temperatures with adiabatic sidewalls. They showed that the Nusselt number at the walls is strongly influenced by Richardson mixed convection number (buoyancy parameter), rotational speed of the cylinder and nanoparticle volume fraction.

In the simulations in this PhD both metallic (non-magnetic and magnetic) and non-metallic (carbon-based) nanoparticles are studied in water-based nanofluids. In this PhD the main focus will be on metallic nanoparticles owing to the obvious high thermal conductivities. However I will also study diamond nanoparticles in the trapezium solar collector simulation and compare with zinc nanoparticles. Many different forms of carbon-based nanoparticle are available including carbon nanotubes (CNTs), graphene sheets, graphite nanoparticles etc. Unfortunately, CNTs have an inherent hydrophobic nature of carbon nanotubes which makes them problematic for solar collectors, although in recent years engineers have developed new dispersion procedures (treating carbon nanotubes with base media) to prepare nanofluids. Water-based alkaline functionalized carbon nanotubes as absorber fluids can now therefore perform more efficiently as sunlight harvesting devices. Of course, again optical properties of carbon-based water nanofluids are critical and detailed knowledge of spectral absorbance

analysis is beneficial in simulations. Carbon nanomaterials can also achieve impressive thermal conductivity improvements of up to 30% with relatively small volume fractions, as observed by Karamia *et al* (2014). These are comparable to metallic nanoparticles e. g. gold, silver, iron, copper etc, which perform equally well for solar radiation absorption due to the plasmon resonance absorption band in the visible and near IR spectrum that can be tuned modifying the NP shape, as noted by (Rativa & Gómez-Malagón, 2015). They also showed that for a nanofluid-based direct absorption collector with 1 cm thickness, and a nanofluid of gold nanoparticles with a low volume fraction, small dimensions (2.5 nm) and a high aspect ratio (AR = 4), an optimal solar weighted absorption coefficient is achievable which is much closer to the ideal solar radiation absorber condition. Further interesting studies of carbon-based nanofluids have been reported by (Otanicar, et al., 2010), (Ni, et al., 2015), (Liu, et al., 2015), (Taylor, et al., 2011), (Pop, et al., 2012), (Bhalla & Tyagi, 2017) who deployed cobalt oxide nanoparticles and (Liu, et al., 2018) who explored graphene/ionic nanofluids. Quite recently, (Tafarroj, et al., 2019) investigated nanosilica and multi-wall carbon nanotube (MWCNT) with two different volume fractions in ethylene glycol (EG)-based nanofluids for a solar direct absorption parabolic trough collector (DAPTC). They studied both experimentally and numerically (with the ANSYS FLUENT software) the cases of volume fractions of the nanoparticles in the base-fluid of 0.1–0.5% and 0.1–0.6% for nanosilica and MWCNT, respectively. They observed that nanofluid including 0.6% MWCNT/EG achieves the best outlet temperature of 346.1 K. (Lee & PilJang, 2013) determined experimentally the extinction coefficients in radiative-convective flow of water-based multi-walled carbon nanotubes (MWCNT) nanofluids in a direct-absorption solar collector (DASC). They synthesized water-based MWCNT nanofluids with low volume fraction with the extinction coefficients are initially measured using the Lambert–Beer law at a fixed wavelength (632.8 nm). The results

indicated that incident solar energy may be totally absorbed in the penetration depth of 10 cm using the nanofluids with extremely low volume fraction of 0.0005 Vol.%. They also compared their results with the Maxwell-Garnett model for cylindrical nanoparticles and the Rayleigh scattering approximation, confirming that both approaches achieve good accuracy in theoretical simulations of radiative transfer in water-based MWCNT nanofluids.

In chapter 7 I will provide detailed ANSYS FLUENT simulations of copper, copper oxide/silver/graphite water-based nanofluids in a flat plate solar collector geometry with inlet and outlet features (for controlling flow rates). 3-dimensional steady state incompressible flow will be assumed under forced convection conditions i. e. thermal buoyancy effect is neglected. The Tiwari-Das nanoscale model will be deployed in ANSYS FLUENT (version 19.2, 2020). To cater for variable optical properties of nanofluids, a more advanced radiative approximation model is deployed, namely the Chandrasekhar discrete ordinates method (DOM) which is described at length in Chapter 2. Extensive visualization of different geometric and nanoscale effects is included. The relative performance of the different metallic and non-metallic nanoparticles on thermal efficiency e. g. local Nusselt number at the enclosure (collector) boundaries is also described. Detailed streamline and isotherm characteristics are computed, and it is identified that specific volume fractions of different metallic and non-metallic nanoparticles under carefully selected flow rates produce optimum heat transfer performance.

#### **1.5-2.4 Modelling a magnetic nanofluid-based hybrid magneto-biomimetic deformable nano-collector with Buongiorno's two-component nanoscale model**

Modern trends in renewable and sustainable energy systems have witnessed a proliferation of novel designs. Pre-eminent in such systems is the *solar energy collector* which exploits, the key energy source available to the earth, namely the sun. Pioneering studies of radiative transport in solar collectors and surface properties were led by Hottel at MIT from the 1930s

to the 1960s and much of this work is summarized in an excellent monograph (Hottel & Sarofim, 1967). Since 1970 a worldwide effort has been underway to increase the durability, resilience and thermal efficiency of solar collector systems. Solar technology has subsequently infiltrated a vast array of devices including solar ponds (Jubran, et al., 1997), solar absorption chillers (Petela, et al., 2017), solar towers (Padki & Sherif, 1999), solar cooling systems (Rashidi & Bég, 2012), CHP refrigeration solar hybrid plants (Rashidi & Bég, 2012), solar-chemical steam control plants (Zhang, et al., 2017), green buildings (photovoltaic facades) (Sze, et al., 2011) and solar automobiles (De Schepper, et al., 2015). Another important application of solar technology is the solar-powered pump (Tiwari & Kalamkar, 2018) which has many uses including heating, waste transport, medical fermentation batch processing etc. A significant development in solar technology has also been the advent of nanofluids. Nanofluids were introduced by Choi (Choi & Eastman, 1995) and constitute a significant advance in fluid dynamics technology and are synthesized by doping conventional base fluids (e.g., water, mineral oil, air, etc.) with carefully designed nano-particles. The resulting suspension achieves improved thermal conductivity and modified viscosity properties. The surface area per unit volume of nanoparticles is much larger (millions of times) than that of conventional microparticles. The number of surface atoms per unit of interior atoms of nanoparticles is very large. These characteristics can be exploited in many complex systems including medical engineering, energy engineering and materials processing. Nanofluids have infiltrated into many areas of energy and also biomedical technology as they may be manipulated to yield more biologically friendly, sustainable and durable products. (Khanafar & Vafai, 2018) presented a lucid summary of solar nanofluid device applications, emphasizing that efficiency of any solar thermal system is dictated by thermophysical properties (viscosity, density, thermal conductivity and specific heat) of the operating fluid and the geometric

characteristics. Critical features of nanofluids for improving solar collector and pump efficiency are types of the nanoparticles (metallic based work best e.g., copper, silver, titanium), nanoparticles volumetric concentration in the base fluid and the nanofluid viscosity and conductivity. The inclusion of copper nanoparticles considerably elevates the heat gain capacity of a solar pump. Carbon nanotube nanofluids not only improve the efficiency of solar collectors but have the added advantage of decreasing CO<sub>2</sub> emissions. It should also be noted that there are a diverse range of mathematical models available for simulating nanofluid transport phenomena which have also been addressed in (Khanafer & Vafai, 2018). These include the Buongiorno two-component model (Buongiorno, 2006) which emphasizes thermophoretic forces and Brownian motion dynamics as the key contributors to thermal conductivity enhancement. The other popular model is Tiwari and Das model (Tiwari & Das, 2007) which simulates the nanoscale effect based on volume fraction (concentration) of the nano-particles. This model prioritizes thermal conductivity and viscosity of the nanofluid by appropriate functions formulated in terms of the nanoparticle volume fraction. However, it is restricted only to a momentum and energy balance and does not feature a separate species concentration balance equation for the nanoparticles. The Tiwari-Das model has the serious drawback of confining the nanoparticle contribution to volume fraction rather than via a separate species conservation equation. The Buongiorno model therefore while it ignores volume fraction effects does compensate for this by a discrete equation for the nano-particle concentration diffusion and is more comprehensive therefore for complex flow simulations where Brownian motion can be modelled. Many recent studies have been communicated on nanofluid solar pumps and collector systems including (Shamshirgaran, et al., 2018) (on energy dynamics of copper nanofluid flat plate collectors), (Owolabi, et al., 2017) (on integrated silver oxide doped nano-solar cells), (Cingarapu, et al., 2014) (on tin-based nanofluids for solar



pumping designs), (Ravindran, 2017) (on nano-fuels for rocket propulsion and solar power), (Abid, et al., 2016) (on salt-based ionic nanofluids for parabolic collectors) and (Alashkar & Gadalla, 2018) (focused on gold and zinc oxide nanofluids for solar power pumps). All these studies confirmed the considerable elevation in thermal efficiency and sustainability of solar power designs attained with judicious deployment of metallic nanoparticles.

Another important renewable pump design is the magnetohydrodynamic (MHD) pump (Lim & Choi, 2009) (Das, et al., 2013). These pumps employ the Lorentz magnetic body force effect, based on the injection of an electric current into two electrodes located at sidewalls facing each other in a microchannel. This charge injection produces a significant transversal ionic current in the microchannel, which is simultaneously subjected to a magnetic field oriented at an angle of  $90^\circ$  to the current direction and microchannel axis. Conventional MHD micropumps can generate only small values for pump rate and achievable pressure and the performance is strongly controlled by the ionic conductivity of the pumping fluid. In DC MHD pumps, in particular, electrolytic bubble generation at the injection electrodes can be a key problem (Ho, 2007) (Leboucher, et al., 1995) (Wang, et al., 2004). However, recent studies with magnetized nanofluids have largely mitigated these and other issues and have simultaneously achieved the marked enhancement in pump efficiency and longevity. Important efforts in this regard include the work of (Shahidian, et al., 2009) which explored the impact of different electrical conductivities of nano-particle doped ionic fluids on overall efficiency. Further studies emphasizing the promise of nanofluid-based MHD pumps includes (Qian & Bau, 2009), (Shahidian, et al., 2009) and (Joo & Lee, 2018). Another exciting development in renewable energy has been the amalgamation of solar pump technology with magnetohydrodynamics (MHD). Recent Work at RPI [30], has established that due to higher temperature generated, solar MHD pumps attain a demonstrably greater efficiency than standard solar thermal pump

technologies which only operate at a much lower temperature. This new branch of renewables is termed concentrating solar MHD Power Utility and is currently being commercialized in the USA. It combines the benefits of high energy radiative power sources (solar) with excellent flow control abilities of magnetohydrodynamic pumps. Other excellent investigations of this technology include (Satyamurthy, et al., 1999) (for liquid metal solar MHD pumps, based on an extension of the Faraday law of induction to liquid metals), (Kaushik, et al., 1995) (on solar-powered liquid metal LMMHD power generation systems with smaller cost per unit of installed power), (Romero & González-Aguilar, 2017) (on MHD concentrating solar thermal (CST) central tower systems).

Although purely nanofluid media have been exploited to great effect in modern solar and solar MHD pumps, it is also possible to enhance heat transfer characteristics via the incision of a *porous material* in the pumping duct (channel). Solar porous absorbers have demonstrated exceptional benefits in regulating flows in such pumps and concurrently elevating thermal transfer efficiencies. (Wang, et al., 2017) showed the optimal performance was possible in solar collectors containing a variable porosity medium. Other examples of porous media solar pump systems include the solar pond studied by (Shi, et al., 2011) (where hydrodynamic stability is controlled more effectively with permeability) and (Ren, et al., 2017) who observed that porous media solar pumps and receivers with larger thickness produce better retention of solar thermal energy. (Vasiliev, et al., 2001) have explored the advantages of porous media in solar-gas solid sorption heat pumps. (Al-Nimr & Alkam, 1998) have analyzed the benefits of porous media matrices in tubeless solar collectors and pumps.

A critical aspect of accurately simulating and designing solar pumps is the proper simulation of thermal radiative heat transfer. Radiation is the dominant mode of heat transfer in sunlight

and is the most complex mode of thermal transport. It involves many complex features including spectral effects, optical thickness, reflection, absorption, transmission etc. To simulate radiative heat transfer problems, very sophisticated numerical algorithms must be employed to cater for a multitude of thermo-physical phenomena which is both time-consuming and expensive. Many approaches have been developed to overcome this challenge and popular models emerging in engineering sciences include the Milne-Eddington approximation, Chandrasekhar discrete ordinates method, P1 differential approximation, Schuster-Schwartzchild two-flux model and the Rosseland diffusion model. These methods convert the integro-differential radiative equation into either partial differential equations or algebraic flux equations which are much easier to implement. Many simulations have been presented using these radiative models and are lucidly summarized in (Tien & Vafai, 1989). Radiative (optical) properties of nanofluids are also crucial in their efficient implementation in solar power technology. (Said, et al., 2013) described the application of a direct absorbing nanofluid (suspension formed by mixing nanoparticles and a liquid) for harvesting solar thermal energy, providing extensive details of radiative properties of nanofluids (optical thickness, scattering coefficients etc). (Du & Tang, 2015) elaborated on the transmission and scattering characteristics of nanofluids with agglomeration effects. (Bég, et al., 2016) utilized both network electro-thermal and finite difference algorithms to simulate thermal convection and radiation heat transfer in an annular porous medium solar energy absorber with a Traugott's P1-radiative differential approximation.

Recent trends in engineering design have strongly gravitated towards *bio-inspired designs*. Biological systems have perfected many intricate mechanisms which can be applied to upgrade conventional engineering systems to a new level of performance and endurance. One of these mechanisms is known as peristalsis and features in an impressive spectrum of natural

phenomena. Peristalsis embodies continuous contraction and expansion of a flexible hollow, tubular structure containing fluid. Peristaltic pumping uses this mechanism where direct contact of any inside moving parts with the fluid is undesirable or inefficient. It is ideal for transferring fluids from lower pressure to higher pressure regions. This mechanism is observed in reptilian breathing (Du, et al., 2014), robotic endoscopy (Slawinski & Terry, 2014), intestinal physiology (Pal & Brasseur, 2002), human speech (laryngeal phonation) (Zheng, et al., 2010), and multidrug efflux pumps to export toxic substrates through their cell membranes (Schulz, et al., 2010). Many excellent mathematical models for peristaltic pumping dynamics have been developed. (Pal & Brasseur, 2002) who showed that in esophageal peristalsis, local pressure and shear stress in the contraction zone are strongly diminished via local longitudinal shortening (LLS) and that a peristaltic wave of local longitudinal muscle contraction coordinated with the circular muscle contraction wave has served to concentrate circular muscle fibers and reduces the magnitude of contractile force required to transport a parcel of trapped fluid (bolus), collectively enhancing circular muscular efficiency. (Tsui, et al., 2014) conducted numerical computations on peristaltic pumping in a finite length distensible channel in which the unstructured computational grid moved according to the oscillation of the wall. (Dobrolyubov & Douchy, 2002) developed a theory of peristaltic waves based on the travelling deformation waves and wave mass transfer theory. (Kumar, et al., 2010) presented perturbation solutions for peristaltic transport due to a sinusoidal wave travelling on the boundary of a permeable tube filled with an incompressible fluid. (Moradi, et al., 2017) described a spectrally accurate algorithm for peristaltic flows in annular geometries and deployed a numerical discretization method based on Fourier and Chebyshev expansions in the streamwise and radial directions, showing that modifications in the mean axial pressure gradient vary proportionally to the second power of the wave amplitude for waves with small enough amplitudes. Further

Newtonian viscous peristaltic pumping modelling studies include (Reddy, et al., 2005) and (Mandviwalla & Archer, 2008). (Ramesh, 2016) considered magnetohydrodynamic thermo-solutal peristaltic pumping of a Stokesian couple stress non-Newtonian fluid in a two-dimensional inclined channel containing a permeable medium. (Tripathi & Bég, 2012) presented closed-form solutions for time-dependent peristaltic magnetohydrodynamic heat transfer through a finite length channel. Nanofluid peristaltic pumping has also been addressed in recent years. (Bég & Tripathi, 2011) presented the first analytical study of thermo-solutal nanofluid peristaltic dynamics in a channel, explicitly considering thermal and species Grashof number buoyancy effects. Further investigations have considered non-Newtonian effects and titanium nanoparticles (Bhatti, et al., 2016), shape geometric effects (Akbar, et al., 2016), combined electrical and magnetic field effects (Tripathi, et al., 2017).

As noted earlier in solar magnetohydrodynamic pumps, radiative heat transfer is a key consideration. The purpose of chapter 8 is to further modify this concept to include biomimetic channel wall features, specifically deformability of the walls. Peristaltic magnetohydrodynamic nanofluid solar pumps must, therefore, feature wall distensibility, nanofluid behavior, magnetohydrodynamics and radiative heat transfer characteristics. Chapter 8 uses a Rosseland optically thick radiative flux model to simulate uni-directional thermal radiation effects. This approach has been utilized in many analyses of peristaltic pumping including (Bhatti, et al., 2016) for two-phase viscoelastic working fluids and (Hayat, et al., 2017) for magnetic nanofluids. A variable-viscosity model is employed for the nanofluid. Darcy's law is employed to simulate porous medium drag effects. Heat source/sink and buoyancy effects are included. The conservation equations for mass, momentum, energy and nano-particle volume fraction (concentration) are transformed from a stationary to a moving coordinate system with lubrication theory. The resulting non-dimensional two-point boundary

value problem is solved with both a perturbation method and an efficient numerical quadrature technique (Maple 17). The influence of relevant physical parameters on axial velocity, temperature, nanoparticle volume fraction and stream function distributions are depicted and discussed briefly. The simulations in Chapter 8 therefore provides an alternative approach to nanofluid direct absorber solar collectors (DASCs) which have not been explored in other chapters.

## Chapter 2 Theoretical and Numerical Methodology

### Abstract

In this chapter we present all the fundamental theory and computational methods implemented in this PhD in subsequent chapters. The PhD involves many aspects of multi-physics – different geometrical configurations, viscous flow, nanoscale models (principally the *Tiwari-Das model for chapters 3-7* and the *Buongiorno MIT Brownian motion-thermophoresis model for chapter 8*), multiple metallic (and carbon) nanoparticles, thermal convection heat transfer (both forced and natural), thermal radiation heat transfer, solar daylight tracking, nanoparticle mass transfer, deformable collector boundaries (peristaltic biomimetic design), magnetohydrodynamics, magnetic nanoparticle physics and dimensional analysis. All these are succinctly elaborated. Furthermore, two basic numerical techniques have been used for simulating a diverse range of problems described in **Chapters 3- 8**; these are ANSYS FLUENT (finite volume method for partial differential equation boundary value problems with mesh design for **chapters 3-7**) and MAPLE shooting quadrature (stepping technique for ordinary differential equation boundary value problems, **chapter 8**). Both are explained in detail. In all subsequent chapters, elements of these topics are again incorporated where appropriate. A full reference list is given including some of my publications based on this PhD.

### 2.1-1 Solar Collector Classification

Solar collectors are devices that can convert solar energy into electrical energy, thermal energy, or other useful form of energy. Traditionally, solar collectors can be classified into two major categories which are based upon the method of conversion: heat (solar thermal collectors) or electricity (Photovoltaic PV solar collectors). A photovoltaic thermal hybrid solar collector

(PVT) is a combination of photovoltaic and thermal solar systems and is considered to be less popular and requires further research. Classification of various solar collectors is illustrated in Figure 2-1.

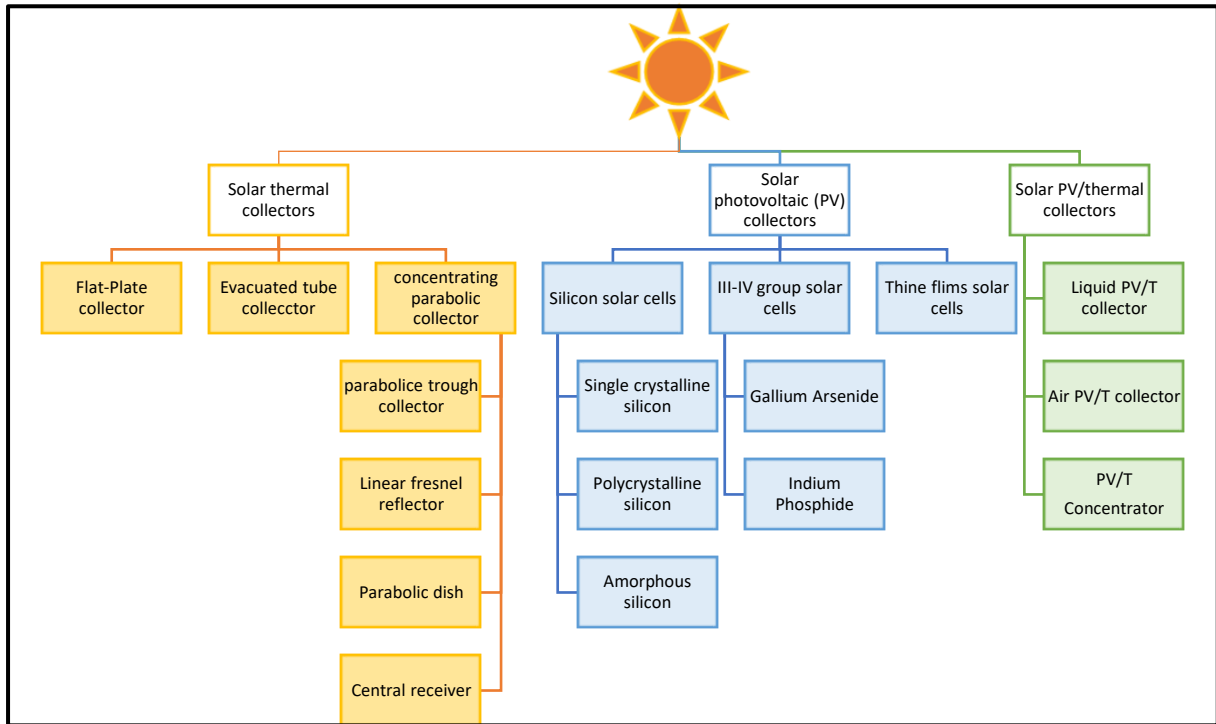


**Figure 2-1** Classification of various solar collectors

**Solar thermal collectors** are the focus of this study, where the collectors are a special kind of heat exchangers that are able to convert solar radiation into thermal energy through a transport medium or a heat transfer fluid (HTF). A system for converting solar energy into thermal energy is generally provided with the following equipment, as shown in Figure 2-2 solar collectors, heat storage devices, circulating pumps, heat transport and distribution network, automation, control, and safety devices. The solar collector collects solar radiation energy and transforms it into thermal energy and transports heat to the heat exchanger or solar storage tank via the heat transfer fluid (HTF). While traditionally HTFs are water, antifreeze-water mix, oils or air, this research uses aqueous-based nanofluid (water in combination with nanoparticle



doping) as a new kind of HTF that can be used in thermal solar collectors. This system can be supplied heat for a house heating system or commercially.

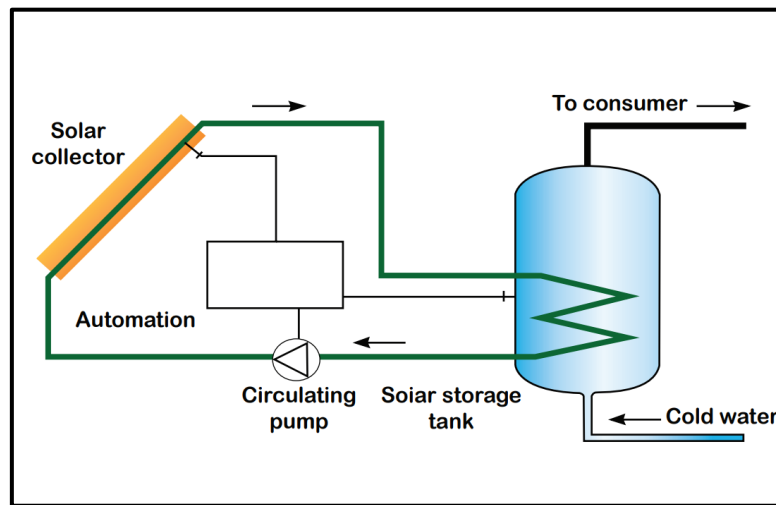


Figure 2-2 Solar energy conversion to thermal energy

Most thermal solar collectors in the current market are conventional surface absorption-based solar collectors, which use a black surface or spectrally selective surface to absorb solar irradiance and heat the heat transfer fluids (HTF) Figure 2-3 (a). The thermal resistance between the absorber and the fluids and the low thermal conductivity of HTFs, however, limit the heat transfer from the absorber surface to the HTF. However, the working fluid of a Direct Absorber Solar Collectors (DASC) is used as the absorbing medium for solar radiation instead of limiting the absorption to the absorber plate. By contrast, DASCs uniformly heat up the nanofluids. Figure 2-3 (b) *reduce the heat losses and thereby increase the collector thermal efficiency*. The modern theory of DASCs was first presented in the 1970s by (Minardi & Chuang, 1975).

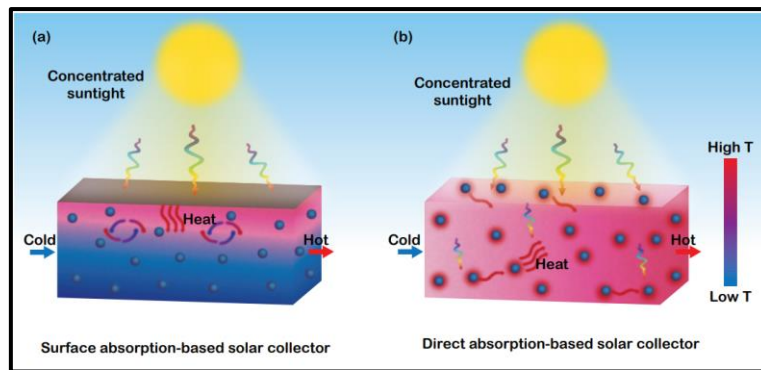


Figure 2-3 a) Surface vs b) Direct surface absorption-based-

**Flat-Plate Collectors (FPCs)** are one of the well-known solar thermal collector types, designed for operation in low to medium temperature ranges below 100 Celsius. The collectors are used to direct and diffuse solar radiations and do not require tracking of the Sun, therefore they require little maintenance in comparison to others. The main applications of these units are in solar water heating, building heating, air conditioning and industrial process heating.

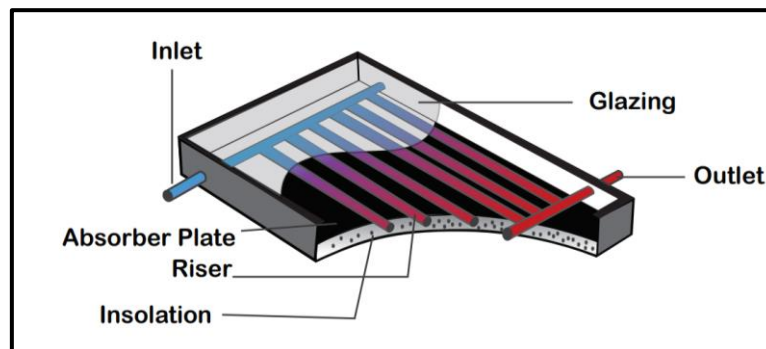
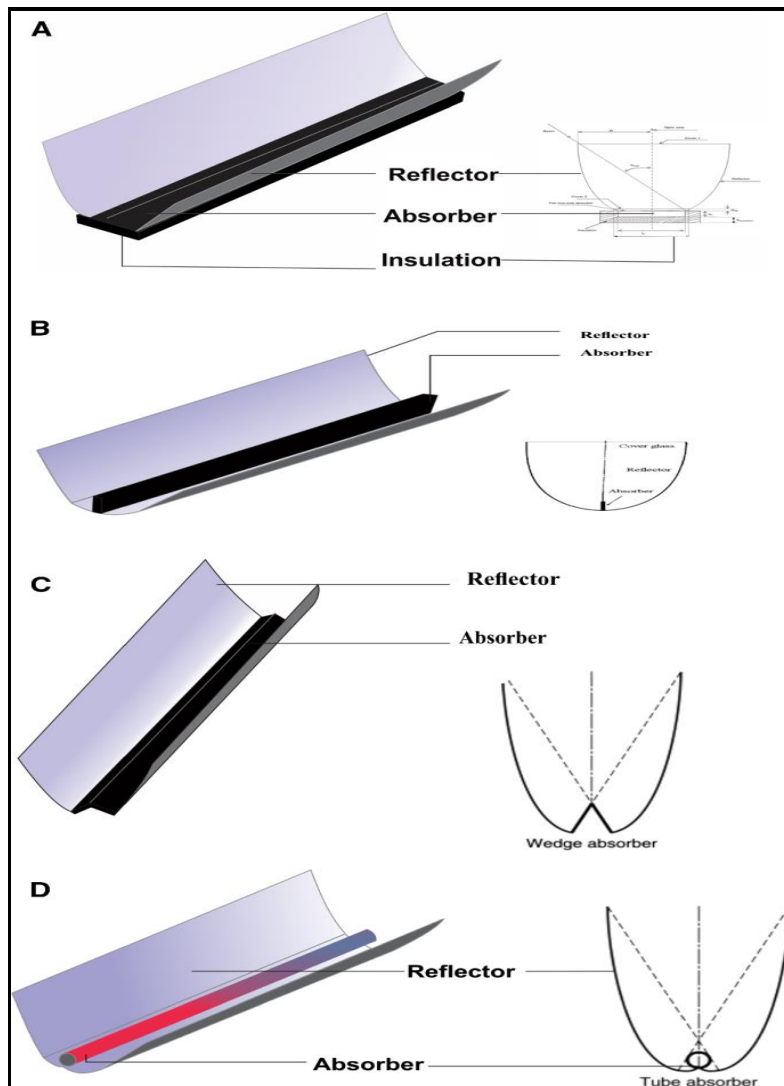


Figure 2-4 Flat plate solar collector

**Concentrating Collectors (PTCs)** are also a solar thermal collector, comprising with a receiver, where the radiation is absorbed and converted to another form of energy, and a concentrator, which is the optical system that directs beam radiation onto the receiver. Concentrating collectors provide energy at temperatures higher than FPCs. They redirect solar radiation passing through an aperture into an absorber and some devices usually require tracking of the Sun. Examples are shown below:



**Figure 2-5 CPC (a) flat one-sided absorber, (b) flat bifacial absorbers, (c) wedge-shaped absorber, (d) tubular absorber**

Both collectors have the same heat transfer working principles i.e., natural and forced convection heat transfer. However, the major differences in the two collectors are the operating temperature and the geometry. Three different geometries are simulated in this regard- a 3-D prismatic geometry with gold nanofluids in **chapter 5**; an annular (tubular concentric- SEE BELOW) geometry in **chapter 6**, and a 3-D flat plate collector geometry in **chapter 7**. It is also noteworthy that evacuated tube solar collectors are based on vaporisation to transfer heat,

which is outside of the research in this PhD but may constitute an interesting pathway for post-doctoral work.

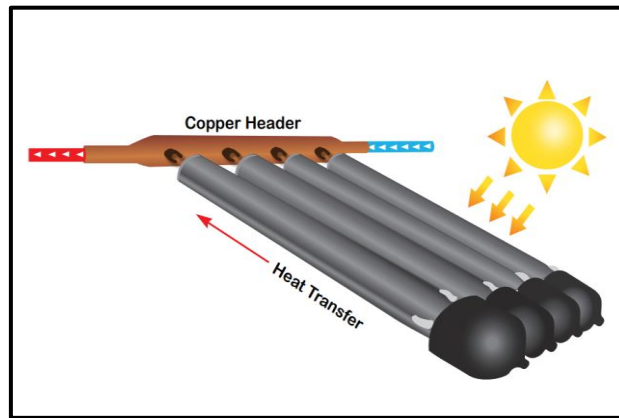


Figure 2-6 Tubular DASC system (Beg, et al., 2020)

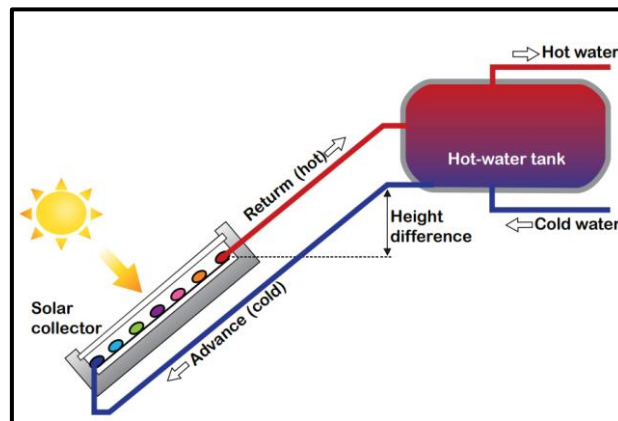


Figure 2-7 Annular tilted composite DASC system (Kuharat, 2019)

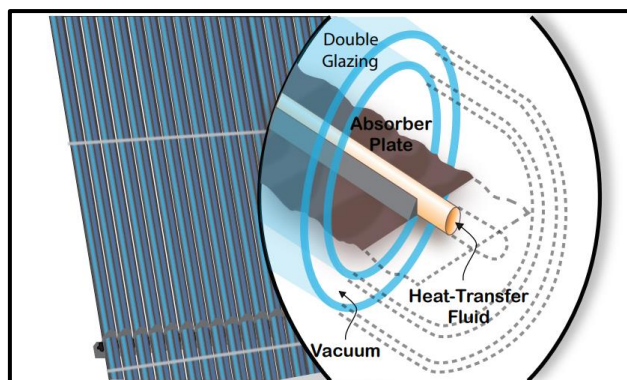
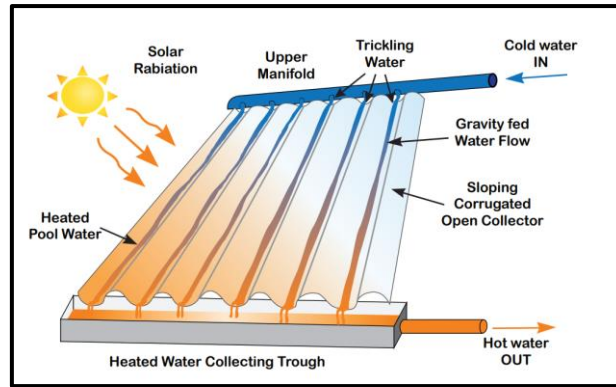
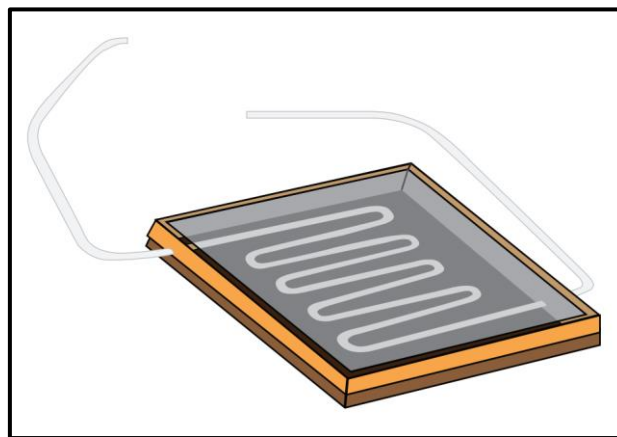


Figure 2-8 Evacuated tube annular DASC system (Kuharat, 2019)



**Figure 2-9 Corrugated (wavy) DASC system (Kuharat, 2019)**



**Figure 2-10 Serpentine DASC system (Kuharat, 2019)**

Since DASCs use a fluid medium to capture heat and contain solid components also, the thermo-physics of such solar devices inevitably involves *all three modes of heat transfer* (conduction, convection and radiation) although the individual contributions may vary with the particular design adopted, as elaborated by Duffie and Beckman (Duffie & Beckman, 2013).

## **2.1-2 Nanofluids**

Nanofluids constitute a solid-liquid (composite) mixture or suspension produced by dispersing tiny metallic or non-metallic solid nano particles in base liquids. Nanofluids are a new class of fluids engineered by dispersing nanometre sized materials (Nanoparticles, Nanofibers, Nanotubes, Nanowires and Nanorods) in base fluids. The size of nanoparticles (usually less

than 100nm) in liquids mixture gives them the ability to interact with liquids at a molecular level and so conducts heat better than modern day heat transfer fluids that depend on nano particles. Nanofluids can express enhanced heat transfer characteristics because of the combination of convection & conduction and an additional energy transfer through the particles' dynamics and collisions (molecular simulation). Metallic nanofluids have been found to possess enhanced thermophysical properties such as thermal conductivity, thermal diffusivity, viscosity, and convective heat transfer coefficients compared to those of base fluids like oil or water. Recently nanofluids have been utilized in peristaltic nano-pumps in medical engineering, pharmaco-dynamic delivery systems, petroleum drilling operations and smart coating systems for offshore applications. Some of these applications are shown in Figure 2-11.

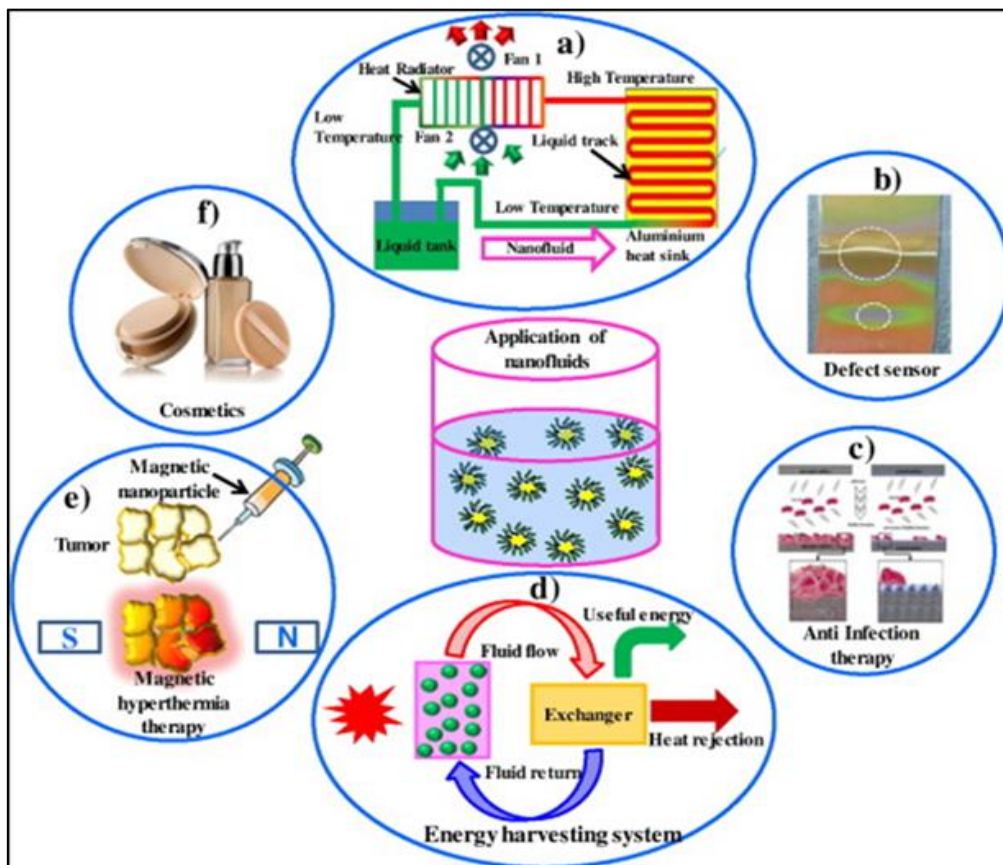


Figure 2-11 Applications of nanofluids in engineering

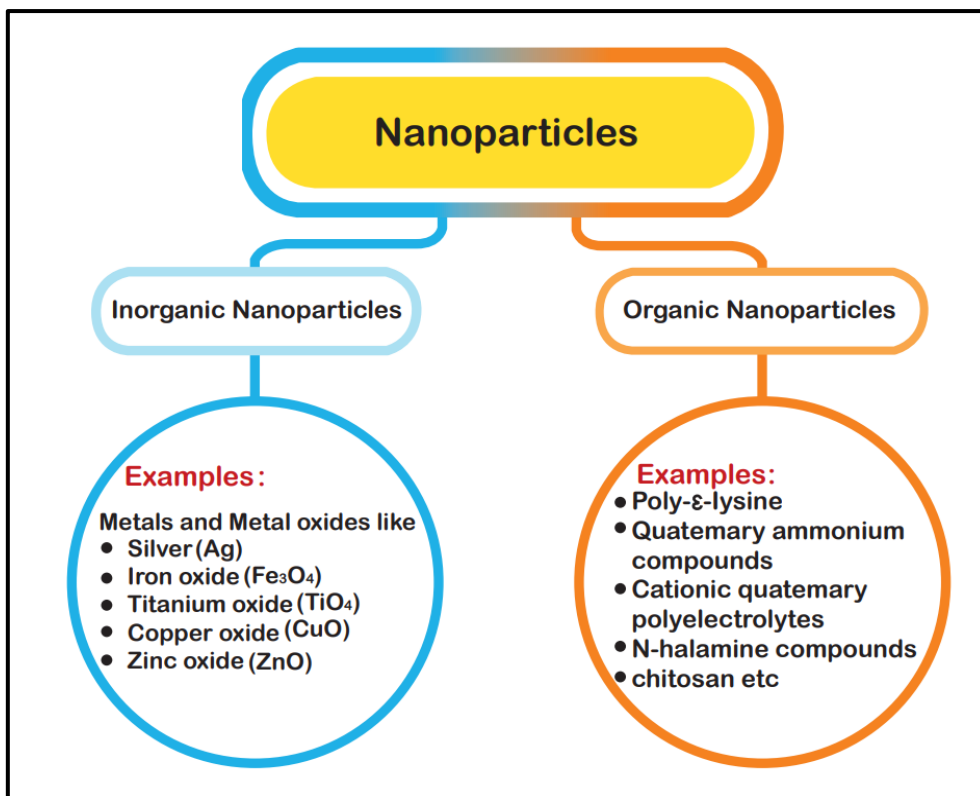


Figure 2-12 Nanoparticle types

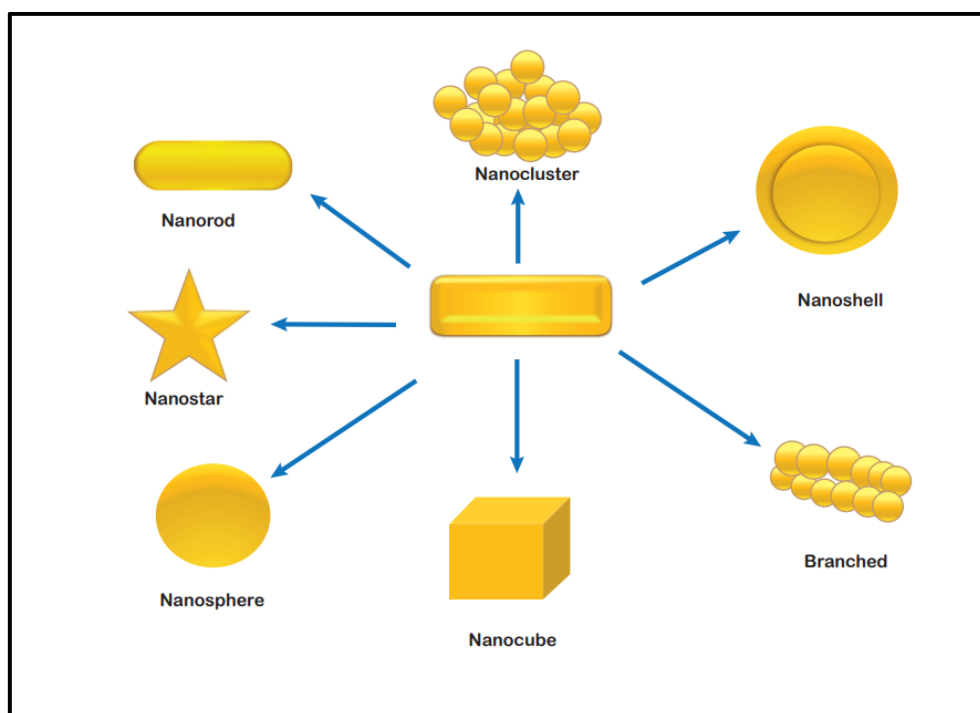


Figure 2-13 Shapes of Nanoparticles





Figure 2-14 Types of Nanoparticles

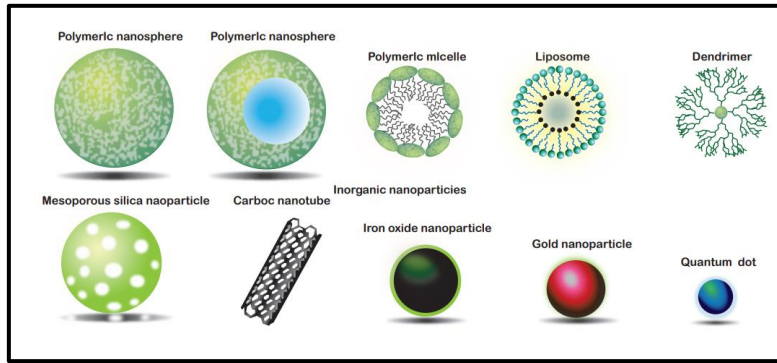


Figure 2-15 Organic Nanoparticles

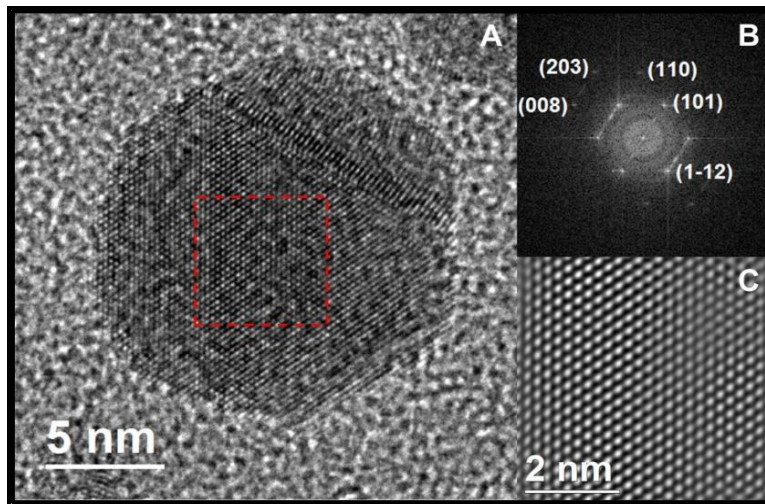


Figure 2-16 SEM image of silver nanoparticles- studied in chapter 3



Nanoparticles can be synthesized chemically or biologically. Metallic nanoparticles that have immense applications in industries are of different types, namely, Gold, Silver, Alloy, magnetic etc.

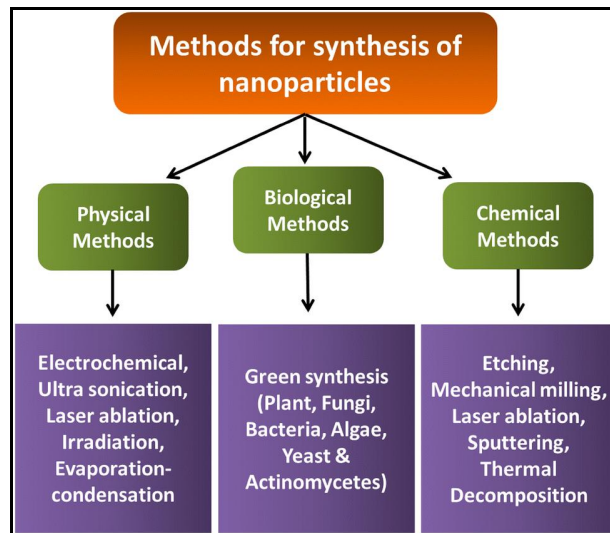


Figure 2-17 Nanoparticle synthesis methods- classification

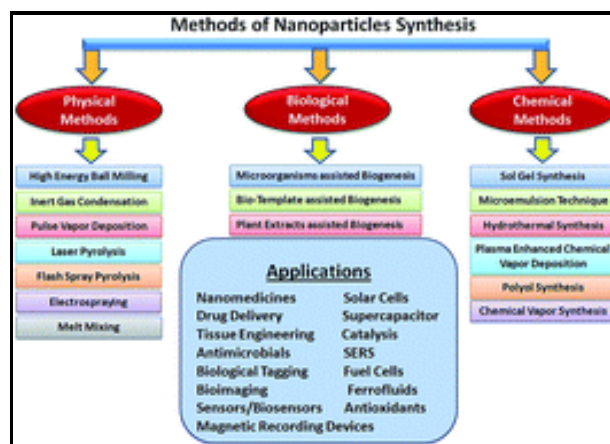


Figure 2-18 - Nanoparticle synthesis methods- types

## 2.2 Analytical Approach

In this study, there are two approaches used - **theoretical and computational fluid dynamics** (CFD) to investigate natural and forced convection internally within nanofluid-based solar

collectors. Before any simulations can be conducted, the correct theoretical model must be established. Data must be verified from experimental sources. Geometry must be carefully considered with boundary conditions and many other aspects. Simulating nanofluid multi-physical convection in enclosures essentially amounts to the computational solution and visualization of strongly coupled, nonlinear boundary value problems. Validation may be achieved via comparison of a simpler version of the final simulation with earlier published numerical studies using alternative algorithms or software or by benchmarking with experiments conducted in other laboratories worldwide and disseminated in the scientific literature. Although some work was conducted in designing a simple nanofluid-based solar circuit in Year 3, this could not be completed due to corona virus pandemic which ruled out access to the evolving rig design in Newton Building from March 2020 to present. Therefore, the experience gained from this sub-section of my work was used to identify previous experiments conducted by other research groups and to use this as a validation benchmark. These are elaborated in the respective chapters.

### 2.2-1 Viscous flow

The fundamental equations for steady viscous, incompressible laminar flow are the three-dimensional time-independent **Navier-Stokes equations**, which in a Cartesian coordinate system (x, y, z) take the following form:

D'Alembert mass conservation (3-D continuity)

$$\left[ \frac{\partial u}{\partial x} + \frac{\partial v}{\partial y} + \frac{\partial w}{\partial z} \right] = 0 \quad \text{Equation 2-1}$$

X-direction momentum conservation

$$\rho \left[ u \frac{\partial u}{\partial x} + v \frac{\partial u}{\partial y} + w \frac{\partial u}{\partial z} \right] = \rho F_x - \frac{\partial p}{\partial x} + \mu \left[ \frac{\partial^2 u}{\partial x^2} + \frac{\partial^2 u}{\partial y^2} + \frac{\partial^2 u}{\partial z^2} \right] \quad \text{Equation 2-2}$$

Y-direction momentum conservation

$$\rho \left[ \mathbf{u} \frac{\partial v}{\partial x} + \mathbf{v} \frac{\partial v}{\partial y} + \mathbf{w} \frac{\partial v}{\partial z} \right] = \rho F_y - \frac{\partial p}{\partial y} + \mu \left[ \frac{\partial^2 v}{\partial x^2} + \frac{\partial^2 v}{\partial y^2} + \frac{\partial^2 v}{\partial z^2} \right] \quad \text{Equation 2-3}$$

Z-direction momentum conservation

$$\left[ \mathbf{u} \frac{\partial w}{\partial x} + \mathbf{v} \frac{\partial w}{\partial y} + \mathbf{w} \frac{\partial w}{\partial z} \right] = \rho F_z - \frac{\partial p}{\partial z} + \mu \left[ \frac{\partial^2 w}{\partial x^2} + \frac{\partial^2 w}{\partial y^2} + \frac{\partial^2 w}{\partial z^2} \right] \quad \text{Equation 2-4}$$

The appropriate energy (heat) conservation equation is:

$$\mathbf{u} \frac{\partial T}{\partial x} + \mathbf{v} \frac{\partial T}{\partial y} + \mathbf{w} \frac{\partial T}{\partial z} = \alpha_m \left( \frac{\partial^2 T}{\partial x^2} + \frac{\partial^2 T}{\partial y^2} + \frac{\partial^2 T}{\partial z^2} \right) + Q_{\text{rad}} \quad \text{Equation 2-5}$$

The transport equations (mass, momentum, and energy) with nanofluid properties are solved subject to the boundary conditions in ANSYS FLUENT:

Here  $\alpha_m = \frac{k}{\rho C_p}$  is the thermal diffusivity, which is a measure of thermal inertia and  $k$  = thermal conductivity (W/mK),  $\rho$  = density (kg/m<sup>3</sup>),  $C_p$  = specific heat capacity of the nanofluid (J/Kg.K). When  $\alpha_m$  is high, the heat moves fast and the nanofluid conducts heat quickly (higher thermal conductivity).  $T$  denotes temperature (K),  $F_{\text{buoyancy}}$  is the buoyancy force (featured in the  $x$ -momentum equation which couples this equation with the energy equation, and is equal to  $-g [1-\beta\Delta T]$  where  $\Delta T$  is the temperature difference between the hot and cold walls i.e., ( $T_H - T_C$ ) and  $Q_{\text{rad}}$  is the *radiative flux term*.

## 2.2-2 Tiwari-Das volume fraction nanofluid model

To simulate nano-particle effects, the (Tiwari & Das, 2007) is employed which allows different concentrations (volume fraction) and types of metallic nanoparticles to be simulated. In ANSYS, this approach is implemented as a “one-phase flow” modification since the particles are very small. A nanofluid is defined in the ANSYS FLUENT workbench as a new fluid with

a new density, viscosity, thermal conductivity, and specific heat obtained as a function of a base fluid and nano-particle type and concentration (volume fraction)

Tiwari-Das model is focused more on the *type and properties* of nanoparticles. Two significant features of nanoparticles which they concentrate on are *thermal conductivity and viscosity*. They make the assumption that the volume fraction is engineered to be between 3 to 5% which enables mechanical behaviour like the base fluid. In the Tiwari-Das model, the nanoparticle contribution is simulated through volume fraction (shown below) instead of in a separate species conservation equation. This model has been used for analysing many metal-oxide nanofluids like zinc oxide, copper oxide, titanium oxide and aluminium oxide.

The volume fraction can be estimated from:

$$\phi = \frac{V_{np}}{V_f} \quad \text{Equation 2-6}$$

Where  $\phi$ =volume fraction,  $V_{np}$ =nano particles volume and  $V_f$ =volume of fluid. The dynamic viscosity can be estimated from:

$$\mu_{nf} = \frac{\mu_f}{(1-\phi)^{2.5}} \quad \text{Equation 2-7}$$

Here  $\mu_{nf}$  = dynamic viscosity of nanofluid (kg/m.s),  $\mu_f$  = dynamic viscosity of base fluid (kg/m.s). The effective density and heat capacity also can be estimated from:

$$\rho_{nf} = (1 - \phi)\rho_f + \phi\rho_s \quad \text{Equation 2-8}$$

$$C_{pnf} = \frac{(1-\phi)(\rho C_p)_f + \phi(\rho C_p)_s}{\rho_{nf}} \quad \text{Equation 2-9}$$

Here  $\rho_{nf}$ =nanofluid density,  $\rho_f$ =base fluid density,  $\rho_s$ =nanoparticle density,  $C_{pnf}$ =nanofluid specific heat capacity. The effective thermal conductivity of fluid can be determined by the Maxwell-Garnet relation which is adopted in Tiwari and Das [24]:

$$\frac{k_{nf}}{k_f} = \frac{k_s + 2k_f - 2\phi(k_f - k_s)}{k_s + 2k_f - \phi(k_f - k_s)} \quad \text{Equation 2-10}$$

Here  $k_{nf}$  =nanofluid thermal conductivity W/(m·K),  $k_f$ = fluid thermal conductivity W/(m·K) and  $k_s$  = nanoparticle thermal conductivity W/(m·K). All calculated nanofluid properties (for the three different metallic nanoparticles studied i.e., copper oxide, silver and titanium oxide) are given in the **Appendix**.

### 2.2-3 Other Nanoscale Models for Nanofluids

Although I have deployed exclusively the Tiwari-Das model in most of the chapters in this PhD, in the penultimate chapter (chapter 8) I explored a novel design with *magnetohydrodynamic solar collector hybrid peristaltic system and utilized the Buongiorno model*. Many other nanoscale models are available for simulating various thermophysical and species diffusion aspects associated with nanofluids. These are briefly described below. Since a number of studies in the literature quoted use these models, it is important to understand them in order to establish useful comparisons with my own simulations and those in the literature. Various formulations for simulating nanofluid transport have been developed, notably by (Buongiorno, 2006) at MIT, (Koo, 2004) and (Li, et al., 2016) at North Carolina State University, USA and (Tiwari & Das, 2007) at the Indian Institute of Technology. While all these models provide robust approaches for simulating thermal conductivity enhancement of nanofluids, they differ considerably. Buongiorno's model includes a separate nanoparticle species diffusion equation in addition to momentum and energy conservation equations; it emphasizes the dominance of Brownian diffusion and thermophoresis body force as

mechanisms contributing to thermal enhancement. The Koo and Li models are modifications of the Tiwari-Das volume fraction model but only include momentum and energy conservation equations. However, they permit the analysis of nanoparticle type or shape effects which is not possible with the Buongiorno model. As such the Koo-Li and Tiwari-Das models are more realistic for smart magnetic coating flows where different magnetic nanoparticle species can be studied. Buongiorno's model however can compute the distribution of nanoparticle species diffusing in nanofluids and has been used in several coating simulations of magnetic nanoparticles by (Bég, et al., 2019) (using a Williamson viscoelastic model and considering wall thermal slip) and (Shukla, et al., 2019) (who considered second law thermodynamic optimization of magnetic nano-coatings).

#### **2.2-4 Buongiorno nanoscale model**

Developed at MIT in 2006, this is also a very popular model in nanofluid dynamics. The nanoparticle suspension is assumed to be stable implying that there is no nanoparticle agglomeration. A dilute suspension of nanoparticles is assumed and large concentration of nanoparticles results in a large suspension viscosity. It is also assumed that the Oberbeck-Boussinesq approximation is valid. Buongiorno considered two-phase non-homogenous model and identified seven slip mechanisms that can produce a relative velocity between the nanoparticles and the base fluid: inertia, Brownian diffusion, thermophoresis, diffusiophoresis, Magnus effect, fluid drainage, and gravity. Of all of these mechanisms, only Brownian diffusion and thermophoresis were found to be important. Buongiorno's analysis [4] consisted of a two-component equilibrium model for mass, momentum, and heat transport in nanofluids; and he found that a non-dimensional analysis of the equations implied that energy transfer by nanoparticle dispersion is negligible, and cannot explain the abnormal heat transfer coefficient increases. He further suggested that the boundary layer has different properties due to the effect

of temperature and thermophoresis. The viscosity may be decreasing in the boundary layer, which would lead to heat transfer enhancement. Under these assumptions, the generalized vectorial form of the conservation equations may be written as:

Continuity (mass conservation) equation:

$$\nabla \cdot \bar{v} = 0 \quad \text{Equation 2-11}$$

Momentum equation:

$$-\frac{\mu}{K} \bar{v} = -\nabla p + [C\rho_p + (1 - C)\{\rho_f(1 - \beta(T - T_\infty))\} + n\gamma\Delta\rho]g$$

Equation 2-12

Energy equation:

$$\bar{v} \cdot T = \alpha_m \nabla^2 T + \tau [D_m \nabla C \cdot \nabla T + (D_T/T_\infty) \nabla T \cdot \nabla T] \quad \text{Equation 2-13}$$

Nanoparticle conservation equation:

$$\bar{v} \cdot \nabla C = D_B \nabla^2 C + (D_T/T_\infty) \nabla^2 T \quad \text{Equation 2-14}$$

With a suitable choice for the reference pressure, the linearized momentum equation can be obtained by writing Eqn. (2) as follows:

$$-\frac{\mu}{K} \mathbf{v} = -\nabla p + [(\rho_p - \rho_{f\infty})(C - C_\infty) + (1 - C_\infty)\rho_{f\infty}\beta(T - T_\infty) + m\Delta\rho]g \quad \text{Equation 2-15}$$

Here  $\bar{v} = (u, v)$  is the nanofluid velocity,  $\tilde{v}$  is the average directional swimming velocity of a microorganism,  $T$  is the temperature,  $C$  is the nanoparticle concentration,  $K$  is permeability of the homogenous, isotropic, saturated porous medium,  $p$  is the pressure,  $g$  is the gravity vector,  $\alpha_m = K_m/(\rho c)_f$  is the effective thermal diffusivity of the nanofluid-saturated porous medium,

$\rho_f$ ,  $\mu$  and  $\beta$  are the density, viscosity, and volumetric volume expansion coefficient of the nanofluid,  $\rho_p$  is the density of the particles.  $\Delta\rho = \rho_{m\infty} - \rho_{f\infty}$  is the density difference between the microorganism density ( $\rho_{m\infty}$ ) and base fluid density ( $\rho_{f\infty}$ ),  $D_B$  is the Brownian diffusion coefficient (Buongiorno nanoscale model),  $D_T$  is the thermophoretic diffusion coefficient (Buongiorno nanoscale model),  $\nabla^2$  is the Laplacian operator and  $\tau = (\rho c)_p / (\rho c)_f$  where  $(\rho c)_p$  is the effective heat capacity of the nanoparticle material and  $(\rho c)_f$  is the heat capacity of the nanofluid.

### **Dimensionless Parameters**

When Buongiorno's model is non-dimensionalized for solar collector flows, two parameters arise of importance—the thermophoresis and Brownian motion parameters arise in both the heat conservation (energy diffusion) and mass conservation (nano-particle species diffusion equations). The elevation in thermal conductivity will also result in an increase in thermal diffusivity. This effectively decelerates the axial flow. There are many mechanisms which link the nanoparticle presence to thermal conduction and to fluid mechanical phenomena. These include interfacial layers, Brownian motion, clustering of nanoparticles and the convection-type effects at the nanoscale (nano-convection) which is associated with the nature of heat transport. With regard to the last of these mechanisms, Brownian motion of nanoparticles can produce thermal conduction elevation either indirectly via nano-convection of the fluid surrounding individual nanoparticles or directly via movement of nanoparticles which convey thermal energy (heat) i.e., particle to particle direct solid-solid transport of heat. Whichever mechanism is in action, the global effect on flow is a deceleration i.e., slowing.

The thermophoretic effect is a species-dominated effect and is linked to nano-particle diffusion. Buongiorno thermophoresis number takes the form:



$$Nt = \frac{(T_1 - T_0) D_T (\rho C)_p}{k_{ef} T_0} \quad \text{Equation 2-16}$$

physically thermophoresis takes place on a different timescale is essentially a diffusion limited transport process. Thermophoretic mobility as dictated by the nano-species diffusivity requires a very large thermal load to exert any major influence.

noticed that the temperature and concentration field are both substantially enhanced with increment in  $Nt$ . The mobilization of nanoparticles towards a colder zone driven by a temperature gradient force is called *thermophoresis*. The parameter  $Nt$  therefore plays a significant role in modifying temperature and nanoparticle distribution. As the value of  $Nt$  increases, the nanofluid temperature and concentration are seen to be elevated. i.e., thermal and nanoparticle concentration (species) boundary layer thicknesses are increased. As  $Nt$  increases, the heat transfer away from the wall is boosted and this aggravates nanoparticle deposition away into the nanofluid region, increasing nanoparticle concentrations throughout the boundary layer in proximity to the solar collector boundary.

### **Brownian motion parameter $Nb$**

$$Nb = \frac{(C_1 - C_0) (\rho C)_p D_B}{k_{ef}} \quad \text{Equation 2-17}$$

Larger  $Nb$  values imply smaller nanoparticles. This encourages thermal diffusion via ballistic collisions which energizes the regime and elevates temperatures. Conversely nanoparticle concentration magnitudes are suppressed since nanoparticle diffusion rate is reduced with stronger Brownian motion effect; the nanoparticle species boundary layer thickness is therefore also depleted. Similarly, while heat diffusion however is encouraged with smaller nanoparticles (higher  $Nb$ ). These numbers are further discussed in chapter 8.

## Schmidt number

$$Sc = \nu/D$$

Equation 2-18

This features in some models of Buongiorno nanofluid flows.

Generally, Schmidt number is inversely proportional to mass diffusivity. Larger values of  $Sc$  correspond to weaker mass diffusivity which has the tendency to decrease the nanoparticle concentration. For gaseous diffusion in polymers,  $Sc < 1$  and the momentum diffusion rate is exceeded by the species diffusion rate and higher concentration magnitudes are computed. However, in the present scenario we consider metallic nanoparticles embedded in a rheological coating for which  $Sc > 1$ ; the momentum diffusion rate exceeds the species diffusion rate and this will produce a depression in concentration values. For the case of  $Sc = 1$  both momentum and nano-particle species diffusion rates are equivalent as are the respective boundary layer thicknesses. The diffusivity of nanoparticles i. e. molecular species in the coating is critical to how effectively the nanoparticles become homogeneously distributed throughout the coating providing total and consistent protection to the cylinder. It is noteworthy that the species diffusion is assumed to obey Fickian diffusion, although in the future *non-Fickian diffusion*, which has also been reported, may be examined.

### 2.2-5 Magnetic nanoparticles

Magnetic nanofluids have emerged as a new sub-group of nanofluids in energy (and also biomedical engineering) which exhibit both magnetic and thermal enhancement properties. Interest in solar thermo-magnetic nanofluid devices has also grown significantly in the past decade. Some extremely diverse applications of this technology include solar magneto-nanofluid-heat pipes (**MNHPs**) (Chiang, et al., 2012), sedimentation control of Arc-Submerged Nanoparticle Synthesis Systems (**ASNSSs**) with magnetic fields (Chang, et al., 2004), critical heat flux elevation with magnetic nanofluids in phase change processes (Lee, et al., 2013),

droplet vaporization time modification in novel rocket combustion systems via magnetized nanofluids (Cristaldo, et al., 2011), thermal tribology (Vékás, 2004) and *solar collector magnetic nano-polymer working fluids* (Prabu & Ajay, 2017) (Khalil & Vafai, 2018). In parallel with substantial experimental work, a rich literature has also developed focused on theoretical and computational simulations of magneto-nanofluid dynamic processes. (Rarani, et al., 2012) used CFD simulations to evaluate the effect of electromagnetic fields on viscous properties of iron oxide-ethylene glycol magnetized nanofluids. (Kandasamy, et al., 2011) employed Lie group transformations and **MAPLE** software to study magnetic nanofluid convection from an extending sheet with wall transpiration. (Hamad, 2011) used hypergeometric functions to analyze magnetic field effects on free convection boundary layer flow from a nanofluid stretching surface. (Rana, et al., 2013) used a variational finite element code to model the transient magneto-convective nanofluid dynamics from a rotating extending surface. They employed a Buongiorno model for the nanofluid and showed that primary velocity is strongly retarded with increasing Hartmann number (magnetic parameter) and there is also a reduction in secondary velocity magnitude. Furthermore, temperature and nanoparticle concentrations were found to be accentuated with Hartmann number. Further studies of magnetic nanofluid convective transport have examined mixed convection (Ferdows, et al., 2012), non-isothermal wall conditions (Hamad, et al., 2011), partially heated micro-channels (Aminossadati, et al., 2011), porous media (Eldabe, et al., 2013) and thermal radiative heat transfer (Ferdows, et al., 2014).

## **2.2-6 Magnetohydrodynamics**

A magnetic field is created by the electric current returning to the power supply through the cathode, just like the magnetic field that is created when electrical current travels through a wire. This self-induced magnetic field interacts with the electric current flowing from the anode to the cathode (through the plasma) to produce an electromagnetic (Lorentz) force (cross product of current density and magnetic field) that pushes the plasma out of the engine, creating thrust. An external magnet coil may also be used to provide additional magnetic fields to help stabilize and accelerate the plasma discharge. In MHD steady flow of a Newtonian, electrically conducting, viscous fluid in the presence of an externally applied transverse uniform magnetic

field, the governing equations are the continuity, Navier-Stokes (momentum conservation in vector form), generalized Ohm's law and energy conservation equations, and these may be presented, in the presence of Ohmic (Joule) heating and viscous dissipation, in vectorial form, as follows:

$$\nabla \cdot \mathbf{u} = 0 \quad \text{Equation 2-19}$$

$$\rho(\mathbf{u} \cdot \nabla)\mathbf{u} = -\nabla P + \mu \nabla^2 \mathbf{u} + \mathbf{J} \times \mathbf{B} \quad \text{Equation 2-20}$$

$$\mathbf{J} = \sigma[\mathbf{E} + \mathbf{u} \times \mathbf{B}] \quad \text{Equation 2-21}$$

$$\rho c_p(\mathbf{u} \cdot \nabla)\mathbf{T} = \mathbf{k} \nabla^2 \mathbf{T} + \mu \Phi + \frac{J^2}{\sigma} \quad \text{Equation 2-22}$$

where  $\mathbf{u}$  is velocity vector,  $\rho$  is the density of the conducting fluid,  $\mu$  is dynamic viscosity of fluid,  $\mathbf{B}$  is external uniform magnetic field,  $B_e$  is constant magnetic flux density,  $B_o$  is constant magnetic flux density,  $c_p$  is specific heat at constant pressure,  $\mathbf{E}$  is electrical field,  $\mathbf{J}$  is current density field,  $k$  is thermal conductivity,  $P$  is pressure,  $\sigma$  is electrical conductivity of fluid,  $T$  is temperature,  $\Phi$  is viscous dissipation function. If the applied magnetic field is steady and sufficiently weak to neglect the induced magnetic field i.e., a *low magnetic Reynolds number* is assumed. The external uniform magnetic field  $\mathbf{B}$  is applied transverse to the plane of the flow and possesses a constant magnetic flux density  $B_o$ . Furthermore all thermophysical and fluid properties are assumed to be constant and electrical currents are neglected. The wall surface e.g., solar collector boundary, is electrically non-conducting, so that current density vanishes both at this surface and in the fluid regime. The penultimate and final terms on the right-hand side of eqn. (30) designate the *viscous heating* and *Joule heating* contributions, respectively, and have been shown to be significant in nanofluid solar collectors exploiting magnetic nanoparticles.

We further note that magnetic field effects are negated when  $M = 0$  i.e., the flow is electrically non-conducting. The imposition of magnetic field necessitates extra work expenditure by the fluid which has to be dragged in the disk plane, against the Lorentzian retarding forces. This supplementary work is dissipated in the form of Joule (Ohmic) heating which manifests with a rise in temperature in the fluid, with increasing  $M$  values. The effect is prominent also since the Joule heating term features quadratic functions

### **2.2-7 Natural Convection and Dimensionless Numbers**

Fundamental heat transfer analysis commonly consists of natural convection within cavities which are of great importance for specific technological applications like solar collectors. Natural or free convection is observed as a result of the motion of the fluid due to density changes arising from the heating process. The movement of the fluid in free convection, whether it is a gas or a liquid, results from the buoyancy forces imposed on the fluid when its density in the proximity of the heat-transfer surface is decreased as a result of the heating process. Free-convective flows may be laminar and turbulent. A flow past a solid surface, the temperature of which is higher (lower) than that of the surrounding flowing medium, is the most widespread type of free convection. Figure 2-19 schematically illustrate characteristic examples of free convection.

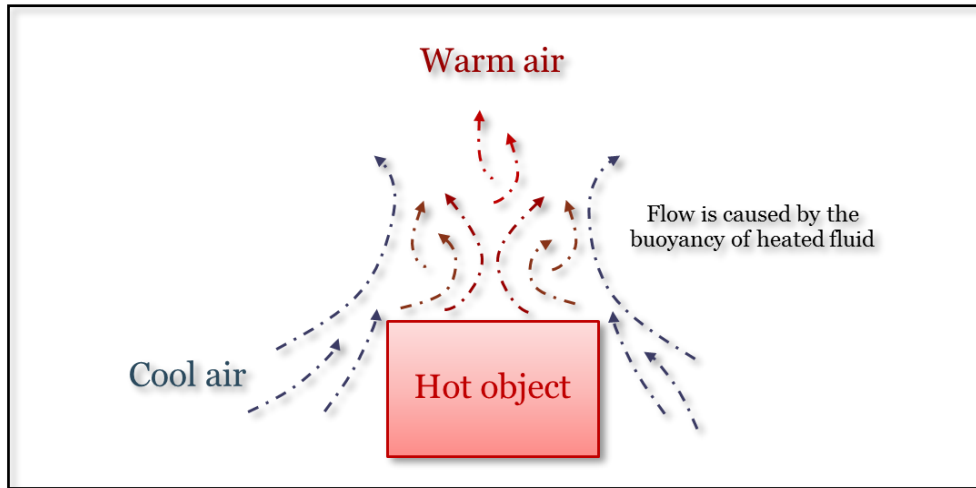


**Figure 2-19 Natural convection**

The buoyancy-generated flows are considered complex due to the combination of transport properties of flow and the thermal fields.

In natural convection related dimensionless numbers are:

**Prandtl number:** ratio of momentum diffusivity to thermal diffusivity:

$$\mathbf{Pr} = \frac{\nu}{\alpha} = \frac{\mu C_p}{k} \quad \text{Equation 2-23}$$

Prandtl number embodies the ratio of *viscous diffusion* to *thermal diffusion* in the boundary layer regime and furthermore expresses the ratio of the *product of specific heat capacity and dynamic viscosity*, to the *fluid thermal conductivity*. When  $Pr$  is high, viscous diffusion rate exceeds thermal diffusion rate. An increase in  $Pr$  from 1 through 3, 5, 7 to 9 greatly decreases temperatures. For  $Pr < 1$ , thermal diffusivity exceeds momentum diffusivity i.e., heat will diffuse faster than momentum. For  $Pr = 1.0$ , both the viscous and energy diffusion rates will be the same as will the thermal and velocity boundary layer thicknesses.

**Grashof number:** ratio of the buoyancy force to the viscous force acting on the fluid:

$$\mathbf{Gr} = \frac{\text{buoyancy forces}}{\text{viscous forces}} = \frac{g\Delta\rho V}{\rho\nu^2} = \frac{g\beta\Delta TV}{\rho\nu} \quad \text{Equation 2-24}$$

$$\mathbf{Gr} = \frac{g\beta(T_s - T_\infty)\delta^3}{\nu^2} \quad \text{Equation 2-25}$$

**Local Rayleigh number:** product of Prandtl and local Grashof numbers:

$$\mathbf{Ra}_x = \frac{g\beta}{\nu\alpha}(T_s - T_\infty)x^3 = \mathbf{Gr}_x\mathbf{Pr} \quad \text{Equation 2-26}$$

$g$  is acceleration due to Earth's gravity ( $\text{m/s}^2$ )

$\beta$  is the coefficient of thermal expansion (equal to approximately  $1/T$ , for ideal gases)

$T_s$  is the surface temperature (K)

$T_\infty$  is the bulk temperature (K)

$L$  is the vertical length (m)

$\nu$  is the kinematic viscosity ( $\text{m}^2/\text{s}$ ).

There are multiple studies that explore a range of variables which influence the natural convection inside enclosures filled with nanofluids. Shape of the enclosure plays a vital role in convection, though the shape depends on practical application. Different types of enclosure filled with nanofluid are studied in recent years. (Ghosh, et al., 2010)

### **Eckert number $Ec$**

Temperatures are therefore elevated in the entire boundary layer regime. Let us briefly consider viscous heating effects. As the value of Eckert number increases positively, this corresponds to an increase in convection currents from the disk to the fluid which transfers greater thermal energy to the boundary layer, manifesting in an increase in fluid temperatures. The opposite case of increasingly negative Eckert numbers implies removal of heat from the boundary layer

regime to the disk via convection currents. As a result, the disk temperature will be enhanced and fluid temperatures will be depressed. The intermediate case of  $Ec = 0$  implies an absence of viscous dissipation where there is no conversion of kinetic energy to thermal energy and the classic profile of monotonic decay is observed. For positive  $Ec$  there will therefore be an increase in thermal boundary-layer thickness whereas with negative  $Ec$  the thermal boundary layer thickness will be reduced.

### **Magnetohydrodynamic Hartmann number**

**Hartmann number (Ha)** is the ratio of electromagnetic force to the viscous force named in honour of the German engineer who performed key experiments in the 1930s. It is defined by:

$$Ha = BL \sqrt{\sigma/\mu} \quad \text{Equation 2-27}$$

$B$  is the magnetic field (Tesla)

$L$  is the characteristic length scale (m)

$\sigma$  is the electrical conductivity (Siemens/m)

$\mu$  is the dynamic viscosity (kg/(ms))

This parameter features only in Chapter 8 where I have studied magnetohydrodynamic nanofluid peristaltic solar collectors (Ghosh, et al., 2010), (Cramer & Pai, 1973).

Solutal Grashof number (Gm or Br)

$$Gm = - \frac{\rho_0(\rho_p - \rho_0)gL^3(C_1 - C_0)}{\mu_0^2} \quad \text{Equation 2-28}$$

It represents the relative magnitude of the *species (nanoparticle) buoyancy force* to the viscous hydrodynamic force in the channel. When  $Br \rightarrow 0$  species (solutal) buoyancy effects vanish



## 2.2-8 Forced Convection and Dimensionless Numbers

Forced convection heat transfer involves fluid motion as well as heat conduction. The fluid motion enhances heat transfer (the higher the velocity the higher the heat transfer rate). The rate of convection heat transfer is expressed by Newton's law of cooling:

$$Q_{\text{conv}}^* = hA(T_s - T_\infty) \quad \text{Equation 2-29}$$

The convective heat transfer coefficient  $h$  strongly depends on the fluid properties and roughness of the solid surface, and the type of the fluid flow (laminar or turbulent). In this research is only focused on **laminar flows**.

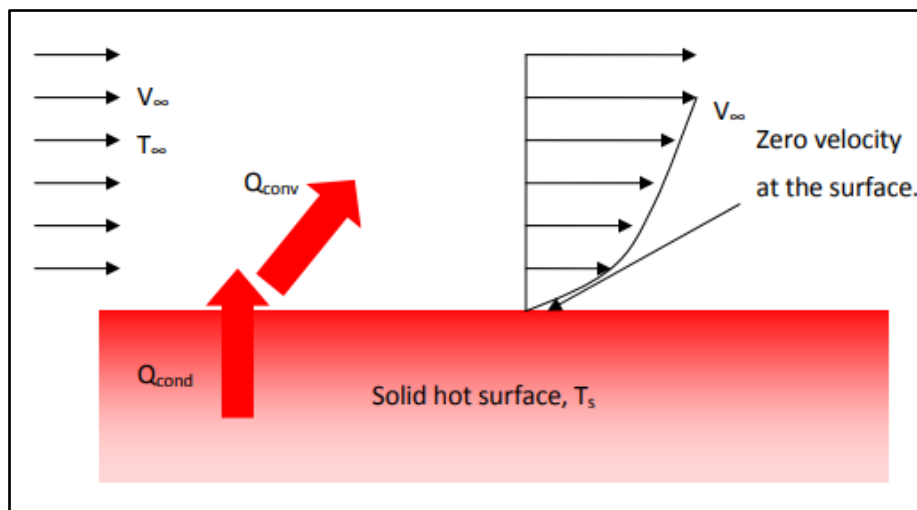


Figure 2-20 Forced Convection

It is assumed that the velocity of the fluid is zero at the wall, this assumption is called no-slip condition. As a result, the heat transfer from the solid surface to the fluid layer adjacent to the surface is by pure conduction since the fluid is motionless. Thus,

$$\dot{q}_{\text{conv}} = \dot{q}_{\text{cond}} = -k_{\text{fluid}} \left. \frac{\partial T}{\partial y} \right|_{y=0} \quad \text{Equation 2-30}$$

Substitute Equation 2.2-15 into Equation 2.2-16 gives:

$$\mathbf{h} = \frac{-k_{\text{fluid}} \left. \frac{\partial T}{\partial y} \right|_{y=0}}{(T_s - T_\infty)} \quad \text{Equation 2-31}$$

The convection heat transfer coefficient (h), in general, varies along the flow direction. The mean or average convection heat transfer coefficient for a surface is determined by averaging the local heat transfer coefficient over the entire surface.

In force convection related dimensionless numbers are:

**Reynolds number:** ratio of inertia forces to viscous forces in the fluid.

$$\mathbf{Re} = \frac{\text{inertia forces}}{\text{viscous forces}} = \frac{\rho \mathbf{v} \delta}{\mu} = \frac{\mathbf{v} \delta}{\nu} \quad \text{Equation 2-32}$$

The Reynolds number (Re) helps predict flow patterns in different fluid flow situations. At low Reynolds numbers, flows tend to be dominated by laminar flow (fluid particles following smooth paths in layers). While at high Reynolds numbers flows tend to be turbulent which is not considered in this research.

**Nusselt number:** ratio of convection over conduction heat transfer.

$$\mathbf{Nu} = \frac{q_{\text{conv}}^*}{q_{\text{cond}}^*} = \frac{h \delta}{k} \quad \text{Equation 2-33}$$

$$\mathbf{Nu} = \frac{q_{\text{CFD}}''(L_x)}{k(T_w - T_b)} \quad \text{Equation 2-34}$$

where  $\delta$  is the characteristic length (m). Nusselt number represents the enhancement of heat transfer through a fluid as a result of convection relative to conduction across the same fluid layer.

## **2.2-9 Magnetic Nanoparticles**

Magnetic nanoparticles are a class of nanoparticle that can be manipulated using magnetic fields. Such particles commonly consist of two components, a magnetic material, often iron, nickel and cobalt, and a chemical component that has functionality. While nanoparticles are smaller than 1 micrometer in diameter (typically 1–100 nanometers), the larger microbeads are 0.5–500 micrometer in diameter. Magnetic nanoparticle clusters that are composed of a number of individual magnetic nanoparticles are known as magnetic nanobeads with a diameter of 50–200 nanometers. Magnetic nanoparticle clusters are a basis for their further magnetic assembly into magnetic nanochains. The addition of magnetic nanoparticles improves the thermal conductivity of the MPCM and increases solar energy absorption, which accelerates the capacity efficiency and expands the storage capacity (Balakinab, et al., 2019).

### **Types of magnetic nanoparticles**

- Oxides: ferrites. Ferrite nanoparticles or iron oxide nanoparticles (iron oxides in crystal structure).
- Ferrites with a shell. TEM image of a maghemite magnetic nanoparticle cluster with silica shell.
- Metallic. Metallic nanoparticles may be beneficial for some technical applications due to their higher magnetic moment.
- Metallic with a shell. The metallic core of magnetic nanoparticles may be passivated by gentle oxidation, surfactants.

## 2.2-10 Direct absorption solar collector with magnetic nanofluid: CFD model and parametric analysis

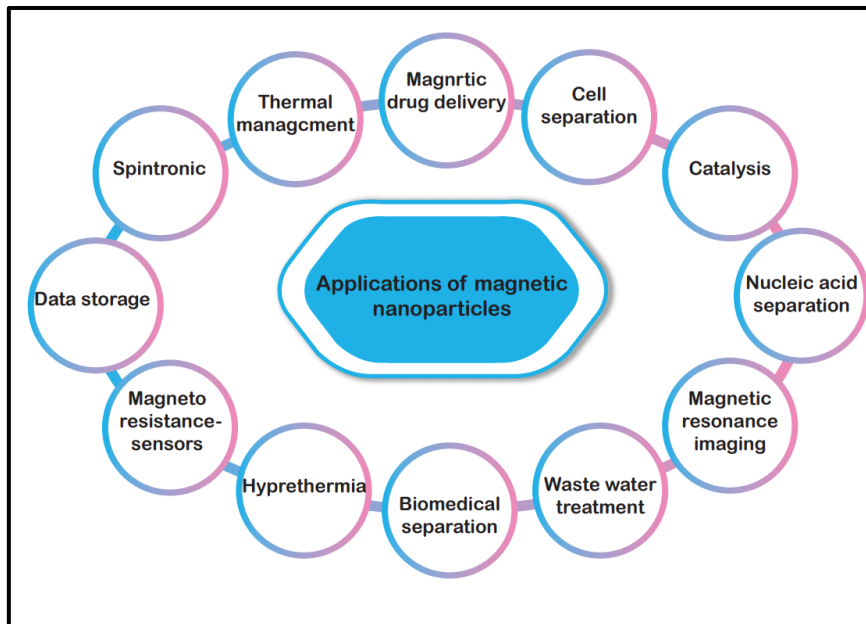


Figure 2-21

Adding nanoparticles is a routine procedure which can easily be carried out in the course of the various methods for manufacturing organic solar cells. It is important, however, not to add too many nanoparticles to the solar cell, because the internal structure of organic solar cells is finely adjusted to optimise the distance between the light-collecting, active materials, so that the pairs of charge carriers can be separated as efficiently as possible. These structures lie in the range of 10 to 100 nanometres.

## 2.2-11 Radiation Models

### 2.2-11.1 Sola Load Model (Solar Ray Tracing and DO (discrete ordinate) irradiation)

Thermal radiation is electromagnetic radiation generated by the thermal motion of charged particles in matter. All matter with a temperature greater than absolute zero emits thermal radiation. Particle motion results in charge-acceleration or dipole oscillation which produce electromagnetic radiation. Sunlight is part of thermal radiation generated by the hot plasma of

the Sun. The Earth also emits thermal radiation, but at a much lower intensity and different spectral distribution (infrared rather than visible) because it is cooler. The Earth's absorption of solar radiation, followed by its outgoing thermal radiation, are the two most important processes that determine the temperature and climate of the Earth in most climate models.

ANSYS FLUENT (2018) provides a solar load model that can be used to calculate the radiation effects from the sun's rays that enters the computational domain. The Solar load is available in the 3D solver only and can be used to model both steady and unsteady flows. Two options available for the model are **Solar Ray Tracing** and **DO (Discrete Ordinate)** radiation. Solar Ray Tracing is used in this simulation due to its highly efficient method and practical means of applying solar loads as heat sources in the energy equations. The solar load model's ray tracing' algorithm can be used to predict the direct illumination energy source that results from incident solar radiation. This approach utilizes a beam that is modelled using the sun position vector and illumination parameters, applies it to any or all wall or inlet/outlet boundary zones specified, performs a face-by-face shading analysis to determine well-defined shadows on all boundary faces and interior walls and finally computes the heat flux on the boundary faces that result from the incident radiation. The solar ray tracing model includes only boundary zones that are adjacent to fluid zones in the ray tracing calculation. In other words, boundary zones that are attached to solid zones are ignored. The resulting heat flux that is computed by the solar ray tracing algorithm is coupled to the ANSYS FLUENT calculation via a source term in the energy equation ( $Q_{\text{rad}}$ ). The heat sources are added directly to computational cells bordering each face and are assigned to adjacent cells in the following order: shell conduction cells, solid cells, and fluid cells. The solar ray tracing algorithm also accounts for internal scattered and diffusive loading. The reflected component of direct solar irradiation is tracked. A fraction of this radiative heat flux, called internally scattered energy is applied to all the surfaces

participating in the solar load calculation, weighted by area. However, Solar Ray Tracing is not a participating radiation model. The model does not deal with emission from surfaces, and the reflecting component of the primary incident load is distributed uniformly across all surfaces rather than being local to the surfaces reflected.

### 2.2-11.2 The radiative transfer equation (RTE)

The radiative transfer equation (RTE) for an absorbing, emitting, and scattering medium at position  $\vec{r}$  in the direction  $\vec{s}$  takes the form (Modest, 1993):

$$\frac{dI(\vec{r}, \vec{s})}{ds} + (a + \sigma_s)I(\vec{r}, \vec{s}) = an^2 \frac{\sigma T^4}{\pi} + \frac{\sigma_s}{4\pi} \int_0^{4\pi} I(\vec{r}, \vec{s}') \Phi(\vec{s} \cdot \vec{s}') d\Omega' \quad \text{Equation 2-35}$$

where  $\vec{r}$  = position vector

$\vec{s}$  = direction vector

$\vec{s}'$  = scattering direction vector

s = path length (m)

a = absorption coefficient ( $m^{-1}$ )

n = refractive index

$\sigma_s$  = scattering coefficient ( $m^{-1}$ )

$\sigma$  = Stefan-Boltzmann constant ( $5.669 \times 10^{-8} W/m^2 - K^4$ )

I = radiation intensity, which depends on position  $\vec{r}$  and direction  $\vec{s}$  ( $W/m^2$ )

T = local temperature (K)

$\Phi$  = phase function

$\Omega'$  = solid angle (steradians)

$(a + \sigma_s)s$  is the optical thickness or opacity of the medium. The refractive index  $n$  is important when considering radiation in semi-transparent media. Figure 2-22 illustrates the process of radiative heat transfer.

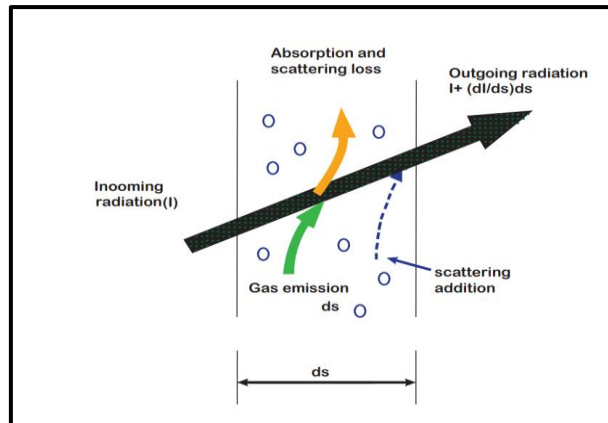


Figure 2-22 Radiative heat transfer process

### 2.2-11.3 Rosseland

Since surface emission is also an important factor in this study, the *Rosseland radiation model* will be implemented in conjunction with Solar Ray Tracing. The Rosseland radiation model assumes that the intensity is the black-body intensity at the fluid temperature. Since the radiative heat flux has the same form as the Fourier conduction law, it is possible to write as follows:

$$q = q_c + q_r = -(k + k_r)\nabla T \quad \text{Equation 2-36}$$

$$k_r = 16\sigma\Gamma n^2 T^3 \quad \text{Equation 2-37}$$

Here  $q_c$  is thermal conduction flux,  $\nabla T$  is temperature gradient,  $k$  is the thermal conductivity (W/mK),  $n$  is the refractive index and  $k_r$  is the radiative conductivity (W/mK). The appropriate substitution for radiative solar flux is made in the energy equation to compute the temperature field. The Rosseland model has the advantage (compared with more complex alternative

models (e.g., Chandrasekhar's discrete ordinates, the Trauggott P1 differential or Schuster-Schwartzchild two flux models as elucidated by (Modest, 1993) in that supplementary transport equation for the incident radiation do not have to be solved and this greatly accelerates computational speed and significantly less memory is required. However, the Rosseland model can be used only for optically thick media. It is recommended for use when the optical thickness exceeds 3. In ANSYS FLUENT the Rosseland model is only available for the pressure-based solver, which is adopted in the present computations. Regarding the nanofluid modelling, the Tiwari-Das model is employed, which allows different concentrations (volume fraction) and types of metallic nanoparticles to be studied in ANSYS.

#### 2.2-11.4 P1

The P-1 radiation model is the simplest case of the more general P-N model, which is based on the expansion of the radiation intensity  $I$  into an orthogonal series of spherical harmonics (first order approximation). The P-1 Model, following equation is obtained for the radiation flux  $q_r$ :

$$\mathbf{q}_r = -\frac{1}{3(a+\sigma_s)-C\sigma_s}\nabla\mathbf{G} \quad \text{Equation 2-38}$$

where  $a$  is the absorption coefficient,  $\sigma_s$  is the scattering coefficient,  $G$  is the incident radiation, and  $C$  is the linear anisotropic phase function coefficient.

$$\Gamma = \frac{1}{3(a+\sigma_s)-C\sigma_s} \quad \text{Equation 2-39}$$

Equation 5.3-2 simplifies to

$$\mathbf{q}_r = -\Gamma\nabla\mathbf{G} \quad \text{Equation 2-40}$$

The transport equation for  $G$  is

$$\nabla \cdot (-\Gamma\nabla\mathbf{G}) = -a\mathbf{G} + 4an^2\sigma\mathbf{T}^4 = \mathbf{S}_G \quad \text{Equation 2-41}$$



where  $n$  is the refractive index of the medium,  $\sigma$  is the Stefan-Boltzmann constant and  $G$  is a user-defined radiation source. ANSYS FLUENT solves this equation to determine the local radiation intensity when the P-1 model is active.

Combining Equations 2.2-26 and 2.2-27 yields the following equation:

$$-\nabla \cdot \mathbf{q}_r = \mathbf{aG} - 4\mathbf{an}^2\sigma\mathbf{T}^4 \quad \text{Equation 2-42}$$

The expression for  $-\nabla \cdot \mathbf{q}_r$  can be directly substituted into the energy equation to account for heat sources (or sinks) due to radiation.

The P-1 model has several advantages over the DTRM. For the P-1 model, the RTE (Equation 2.2-35) is a diffusion equation, which is easy to solve with little computational costs. The model includes the effect of scattering and the P-1 model works reasonably well. In addition, the P-1 model can easily be applied to complicated geometries with curvilinear coordinates.

P-1 model assumes that all surfaces diffuse. This means that the reflection of incident radiation at the surface is isotropic, with respect to the solid angle. The implementation assumes gray radiation. There may be a loss of accuracy, depending on the complexity of the geometry, if the optical thickness is small. P-1 model tends to over-predict radiative fluxes from localized heat sources or sinks.

#### **2.2-11.5 Chandrasekhar Discrete Ordinates Model (DO)**

The DO model covers all range of optical thicknesses. The model also allows the solution of radiation at semi-transparent walls (glass), which is the main component of DASCs. Computational cost is moderate for typical angular discretizations and memory requirements are modest. Thus, it is possible to include scattering, anisotropy, semi-transparent media, and particulate effects.

The DO model considers the radiative transfer equation (RTE) in the direction  $\vec{s}$  as a field equation. Thus, is written as

$$\nabla \cdot (\mathbf{I}(\vec{r}, \vec{s})\vec{s}) + (a + \sigma_s)\mathbf{I}(\vec{r}, \vec{s}) = a n^2 \frac{\sigma T^4}{\pi} + \frac{\sigma_s}{4\pi} \int_0^{4\pi} \mathbf{I}(\vec{r}, \vec{s}') \Phi(\vec{s} \cdot \vec{s}') d\Omega' \quad \text{Equation 2-43}$$

Here  $T$  is the wavelength,  $a$  is the spectral absorption coefficient, and  $I$  is the black body intensity given by the Planck function. The scattering coefficient, the scattering phase function, and the refractive index  $n$  are assumed independent of wavelength.

### Boundary and Cell Zone Condition Treatment at Opaque Walls

The discrete ordinates radiation model allows the specification of opaque walls that are interior to a domain or external to the domain e.g., copper absorber plate of flat plate DASC in chapter 7. Opaque walls are treated as gray radiation is being computed. Figure 5.3.8 shows a schematic of radiation on an opaque wall in ANSYS FLUENT.

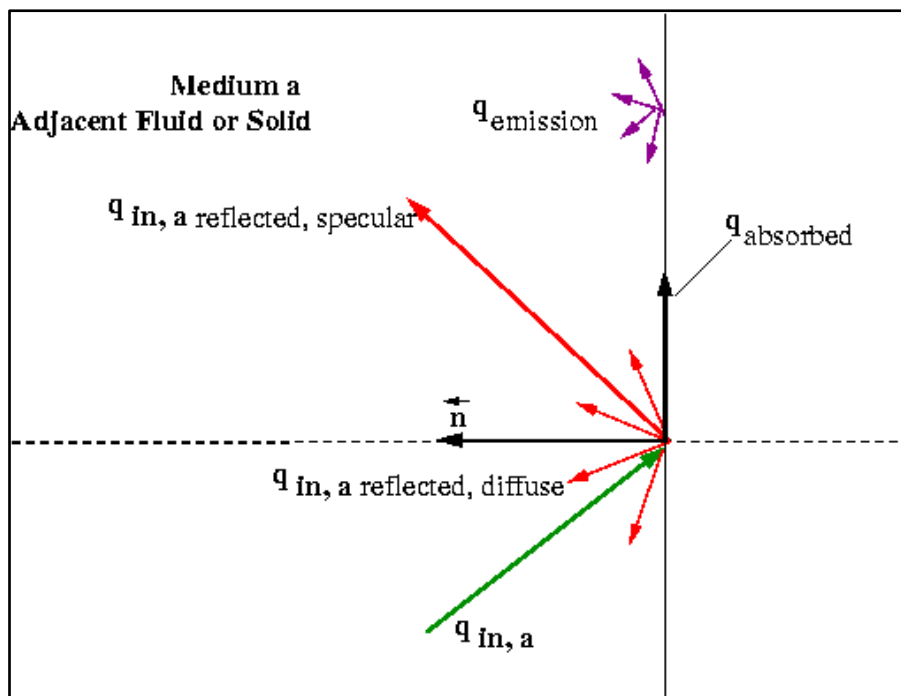


Figure 2-23 Treatment for opaque walls

The diagram in Figure 2-23 shows incident radiation  $q_{in,a}$  on side a of an opaque wall. Some of the radiant energy is reflected diffusely and specularly, depending on the diffuse fraction  $f_d$  for side a of the wall that you specify as a boundary condition.

Some of the incident radiation is absorbed at the surface of the wall and some radiation is emitted from the wall surface as shown in Figure 2.23. The amount of incident radiation absorbed at the wall surface and the amount emitted back depends on the emissivity of that surface and the diffuse fraction  $f_d$ .  $q_{in}$  is the amount of radiative energy incident on the opaque wall, then the following general quantities are computed by ANSYS FLUENT for opaque walls.

$$\text{emission from the wall surface} = n^2 \epsilon_{tb} \sigma T_w^4 \quad \text{Equation 2-44}$$

$$\text{diffusely reflected energy} = f_d (1 - \epsilon_w) q_{in} \quad \text{Equation 2-45}$$

$$\text{specularly reflected energy} = (1 - f_d) (1 - \epsilon_w) q_{in} \quad \text{Equation 2-46}$$

$$\text{absorption at the wall surface} = \epsilon_w q_{in} \quad \text{Equation 2-47}$$

where  $f_d$  is the diffuse fraction,  $n$  is the refractive index of the adjacent medium,  $\epsilon_w$  is the wall emissivity,  $\sigma$  is Boltzmann's Constant, and  $T_w$  is the wall temperature.

### **Semi-Transparent Exterior Walls**

Figure 2-24 shows the general case of an irradiation beam  $q_{in,a}$  applied to an exterior semi-transparent wall with zero thickness and a non-zero absorption coefficient for the material property. An irradiation flux passes through the semi-transparent wall from outside the computational domain (Figure 2-24) into the adjacent fluid or solid medium A. The transmitted radiation can be refracted (bent) and dispersed specularly and diffusely, depending on the refractive index and the diffuse fraction that you provide as a boundary condition input. Note

that there is a reflected component of  $q_{irrad}$  when the refractive index of the wall  $n_b$  is not equal to 1, as shown.

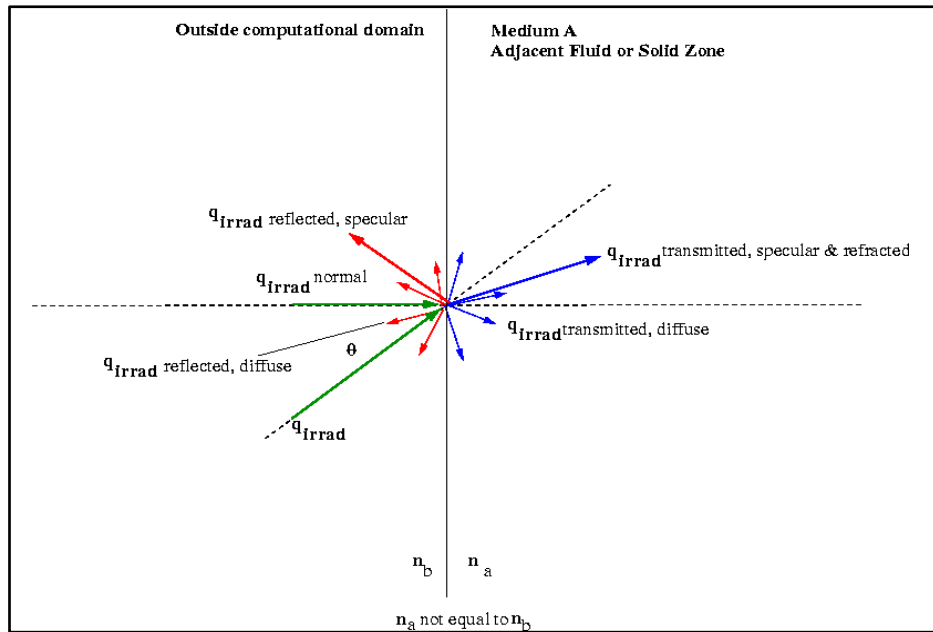


**Figure 2-24 Treatment at semi-transparent walls**

Incident radiation can also occur on external semi-transparent walls. The irradiation beam is defined by the magnitude, beam direction, and beam width that you supply. The irradiation magnitude is specified in terms of an incident radiant heat flux ( $W/m^2$ ). Beam width is specified as the solid angle over which the irradiation is distributed (i.e., the beam  $\theta$  and  $\phi$  extents). The default beam width in ANSYS FLUENT is  $1e^{-6}$  degrees which is suitable for collimated beam radiation. Beam direction is defined by the vector of the centroid of the solid angle. For external solar load, Direct Irradiation Parallel to the Beam in the Wall boundary condition dialog box is applied, then  $q_{irrad}$  for irradiation (Figure 2-25) and ANSYS FLUENT computes and uses the surface normal flux  $q_{irrad,normal}$  in its radiation calculation.

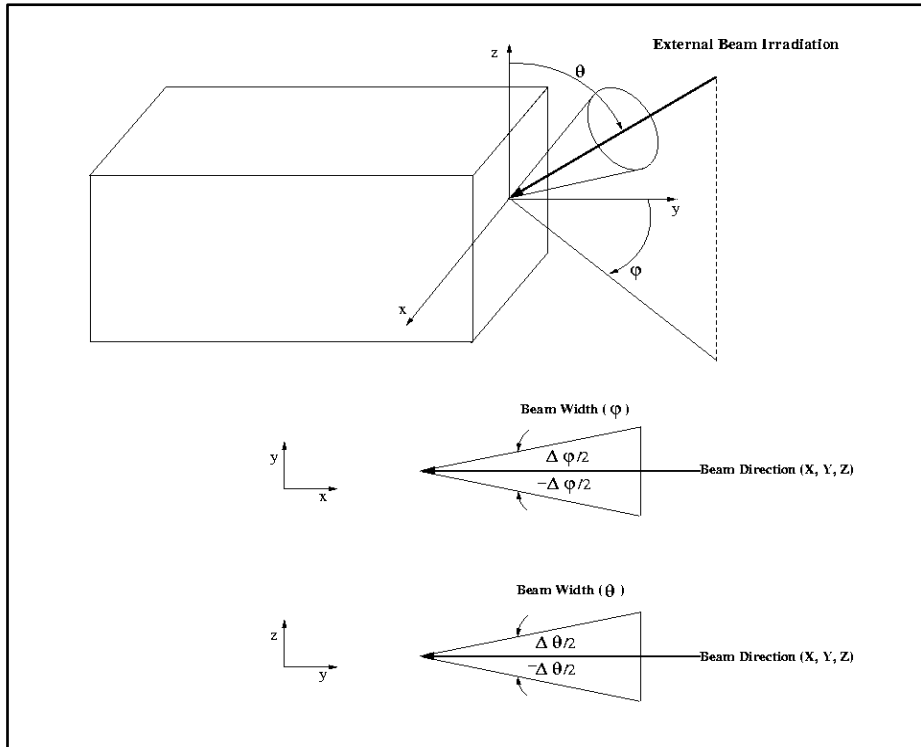


**Figure 2-25 Beam Width and Direction for External Irradiation Beam**

### ***Limitations***

In cases with significant emission or absorption of radiation in a participating solid material, such as the absorption of long wavelength radiation in a glass solar wall, the use of semi-transparent thin walls can result in the prediction of unphysical temperatures in the numerical solution. In a 3-dimensional model this can be overcome by activating the shell conduction option for the respective thin wall. Otherwise, where possible, it is advisable to represent the solid wall thickness explicitly with one or more layers of cells across the wall thickness.

### ***Radiation- dimensionless numbers- Rosseland Number $Rn$***

$$Rn = \frac{16\sigma^* T_0^3}{3k^* \mu_0 C_f}, \quad \text{Equation 2-48}$$

This again features only in chapter 8 where a solar MHD peristaltic collector design is studied theoretically and numerically with MAPLE software.

Rosseland's model assumes radiative equilibrium and that the nanofluid has gray properties which are popular in solar pump designs. Furthermore, Rosseland's model assumes that the intensity is the black-body intensity at the nanofluid temperature and since it is generally confined to incompressible flows it is particularly appropriate for low-speed transport characteristic of porous media hydromagnetic pumping. The parameter  $Rn$  embodies the relative contribution of conduction heat transfer to thermal radiation transfer. It is variously known in thermal physics as the Stark number and Rosseland-Boltzmann number. Large  $Rn$  values imply small radiation contribution and small  $Rn$  values correspond to high radiative flux. As  $Rn \rightarrow 0$ , thermal radiation flux contribution vanishes and the dominant mode of heat transfer is thermal conduction. Hence with smaller  $Rn$  values, thermal radiation is stronger than thermal conduction (the contribution is only equal for both modes of heat transfer when  $Rn = 1$ ). Thermal radiation supplements the fluid thermal conductivity via the energy equation and serves to increase temperatures,

## **2.3 Numerical Aspects**

As noted earlier, ANSYS FLUENT and MAPLE are the two numerical tools that have been employed in this PhD.

### **2.3-1 ANSYS FLUENT**

A summary of the fundamental methodology for building an ANSYS FLUENT solar DASC simulation is given in Figure 2-26 below:

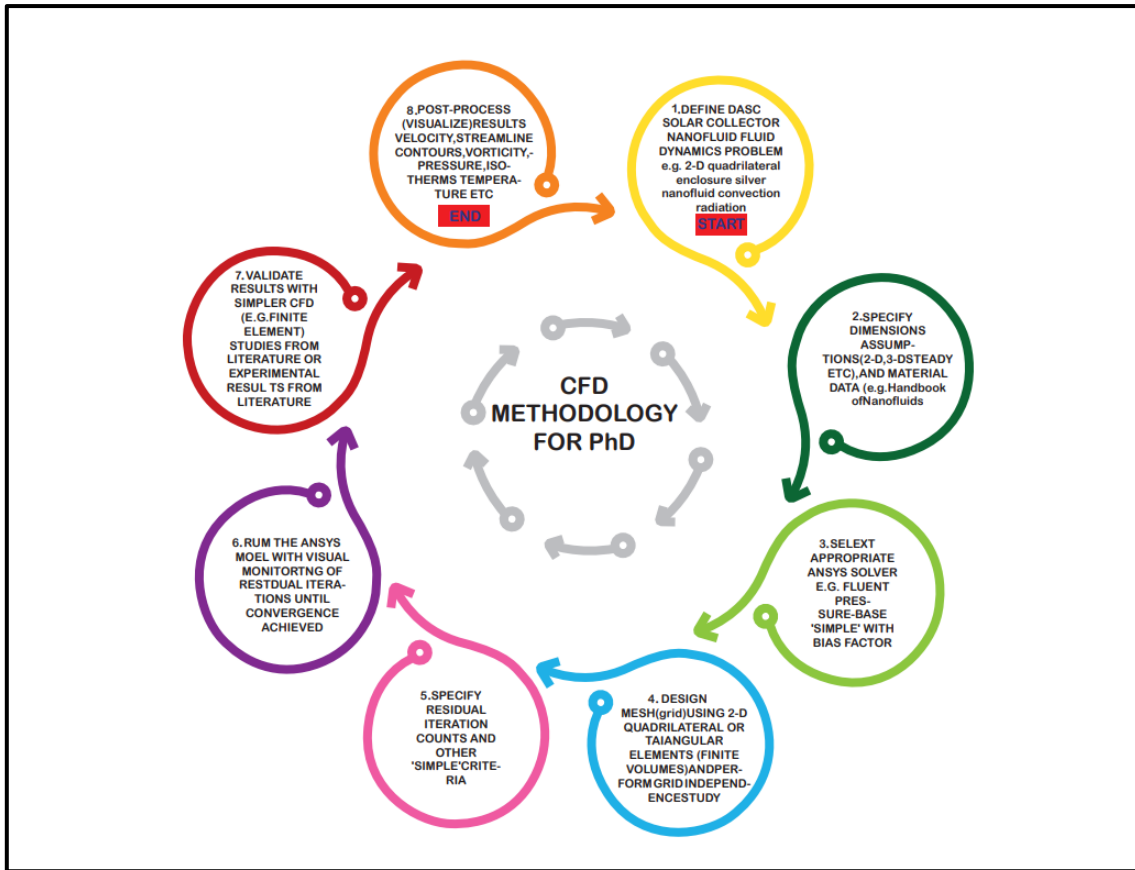


**Figure 2-26 CFD ANSYS FLUENT Methodology for solving nanofluid DASC enclosure boundary value problem**

This research started with a numerical investigation on natural convection in solar enclosures (flat plate solar collector). The two-dimensional square, rectangular and trapezoidal models were studied under the natural convection of constant heat flux with radiation effect, as presented in Chapters 3 and 4 where various types of nanofluids were considered as working fluids, e.g., copper-water, titanium dioxide-water, Aluminium oxide-water, Silver-water and Diamond-water nanofluid, as listed in the Appendix. The three-dimensional box (prism) enclosure models were investigated for the natural convection of a constant temperature in a cube, where the radiation was neglected due to the complexity of the geometry and Gold-water nanofluid was considered in Chapter 5. Three-dimensional annulus DASC model, mixed convection was investigated using a solar flux model, which is available in ANSYS to replicate

solar radiation from the sun coupled with the Rosseland radiation model in Chapter 6. The last simulation is based on the investigation into the forced convection of a three-dimensional flat plate DASC using solar ray tracing model, which is available in ANSYS to replicate solar energy from the sun over a period of time. Discrete Ordinates (DO) radiation model was applied in Chapter 7. All these chapters focused on non-deformable boundary Thermal Direct Absorber Solar Collector and are investigated using computational fluid dynamics software (ANSYS FLUENT). However, in chapter 8 I conducted a parallel investigation on a different deformable peristaltic solar collector configuration in which I also explored magnetic nanoparticles, described in due course. The research methodology validation steps for chapters 3-7 (ANSYS FLUENT simulations) are shown in Figure 2-27.

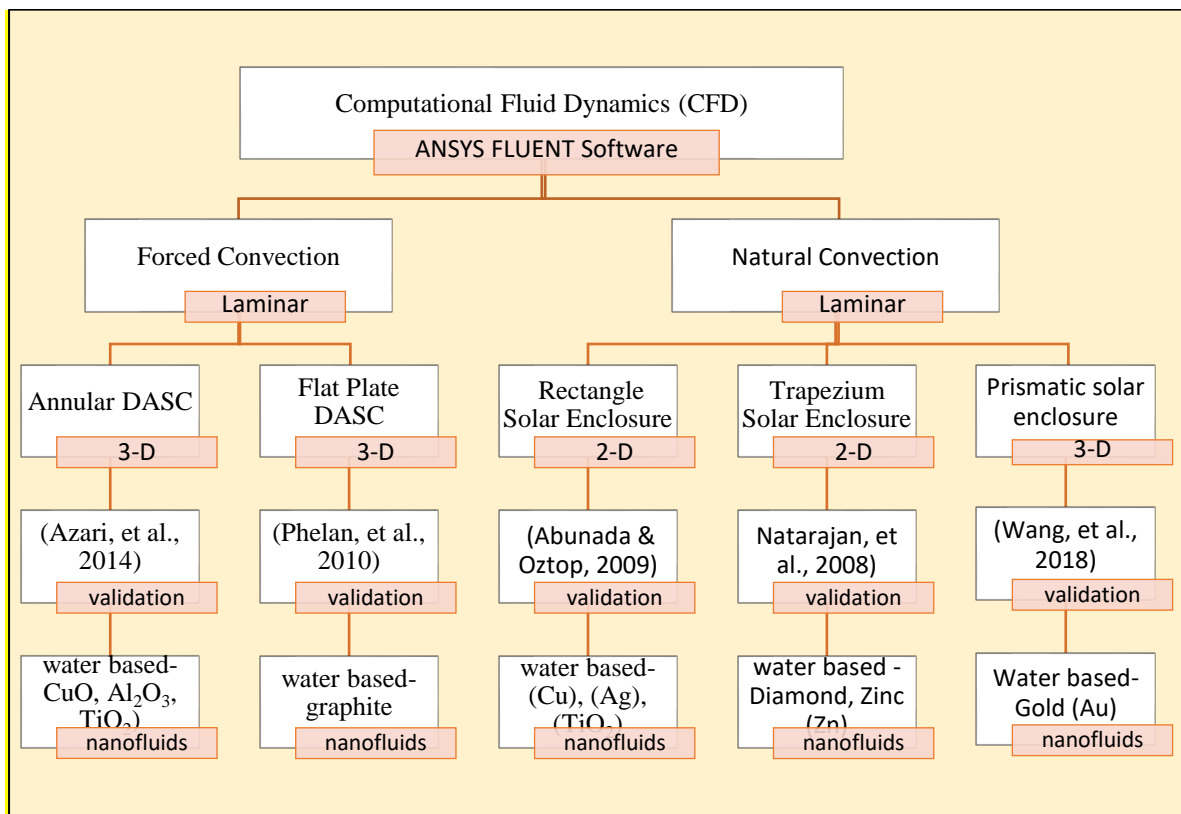


**Figure 2-27 Validation Methodology Diagram**



All numerical simulations **in chapters 3-7** are done with Computational Fluid Dynamic (CFD) software, (ANSYS FLUENT) which is available at the University of Salford. The software solves the **Navier-Stokes equations, Energy (heat) equation, and Radiation heat transfer models (Rosseland, P1 and DO)**. The Tiwari-Das volume fraction nanofluid model is employed to simulate nano-particle effects. Computations are conducted with the **pressure-based solvers** and the use of the **SIMPLE** algorithm available in ANSYS FLUENT, as shown in Figure 2-28 The SIMPLE algorithm can also be referred to the projection method where the 'u,' 'v,' 'w,' and 'p' fields must be solved separately. In the projection method, the constraint of mass conservation (continuity) of the velocity field is achieved by solving a pressure (or pressure correction) equation. The pressure equation is derived from the continuity and the momentum equations in such a way that the velocity field, corrected by the pressure, satisfies the continuity. Since the governing equations are nonlinear and coupled to one another, the solution process involves iterations wherein the entire set of governing equations is solved repeatedly until the solution converges. Then all the flow field variables such as velocity streamline function and temperature are automatically plotted and analysed graphically in the post-processing stage.

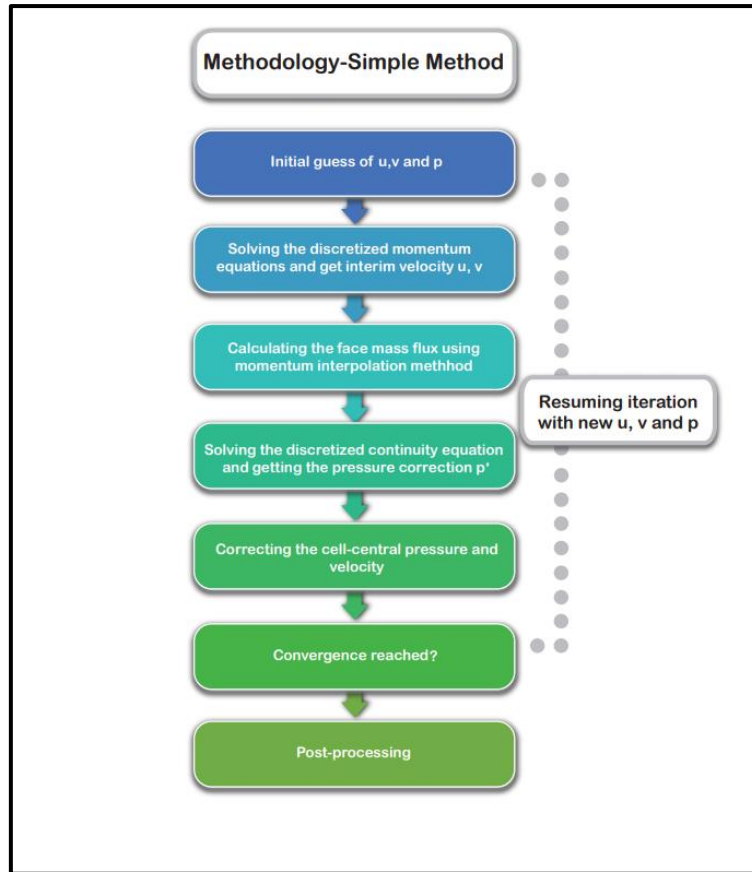


Figure 2-28 Methodology of Simple Method

### 2.3-1.1 Mass Conservation Equation

The unsteady equation for mass conservation or continuity is written as follows:

$$\frac{\partial \rho}{\partial t} + \nabla \cdot (\rho \vec{v}) = S_m \quad \text{Equation 2-49}$$

The equation above is the general form of the mass conservation equation which is valid for both compressible and incompressible flows. The source  $S_m$  is the mass (kg) applied to the continuous phase from the dispersed second phase and any user-defined sources. Here  $(\vec{v})$  is the velocity vector in three dimensions,  $\rho$  is fluid density ( $\text{kg/m}^3$ ),  $t$  is time (s).

### 2.3-1.2 Momentum Conservation Equation

Conservation of momentum in an inertial (non-accelerating) reference frame takes the form.

$$\frac{\partial}{\partial t} (\rho \vec{v}) + \nabla \cdot (\rho \vec{v} \vec{v}) = -\nabla p + \nabla \cdot (\bar{\bar{\tau}}) + \rho \vec{g} + \vec{F} \quad \text{Equation 2-50}$$

Where,  $p$  is the static pressure (Pa),  $\bar{\tau}$  is the stress tensor (N/m<sup>2</sup>),  $\rho\vec{g}$  and  $\vec{F}$  are the gravitational body force (N) and external body force (N) e.g., thermal buoyancy, respectively (e.g. arising from interaction with the dispersed phase).  $\vec{F}$  also has other model-dependent source terms such as user-defined sources and porous-media. The  $\bar{\tau}$  term is given by:

$$\bar{\tau} = \mu \left[ (\nabla\vec{v} + \nabla\vec{v}^T) - \frac{2}{3} \nabla \cdot \vec{v} \mathbf{I} \right] \quad \text{Equation 2-51}$$

Here  $\mu$  is the dynamic viscosity (kg/(ms)),  $\mathbf{I}$  is the unit tensor and the last term shown is the effect of volume dilation. No slip velocity conditions are applied at the rigid walls and a moving boundary velocity at the top wall.

### 2.3-1.3 ANSYS FLUENT

The parameters analyzed are:

Pressure

Streamline velocity

Temperature

Isotherms

Vorticity (this is a gradient of certain velocity components)

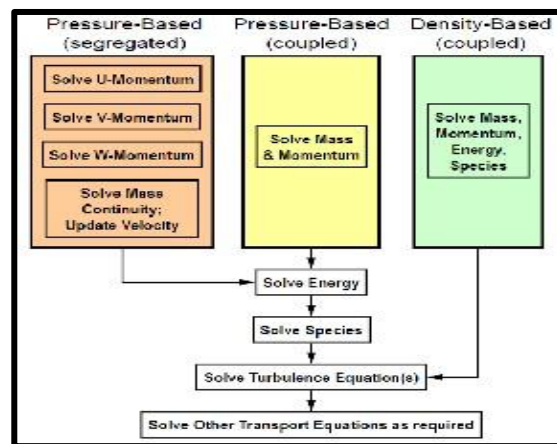


Figure 2-29 ANSYS Fluent explained in further detail

ANSYS Fluent utilises meshes comprised of either triangular or quadrilateral cells or a combination of the two in 2D, whereas for 3D tetrahedral, hexahedral, polyhedral, pyramid, wedge cells or a combination of these are used. The choice of which mesh type to use will depend on the problem that needs solving. To decide on mesh type 3 main factors need to be considered they are: setup time, computational expense, and numerical diffusion.

### **Set up time**

Ideally in a flow problem in engineering it comprises of complicated geometries, to solve this quadrilateral or hexahedral elements for such problems is disadvantageous as it can be extremely time consuming and, in some cases, can be impossible. Set up time for complicated geometries is the critical reason that when using unstructured meshes to utilise either triangular or tetrahedral cells. Other drawbacks which are associated with using quadrilateral or hexahedral elements (*also known as structured or block structured meshes*) includes the geometry may become oversimplified, mesh quality issues, and a less efficient mesh distribution i.e., finite resolution in regions of less importance which can result in a high cell count.

### **Computational expense**

In the case of complicated geometries or the range of length scales of the flow is significant then a triangular/tetrahedral mesh can be developed with little cells than the equivalent mesh which consists of quadrilateral/hexahedral elements. This is due to a triangular/tetrahedral mesh permits clustering of cells in chosen regions of the flow domain. Whereas structured quadrilateral/hexahedral meshes usually force cells to be positioned in areas where they are not required. A property of quadrilateral/hexahedral elements that may make this more cost

effective in some scenarios includes that since they allow a much larger aspect ratio than triangular/tetrahedral then this will invariably influence the skewness of the cell, this can be undesired and can affect the accuracy and convergence. In the situation of a simple geometry in where the flow fits well to the shape of the geometry, i.e., a long thin duct then uses a mesh of relatively high aspect ratio quadrilateral/hexahedral cells. The mesh is likely to have less cells than triangular/tetrahedral cells. Furthermore, by changing the domain of a tetrahedral mesh into a polyhedral mesh will cause fewer cell count than the original mesh. Whereas the result in a coarser mesh, convergence will usually be quicker, save time and computational expense.

### **Numerical diffusion**

Main source of error in multidimensional situations is numerical diffusion this is known as “false diffusion”. This term is being expressed because the diffusion is not real but its effect on a flow calculation is analogous to that of increasing the real diffusion coefficient. This is visible when the actual diffusion is much small than expected when the situation is convection-dominated. Finite amount of numerical diffusion can be found in all practical numerical methods for resolving fluid flow. This is due to as numerical diffusion evolves from errors which are generated by representing the fluid flow equations in discrete form. To manage numerical diffusion could be to refine the mesh and is minimised when the flow is aligned with the mesh (Kuharat, 2017).

### **2.3-2 Maple numerical quadrature**

MAPLE is an excellent symbolic software with many libraries of built in ready-to-use numerical solvers for ordinary and partial differential problems. One of the most powerful methods available is Runge–Kutta–Merson numerical quadrature (“RK45 algorithm”)

(maplesoft, 2019) which can solve numerous radiative-convection nonlinear flow problems. In MAPLE this quadrature is used to yield temperature and stream function. The appropriate velocity is then computed in a sub-iteration loop. This approach has been extensively implemented recently in many heat transfer problems including peristaltic thermal convection flows (Tripathi & Bég, 2012), thermo-solutal slip radiative convection flows (Bég, et al., 2014), magnetic materials processing (Uddin, et al., 2014) (Bég, et al., 2015), nanofluid dynamics with radiation heat transfer (Uddin, et al., 2015), non-Newtonian bioconvection (Bég, et al., 2015) (Uddin, et al., 2016) (Latiff, et al., 2016), variable thermophysical property convection (Bég, et al., 2016), rotating thermal convection (Bég, et al., 2016), hypoxia biofluid dynamics (Srivastava, et al., 2016), porous media multi-physical convection (Uddin, et al., 2016) (Uddin, et al., 2016), radiative-convective-conductive energy conversion (Uddin, et al., 2016), enclosure bioprocessing flows (Bhargava, et al., 2017), bio-nano fuel cells (Uddin, et al., 2017) (Bég, et al., 2017), electro-osmotic pumping (Tripathi, et al., 2017), melting convection (Amirson, et al., 2019) and anisotropic mass transfer coating flows (Bég, et al., 2019). The robustness and stability of this numerical method is therefore well established- it is highly adaptive since it adjusts the quantity and location of grid points during iteration and thereby constrains the local error within acceptable specified bounds. Many different wall boundary conditions which arise in DASC enclosure flows are easily accommodated. The stepping formulae although designed for nonlinear problems, are even more efficient for any order of linear differential equation and are summarized below (Bég, et al., 2019):

$$k_0 = f(x_i, y_i) \quad \text{Equation 2-52}$$

$$k_1 = f\left(x_i + \frac{1}{4}h, y_i + \frac{1}{4}hk_0\right) \quad \text{Equation 2-53}$$

$$k_2 = f\left(x_i + \frac{3}{8}h_3 y_1 + \left(\frac{3}{32}k_0 + \frac{9}{32}k_1\right)h\right) \quad \text{Equation 2-54}$$

$$k_3 = f\left(x_i + \frac{12}{13}h, y_i + \left(\frac{1932}{2197}k_0 - \frac{7200}{2197}k_1 + \frac{7296}{2197}k_2\right)h\right) \quad \text{Equation 2-55}$$

$$k_4 = f\left(x_i + h, y_i + \left(\frac{439}{216}k_0 - 8k_1 + \frac{3860}{513}k_2 - \frac{845}{4104}k_3\right)h\right) \quad \text{Equation 2-56}$$

$$k_5 = f\left(x_i + \frac{1}{2}h, y_i + \left(-\frac{8}{27}k_0 + 2k_1 - \frac{3544}{2565}k_2 + \frac{1859}{4101}k_3 - \frac{11}{40}k_4\right)h\right) \quad \text{Equation 2-57}$$

$$y_{i+1} = y_i + \left(\frac{25}{216}k_0 + \frac{1408}{2565}k_2 + \frac{2197}{4101}k_3 - \frac{1}{5}k_4\right)h \quad \text{Equation 2-58}$$

$$z_{i+1} = z_i + \left(\frac{16}{135}k_0 + \frac{6656}{12825}k_2 + \frac{28561}{56430}k_3 - \frac{9}{50}k_4 + \frac{2}{55}k_5\right)h \quad \text{Equation 2-59}$$

Here  $y$  denotes fourth order Runge-Kutta phase and  $z$  is the fifth order Runge-Kutta phase. An estimate of the error is achieved by subtracting the two values obtained. If the error exceeds a specified threshold, the results can be re-calculated using a smaller step size. The approach to estimating the new step size is shown below:

$$h_{new} = h_{old} \left(\frac{\epsilon h_{old}}{2|z_{i+1} - y_{i+1}|}\right)^{1/4} \quad \text{Equation 2-60}$$

This technique is particularly suitable for use with the Rosseland diffusion flux radiative model (Bég, et al., 2014) (Uddin, et al., 2015). This method is used in chapter 8 to solve the Buongiorno nanoscale solar collector MHD equations.

## SUMMARY

In this base chapter for the entire PhD, all the fundamental theory and computational methods implemented in this PhD in subsequent chapters have been presented. All relevant aspects of multi-physics have been covered – different geometrical solar collector configurations, viscous flow, nanoscale models (principally the Tiwari-Das model for chapters 3-7 and the Buongiorno

MIT Brownian motion-thermophoresis model for chapter 8) , multiple metallic (and carbon) nanoparticles, thermal convection heat transfer (both forced and natural), thermal radiation heat transfer, solar daylight tracking, nanoparticle mass transfer, deformable collector boundaries (peristaltic biomimetic design), magnetohydrodynamics, magnetic nanoparticle physics and dimensional analysis. All these are succinctly elaborated. Furthermore, two basic numerical techniques have been reviewed: **ANSYS FLUENT** (finite volume method for partial differential equation boundary value problems with mesh design for **chapters 3-7**) and **MAPLE** shooting quadrature (stepping technique for ordinary differential equation boundary value problems, **chapter 8**). In all subsequent chapters, elements of these topics are again incorporated where appropriate.



# **Chapter 3 Natural Convection of Nanofluids Inside a Two-dimensional Quadrilateral Solar Enclosure with Copper, Silver and Titania Metallic nanoparticles and multiple radiative transfer models**

## **Abstract**

Having established the theoretical and computational methodologies in Chapter 2, in this first DASC simulation I will explore the use of three different metallic nanoparticles (silver, copper and titanium oxide) in a simple 2-dimensional quadrilateral enclosure. Natural convection is considered i. e. thermal buoyancy is the dominant effect and therefore Rayleigh number is the critical control parameter. The Tiwari-Das nanoscale model is deployed in ANSYS FLUENT. The simple Rosseland and P1 radiative flux approximations are implemented, as described in Chapter 2. Extensive visualization of different geometric and nanoscale effects is included. The relative performance of the *different metallic nanoparticles* and *different radiative approximations* on thermal efficiency e. g. local Nusselt number to the enclosure (collector) boundaries is also described. To establish confidence in using ANSYS FLUENT CFD for nanofluid dynamics, the geometry considered is the simplest possible. In subsequent chapters it is modified to more complex configurations e. g. Finite volume numerical analysis of diamond and zinc nanoparticles performance in a water-based trapezium direct absorber solar collector with buoyancy effects in chapter 4, 3-dimensional tilted prismatic solar enclosure with aspect ratio and gold nanoparticles in chapter 5, forced convection in a nanofluid-based

annular solar collector with different metallic nanoparticles (copper, titania, alumina) in chapter 6 etc.

### **a. Introduction and Mathematical Model**

From the extensive literature review given in Chapter 1, the numerical analysis of natural convection heat transfer and fluid flow in enclosures has extensively been developed using different computational techniques as it is a fundamental compliment to experimental studies of solar collectors. (Abu-Nada & Oztop, 2009) investigated the effects of inclination angle on natural convection heat transfer and fluid flow in a two-dimensional enclosure filled with Cu-nanofluid. This excellent benchmark from the scientific literature was selected to use for the case study and validation- the authors of this work solved the governing equations with a finite volume technique, which is the same algorithm to that deployed in ANSYS FLUENT. They studied however the *case of zero inclination*. The direct absorber solar collector geometry considered is visualized in **Figure 3.1** in an (x,y) coordinate system.

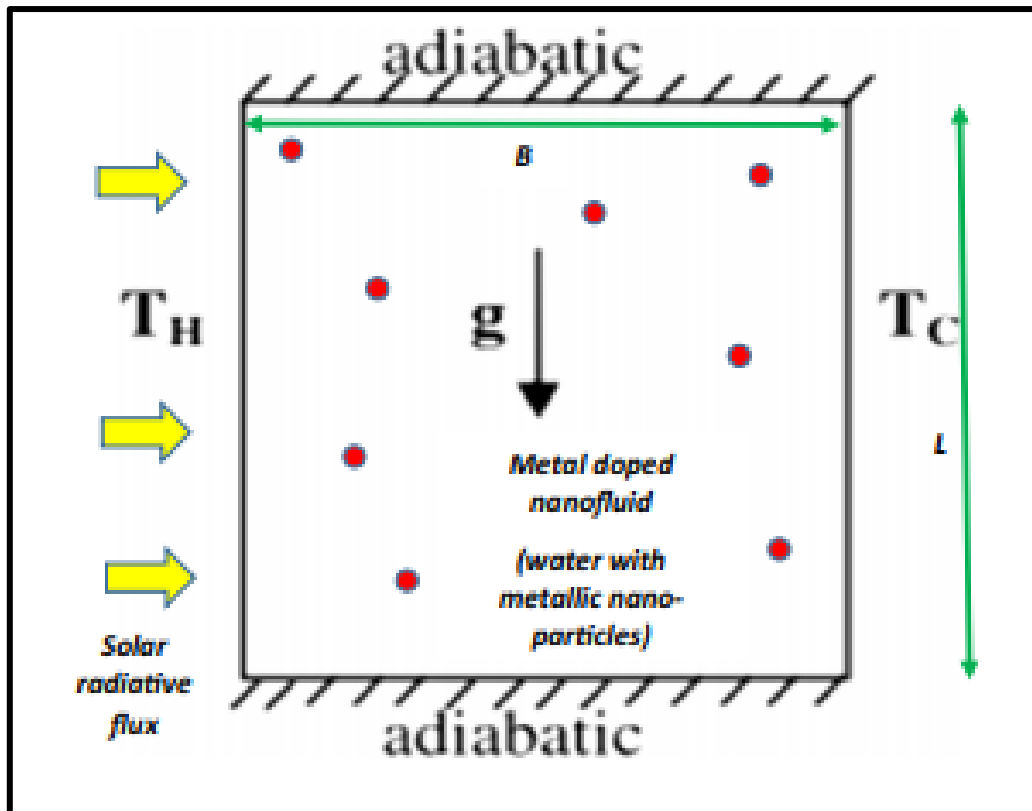


Figure 3.1 Direct absorber solar nanofluid collector enclosure geometry

The fluid in the enclosure is a water-based nanofluid containing copper nanoparticles. It is assumed that the base fluid (i.e., water) and the nanoparticles are in thermal equilibrium and no slip occurs between them. The thermo-physical properties of the nanofluid are given in **Table 3.1**. The left wall is maintained at a constant temperature ( $T_H$ ) higher than the right wall ( $T_C$ ). The thermophysical properties of the nanofluid are assumed to be constant except for the density variation, which is approximated by the Boussinesq model. The two-dimensional model of heat and fluid flow in the enclosure is designed in ANSYS FLUENT. Laminar, steady-state, incompressible flow is considered with *forced convective heat transfer*. The nanofluid is filled inside the enclosure and the Tiwari-Das nano-particle volume fraction model is deployed, which is described previously. The fundamental equations for steady viscous, incompressible laminar flow are the two-dimensional time-independent Navier-Stokes

equations, which in a Cartesian coordinate system are reduced from the general 3-D equations given in section 2.2-1 of chapter 2. The appropriate equations are now:

D'Alembert mass conservation (2-D continuity)

$$\left[ \frac{\partial u}{\partial x} + \frac{\partial v}{\partial y} \right] = 0 \quad \text{Equation 3-1}$$

x-direction momentum conservation

$$\rho_f \left[ u \frac{\partial u}{\partial x} + v \frac{\partial u}{\partial y} \right] = \rho_f F_x - \frac{\partial p}{\partial x} + \mu_f \left[ \frac{\partial^2 u}{\partial x^2} + \frac{\partial^2 u}{\partial y^2} \right] - g [1 - \beta \Delta T] \quad \text{Equation 3-2}$$

y-direction momentum conservation

$$\rho_f \left[ u \frac{\partial v}{\partial x} + v \frac{\partial v}{\partial y} \right] = \rho_f F_y - \frac{\partial p}{\partial y} + \mu_f \left[ \frac{\partial^2 v}{\partial x^2} + \frac{\partial^2 v}{\partial y^2} \right] \quad \text{Equation 3-3}$$

Energy conservation

$$u \frac{\partial T}{\partial x} + v \frac{\partial T}{\partial y} = \alpha_m \left( \frac{\partial^2 T}{\partial x^2} + \frac{\partial^2 T}{\partial y^2} \right) + Q_{\text{rad}} \quad \text{Equation 3-4}$$

Here  $(u, v)$  are velocity components in the  $(x, y)$  directions,  $\alpha_m = \frac{k_f}{\rho_f C_p}$  is the thermal diffusivity,

which is a measure of thermal inertia and  $k_f =$  fluid thermal conductivity (W/mK),  $\rho_f =$  density

(kg/m<sup>3</sup>),  $C_p =$  specific heat capacity of the nanofluid (J/Kg.K). When  $\alpha_m$  is high, the heat moves

fast and the nanofluid conducts heat quickly (higher thermal conductivity).  $T$  denotes

temperature (K),  $-g [1 - \beta \Delta T]$  is the thermal buoyancy force (featured in the  $x$ -momentum

equation which couples this equation with the energy equation, where  $\Delta T$  is the temperature

difference between the hot and cold walls (i.e.  $T_H - T_C$ ) and  $Q_{\text{rad}}$  is the *radiative heat flux*.

ANSYS FLUENT software provides a solar load model (for both steady and time-dependent flows) which may be implemented to compute the radiation effects from the sun rays entering

the computational domain; however, the solar load model is only available for 3-dimensional modelling. In the present simulation, the Rosseland and P1 algebraic flux models are therefore employed to simulate radiative heat transfer via the radiative flux term,  $Q_{rad}$ . The principal focus is to study the *heat absorption capability* of various types of nanofluids. The solar radiative flux is therefore fixed in the y-direction (imposed on the hot left wall) with a specific intensity of 877 W/m<sup>2</sup>. The solar calculator utility in ANSYS FLUENT (solar load model) is de-selected. To simulate nano-particle effects, the Tiwari-Das model is employed which allows different concentrations (volume fraction) and types of metallic nano-particles to be simulated. In ANSYS, this approach is implemented as a “one-phase flow” modification since the particles are very small. A nanofluid is defined in the ANSYS FLUENT workbench as a *new fluid* with a new density, viscosity, thermal conductivity and specific heat obtained as a function of a base fluid and nano-particle type and concentration (volume fraction). The volume fraction can be estimated from:

$$\phi = \frac{V_{np}}{V_f} \quad \text{Equation 3-5}$$

Where  $\phi$  = volume fraction,  $V_{np}$  = nano particles volume and  $V_f$  = volume of fluid. The dynamic viscosity can be estimated from:

$$\mu_{nf} = \frac{\mu_f}{(1-\phi)^{2.5}} \quad \text{Equation 3-6}$$

Here  $\mu_{nf}$  = dynamic viscosity of nanofluid (kg/m.s),  $\mu_f$  = dynamic viscosity of base fluid. The effective density and heat capacity also can be estimated from:

$$\rho_{nf} = (1 - \phi)\rho_f + \phi\rho_s \quad \text{Equation 3-7}$$

$$C_{pnf} = \frac{(1-\phi)(\rho C_p)_f + \phi(\rho C_p)_s}{\rho_{nf}}, \quad \text{Equation 3-8}$$

Here  $\rho_{nf}$  = nanofluid density,  $\rho_f$  = base fluid density,  $\rho_s$  = nanoparticle density,  $C_{pnf}$  = nanofluid specific heat. The effective thermal conductivity of fluid can be determined by the Maxwell-Garnet relation which is adopted in Tiwari and Das:

$$\frac{k_{nf}}{k_f} = \frac{k_s + 2k_f - 2\phi(k_f - k_s)}{k_s + 2k_f - \phi(k_f - k_s)} \quad \text{Equation 3-9}$$

Here  $k_{nf}$  = nanofluid thermal conductivity,  $k_f$  = fluid thermal conductivity and  $k_s$  = nanoparticle thermal conductivity. All calculated nanofluid properties (for the three different metallic nanoparticles studied i. e. copper, silver and titanium oxide) at the two volume fractions studied are given in the **Appendix**. The key local dimensionless parameters which may be computed in ANSYS FLUENT are *local Rayleigh number* (ratio of thermal buoyancy and viscous hydrodynamic force) and the *Nusselt number* (heat transfer rate along the left wall). These may be defined as:

**Rayleigh number:**  $Ra_y = \frac{g\beta}{\nu\alpha_m} (\Delta T)y^3$  Equation 3-10

**Nusselt number:**  $Nu = \frac{hL}{k_{nf}} = \frac{q''_{wCFD}(L)}{k_{nf}(\Delta T)}$  Equation 3-11

Here  $g$  denotes is gravity,  $\beta$  is coefficient of thermal expansion,  $\alpha_m$  is thermal diffusivity,  $y$  is coordinate,  $h$  is convective heat transfer coefficient,  $B$  is the width of the enclosure,  $L$  is height of the enclosure (aspect ratio  $AR = L/B$ ),  $q''_{wCFD}$  is the heat flux rate computed in ANSYS FLUENT. In addition to no-slip boundary conditions at the walls of the enclosure, the following thermal boundary conditions are imposed:

Left wall: Constant temperature,  $T= 390$  K

Right wall: Constant temperature,  $T= 290$  K

Top and Bottom walls: Adiabatic

Radiative heat transfer is also incorporated using the ANSYS P1 model and Rosseland radiative models. The Rosseland radiation model assumes that the intensity is the black-body intensity at the nanofluid temperature. The standard thermal conduction flux is augmented with the radiative flux,  $Q_{rad}$ . The Rosseland model is simpler but less realistic than the Trauggott P1 differential since the latter is not restricted to optically thick fluid media. However significantly higher mesh density is required for the P1 model. Both models are available in ANSYS with the pressure-based solver, which is therefore deployed in the present computations.

### 3.1 Grid Sensitivity Analysis

In a CFD solution, the sum is never identically zero, but (hopefully) decreases with progressive iterations. A residual can be thought of as a measure of how much the solution to a given transport equation deviates from. The average residual associated with each transport equation is monitored, to help determine when the solution has converged. For this simulation, thousands of iterations are required to converge on a final solution and the residuals may decrease by several orders of magnitude. In addition to the convergence from ANSYS residual print plot, as explained above, the grid sensitivity analysis was conducted by refining the mesh of the model until the results were constant as shown in **Figure 3.2**.

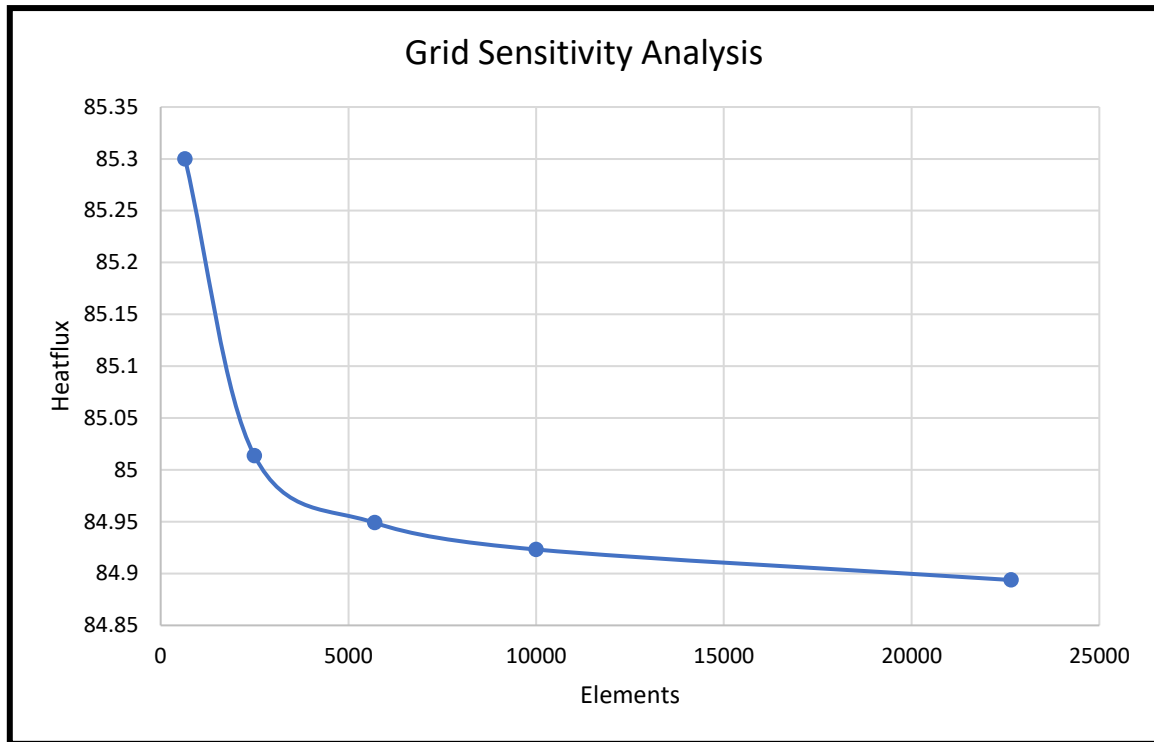


**Figure 3.2: Grid Sensitivity Analysis**

### **3.2 Validation with Published Studies**

To validate the results obtained from the ANSYS Model of the natural convection inside an enclosure filled with copper-water nanofluid, with a Rayleigh number of  $10^3$ , was compared with a study conducted by (Abu-Nada & Oztop, 2009) as shown in Figure 3.3 and Figure 3.4. Since the study used dimensionless units, to show stream function and temperature, it is difficult to replicate the values of the result. Therefore, the result will be only compared with the pattern of the stream function and temperature contour. The CFD simulation, using ANSYS fluent, agrees with the results produced by (Abu-Nada & Oztop, 2009) since both of the stream function and temperature contour patterns show very close similarity. Other test cases were also conducted to further confirm confidence in the ANSYS FLUENT model. Once confidence has been established in the simulations it is possible to progress with complexity in the geometry.



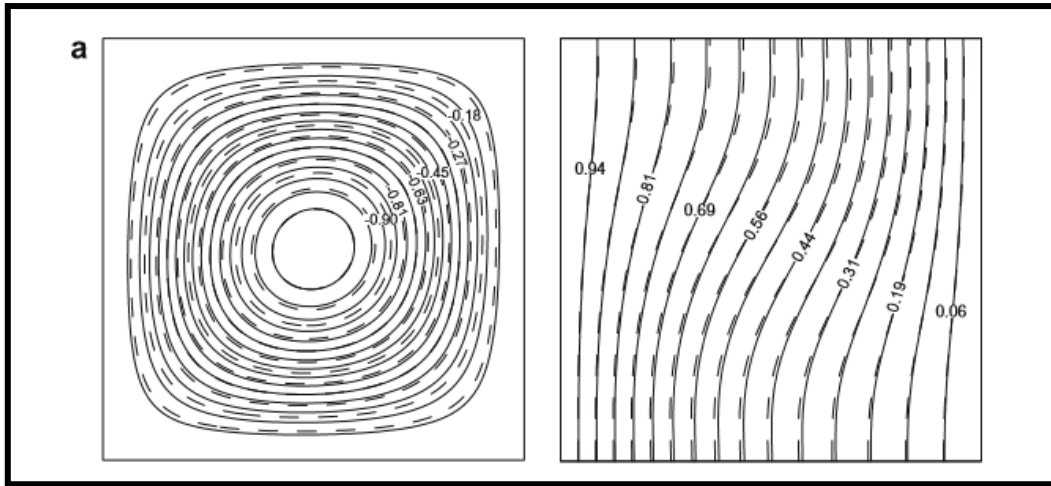


Figure 3.3 Finite Volume results for Streamline and Isotherm plots for copper-water nanofluid, with a Rayleigh number of 103, volume fraction of 0.01 (Abu-nada & Oztop, 2009)

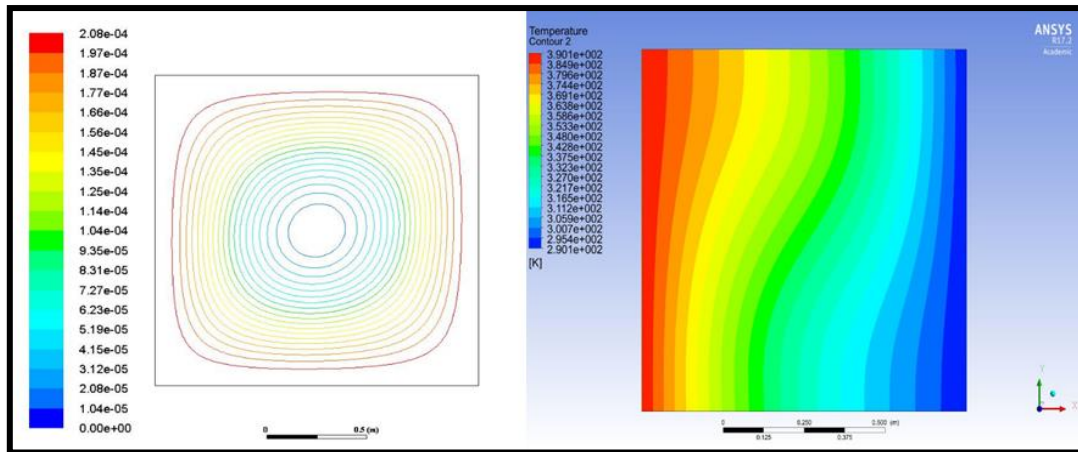


Figure 3.4 ANSYS FLUENT Streamline and Isotherm plots for copper-water nanofluid, with a Rayleigh number of  $10^3$ , volume fraction of 0.01

### 3.3 Results and Discussion

The ANSYS FLUENT results are depicted in Figure 3.5, Figure 3.6, and Figure 3.7 illustrate the results obtained with different radiative flux models, for temperature contour (isotherm) plots for Silver-water nanofluid with low volume fraction = 0.01 (1%), for a square enclosure ( $AR = 1$ ) with Rayleigh number,  $Ra = 10^4$  and radiative absorption coefficient of 0.2.

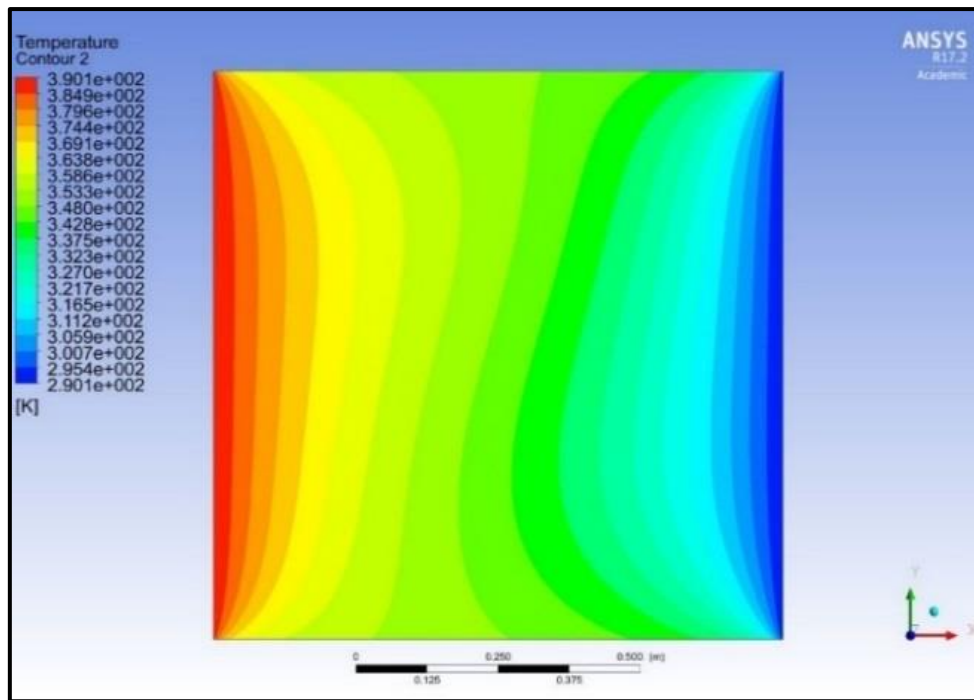


Figure 3.5 Isotherms for silver-water nanofluent,  $Ra = 10^4$ , Rosseland flux model with  $\Phi = 0.01$ .

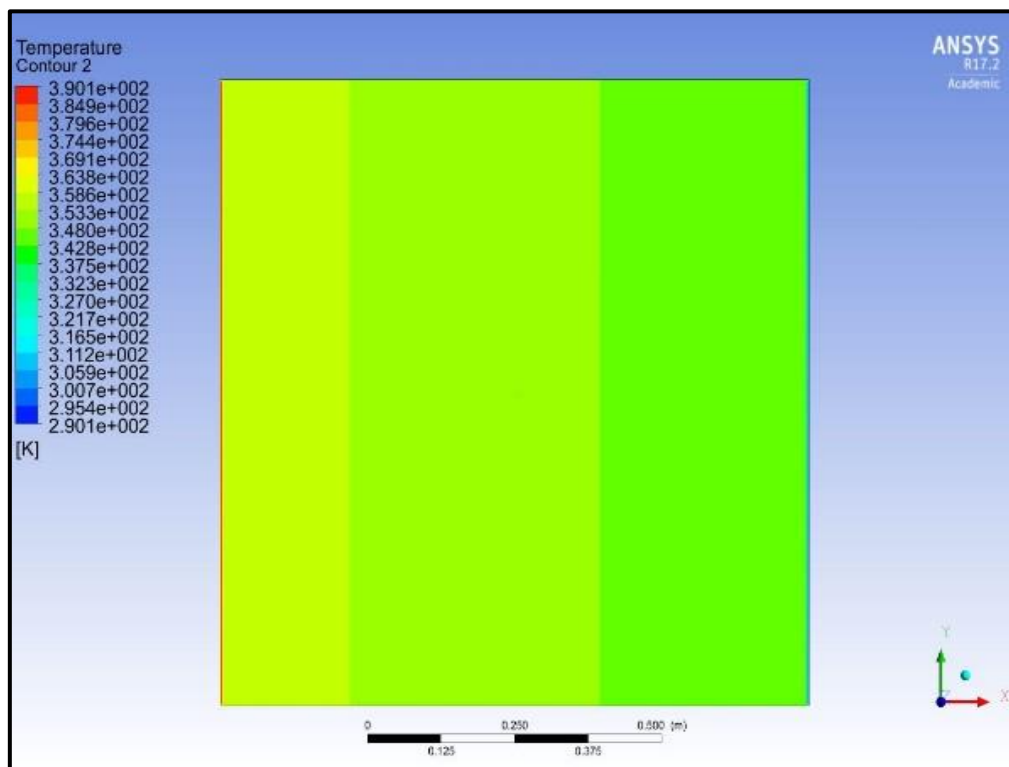
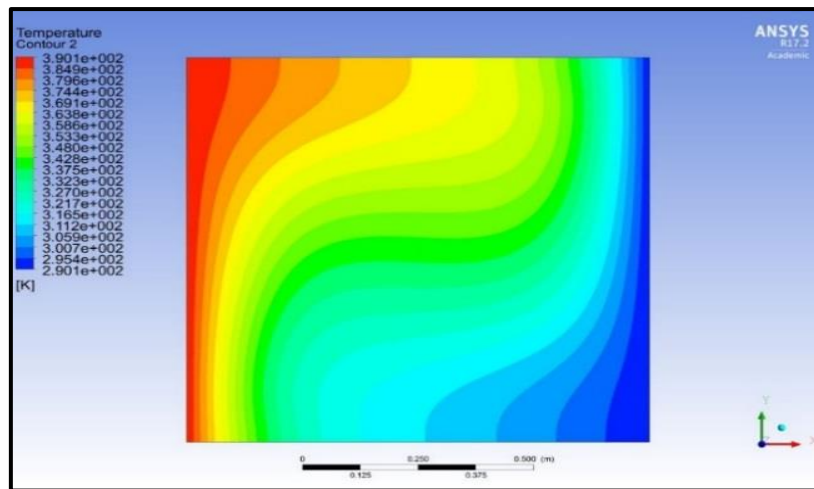


Figure 3.6 Isotherms for silver-water nanofluent,  $Ra = 10^4$ , no radiative flux with  $\Phi = 0.01$ .



**Figure 3.7 Isotherms for silver-water nanofluid,  $Ra = 10^4$ , P1 radiative flux with  $\Phi = 0.01$ .**

Silver water nanofluid is studied since it has proved very promising for achieving high heat transfer rates, and silver has the advantage of anti-microbial properties and requiring less maintenance than other metallic nanoparticles (Nasrin, et al., 2004). (Roy, et al., 2015) have also confirmed experimentally that silver-water nanofluids achieve improved heat transfer even at relatively low volume fractions (less than 5 %) although they considered only flat plate solar collectors. In the present study a solar flux is specified of  $877\text{W/m}^2$  which is also consistent with the solar radiation flux values examined by (Roy, et al., 2015) (among others) who considered the range  $800\text{ W/m}^2$  to  $1000\text{ W/m}^2$ . (Ozsoy & Corumlu, 2018) have also verified the superior thermal efficiency and long-term stability of silver-water nanofluids in thermosyphon heat pipes in evacuated tube solar collectors. They found that silver nanoparticles enhance solar collector efficiency from 20.7% and 40% compared with the pure water. In the simulations conducted therefore we first elaborate on silver-water nanofluid performance and thereafter compare with an alternative metallic nanofluid, namely Titanium oxide-water.

It is evident that the Rosseland flux model Figure 3.5 predicts a temperature field significantly different from that obtained without radiation Figure 3.6. For the low optical thickness in this

problem, the temperature field predicted by the Rosseland model is not physically realistic. The P-1 differential radiative model Figure 3.7 produces a more homogenous thermal effect adjacent to the hot wall and enables radiative flux to penetrate more evenly through the nanofluid enclosure, whereas the Rosseland model predicts a biased temperature enhancement only in the top left corner. The isotherms are weakly distorted with the Rosseland model whereas they are substantially morphed with the P1 flux model and heat permeates the enclosure more strongly in the upper zone with cooler fluid in the lower zone. There however remains a dominant thermal zone associated with radiative flux in the vicinity of the left (heated) solar receiving wall. Furthermore, the hotter isotherms are more widely dispersed for the P1 flux model case which clearly simulates the absorption of radiation more accurately than the Rosseland flux model. With no radiation present no tangible thermal penetration is achieved and there is no distortion in isotherms. Radiative flux therefore exerts a considerable role and the simulations since it augments the thermal diffusivity of the working fluid. Apparently solar collector models including this mode of heat transfer produce more realistic representations of solar heat flux absorption.

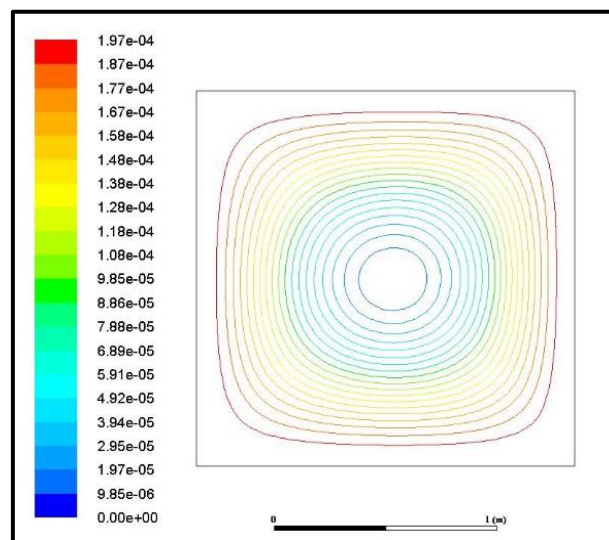


**Figure 3.8 Streamline distributions for silver-water nanofluid,  $Ra = 10^4$ , P1 flux model with  $\Phi = 0.01$ .**

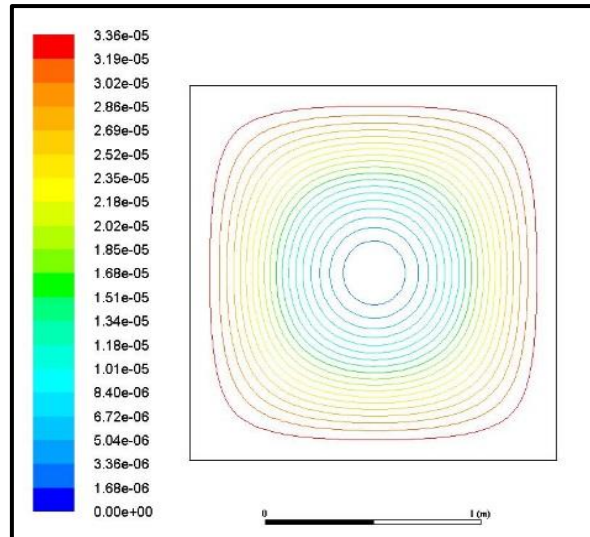


**Figure 3.9** Streamline distributions for silver-water nanofluid,  $Ra = 10^4$ , Rosseland flux with  $\Phi = 0.01$ .

Figure 3.8 and Figure 3.9 visualize the streamline (velocity contour) plots obtained again for Silver-water nanofluid with low-volume fraction = 0.01 (1% doping), for a square enclosure ( $AR = 1$ ) with Rayleigh number,  $Ra = 10^4$  and radiative absorption coefficient of 0.2. Although a single cell is computed for both cases, significantly higher magnitudes are observed with the P1 flux model (Figure 3.8) compared with the Rosseland model (Figure 3.9). An almost stagnant zone arises at the centre of the enclosure where vorticity effects are minimized. The streamlines are also in closer proximity especially in the periphery of the enclosure where higher temperature is generated for the P1 model case (Figure 3.8). In the vicinity of the enclosure walls, there is elevated mobility of silver nanoparticles and a reduction in viscosity. Acceleration is therefore computed in this region and this concurs with the findings of Qi *et al.* [34] although they considered Gallium as the base fluid. Since the velocity field is coupled to the temperature field in natural convection, it is influenced by radiative transfer flux. The P1 model yields the correct velocity profiles since the radiation source in the energy equation, which is proportional to the absorption coefficient, is small. The Rosseland model uses an effective conductivity to account for radiation, and yields the wrong temperature field, which

in turn results in markedly lower accuracy in the computation of the velocity field and streamline distribution.

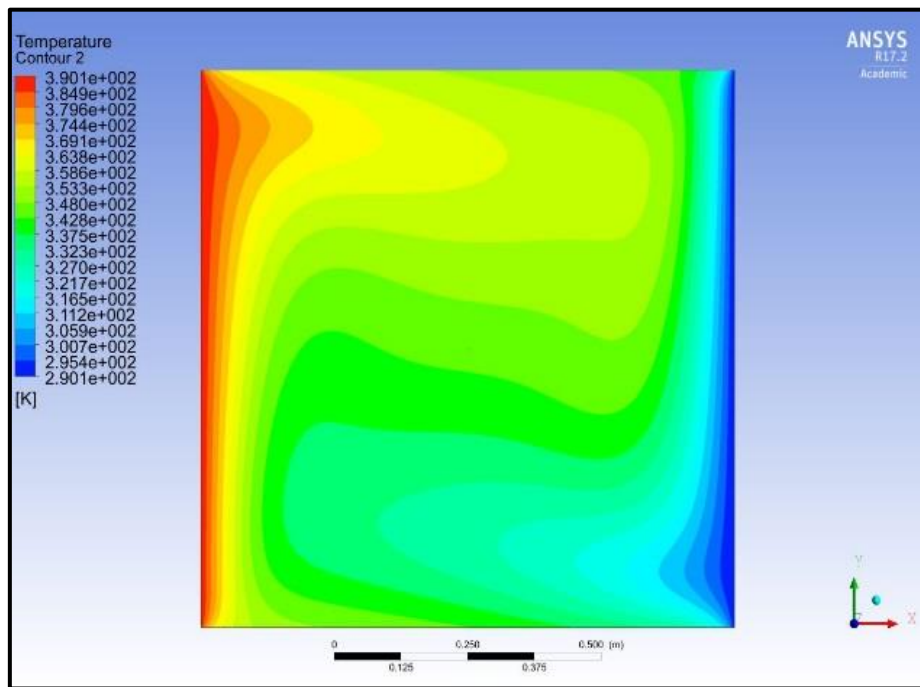


Figure 3.10 Isotherms for silver-water nanofluid,  $Ra = 10^5$ , P1 radiative flux with  $\Phi = 0.04$ .

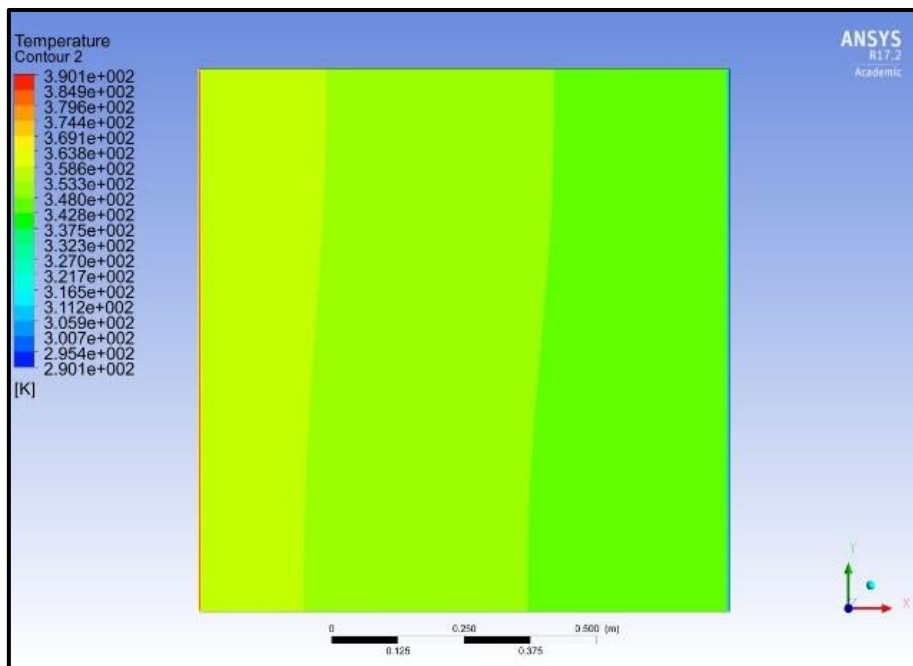
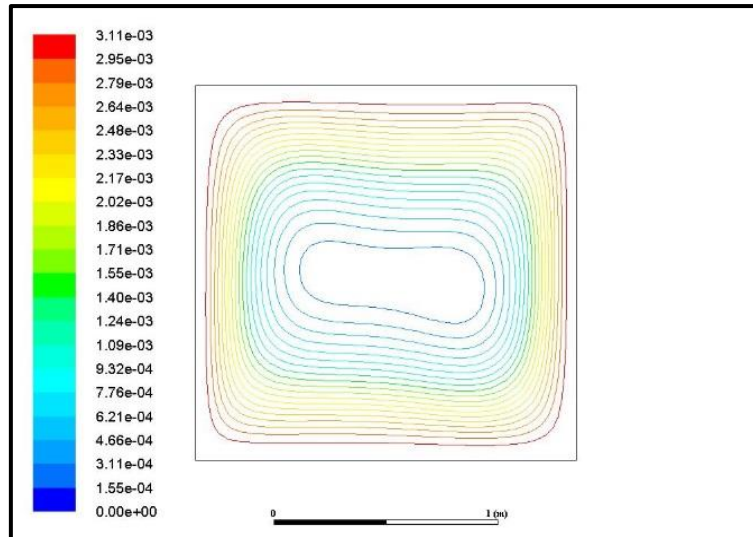
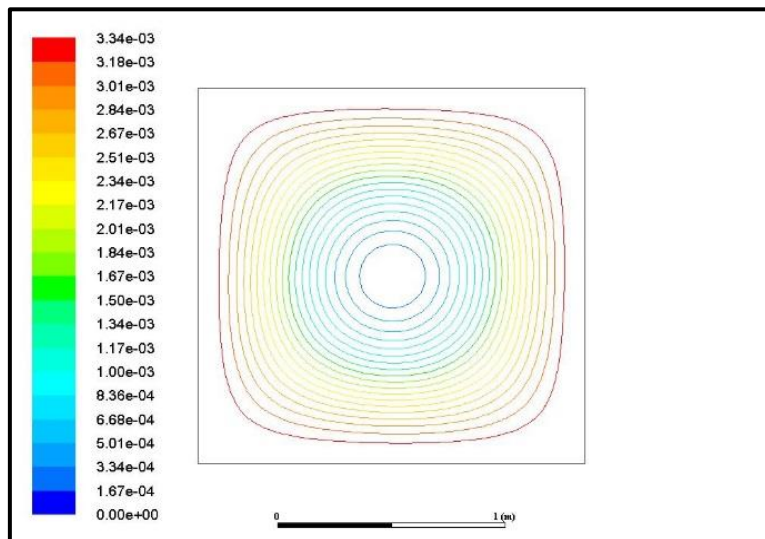


Figure 3.11 Isotherms for silver-water nanofluid,  $Ra = 10^5$ , no radiative flux with  $\Phi = 0.04$





**Figure 3.12** Streamline distributions for silver-water nanofluid,  $Ra = 10^5$ , P1 radiative flux with  $\Phi = 0.04$



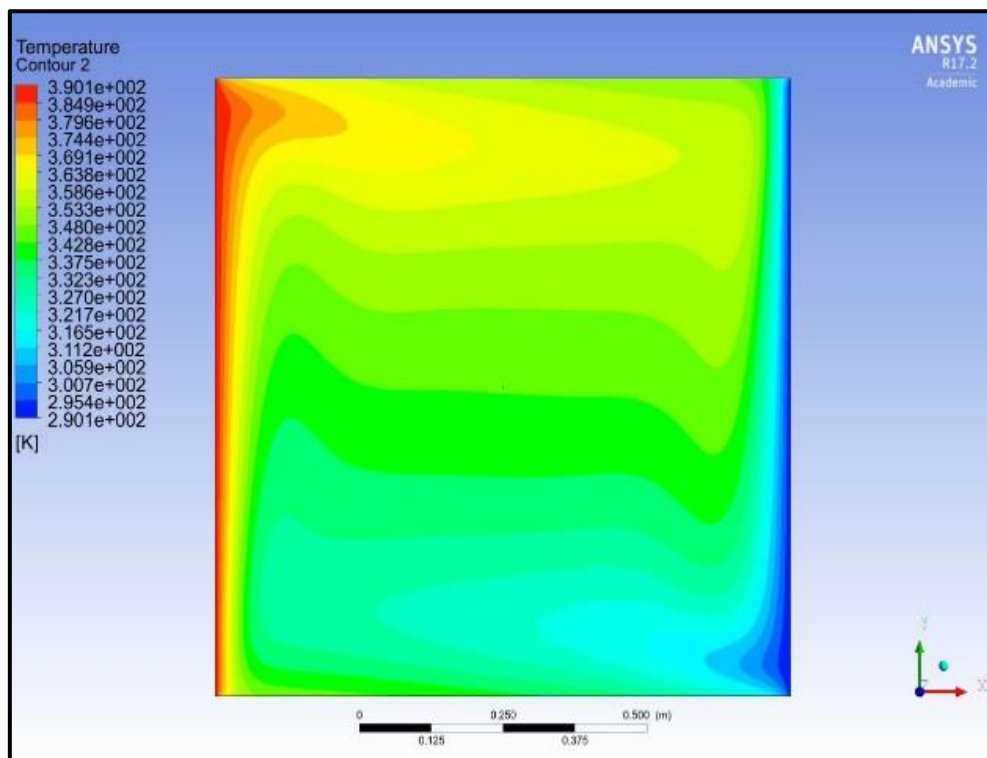
**Figure 3.13** Streamline distributions for silver-water nanofluid,  $Ra = 10^5$ , no radiative flux with  $\Phi = 0.04$ .

Figure 3.10 and Figure 3.11 depict the isotherm plots for silver-water nanofluid with stronger natural convection i.e., thermal buoyancy ( $Ra = 10^5$ ) with a much higher nano-particle volume fraction ( $\Phi = 0.04$ ) for the P1 flux case and no radiative heat transfer cases, respectively. Compared with figs Figure 3.6 and Figure 3.7 (P1 flux case) a significant modification is only observed with the P1 flux case (Figure 3.10). The hotter fluid zone is found to push further from the hot wall and occupies a greater proportion of the enclosure. The colder zone which

occupies the lower wall is largely eliminated and the lower right corner of the enclosure features a much-contracted cold zone. The enhanced thermal buoyancy coupled with the four hundred percent increase in silver nanoparticles occupying the cavity contribute strongly to encouraging thermal diffusion and transporting heat more effectively throughout the enclosure. Thermal conductivity of the nanofluid increases with increase in volume concentration. There is also a reduction in thermal boundary layer thickness at the walls and colder nanofluid is confined to the right wall with a narrower (constricted) zone in the lower half space of the enclosure. Higher doping of silver nanoparticles successfully improves the circulation of heat in the enclosure and is assisted by thermal buoyancy. There is a weak transition in the isothermal profiles for the non-radiative case (Figure 3.11) compared with earlier case (Figure 3.6) - isotherms are skewed towards the right wall- however there is no tangible change in temperatures with yellow-green zones persisting in the vicinity of the hot wall, and becoming progressively cooler (green) towards the central area and eventually cooling further (dark green zones) near the cold right wall. The absence of radiative heat transfer therefore has a critical influence on the impact of higher thermal buoyancy (Rayleigh number) and increased silver nano-particle doping. Inclusion of radiative heat transfer is essential since the entire energy in the enclosure is received from the exterior by radiation, as noted by (Gómez, et al., 2013). However, it is further of note that radiative heat transfer modelling could be improved especially for directional accuracy and high participating media with alternate models such as the Chandrasekhar discrete ordinates model, as elaborated by (Howell & Pinar Menguc, 2015). Also, more advanced radiative models may provide deeper insight into thermophysical behaviour of silver nano-particles, as described by (Maddah, et al., 2013). Figure 3.12 and Figure 3.13 illustrate the streamline plots again for silver-water nanofluid with stronger thermal buoyancy ( $Ra = 10^5$ ) with a higher nano-particle volume fraction ( $\Phi = 0.04$ ) for the P1 flux



case and no radiative heat transfer cases, respectively. Compared with Figure 3.9 (Rosseland) and Figure 3.8 (P1 flux case) a significant modification is only observed with the P1 flux case (Figure 3.12). The central cell is warped into a peanut-shaped zone and there is a narrowing in streamlines especially at the periphery of the enclosure. Significantly higher magnitudes are computed compared with the lower Rayleigh number and lower volume fraction case shown earlier (Figure 3.7). The central zone is expanded laterally but constricted vertically with greater intensity around the periphery of the distorted inner cell. Flow acceleration is therefore generated for the P1 flux model. Although no significant modification is observed in the topology of the streamlines in the non-radiative case Figure 3.13 compared with Figure 3.6, there is a notable increase in streamline magnitudes. Again, therefore the nanofluid circulation is accelerated albeit with no distortion of the inner cell.



**Figure 3.14 Isotherms for silver-water nanofluid,  $Ra = 10^6$ , P1 radiative flux with  $\Phi = 0.04$ .**

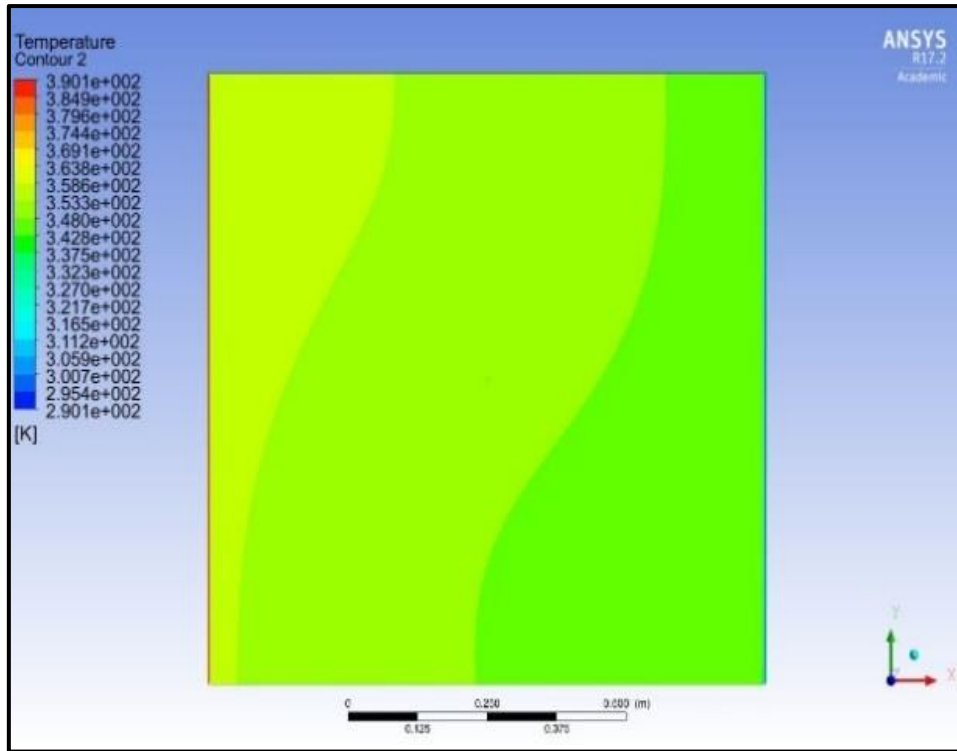


Figure 3.15 Isotherms for silver-water nanofluid,  $Ra = 10^6$ , no radiative flux with  $\Phi = 0.04$ .

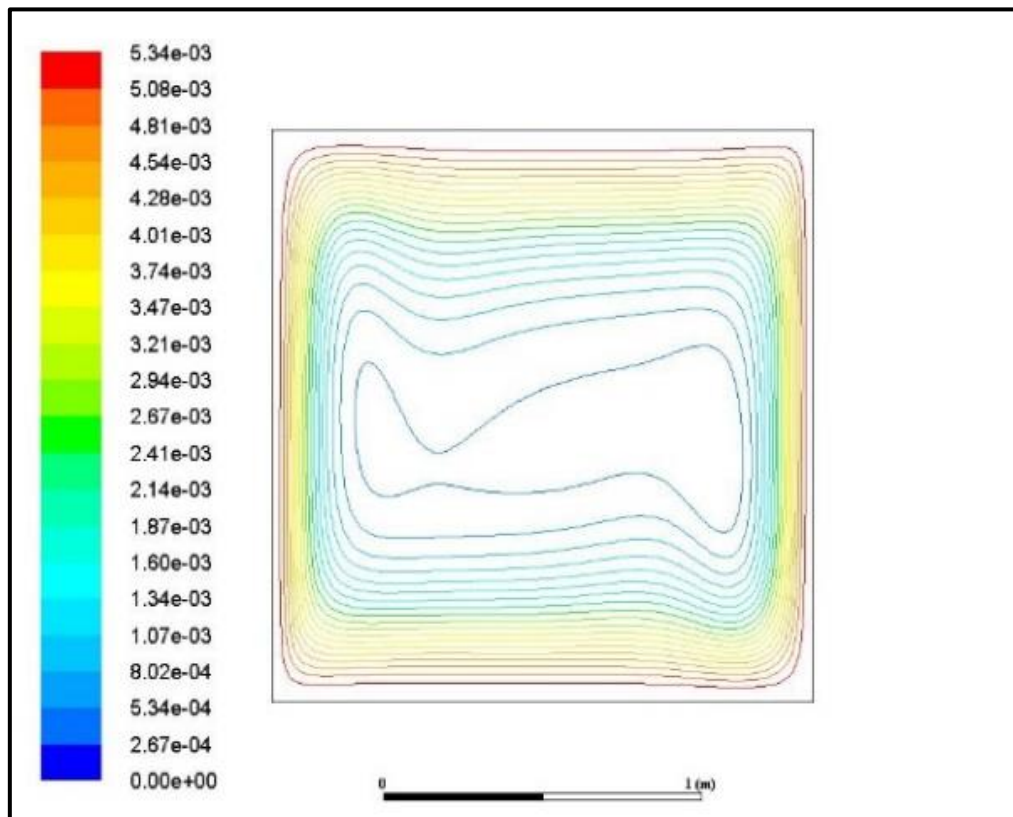
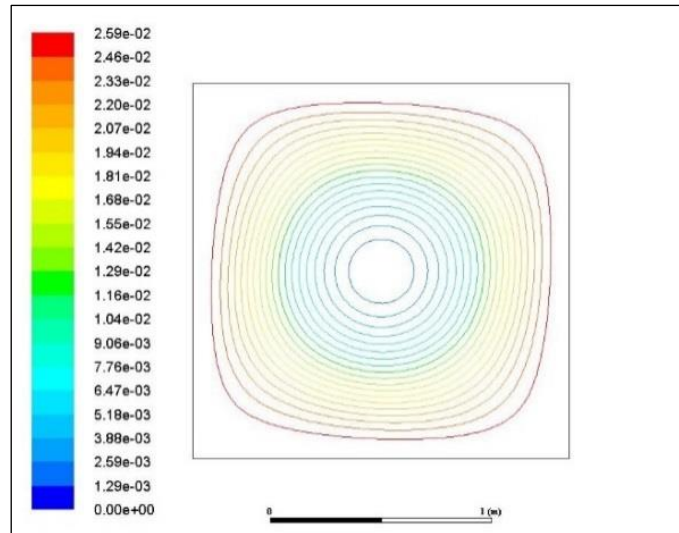


Figure 3.16 Streamline distributions for silver-water nanofluid,  $Ra = 10^6$ , P1 radiative flux with  $\Phi = 0.04$ .



**Figure 3.17 Streamline distributions for silver-water nanofluid,  $Ra = 10^6$ , no radiative flux with  $\Phi = 0.04$ .**

Figure 3.14, Figure 3.15, Figure 3.16 and Figure 3.17 present the isotherm plots and streamline plots for silver-water nanofluid with even stronger natural convection i.e. thermal buoyancy ( $Ra = 10^6$ ) again with high nano-particle volume fraction ( $\Phi = 0.04$ ) for the P1 flux case and no radiative heat transfer cases, respectively. Comparing Figure 3.14 with Figure 3.10, there is an even deeper penetration of hot nanofluid towards the cold (right) wall. Higher temperature contours dominate the upper half space of the enclosure with the colder zone isolated in the lower half space and this applies across the width of the enclosure. The maximum temperature zone is extended in the upper left of the enclosure and orange zones protrude further into the enclosure. Evidently higher Rayleigh number therefore mobilizes strong thermal convection currents in the enclosure and allows enhanced transfer of thermal energy across the enclosure. The cold blue narrow zone immediately adjacent to the right cold wall is also narrowed noticeably and warmer nanofluid (green contours) penetrates deeper approaching more closely to the cold wall. Figure 3.15 shows that the isotherms are further distorted with higher Rayleigh number although yellow and green (warm) zones remain without the hotter zones extending from the left wall. The absence of radiation therefore again leads to inadequate capturing of the

modified thermal distribution. Figure 3.16 illustrates that yet greater distortion of the cellular structure in the enclosure is induced with greater Rayleigh number. The central zone is further modified into an asymmetric topology and extends further towards the left and right walls. Much higher velocities are computed in Figure 3.12 compared with Figure 3.13 since the buoyancy effect is ten times stronger ( $Ra$  is  $10^5$  in Figure 3.12). The peanut shaped central cell in Figure 3.13 is distinctly morphed in Figure 3.12. Streamlines are constricted again near all the edges of the enclosure indicating intensification in the flow. The trend is that the flow is tending towards a bifurcating cellular structure where multiple zones are synthesized in the central area of the enclosure. Instability can be induced thereafter, and attention is therefore limited in the simulations to  $Ra = 10^6$  as the maximum Rayleigh number studied. Figure 3.17 shows that the streamline distributions are skewed slightly towards the upper right of the enclosure with  $Ra = 10^6$  compared with Figure 3.13 ( $Ra = 10^5$ ). The central zone is also somewhat expanded compared with higher Rayleigh number i.e., stronger natural convection. However, there is a distinct deceleration in the flow i.e., streamline magnitudes are reduced with greater Rayleigh number for the non-radiative case.

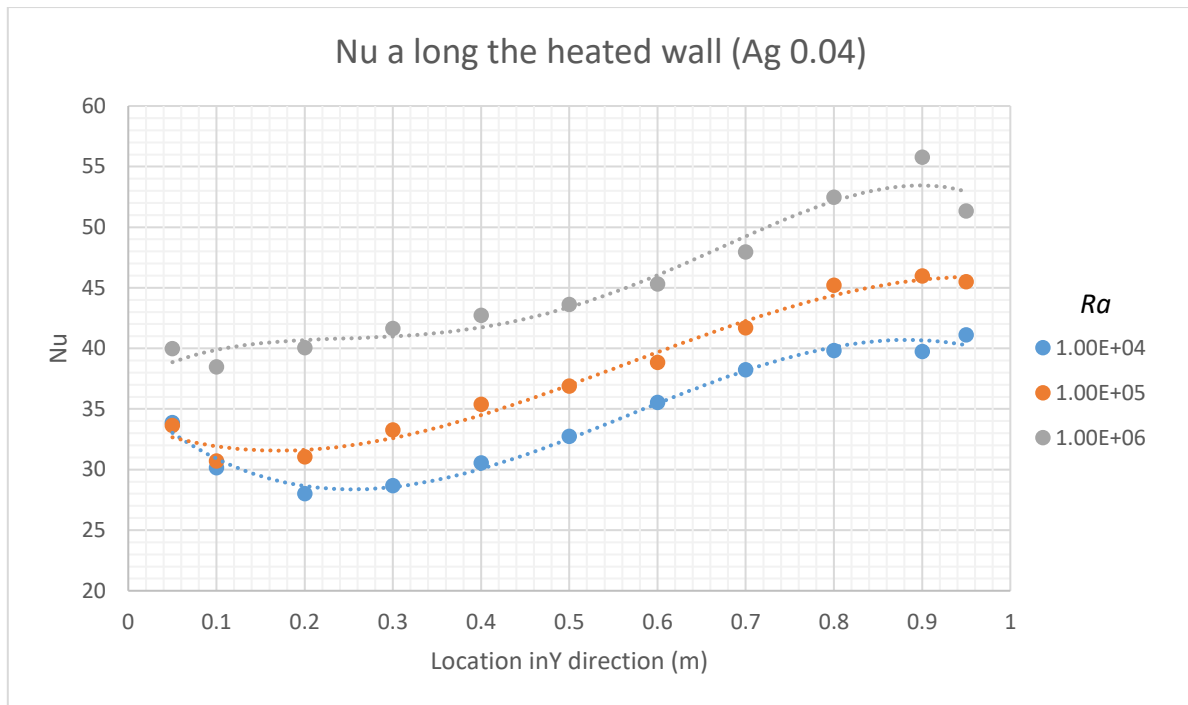


**Figure 3.18 Nusselt numbers along hot wall for silver-water nanofluid, P1 flux with  $\Phi = 0.04$  for different Rayleigh numbers**

Figure 3.18 depicts the influence of Rayleigh number on Nusselt number along the heated (left) wall for silver water nanofluid at 4% volume fraction, once again for a square enclosure (aspect ratio,  $AR = 1$ ). These profiles correspond only to the P1 radiative flux model. An increase in Rayleigh number clearly elevates strongly the local Nusselt number magnitudes. There is also a considerable elevation in Nusselt number as we progress from the base of the enclosure ( $y = 0$ ) to the top of the enclosure ( $y = 1$ ). Minimal Nusselt number is consistently computed at the base of the left wall and maximum Nusselt number at the top of the wall, irrespective of the Rayleigh number. Increasing thermal buoyancy therefore exerts a significant influence on wall heat transfer characteristics at the solar flux loaded boundary (hot left wall).

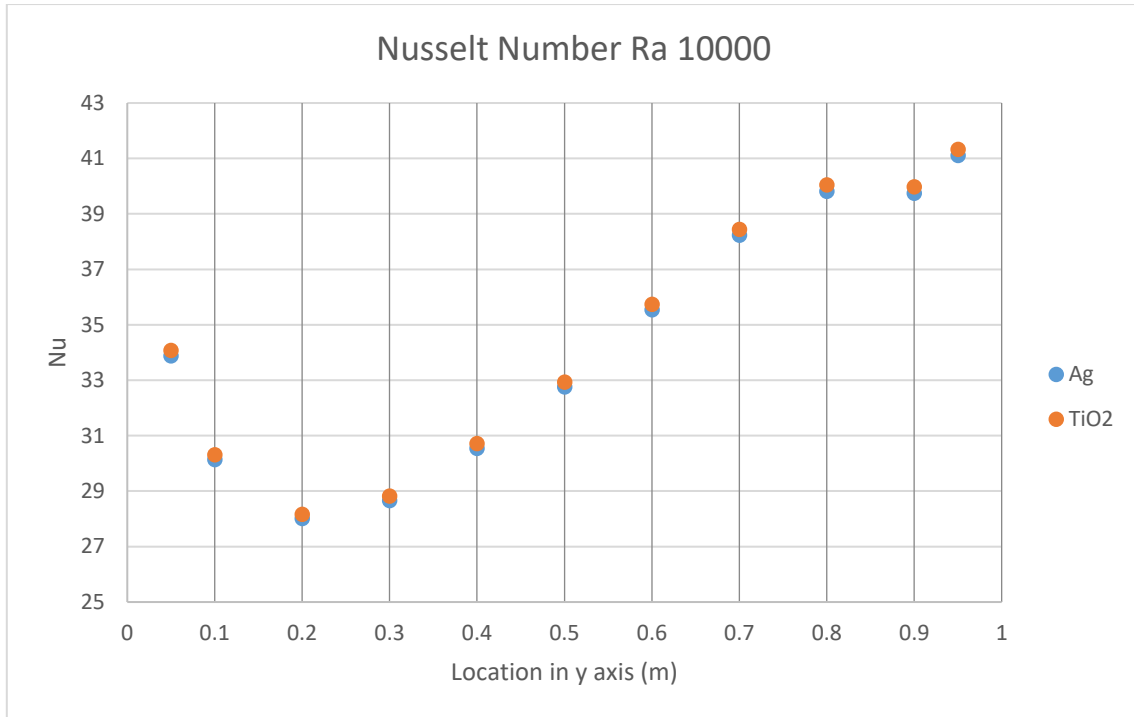


Figure 3.19 Nusselt numbers for different nanofluids, P1 flux with  $\Phi = 0.04$ ,  $Ra = 10^4$ .

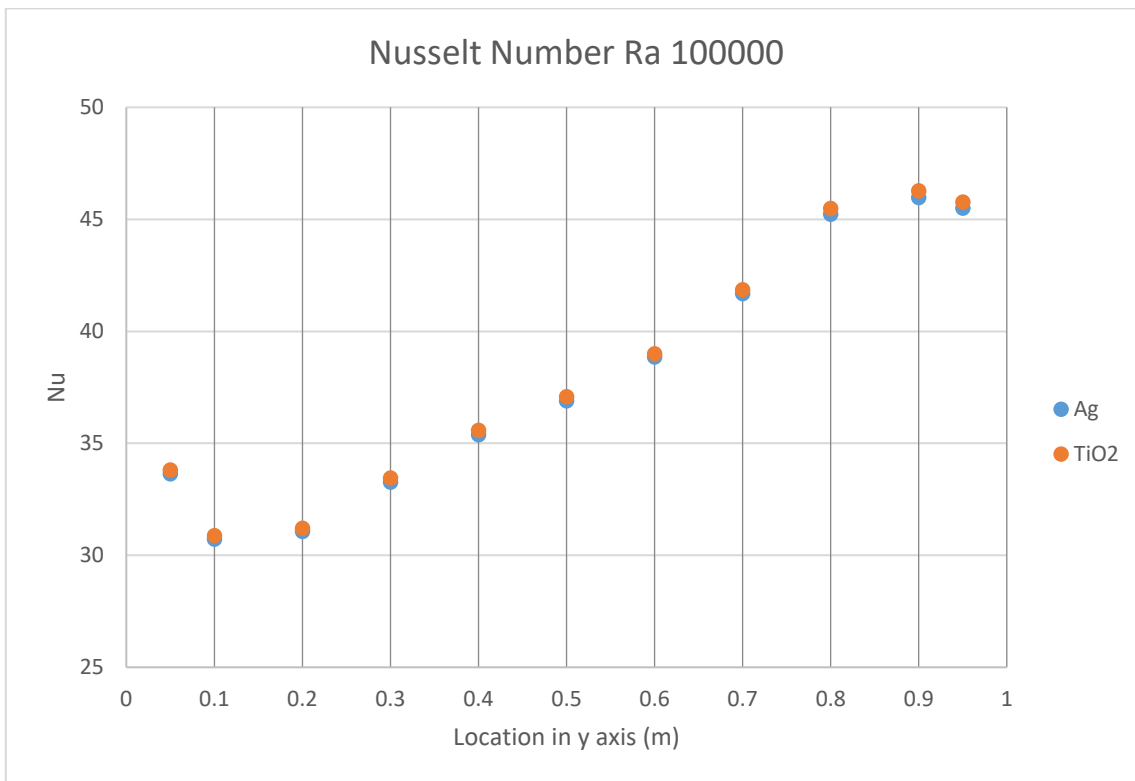
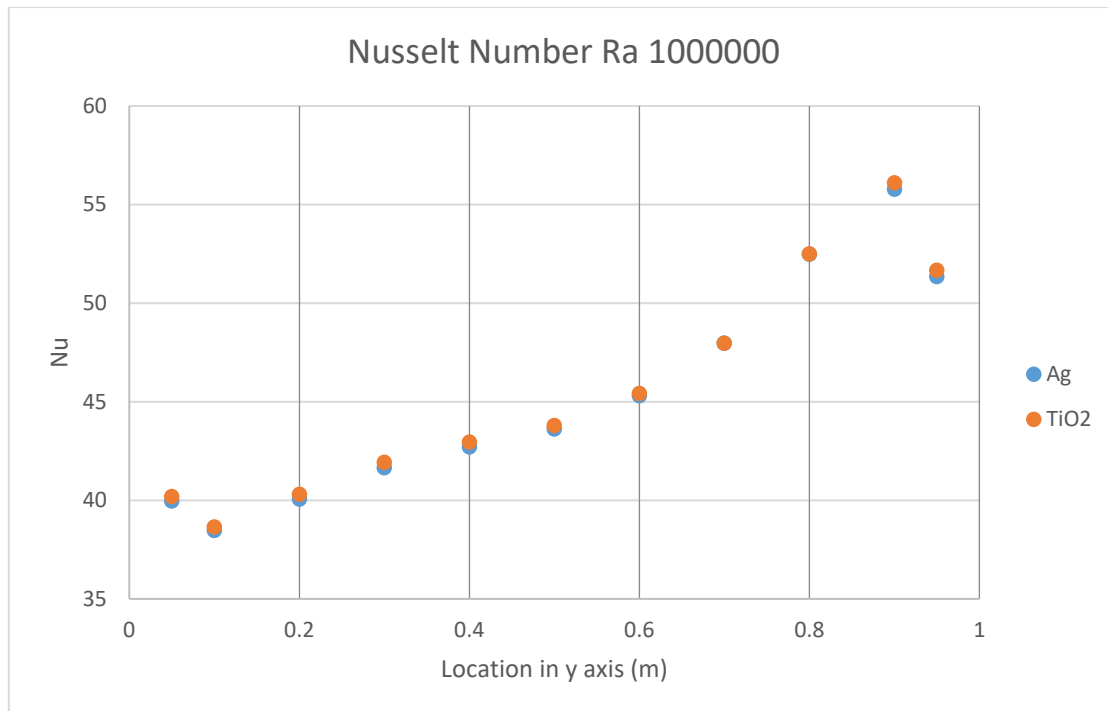


Figure 3.20 Nusselt numbers for different nanofluids, P1 flux with  $\Phi = 0.04$ ,  $Ra = 10^5$



**Figure 3.21 Nusselt numbers for different nanofluids, P1 flux with  $\Phi = 0.04$ ,  $Ra = 10^6$ .**

Figure 3.19, Figure 3.20 and Figure 3.21 illustrate the relative performance, in terms of Nusselt number achieved with silver-water nanofluid and Titanium oxide-water nanofluid, again with the P1 flux radiative model and 4% volume fraction. Titanium oxide has a significantly lower thermal conductivity than silver and the latter is also more stable (longer shelf life) when suspended in base water (Gómez, et al., 2013). Silver has superior optical (reflective) properties whereas titanium has anti-corrosion properties. However, Titanium is less than half the density of silver and therefore less liable to settle towards the base of the solar collector over longer periods of use. All metallic nanoparticles tend to agglomerate or aggregate due to the van der Waals forces, which can bind several particles together into a lump of particles. As a result of gravitational effects, these denser metallic nanoparticles will conglomerate at the base of the container (solar collector). The overall nanofluid thermal conductivity will therefore be modified since better performance requires uniform distribution of nanoparticles throughout the base fluid. While silver water nanofluid will have a significantly greater overall thermal

conductivity than titanium oxide water nanofluid, the latter will still have a much greater thermal conductivity compared to water. (Fedele, et al., 2012) and (Saleh, et al., 2014) have further elaborated that the interfacial layer of water molecules engulfing the metallic nanoparticles enhances thermal conductivity since the water molecules surrounding the nanoparticles exhibit greater order and uniform distribution compared with pure water molecules further from the nano-particles. Very close magnitudes are computed for the Nusselt numbers with both silver and titanium oxide nanofluids at any given Rayleigh number, although the magnitudes are marginally higher for titanium oxide. Initially all profiles descend from the hot wall and thereafter rise steadily with distance along the wall culminating in the maximum Nusselt number near the top of the left hot wall. With increasing Rayleigh number from  $10^4$  (Figure 3.19) to  $10^5$  (Figure 3.20) to  $10^6$  (Figure 3.21) there is a progressive increase in Nusselt number indicating greater heat transfer to the enclosure nanofluid. Other mechanisms may also contribute in addition to thermal buoyancy, such as thermophoresis and Brownian motion. However, these cannot be simulated with the Tiwari-Das nanofluid model and require alternative nanoscale mathematical models (Vasu, et al., 2019) and (Prakash, et al., 2019) which are not available in ANSYS FLUENT software.



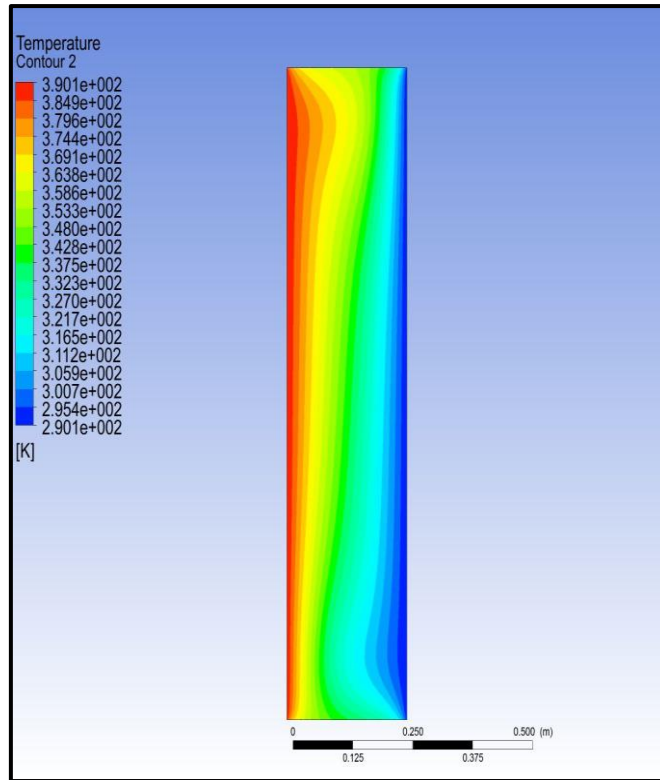


Figure 3.22 Isotherms for Titanium oxide-water nanofluid, P1 flux with  $\Phi = 0.04$ ,  $Ra = 10^5$  and absorption coefficient of 0.2 for aspect ratio  $AR = 4$ .

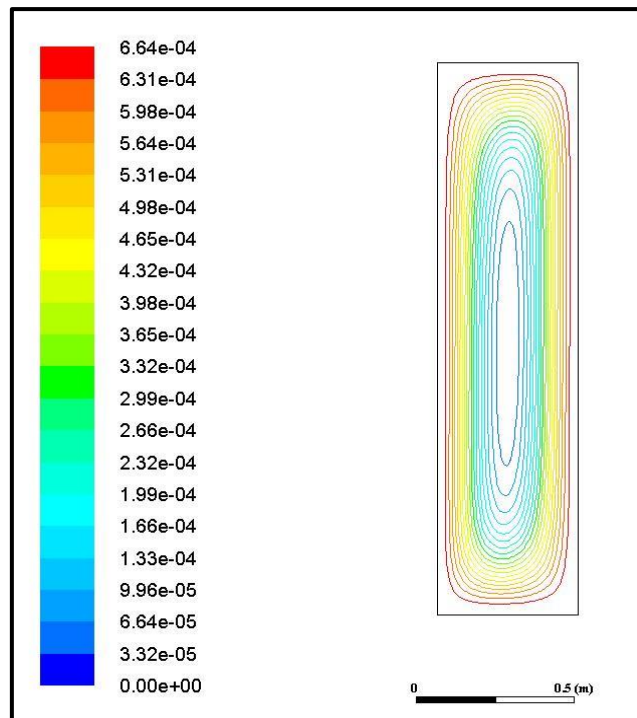
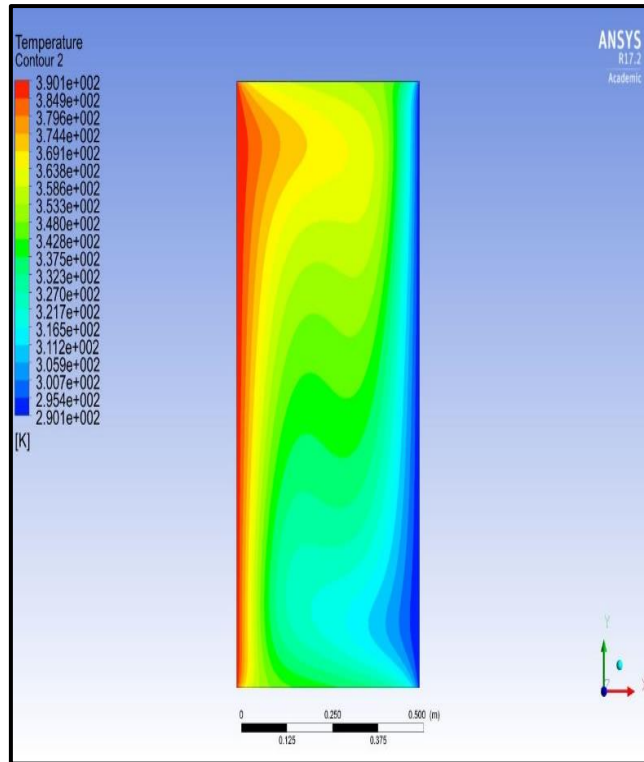
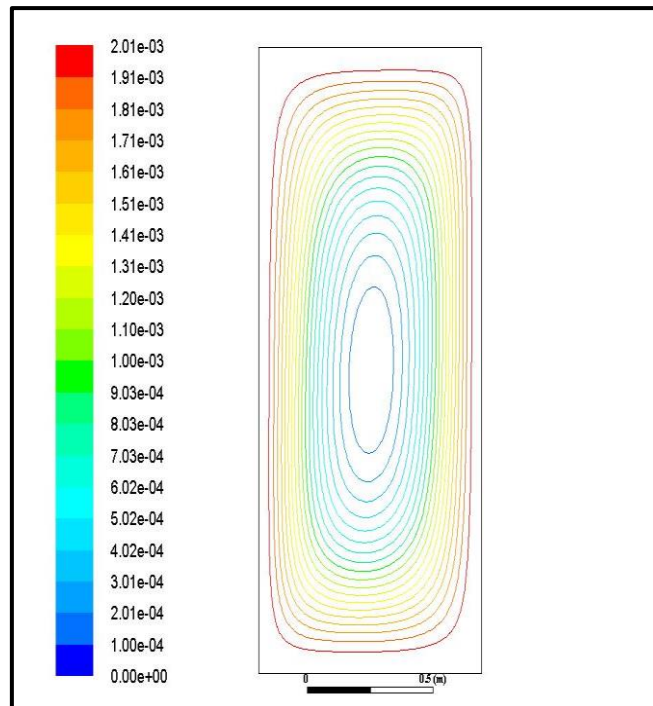


Figure 3.23 Streamlines for Titanium oxide-water nanofluid, P1 flux with  $\Phi = 0.04$ ,  $Ra = 10^5$  and absorption coefficient of 0.2 for aspect ratio  $AR = 4$ .



**Figure 3.24 Isotherms for Titanium oxide-water nanofluid, P1 flux with  $\Phi = 0.04$ ,  $Ra = 10^5$  and absorption coefficient of 0.2 for aspect ratio  $AR = 2$**



**Figure 3.25 Streamlines for Titanium oxide-water nanofluid, P1 flux with  $\Phi = 0.04$ ,  $Ra = 10^5$  and absorption coefficient of 0.2 for aspect ratio  $AR = 2$ .**

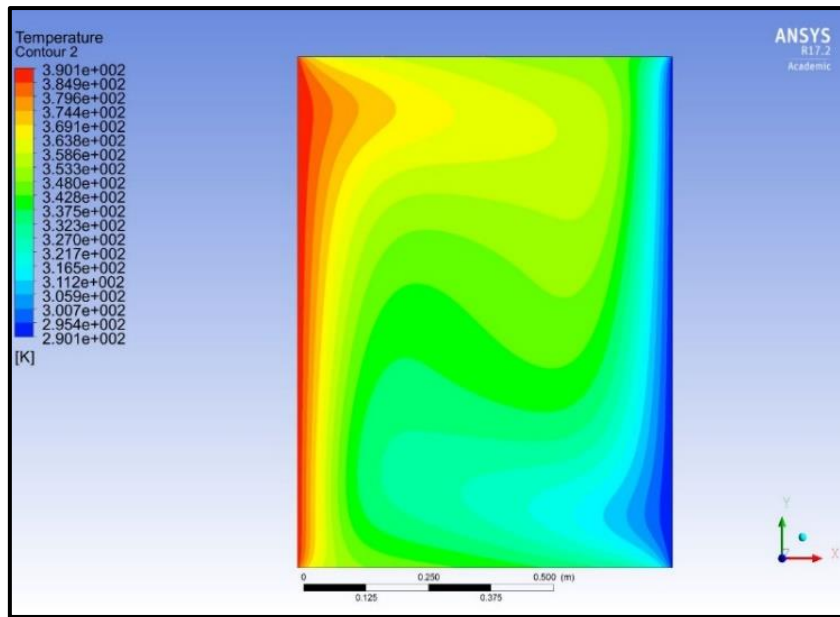


Figure 3.26 Isotherms for Titanium oxide-water nanofluid, P1 flux with  $\Phi = 0.04$ ,  $Ra = 10^5$  and absorption coefficient of 0.2 for aspect ratio  $AR = 4/3$ .

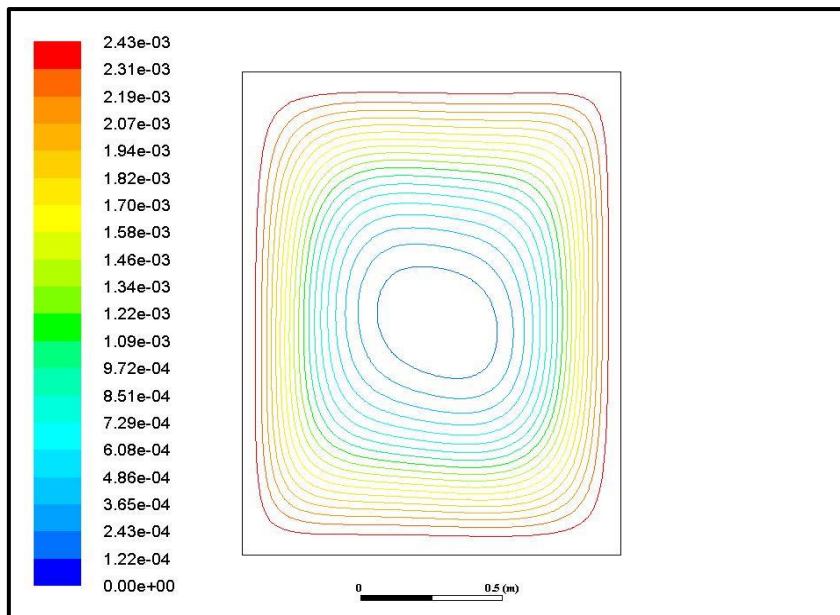


Figure 3.27 Streamlines for Titanium oxide-water nanofluid, P1 flux with  $\Phi = 0.04$ ,  $Ra = 10^5$  and absorption coefficient of 0.2 for aspect ratio  $AR = 4/3$ .

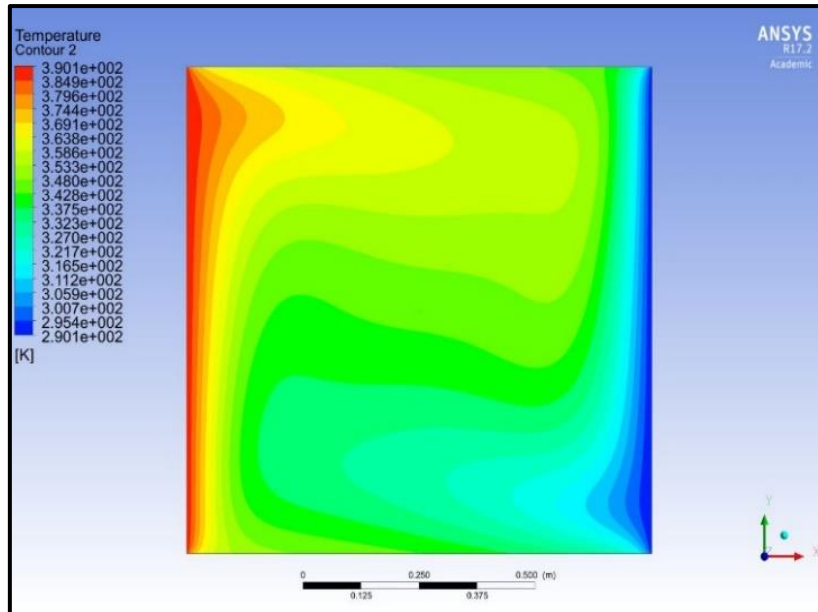


Figure 3.28 Isotherms for Titanium oxide-water nanofluid, P1 flux with  $\Phi = 0.04$ ,  $Ra = 10^5$  and absorption coefficient of 0.2 for aspect ratio  $AR = 1$  (square cavity).

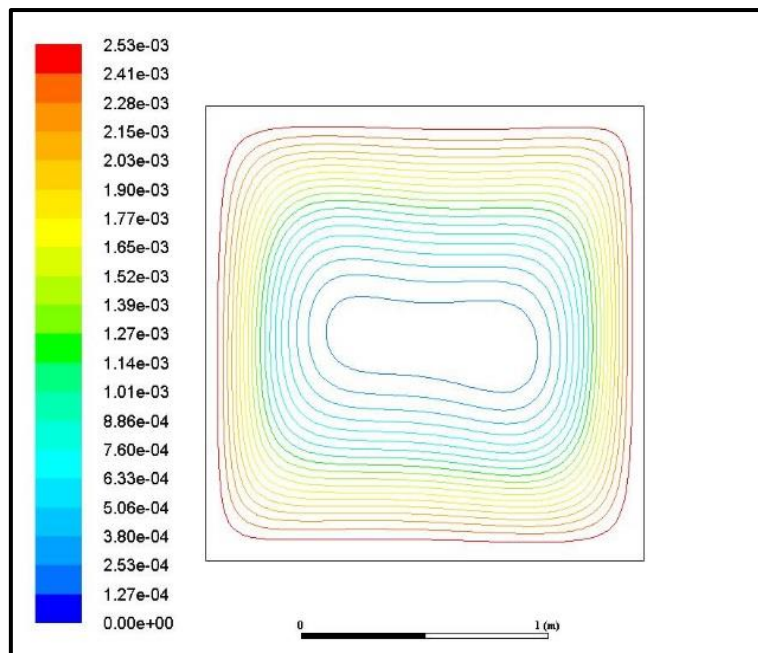


Figure 3.29 Streamlines for Titanium oxide-water nanofluid, P1 flux with  $\Phi = 0.04$ ,  $Ra = 10^5$  and absorption coefficient of 0.2 for aspect ratio  $AR = 1$  (square cavity).

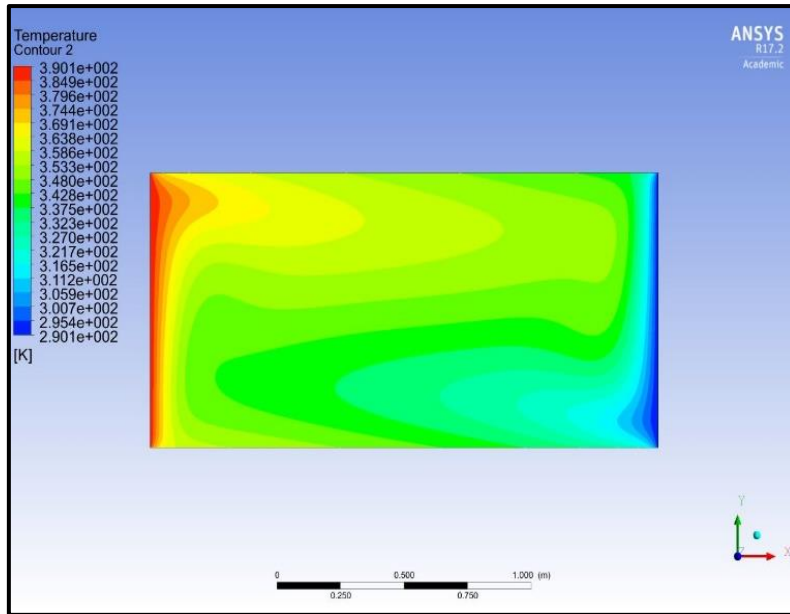


Figure 3.30 Isotherms for Titanium oxide-water nanofluid, P1 flux with  $\Phi = 0.04$ ,  $Ra = 10^5$  and absorption coefficient of 0.2 for aspect ratio  $AR = 0.5$  (shallow cavity).

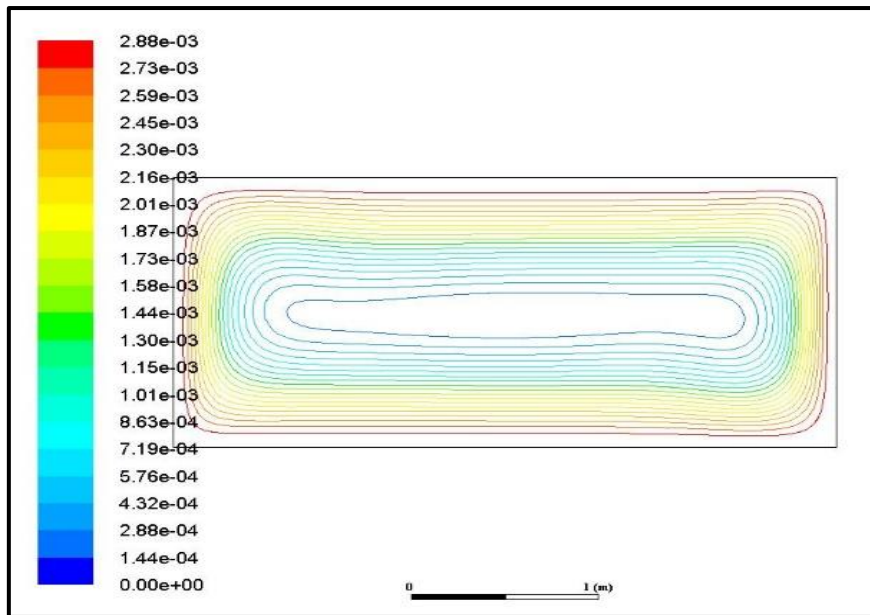
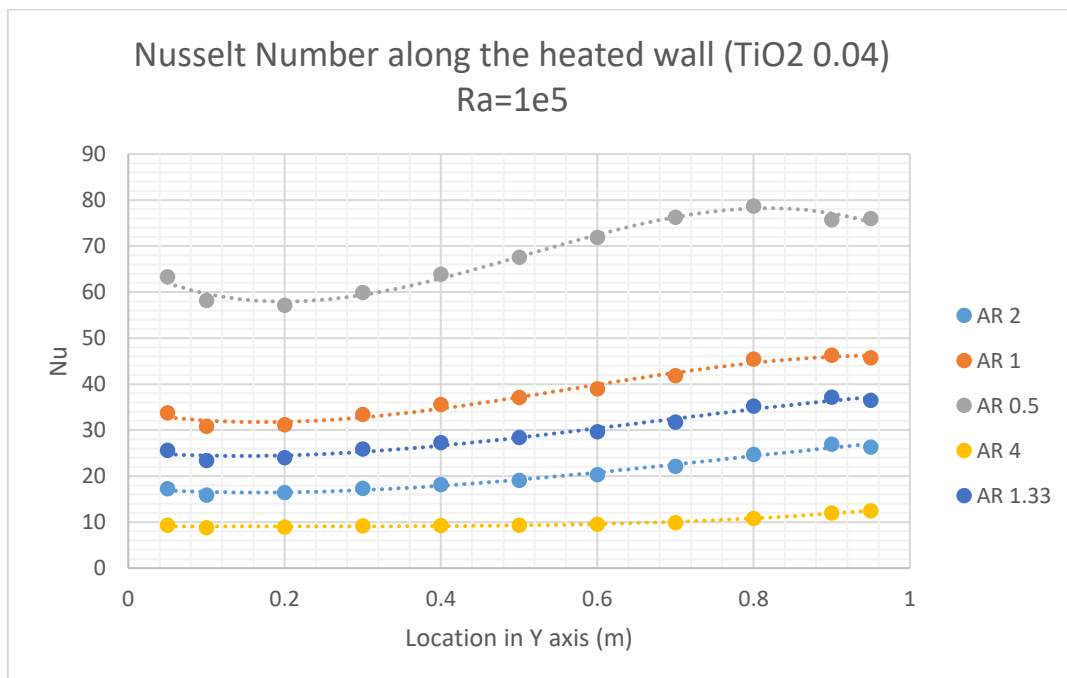


Figure 3.31 Streamlines for Titanium oxide-water nanofluid, P1 flux with  $\Phi = 0.04$ ,  $Ra = 10^5$  and absorption coefficient of 0.2 for aspect ratio  $AR = 0.5$  (shallow cavity).

From Figure 3.22-Figure 3.31 illustrate the impact of aspect ratio on isotherms and streamline plots. In these figures we consider *Titanium oxide-water nanofluid with the P1 radiative flux model, volume fraction of  $\Phi = 0.04$ , and  $Ra = 10^5$* . The solar heat flux is maintained at the

same value on the left hot wall. **Five different aspect ratios (AR) are considered:** 4 (very tall enclosure), 2 (tall enclosure), 4/3 (an enclosure which is slightly taller than wide), 1 (square), to 0.5 (shallow enclosure). Comparing isotherms first we consider the variation in Figure 3.22 (AR = 4), Figure 3.24 (AR = 2), Figure 3.26 (AR = 4/3), Figure 3.28 (AR = 1) and finally Figure 3.30 (AR = 0.5). Significant alteration in the temperature contours is instigated with a progressively decreasing aspect ratio. With decreasing aspect ratio (AR = ratio of height of enclosure to width of enclosure) hotter nanofluid begins to penetrate deeper into the upper half space. The cold zone (blue contours) adjacent to the right wall becomes increasingly localized in the lower half space of the enclosure. This process is accentuated as we reduce the AR from 4.3 to 1 and then eventually dominates with a shallow enclosure yellow and green contours occupying most of the enclosure space indicating enhanced thermal diffusion and more homogenous heat distribution throughout the collector geometry. Lower aspect ratio therefore encourages the synthesis of dual thermal zones at the upper and lower zones of the enclosure. Overall, the isotherms are compressed towards the hot wall and the cold ceiling and most of the enclosure is occupied by warmer fluid at higher aspect ratios. Due to this effect, the single cell is expanded in both vertical and horizontal directions at higher aspect ratio with lesser distortion in the flow. This expansion results in boundary layer formation and is opposed at lower aspect ratios. The colder zone morphs from a blunt topology into a sharper bullet-shaped profile with smaller aspect ratio. Similar observations have been reported by (Sheikhzadeh & Nikfar, 2013). Comparing streamline plots (based on stream function) we study the variation in Figure 3.23 (AR = 4), Figure 3.25 (AR = 2), Figure 3.27 (AR = 4/3), Figure 3.29 (AR = 1) and finally Figure 3.31 (AR = 0.5). Significant alteration in the temperature contours is instigated with a progressively decreasing aspect ratio. For aspect ratio greater than unity (Figures 18, 20 and 22) there is a distinct singular cell structure to the enclosure circulation.

The structure is elongated in the vertical direction in Figure 3.22 and Figure 3.24 but disperses more laterally in Figure 3.26. A significant deceleration in the flow accompanies a decrease in aspect ratio from 4 to 2 i.e., lower magnitudes of stream function are computed. However, this trend is reversed with subsequent decrease in aspect ratio to 4/3 for which acceleration is computed and this pattern continues with even further decrease in aspect ratio to unity and finally to 0.5 (Figure 3.30). The singular cell structure is retained however only down to an aspect ratio of 4/3 and there is an increasing skewness in distributions towards the upper right corner of the cavity. At AR = 1 (Figure 3.28) a dual structure begins to emerge in the centre of the enclosure. At higher aspect ratio, the streamline distributions are more symmetrical whereas for AR = 1 and more so for AR = 0.5 (Figure 3.30) a dis-symmetry is observed, and a skewness emerges in the circulation which is biased towards the opposite wall i.e., the left hot wall of the solar enclosure. Vortex structure is therefore clearly influenced by aspect ratio. The central cell zone becomes increasingly elongated and distorted for AR = 0.5.



**Figure 3.32** Nusselt numbers along hot wall for Titanium oxide-water nanofluid, P1 flux with  $\Phi = 0.04$ ,  $Ra = 10^5$  with different enclosure aspect ratios (AR)

Figure 3.32 shows the Nusselt number distribution along the left hot wall for *Titanium oxide-water nanofluid with the P1 radiative flux model, volume fraction of  $\Phi = 0.04$ , and  $Ra = 10^5$* . Nusselt number at the left hot wall is maximized at low aspect ratio ( $AR = 0.5$ ) and minimized at high aspect ratio ( $AR = 4$ ) indicating that shorter and wider solar enclosures achieve significantly better heat transfer rates than taller and narrower enclosures. At highest aspect ratio ( $AR = 4$ ) Nusselt number remains invariant from the base of the hot wall for most of the length and is only increased marginally in the vicinity of the uppermost region along the wall. However, for lower aspect ratios Nusselt number generally grows consistently with progression along the heated wall from the base to the upper end. Generally, titanium oxide-water nanofluid produces quite good thermal enhancement compared with pure water.

### **3.4 Conclusions**

Computational simulations of steady-state nanofluid natural convection with thermal radiation in a two-dimensional solar collector enclosure have been presented. ANSYS FLUENT finite volume code (version 19.1) has been deployed. The Tiwari-Das volume fraction nanofluid model is used and three different nanoparticles are studied (Copper (Cu), Silver (Ag) and Titanium Oxide ( $TiO_2$ )) with water as the base fluid. The Traugott P1 flux and Rosseland diffusion models have been utilized to analyse radiative heat transfer which is imposed as solar thermal radiative flux at the hot left wall of the enclosure. Mesh-independence tests have been included. ANSYS isotherm and streamline computations have been validated with published studies from the literature for the copper-water nanofluid case. Extensive results have been presented for temperature contours, streamlines and Nusselt number distribution along the heated wall for both silver-water and titanium oxide-water nanofluids. The present investigation has shown that:



i) P1 model more accurately predicts the actual influence of solar radiative flux on thermal fluid behaviour compared with Rosseland radiative model and accurately reproduces the penetration of heat deeper into the enclosure.

ii) With increasing Rayleigh number (natural convection i.e. buoyancy effect), significant modification in the thermal flow characteristics is induced with emergence of a dual structure to the circulation. Temperatures are generally enhanced with greater Rayleigh number for both the silver-water nanofluid case and titanium oxide water nanofluid case, although greater temperatures are computed in the former and slightly higher Nusselt numbers in the latter.

iii) With decreasing aspect ratio (wider base relative to height of the solar collector geometry) higher temperatures are generated in the enclosure and hotter titanium oxide water nanofluid reaches deeper into the enclosure space. At lower aspect ratio (less than or equal to unity) dual thermal zones are generated in the upper and lower zones of the enclosure.

iv) A substantial deceleration in the titanium oxide water nanofluid flow is induced initially with a decrease in aspect ratio from 4 to 2; however, this pattern is reversed with subsequent decrease in aspect ratio (aspect ratio of  $4/3$ , 1 and 0.5) and flow is accelerated. The singular symmetric cell structure observed at higher aspect ratio is modified into a non-symmetric laterally elongated structure at low aspect ratios.

v) With increasing nano-particle volume fraction of silver nanoparticles, heat circulation in the enclosure is encouraged, thermal conductivity is enhanced, and this is also assisted at greater Rayleigh numbers.

vi) Higher Rayleigh number and nano-particle fraction also causes the central cell to be warped in the streamline distribution and accelerates the flow in the enclosure.

CFD has been shown to be a useful tool in studying metallic nanofluid-solar collector performance. The present simulations provide a solid benchmark for the subsequent chapters and established great confidence in ANSYS FLUENT. In chapter 4 I shall describe a trapezium geometrical solar enclosure with zinc and diamond (carbon-based) nanoparticles. The model in chapter 4 is the last of the 2-D simulations- all subsequent chapters address fully 3-D models.

## **PUBLICATION NOTE**

A version of this chapter was published in **S. Kuharat**, O. Anwar Bég, Ali Kadir and B. Vasu, Computation of metallic nanofluid natural convection in a two-dimensional solar enclosure with radiative heat transfer, aspect ratio and volume fraction effects, *Arabian J. Science and Engineering* (2020). (19 pages). [doi.org/10.1007/s13369-020-04678-1](https://doi.org/10.1007/s13369-020-04678-1) [Impact factor 1.8]. A shorter version was presented at the *International Conference on Innovative Applied Energy (IAPE'19)*, Oxford, United Kingdom, 14-15 March (2019).

---

# **Chapter 4 Diamond and Zinc Nanoparticles Performance in A Water-Based Trapezium Direct Absorber Solar Collector**

## **Abstract**

Following from chapter 3 which investigated heat transfer behaviour in a simple 2-dimensional quadrilateral enclosure with Copper, Silver and Titania Metallic nanoparticles in base water fluid, this chapter will investigate the slightly more complex geometry of a trapezium where a change in inside walls angles influences the heat and flow circulation. These include both carbon-based (e.g. silicates, diamond, carbon nanotubes) and metallic nanoparticles (gold, silver, copper, tin, zinc etc). By combining these nanoparticles with water base fluids, to create nanofluids, improved performance can be achieved in direct absorber solar collector (DASC) systems. In the current work, motivated by these developments, a finite volume code (ANSYS FLUENT ver. 19.1) is employed to simulate the relative performance of both carbon-based (i.e., diamond) and metal-based (i.e., zinc) nanoparticles in a trapezium geometry. The Tiwari-Das formulation is implemented to compute viscosity, thermal conductivity and heat capacity properties for diamond-water and zinc-water nanofluids at different volume fractions. Steady state nanofluid buoyancy-driven incompressible laminar Newtonian convection is examined. The SIMPLE solver is deployed, and residual iterations utilized for convergence monitoring. Mesh independence is included. Verification with the penalty finite element computations of Natarajan et al. (*Int. J. of Heat and Mass Transfer*, 51:747-756, 2008) for the case of a Newtonian viscous fluid (zero volume fraction) is also conducted and excellent correlation achieved. Isotherm, streamline and local Nusselt number plots are presented for different volume fractions, sloping wall inclinations (both negative and positive slopes are considered)

and Rayleigh numbers. Vortex structure and thermal distributions are shown to be modified considerably with these parameters. Overall diamond achieves higher heat transfer rates while more stable velocity distributions are produced with zinc nanoparticles. These trends are amplified at higher volume fractions. The present computations may be further generalized to the three-dimensional case although this requires significantly greater mesh densities and compilation times.

## 4.1 Mathematical Model

Computational Fluid Dynamics software (ANSYS FLUENT) (ANSYS, Inc, 2018) is used to simulate a two-dimensional model of natural convection flow of diamond and zinc-water-based nanofluids in a trapezium enclosure, illustrated in Figure 4.1. The nanofluid (solar absorber liquid) flow is considered to be laminar, steady-state and incompressible. The Tiwari-Das nano-particle volume fraction model is deployed (Bég, et al., 2019) and is described in due course.

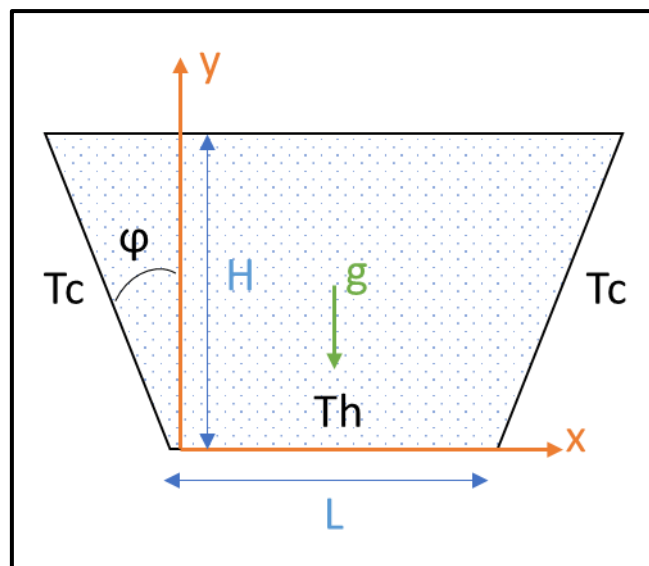


Figure 4.1 Trapezium water nanofluid direct absorber solar collector

The fundamental equations for steady viscous, incompressible laminar flow i.e. Navier-Stokes equations with the thermal convection energy equation are solved where the simulation is two-dimensional and time independent in a Cartesian coordinate system. These equations take the following form:

***Continuity Equation:***

$$\frac{\partial u}{\partial x} + \frac{\partial v}{\partial y} = 0 \quad \text{Equation 4-1}$$

***x-direction momentum***

$$u \frac{\partial u}{\partial x} + v \frac{\partial u}{\partial y} = -\frac{1}{\rho} \frac{\partial p}{\partial x} + \nu \nabla^2 u \quad \text{Equation 4-2}$$

***y-direction momentum***

$$u \frac{\partial v}{\partial x} + v \frac{\partial v}{\partial y} = -\frac{1}{\rho} \frac{\partial p}{\partial y} + \nu \nabla^2 v + g\beta(T - T_c) \quad \text{Equation 4-3}$$

***Energy equation***

$$u \frac{\partial T}{\partial x} + v \frac{\partial T}{\partial y} = \frac{k_{nf}}{\rho_{nf} c_p} \nabla^2 T \quad \text{Equation 4-4}$$

There is no heat transfer through the top wall (adiabatic condition). No slip boundary conditions are assumed on all walls of the enclosure (cavity). Furthermore, the following thermal

boundary conditions are imposed:

Left cold wall: Constant temperature,  $T = 300 \text{ K}$

Right cold wall: Constant temperature,  $T = 300 \text{ K}$

Bottom hot wall: Constant temperature,  $T = 305 \text{ K}$  Equation 4-5

The remaining walls: Adiabatic

A Rayleigh number can also be defined as follows:

$$Ra = \frac{g\beta}{\nu\alpha m} (T_s - T_\infty) y^3 \quad \text{Equation 4-6}$$

Rayleigh number can also be explained as follows: Rayleigh number ( $Ra$ ) is a dimensionless number that signifies the ratio of thermal buoyancy and viscous force. Nusselt number ( $Nu$ ) gives a measure for heat transfer rate along the hot wall of the two-dimensional enclosure. In Eqn. (4-3), the term  $(\rho\beta)nf g(T - Tw)$  symbolizes the thermal buoyancy force. Since the changes in temperature and density of the nanofluid in this simulation are small, thus the Boussinesq model is employed. Boussinesq's model (named in honour of the great French engineer and mathematician J. Boussinesq) considers density to be invariant for all the solved equations in (ANSYS, Inc, 2018); this provides faster convergence in comparison to setting up the problem with fluid density as a function of temperature. This approximation is accurate provided  $\beta(T-Tw)$  is less than or equal to unity. Absorber fluid i.e. nanofluid transport is modelled as a "pseudo single-phase flow" since the nanoparticles are very small (the scale is one billionth of a metre). Eqns. (4-1)-(4-4) with the associated boundary conditions (4-5) are solved by (ANSYS, Inc, 2018) software and the temperature along the solid-air interfaces is computed as part of the solution. This finite volume code has been deployed extensively by the authors in many areas including photovoltaic thermofluids (Sze, et al., 2011), aerodynamics and gas dynamics (Daud, et al., 2012) (Daud, et al., 2011) (Bég, et al., 2018) (Bég, et al., 2019) (Kadir, et al., 2019) and nanofluid solar collector simulations (Kuharat, et al., 2019) (Kuharat & Bég, 2019) (Bég, et al., 2020) (Al-Srayyih, 2019). The solution of the model gives the temperature and velocity fields and hence total heat flux across the heated wall, local and average Nusselt numbers along the heated wall, as well as the flow streamlines and surface

shear stress. A nanofluid is defined in ANSYS FLUENT workbench as a “new fluid” with a new density, viscosity, thermal conductivity and specific heat obtained as a function of a base fluid and nano-particle type and concentration (volume fraction), according to Brinkman as described in (Akbarzadeh & Fardi, 2018).

## 4.2 Grid Sensitivity Analysis

Extensive grid independence tests were conducted of the trapezium mesh for air inside trapezium geometry with  $\phi=30$  and  $Ra 10^5$  shown in Figure 4.2. within the grid dependet study five different uniform grids system of 1288, 2030, 3572, 4472 and 5244 are conducted. The result in an averagee nusselt number of the fluid is increase with a number of the elements untill a small difference is observed between 4472 elements and 5244 elements which can be consider nelegible which indicated that the simulation is convergent. The finalized mesh is shown in Figure 4.3. 5244 triangular elements were deployed.

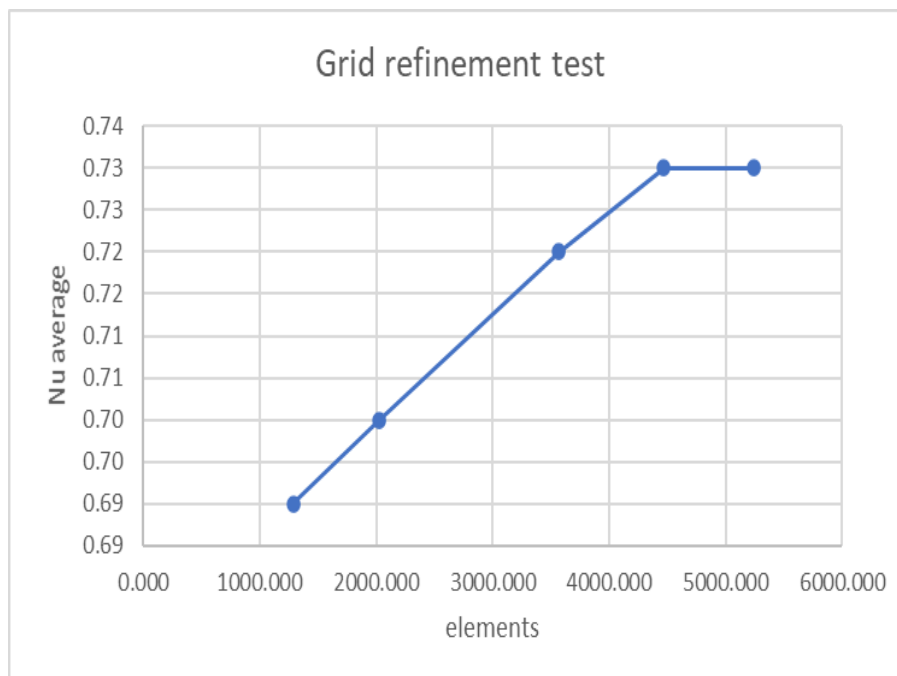
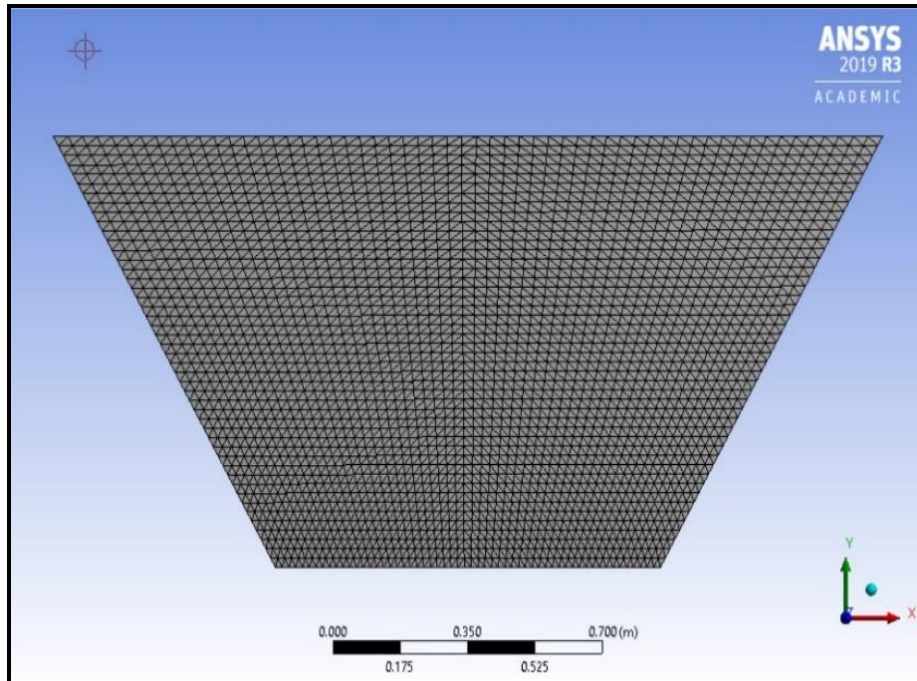
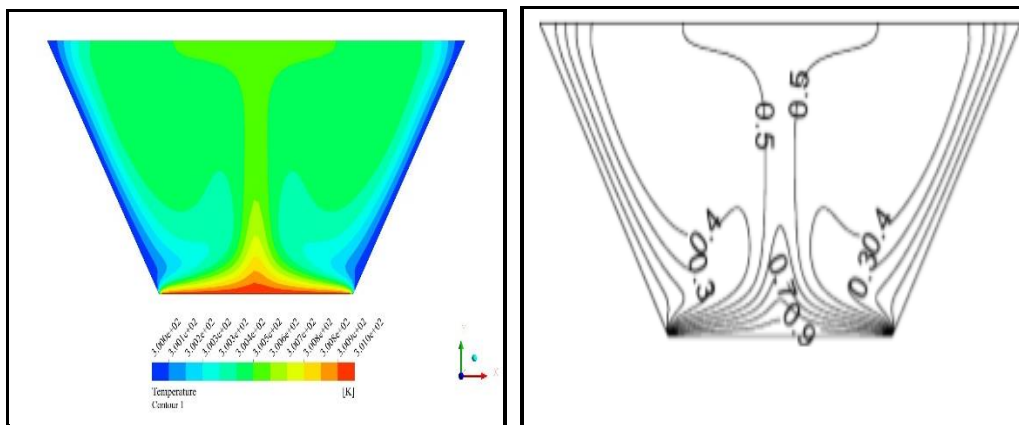


Figure 4.2 Grid refinement test



**Figure 4.3 Final Mesh design for nanofluid DASC**

To verify the accuracy of the ANSYS FLUENT computations, a comparison has also been made for the purely Newtonian fluid case with the exact trapezium geometry and boundary conditions employed in the finite element simulations of (Natarajan, et al., 2008). The comparison of temperature contours (isotherms) is shown in Figure 4.4.



**Figure 4.4 Comparison of ANSYS FLUENT and FEM solution of (Natarajan, et al., 2008).**

Excellent correlation is achieved and therefore confidence in the present ANSYS FLUENT code is justifiably high.

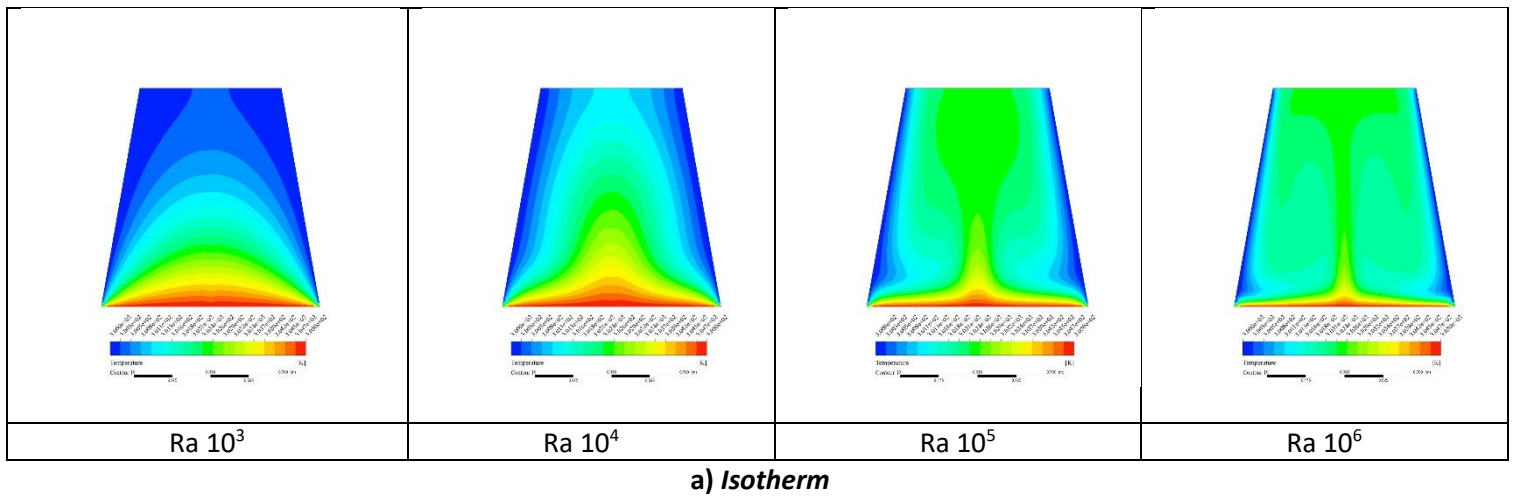


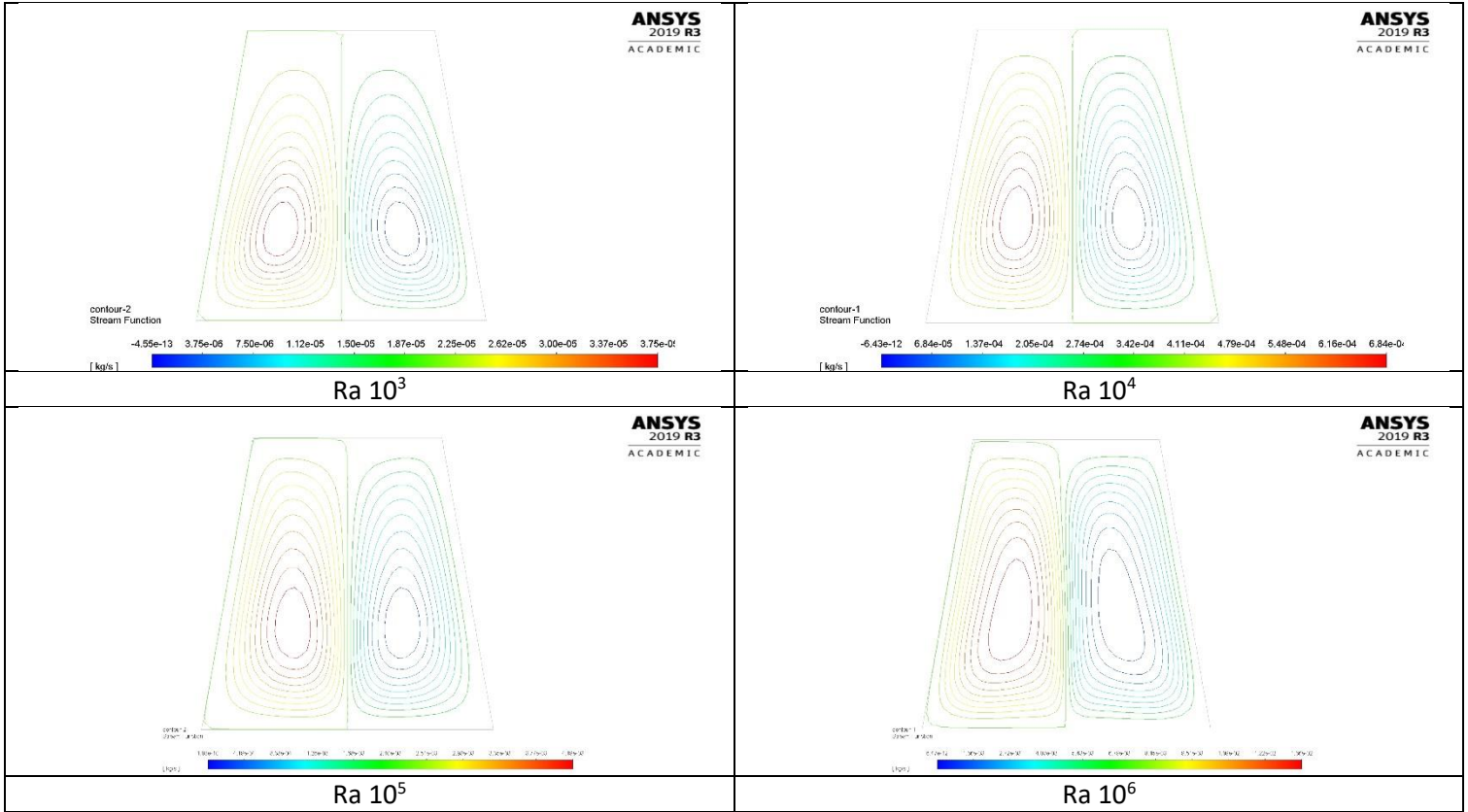
### 4.3 Results and Discussion

Ansys fluent results are presented in Figure 4.5-Figure 4.16. We consider the influence of individual parameters in turn in the ensuing discussion.

#### *Effects of Rayleigh number and inclination on the streamlines and isotherms (diamond)*

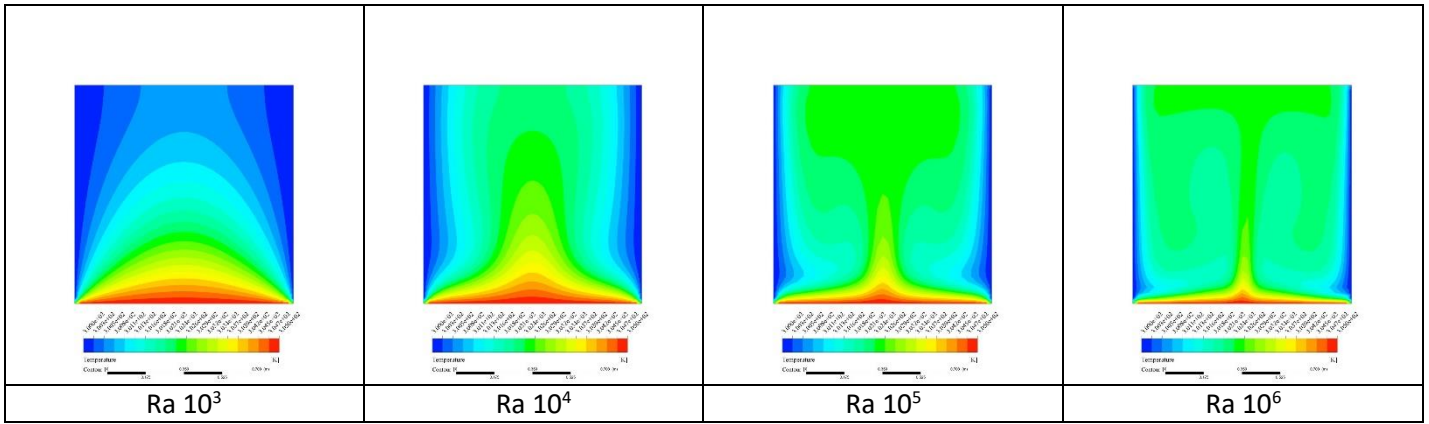
The progression of flow and thermal fields within the trapezoidal enclosure for  $Ra = 10^3, 10^4, 10^5, \text{ and } 10^6$  and tilt angle,  $\phi = 30^\circ, 20^\circ, 10^\circ, 0^\circ, \text{ and } -10^\circ$  are presented in Figure 4.5-Figure 4.9. The flow and temperature fields are symmetrical about the vertical y-axis as boundary conditions are the same for both left and right inclined sidewalls. As predicted, hot fluid mainly rises up from the middle of the heated wall due to an effect of thermal buoyancy force. The flow is redirected down along the walls forming two symmetric vortex cells with clockwise and anticlockwise rotations inside the cavity.



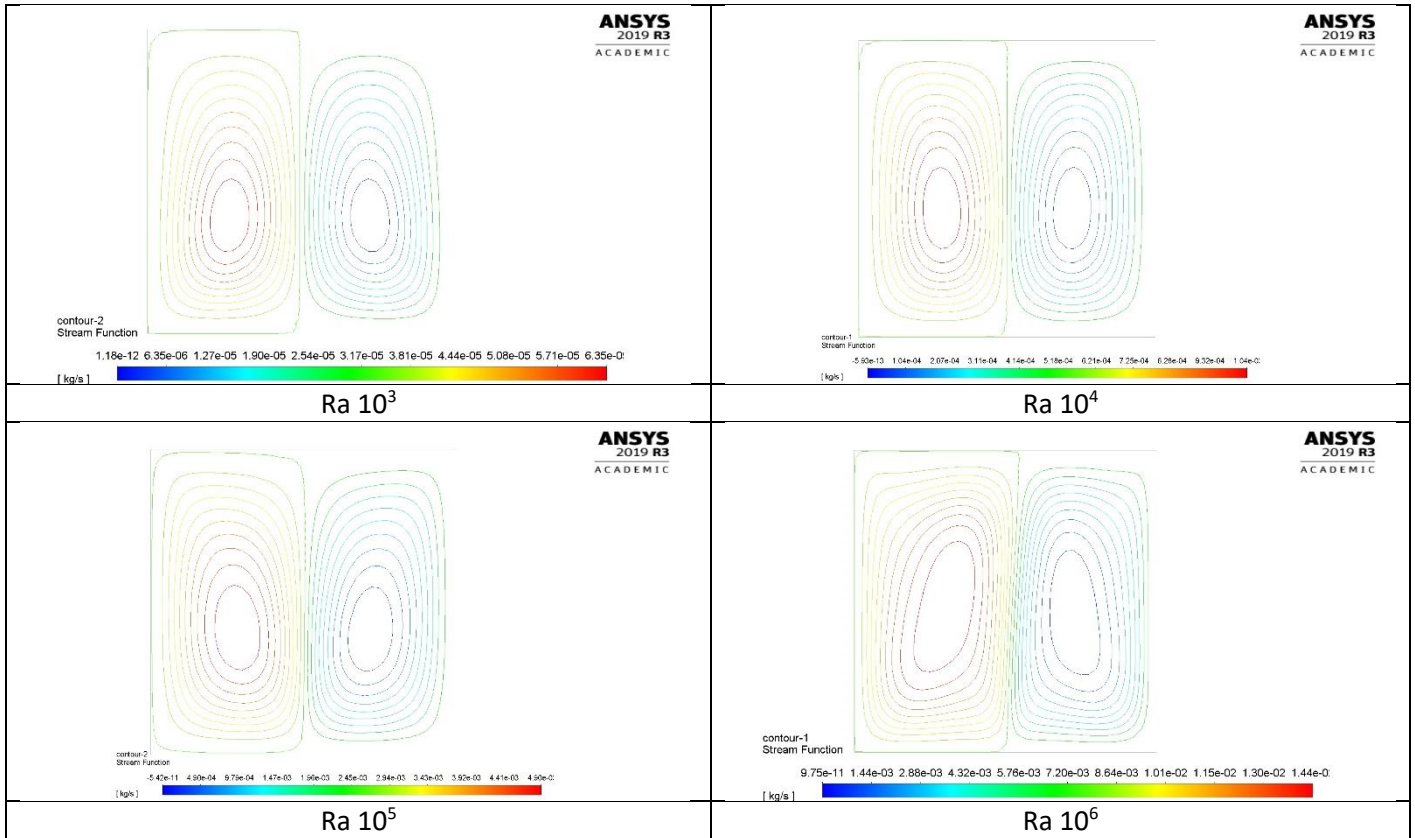


b) Streamline fuction

Figure 4.5 Diamond-Water Based Nanofluid with volume fraction  $\phi = 0.02$ , angle ( $\theta$ ) =  $-10^\circ$

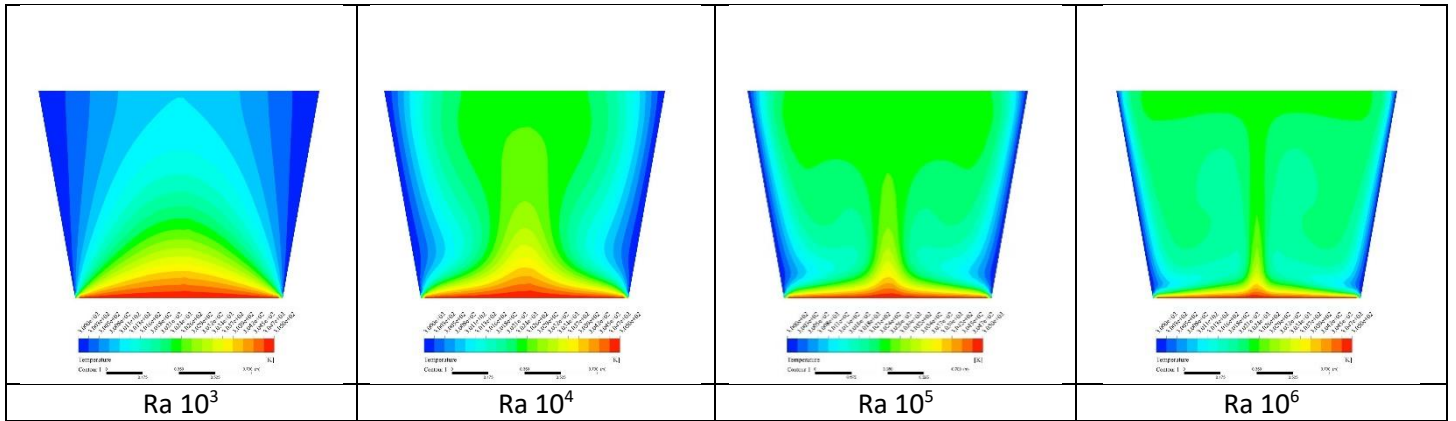


a) Isotherm

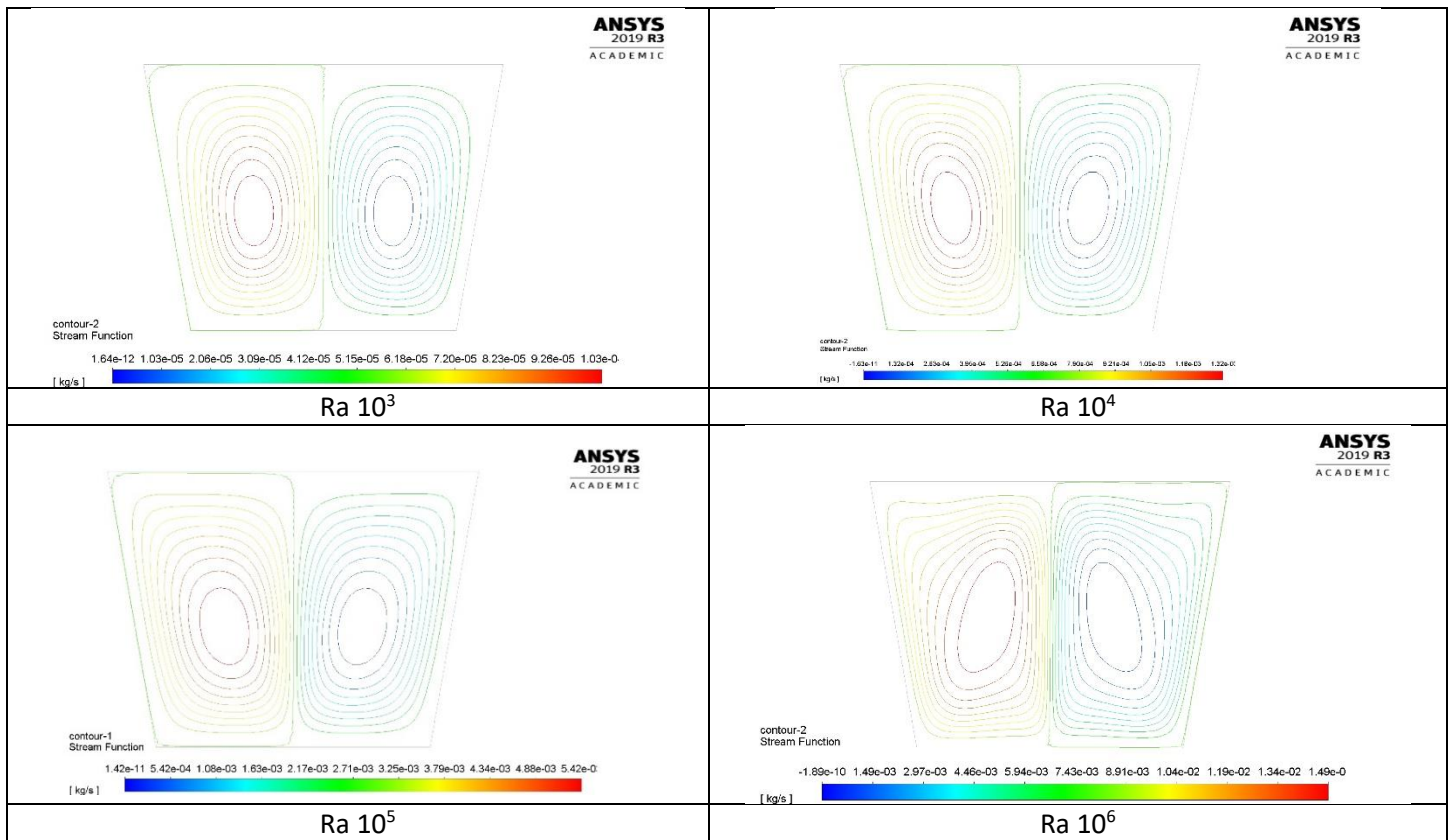


**b) Streamline fuction**

**Figure 4.6 Diamond-Water Based Nanofluid with volume faction  $\phi = 0.02$ , angle  $(\theta) = 0^\circ$**

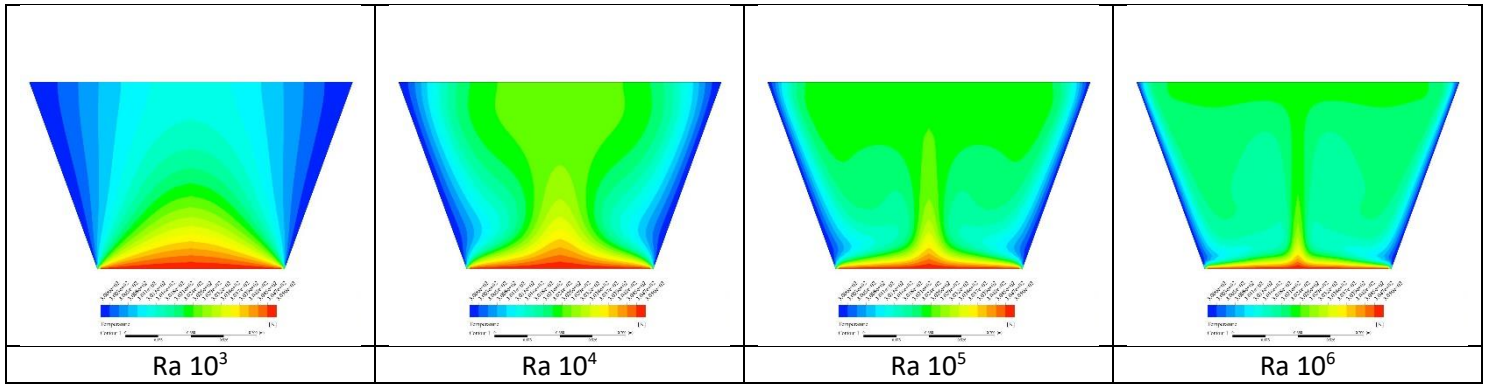


a) Isotherm

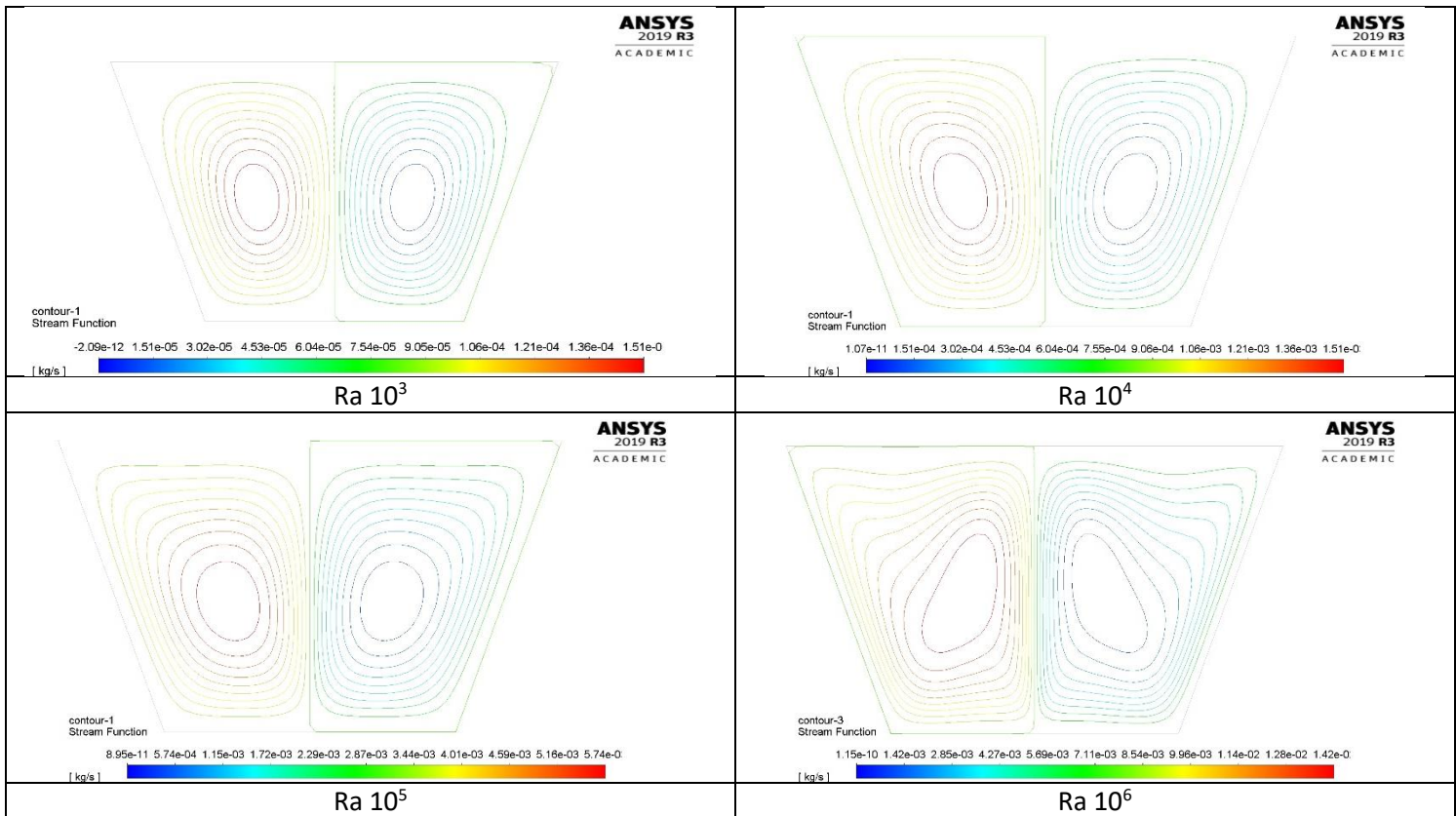


b) Streamline function

Figure 4.7 Diamond-Water Based Nanofuid with volume fraction  $\phi = 0.02$ , angle  $(\theta) = 10^\circ$



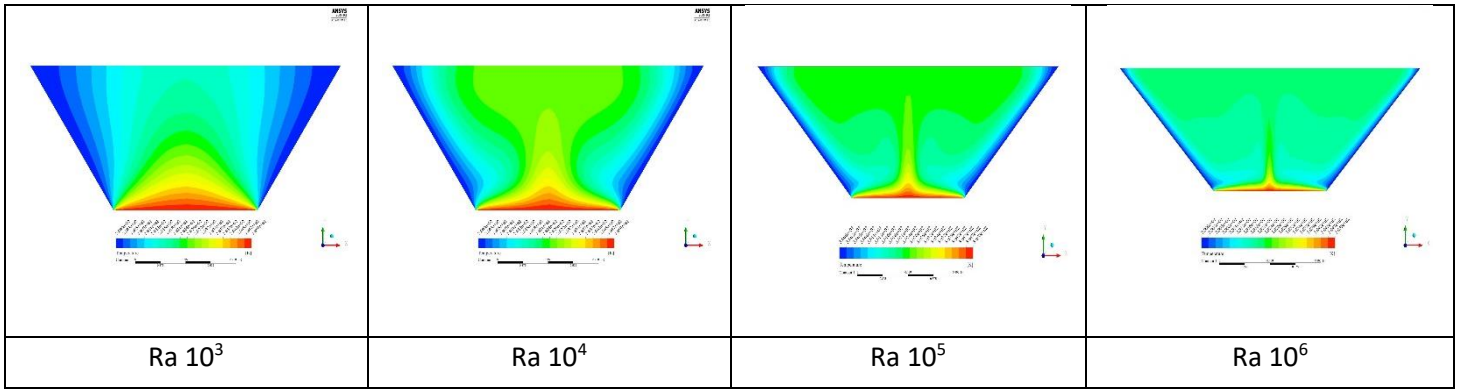
a) Isotherm



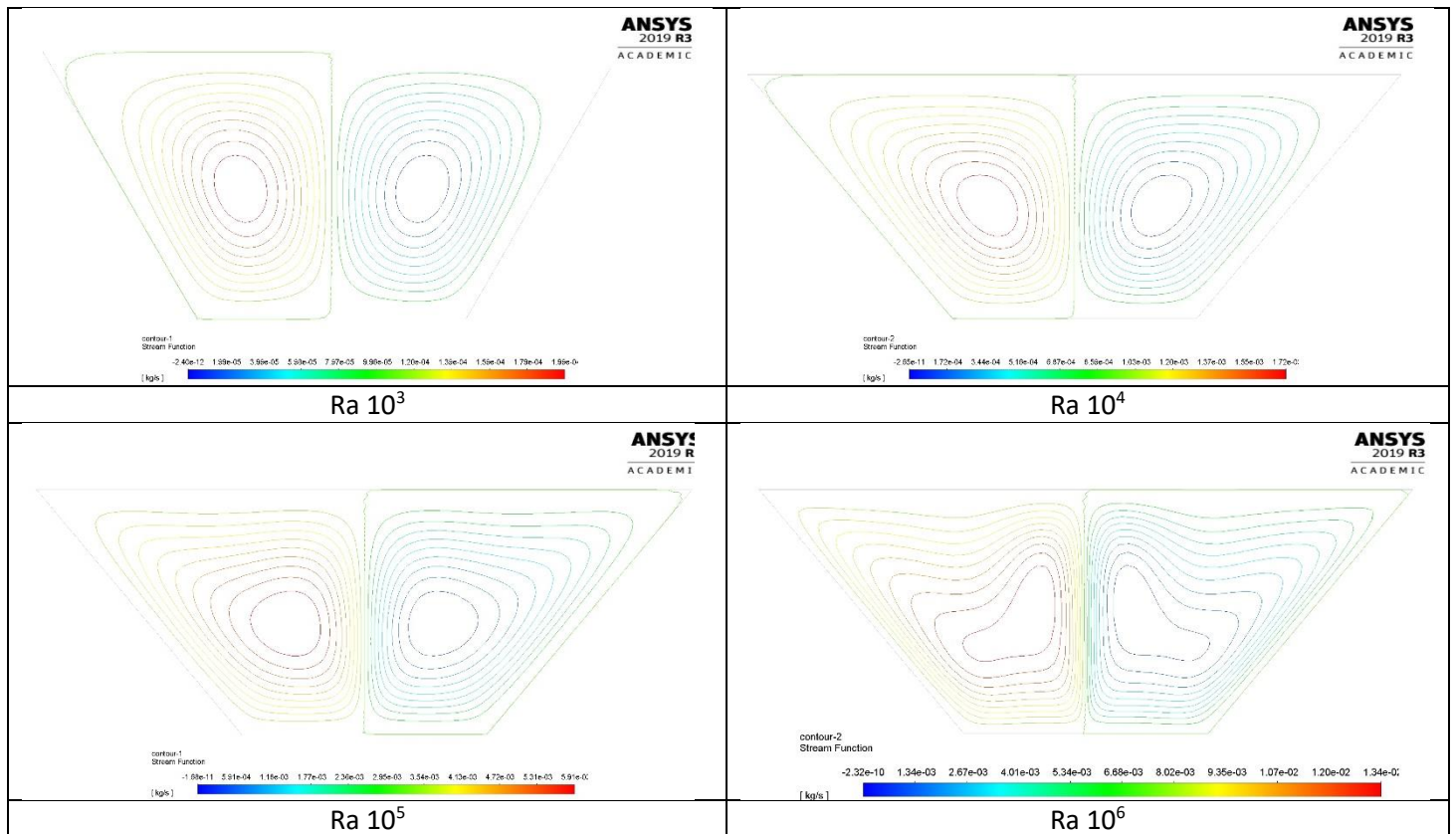
b) Streamline fuction

Figure 4.8 Diamond-Water Based Nanofluid with volume fraction  $\phi = 0.02$ , angle ( $\phi$ ) =  $20^\circ$



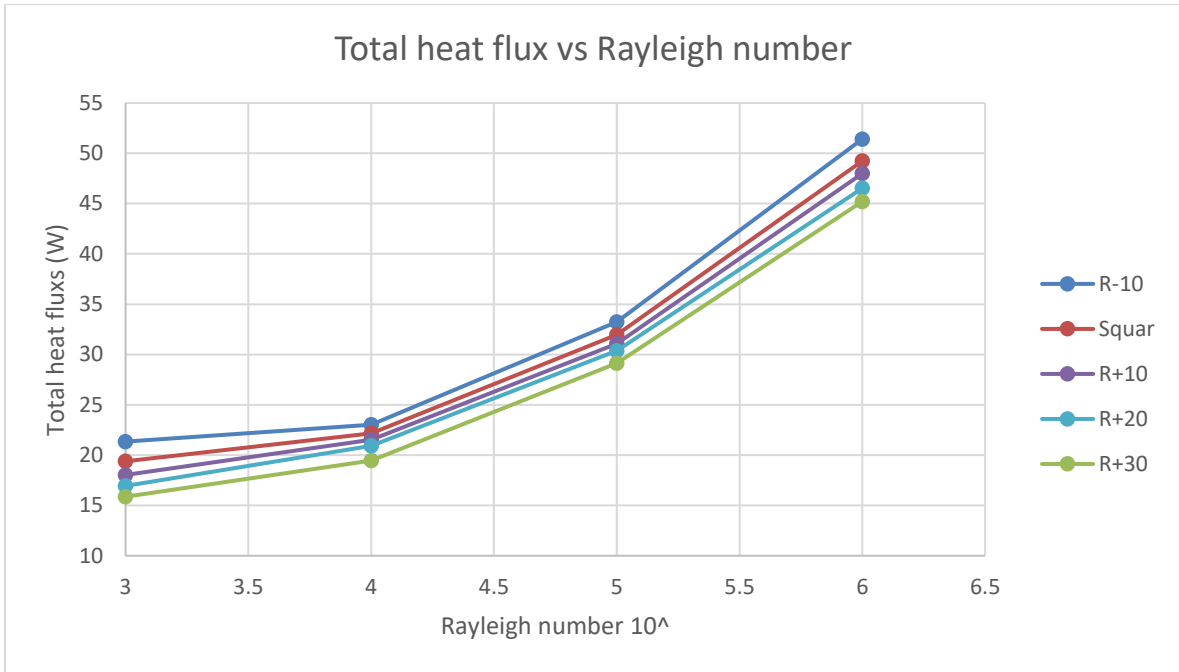


a) Isotherm



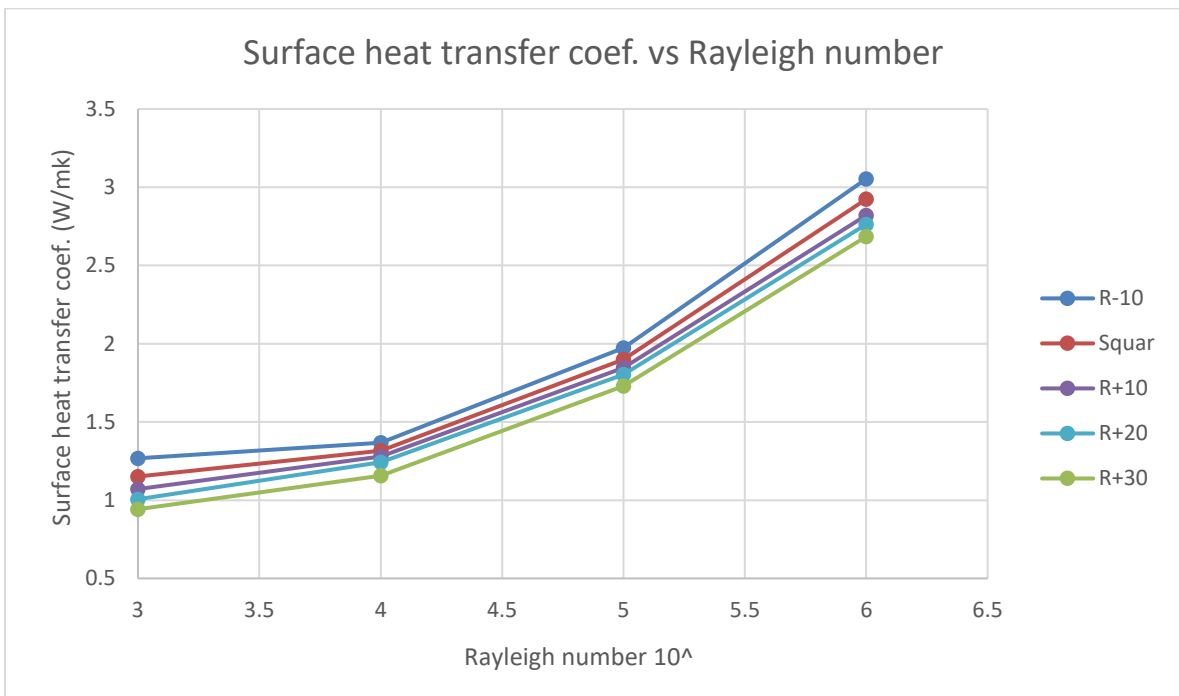
b) Streamline function

Figure 4.9 Diamond-Water Based Nanofluid with volume fraction  $\phi = 0.02$ , angle ( $\theta$ ) =  $30^\circ$



**Figure 4.10 Total heat flux vs Rayleigh number**

***Diamond-Water Based Nanofluid with volume fraction  $\phi = 0.02$***



**Figure 4.11 Surface heat transfer coef. vs Rayleigh number**

***Diamond-Water Based Nanofluid with volume fraction  $\phi = 0.02$***

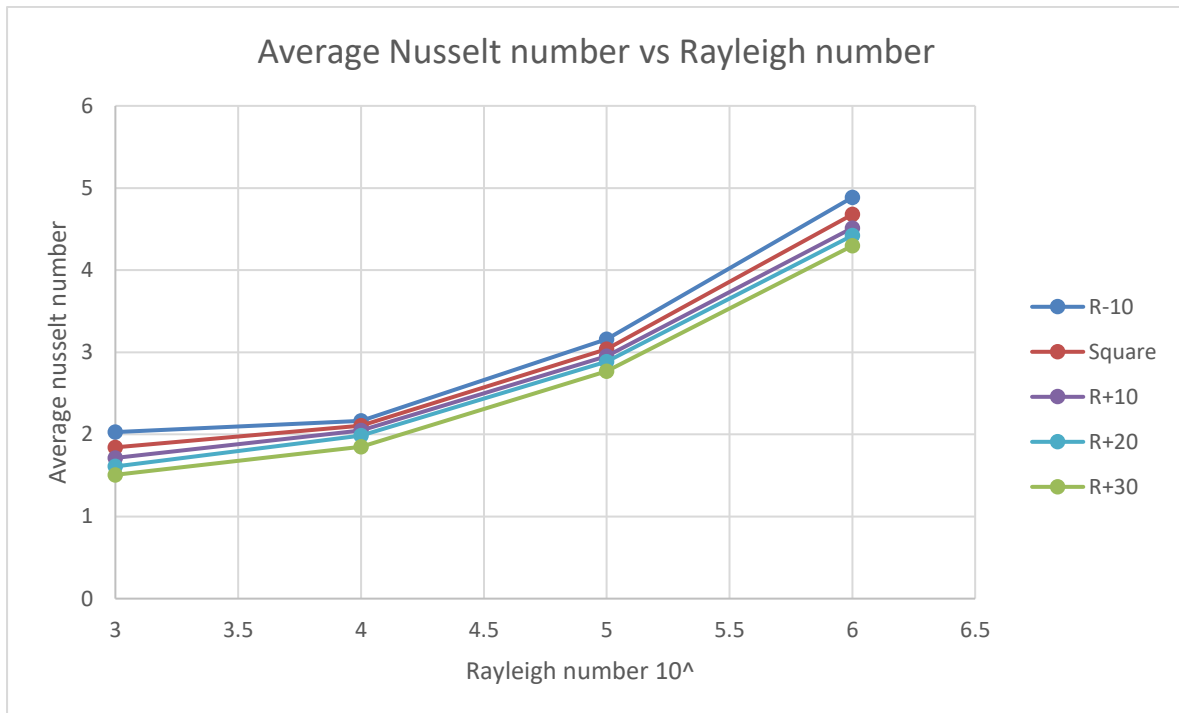


**Figure 4.12 Average Nusselt number vs Rayleigh number**  
***Diamond-Water Based Nanofluid with volume fraction  $\phi = 0.02$***



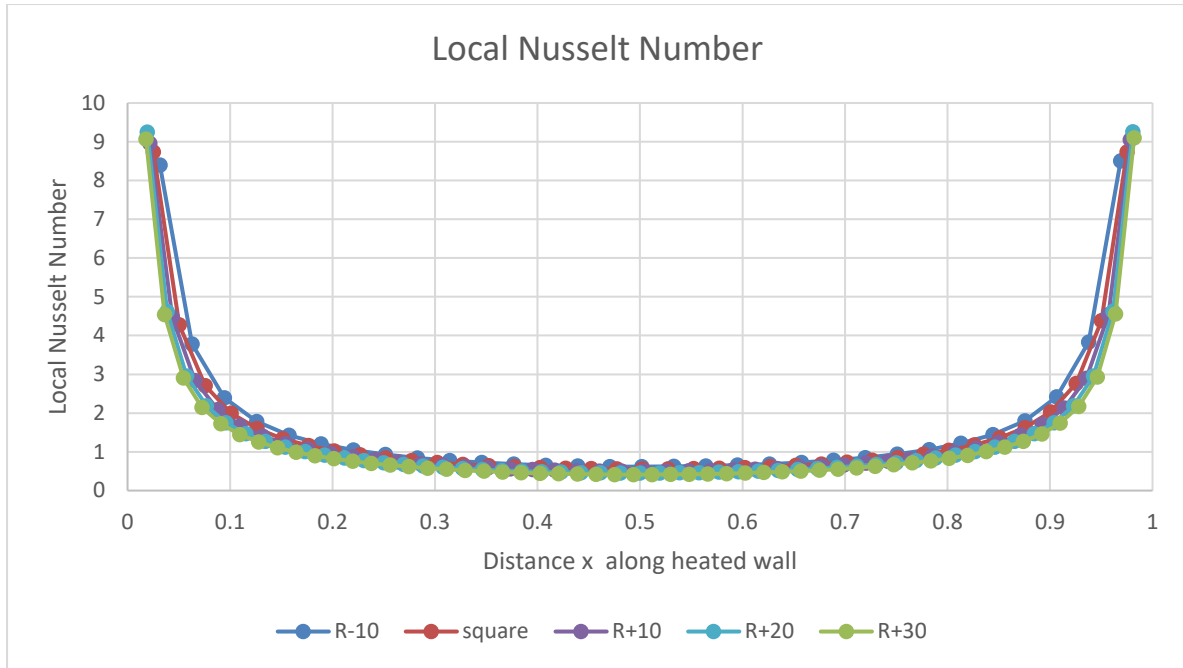


Figure 4.13 Local Nusselt Number

**Diamond-Water Based Nanofluid with volume fraction  $\phi = 0.02$**

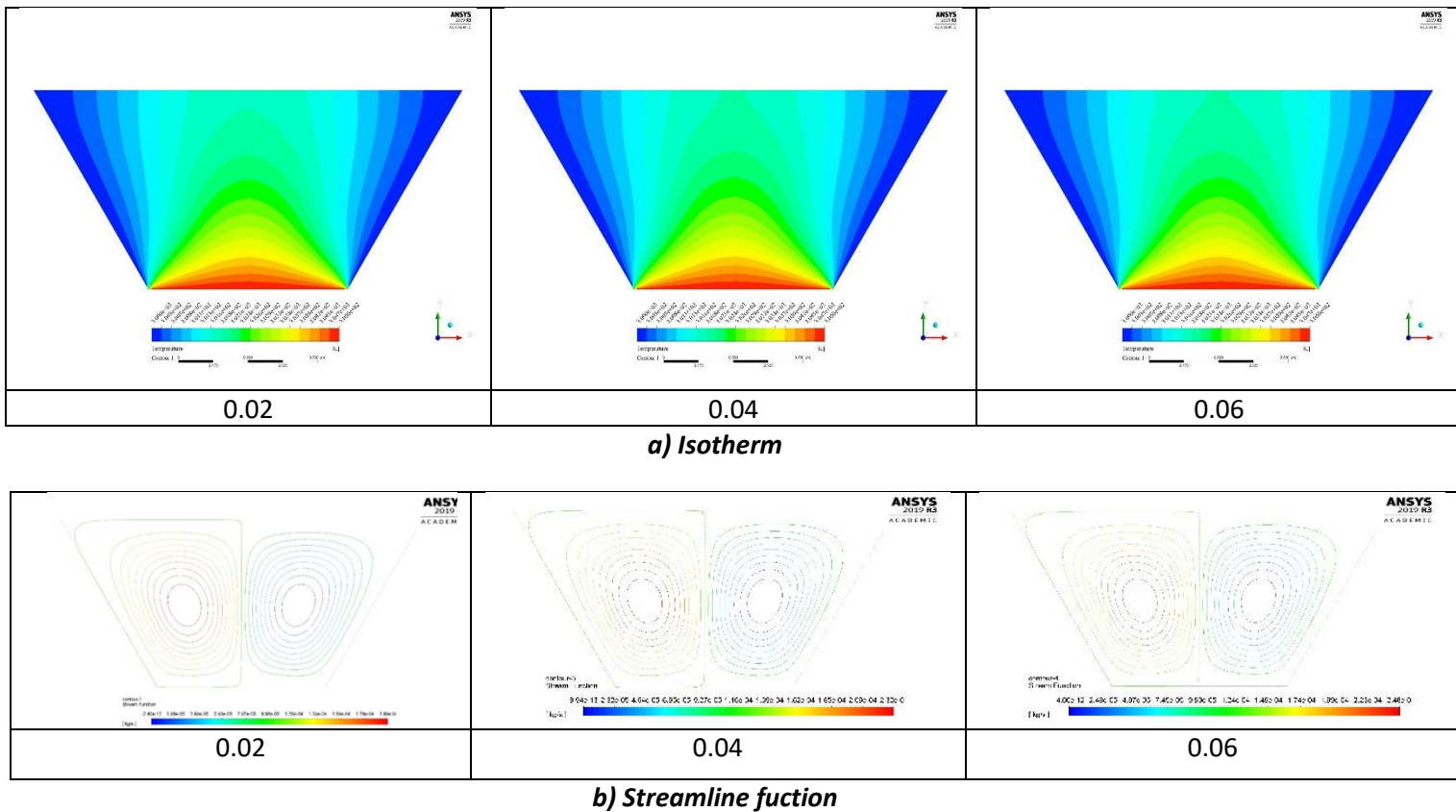
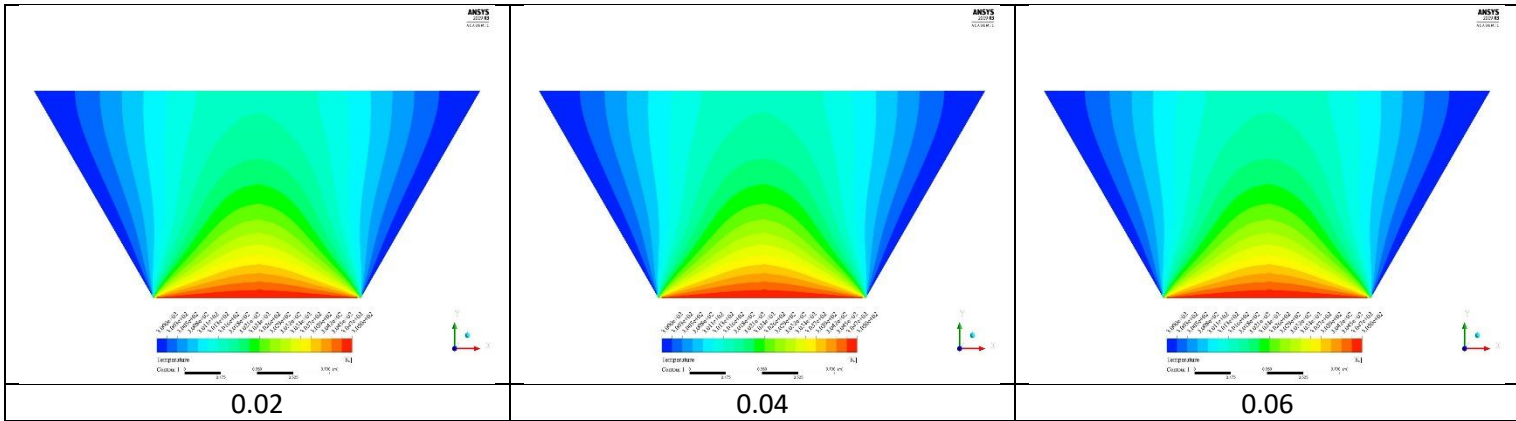
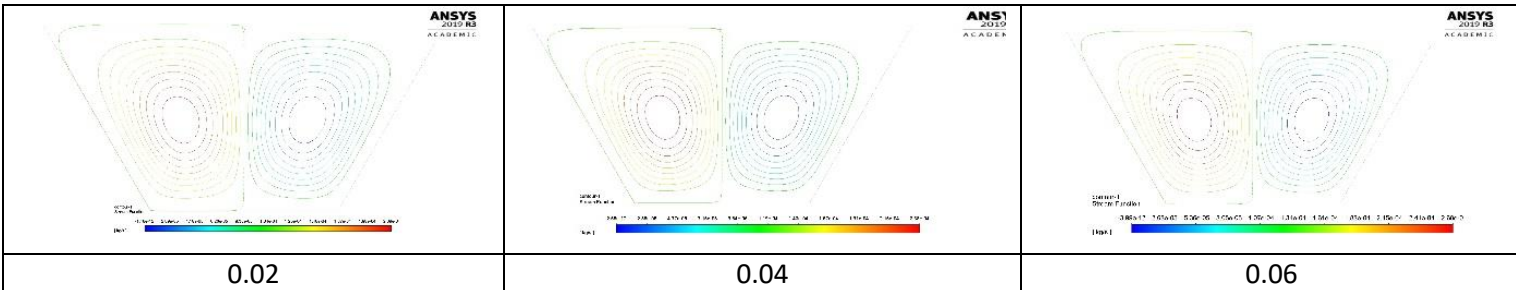


Figure 4.14 Diamond nanofluid in Trapezium with 30 degree slope at Rayleigh number  $10^3$  with different volume fraction



a) Isotherm



b) Streamline function

Figure 4.15 Zinc nanofluid in Trapezium with 30 degree slope at Rayleigh number  $10^3$  at different volume fraction

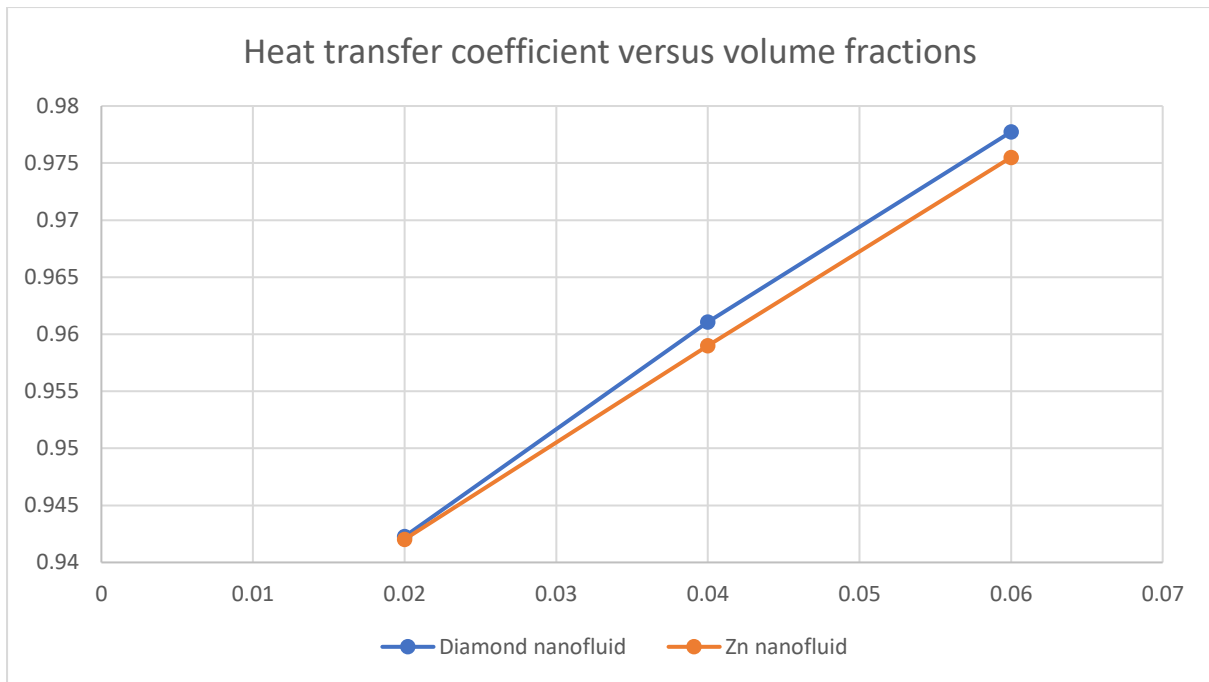


**Figure 4.16 Heat transfer coef. vs volume fractions**

With increasing Rayleigh number, the hot zone at the trapezium base is progressively suppressed. Heat transfer to the wall is therefore inhibited. However, there is a concurrent expansion in warmer fluid through the core region and the cooler zones at the sidewalls are contracted. Heat is therefore circulated more efficiently in the enclosure with increasing thermal buoyancy effect. At very high Rayleigh number (with volume fraction fixed at 2%, diamond nanofluid case, Figure 4.5) the streamlines are also morphed considerably, and the dual vortex structure is stretched in the vertical direction. The cells are increasingly lop-sided as compared with lower Rayleigh numbers. For the rectangular case (slope angle = 0) and the same volume fraction (2%, diamond case), the green zones are significantly expanded in the upper section of the enclosure with increasing Rayleigh number. Also, there is an elimination in the skewing of the dual vortex zones at higher Rayleigh numbers; however some distortion is induced at the upper and lower wall zones in the streamlines which are not as controlled as in the trapezium case. With positive side wall inclination (10 degrees), as observed in Figure 4.7, there is a much more consistent distribution of heat achieved throughout the trapezium and

this is encouraged with greater Rayleigh number. However, at highest Rayleigh number, colder regions emerge in a symmetric fashion which implies that a critical Rayleigh number between 106 and 107 exists where the best temperature distribution is obtained in the solar collector. The dual vortex structure witnessed in the streamlines is much more stable in Figure 4.7 than in previous figures (negative slope case, Figure 4.5 and rectangular case, Figure 4.6). This would indicate that the strong positive slope trapezium produces the most regulated circulation compared with the other configurations. However, it does not achieve the best heat transfer to the boundaries, which is generally obtained with the strong negative slope case (Figure 4.5 i.e., -10 degrees inclination). While the trend in isotherms is sustained with even greater positive sidewall slope (Figure 4.8) i.e. expansion in homogenous heat distribution, the vortex cells (streamlines) are increasingly warped with higher Rayleigh numbers, in particular at the top left and right corners of the cavity. A counterproductive distribution in both isotherms and streamlines is further witnessed with even greater side wall slope angle ( $\theta = 30$  degrees i.e. gentle slope) in Figure 4.9 It would appear therefore that optimum results in terms of heat transmission to the boundaries, are produced for the strong negative slope (-10 degrees i.e. Figure 4.5) even at relatively low diamond nanoparticle volume fraction (2%). It is also noteworthy that even at low Rayleigh numbers, e.g.  $Ra = 10^3$ , viscous forces are considerably greater than the buoyancy forces and, therefore heat transfer is essentially diffusion dominated and the shape of the streamline tends to follow the geometry of the enclosure. For  $Ra = 10^5$  and  $10^6$ , it is remarkable to observe that the streamline of temperature contours near the walls tend to have a neck formation cause by a strong circulation of a higher Rayleigh number which contrasts the flow pattern for  $Ra = 10^3$ . The core of the circulating rolls narrower with the increase of  $Ra$  indicating a significant increase in the intensity of convection.

### ***Total heat flux***

**Figure 4.10** shows results of total heat flux with change in Rayleigh number for diamond-water based nanofluid with volume fraction,  $\phi = 0.02$  at different sidewall inclination angles (30, 20, 10, 0 and -10). For a constant surface temperature, increase in the total heat flux indicates a boost in the heat transfer to the walls. This corresponds to a decrease in temperature contour magnitudes within the enclosure.

### ***Surface heat transfer coefficient***

**Figure 4.11** shows the results for average surface heat transfer coefficient at various Rayleigh numbers for different sidewall inclination angles, again for diamond-water based nanofluid with volume fraction  $\phi = 0.02$ . Again, as in Figure 4.10, the negative side wall case (angle of -10 degrees) achieves the best heat flux to the wall, whereas a=intermediate performance is given with the positive strong slope case (+10 degrees).

### ***Average Nusselt number***

**Figure 4.12** illustrates results of Average Nusselt number along the heated wall with different Rayleigh numbers at different sidewall inclination angles, diamond-water based nanofluid with volume fraction  $\phi = 0.02$ . At lower  $Ra$  for all cases of the sidewall inclination angle (30, 20, 10, 0 and -10), graphs retain a flat trend indicating slight increase in  $Nu$  later rises rapidly after Rayleigh number reached  $10^4$ . However, the average Nusselt number is higher for a lower sidewall inclination angle. For this case therefore compared with other geometries, a superior heat transfer rate is attained to the boundaries, at all Rayleigh numbers. As the sidewall inclination angles decrease, the trapezium morphs into a rectangular geometry and then an obtuse trapezium with positive sloping walls. The constant temperature sidewalls in the case

of negative slope (-10 degrees) act as heat sinks which move closer to the heat source resulting in improved heat transfer to the walls of the cavity.

### ***Local Nusselt Number***

The trends observed in Figure 4.12 are confirmed also in Figure 4.13 wherein the strong negative trapezium sloped case (inclination = -10 degrees) again attains the highest magnitudes of local Nusselt number at all locations ( $x$  values) along the heated wall. Clearly local Nusselt number is a maximum at  $x = 0$  and  $x = 1$  corresponding to the extremities of the heated boundary.

### ***Effects of volume fraction on the streamlines and isotherms (diamond and zinc)***

**Figure 4.14-Figure 4.15** illustrate the relative performance of diamond and zinc nanoparticles at different percentage doping i.e. volume fractions,  $\phi$ . The gentlest positive slope trapezium case of  $\Phi = 30$  degrees is considered with lowest Rayleigh number,  $Ra = 10^3$ . In both cases there is a significant enhancement in temperature magnitudes with greater volume fraction. The hot zone at the base wall is expanded and warmer fluid (green/yellow zones) progressively replaces colder blue zones in the core region. Thermal diffusion in the regime is therefore clearly modified with greater quantities of nanoparticles. Slightly higher temperatures are computed for the zinc nanofluid compared with diamond nanofluid which is probably due to thermal conductivity differences. This inevitable leads to a difference in the heat transfer coefficient.

### ***Heat Transfer Coefficient***

**Figure 4.16** depicts the variation in heat transfer coef. vs volume fractions for both diamond and zinc-water nanofluid. At low volume fraction (2%) both achieve approximately the same

magnitude in heat transfer coefficient. However, with increasing volume fraction, the profiles diverge significantly and diamond-water nanofluid produces a markedly higher heat transfer coefficient which is maximum at the highest volume fraction of 6%.

## 4.4 Conclusions

A theoretical and numerical study of the relative performance of both carbon-based (i.e. diamond) and metal-based (i.e. zinc) water -nanofluids in a trapezoidal geometry has been presented. The Tiwari-Das formulation is implemented to compute viscosity, thermal conductivity and heat capacity properties for diamond-water and zinc-water nanofluids at different volume fractions. Steady state nanofluid buoyancy-driven incompressible laminar Newtonian convection is examined. A finite volume code (ANSYS FLUENT ver 19.1) is employed for the simulations with the SIMPLE solver, residual iterations utilized for convergence monitoring. Mesh independence is included. Verification with the penalty finite element computations of (Natarajan, et al., 2008) for the case of a Newtonian viscous fluid (zero volume fraction) is also conducted and excellent correlation achieved. Isotherm, streamline and local Nusselt number plots are presented for different volume fractions, sloping wall inclinations (both negative and positive slopes are considered) and Rayleigh numbers. The simulations have shown that:

- 1) Vortex structure and thermal distributions are modified considerably with volume fraction, enclosure side wall inclination and Rayleigh number.
- ii) Diamond achieves higher heat transfer rates than zinc nanoparticles.
- iii) Increasing heat transfer coefficients are computed with a rise in nanoparticle volume fraction for both diamond and zinc.

iv) Constant temperature sidewalls in the case of a strong negative slope (-10 degrees) act as heat sinks which move closer to the heat source resulting in improved heat transfer to the walls of the cavity.

v) The strong positive slope trapezium case (inclination of +10 degrees) produces the most regulated circulation compared with the other configurations, although it does not achieve the best heat transfer to the boundaries – this is obtained with the strong negative slope case (i.e., -10 degrees inclination).

vi) For the rectangular case (slope angle = 0) in the diamond water nanofluid case, more homogeneous temperature distribution is achieved throughout the enclosure compared with any trapezium scenario and the skewing of the dual vortex zones at higher Rayleigh numbers is eliminated.

vii) For the strong positive slope trapezium case (+10 degrees inclination) compared with the strong negative slope trapezium case (-10 degrees inclination), at very high Rayleigh number (volume fraction 2%, diamond nanofluid case) the streamlines are also morphed considerably, and the dual vortex structure is stretched in the vertical direction. The cells are increasingly lop-sided as compared with lower Rayleigh numbers for both sloped wall cases.

The present computations have furnished some interesting insights into the relative performance of zinc and diamond water nanofluids in trapezium and rectangular colar enclosures. However they have been confined to stady state and ignored porous media (Al-Srayyih, 2019) and magnetohydrodynamic effects (magnetic nanoparticles). Magnetic nanofluids are considered in chapter 8. The next model in chapter 5 is a 3-D simulation of natural convection in solar collector.

#### **PUBLICATION NOTE**

A version of this chapter has been accepted in *IMECHE J Nanoengineering, Nanomaterials and Nanosystems (2021)* and a shorter version will be presented at the *8<sup>th</sup> BUU Virtual Interdisciplinary Conference (Thailand) in September 2021*.



# **Chapter 5 Three-dimensional tilted prismatic solar enclosure with aspect ratio and volume fraction effects**

## **Abstract**

Building on the CFD simulations in chapter 3 and 4 which examined 2-D solar enclosure configurations, this chapter presents finite volume numerical simulations of natural convection in an inclined *3-dimensional* prismatic direct absorption solar collector (DASC) containing gold-water nanofluid. Steady-state, incompressible laminar Newtonian viscous flow is assumed. The enclosure has two adiabatic walls, one hot (solar receiving) and one colder wall. ANSYS FLUENT software (version 19.1) is employed. The Tiwari-Das volume fraction nanofluid model is again utilized to simulate nanoscale effects and allows a systematic exploration of volume fraction effects. The effects of thermal buoyancy (Rayleigh number), geometrical aspect ratio and enclosure tilt angle on isotherm and temperature contour distributions are presented with extensive visualization in three dimensions. Grid-independence tests are included. Validation with published studies from the literature is also conducted. A significant modification in vortex structure and temperature distribution is computed with volume fraction, Rayleigh number, aspect ratio and tilt angle. Heat flux and average Nusselt number results are also included. Gold nanoparticles even at relatively low volume fractions are observed to achieve substantial improvement in heat transfer characteristics.

## **5.1 Computational Mathematical Model**

The three-dimensional model of heat and fluid flow in the solar nanofluid absorber geometry (prismatic enclosure) is designed in ANSYS FLUENT computational fluid dynamics software (Kuharat & Bég, 2018). The geometric configuration is illustrated in Figure 5.1. Laminar, steady-state, incompressible flow is considered. The nanofluid is the absorber fluid and the

Tiwari-Das nano-particle volume fraction model is deployed (Tiwari & Das, 2007), which is described in due course.

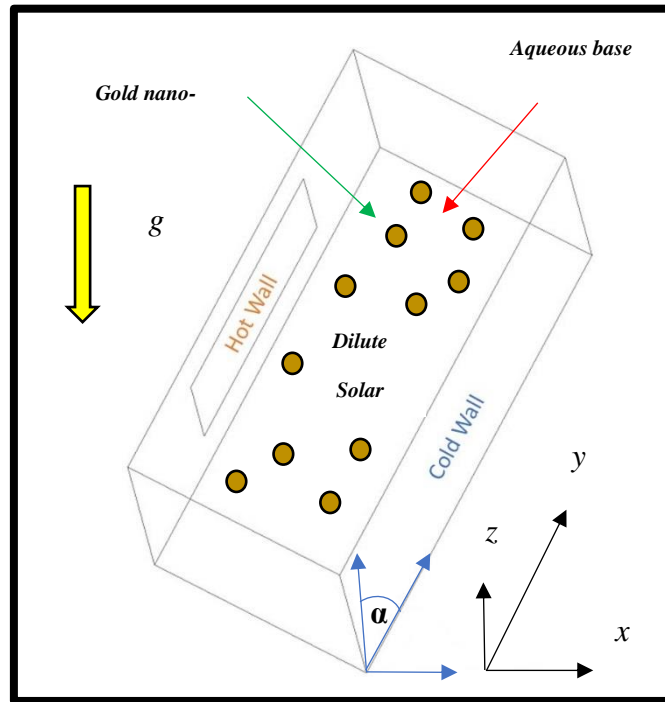


Figure 5.1 3-dimensional solar nanofluid absorber prismatic geometry

A dilute nanofluid suspension is assumed, and the nanoparticles are taken to be in thermal equilibrium with the base fluid. There is no heat transfer through the top wall (adiabatic end condition). No slip boundary conditions are assumed on all walls of the enclosure (cavity). The walls are solid (impermeable). The fundamental equations for steady viscous, incompressible laminar flow and thermal convection are the three-dimensional time-independent Navier-Stokes equations and energy equation, which in a Cartesian coordinate system, take the following form (more details of the equations are given in section 2.2-1 of chapter 2):

$$\frac{\partial v_i}{\partial x_i} = 0 \quad (5.1)$$

$$\rho_{nf} v_j \frac{\partial v_j}{\partial x_j} = -\frac{\partial p}{\partial x_i} + (\rho\beta)_{nf} g(T - T_w) \cos\alpha + \frac{\partial}{\partial x_j} \left[ \mu_{nf} \left( \frac{\partial v_i}{\partial x_j} + \frac{\partial v_j}{\partial x_i} \right) \right] \quad (5.2)$$

$$(\rho c_p)_{nf} v_j \frac{\partial T}{\partial x_j} = \frac{\partial}{\partial x_j} \left( k_{nf} \frac{\partial T}{\partial x_j} \right) \quad (5.3)$$

Here  $v_j$  is the velocity vector (u,v,w),  $x_j$  denotes (x,y,z) coordinates,  $\rho_{nf}$  is density of the nanofluid (kg/m<sup>3</sup>),  $\mu_{nf}$  is dynamic viscosity of the nanofluid (kg.m/s),  $c_p$  = specific heat capacity of the nanofluid (J/kg.K),  $k_{nf}$  is thermal conductivity of nanofluid (W/m.K), T denotes temperature (K), g denotes gravity,  $\beta$  is coefficient of thermal expansion and  $\alpha$  is the enclosure orientation angle (tilt) to the vertical. When heat is added to the nanofluid, the density varies with temperature and flow can be induced due to the force of gravity mobilizing natural convection currents. In eqn. (5.2), the term  $(\rho\beta)_{nf}g(T - T_w)\cos\alpha$  denotes the buoyancy force. Natural convection (buoyancy-driven flows) frequently employ the Boussinesq model. In this approach, constant density is specified, so the mass is properly calculated. This approach is valid provided the temperature differences in the domain are not excessive. The main benefit of Boussinesq model is that the simulation has faster convergence in comparison to setting up the problem with fluid density as a function of temperature. This model treats density as a constant value in all the solved equations in ANSYS FLUENT (Kuharat, et al., 2019). This approximation is accurate if changes in actual density are small; specifically, the Boussinesq approximation is valid when  $\beta(T - T_w) \leq 1$ . In ANSYS, this approach is implemented as a “one-phase flow” modification since the nano-particles are very small. A nanofluid is defined in the ANSYS FLUENT workbench as a “new fluid” with a new density, viscosity, thermal conductivity and specific heat obtained as a function of a base fluid and nano-particle type and concentration (volume fraction), according to Brinkman as described in Bég (Bég, 2018).

The key local dimensionless parameters which may be computed in ANSYS FLUENT (Kuharat, et al., 2019), (Kuharat & Bég, 2018), (Kuharat & Bég, 2019)] are *local Rayleigh*

number (ratio of thermal buoyancy and viscous hydrodynamic force) and the *average Nusselt number on the hot wall* ( $\overline{Nu}$ ). These may be defined as:

$$\text{Rayleigh number: } Ra_y = \frac{g\beta}{\nu\alpha m} (T_s - T_\infty)y^3 \quad (5.4)$$

$$\text{Average Nusselt number: } \overline{Nu} = \frac{\bar{h}L}{k} = \frac{q''_{w\text{CFD}}(L)}{k(T_s - T_\infty)} \quad (5.5)$$

Here,  $y$  is coordinate,  $h$  is convection coefficient,  $L$  is height of the enclosure,  $q''_{w\text{CFD}}$  is the heat flux rate computed in ANSYS FLUENT (CFD code). *Local Rayleigh number* represents the ratio of thermal buoyancy and viscous hydrodynamic force. *Average Nusselt number* provides a measure for heat transfer rate along the hot wall of the three-dimensional enclosure. In addition to the *no-slip* boundary conditions at the walls of the enclosure, the following thermal boundary conditions are imposed:

*Left hot wall: Constant temperature,  $T = 325\text{ K}$*

*Right cold wall: Constant temperature,  $T = 315\text{ K}$*

*The remaining walls: Adiabatic* (5.6)

## 5.2 Grid Sensitivity Analysis

An extensive mesh testing procedure was conducted to guarantee a grid-independent solution. The grid independence test has been performed on a cubical enclosure (i.e. aspect ratio =1) with  $Ra = 10^5$ ,  $\phi$  (volume fraction) = 0.02 i.e. 2% gold nanoparticles by volume. The tests were conducted for maximum element size of 0.08, 0.06, 0.05 and 0.04 m. The average heat flux ( $Q$ ) on the hot wall is selected as a sensitive parameter. The results of the mesh variation are shown in Figure 5.2. It is evident that the simulations attain mesh-independent convergence

with approximately 40,000 tetrahedral (pyramid) elements. Therefore, this mesh density is deployed in all subsequent simulations. The meshed prismatic enclosure model is shown in Figure 5.3

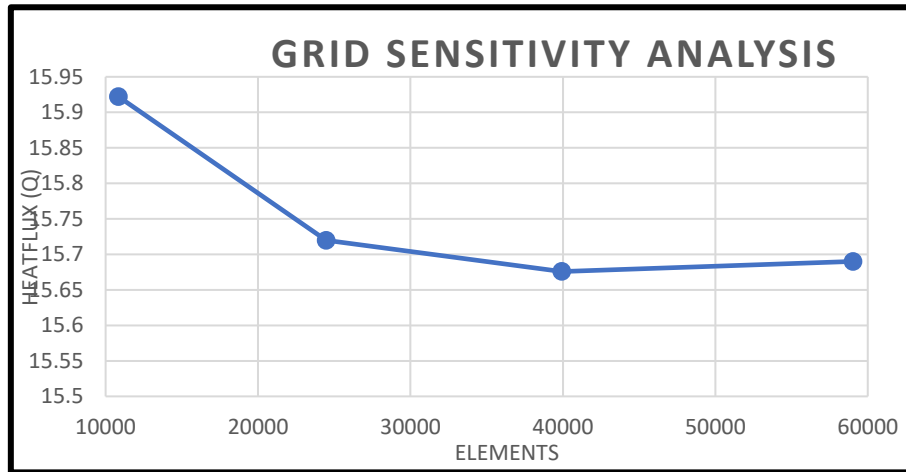


Figure 5.2 Finite volume ANSYS FLUENT grid independence study

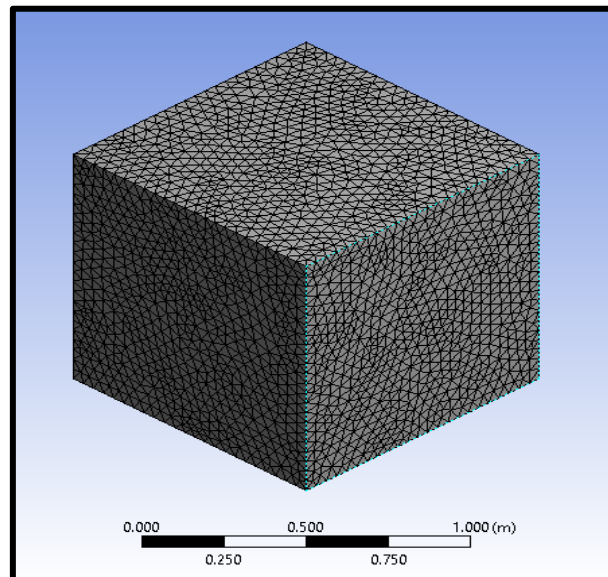


Figure 5.3 ANSYS 3-D mesh for nanofluid prismatic collector

### 5.3 Validation with Published Studies

To validate the results obtained from the ANSYS Model for natural convection inside a 3-D enclosure filled with aluminium oxide-water nanofluid, with a Rayleigh number of  $10^5$ , a

comparison is conducted with the earlier study (Wang, et al., 2018) for an aspect ratio of 1 (square enclosure) as shown in Figure 5.4 and Figure 5.5. The CFD simulation, using ANSYS FLUENT achieves close correlation with the results in (Wang, et al., 2018) as is evident from the good agreement in streamline (iso-velocity) and temperature contour patterns. The progressive distortion in temperature contours with distance from the heated left wall is clearly captured as is the strong vortex structure of the streamlines. Other test cases were also conducted to further confirm confidence in the ANSYS FLUENT model. Once confidence was established in the simulations further new simulations can be performed to examine specific effects of aspect ratio, Rayleigh number (buoyancy), volume fraction and enclosure inclination angle.

Figure 5.6 illustrates the comparison of the ANSYS FLUENT computation non-dimensional temperature distribution along the horizontal centreline in the  $Y/L=0.5$  plane with the Lattice Boltzmann method solution of (Wang, et al., 2018). Very close agreement is achieved confirming the accuracy of the ANSYS FLUENT simulations. Furthermore, Figure 5.6 also confirms that the grid resolution of the ANSYS FLUENT simulation (40,000 elements) is of the requisite accuracy to produce the correct results.

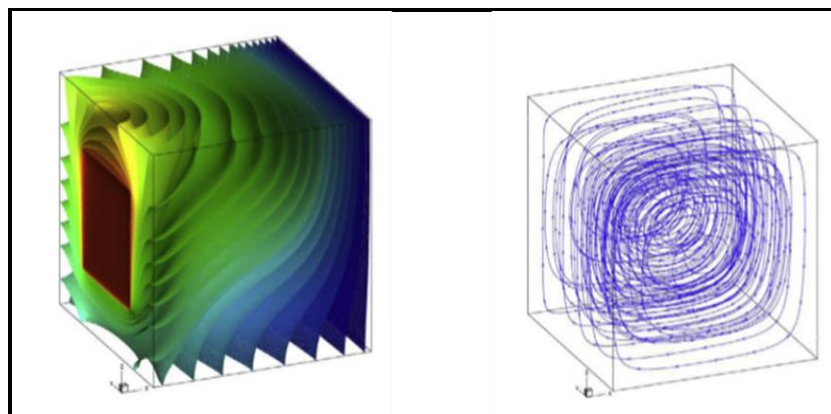


**Figure 5.4 Benchmark case for validation with LBM results of (Wang, et al., 2018).**

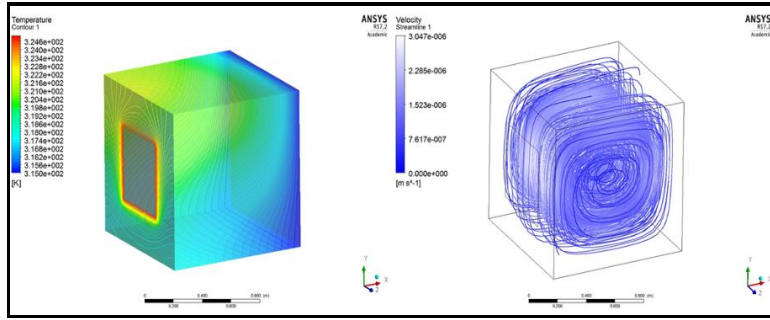


Figure 5.5 Present ANSYS FLUENT streamline and isotherm results

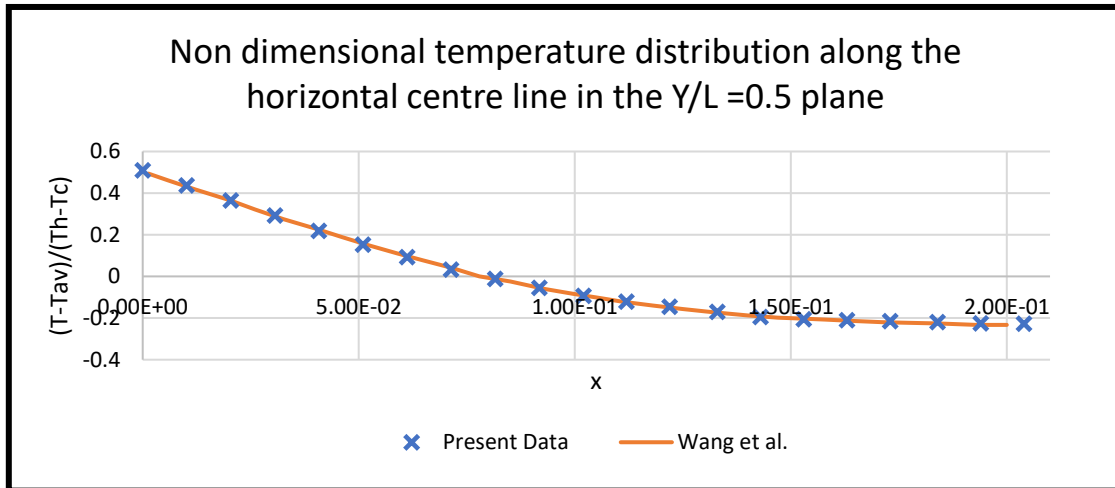


Figure 5.6 Comparison of ANSYS FLUENT solution (x) and LBM results (-) of (Wang, et al., 2018)

## 5.4 Results and Discussion

The ANSYS FLUENT results are depicted in Figure 5.7-Figure 5.11, Figure 5.12-Figure 5.13, Figure 5.14-Figure 5.16, Figure 5.17-Figure 5.21, Figure 5.22-Figure 5.25 and Tables 2-4. The data utilized in a typical computation, for example with a gold nano-particle volume fraction  $\phi$  of 5%, based on the Tiwari-Das nanoscale model calculations is given in **Table 1**.

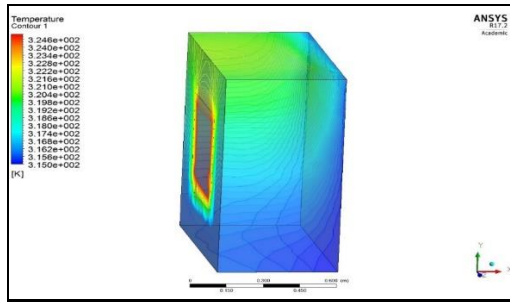


Figure 5.7 3-D full body temperature contours for gold-water nanofluid, with  $\phi = 5\%$ ,  $AR = 2$  and  $Ra = 10^5$  for inclination ( $\alpha$ ) = 0 degrees (vertical orientation).

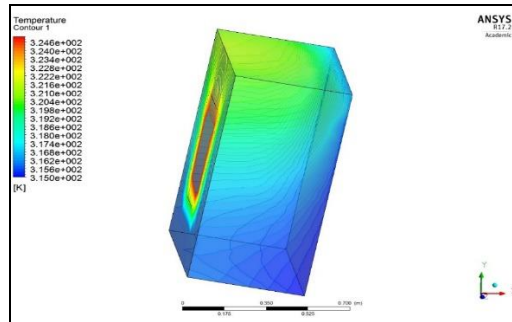


Figure 5.8 3-D full body temperature contours for gold-water nanofluid, with  $\phi = 5\%$ ,  $AR = 2$  and  $Ra = 10^5$  for inclination ( $\alpha$ ) = 10 degrees (weak tilt orientation).

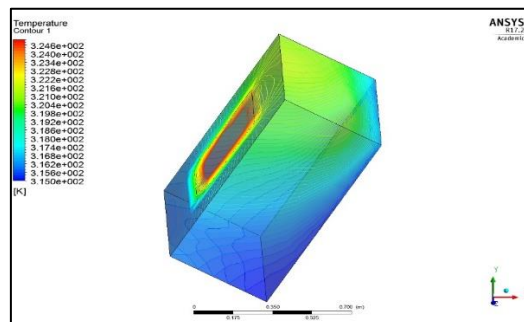


Figure 5.9 3-D full body temperature contours for gold-water nanofluid, with  $\phi = 5\%$ ,  $AR = 2$  and  $Ra = 10^5$  for inclination ( $\alpha$ ) = 30 degrees.

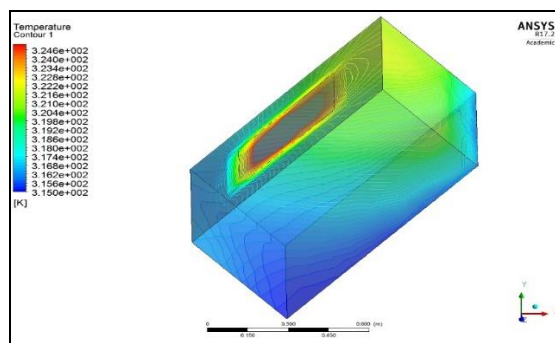
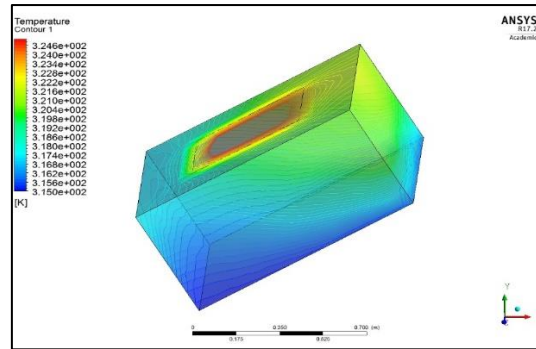


Figure 5.10 3-D full body temperature contours for gold-water nanofluid, with  $\phi = 5\%$ ,  $AR = 2$  and  $Ra = 10^5$  for inclination ( $\alpha$ ) = 45 degrees.

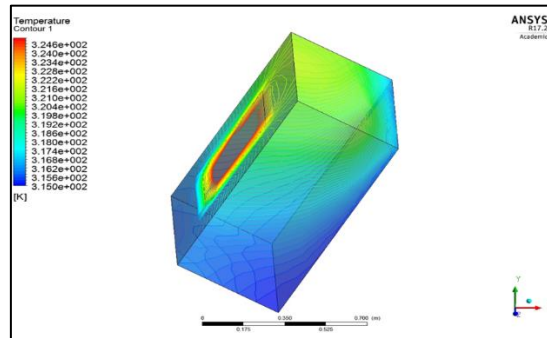




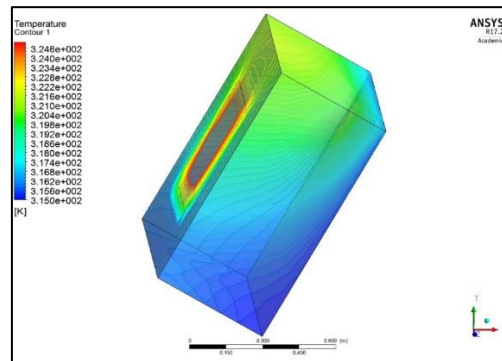
**Figure 5.11 3-D full body temperature contours for gold-water nanofluid, with  $\phi = 5\%$ ,  $AR = 2$  and  $Ra = 10^5$  for inclination ( $\alpha$ ) = 60 degrees.**

Figure 5.7-Figure 5.11 illustrate 3-dimensional temperature contour plots for impact of inclination angle ( $\alpha$ ) with volume fraction of 5%, aspect ratio of 2 and a higher Rayleigh number of  $Ra = 10^5$ . Although five orientation (tilt) cases are studied ( $\alpha = 0, 10, 30, 45$  and  $60$  degrees) there are *two plots per case*. **Table 2** shows the heat fluxes for the 5 tilt angles. It is apparent that with greater inclination of the enclosure there is a gradual enhancement in heat transfer from the left hot face (heated wall) towards the opposite cold wall, although this is concentrated in the uppermost section of the enclosure. Only at higher tilt angles does the green warmer zone penetrate deeper into the enclosure space and also dominates the upper face, left face completely. Temperature contours are also significantly expanded on the hot face around the central zone with increasing orientation of the enclosure. The thermal buoyancy force,  $F_{buoyancy}$  equals  $g\beta(T-T_w) \cos\alpha$ , in the momentum equation (2) is clearly reduced with increasing angle of inclination. It is maximized for the vertical enclosure case and progressively reduced with increasing tilt angle. It is minimized for the horizontal enclosure case ( $\alpha \rightarrow 90$  degrees,  $\cos\alpha \rightarrow 0$ ). Scaling thermal buoyancy contribution via tilting the enclosure is therefore a simple but powerful mechanism for regulating temperature distribution in the solar collector. **Table 2** shows the heat flux to the left wall (Nusselt number function) is decreased as inclination angle

is increased since greater transfer of thermal energy deeper into the enclosure away from the hot wall is generated.



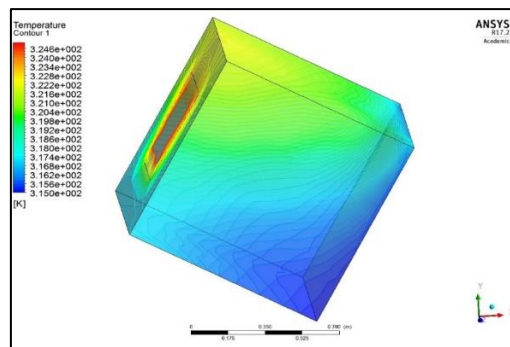
**Figure 5.12 3-D full body temperature contours for gold-water nanofluid, with  $\alpha = 30$  degrees, AR =2 and  $Ra = 10^5$  for gold volume fraction ( $\phi$ ) = 5%.**



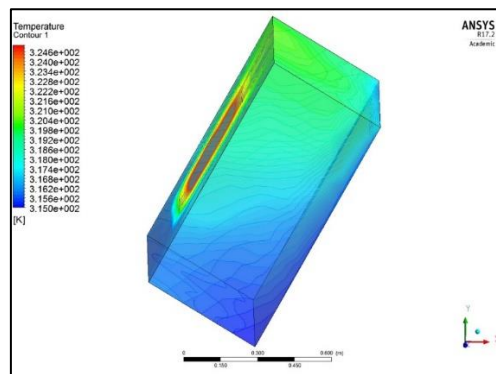
**Figure 5.13 3-D full body temperature contours for gold-water nanofluid, with  $\alpha = 30$  degrees, AR =2 and  $Ra = 10^5$  for gold volume fraction ( $\phi$ ) = 8%.**

Figure 5.12 and Figure 5.13 illustrate the 3-dimensional temperature contours in the solar enclosure for an increase in nano-particle volume fraction,  $\phi = 5, 8\%$ . A substantial heating of the enclosure accompanies an increase in nano-particle volume fraction. The warm localized yellow-green contours originating at the left hot wall, are noticeably expanded and push the cooler central light blue contours further into the enclosure towards the opposite wall and sections of the dark blue colder zone vanish. The upper section of the opposite wall is heated with lighter blue (warmer) contours replacing the original darker blue ones. Nano-particle presence therefore *extends the penetration distance* of heat into the enclosure and increase thermal boundary layer thickness both at the upper face and the left hot face. **Table 3** shows

that heat flux is dramatically increased with greater nano-particle volume fraction. The presence of nano-particles mobilizes micro-convection and encourages thermal diffusion away from the wall. This achieves the thermal enhancement. Similar findings have been reported by numerous authors including Taffarj *et al.* [28], Fattahi *et al.* [30] Balakin *et al.* [31] and Nasrin *et al.* [35] for both carbon-based and metallic nanoparticles although they did not examine the case of gold.



**Figure 5.14 3-D full body temperature contours for gold-water nanofluid, with  $\alpha = 30$  degrees,  $Ra = 10^6$  and gold volume fraction ( $\phi$ ) = 5% for AR = 1 (cubical enclosure).**



**Figure 5.15 3-D full body temperature contours for gold-water nanofluid, with  $\alpha = 30$  degrees,  $Ra = 10^6$  and gold volume fraction ( $\phi$ ) = 5% for AR = 2.**

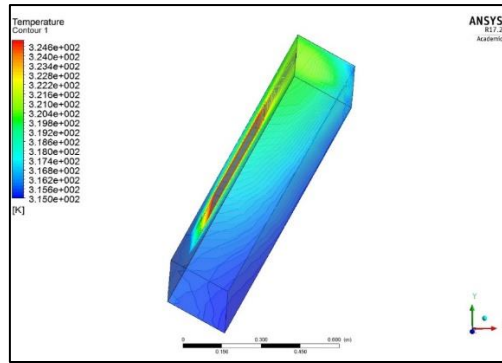


**Figure 5.16 3-D full body temperature contours for gold-water nanofluid, with  $\alpha = 30$  degrees,  $Ra = 10^6$  and gold volume fraction ( $\phi$ ) = 5% for AR = 4 (slender enclosure).**

Figure 5.14-Figure 5.16 illustrate 3-dimensional temperature contour plots for impact of enclosure aspect ratio ( $AR$ ) with nano-particle volume fraction ( $\phi$ ) of 5%, inclination angle of 30 degrees and Rayleigh number  $Ra = 10^6$ .  $AR$  defines the ratio of the height of the enclosure to either base dimension, where the base is always considered to be a square. Since three aspect ratio cases are examined, ( $AR= 1$  i.e. cubic enclosure,2,4) there are two plots per case i.e. a total of six visualizations are given. It is evident that there is a marked expansion of the warmer yellow/green upper left zone deeper into the body of the enclosure with a gradual replacement of darker colder blue contours with lighter blue warmer ones further and further towards the base and the right wall. For the highest aspect ratio yellow/green contours reach the right cold wall although they are confined to the upper area only. **Table 4** shows the heat fluxes for all three aspect ratio cases studied. Aspect ratio is the only geometric parameter investigated and is important for providing some insight into the relative dimensions of the solar collector on heat transfer characteristics. The  $AR$  values selected are representative of actual configurations utilized in solar farms [44]. A significant elevation in surface heat flux is achieved with greater aspect ratio as shown in **Table 4**. This has also been computed by (Esfandiary, et al., 2016) and (Motlagh & Soltanipour, 2017) who also observed the deeper penetration of heat in enclosures with higher aspect ratio.

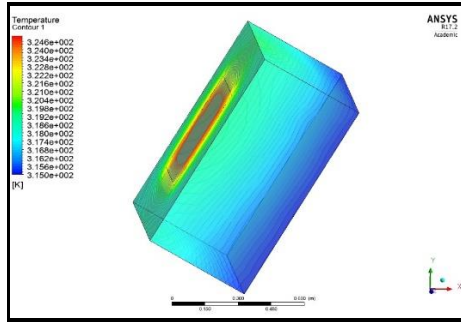


Figure 5.17 3-D full body temperature contours for gold-water nanofluid, with  $\alpha = 30$  degrees,  $AR = 2$  and gold volume fraction ( $\phi$ ) = 5% for  $Ra = 10^3$ .

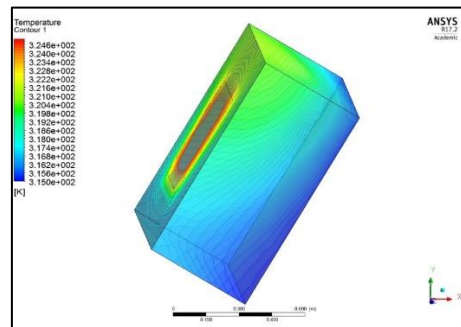


Figure 5.18 3-D full body temperature contours for gold-water nanofluid, with  $\alpha = 30$  degrees,  $AR = 2$  and gold volume fraction ( $\phi$ ) = 5% for  $Ra = 10^4$ .

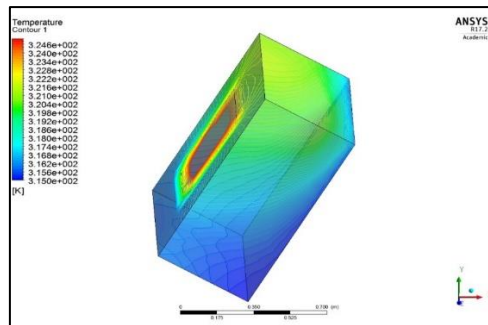


Figure 5.19 3-D full body temperature contours for gold-water nanofluid, with  $\alpha = 30$  degrees,  $AR = 2$  and gold volume fraction ( $\phi$ ) = 5% for  $Ra = 10^5$ .

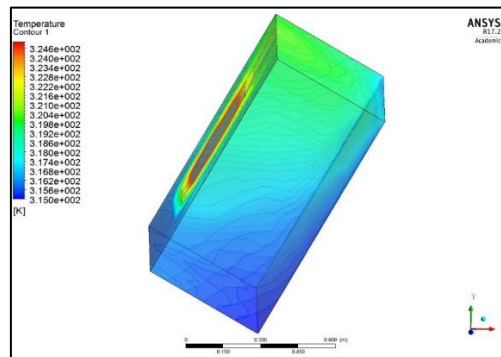
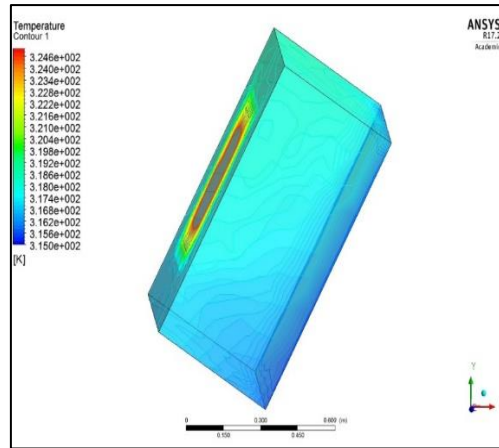
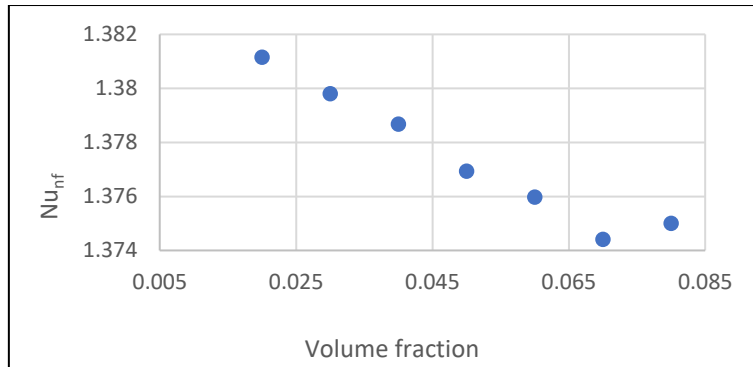


Figure 5.20 3-D full body temperature contours for gold-water nanofluid, with  $\alpha = 30$  degrees,  $AR = 2$  and gold volume fraction ( $\phi$ ) = 5% for  $Ra = 10^6$ .



**Figure 5.21 3-D full body temperature contours for gold-water nanofluid, with  $\alpha = 30$  degrees,  $AR = 2$  and gold volume fraction ( $\phi$ ) = 5% for  $Ra = 10^7$ .**

Figure 5.17-Figure 5.21 show the influence of the Rayleigh number for nano-particle volume fraction ( $\phi$ ) of 5%, inclination angle of 30 degrees and  $AR = 2$ . Five Rayleigh number cases are examined ( $Ra = 10^3, 10^4, 10^5, 10^6$  and  $10^7$ ). Initially there is an intensification in temperature contours only at the left hot wall with cooler light blue zones throughout the body of the enclosure and a cold blue zone at the far wall. This is modified to a localization of heat in the upper left zone of the enclosure with an increase in Rayleigh number from  $10^3$  to  $10^4$ . This trend continues to prevail with further increment in Rayleigh number up to  $10^6$ . However, at very high Rayleigh number of  $10^7$  (the temperature distribution achieved is much more homogenous) and the vast majority of the enclosure space is occupied by light blue warmer contours which also dominate the far wall. Significantly more balanced thermal diffusion through the enclosure is therefore achieved with very strong thermal buoyancy effect and there is a contraction in the yellow/red hot zone on the hot wall for this scenario. Rayleigh number (buoyancy) is overall a very dominant influence on thermo-fluid characteristics in the solar collector.



**Figure 5.22 Average Nusselt number versus volume fraction ( $\phi$ )**

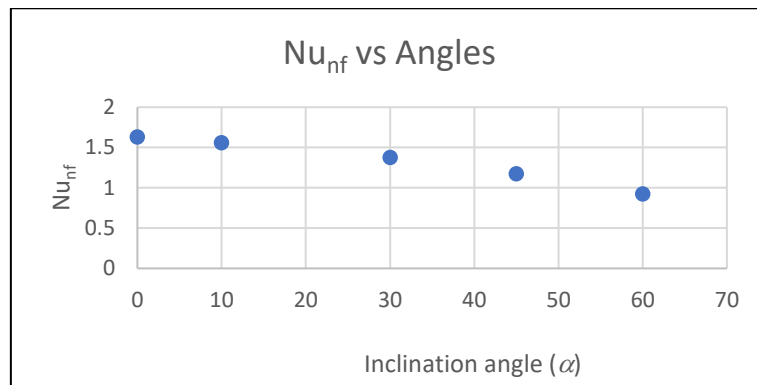


**Figure 5.23 Average Nusselt number versus enclosure inclination angle ( $\alpha$ )**

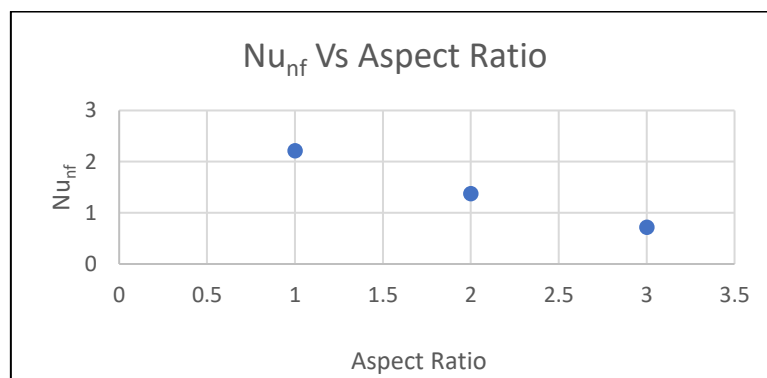


**Figure 5.24 Average Nusselt number versus enclosure aspect ratio**

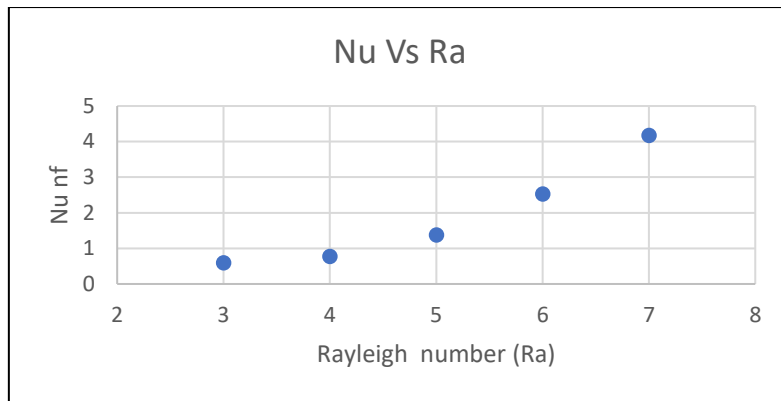


**Figure 5.25 Average Nusselt number versus Rayleigh number (Ra)**

In Figure 5.22 - Figure 5.25 the impact of the different parameters (nano-particle volume fraction, tilt angle, aspect ratio and Rayleigh number) on average Nusselt number at the hot wall are presented.

The average Nusselt number ( $Nu_{nf}$ ) at the region of heat source is calculated and presented in Figure 5.22 for the unity aspect ratio case ( $AR = 1$ ) with a tilt angle of 30 degrees and Rayleigh number of  $10^4$ .  $Nu_{nf}$  clearly decreases with the increase of volume fraction. This can be explained by the fact that thermal conductivity of nanofluid ( $k_{nf}$ ) is elevated with increasing volume fraction, and consequently conductive heat transfer is increased whereas thermal convection heat transfer is reduced. This amplifies the temperature in the nanofluid and results in a transfer of heat from the wall manifesting in a decrease in Nusselt numbers. However, at around 0.08 (8%) volume fraction there is an upturn in Nusselt number which indicates that the heat transfer enhancement from conduction (associated with the nano-particles) decreases and this is also associated with the counter-productive increase in nanofluid effective viscosity. Therefore, the optimum nano-particle volume fraction ( $\phi_{max}$ ) is 0.07 (i.e. 7%) and this is the maximum level of nanoparticle doping which benefits the solar collector performance. It is ideal to keep the Rayleigh number low so that the convective heat transfer from buoyancy force does not overcome the effect of conductive heat transfer from the gold nanoparticles. The



optimal nano-particle volume fraction concurs with many other studies which have also reported an approximate upper limit of 8% volume fraction for thermal enhancement by nanoparticles (Wang, et al., 2018).

Figure 5.23 clearly shows that there is a *linear decay* in the Nusselt number with increasing inclination angle. This is associated with the depletion in thermal buoyancy force with increasing inclination angle. As noted earlier the maximum buoyancy force is achieved with the vertical orientation ( $\alpha = 0$ ) of the prismatic enclosure ( $g\beta(T-T_w) \cos\alpha \rightarrow g\beta(T-T_w)$  since  $\cos\alpha \rightarrow 1$ ). However, with increasing tilt angle,  $\cos\alpha$  is progressively reduced reaching a minimum value of 0 when  $\alpha \rightarrow 90$  degrees i.e., the horizontal enclosure case for which natural convection effects are minimized. Therefore, with greater inclination angle of the enclosure, heat transfer to the wall is reduced (Nusselt number is decreased) whereas thermal enhancement in the nanofluid itself i.e. temperatures within the circulating nanofluid are increased. Again, the ANSYS FLUENT simulations concur well with other studies on inclined nanofluid solar collectors including (Esfandiary, et al., 2016), (Motlagh & Soltanipour, 2017) Motlagh *et al.* and (Ghachem, et al., 2015).

Figure 5.24 shows that for a given nanoparticle volume fraction of 0.05 and Rayleigh number of  $10^6$  (laminar regime), with 30 degrees tilt angle, the average Nusselt number decreases with increasing aspect ratio. Although increasing aspect ratio has been shown to elevate temperatures in the gold-water nanofluid, this indicates that greater heat transfer from the boundary (wall) to the body of nanofluid is achieved with greater aspect ratio. This reduces the heat transfer to the boundary and therefore decreases average Nusselt numbers. Higher Nusselt number is therefore achieved with lower aspect ratio geometries whereas greater temperature enhancement is produced with higher aspect ratios. These trends are consistent with other

investigations including (Trodi & Benhamza, 2017) and (Bouhaleb & Abbassi, 2014). The overall implication is that the influence of aspect ratio is stronger when the enclosure is taller and the Rayleigh number is high (but not too high).

Figure 5.25 presents the variation of Nusselt number with Rayleigh number at fixed volume fraction of 0.05 and inclination angle of 30 degrees and unity aspect ratio for the enclosure. There is a significant escalation in average Nusselt number with increasing Rayleigh number which due to the accentuation in thermal buoyancy force effect. Nusselt number increases significantly up to Rayleigh numbers of  $10^7$  which constitutes the cut-off point for *laminar* convection flows. Beyond this limit the buoyancy forces overcome the viscous forces significantly and the heat transfer is dominated by convection at high Rayleigh number with the onset of turbulence, as noted by (Braga & de Lemos, 2009). Although further ANSYS FLUENT computations have also been made for *shallow enclosures* (aspect ratio  $<1$ ), it was found that the effect of Rayleigh number on heat transfer is less significant for such scenarios and therefore these have been omitted for brevity.

## 5.5 Conclusions

A computational study of natural convection in an inclined 3-dimensional prismatic direct absorber solar collector (DASC) containing gold-water nanofluid has been presented. Steady-state, incompressible laminar Newtonian viscous flow is assumed. The enclosure has two adiabatic walls, one hot (solar receiving) and one colder wall. ANSYS FLUENT software (version 19.1) is employed. The Tiwari-Das volume fraction nanofluid model is utilized to simulate nanoscale effects and allows a systematic exploration of volume fraction effects. The effects of thermal buoyancy (Rayleigh number), geometrical aspect ratio and enclosure tilt

angle on isotherm and temperature contour distributions are presented with extensive visualization in both two and three dimensions. Grid-independence tests are included. Validation with published studies from the literature is also conducted. The computations have shown that:

(i) Higher geometrical aspect ratio leads to improved heat transfer in the regime with deeper penetration of warmer zones in the enclosure.

(ii) Increasing Rayleigh number (thermal buoyancy force relative to viscous hydrodynamic force), there is an intensification in heat transfer from the left wall through the enclosure space and much more homogenous temperature distributions are eventually obtained.

(iii) With increasing nano-particle volume fraction, heat penetrates more effectively into the enclosure from the hot wall and temperature magnitudes are enhanced.

(iv) With greater inclination of the enclosure there is a progressive elevation in heat transfer from the left hot face (heated wall) towards the opposite cold wall, and temperatures are elevated mainly in the upper left zone with a more extensive warming in the central zone.

(v) Heat flux is dramatically increased with greater nano-particle volume fraction, and aspect ratio whereas it is suppressed with greater inclination of the enclosure.

(vi) Higher Nusselt number is therefore achieved with lower aspect ratio geometries whereas greater temperature enhancement is produced with higher aspect ratios.

(vii) There is a substantial boost in average Nusselt number with increasing Rayleigh number associated with the elevation in thermal buoyancy force effect.

(viii) With larger inclination angle of the prismatic enclosure, heat transfer to the wall is decreased (Nusselt number is depleted) whereas greater thermal enhancement in the nanofluid itself is achieved.

(ix) Nusselt number is significantly suppressed with an increase in gold nano-particle volume fraction whereas temperatures are enhanced, both up to the cut-off volume fraction of 7%.

(x) CFD finite volume methods (ANSYS FLUENT) provide an excellent tool for simulating solar nanofluid collector thermal fluid dynamic phenomena and offer a powerful compliment to experimental methods.

The present simulations have neglected *thermal radiative heat transfer* effects. These may be addressed with a number of radiation flux models in ANSYS FLUENT e.g. surface-to-surface (STS) model and the discrete ordinates model (DOM) - which I will consider in chapter 8. Furthermore, the geometry considered has been planar (prismatic). Many solar collector designs are now exploring *curved* geometries e.g. parabolic, sinusoidal, (Abadshapoori & Saidi, 2018) and these are currently also under investigation by the authors which will be invested in the next chapter. Chapter 6 will describe an *annular geometry* and also considers *forced* convection.

## **PUBLICATION NOTE**

A version of this chapter was published in **Kuharat, S., Bég, O.A., Kadir, A., Vasu, B., Bég, T.A. and S. J. Walid, Computation of gold-water nanofluid natural convection in a three-dimensional tilted prismatic solar enclosure with aspect ratio and volume fraction effects. Nanoscience and Technology: An International Journal, 11 (2), 141-167 (2020).**

# **Chapter 6      Computational Fluid Dynamics Simulation of a Nanofluid-Based Annular Solar Collector with Different Metallic Nanoparticles**

## **6.1 Abstract**

Thusfar in Chapters 3-5, regular *straight walled* DASC geometries have been considered e.g. quadrilateral, trapezium, cubic etc. In this chapter we consider curved geometries i.e. convective heat transfer in an annular (concentric tube) pipe solar collector system. The inner tube contains pure water and the annular region contains nanofluid. Three-dimensional steady-state incompressible laminar flow comprising water-based nanofluid containing a variety of metallic nanoparticles (copper oxide, aluminium oxide and titanium oxide nanoparticles) is examined. The Tiwari-Das model is deployed for which thermal conductivity, specific heat capacity and viscosity of the nanofluid suspensions is evaluated as a function of solid nanoparticle volume fraction. Radiative heat transfer is also incorporated using the ANSYS solar flux and Rosseland radiative models. The ANSYS FLUENT finite volume code (version 18.1) is employed to simulate the thermo-fluid characteristics. Mesh-independence tests are conducted. The influence of volume fraction on temperature, velocity, pressure contours is computed and visualized. Copper oxide nanofluid is observed to achieve the best temperature enhancement. Temperature contours at cross-sections of the annulus are also computed.

## **6.2 Computational Mathematical Model**

The 3-D solar collector concentric geometry studied is illustrated in Figure 6.1 in an  $(x, y, z)$  coordinate system. It comprises two concentric cylinders, the inner composed of copper and

the outer composed of glass. The copper tube has inner diameter 22mm, thickness 3 mm and is of 1m in length and contains flowing water. This inner copper tube is submerged in metallic nano-fluid confined in the annular space between the copper tube and an external glass tube with internal diameter of 51 mm and wall thickness of 2.25 mm with the same length (1m). There is no heat transfer though the top wall (adiabatic end condition). No slip boundary conditions are assumed on all walls of the cavity are considered as impermeable. The physical properties of the fluid assumed constant.

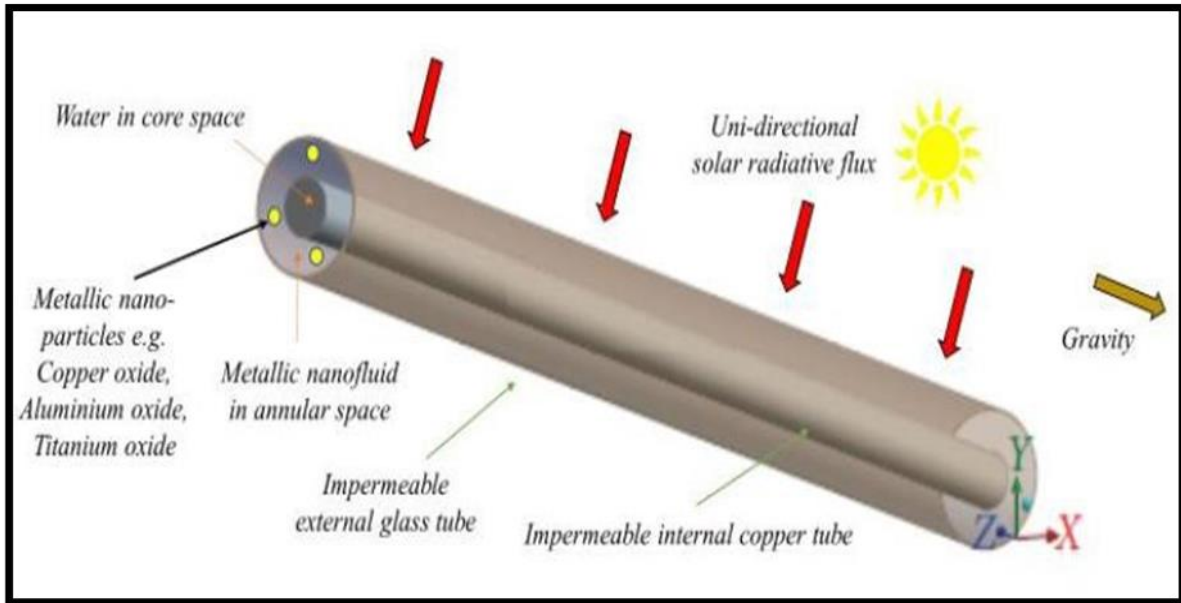


**Figure 6.1 Geometrical and physical model for annular nanofluid solar collector**

The three-dimensional ( $x, y, z$ ) transport equations given in section 2.2-1 of chapter 2 (mass, momentum, and energy) time independent with nanofluid properties are solved subject to the boundary conditions in ANSYS FLUENT:

At the inlet: Volume flow rate inlet of 0.002 kg/s

At the outlet: Zero pressure outlet from one face.

Heat flux: Heat is added as a solar radiation intensity of 877 W/m<sup>2</sup>.

The following volume fractions are considered each for the CuO, Al<sub>2</sub>O<sub>3</sub> and TiO<sub>2</sub> nanofluids: 0.01wt%, 0.05wt%, 0.1 wt%. In ANSYS FLUENT physics, gravity is set as 9.81 m/s<sup>2</sup>.

### 6.3 Grid Sensitivity Analysis

The annular solar collector mesh used a combination of unstructured grids (inner tube) and a structure grid (annulus) as shown in 6.2. Hexahedral (“hex”) elements (finite volumes) are used in this simulation, as the hex mesh can provide the same resolution of the flow physics as tetrahedron mesh but with significantly fewer elements required. It is also important that the model does not contain any sliding mesh as this is not compatible with the solar load model.

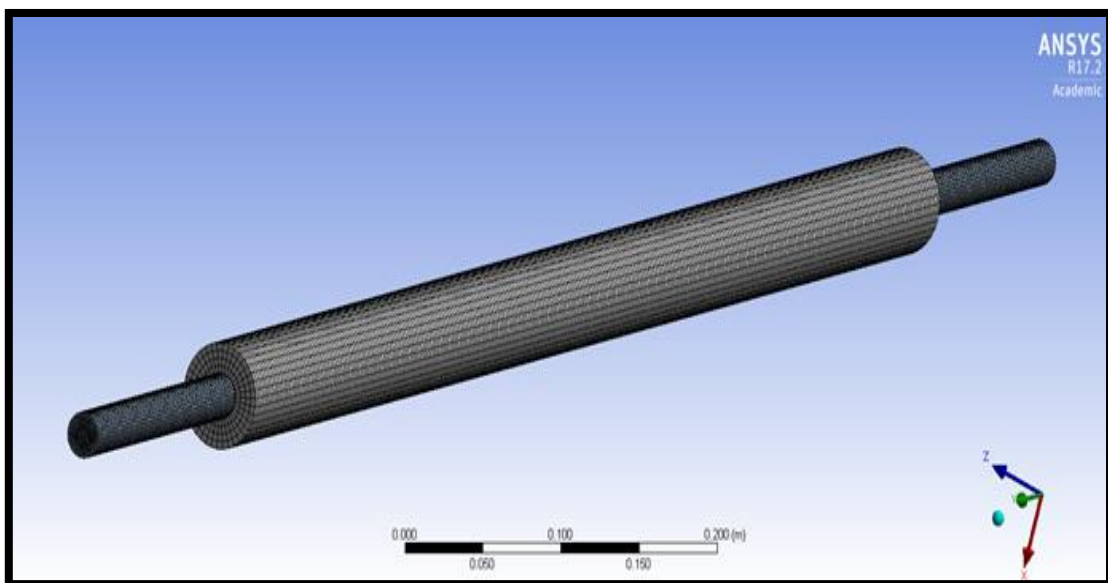


**Figure 6.2 ANSYS FLUENT 3-dimensional mesh of solar configuration (Mesh density Nodes: 479188, elements: 443970)**

Figure 6.2 shows the grid sensitivity analysis. The largest elements used in case one can be considered as a coarse mesh with 103068 elements. On increasing the number of elements by 100000 (case two), the graph shows a variation indicating that the simulation is not convergent. The next part of the grid dependent study covers cases three, four and five. Upon observation

of cases four (325951 elements) and five (448836 elements), these cases utilize a fine mesh, where the difference between the two values are infinitesimal and hence considered negligible. This shows that the simulation is convergent at case four with 448836 elements. This grid-independence study provides an appropriate grid size (case four) which is subsequently adopted for all further simulations and is of sufficient quality to guarantee mesh-independent and converged results i.e., the most accurate results possible with the minimum number of elements.

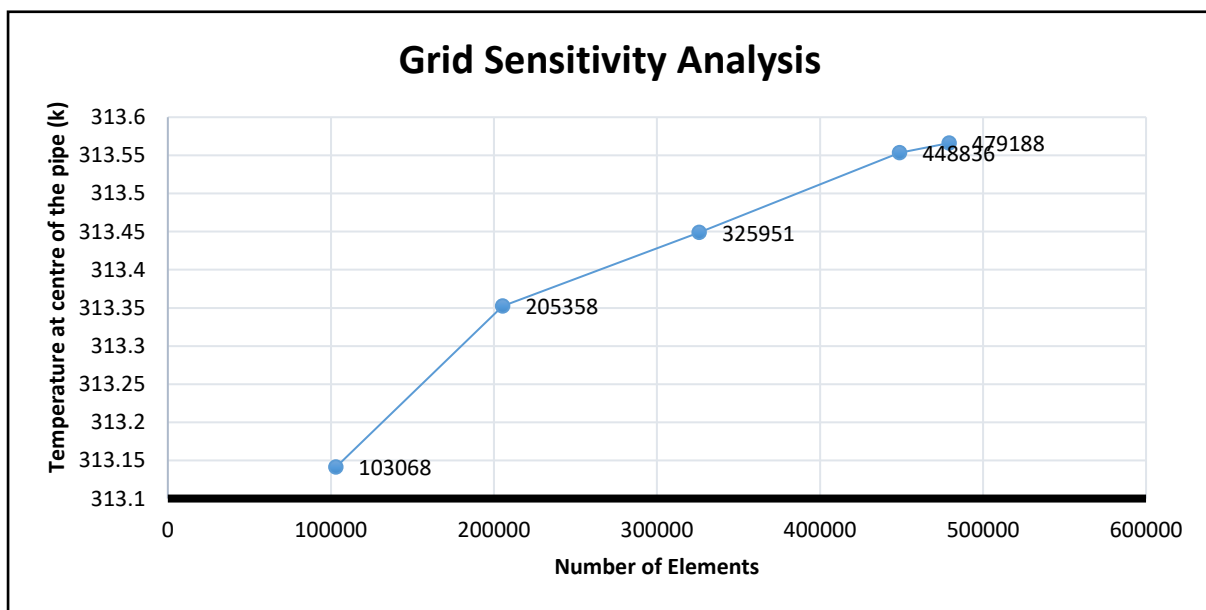


Figure 6.3 ANSYS FLUENT grid independence study

## 6.4 Results and Discussion

In the ANSYS simulations,  $T_w$  is the pipe wall temperature at a given location along the pipe and  $T_m$  is the mean temperature in the pipe at the location where  $T_w$  is defined. The ANSYS FLUENT results are depicted in Figure 6.4-Figure 6.38 Three different sets of results are visualized for the three metallic nano-particle cases i.e., *Copper oxide*, *Aluminium oxide* and *Titanium oxide*. In each of these three nanofluid cases, *three different volume fractions* are studied. Therefore 9 sets of computations are presented, three each for each different metallic



nano-particle studied. We consider each set of three in turn. Volume fractions examined are  $\phi = 0.01, 0.05$  and  $0.1$  i.e., 1%, 5% and 10%. Each set of figures illustrates respectively the temperature, temperature cross-section slice views, velocity and pressure distributions.

**Figure 6.4 to Figure 6.15** correspond to the Copper oxide case. Figure 6.4-6.7 correspond to  $\phi = 0.01$ , Figs. 12a-d to  $\phi = 0.05$  and Figs. 11a-d to  $\phi = 0.1$  respectively. To gain a perspective of the influence of volume fraction, one has to compare the *respective plots* with each other i.e., **Figure 6.4, Figure 6.8 and Figure 6.12** consider the *temperature contours* for copper oxide nanofluid with the three different volume fractions. Similarly, we compare **Figure 6.5, Figure 6.9 and Figure 6.13** (temperature cross-section slice views), then compare **Figure 6.6, Figure 6.10 and Figure 6.14** (velocity) and finally Figure 6.7, Figure 6.11 and **Figure 6.15** (pressure distributions).

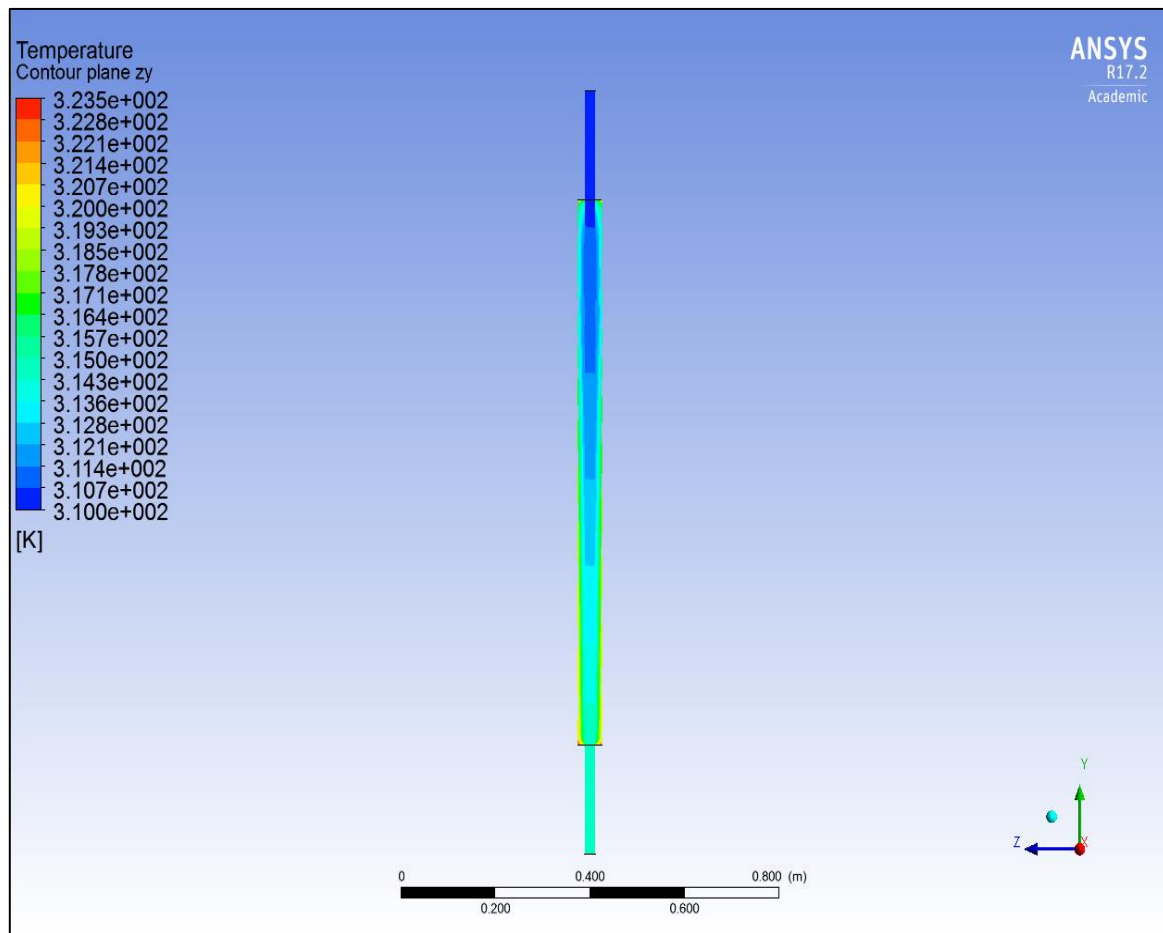


**Figure 6.4 Temperature Contour for CuO nanofluid,  $\Phi = 0.01$**

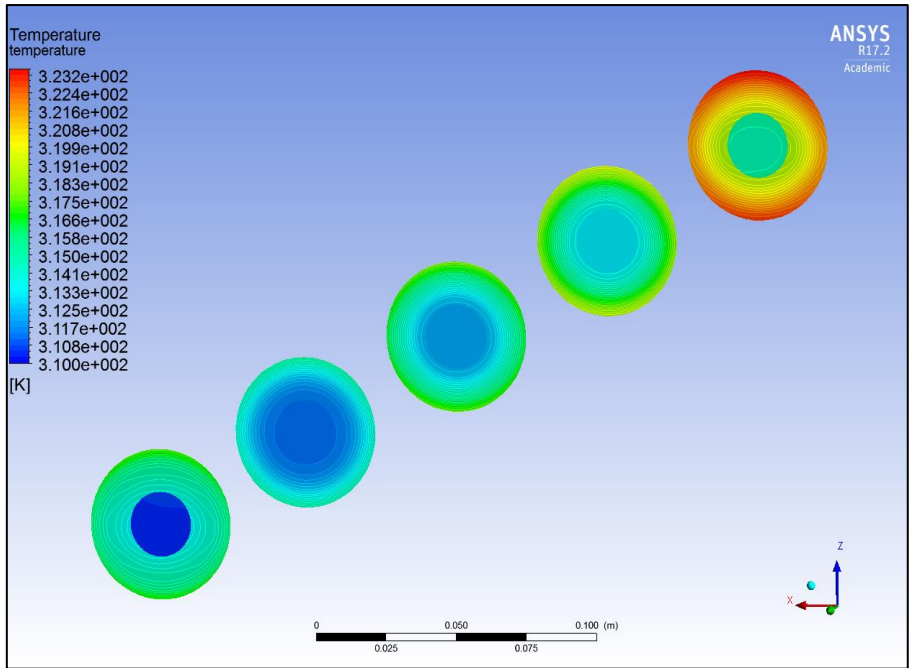


**Figure 6.5 Temperature Contour Cross-sections for CuO nanofluid,  $\Phi = 0.01$**

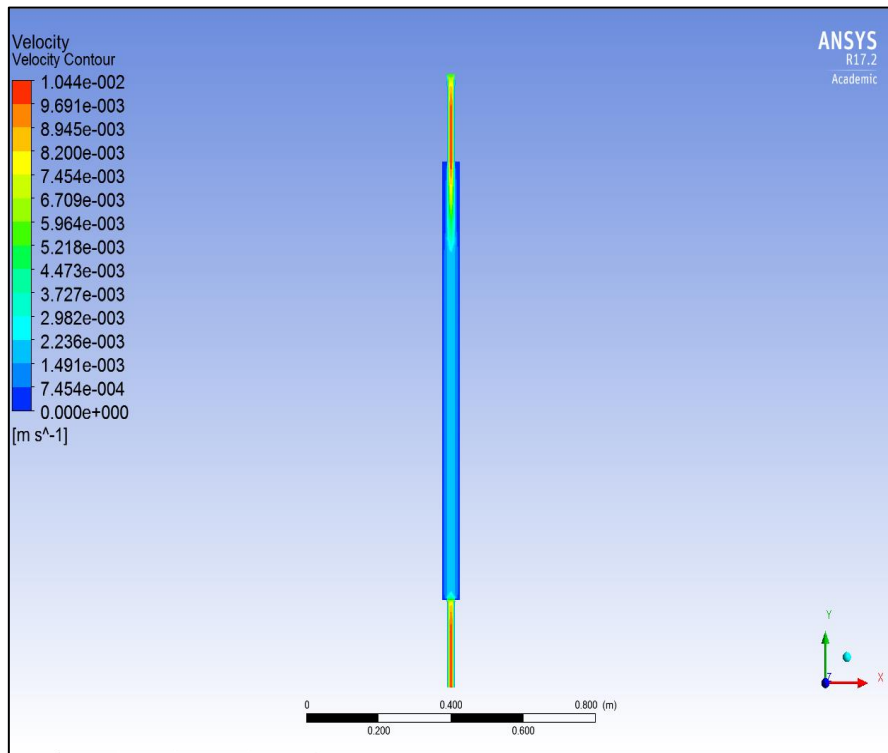


**Figure 6.6 Velocity Contours for CuO nanofluid,  $\Phi = 0.01$**

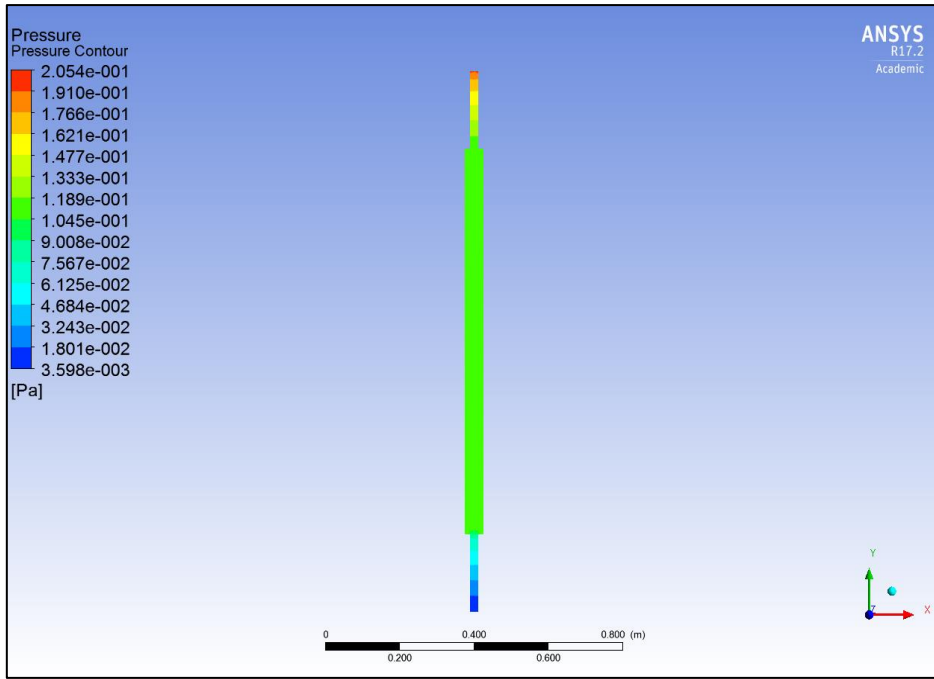


Figure 6.7 Pressure Contours for CuO nanofluid,  $\Phi = 0.01$

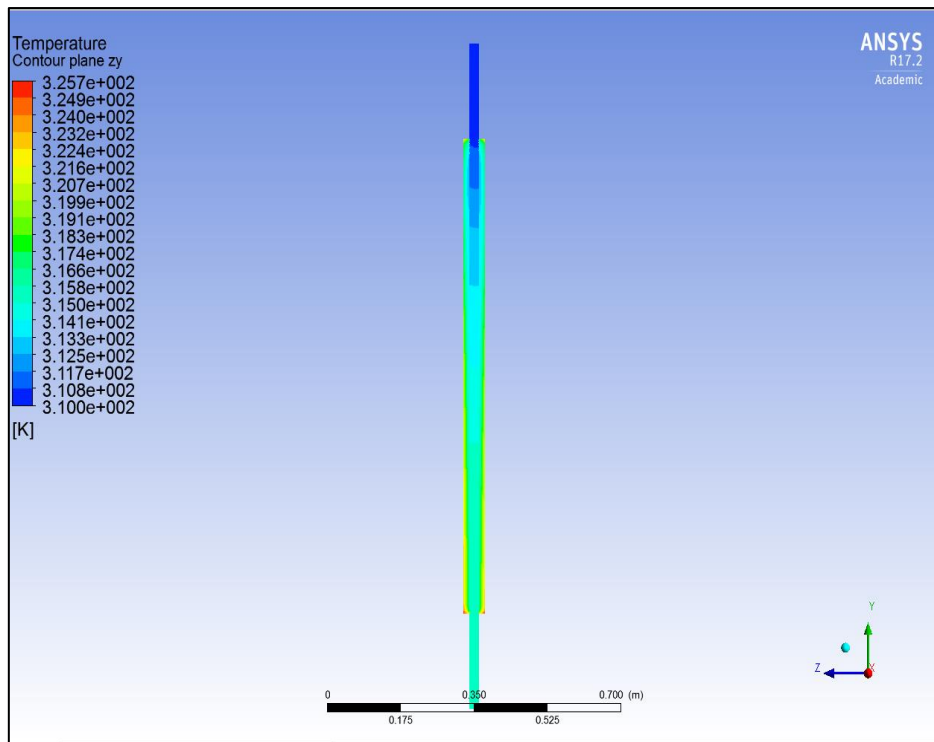


Figure 6.8 Temperature Contour for CuO nanofluid,  $\Phi = 0.05$

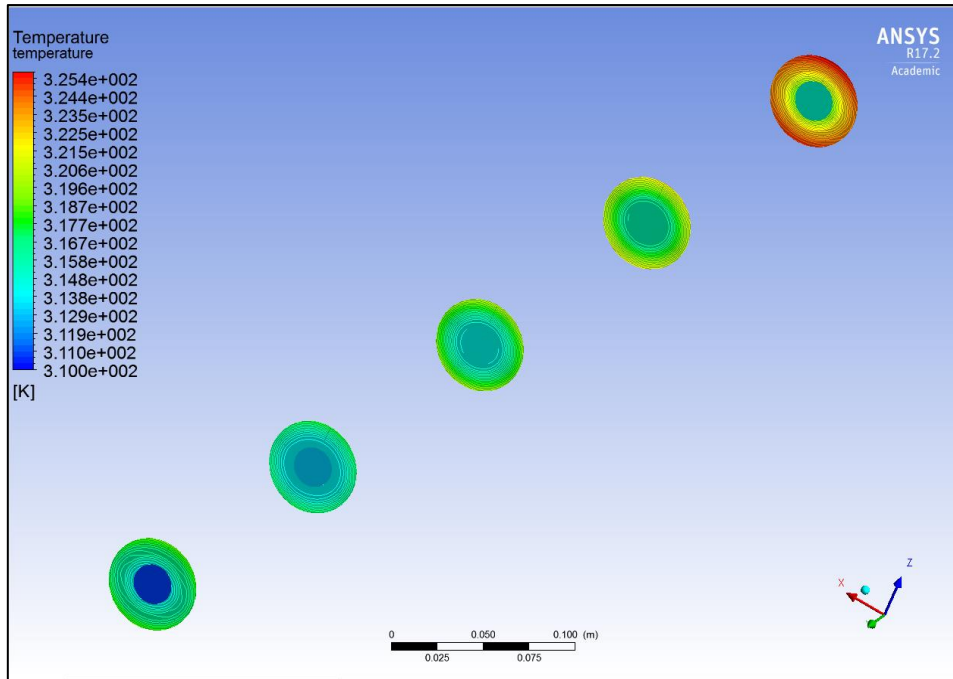


Figure 6.9 Temperature Contour cross sections for CuO nanofluid,  $\Phi = 0.05$

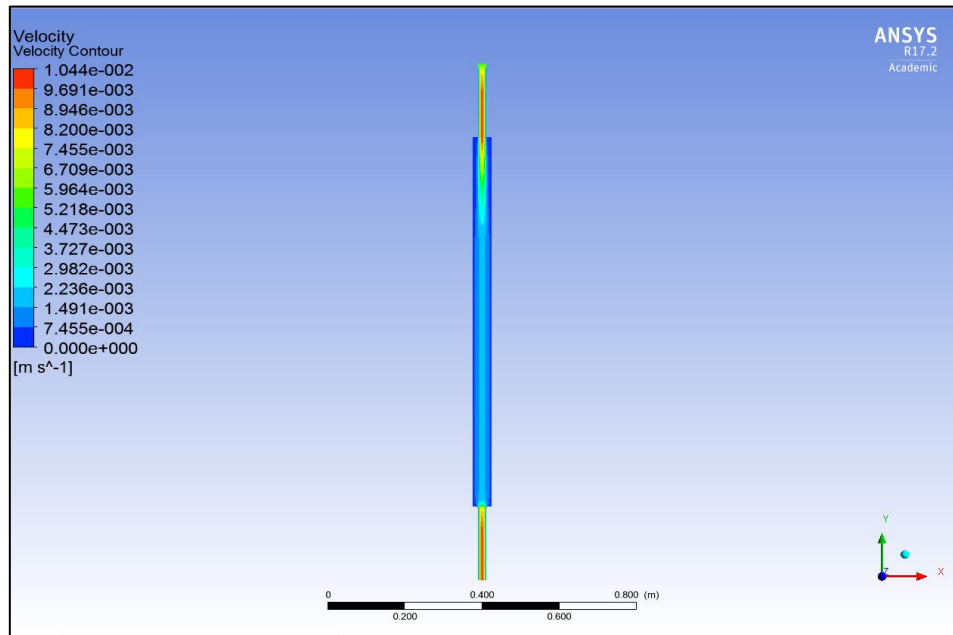


Figure 6.10 Velocity Contours for CuO nanofluid,  $\Phi = 0.05$

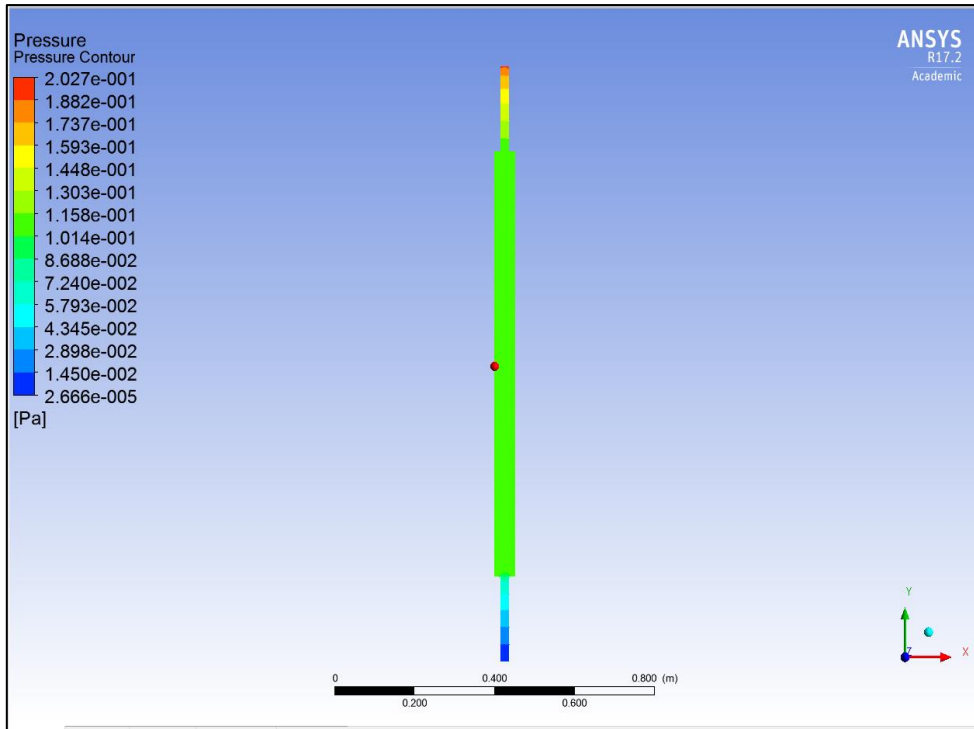


Figure 6.11 Pressure Contours for CuO nanofluid,  $\Phi = 0.05$

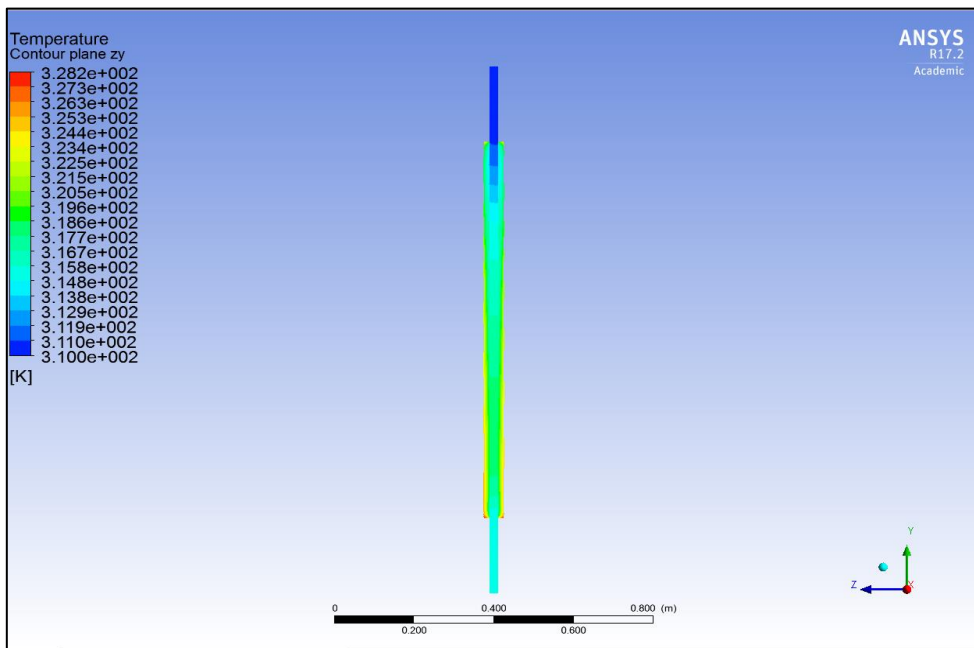


Figure 6.12 Temperature Contour for CuO nanofluid,  $\Phi = 0.1$

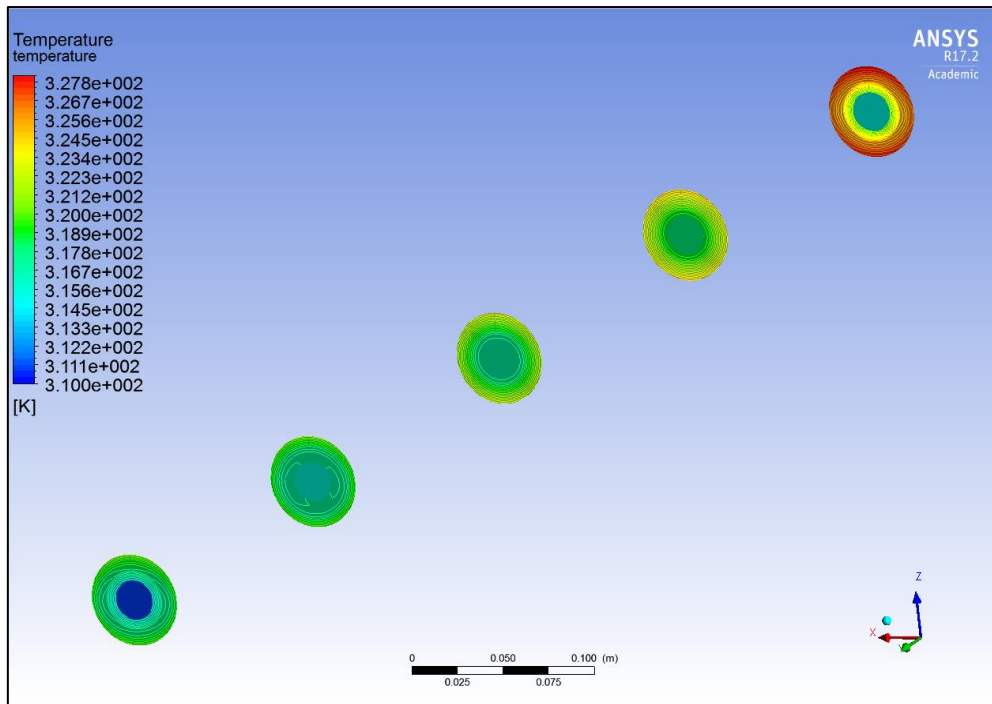


Figure 6.13 Temperature Contour cross sections for CuO nanofluid,  $\Phi = 0.1$

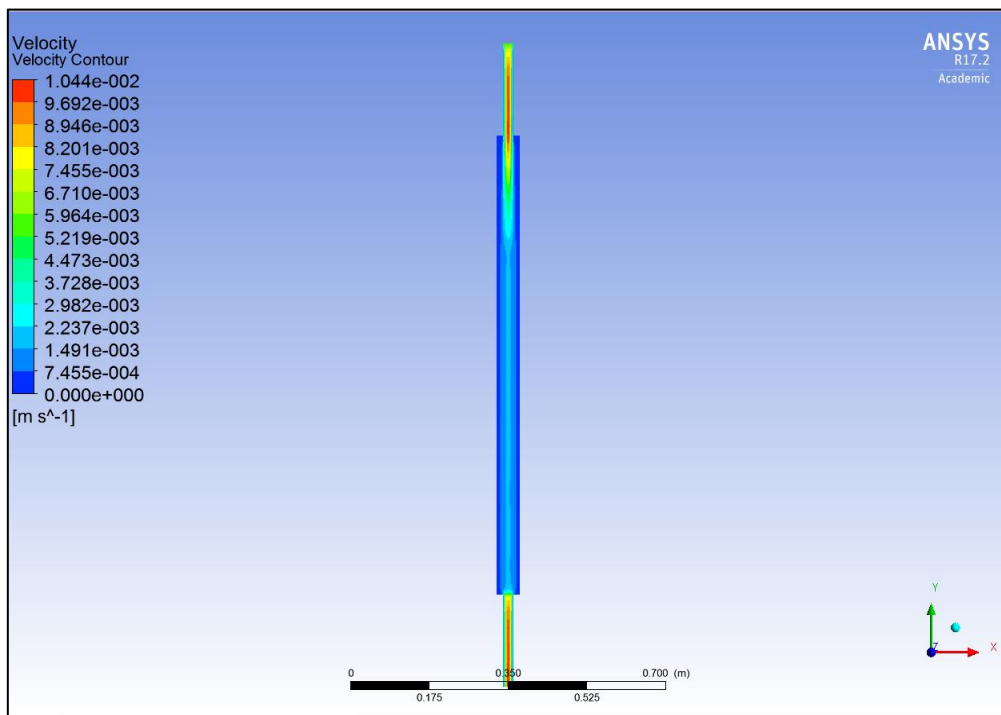


Figure 6.14 Velocity Contours for CuO nanofluid,  $\Phi = 0.1$

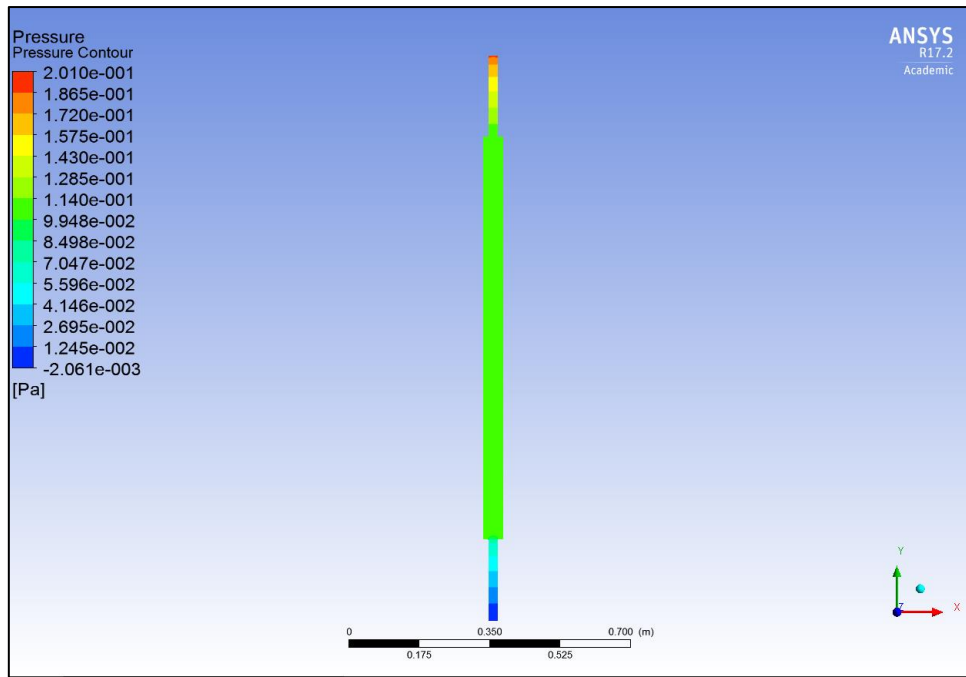


Figure 6.15 Pressure Contours for CuO nanofluid,  $\Phi = 0.1$

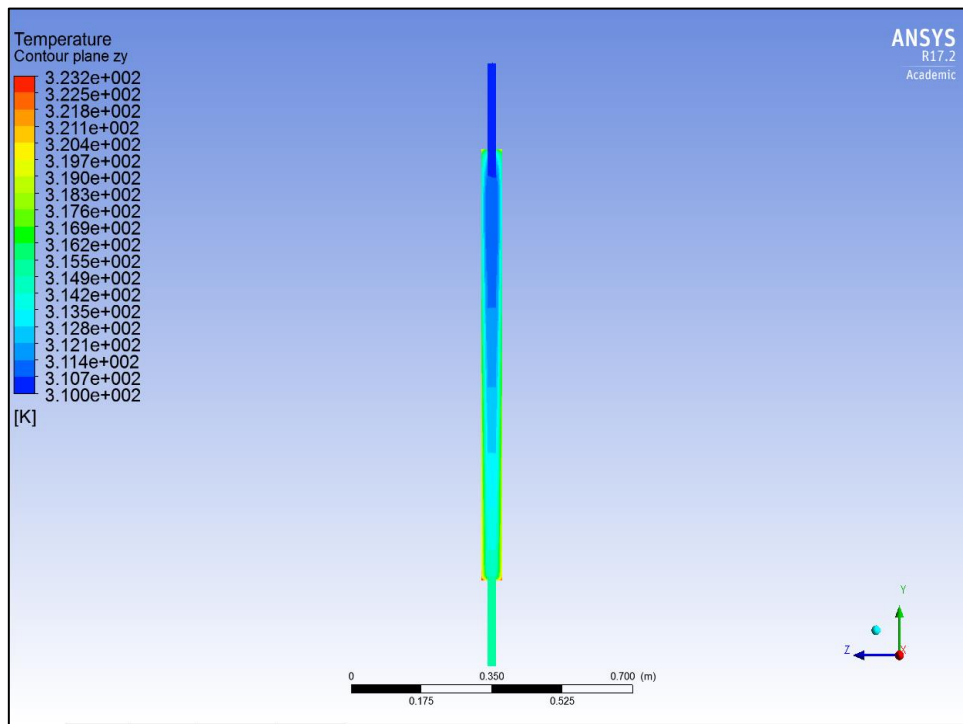


Figure 6.16 Temperature Contour for Al<sub>2</sub>O<sub>3</sub> nanofluid,  $\Phi = 0.01$

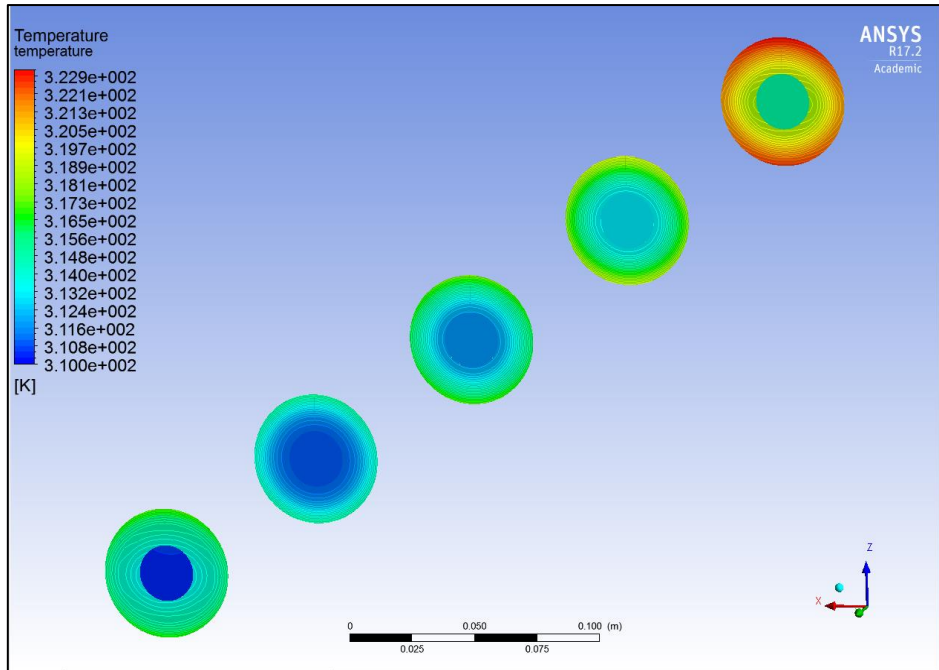


Figure 6.17 Temperature Contour cross sections for  $\text{Al}_2\text{O}_3$  nanofluid,  $\Phi = 0.01$

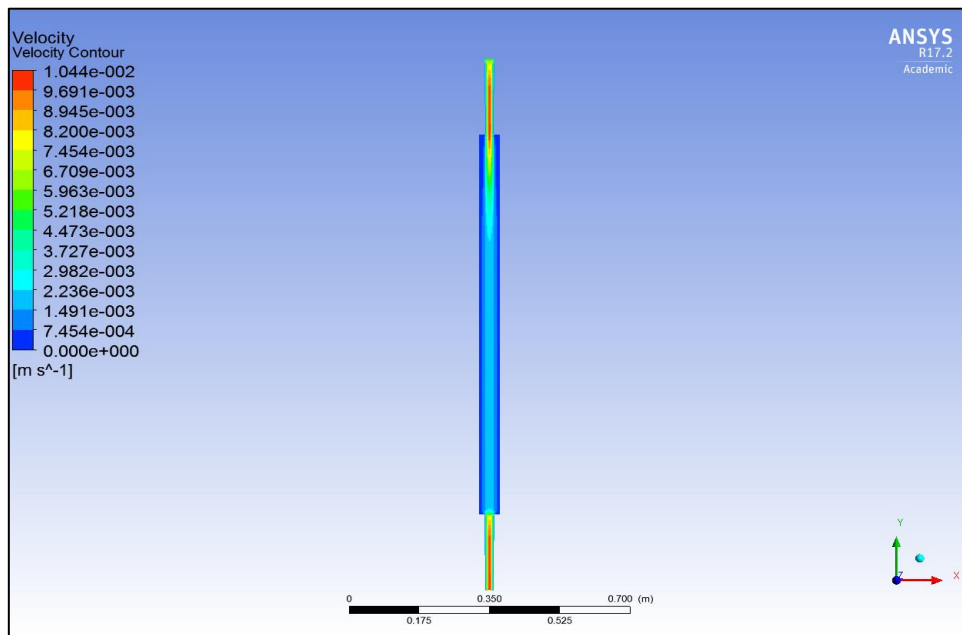


Figure 6.18 Velocity Contours for  $\text{Al}_2\text{O}_3$  nanofluid,  $\Phi = 0.01$



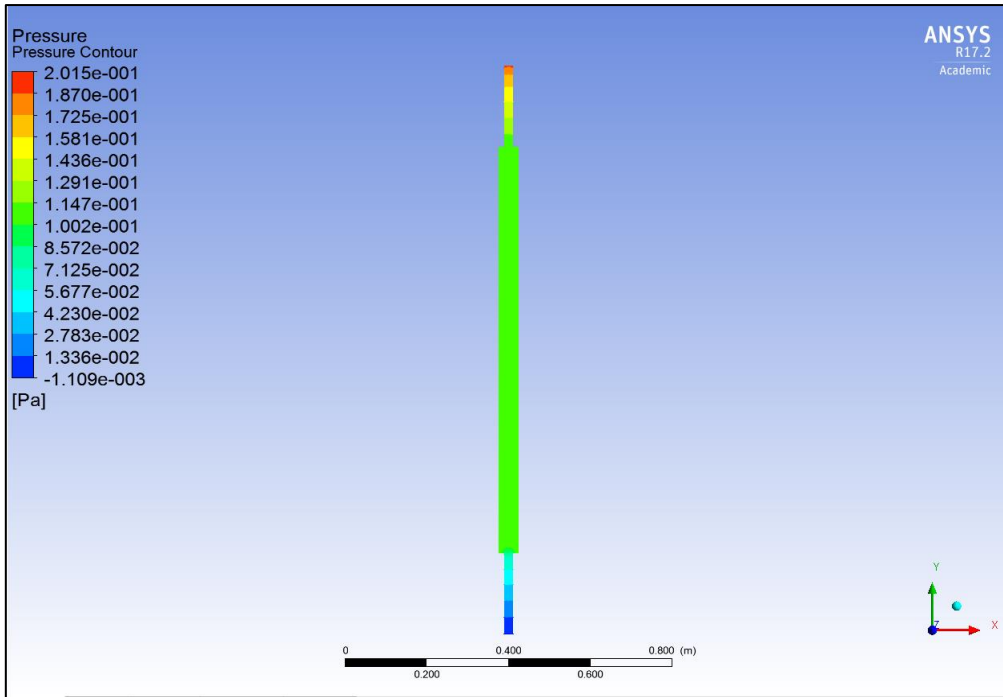


Figure 6.19 Pressure Contours for  $\text{Al}_2\text{O}_3$  nanofluid,  $\Phi = 0.01$

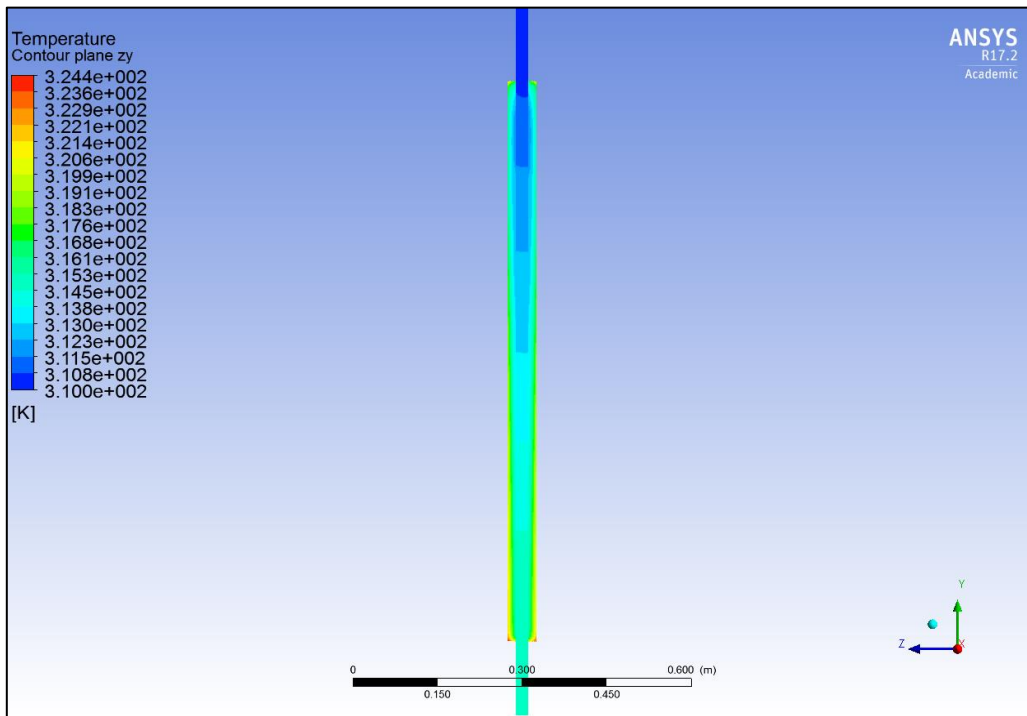


Figure 6.20 Temperature Contours for  $\text{Al}_2\text{O}_3$  nanofluid,  $\Phi = 0.05$

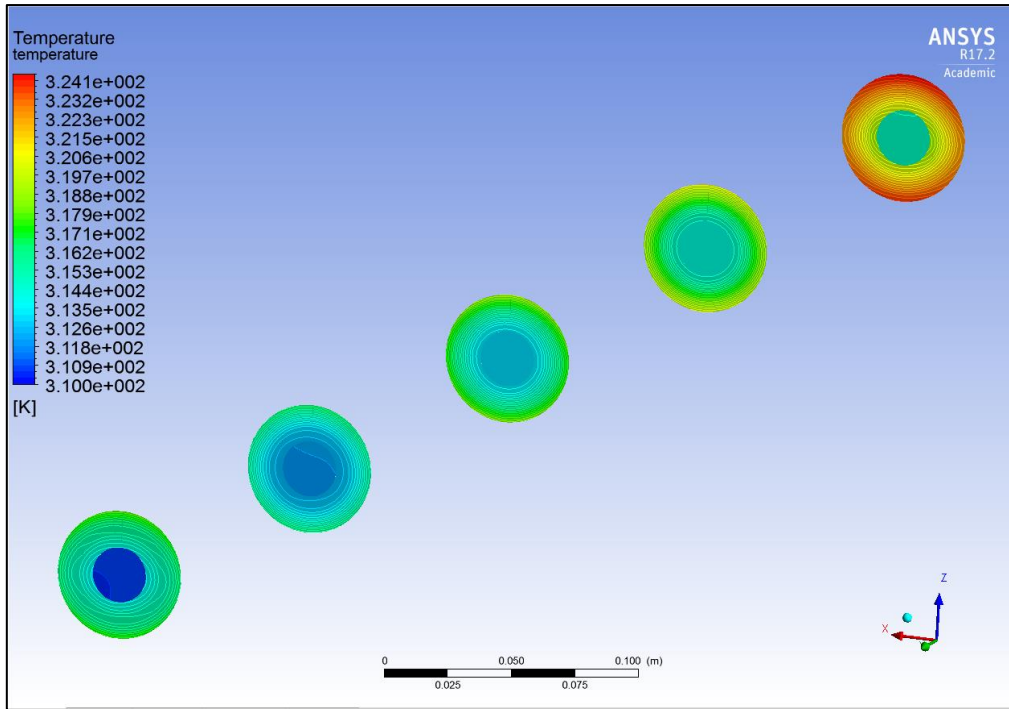


Figure 6.21 Temperature Contour cross sections for  $\text{Al}_2\text{O}_3$  nanofluid,  $\Phi = 0.05$

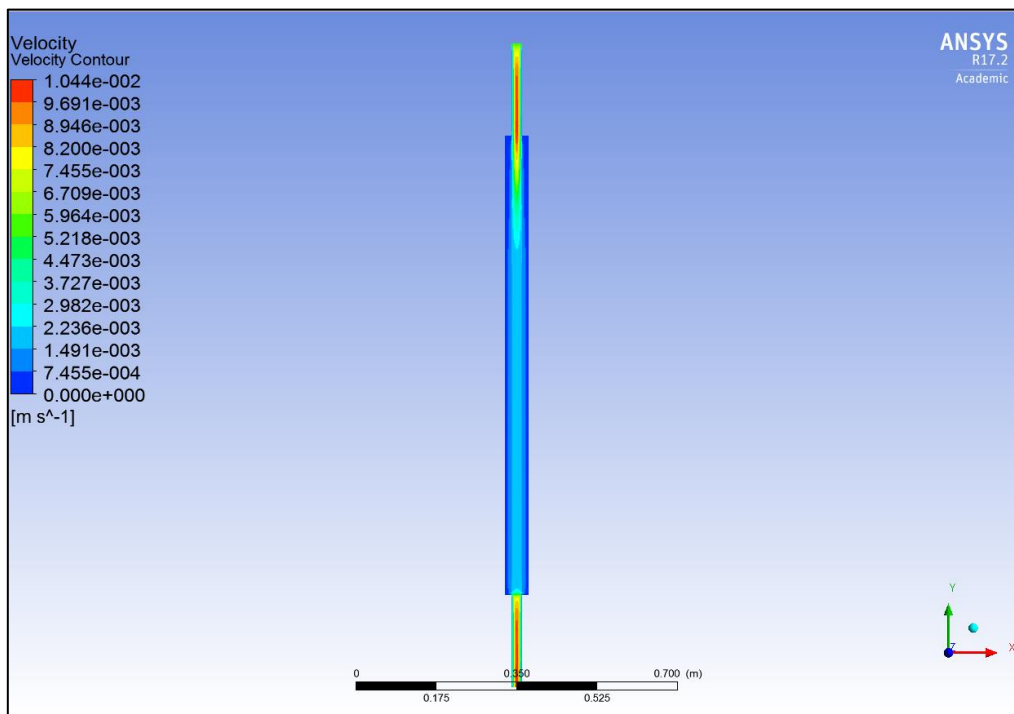


Figure 6.22 Velocity Contours for  $\text{Al}_2\text{O}_3$  nanofluid,  $\Phi = 0.05$

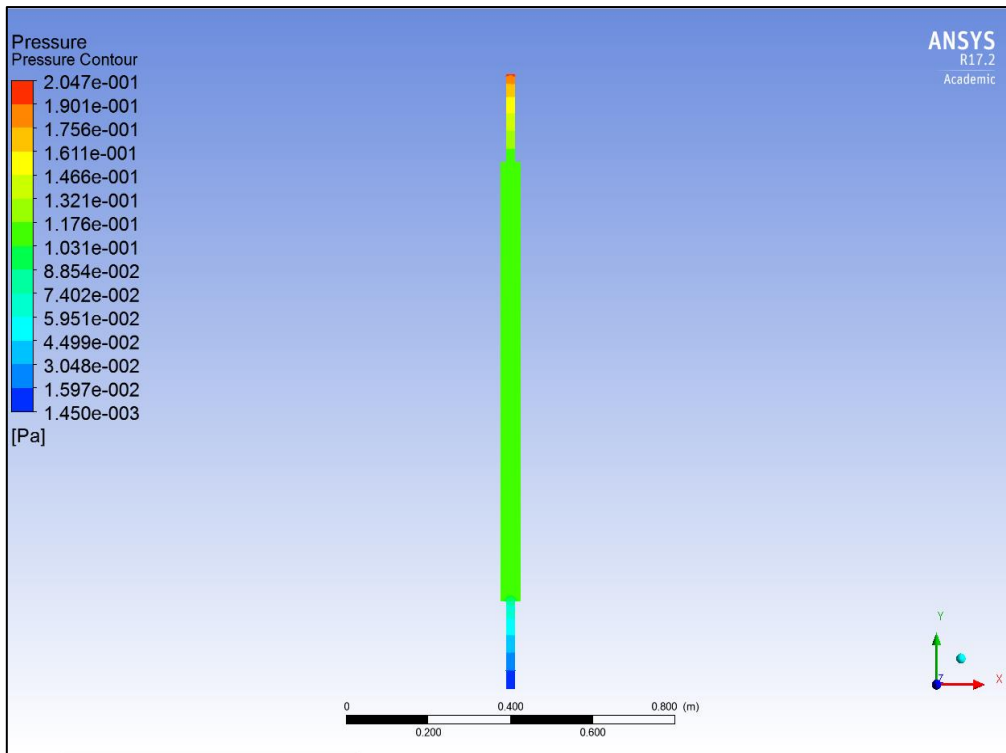


Figure 6.23 Pressure Contours for Al<sub>2</sub>O<sub>3</sub> nanofluid,  $\Phi = 0.05$

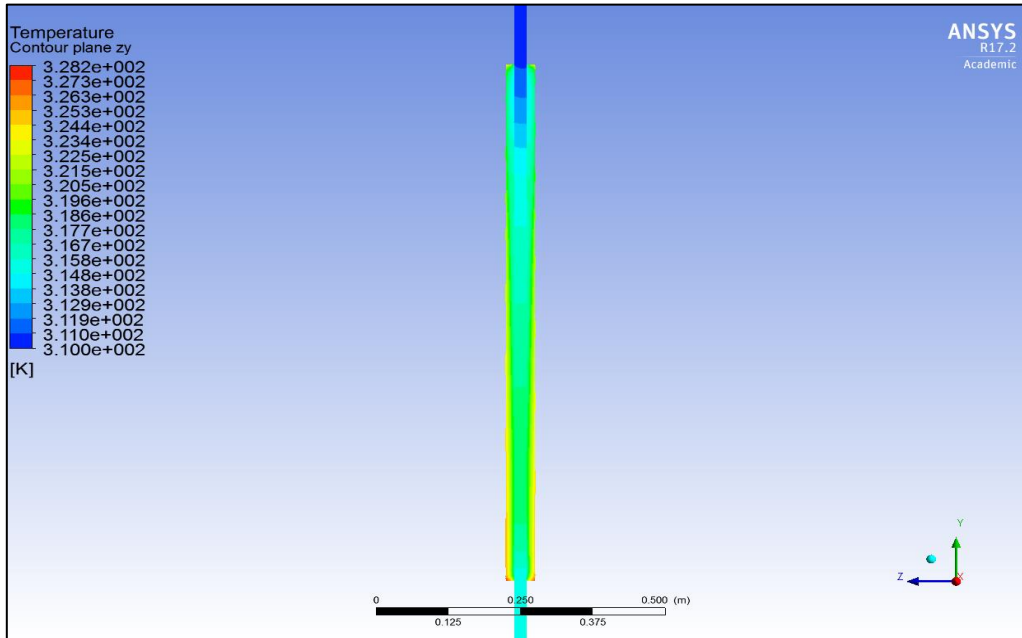


Figure 6.24 Temperature Contours for Al<sub>2</sub>O<sub>3</sub> nanofluid,  $\Phi = 0.1$

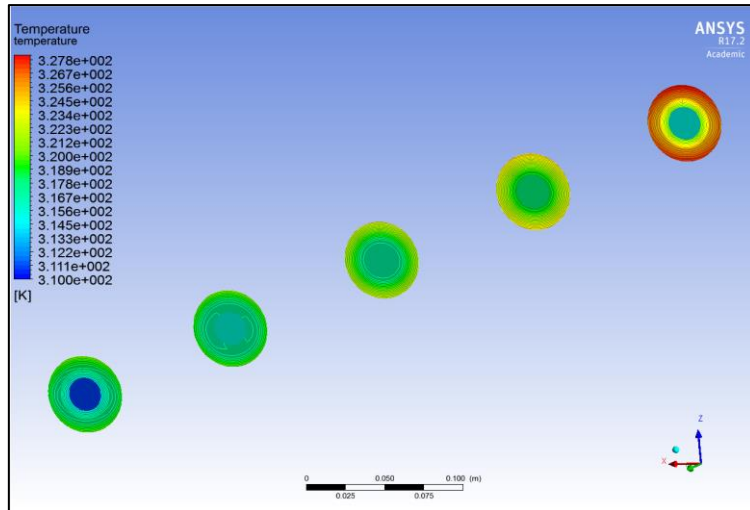


Figure 6.25 Temperature Contour cross sections for  $\text{Al}_2\text{O}_3$  nanofluid,  $\Phi = 0.1$

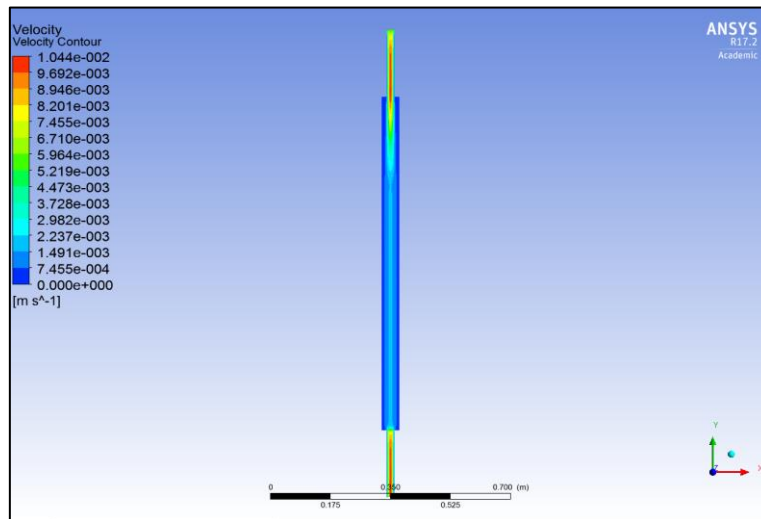


Figure 6.26 Velocity Contours for  $\text{Al}_2\text{O}_3$  nanofluid,  $\Phi = 0.1$

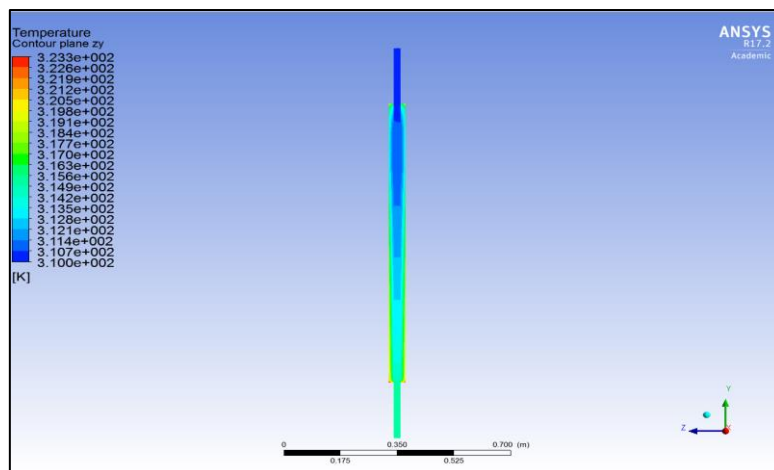


Figure 6.27 Temperature Contours for  $\text{TiO}_2$  nanofluid,  $\Phi = 0.01$

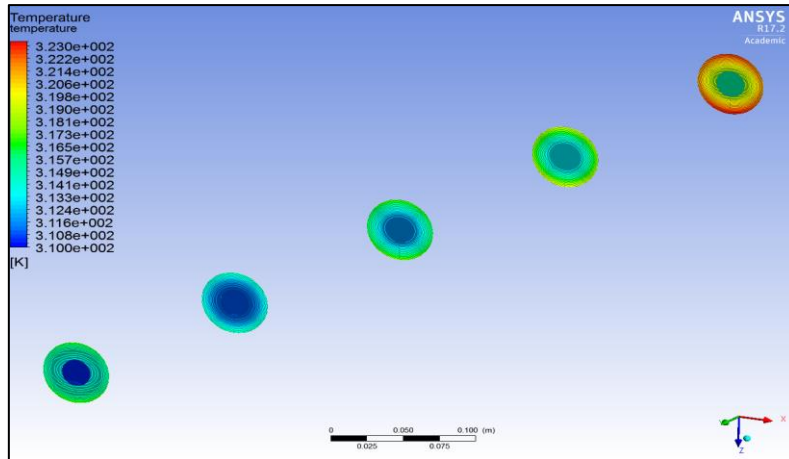


Figure 6.28 Temperature Contour cross sections for  $\text{TiO}_2$  nanofluid,  $\Phi = 0.01$

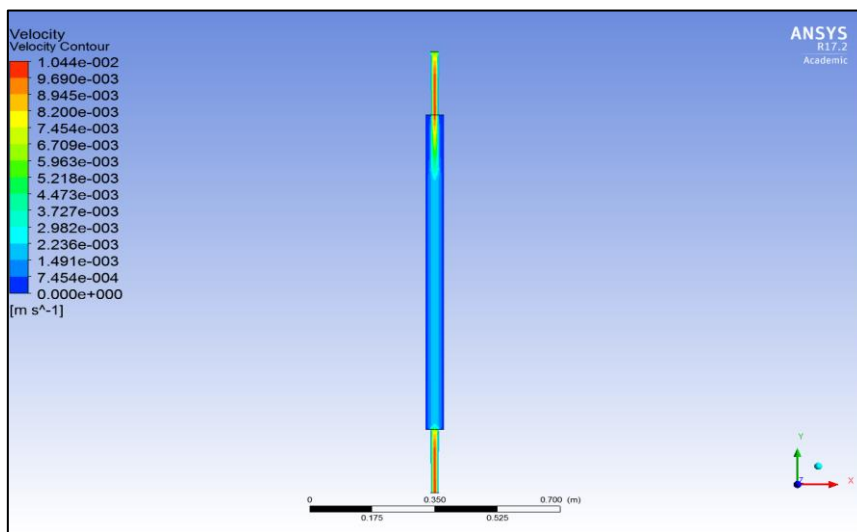


Figure 6.29 Velocity Contours for  $\text{TiO}_2$  nanofluid,  $\Phi = 0.01$

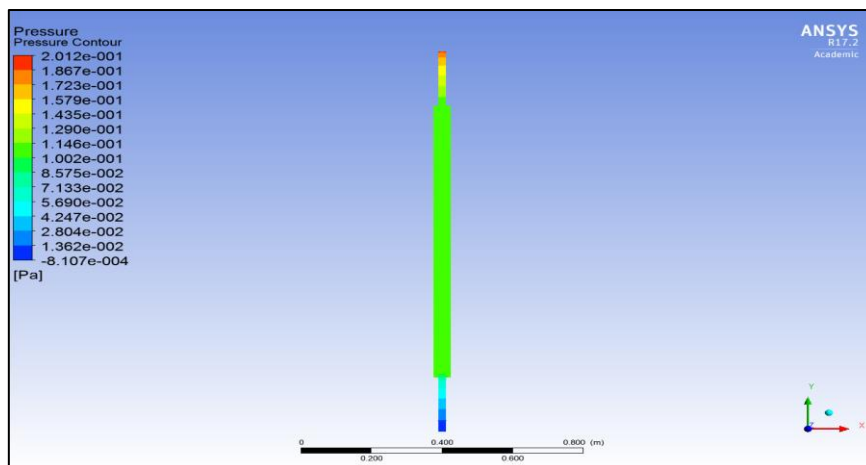


Figure 6.30 Pressure Contours for  $\text{TiO}_2$  nanofluid,  $\Phi = 0.01$

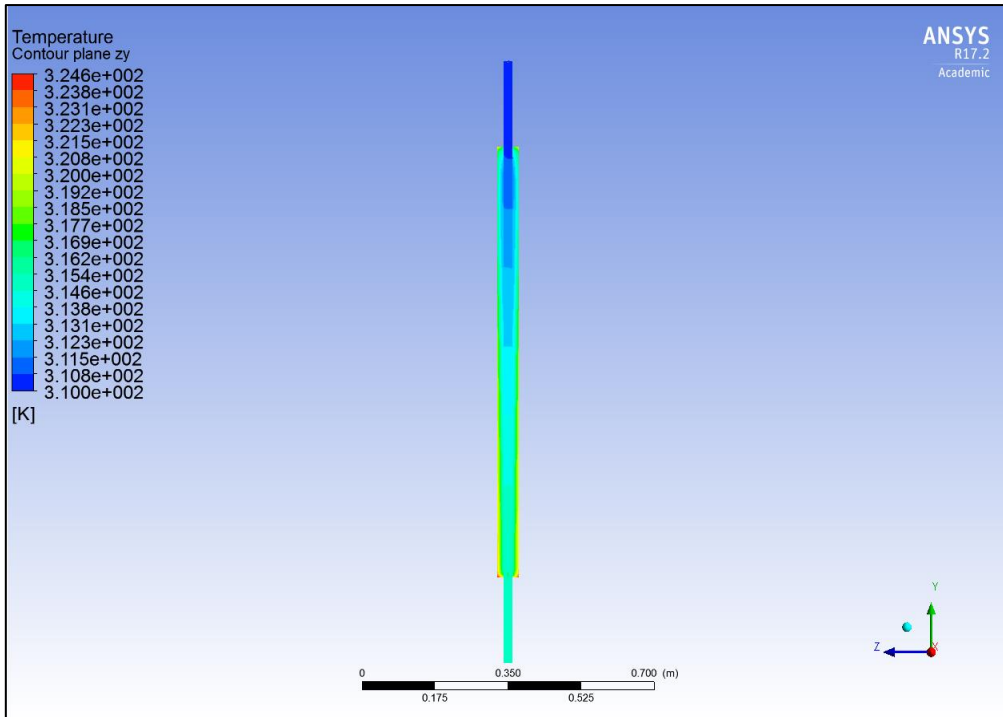


Figure 6.31 Temperature Contours for  $\text{TiO}_2$  nanofluent,  $\Phi = 0.05$

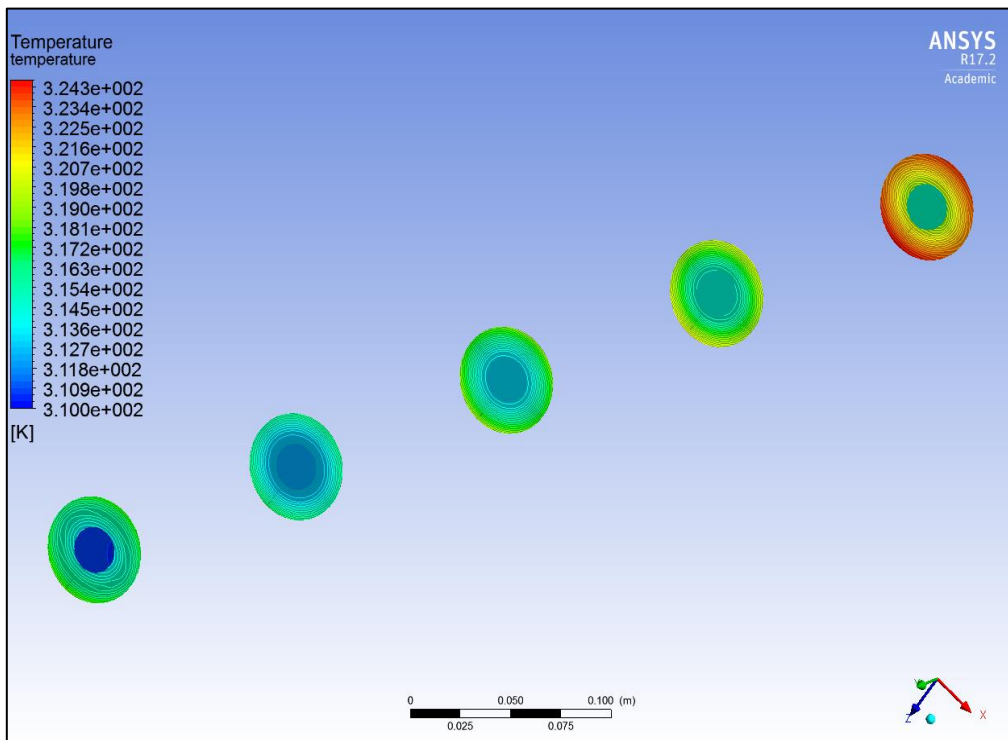


Figure 6.32 Temperature Contours cross sections for  $\text{TiO}_2$  nanofluent,  $\Phi = 0.05$

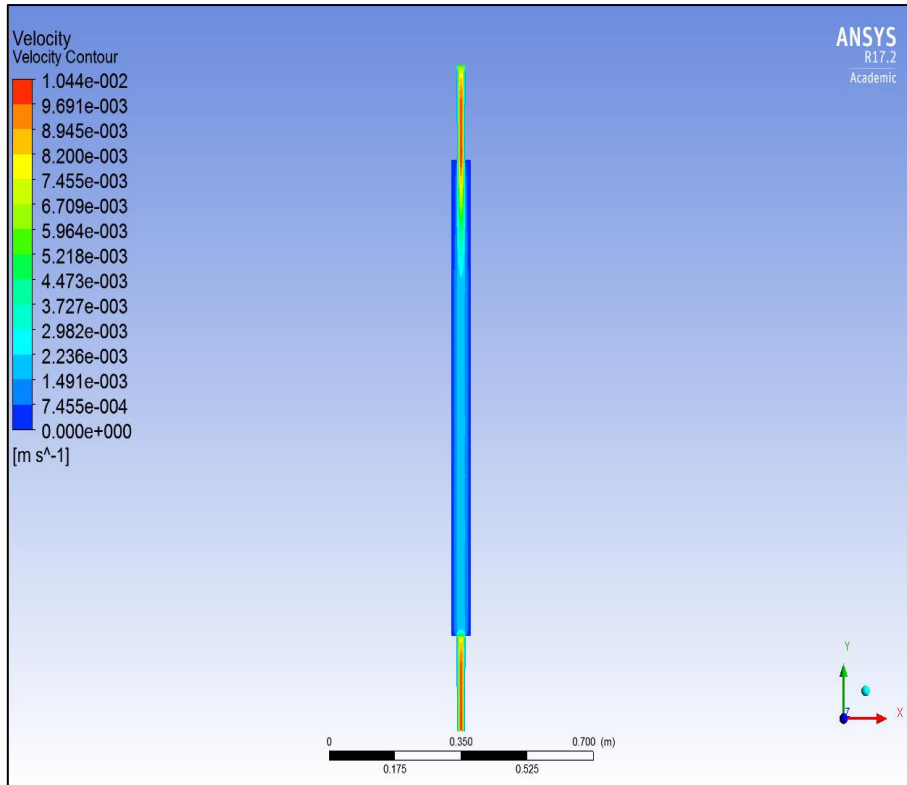


Figure 6.33 Velocity Contours for TiO<sub>2</sub> nanofluid,  $\Phi = 0.05$

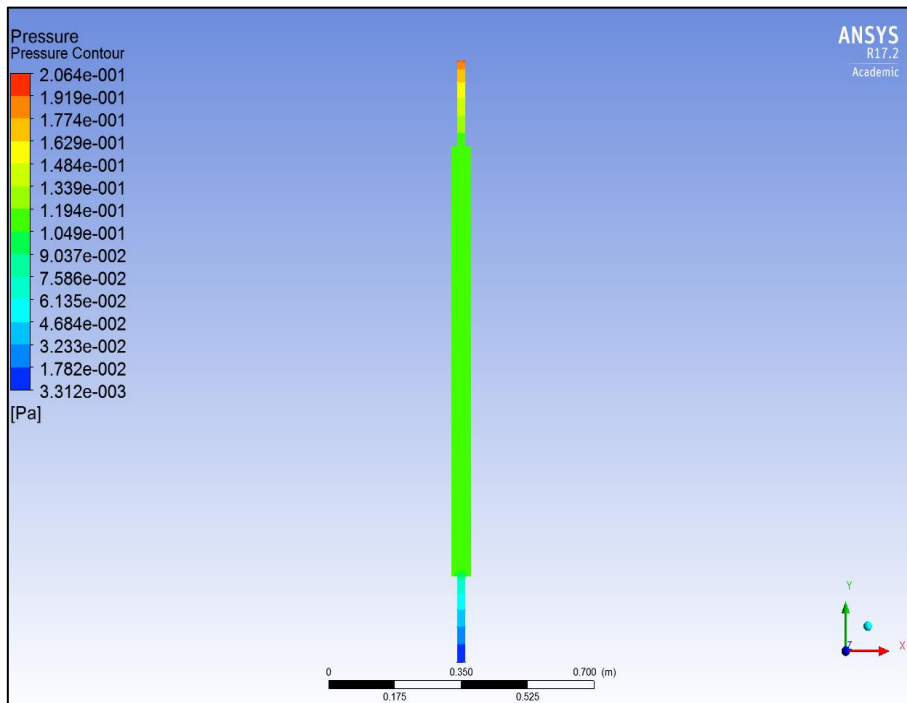


Figure 6.34 Pressure Contours for TiO<sub>2</sub> nanofluid,  $\Phi = 0.05$

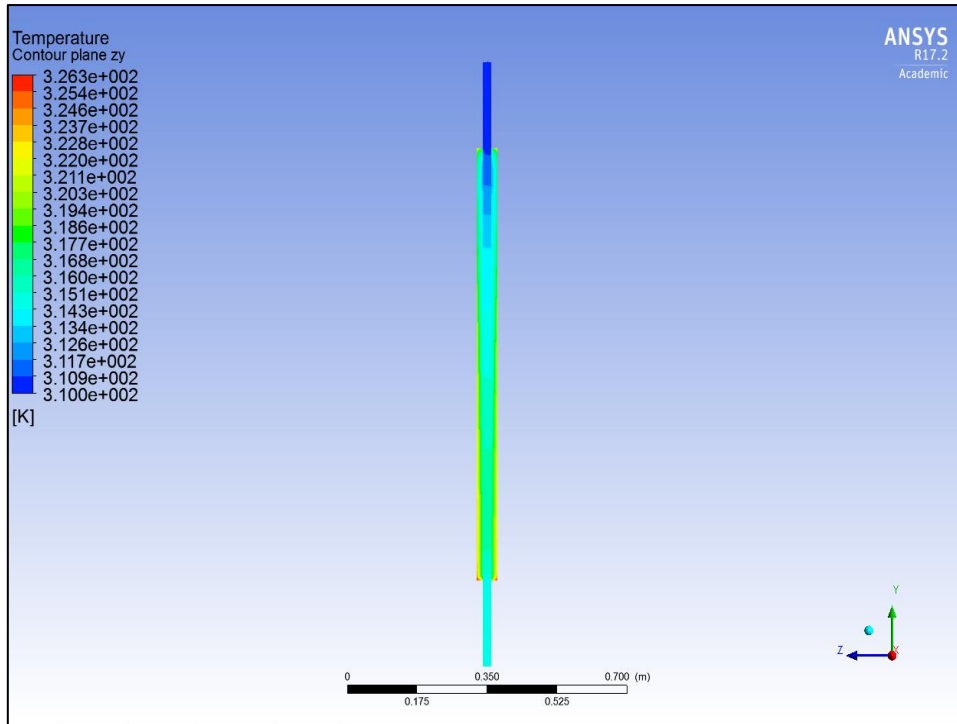


Figure 6.35 Temperature Contours for TiO<sub>2</sub> nanofluid,  $\Phi = 0.1$

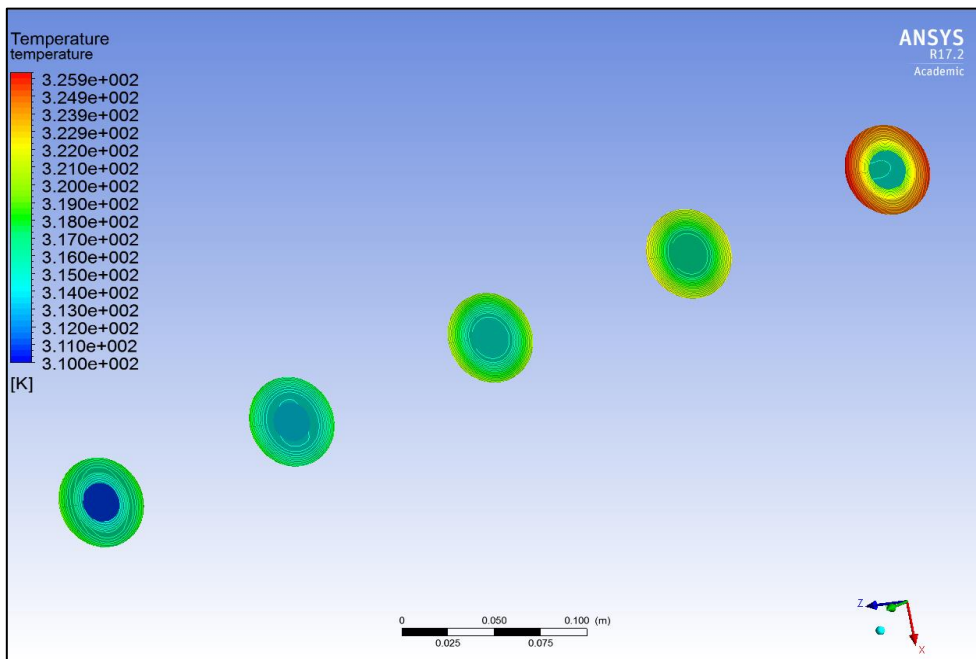


Figure 6.36 Temperature Contour cross sections for TiO<sub>2</sub> nanofluid,  $\Phi = 0.1$



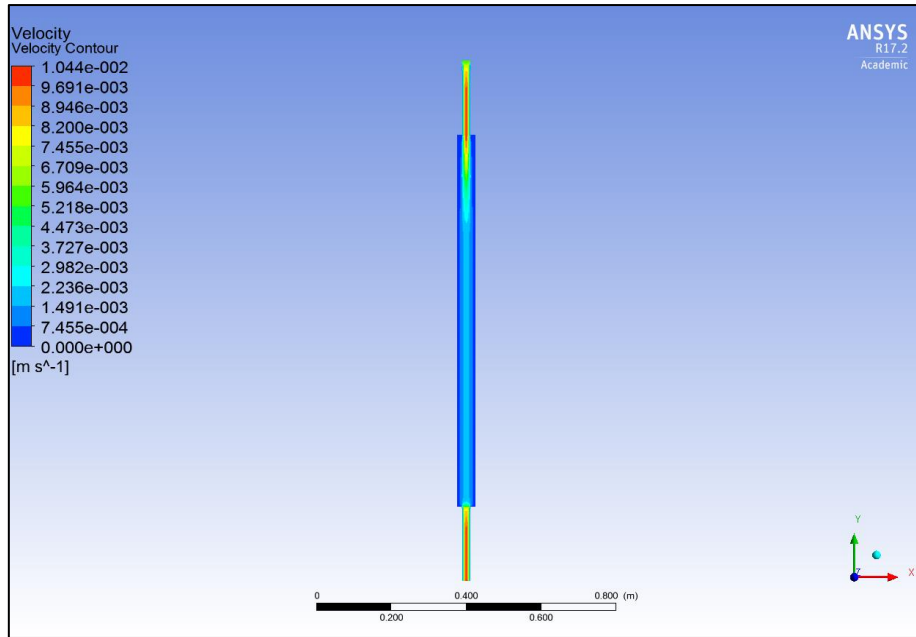


Figure 6.37 Velocity Contours for TiO<sub>2</sub> nanofluid,  $\Phi = 0.1$

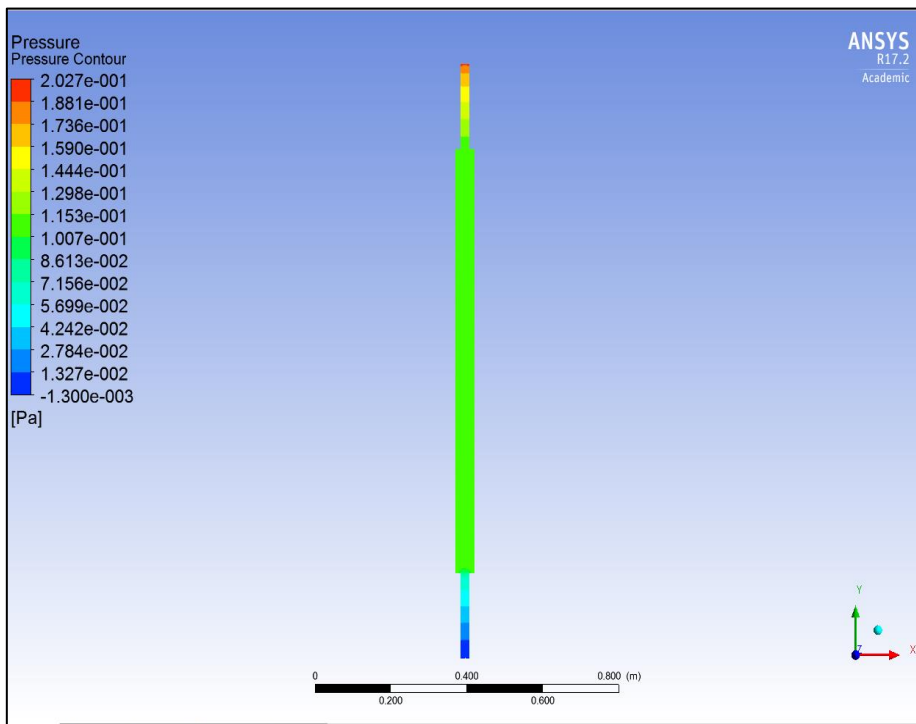
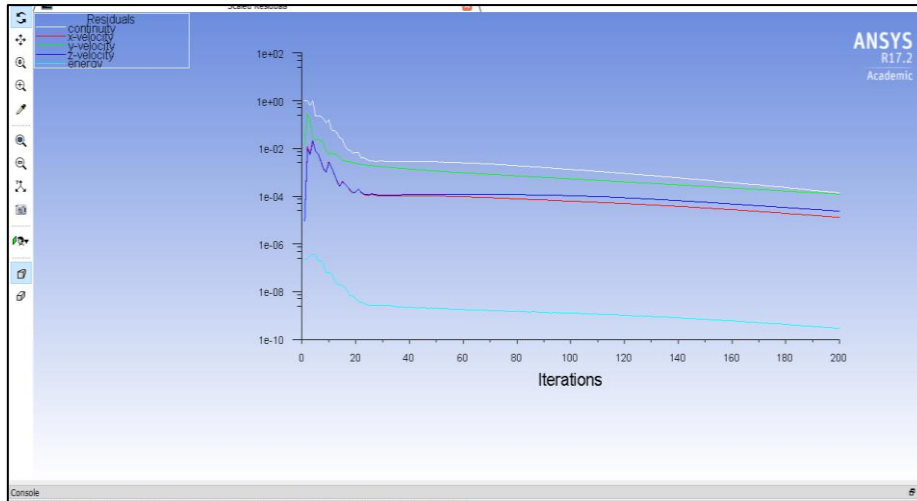


Figure 6.38 Pressure Contours for TiO<sub>2</sub> nanofluid,  $\Phi = 0.1$



**Figure 6.39 Residual iterations for ANSYS FLUENT simulation ( $\text{TiO}_2$  nanofluid,  $\Phi = 0.1$ )**

**Figure 6.4, Figure 6.8, Figure 6.12 Figs. 11a, 12a and 13a** show a significant modification in temperature distributions as volume fraction is enhanced from  $\phi = 0.01$ , to  $\phi = 0.05$  and finally  $\phi = 0.1$ . There is progressive heating from the base upwards of the annular region with increasing volume fraction. The blue zones are progressively eliminated, and green zones (higher temperature) extend further towards the upper adiabatic end. Red (maximum temperature zones) begin to appear at the highest volume fraction (**Figure 6.12**). The increase in concentration of metallic nanoparticles clearly enhances thermal conductivity of the nanofluid in the annular region and this intensifies thermal diffusion and heat transfer. **Figure 6.5, Figure 6.9 and Figure 6.13** (temperature cross-section slice views) provide a clearer visualization of the temperature at distinct locations in the annular space from the base of the solar collector to the top end (adiabatic end). There is a systematic evolution in contours. For the lowest volume fraction case, generally blue and green contours are prevalent (low temperatures) for the majority of the annular length. As volume fraction is increased, yellow and red zones are generated and become intensified towards the upper region of the annulus. Evidently therefore the enhancement in thermal conductivity encourages thermal diffusion and mobilizes a heating in the annulus indicating that more solar energy is captured, and that thermal efficiency is boosted (solar flux is fixed although it may be varied in the ANSYS specification). The presence of metallic nanoparticles achieves an elevation in interfacial thermal conductivity and even in the absence of buoyancy forces (forced convection is considered) encourages significantly thermal absorption. These patterns are consistent with numerous other studies on metallic nanofluids including (Moghadam, et al., 2014) and

(Maddah, et al., 2013). **Figure 6.6, Figure 6.10 and Figure 6.14** illustrate the evolution in velocity through the annular space. A less tangible influence is computed with increasing volume fraction. In all case high velocity zones arise at the inlet and outlet with slower zones in the interim sections. The primary influence on velocity is via the viscosity modification in the Tiwari-Das model. Although there is a slight intensification in velocity i.e. flow acceleration at the highest volume fraction (fig. 13c), this is only identified in the extremity zones of the annular geometry. Finally pressure distributions are depicted in **Figure 6.7, Figure 6.11 and Figure 6.15**. Generally intermediate pressure are clearly computed (green zones) through the main body of the annulus at any volume fraction. There is a slight pressure drop at the extremities (corresponding to acceleration in the flow); however, the dominant influence of metallic nano-particles (copper oxide) is on the temperature field as noted earlier in **Figure 6.4, Figure 6.5, Figure 6.8, Figure 6.9, Figure 6.12 and Figure 6.13**. Effectively, the enhanced heat absorbed at high volume fraction in the annular nanofluid space is transferred via the inner copper cylinder to the central space (pure water) leading to an elevation in solar thermal efficiency.

**Figure 6.16-Figure 6.19 to Figure 6.24-Figure 6.26** correspond to the Aluminium oxide nanofluid case, again at three different values of nano-particle volume fraction, viz  $\phi = 0.01$ ,  $\phi = 0.05$  and  $\phi = 0.1$  respectively. **Figure 6.16, Figure 6.20 and Figure 6.24** show a significant modification in temperature distributions as volume fraction is enhanced from  $\phi = 0.01$ , to  $\phi = 0.05$  and finally  $\phi = 0.1$ . At lower volume fractions, there is a dominant blue zone throughout the main annular space with weak peripheral green zones (low temperatures). However, for the highest volume fraction, (**Figure 6.24**) there is a marked growth in the green zone and emergence of yellow and very small red zones at the lower zone in the annulus, indicating that temperatures are increased, albeit weakly. Temperatures are however not as high as in the copper oxide cases (Figure 6.4, Figure 6.8, Figure 6.12) and this is probably attributable to the lower thermal conductivity of aluminium oxide compared with copper oxide. Inspection of the temperature cross-sections (Figure 6.17, Figure 6.21, Figure 6.25) confirms the intensification in temperatures, in particular, near the periphery of the glass tube in the upper zone of the annulus with an increase in volume fraction. Progressively we observe the emergence of yellow zones in the later cross-sections at  $\phi = 0.1$  which are absent at lower volume fractions. Darker blue and green zones vanish with stronger aluminium oxide nano-particle concentrations.

However again there are lower temperatures achieved at the equivalent volume fraction for aluminium oxide compared with copper oxide (Figure 6.5, Figure 6.9, Figure 6.13). Velocity is initially observed to be increased somewhat (Figure 6.18, Figure 6.22) with increase in volume fraction from  $\phi = 0.01$  to  $\phi = 0.05$ , especially in the inlet and outlet zones (blue slow zones are phased out with higher velocity green zones); however, with further elevation in volume fraction (Figure 6.26) the trend is inhibited and there is a slight deceleration in flow near the upper zone of the annulus (inlet) and the re-emergence of blue zones. Negligible alteration in pressure is computed with an increase in volume fraction from  $\phi = 0.01$  to  $\phi = 0.05$  (Figure 6.19 and Figure 6.23) and further numerical experiments revealed that greater volume fractions of aluminium oxide nano-particles to do not instigate any significant modification in pressure distributions.

**Figure 6.27 to Figure 6.38** correspond to the Titanium oxide nanofluid case, again at three different values of nano-particle volume fraction, viz  $\phi = 0.01$ ,  $\phi = 0.05$  and  $\phi = 0.1$  respectively. Figure 6.27, Figure 6.31 and Figure 6.35 show a significant increase in temperature magnitudes as volume fraction is enhanced from  $\phi = 0.01$ , to  $\phi = 0.05$  and finally  $\phi = 0.1$ . At lower volume fractions, there is a prevalent blue zone (lowest temperatures) throughout the majority of the annulus with subsequent green zones (intermediate temperatures) as we approach the upper end and lower peripheral yellow zones (higher temperatures). However, as volume fraction is increased, (Figure 6.31) there is a marked development in the green zone which extends further towards the upper end and a thickening in the yellow peripheral streaks with some presence of high temperature (red micro-zones at the base of the annulus). The temperatures are further increased for maximum volume fraction (Figure 6.35) and the green zone extends yet further upwards with some yellow areas at the tube walls. The temperature magnitudes exceed those computed at the same values of volume fraction for Aluminium oxide (Figure 6.16, Figure 6.20, Figure 6.24) but are substantially lower than those obtained for Copper oxide (Figure 6.8, Figure 6.12). This confirms the superior performance of Copper oxide in achieving thermal enhancement in the solar annular collector. Figure 6.28, Figure 6.32 and

Figure 6.36 (temperature cross-section slice views) also show that temperatures are markedly enhanced with increasing volume fraction of titanium oxide nano-particles, as we progress from the lower end of the annular region to the upper end. Stronger red (high temperature) and yellow zones (quite high temperature) appear to grow considerably. The magnitudes achieved

are larger than those for the Aluminium oxide cases (Figure 6.17, Figure 6.21 and Figure 6.25). However, they are still somewhat less than those attained for the Copper oxide cases (Figure 6.5, Figure 6.9 and Figure 6.13). Apparently therefore higher nano-particle concentrations (volume fractions) of Copper oxide attain the best thermal performance since the best absorption of solar thermal energy is achieved. Intensified thermal convection currents are generated for this case. Titanium oxide is the next best option, whereas Aluminium oxide is the least successful option. These findings are important since they generalize previous studies in which a single metallic nano-particle was examined e.g. Copper oxide by (Moghadam, et al., 2014) or two metallic nanofluids (silver oxide and aluminium oxide) by (Maddah, et al., 2013). Figure 6.29, Figure 6.33 and Figure 6.37 visualize the velocity contours again for three different volume fractions. No substantial modification is generated in the velocities for the Titanium oxide case. Finally pressure distributions are depicted in Figure 6.30, Figure 6.34 and Figure 6.38 and it is evident that no tangible change arises in the pressure field with a change in volume fraction of titanium oxide nano-particles, concurring with the observations of (Maddah, et al., 2013). Finally, in Figure 6.39 we have presented residual iterations for the ANSYS FLUENT simulations for a sample case (Aluminium Oxide) indicating how excellent convergence is achieved and good accuracy is maintained.

## 6.5 Conclusions

3-D computational simulations have been presented in this chapter for forced convective heat transfer in an annular pipe solar collector system under solar radiative heat flux. **ANSYS FLUENT 18.1** computational fluid dynamics software has been employed to analyse the three-dimensional steady-state incompressible laminar flow comprising water-based nanofluid containing a variety of metallic nanoparticles (copper oxide, aluminium oxide and titanium oxide nanoparticles). The Tiwari-Das model which utilizes the Maxwell-Garnett approach has been employed to simulate nanoscale effects. This model provides accurate expressions for thermal conductivity, specific heat capacity and viscosity of the nanofluid suspensions as a function of solid nano-particle volume fraction and is easily implemented in the FLUENT material physics option (under “one-phase flow”). Mesh-independence tests have been included. The influence of volume fraction on temperature, temperature cross-sections, velocity and pressure contours has been computed. The present analysis has shown that:

- (i) 2-D model validation shows confidence in the nanofluid ANSYS approach.
- (ii) The Tiwari-Das nanoscale model is proven to be compatible with the ANSYS multi-physics and produces robust accurate results for enclosure nanofluid solar collector simulations.
- (iii) For the 3-D annular model Copper oxide nanofluid is observed to achieve the best temperature enhancement. Temperature contours at cross-sections of the annulus are also computed.
- (iv) For the 3-D annular model Titanium Oxide achieves higher temperatures than Aluminium Oxide but significantly lower temperatures than Copper Oxide.
- (v) For the 3-D annular model temperature cross-sections exhibit significant enhancement in magnitudes with volume fraction for all three metallic nano-particles, although the best performance again is with Copper Oxide.
- (vi) For the 3-D annular model there is flow acceleration for the Copper oxide case at the highest volume fraction although it is confined to the extremity zones of the annular geometry (inlet and outlet).
- (vii) For the 3-D annular model velocities are initially increased with volume fraction for the Aluminium Oxide case but subsequently with maximum volume fraction they are reduced.
- (viii) For the 3-D annular model pressures are also reduced somewhat with increasing volume fraction for the Copper oxide case but not altered significantly for either Titanium Oxide or Aluminium Oxide cases.

## **PUBLICATION NOTE**

A version of this chapter was published in **Kuharat, S. and Bég, O. Anwar**, 'Computational fluid dynamics simulation of a nanofluid-based annular solar collector with different metallic nano-particles', *Heat and Mass Transfer Research Journal (HMTRJ)*, 3 (1) 1-23 (2019). A shorter version (poster) was presented earlier at the *ICHTFM 2018: 20th International Conference on Heat Transfer and Fluid Mechanics, WASET, Istanbul, Turkey, August 16 – 17 (2018)*.

# **Chapter 7 Numerical simulation of forced convection-radiation transfer in a flat plate prismatic 3-d solar collector with inlet/outlet conditions, metallic/carbon nanoparticles and the Chandrasekhar discrete ordinates method.**

## **7.1 Introduction**

From the research conducted in chapters 3-6, it has been demonstrated that nanofluids provide significant thermal enhancement in a variety of direct absorber solar collectors i.e., prismatic, trapezoidal, annular etc. A range of metallic nanoparticles (copper, titanium oxide, aluminium oxide, zinc, silver diamond) and different volume fractions have been explored. However, other thermal solar collectors in the current market have different features such as conventional surface absorption-based solar collectors, which use a *black surface or spectrally selective surface* to absorb solar irradiance and heat the heat transfer fluids (HTF). In these systems the efficiency depends on the absorber capturing solar energy and how effectively heat is transferred to the working fluid. Heat transfer in surface absorption-based solar collectors mostly relies on thermal conductivity of nanofluids, flow rate (forced convection) and temperature gradient (radiation). In the present chapter (and final ANSYS FLUENT simulation in this PhD) therefore the flat plate solar collector geometry with inlet and outlet features (for controlling flow rates) is examined. Three different metallic (copper, copper oxide, silver) and one non-metallic (Graphite) nanoparticles are simulated in a 3-dimensional solar collector geometry. Forced convection is considered i. e. thermal buoyancy effect (neglected), and therefore Reynolds and Prandtl numbers and volume fraction are the critical control

parameters. The Tiwari-Das nanoscale model is deployed in ANSYS FLUENT. To cater for variable optical properties of nanofluids, a more advanced radiative approximation model is deployed, namely the Chandrasekhar discrete ordinates method (DOM) which has been described at length, earlier in Chapter 2. Extensive visualization of different geometric and nanoscale effects is included. The relative performance of the different metallic and non-metallic nanoparticles on thermal efficiency e. g. local Nusselt number at the enclosure (collector) boundaries is also described. Interesting thermofluid characteristics are computed and it is identified that specific volume fractions of different metallic and non-metallic nanoparticles under carefully selected flow rates produce optimum heat transfer performance.

## **7.2 Mathematical Model**

From the extensive literature review given in Chapter 1, the numerical analysis of natural/forced convection heat transfer and fluid flow in enclosures has extensively been developed using different computational techniques as it is a fundamental compliment to experimental studies of solar collectors. As described earlier, (Otanicar, et al., 2010) investigated the radiative properties of nanofluids, leading to an increase in the efficiency of direct absorption solar collector. This excellent benchmark from the scientific literature has been selected to use as a case study and validation-the authors of this work report on the experimental results of a micro-solar-thermal-collector that measures  $3 \times 5 \text{ cm}^2$  with a channel depth of  $150 \text{ }\mu\text{m}$ . However, their study only focused on radiative properties. In the present analysis, we extend and generalize their study to also consider forced convection effects in a real solar collector dimension (W  $0.5 \text{ m} \times$  L  $1 \text{ m}$  and depth of  $0.05 \text{ m}$ ). The direct absorber solar collector geometry simulated is visualized in Figure 7.1 below in an (x,y,z) coordinate system.



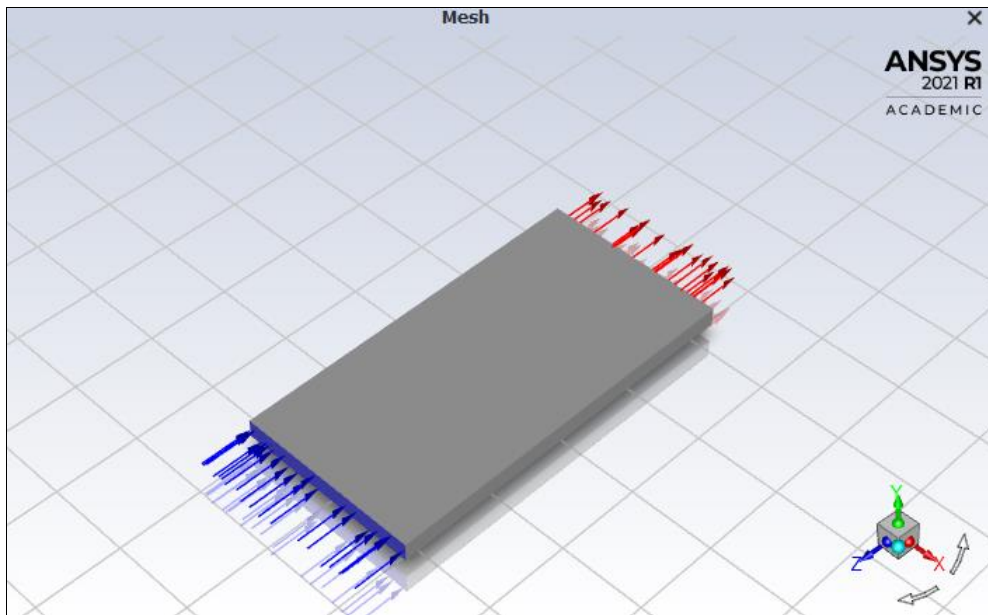


Figure 7.1 Direct absorber solar nanofluid collector

The fluid in the enclosure is a water-based nanofluid containing copper, copper oxide, silver, or graphite nanoparticles. It is assumed that the base fluid (i.e., water) and the nanoparticles are in thermal equilibrium and no slip occurs between them. The thermo-physical properties of the nanofluid are given in **Table 7.1**. The collector glazing is a low reflectance glass with directly receive a solar irradiation of  $1423 \text{ W/m}^2$  where the copper absorber plate is assumed to be coated with a reflective material (adiabatic). Left and right walls are taken as adiabatic. The thermophysical properties of the nanofluid are assumed to be constant. Laminar, steady-state, incompressible flow is considered with *forced convective heat transfer*. The nanofluid completely fills the flat plate solar enclosure and the Tiwari-Das single-phase nano-particle volume fraction model is deployed, which has been elaborated in detail in Chapter 2. The fundamental equations for steady viscous, incompressible laminar flow are the three-dimensional time-independent Navier-Stokes equations, which in a Cartesian coordinate system are reduced from the general 3-D equations given in section 2.2-1 of chapter 2.

ANSYS FLUENT software provides a solar irradiation model (for both steady and time-dependent flows) which implemented to compute the radiation effects from the sun rays entering the computational domain. In the present simulation, the discrete ordinate model is therefore employed to simulate radiative heat transfer via the radiative flux term,  $Q_{rad}$ . DOM is a non-gray model which allows wavelength-dependent optical properties of working fluid to be included in radiative transfer analysis. The sun's rays that enter the computational domain can be modeled by the ray tracing algorithm. By applying the solar load in ANSYS-Fluent, the calculated heat by the ray tracing algorithm is coupled to the energy equation via a heat source term. Only the DOM option needs to be selected in addition to "Solar Ray Tracing" settings under "Radiation Tab" in the ANSYS graphical user interface. The principal focus is to study the heat absorption capability of various types of nanofluids. The solar radiative flux is therefore fixed in the y-direction with a specific intensity of  $1423 \text{ W/m}^2$ . To simulate nano-particle effects, the Tiwari-Das model allows different concentrations (volume fraction) and types of metallic nanoparticles to be examined. The optical properties i. e. extinction coefficients of nanofluids are taken from experimental conducted in (Taylor, et al., 2011). In ANSYS, this approach is implemented as a "one-phase flow" modification since the particles are very small. A nanofluid is defined in the ANSYS FLUENT workbench as a new fluid with a new density, viscosity, thermal conductivity and specific heat obtained as a function of a base fluid and nano-particle type and concentration (volume fraction. The volume fraction can be estimated from:

$$\phi = \frac{V_{np}}{V_f} \quad \text{Equation 7.1}$$

Where  $\phi$  =volume fraction,  $V_{np}$  = nano particles volume and  $V_f$  = volume of fluid. The dynamic viscosity can be estimated from:

$$\mu_{nf} = \frac{\mu_f}{(1-\phi)^{2.5}} \quad \text{Equation 7.2}$$

Here  $\mu_{nf}$  = dynamic viscosity of nanofluid (kg/m.s),  $\mu_f$  = dynamic viscosity of base fluid. The effective density and heat capacity also can be estimated from:

$$\rho_{nf} = (1 - \phi)\rho_f + \phi\rho_s \quad \text{Equation 7.3}$$

$$C_{pnf} = \frac{(1-\phi)(\rho C_p)_f + \phi(\rho C_p)_s}{\rho_{nf}}, \quad \text{Equation 7.4}$$

Here  $\rho_{nf}$  = nanofluid density,  $\rho_f$  = base fluid density,  $\rho_s$  = nanoparticle density,  $C_{pnf}$  = nanofluid specific heat. The effective thermal conductivity of fluid can be determined by the Maxwell-Garnet relation which is adopted in Tiwari-Das model:

$$\frac{K_{nf}}{k_f} = \frac{k_s + 2k_f - 2\phi(k_f - k_s)}{k_s + 2k_f - \phi(k_f - k_s)} \quad \text{Equation 7.5}$$

Here  $k_{nf}$  = nanofluid thermal conductivity,  $k_f$  = fluid thermal conductivity and  $k_s$  = nanoparticle thermal conductivity. All calculated nanofluid properties (for the four different metallic nanoparticles studied i.e., copper, copper oxide, silver, and graphite) at the two volume fractions studied are given in the **Appendix**. The key local dimensionless parameters which may be computed in ANSYS FLUENT are *local Nusselt number and volume average Nusselt number* (heat transfer rate along the left wall). The latter may be defined as:

$$\text{Nusselt number: } Nu = \frac{hL}{k_{nf}} = \frac{q''_{w\text{CFD}}(L)}{k_{nf}(\Delta T)} \quad \text{Equation 7.6}$$

$h$  is convective heat transfer coefficient,  $B$  is the width of the enclosure,  $L$  is height of the enclosure,  $q''_{w\text{CFD}}$  is the heat flux rate computed in ANSYS FLUENT. In addition to no-slip boundary conditions at the walls of DASC, the following thermal boundary conditions are imposed:

$$\text{Inlet: Constant temperature, } T = 300 \text{ K} \quad \text{Equation 7.7-a}$$

Outlet: Constant Flow rate weight of 1

Equation 7.7-b

Left, Right and Bottom walls: Adiabatic

Equation 7.7-c

Solar irradiation,  $Q_{rad}=1423 \text{ W/m}^2$

Equation 7.7-d

Radiative heat transfer is also incorporated using the ANSYS DO model. The scattering effect is ignored. The standard thermal conduction flux (Fourier model) is augmented with the radiative flux,  $Q_{rad}$ .

### 7.3 Grid Sensitivity Analysis

In a CFD solution, the sum is never identically zero, but (hopefully) decreases with progressive iterations. A residual can be thought of as a measure of how much the solution to a given transport equation deviates from the actual correct solution.

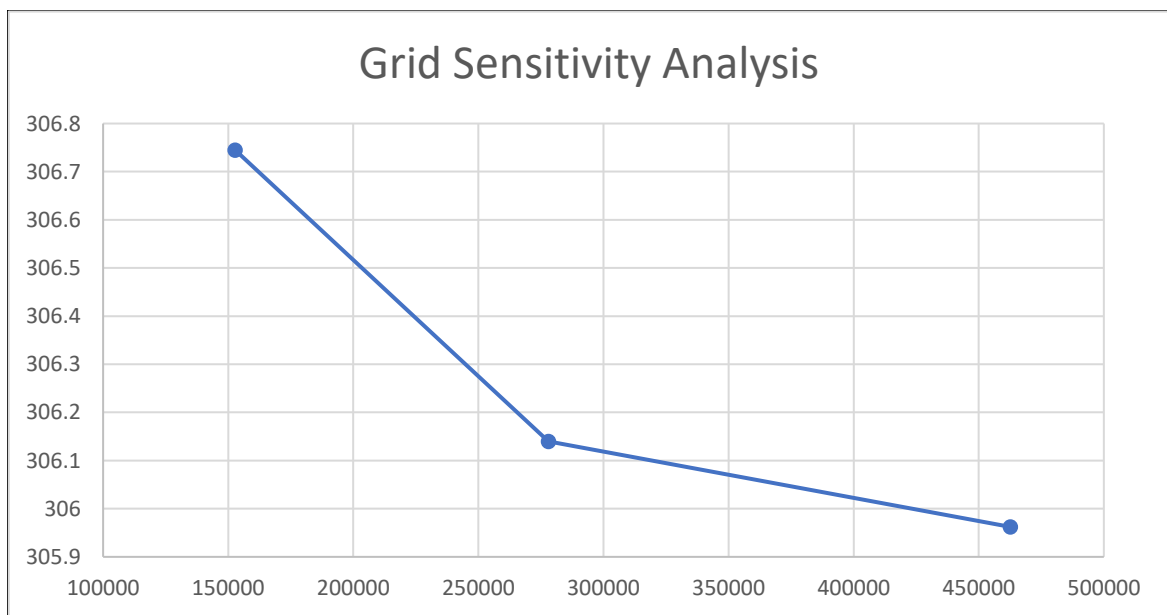


Figure 7.2: Grid Sensitivity Analysis

The *average residual* associated with each transport equation is monitored, to help determine when the solution has converged. For this simulation, ten thousand of iterations are required to

get the residuals decrease below  $1e^{-6}$  for all the equations which a very accurate criterion for the final solution. In addition to the convergence generated by the ANSYS residual print plot, as explained above, the grid sensitivity analysis was conducted by refining the mesh of the model until the results were reduced as shown in **Figure 3.2**. Further refinement cannot be conducted due to the software licence restriction (limited to maximum of 500,000 elements).

## 7.4 Validation with Published Studies

To validate the results obtained from the ANSYS Model for forced convective heat transfer inside a direct absorption solar collector filled with *graphite-water nanofluid*, results were benchmarked with the experimental study conducted by (Otanicar, et al., 2010) as shown in Figure 3.3. Figure 7.4 shows a similar pattern of temperature contours, as both studies show a cool temperature at the inlet and a high temperature at the outlet. The top edge of the collector is at the highest temperature. However, in the infrared image of the experiment there are some non-uniform cooler zones at the top right and bottom left corners of the collector which are perhaps associated with experimental errors since the flow field studied by (Otanicar, et al., 2010) is not fully developed hydrodynamically. Also, in their experiments errors arise due to nanoparticle deposition resulting in local thermal leaks. Figure 7.5 shows a comparison of collector efficiency from the ANSYS FLUENT modelling and experimental results of graphite-water based nanofluids. The graph indicates that simulation results are slightly higher than experimental ones which is expected. As the simulation model does not consider the effect of thermophoresis and Brownian motion (available in a different nanoscale model known as Buongiorno's model, which was earlier described in chapter 2 and will be used next in Chapter 8), inevitably some discrepancy is to be found. The Buongiorno model is currently not available in ANSYS FLUENT material physics and therefore could not be used. The

experimental study of (Otanicar, et al., 2010) agrees also quite well with CFD model of a direct absorption solar collector presented by (Bardsgard, et al., 2020). Overall, however the Tiwari-Das based ANSYS FLUENT CFD simulation gives a good prediction of accuracy to within 8% of the experimental results across a wide range of volume fractions.

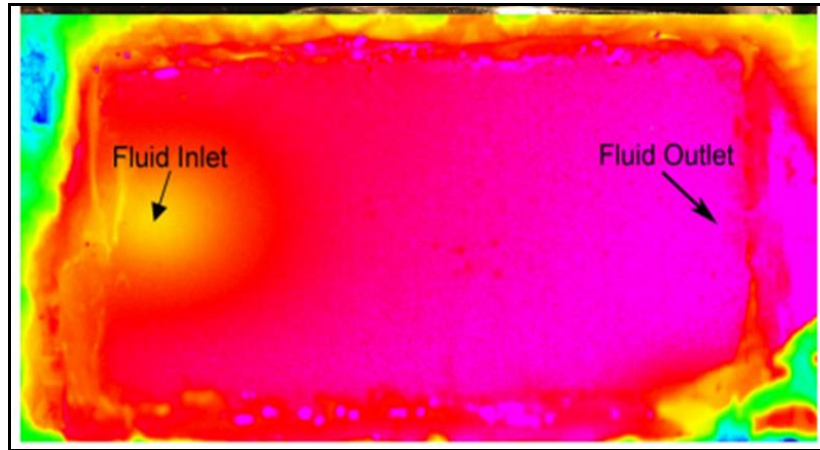


**Figure 7.3 Infrared image demonstrating rapid temperature increase (blue: coolest and Pink: warmest) (Otanicar, et al., 2010)**

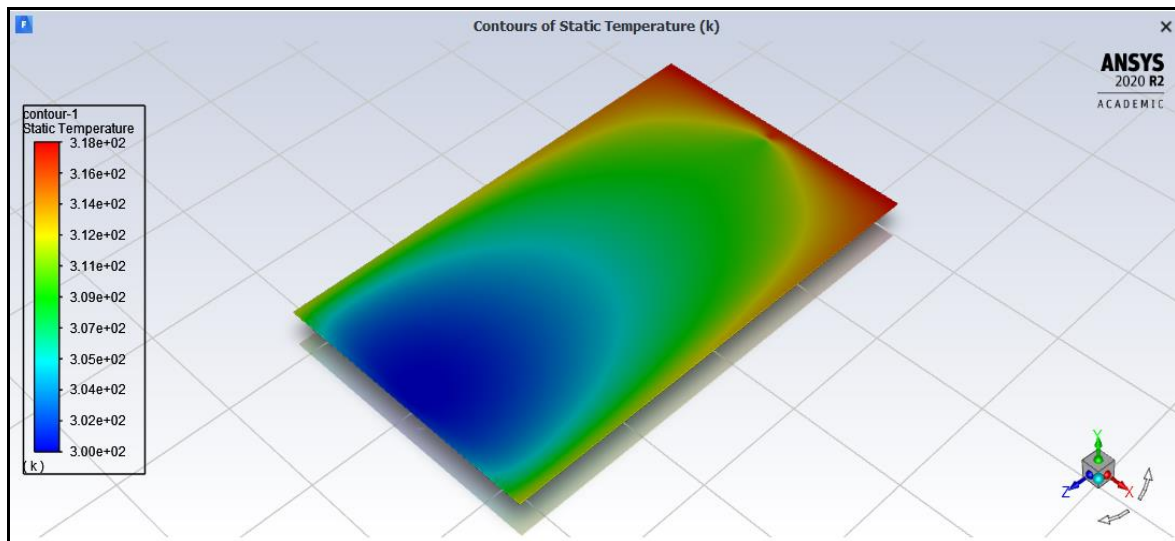


**Figure 7.4 ANSYS FLUENT Temperature Contour Plot for Graphite-water based nanofluid (blue: coolest and red: warmest).**

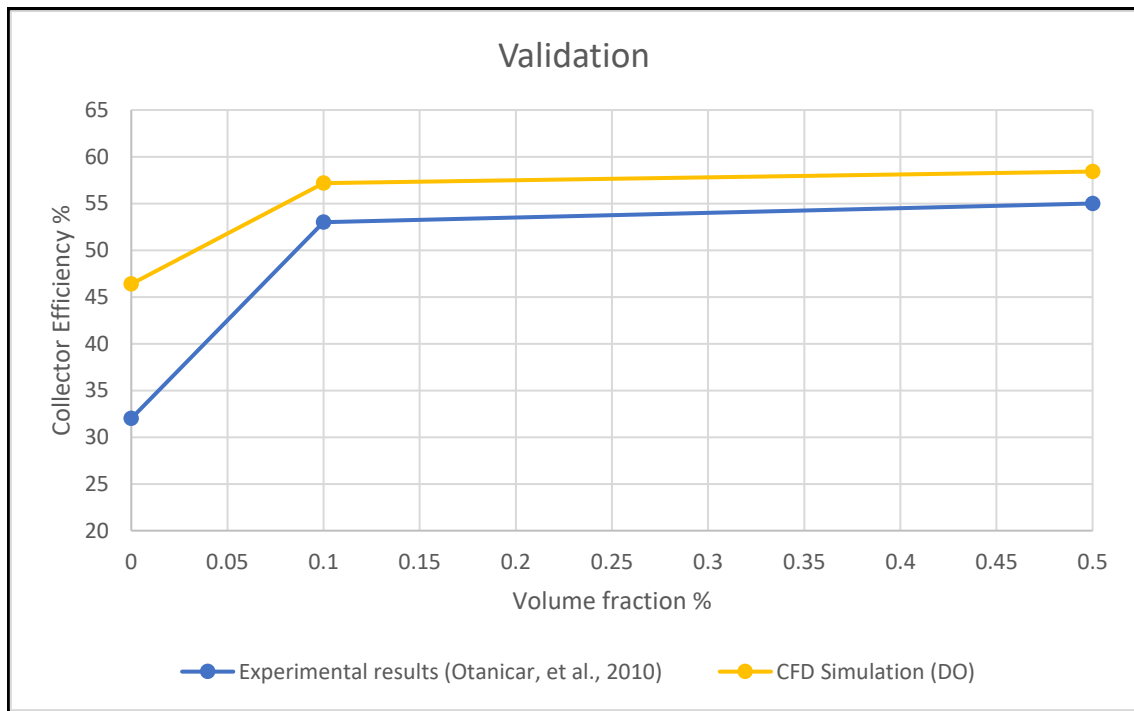


**Figure 7.5 Comparison of modelling and experimental results of graphite- water based nanofluid.**

## **7.5 Results and Discussion**

From the previous chapters 3-6, all the studies have covered the subject of natural convection, forced convection and radiation of nanofluids in various solar collector geometries. *However optical properties of nanofluids have not been included.* Hence, this chapter investigates the behaviour of heat transfer, with the *nanofluid optical properties taken into consideration*, along with the parametric analysis of nanofluids, volume fraction and mass flow rate of a direct absorption solar collector. Extensive temperature computations (coloured contour plots) are included for many different cases.

### **7.5-1 Parametric analysis of various working fluids (water and water based nanofluids)**

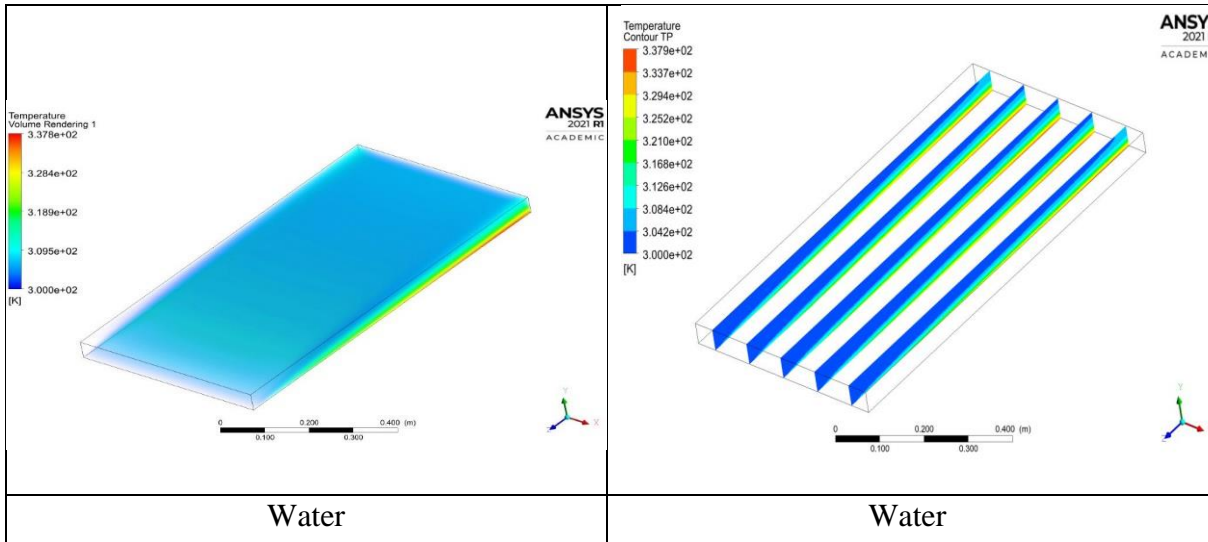
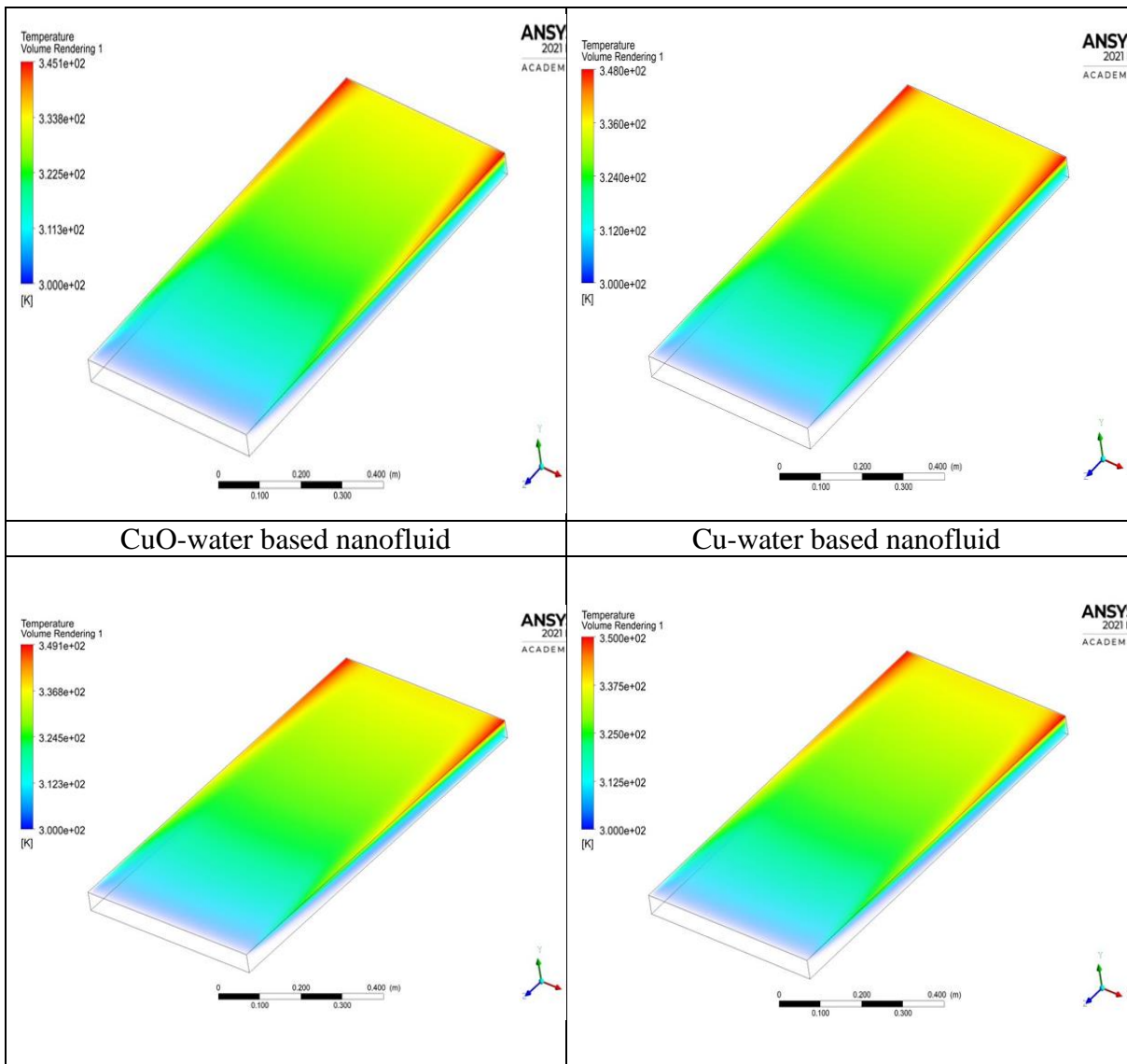


Figure 7.6 Temperature contour of water based solar collector.





Graphite-water based nanofluid	Silver-water based nanofluid
--------------------------------	------------------------------

**Figure 7.7 Temperature contour of 4 types of nanofluids at 0.04 percentage volume fraction**

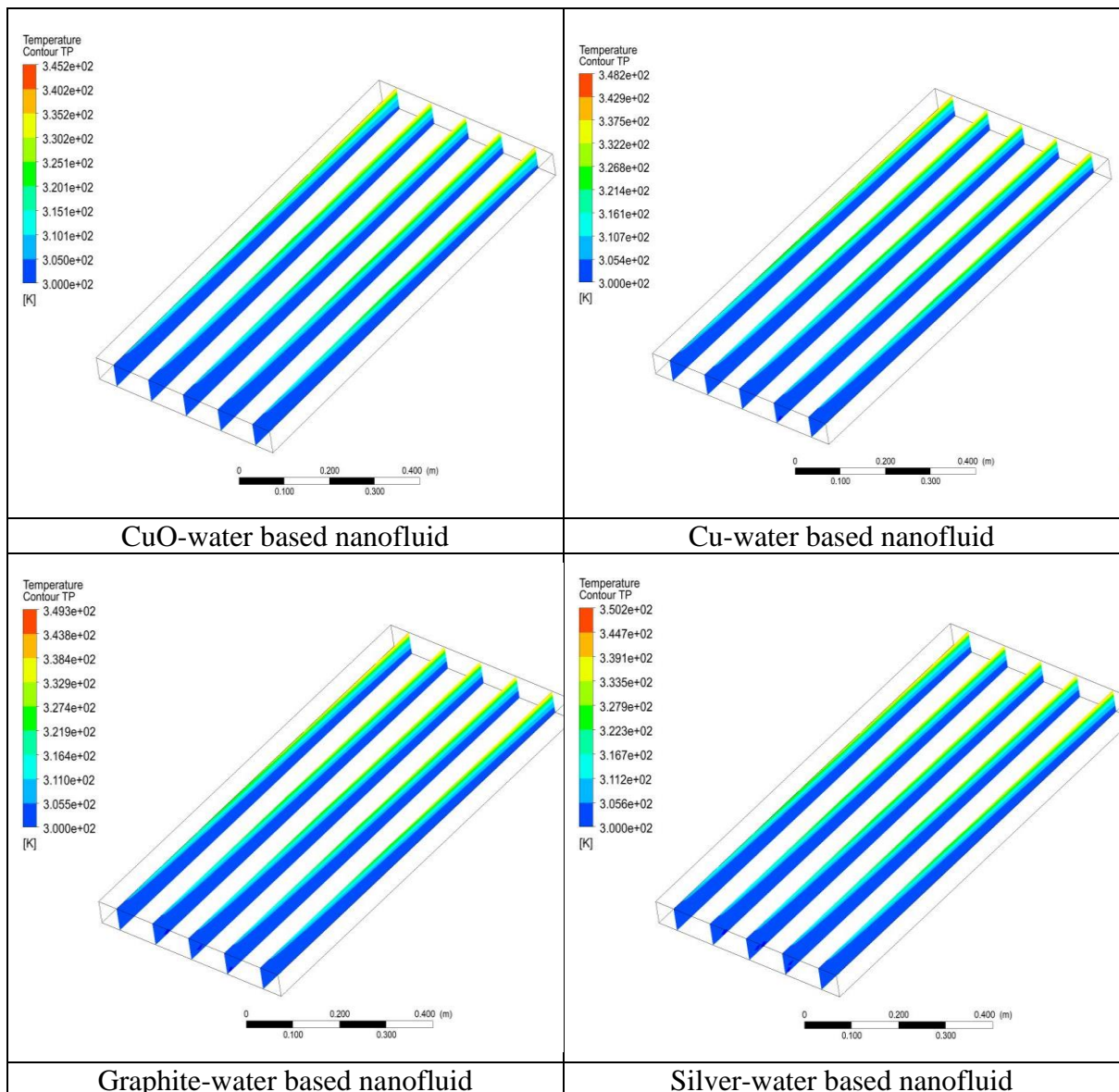


**Figure 7.8 Temperature contour of 3 types of nanofluids at 0.04 percentage volume fraction**

Figure 7.6-Figure 7.8 show temperature contours of various nanofluid types (Graphite, Silver, CuO and Cu water based nanofluid) with the same percentage volume fraction of 0.004 and the same mass flow rate of 0.01 kg/s. Figure 7.6 shows temperature contour of pure water in that begins to heat up from the copper absorber plate at the bottom of the collector, as water

has a very low absorption coefficient, which allows all the solar rays to pass through and heat up the copper plate. Most of the solar radiation heat is however transferred by convection.

Figure 7.7 and Figure 7.8 show temperature volume contour plots of 4 types of water based nanofluids, where all the nanofluids behave in a similar manner when heated from the top of the DASC; heat penetrates efficiently to the bottom of the collector. This is due to nanoparticles increasing the absorption coefficient of nanofluids, where these properties are collected from an experiment (Taylor, et al., 2011). Since the flow is considered as laminar flow, heat is transported via forced convection in the same way. The main difference between each nanofluid contour plot is the temperature magnitude. The CuO water-based nanofluid maximum temperature is the lowest of the 4 nanofluids. Then Cu water based nanofluid has a slightly higher temperature and this is due to a higher absorption coefficient and thermal conductivity. In the same way graphite and silver nanofluids can absorb solar radiation better than Cu and CuO due to higher absorption coefficients. However, to compare a non-metallic (graphite) nanofluid to metallic (silver) nanofluid can be difficult, since the absorption coefficient of both nanofluids are very high. (Otanicar, et al., 2010). It has been shown experimentally that adding even a small fraction of graphite nanoparticles to the fluid makes the clear fluid completely opaque to the naked eye and results in a rapid increase in thermal efficiency. Silver nanofluid thermal conductivity is much greater than thermal conductivity of graphite nanofluid and this is the principal reason for silver attaining the highest temperature. A further advantage of silver is the anti-bacterial characteristic which makes it ideal for sustainable and biocompatibility of future nanofluid-based solar absorbers, as elucidated in previous chapters (rectangular solar geometry).

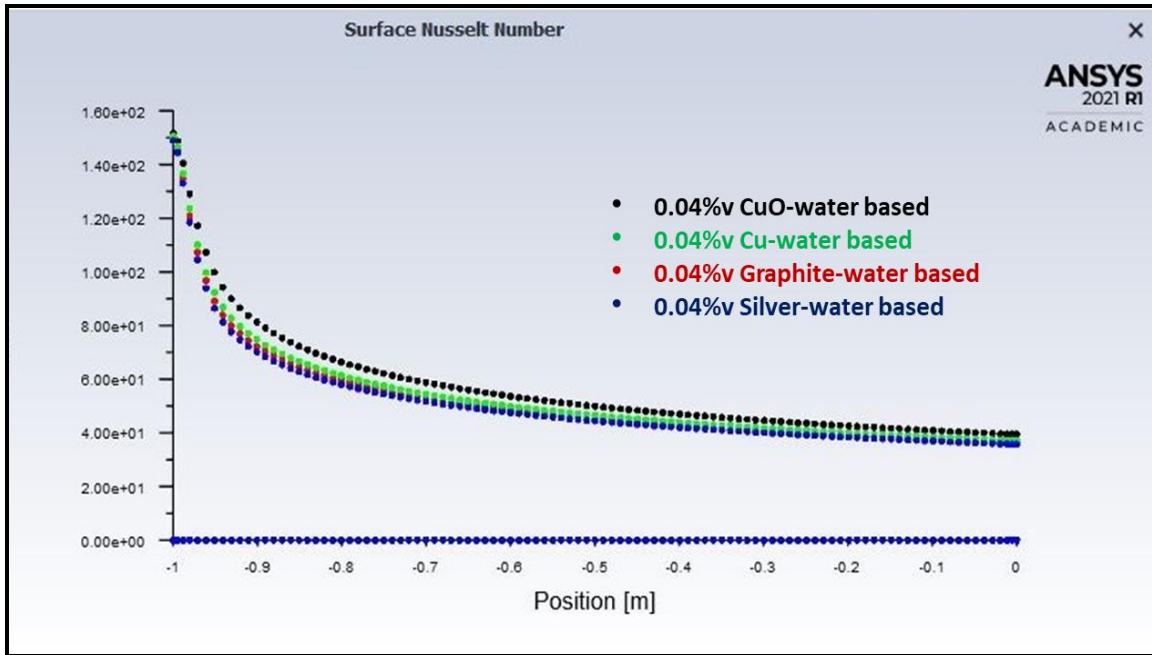


Figure 7.9 Local Surface Nusselt Number of various nanofluids with 0.004 percentage volume fraction

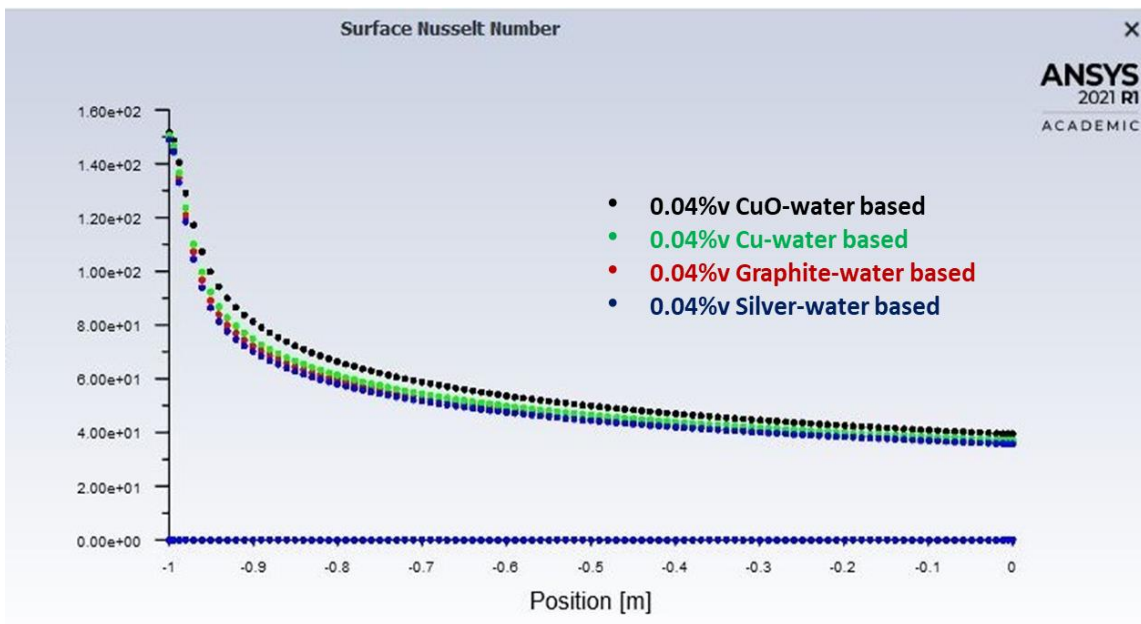
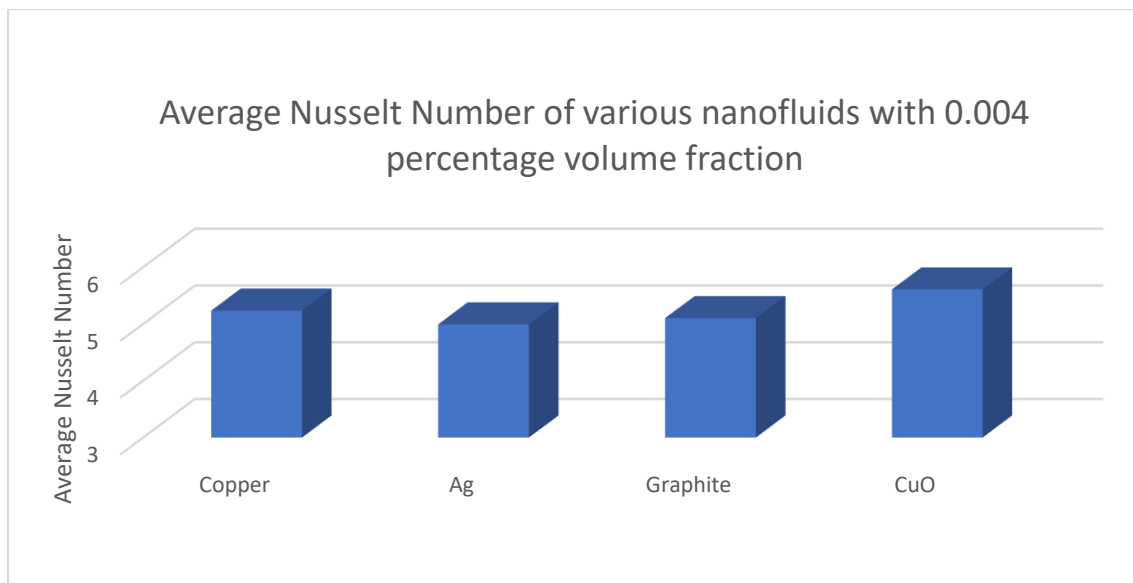


Figure 7.9 shows the local Nusselt number at the middle of the flat plate collector. As explained earlier, CuO has the lowest thermal conductivity which results in heat transfer mainly by convection. In other nanofluids which have a higher thermal conductivity like Cu, Graphite and Silver heat is more efficiently transferred by thermal conduction. When comparing the

local Nusselt number of graphite nanofluid and silver nanofluid, the silver nanofluid has a slightly lower Nusselt number even though thermal conductivity of silver is a lot higher than graphite. Since higher temperatures are generated in the silver nanofluid, there is a lower net transfer of heat to the surface i. e. a lower Nusselt number. Additionally, there is a limited surface area of the solar geometry which receives solar radiation and there is only so much heat that can be conducted at constant mass flow rate.



**Figure 7.10 shows the average Nusselt Number distributions for various nanofluids with 0.004 percentage volume fraction for the same mass flow rate of 0.01 kg/s. CuO and Cu nanofluid transfer heat more through convection which depends on mass flow rate (hydrodynamics). The average Nusselt number of silver (Ag) and graphite nanofluids are lower than for CuO and Cu nanofluids. Noting that Nusselt number is also a quantification of the ratio of convection heat transfer to conduction heat transfer, therefore these two nanofluids also absorb and transfer heat largely through conduction, which depends**

on fluid properties (thermal conductivity).

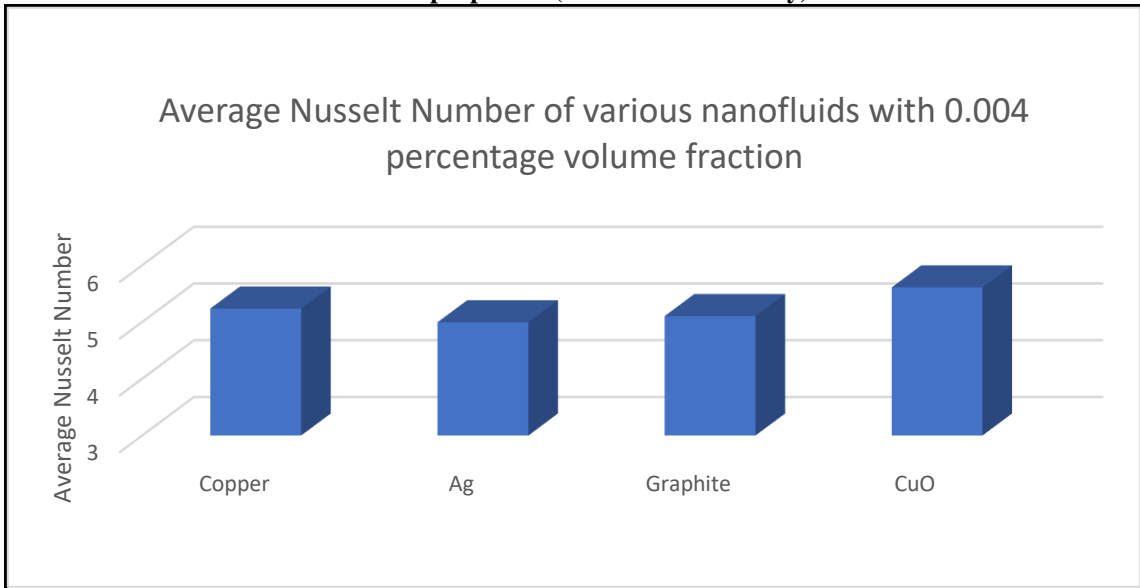


Figure 7.10

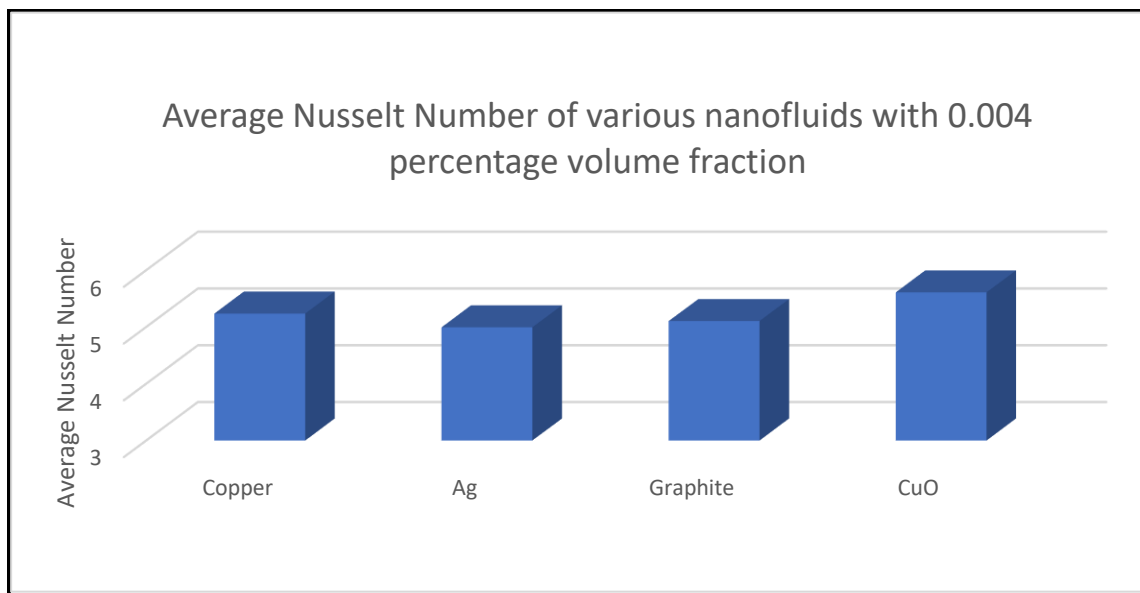
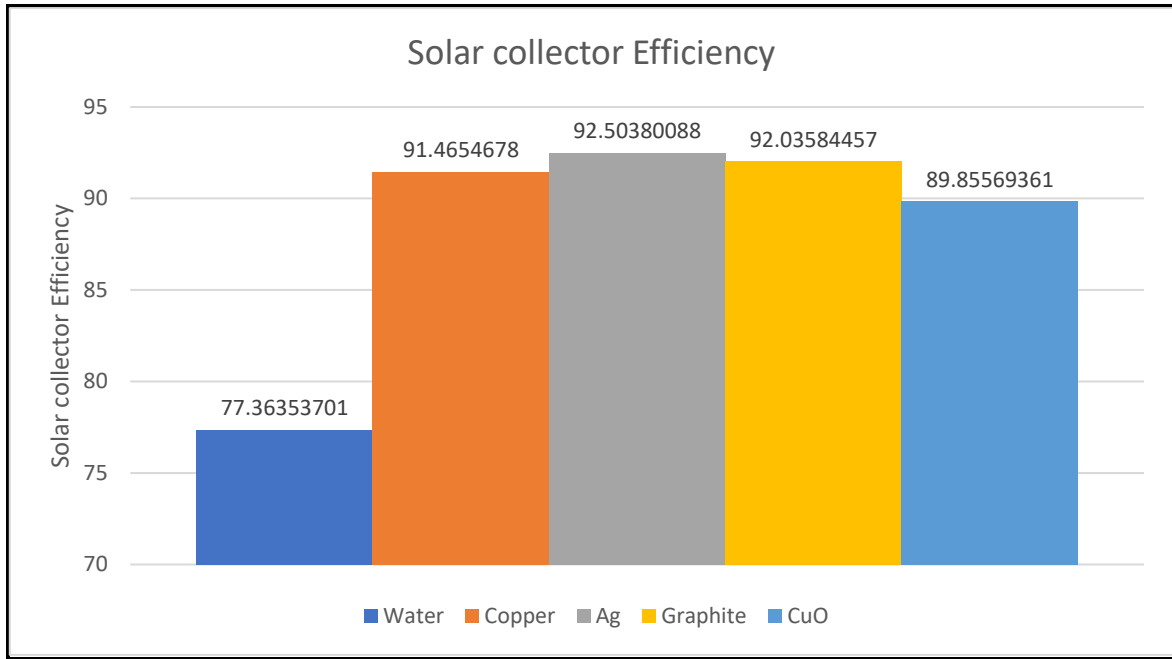


Figure 7.10 Average Nusselt Number of various nanofluids with 0.004 percentage volume fraction



**Figure 7.11 Solar collector efficiency with various nanofluids**

Figure

7.7-

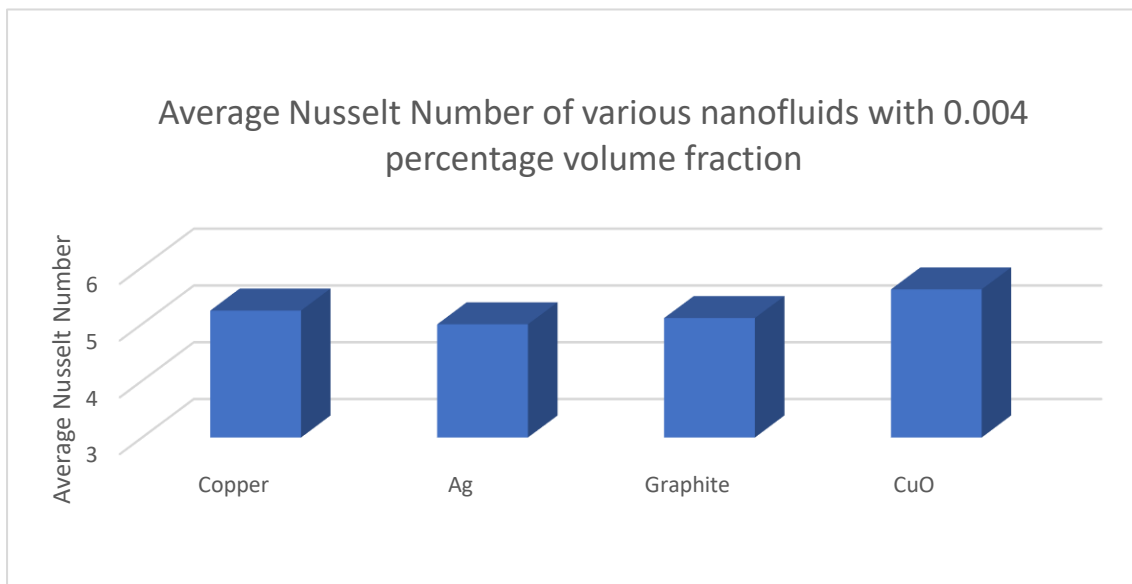


Figure 7.10 describe the heat transfer behaviour of working nanofluids inside solar collectors and elucidate whether they are more convection or conduction based. Figure 7.11 shows solar collector efficiency with various nanofluids using the following equation:

$$\eta = \frac{\dot{m}C_p(T_{outlet}-T_{inlet})}{G_T A} \quad (7.13)$$

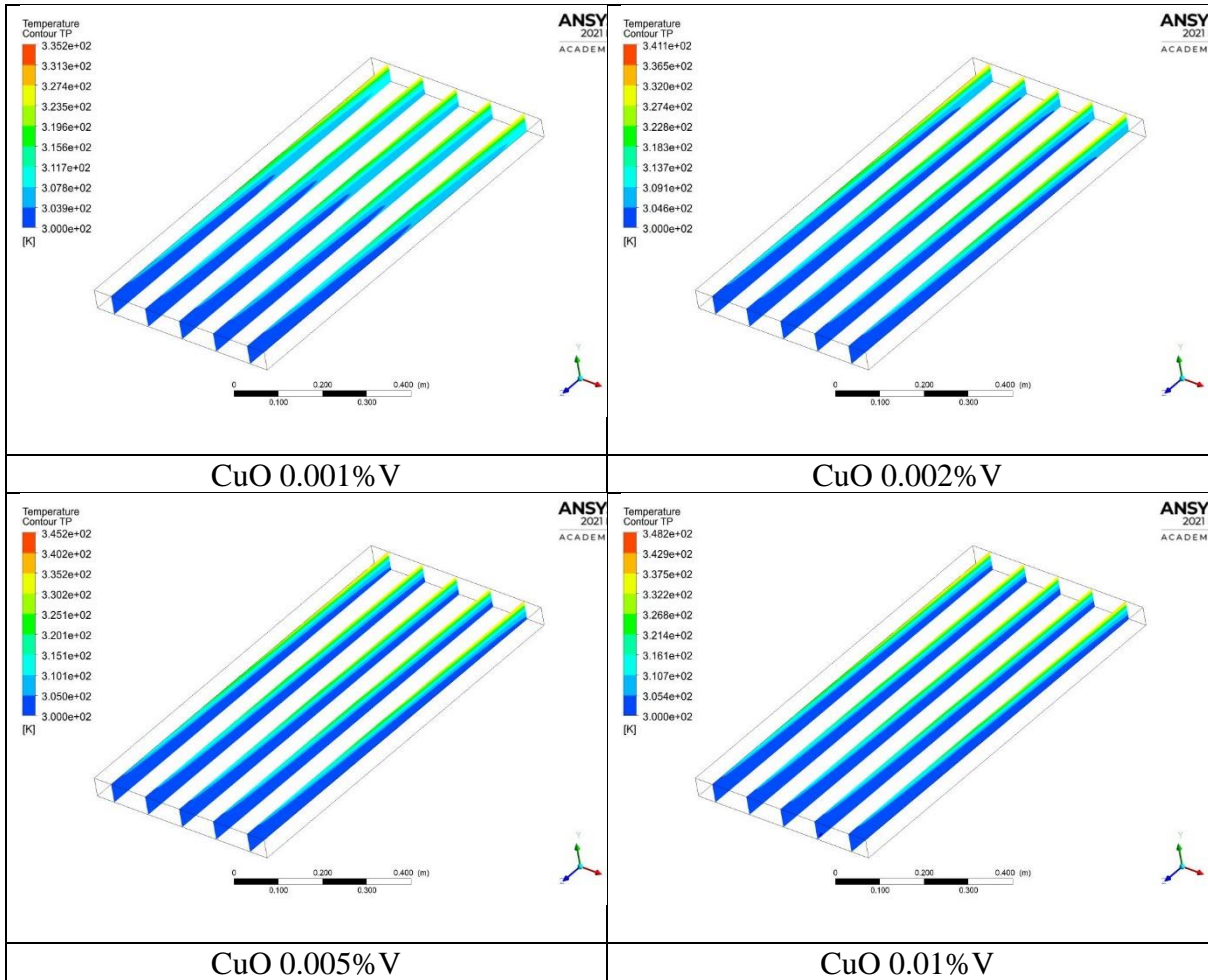
Here  $\dot{m}$  is the mass flow rate in kg/s,  $C_p$  is specific heat capacity of nanofluid,  $T_{inlet}$  is the average inlet temperature,  $T_{outlet}$  is the average outlet temperature of the collector,  $G_T$  is solar irradiance which set to be 1423 W/m<sup>2</sup> and  $A$  is the collector area (m<sup>2</sup>).

Figure 7.11 shows that at the same volume fraction of 0.004 and flow rate of 0.001 kg/s, silver (Ag) nanofluids give the highest thermal efficiency of 92.5 percent then followed by graphite (92 percent), Copper (91.5 percent) and Copper oxide nanofluid (90 percent). Clearly pure water is the least efficient fluid to use in this collector with a maximum thermal efficiency of 77.3 percent. The deployment of nanoparticles is therefore clearly verified with the results.

### **7.2.1 Parametric analysis of varies volume fractions of nanofluid (CuO water based nanofluid and Graphite water based nanofluid)**

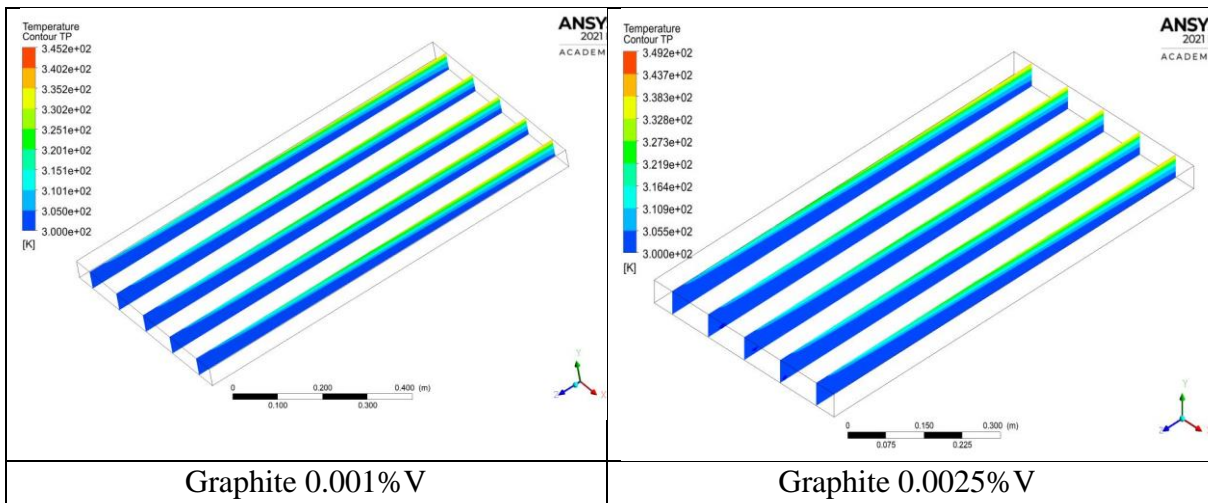
The previous parametric analysis of varies type of nanofluids suggested that the heat transfer inside collector also depend on fluids properties (thermal conductivity and extinction coefficient). As the experimental data range for extinction coefficients is only available for two type of nanofluid CuO and graphite nanofluid, therefore, only two nanofluids are investigated- CuO metallic nanofluid and non-metallic graphite nanofluid. In the simulations, volume fraction is varied whereas the mass flow rate is kept at constant of 0.01 kg/s.

Figure 7.12 shows the temperature contour plots of copper oxide nanofluid with an increase in particle volume fraction from 0.001 % V to 0.01% V.



**Figure 7.12 Temperature contour of CuO- water based nanofluids at various percentage volume fractions.**

Figure 7.13 shows temperature contour plots of graphite nanofluid with an increase in nanoparticle volume fraction from 0.001 % V to 0.01% V.





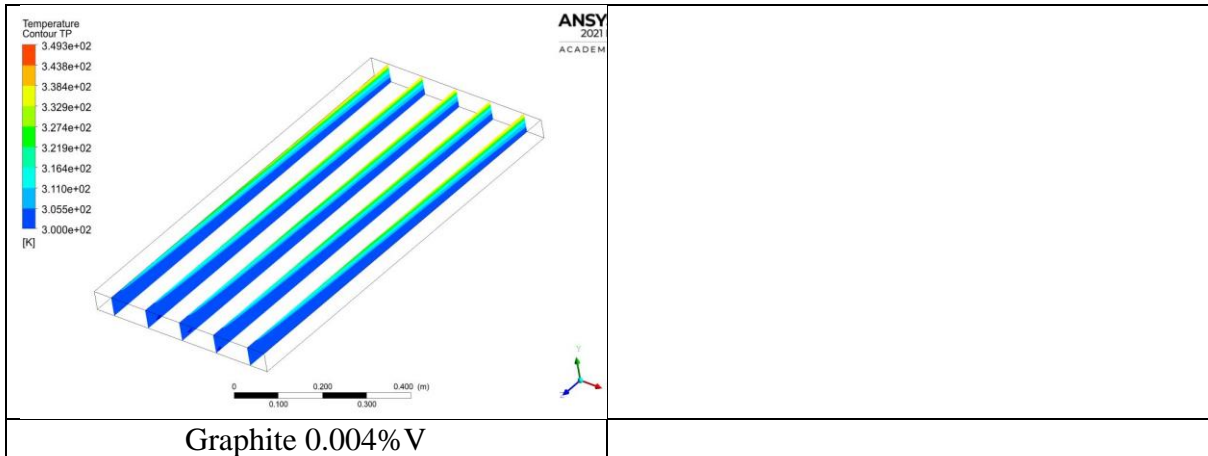


Figure 7.13 Temperature contour of Graphite - water based nanofluids at various percentage volume fractions.

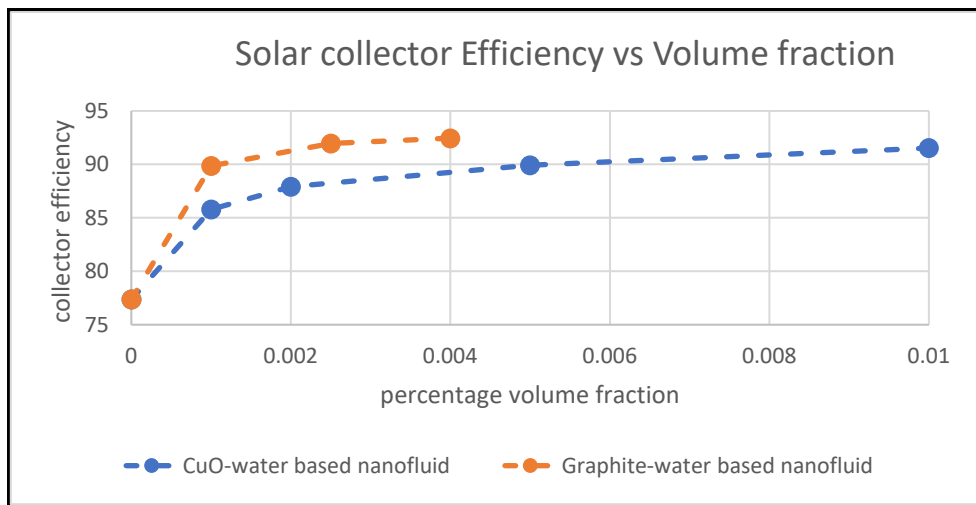


Figure 7.14 Solar collector Efficiency vs Volume fraction (CuO-water based nanofluid)

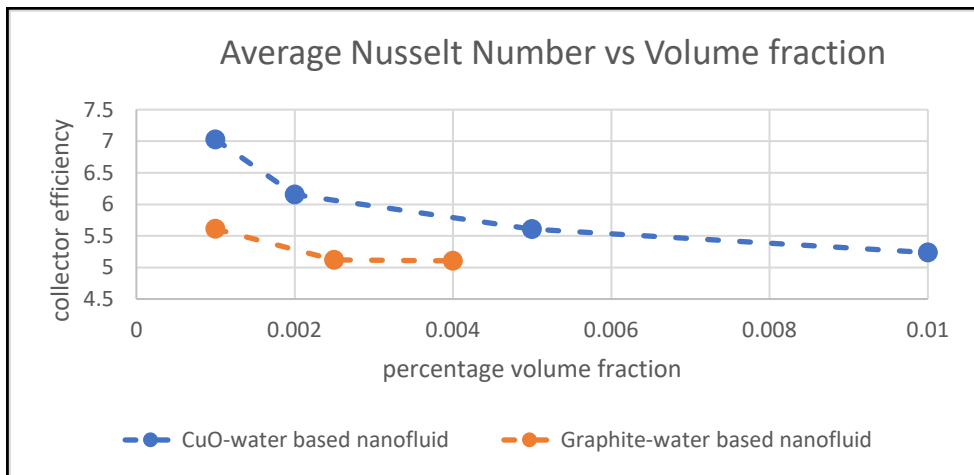


Figure 7.15 Average Nusselt Number vs Volume fraction (CuO-water based nanofluid)

## 7.2.2 Parametric analysis of varies mass flow rates of CuO water based nanofluid and Graphite water based nanofluid.

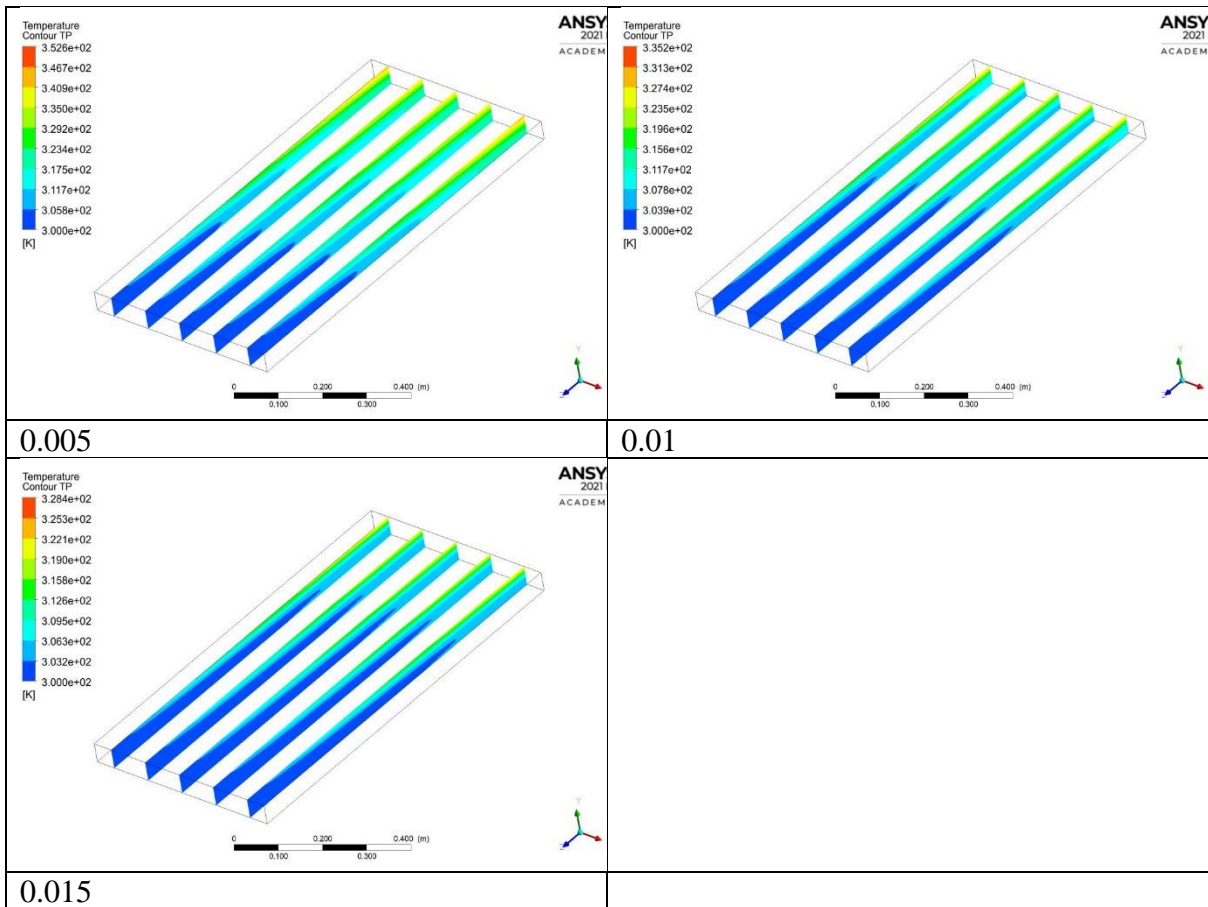
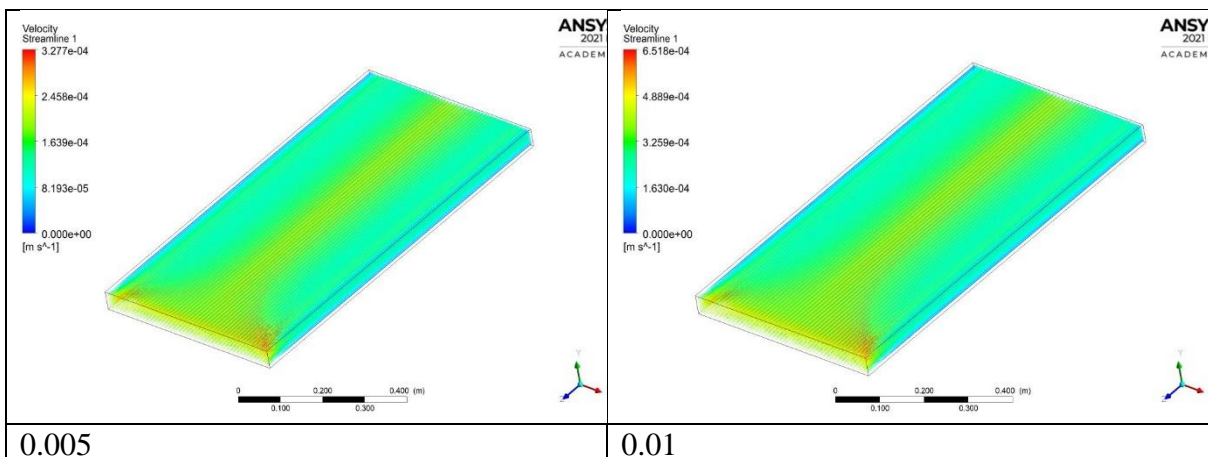


Figure 7.16 Temperature Contour of CuO-water based nanofluid (0.001 %V) with various mass flowrates.



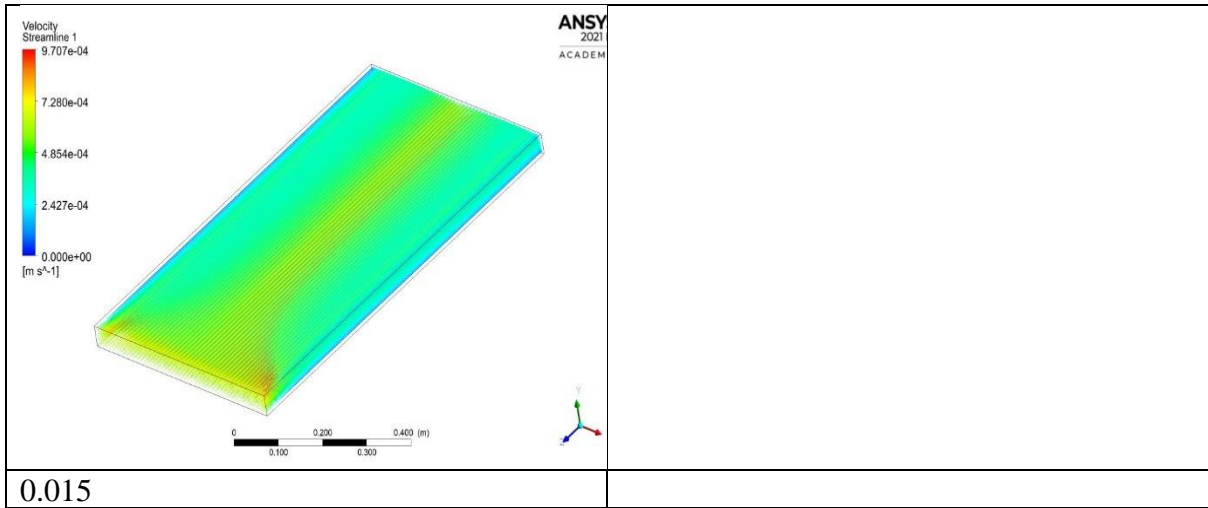


Figure 7.17 Velocity streamlines of CuO-water based nanofluid (0.001 %V) with various mass flowrates.

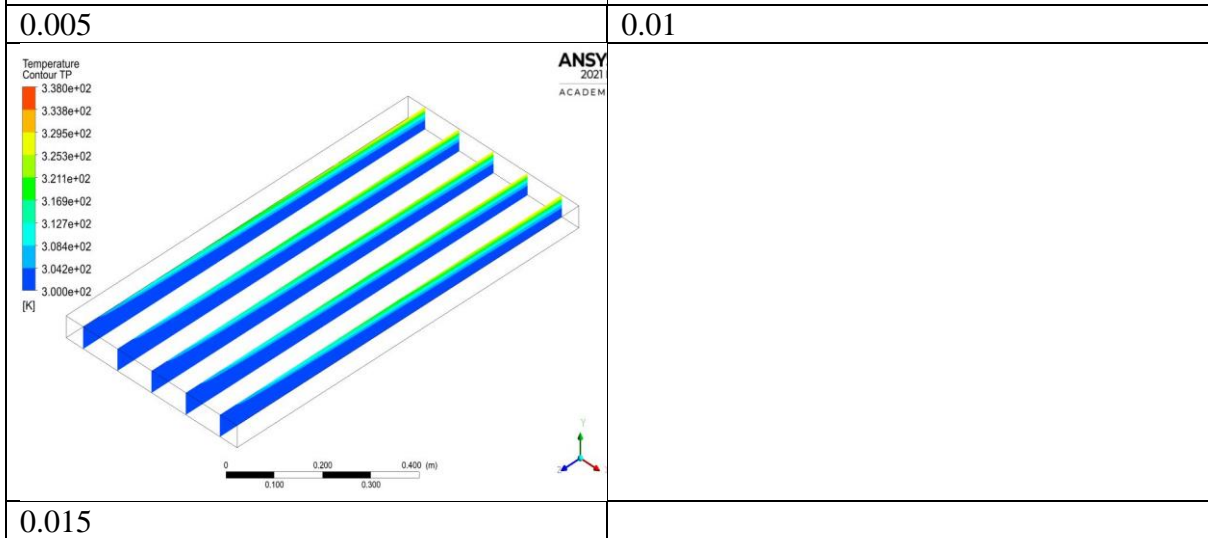
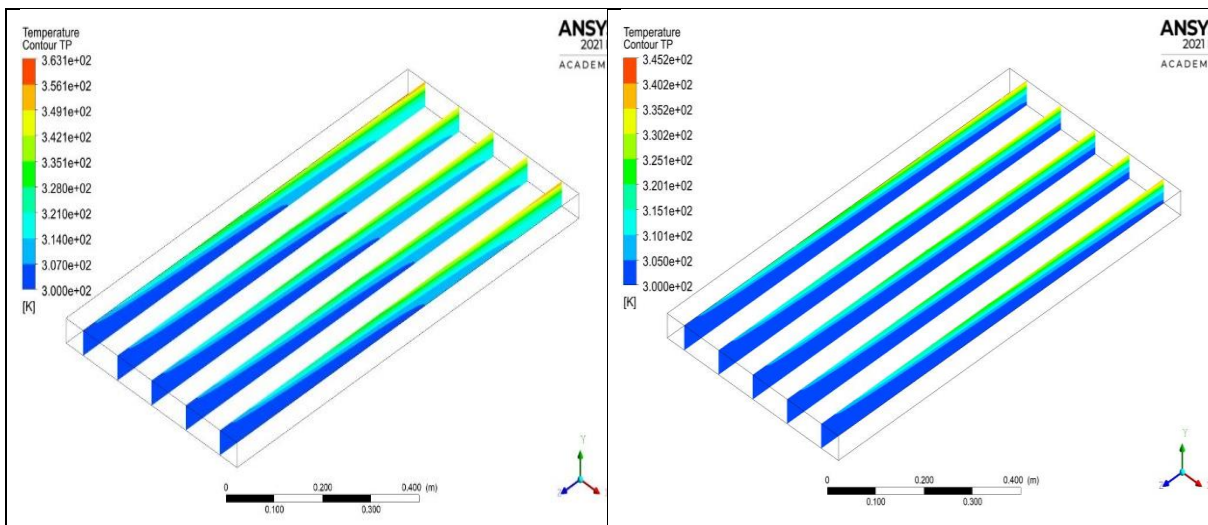


Figure 7.18 Temperature Contour of Graphite-water based nanofluid (0.001 %V) with various mass flowrates.

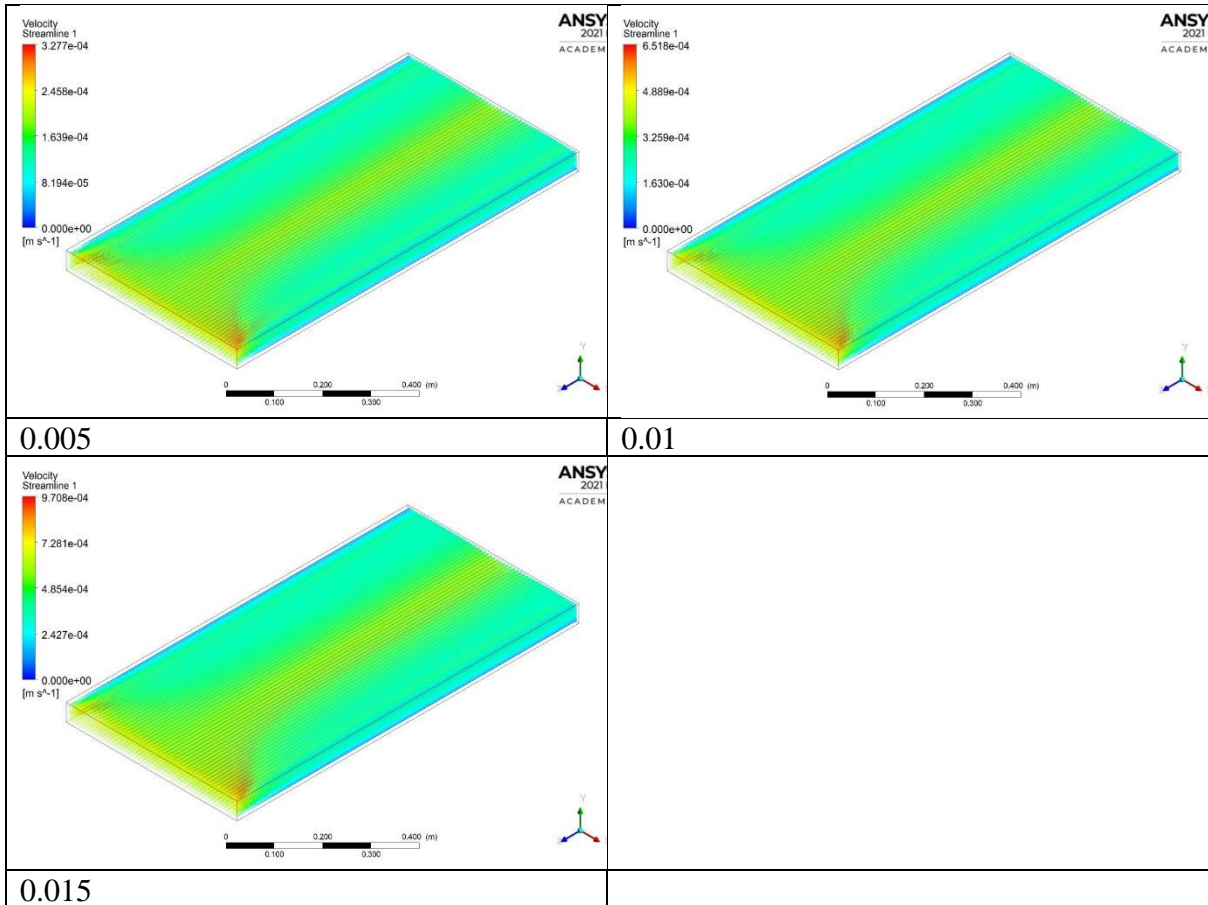
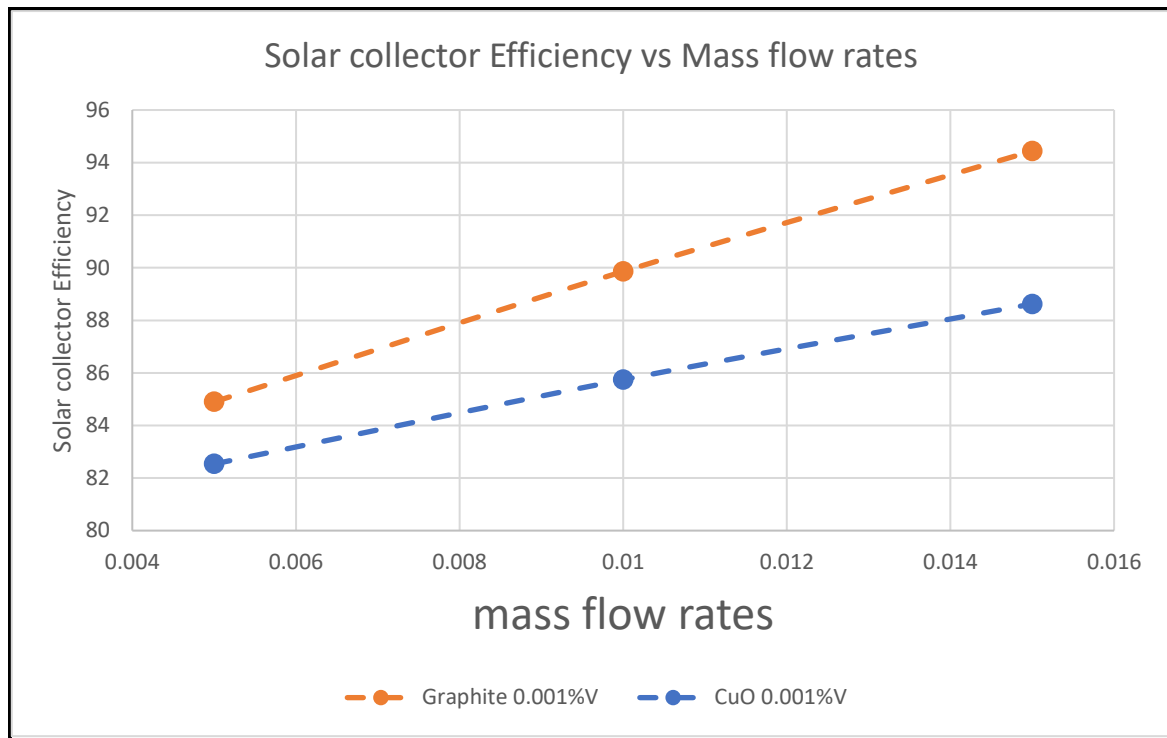


Figure 7.19 Velocity streamlines of Graphite-water based nanofluid (0.001 %V) with various mass flowrates.



**Figure 7.20 Solar collector Efficiency vs Mass flow rates**

Further results are shown in Figs. 7.14 to 7.20. Graphite nanofluid obtains a higher solar collector efficiency than silver nanofluid (Fig. 7.14) whereas copper oxide nanofluid achieves superior average Nusselt number (Fig. 7.15). An increase in mass flow rate progressively inhibits thermal diffusion in the solar collector with green zones contracting significantly and the proliferation of larger blue zones in the temperature contours (Fig. 7.16). With increasing mass flow rate the tower-like structure for flow streamlines is also expanded laterally and the higher velocity (red bands) are expanded near the base of the flat plate enclosure (Fig. 7.17). For graphite based nanofluid, the blue zones are much more pronounced in the temperature contour plots (Fig. 7.18) which indicates much lower temperatures are produced throughout the geometry compared with copper oxide nanofluid. However, Fig. 7.19 shows that larger velocities are computed especially near the base of the enclosure with graphite nanofluid and the central green/yellow core zone is also wider. Finally, in Fig. 7.20 a much higher solar

thermal efficiency is computed for graphite water nanofluid compared with copper oxide water nanofluid, at the same nanoparticle volume fraction of 0.001%.

## 7.6 Conclusions

3-dimensional ANSYS FLUENT finite volume simulations have been described for laminar, incompressible forced convection heat transfer in *a flat plate solar collector geometry with inlet and outlet features (for controlling flow rates)*. Three different metallic (copper, copper oxide, silver) and one non-metallic (Graphite) nanoparticles have been considered. The Tiwari-Das single-phase nanoscale model has been implemented to allow volume fraction variation and different nanoparticle material properties to be analyzed. To cater for variable optical properties of nanofluids, a more advanced radiative approximation model has also been deployed, namely the Chandrasekhar discrete ordinates method (DOM) which allows optical property variation for nanofluids. Extensive visualization of different geometric and nanoscale effects is included. The relative performance of the different metallic and non-metallic nanoparticles on thermal efficiency e. g. local Nusselt number at the enclosure (collector) boundaries has also been described. The main findings of the present study may be summarized as follows:

(i) At the same volume fraction of 0.004 and flow rate of 0.001 kg/s, silver (Ag) nanofluids give the highest thermal efficiency of 92.5 percent then followed by graphite (92 percent), Copper (91.5 percent) and Copper oxide nanofluid (90 percent).

(ii) Pure water is the least efficient fluid to use in flat plate solar collectors with a maximum thermal efficiency of 77.3 percent. The thermal enhancement properties of nanoparticles are

clearly justified based on the ANSYS simulations which also corroborate well with earlier experimental investigations.

(iii) Graphite nanofluid obtains a higher solar collector efficiency than silver nanofluid whereas copper oxide nanofluid achieves superior average Nusselt number.

(iv) An increase in mass flow rate progressively inhibits thermal diffusion in the solar collector with green zones contracting significantly and the proliferation of larger blue zones in the temperature contours for graphite nanofluids.

(v) For graphite based nanofluid, the blue cooler zones are much more pronounced in the temperature contour plots implying that lower temperatures are produced throughout the geometry compared with copper oxide nanofluid.

(vi) Larger velocities are computed especially near the base of the enclosure with graphite nanofluid and the central green/yellow core zone is also wider compared with copper oxide nanofluid.

(vii) A higher solar thermal efficiency is computed for graphite water nanofluid compared with copper oxide water nanofluid, at the same nanoparticle volume fraction of 0.001%.

The present study has ignored magnetic properties of nanoparticles. These also offer another mechanism of functionality and controlling heat transfer rates in DASCs. Furthermore, Brownian motion and thermophoresis effects have also been neglected which can be addressed with Buongiorno's model. Both aspects are considered in chapter 8.

## **PUBLICATION NOTE**

A long version of this chapter has been submitted to *Applied Nanoscience* (Springer, Impact factor = 3.5) and a shorter version is to be presented at the 8<sup>th</sup> BUU Int. Interdisciplinary Research Conference, Thailand, September 2021.

## **Chapter 8 Modelling a magnetic nanofluid-based hybrid magneto-biomimetic deformable nano-collector with Buongiorno's two-component nanoscale model**

### **Abstract**

Thus far in the PhD, I have used the Tiwari-Das nanoscale model, ANSYS FLUENT finite volume method and rigid boundaries. Additionally, *non-magnetic metallic nanoparticles* only have been considered. In this chapter we explore a different nanoscale formulation, namely Buongiorno's nanofluid model which features Brownian motion and thermophoresis. Most designs of solar collectors involve fixed (rigid) geometries which may be cylindrical, parabolic, tubular or flat-plate types. Modern developments in biomimetics have identified that deformable conduit structures may be beneficial for sustainable energy systems. Motivated by these aspects, in this chapter I will describe a mathematical model and computational solution for a biomimetic peristaltic solar magnetohydrodynamic nanofluid-based solar collector. The working fluid is a magnetized nanofluid which comprises a base fluid containing suspended magnetic nanoparticles. Heat is transferred via distensibility of the conduit in the form of peristaltic thermal waves and buoyancy effects. An externally applied magnetic field achieves the necessary circuit design for generating Lorentzian magnetic body force in the fluid. A variable viscosity modification is employed using Reynolds exponential model. To simulate solar loading conditions the Rosseland thermal radiative flux model is also deployed which has been described in previous chapters. An asymmetric porous channel is investigated with multiple amplitudes and phases for the wall wavy motion. The channel also contains a



homogenous, isotropic porous medium which is simulated with a modified Darcy model. Heat generation/absorption effects are also examined. The electrically conducting nature of the nanofluid invokes magnetohydrodynamic (MHD) effects. The moving boundary value problem is normalized and linearized using the lubrication approach. Analytical solutions are derived for axial velocity, temperature and nanoparticle volume fraction. Validation is conducted with Maple numerical quadrature. This symbolic software is more appropriate than ANSYS FLUENT since the formulation explored herein is novel and not available in ANSYS materials physics. Extensive visualization of important transport characteristics including “trapping phenomena” are presented. The observations demonstrate promising features of the solar magnetohydrodynamic peristaltic nanofluid hybrid collector which may also be exploited in spacecraft applications.

## 8.1 Mathematical formulation

In this simulation, we consider two-dimensional flow of magnetite nanofluids driven by peristaltic pumping through an asymmetric channel (DASC geometry) containing a homogenous, isotropic porous wafer material, in the presence of an externally applied transverse magnetic field. The channel walls are propagating with constant wave velocity ( $c$ ) as sinusoidal wave trains. Let  $Y = H_1$ , and  $Y = H_2$  be respectively the left and right wall boundaries of the asymmetric channel of width  $(d_1 + d_2)$ . The temperature ( $T$ ) and nanoparticle volume fraction ( $C$ ) are prescribed values of  $T_0, C_0$  and  $T_1, C_1$  at  $Y = H_1$  and  $Y = H_2$  respectively. The geometry of the biomimetic solar magnetohydrodynamic nanofluid pump is depicted in **Fig.1** and mathematically expressed as:

$$H_1(X, t) = d_1 + a_1 \cos\left(\frac{2\pi}{\lambda}(X - ct)\right), \quad (8.1a)$$

$$H_2(X, t) = -d_2 - a_2 \cos\left(\frac{2\pi}{\lambda}(X - ct) + \phi\right). \quad (8.1b)$$

in which  $a_1, a_2, \lambda, t$  and  $\phi$  are the amplitudes of the left and right waves, wavelength, dimensional time and phase difference, further  $a_1, a_2, d_1$  and  $d_2$  satisfy the inlet of the condition:

$$a_1^2 + a_2^2 + 2a_1^2 a_2^2 \cos \phi \leq (d_1 + d_2)^2. \quad (8.2)$$

Buongiorno's [13] model is deployed for the nanofluid. This emphasizes thermophoretic forces and Brownian motion dynamics as the key contributors to thermal conductivity enhancement. This model which has the advantage of being very easily incorporated into the framework of viscous fluid dynamics. It also allows the inclusion of a species diffusion (concentration) boundary layer equation which is not possible with other models such as the (Tiwari & Das, 2007) It is a two-component laminar four-equation non-homogeneous equilibrium model for mass, momentum, and heat transport in nanofluids highlights the dominance of Brownian diffusion and thermophoresis over other nanoscale mechanisms e.g. diffusion-phoresis, Magnus effect, fluid drainage, micro-convection and ballistic collisions. The model further assumes that energy transfer via nano-particle dispersion is negligible and that Dufour (diffuso-thermal) effects may be negated. Implementing the Buongiorno formulation (Buongiorno, 2006) the resulting governing unsteady equations for conservation of mass, momenta (incorporating external magnetic field and Darcy porous matrix resistance), energy and

nanoparticle volume fraction (nano-species concentration) in an  $(X, Y)$  coordinate system emerge as (Nadeem & Akbar, 2009):

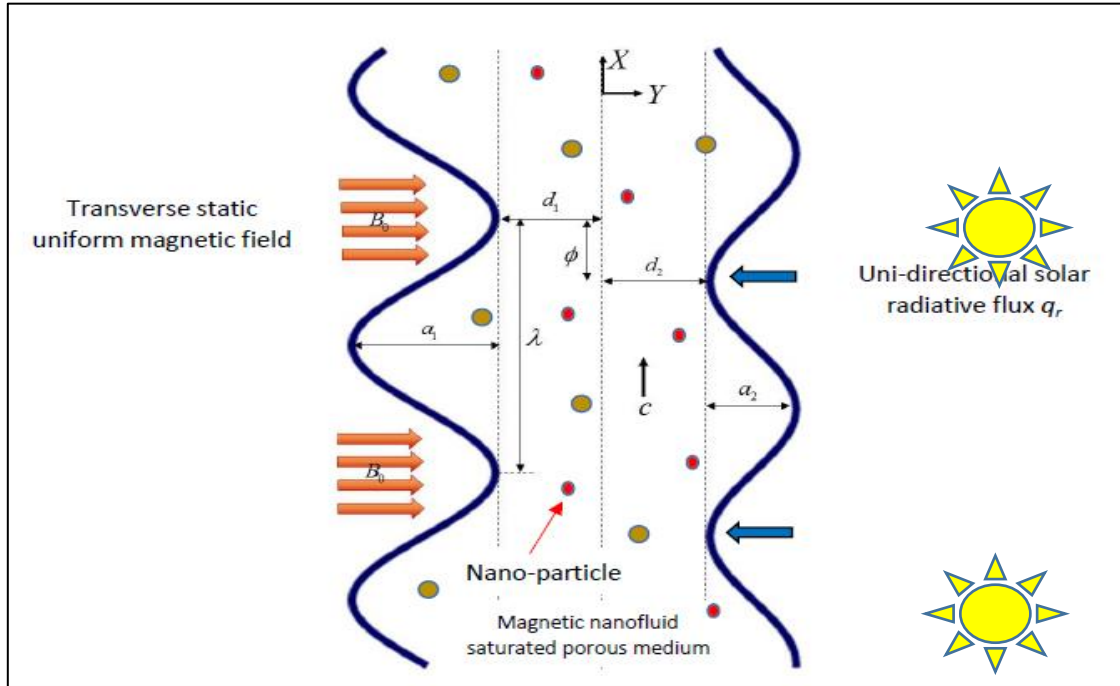


Figure 8.1 Schematic diagram of the solar magnetic nanofluid peristaltic pump collector (asymmetric channel).

$$\frac{\partial U}{\partial X} + \frac{\partial V}{\partial Y} = 0, \quad (8.3)$$

$$\rho_f \left( \frac{\partial U}{\partial t} + U \frac{\partial U}{\partial X} + V \frac{\partial U}{\partial Y} \right) = -\frac{\partial P}{\partial X} + 2 \frac{\partial}{\partial X} \left[ \mu(T) \frac{\partial U}{\partial X} \right] + \frac{\partial}{\partial Y} \left[ \mu(T) \left( \frac{\partial V}{\partial X} + \frac{\partial U}{\partial Y} \right) \right] - \frac{\mu(T)}{k_0} U - \sigma' B_0^2 U + (1 - C_0) \rho_0 g \beta_i (T - T_0) - (\rho_p - \rho_0) g (C - C_0), \quad (8.4)$$

$$\rho_f \left( \frac{\partial V}{\partial t} + U \frac{\partial V}{\partial X} + V \frac{\partial V}{\partial Y} \right) = -\frac{\partial P}{\partial Y} + 2 \frac{\partial}{\partial Y} \left[ \mu(T) \frac{\partial V}{\partial Y} \right] + \frac{\partial}{\partial X} \left[ \mu(T) \left( \frac{\partial V}{\partial X} + \frac{\partial U}{\partial Y} \right) \right] - \frac{\mu(T)}{k_0} U, \quad (8.5)$$

$$(\rho C')_f \left( \frac{\partial T}{\partial t} + U \frac{\partial T}{\partial X} + V \frac{\partial T}{\partial Y} \right) = k_{ef} \left[ \frac{\partial^2 T}{\partial X^2} + \frac{\partial^2 T}{\partial Y^2} \right] + (\rho C')_p \left[ D_B \left( \frac{\partial C}{\partial X} \frac{\partial T}{\partial X} + \frac{\partial C}{\partial Y} \frac{\partial T}{\partial Y} \right) \right] + \frac{D_T}{T_0} \left[ \left( \frac{\partial T}{\partial X} \right)^2 + \left( \frac{\partial T}{\partial Y} \right)^2 \right] + Q_0 - \frac{\partial q_r}{\partial Y}, \quad (8.6)$$

$$\left( \frac{\partial C}{\partial t} + U \frac{\partial C}{\partial X} + V \frac{\partial C}{\partial Y} \right) = D_B \left[ \frac{\partial^2 C}{\partial X^2} + \frac{\partial^2 C}{\partial Y^2} \right] + \frac{D_T}{T_0} \left[ \frac{\partial^2 T}{\partial X^2} + \frac{\partial^2 T}{\partial Y^2} \right], \quad (8.7)$$

where,  $U$ ,  $V$  are the velocity components in  $X$ ,  $Y$  directions,  $\rho_f$  is fluid density,  $P$  is pressure,  $\mu(T)$  is temperature dependent viscosity,  $k_0$  is the permeability parameter,  $\sigma'$  is electrical conductivity,  $B_0$  is transverse magnetic field,  $g$  is acceleration due to gravity,  $\beta_t$  is volumetric thermal expansion coefficient of the fluid,  $\beta_c$  is volumetric solutal expansion coefficient of the fluid,  $\rho_0$  is the nanofluid density at the reference temperature ( $T_0$ ),  $\rho_p$  is nanoparticle mass density,  $(\rho C')_f$  is heat capacity of fluid,  $k_{ef}$  is thermal conductivity,  $(\rho C')_p$  is effective heat capacity of nanoparticle,  $D_B$  is Brownian diffusion coefficient,  $D_T$  is thermophoretic diffusion coefficient,  $Q_0$  is the constant heat addition/absorption. We further note that in the solar MHD nanofluid pump circuit, the direction of the current density  $J$  determines whether the system behaves as a pump or as a generator. When electric current passes through an electrically neutral conducting medium in the presence of a magnetic field, a vector body force per unit volume  $F$  ( $N/m^3$ ) affects the medium.  $F$  is referred to as Lorentz force and is given by  $-\sigma B_o^2 u$  i.e. the fifth term on the right-hand side of the X-momentum equation (4). We consider the case where the current density accelerates the flow i. e. works as a *solar collector pump* (the opposite case of a generator is produced when the current density is reversed and as a result so is the Lorentz body force). We neglect magnetic field leakage and assume that the magnetic field is uniform during operation. Since the magnetic Reynolds number of the flow is taken to be very small, the induced magnetic field is negligible, and it is further assumed that no external electric field is applied. Therefore, the electric field due to polarization of charges is negligible so that no energy is added or extracted from the fluid by electrical means. Ohmic (Joule) heating is neglected as are Soret and Dufour cross-diffusion

effects. The radiative heat flux ( $q_r$ ) is given by using Rosseland's approximation. This approximation is valid for optically-thick fluids which can absorb or emit radiation at their boundaries [1].

$$q_r = -\frac{4\sigma^*}{3k^*} \frac{\partial T^4}{\partial Y}. \quad (8.8)$$

Here  $\sigma^*$  and  $k^*$  are the Stefan-Boltzmann constant and the mean absorption coefficient, respectively. We assume that the temperature difference within the flow is adequately small.

The term  $T^4$  is expanded as a Taylor series about a free stream temperature  $T_0$  and ignoring higher order terms in the first order in  $(T - T_0)$ , we get:

$$q_r = -\frac{16\sigma^* T_0^3}{3k^*} \frac{\partial T}{\partial Y}. \quad (8.9)$$

The transformations from the fixed frame of reference ( $X, Y$ ) to the wave frame of reference ( $\bar{x}, \bar{y}$ ) are given by:

$$\bar{x} = X - c\bar{t}, \bar{y} = Y, \bar{u} = U - c, \bar{v} = V \text{ and } p(\bar{x}) = P(X, \bar{t}). \quad (8.10)$$

After utilizing the transformations (8.10), equations (8.1a, b) - (8.7) retract to the following form:

$$\frac{\partial \bar{u}}{\partial \bar{x}} + \frac{\partial \bar{v}}{\partial \bar{y}} = 0, \quad (8.11)$$

$$\rho_f \left[ (\bar{u} + c) \frac{\partial \bar{u}}{\partial \bar{x}} + \bar{v} \frac{\partial \bar{u}}{\partial \bar{y}} \right] = -\frac{\partial \bar{p}}{\partial \bar{x}} + 2 \frac{\partial}{\partial \bar{x}} \left[ \mu(T) \frac{\partial \bar{u}}{\partial \bar{x}} \right] + \frac{\partial}{\partial \bar{y}} \left[ \mu(T) \left( \frac{\partial \bar{v}}{\partial \bar{x}} + \frac{\partial \bar{u}}{\partial \bar{y}} \right) \right] - \frac{\mu(T)}{k_0} \bar{u} - \sigma' B_0^2 \bar{u} + (1 - C_0) \rho_0 g \beta_t (T - T_0) - (\rho_p - \rho_0) g (C - C_0), \quad (8.12)$$

$$\rho_f \left[ (\bar{u} + c) \frac{\partial \bar{v}}{\partial \bar{x}} + \bar{v} \frac{\partial \bar{v}}{\partial \bar{y}} \right] = -\frac{\partial \bar{p}}{\partial \bar{y}} + 2 \frac{\partial}{\partial \bar{y}} \left[ \mu(T) \frac{\partial \bar{v}}{\partial \bar{y}} \right] + \frac{\partial}{\partial \bar{x}} \left[ \mu(T) \left( \frac{\partial \bar{v}}{\partial \bar{x}} + \frac{\partial \bar{u}}{\partial \bar{y}} \right) \right] - \frac{\mu(T)}{k_0} \bar{v}, \quad (8.13)$$

$$\begin{aligned}
(\rho C')_f \left[ (\bar{u} + c) \frac{\partial T}{\partial \bar{x}} + v \frac{\partial T}{\partial \bar{y}} \right] &= k_{ef} \left[ \frac{\partial^2 T}{\partial \bar{x}^2} + \frac{\partial^2 T}{\partial \bar{y}^2} \right] + (\rho C')_p \left[ D_B \left( \frac{\partial C}{\partial \bar{x}} \frac{\partial T}{\partial \bar{x}} + \frac{\partial C}{\partial \bar{y}} \frac{\partial T}{\partial \bar{y}} \right) \right] \\
&+ \frac{D_T}{T_0} \left[ \left( \frac{\partial T}{\partial \bar{x}} \right)^2 + \left( \frac{\partial T}{\partial \bar{y}} \right)^2 \right] + Q_0 - \frac{\partial q_r}{\partial \bar{y}}, \tag{8.14}
\end{aligned}$$

$$\left[ (\bar{u} + c) \frac{\partial C}{\partial \bar{x}} + v \frac{\partial C}{\partial \bar{y}} \right] = D_B \left[ \frac{\partial^2 C}{\partial \bar{x}^2} + \frac{\partial^2 C}{\partial \bar{y}^2} \right] + \frac{D_T}{T_0} \left[ \frac{\partial^2 T}{\partial \bar{x}^2} + \frac{\partial^2 T}{\partial \bar{y}^2} \right]. \tag{8.15}$$

We now introduce the following dimensionless variables:

$$\begin{aligned}
x &= \frac{\bar{x}}{\lambda}, y = \frac{\bar{y}}{d_1}, u = \frac{\bar{u}}{c}, v = \frac{\lambda \bar{v}}{d_1 c}, p = \frac{d_1^2 p}{\mu_0 c \lambda}, t = \frac{c \bar{t}}{\lambda}, h_1(x) = \frac{H_1(\bar{x})}{d_1}, h_2(x) = \frac{H_2(\bar{x})}{d_1}, a = \frac{a_1}{d_1}, b = \frac{a_2}{d_1}, \\
d &= \frac{d_2}{d_1}, M^2 = \frac{\sigma' B_0^2 d_1^2}{\mu_0}, \theta = \frac{T - T_0}{T_1 - T_0}, \sigma = \frac{C - C_0}{C_1 - C_0}, \mu(\theta) = \frac{\mu(T)}{\mu_0}, R = \frac{\rho_f c d_1}{\mu_0}, K = \frac{k_0}{d_1^2}, \\
Gr &= \frac{(1 - C_0) \rho_0^2 g \beta_t d_1^3 (T_1 - T_0)}{\mu_0^2}, Br = -\frac{\rho_0 (\rho_p - \rho_0) g d_1^3 (C_1 - C_0)}{\mu_0^2}, Pr = \frac{C_f' \mu_0}{k_{ef}}, Rn = \frac{16 \sigma^* T_0^3}{3k^* \mu_0 C_f'}, \\
\beta &= \frac{d_1^2 Q_0}{(T_1 - T_0) \mu_0 C_f'}, Nt = \frac{(T_1 - T_0) D_T (\rho C')_p}{k_{ef} T_0}, Nb = \frac{(C_1 - C_0) (\rho C')_p D_B}{k_{ef}}. \tag{8.16}
\end{aligned}$$

Here  $R$ ,  $Rn$ ,  $d$ ,  $a$  and  $b$ ,  $M$ ,  $K$ ,  $Gr$ ,  $Br$ ,  $Pr$ ,  $\beta$ ,  $Nb$ ,  $Nt$ ,  $\theta$  and  $\sigma$  are the Reynolds number, radiation parameter, width of the channel, amplitudes of left and right walls, Hartmann number, permeability parameter, thermal Grashof number, local nanoparticle Grashof number, Prandtl number, heat source/sink parameter, Brownian motion parameter, thermophoresis parameter, non-dimensional temperature and nano-particle volume fraction, respectively. Applying the long wavelength and low Reynolds number approximations and introducing the stream

function  $u = \frac{\partial \psi}{\partial y}$ , eqns. (8.12-8.15) reduce to:

$$0 = -\frac{\partial p}{\partial x} + \frac{\partial}{\partial y} \left[ \mu(\theta) \frac{\partial^2 \psi}{\partial y^2} \right] - \left( \frac{1}{K} + M^2 \right) \left( \frac{\partial \psi}{\partial y} + 1 \right) + Gr\theta + Br\sigma, \tag{8.17}$$

$$0 = -\frac{\partial p}{\partial y}, \quad (8.18)$$

$$0 = \left( \frac{1}{Pr} + Rn \right) \frac{\partial^2 \theta}{\partial y^2} + Nb \left( \frac{\partial \sigma}{\partial y} \frac{\partial \theta}{\partial y} \right) + Nt \left( \frac{\partial \theta}{\partial y} \right)^2 + \beta, \quad (8.19)$$

$$0 = \frac{\partial^2 \sigma}{\partial y^2} + \frac{Nt}{Nb} \frac{\partial^2 \theta}{\partial y^2}. \quad (8.20)$$

Eqn. (8.18) implies that  $p$  is not function of  $y$ . Differentiating Eqn. (8.17) with respect to  $y$ , yields:

$$0 = \frac{\partial^2}{\partial y^2} \left[ \mu(\theta) \frac{\partial^2 \psi}{\partial y^2} \right] - N^2 \frac{\partial^2 \psi}{\partial y^2} + Gr\theta + Br\sigma, \quad (8.21)$$

Where  $N^2 = \frac{1}{K} + M^2$ .

The volumetric flow rate in the wave frame is given by:

$$q = \int_{h_1}^{h_2} u dy = \int_{h_1}^{h_2} (U - 1) dy, \quad (8.22)$$

On integration, eqn. (8.22) yields:

$$q = Q + h_1 - h_2, \quad (8.23)$$

Averaging the volumetric flow rate along one time-period, we get:

$$\Theta = \int_0^1 Q dt = \int_0^1 (q + h_2 - h_1) dt, \quad (8.24)$$

which yields:

$$\Theta = q + 1 + d \quad (8.25)$$

The appropriate boundary conditions may be presented in the following form:

$$\psi = \frac{q}{2}, \frac{\partial \psi}{\partial y} = -1, \theta = 0 \text{ and } \sigma = 0 \text{ at } y = h_1(x) = 1 + a \cos 2\pi x, \quad (8.26a)$$

$$\psi = -\frac{q}{2}, \frac{\partial \psi}{\partial y} = -1, \theta = 1 \text{ and } \sigma = 1 \text{ at } y = h_2(x) = -d - b \cos(2\pi x + \phi), \quad (8.26b)$$

This satisfies the condition:  $a^2 + b^2 + 2ab \cos(\phi) \leq (1+d)^2$ . Solving the Eqns. (8.19-8.20) subject to boundary condition (8.26), the temperature and nanoparticle fraction field are obtained as:

$$\theta(y) = A_3 e^{-A_1 y} - \frac{A_2 y}{A_1} - A_4, \quad (8.27)$$

$$\sigma(y) = A_5 y - A_6 e^{-A_1 y} - A_7. \quad (8.28)$$

## 8.2 Validation with Maple17

The linear dimensionless two-point moving boundary value problem (BVP) i. e. eqns. (8.19), (8.20) and (8.21) with conditions (8.26a, 8.26b) are easily solved using Runge–Kutta–Merson numerical quadrature to yield temperature, nano-particle volume fraction and stream function.

The axial velocity is then computed in a sub-iteration loop based on the definition,  $u = \frac{\partial \psi}{\partial y}$ .

The computations are executed in **MAPLE17** software (RK45 algorithm). This approach has been extensively implemented recently in non-Newtonian nanofluid flows [63]. The robustness and stability of this numerical method is therefore well established- it is highly adaptive since it adjusts the quantity and location of grid points during iteration and thereby constrains the local error within acceptable specified bounds. In the current problem, the wall boundary conditions given in Eqns. (8.26a, b) are easily accommodated. The stepping formulae although designed for nonlinear problems, are even more efficient for any order of linear differential equation are already given in Chapter 2 and are therefore not repeated here [63]. A comparison

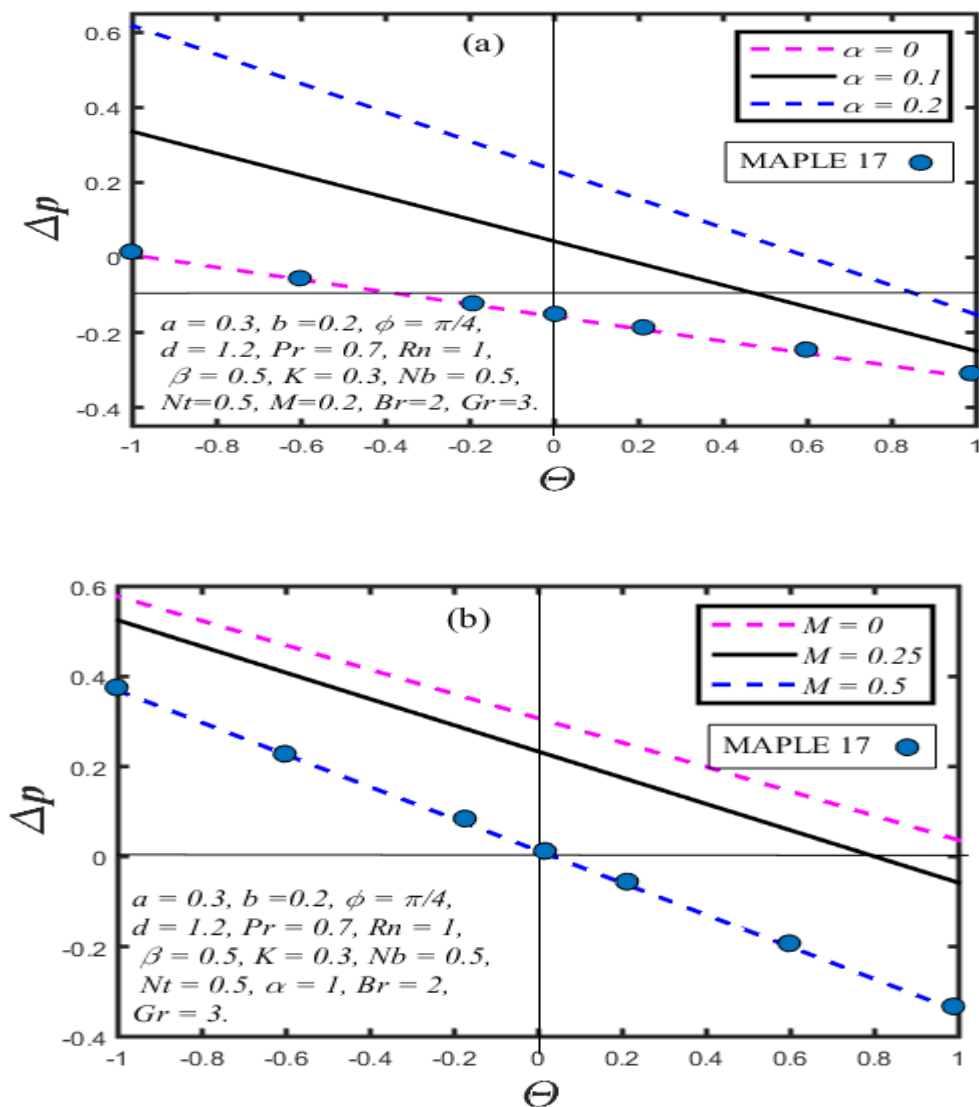


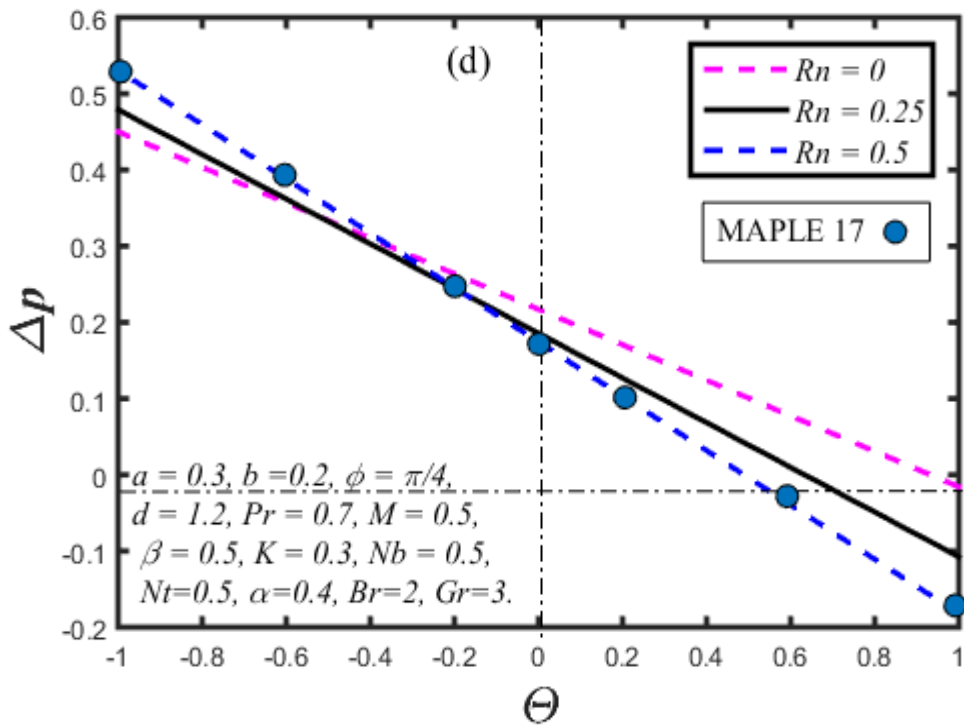
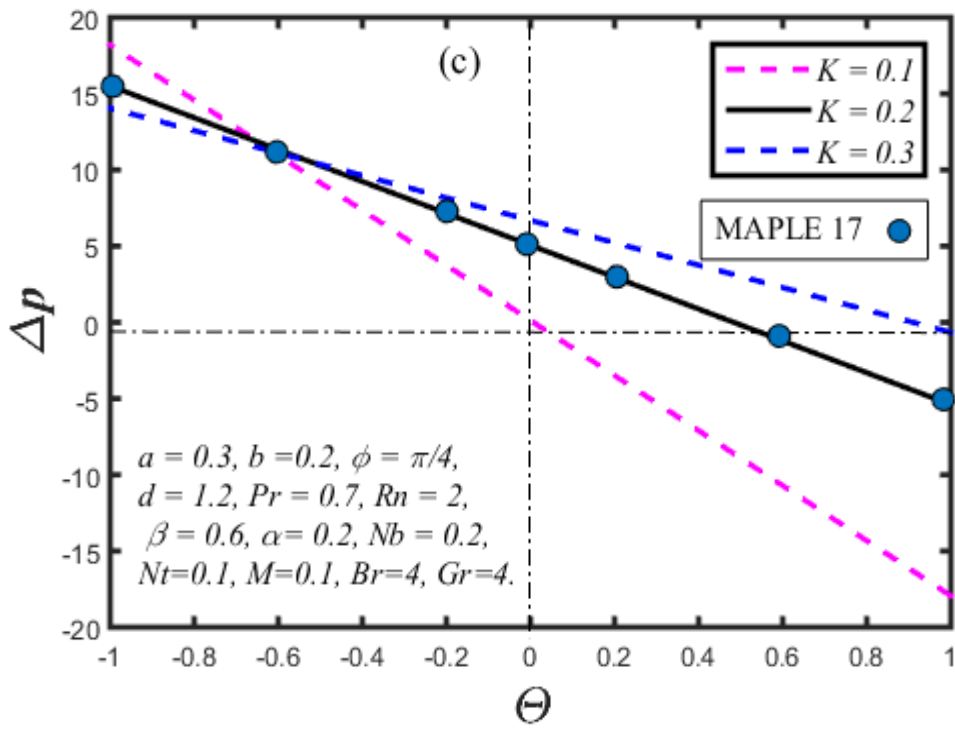
of the analytical and MAPLE numerical quadrature solutions (blue dots) is documented in **Figs. 8.2a-f** for pressure rise profile with variation in (a)  $\alpha$ , (b)  $M$ , (c)  $K$ , (d)  $Rn$ , (e)  $\beta$  and (f)  $Br$  and also **Figs. 8.3a-f** for axial velocity distributions (axial velocity vs. transverse coordinate) for (a)  $M$ , (b)  $Rn$ , (c)  $Pr$ , (d)  $K$ , (e)  $\beta$ , (f)  $\alpha$  and finally in **Figs. 8.4a-d** for temperature and nanoparticle volume fraction profiles with variation in (a)  $\beta$ , (b)  $Nt$ , (c)  $Pr$ , (d)  $Rn$ . Only one case is validated in each plot. Excellent correlation is achieved in all cases. Confidence in the present analytical solutions is therefore high. Maple quadrature is of comparable accuracy to many other sophisticated semi-numerical methods including homotopy analysis methods (HAM), Adomian decomposition methods (ADM), spectral collocation Chebyshev polynomial methods and Variational iterative methods (VIMs) which accurately compute series solution, although Maple quadrature is less algebraically rigorous and can be applied directly for all types of differential and integral equations, linear or nonlinear, homogeneous or inhomogeneous, with constant coefficients or with variable coefficients. Another important advantage is that the method is capable of greatly reducing the size of computation work while still maintaining high accuracy of the numerical solution [63].

### **8.3 Numerical evaluation of results and discussion**

The primary aim of this investigation is to analyze the influence of temperature-dependence of the nanoliquid viscosity, thermal radiative flux, wafer permeability and heat source/sink effects on thermal flow characteristics of the solar peristaltic nanofluid magnetohydrodynamic micro-pump. In this regard, herein we elaborate on the impact of various pertinent hydrodynamic, magnetic, thermal and porous medium parameters i.e. Reynolds number viscosity parameter ( $\alpha$ ), heat source/sink parameter ( $\beta$ ), Prandtl number ( $Pr$ ), Hartmann number ( $M$ ), thermal

radiation ( $Rn$ ), Permeability parameter ( $K$ ) and local nanoparticle Grashof number ( $Br$ ) at a pre-determined axial location along the pump channel ( $x = 0.5$ ) on the evolution of axial velocity of the fluid ( $u$ ), pressure gradient ( $dp/dx$ ), temperature distribution ( $\Theta$ ) and nanoparticle volume fraction of the fluid ( $\sigma$ ). The distributions are depicted in **Figs. 8.2-8.7**. Evaluation of the closed form solutions is conducted via the symbolic software **Maple** which is very versatile for peristaltic and hydromagnetic pump simulations.





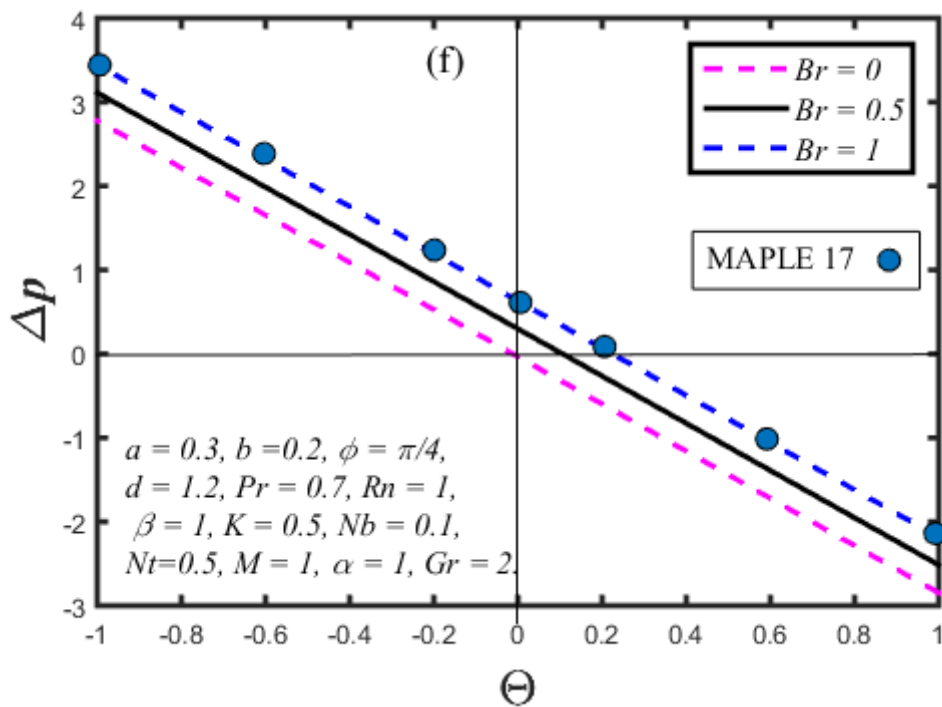
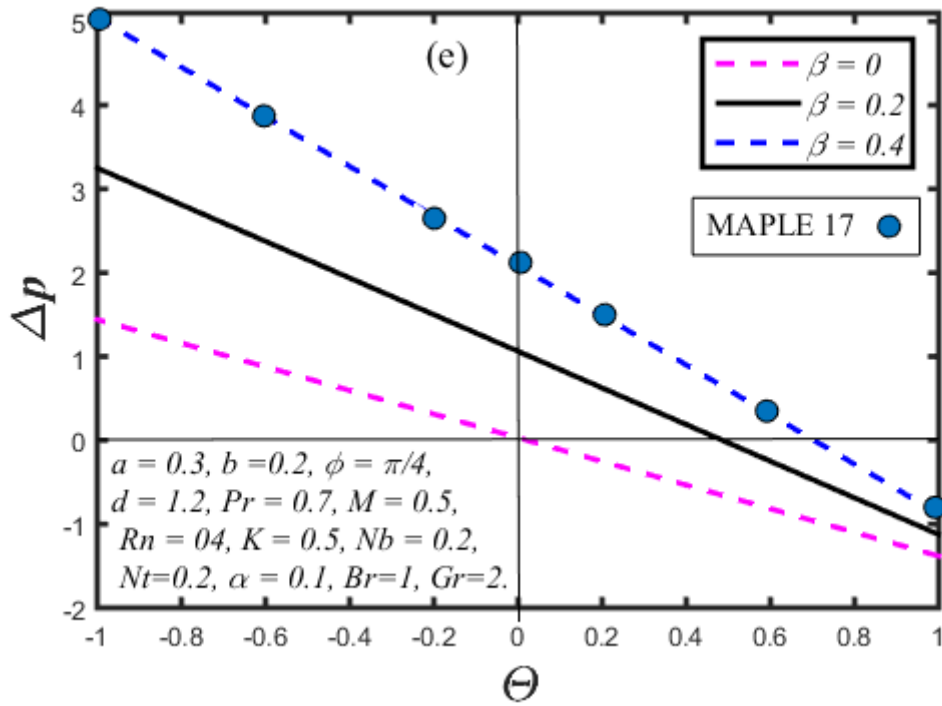
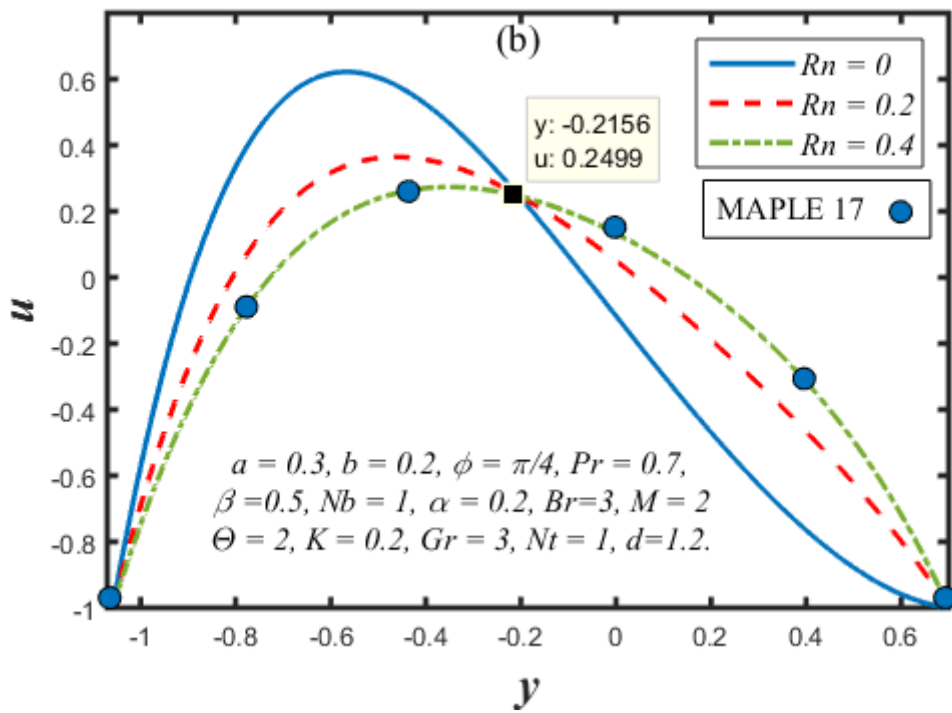
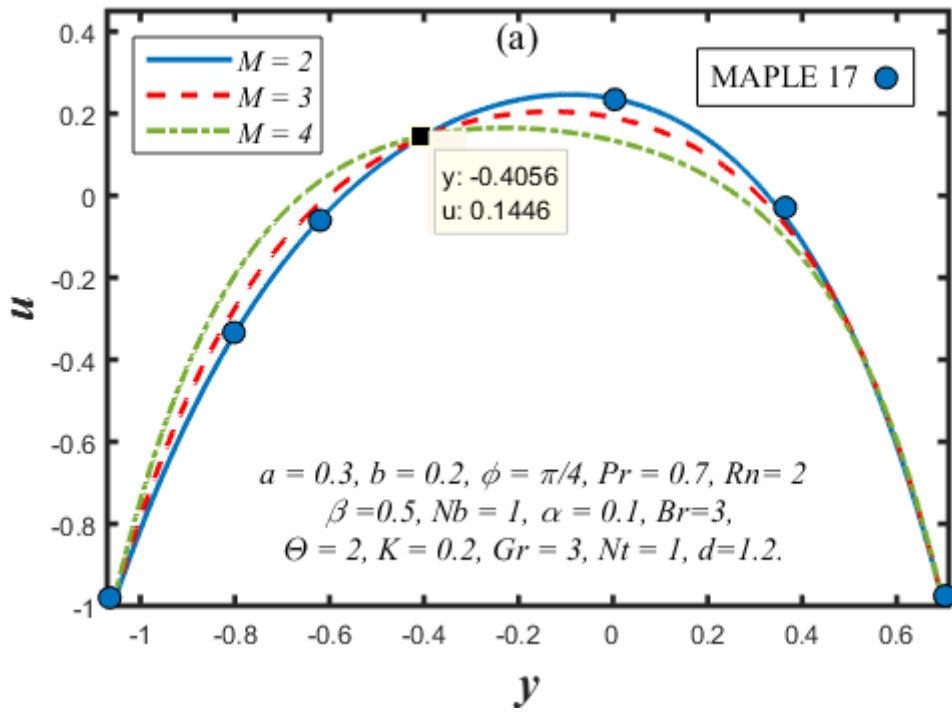
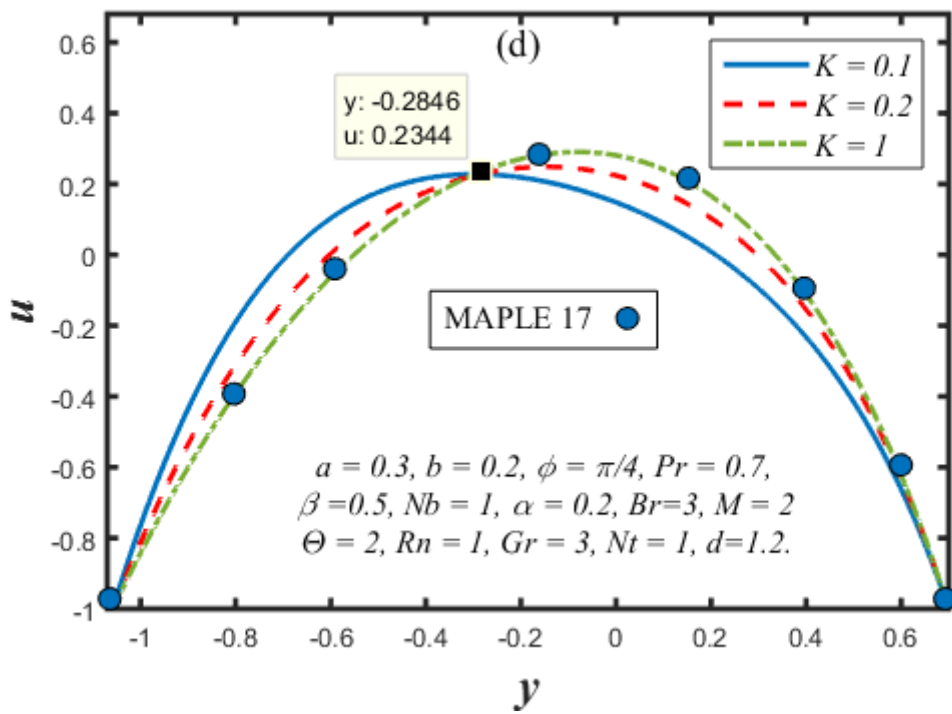
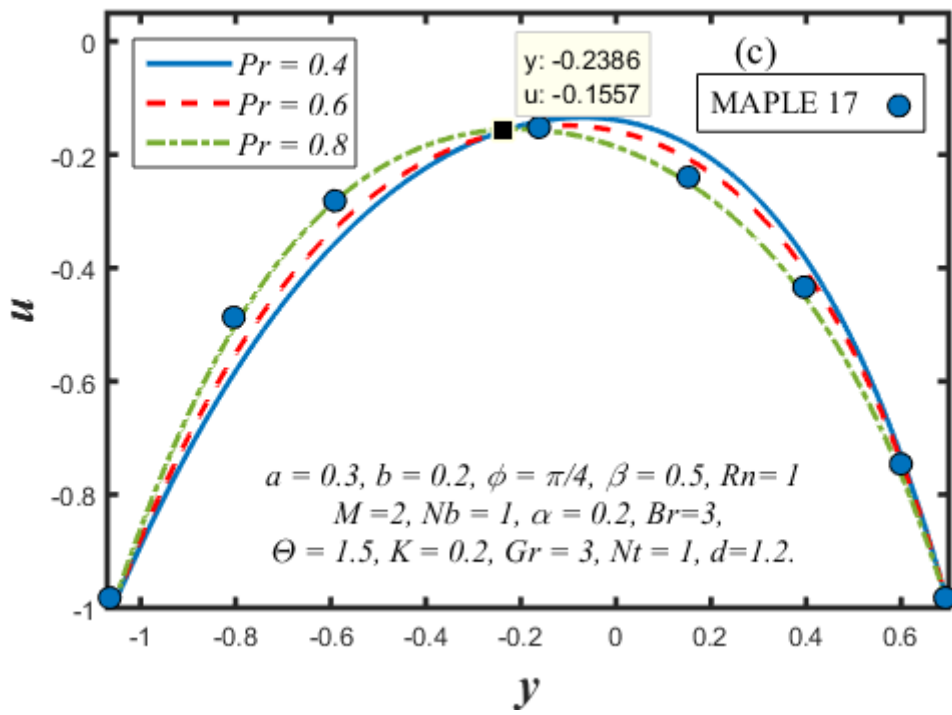


Figure 8.2 Pressure rise profile with variation in (a)  $a$ , (b)  $M$ , (c)  $K$ , (d)  $Rn$ , (e)  $\beta$  and (f)  $Br$ .





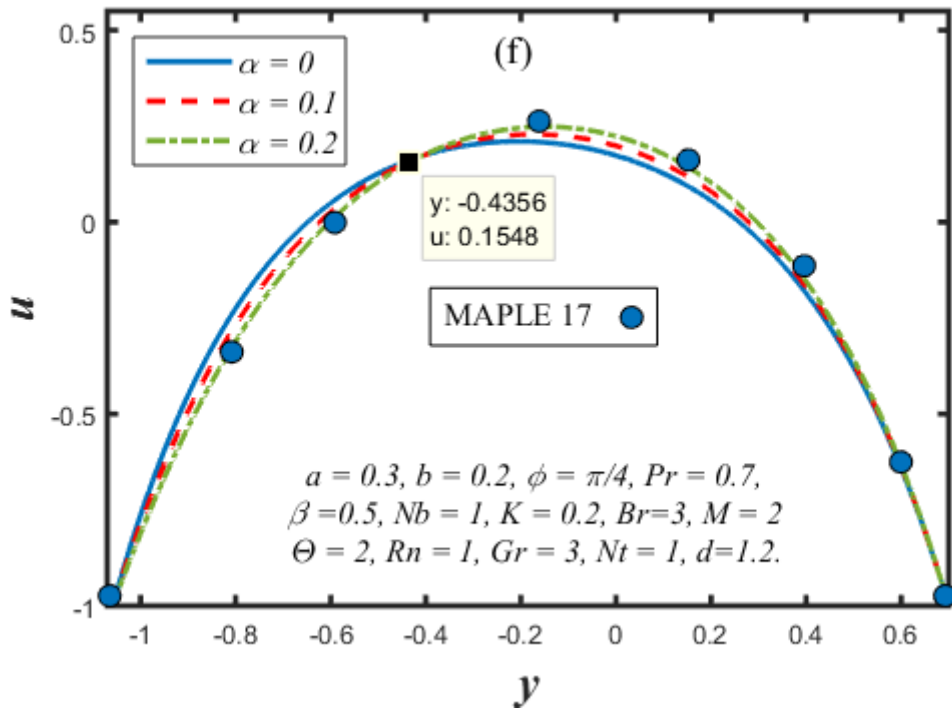
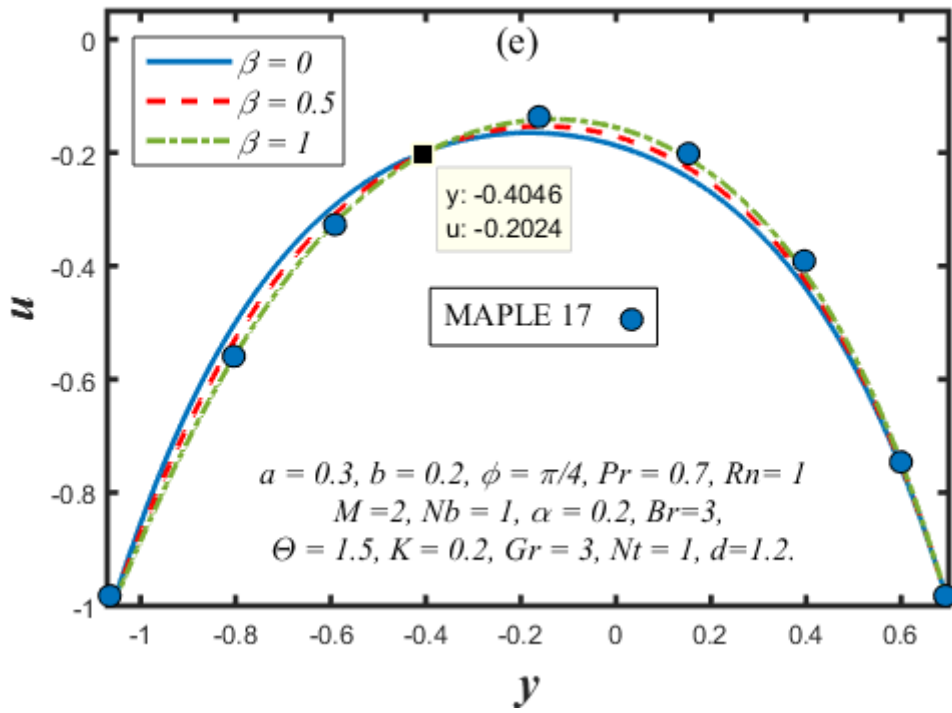
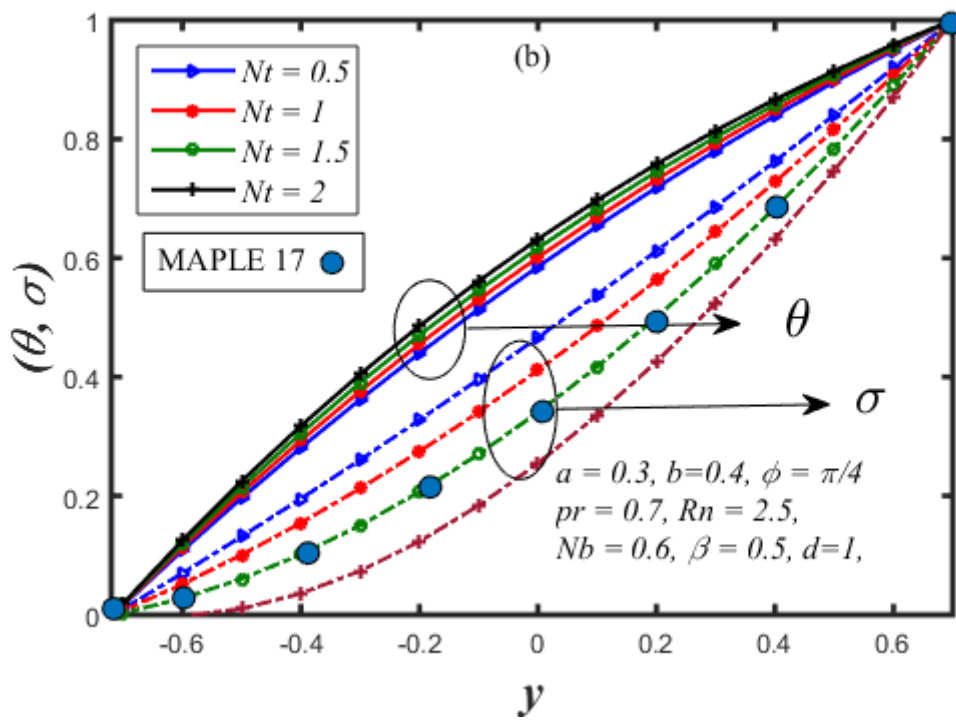
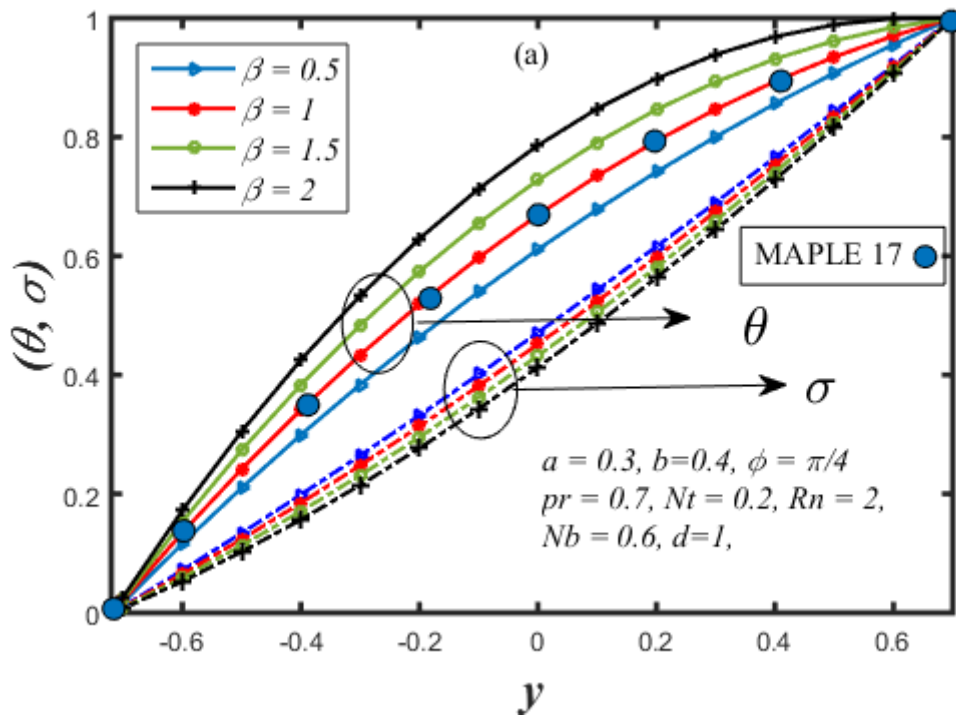


Figure 8.3 Axial velocity distributions (axial velocity vs. transverse coordinate) for (a)  $M$ , (b)  $Rn$ , (c)  $Pr$ , (d)  $K$ , (e)  $\beta$ , (f)  $\alpha$ .





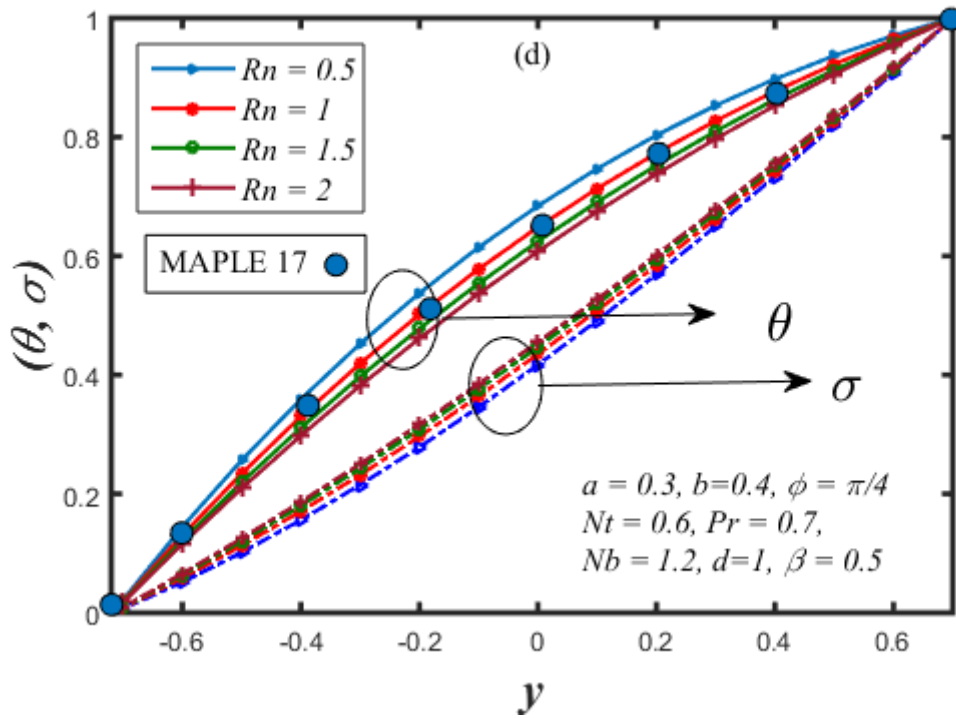
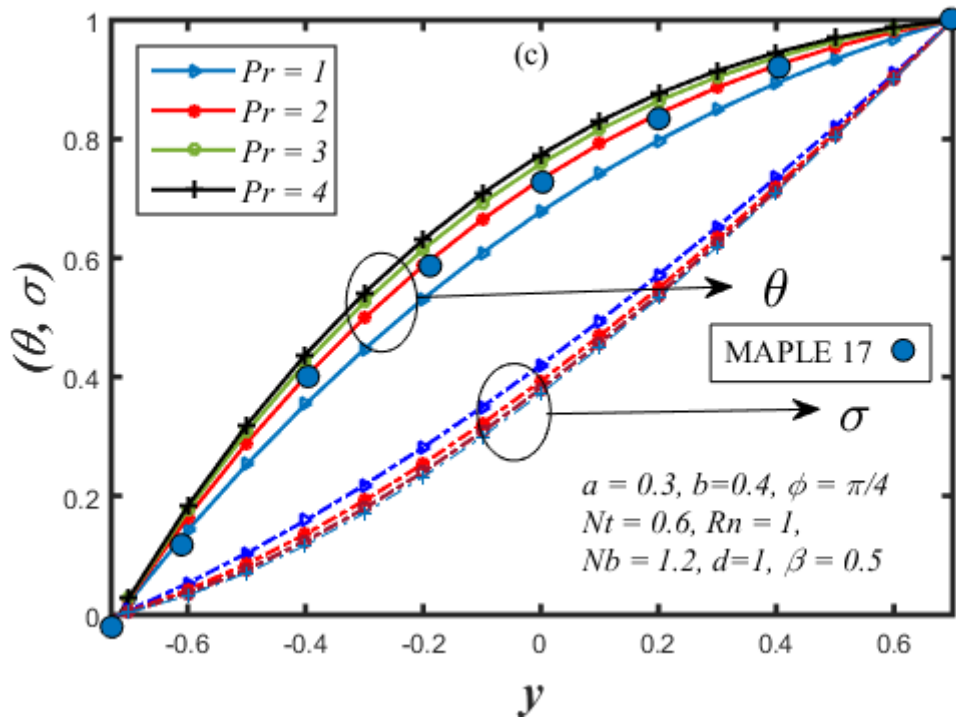
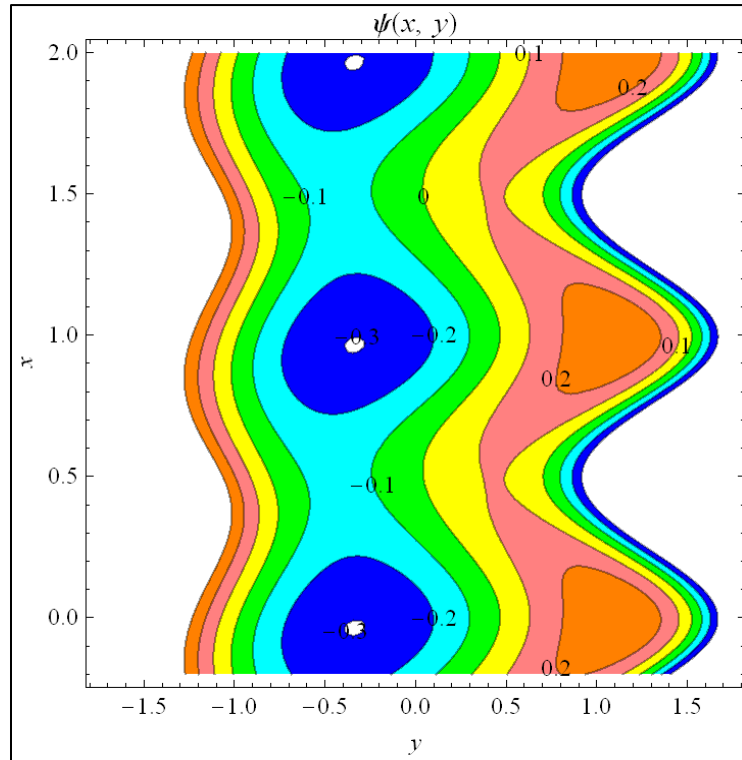
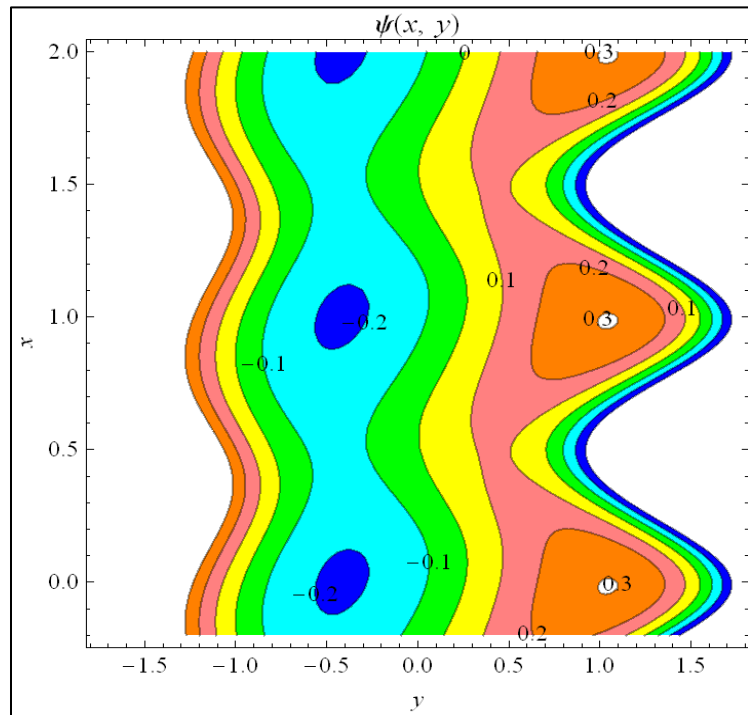


Figure 8.4 Temperature and nanoparticle volume fraction profiles with variation in (a)  $\beta$ , (b)  $Nt$ , (c)  $Pr$ , (d)  $Rn$

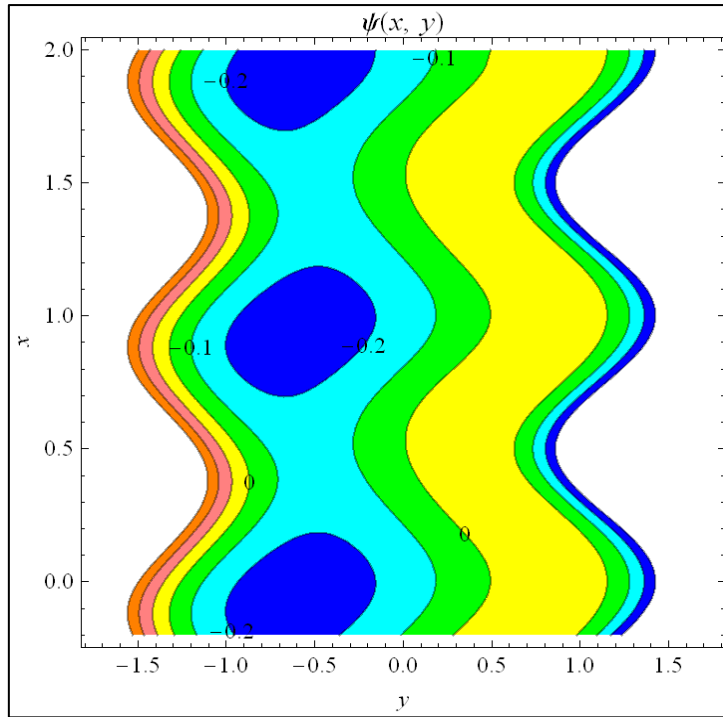


(a)

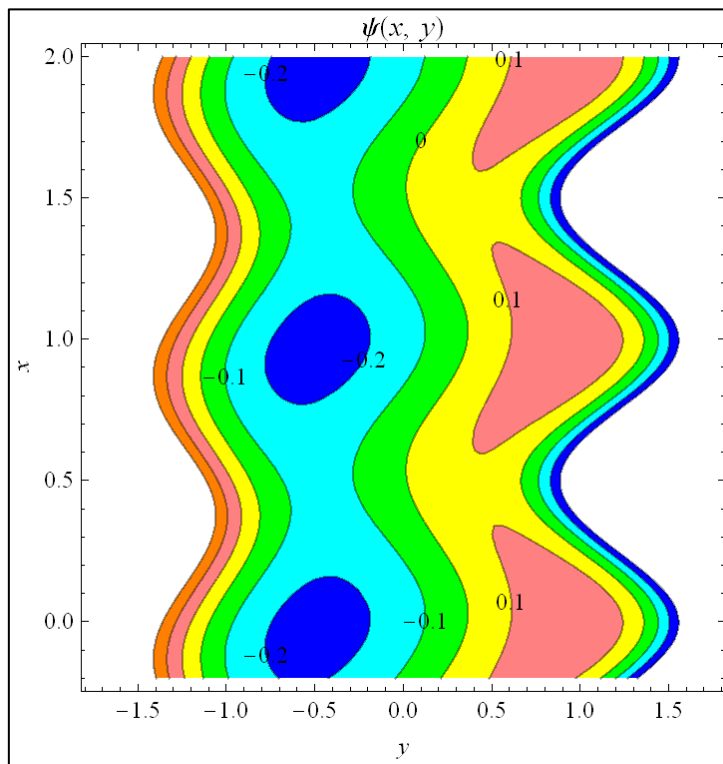


(b)

Figure 8.5 Stream lines at  $a=0.3, b=0.2, Pr=0.7, Rn=0.5, \beta=0.5, Nb=0.5, Nt=0.5, M=1, d=1.1, Br=3, \Theta=2, K=0.2, \phi=\pi/4, Gr=2, Pr=2, Nt=1$ , for (a)  $\alpha=0$ , (b)  $\alpha=0.1$ .

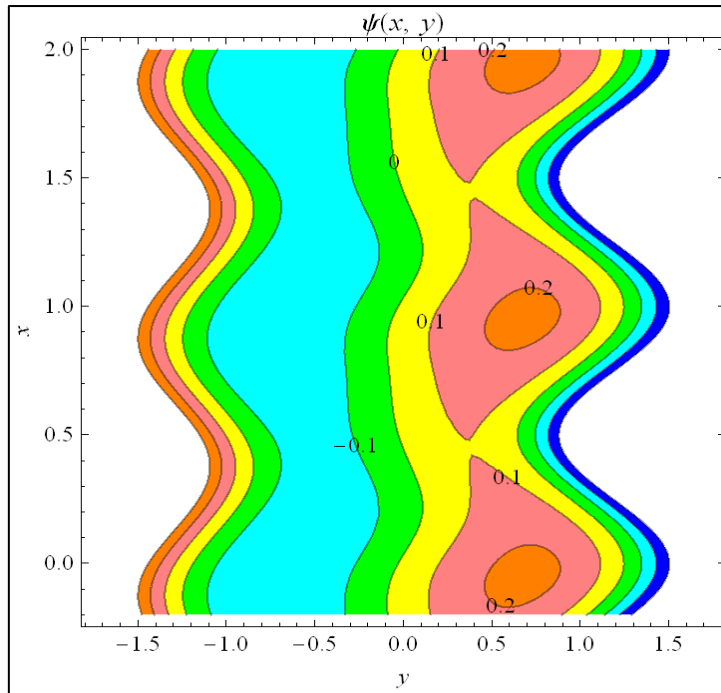


(a)

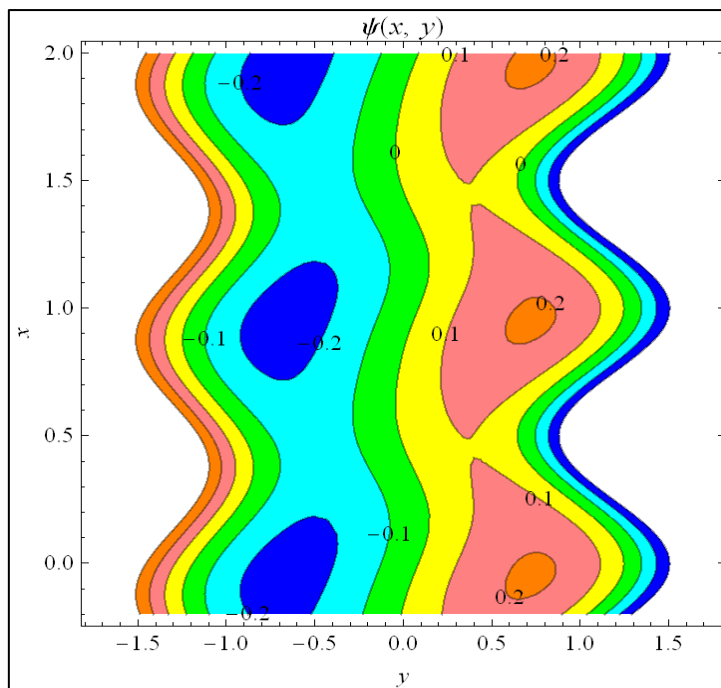


(b)

Figure 8.6 Stream lines at  $a=0.3, b=0.2, Pr=0.7, Rn=0.5, a=0, Nb=0.5, Nt=0.5, M=1, d=1.1, Br=3, \Theta=2, K=0.2, \phi=\pi/4, Gr=2, Pr=2, Nt=1$ , for (a)  $\beta=0$  (b)  $\beta=0.5$ .



(a)



(b)

**Figure 8.7** Stream lines at  $a=0.3$ ,  $b=0.2$ ,  $Pr=0.7$ ,  $Rn=0.5$ ,  $\alpha=0$ ,  $Nb=0.5$ ,  $Nt=0.5$ ,  $\beta=0.25$ ,  $d=1.1$ ,  $Br=3$ ,  $\Theta=2$ ,  $K=0.2$ ,  $\phi=\pi/4$ ,  $Gr=2$ ,  $Pr=2$ ,  $Nt=1$ , for (a)  $M=0$ , (b)  $M=1$ .

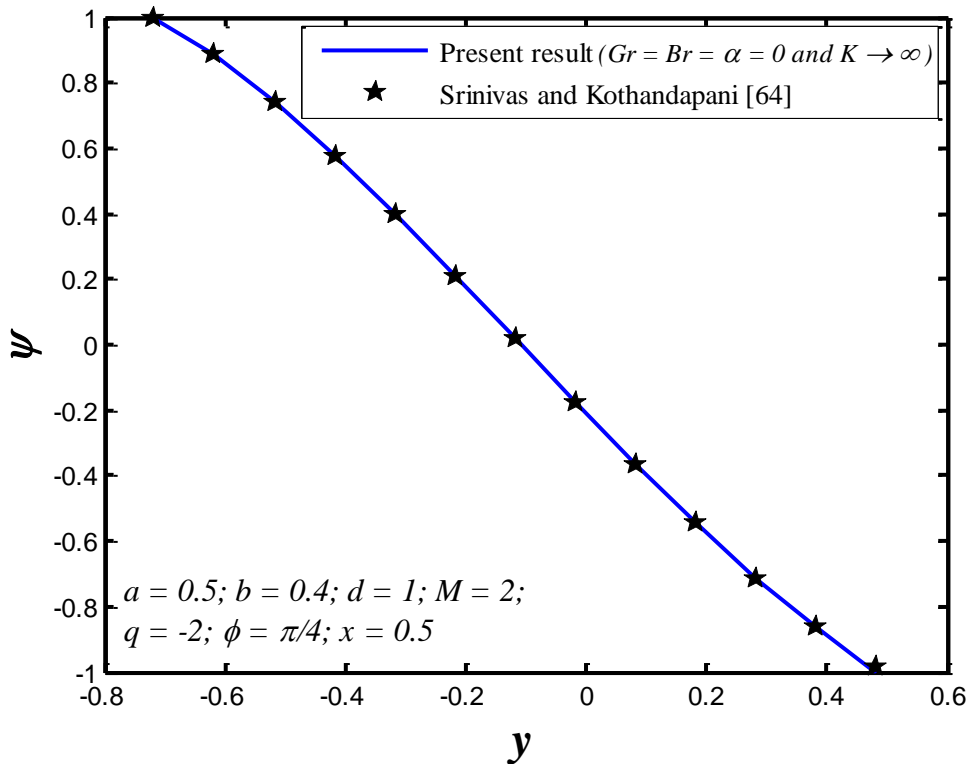


Figure 8.8 Comparison result of stream function versus transverse axis.

### 8.3-1 Pumping characteristics

The pressure rise per wavelength can be calculated by using the form  $\Delta p = \int_0^1 \left( \frac{\partial p}{\partial x} \right) dx$ . The pressure rise is computed numerically using the symbolic software Mathematica for the perturbation solutions and MAPLE17 for the Runge-Kutta-Merson numerical solutions. The pressure rise ( $\Delta p$ ) versus mean flow rate ( $\Theta$ ) for various values of  $\alpha$ ,  $M$ ,  $K$ ,  $Rn$ ,  $\beta$  and  $Br$  is illustrated in Figs. 8.2 (a-f). Fig. 8.2(a) portrays that the influence of Reynolds viscosity parameter on the pressure rise versus the mean flow rate. One can insure that the pressure rise increases with increasing Reynolds viscosity parameter ( $\alpha$ ) for the pumping region (

$\Delta p > 0, \Theta > 0$ ). It is also evident that volumetric flow rate is elevated for Newtonian nanofluid ( $\alpha = 0$ ) and depressed for non-Newtonian nanofluid i.e., for non-zero Reynolds viscosity parameter ( $\alpha > 0$ ). Additionally, peristaltic pumping is inhibited with increasing temperature-dependence of the nanofluid viscosity. This is also consistent with the simultaneous deceleration in the axial flow with greater nanofluid viscosity. Pressure and velocity (linked to flow rate) respond in opposite ways in hydrodynamics- the inverse relationship is clearly demonstrated in all the negative gradients in the profiles in the plot. Evidently pressure rise is minimized with the Newtonian nanofluid (least viscosity) and maximized with strongly non-Newtonian nanofluid (highest viscosity). The implication for solar pump performance is that if greater pressures are required (as opposed to flow acceleration), this may be achieved via increased doping of the working fluid with nanoparticles.

(Choi & Eastman, 1995) have highlighted the strong modification in nanofluid rheology with increased concentrations of nanoparticles. The change in viscosity is intimately related to heat transfer enhancement of nanofluids in particular when buoyancy forces are present, as in the present study, as will be elaborated in due course. Thus viscosity variation as studied by the Reynolds model may provide a good insight into the improved efficiencies reported in solar energy systems doped with nanofluids at higher temperatures as noted by (Cingarapu, et al., 2014), (Alashkar & Gadalla, 2018). Furthermore, since magnetic pumping is also present it is noteworthy that the present computations are consistent with the earlier simulations of (Shahidian, et al., 2012) where rheological and higher viscosity was observed to also generate pressure difference elevation in pump operations. In Fig. 8.2(b), we examine the effect of Hartmann number ( $M$ ) on the pressure rise verse mean flow rate. Clearly pressure rise diminishes with growing values of Hartmann number for the peristaltic pumping region (

$\Delta p > 0, \Theta > 0$ ). The Lorentz magnetic drag force i.e.  $-M^2 \partial^2 \psi / \partial y^2$  in eqn. (8.21) is generated by the application of magnetic field in the Y-direction (transverse to the axial velocity direction i.e. the X-direction). This accelerates the flow and concurrently depletes the pressure rise in the solar magnetic pump channel. The profiles are all therefore linear decays i.e., with maximum pressure rise there is a corresponding minimal flow rate and vice versa. This concurs with the findings of (Lim & Choi, 2009) for the similar scenario of a two-dimensional channel with side-walled electrodes, although in our study wall deformability is present i.e. the channel walls propagate peristaltic waves (we have set the amplitudes of left and right walls i.e.  $a, b$  as 0.3 and 0.2 respectively and also the phase difference is prescribed as  $\pi/4$ ). Similar observations have also been reported by (Das, et al., 2013), (Ho, 2007) and (Leboucher, et al., 1995). These studies have also shown in agreement with our computations that pressure rise in magnetohydrodynamic pumping is lowest with strong magnetic field ( $M = 0.5$ ) and highest with absence of magnetic field i.e. electrically non-conducting nanofluid ( $M = 0$ ). These trends are sustained at all values of volumetric flow rate ( $\Theta$ ). Fig. 8. 2(c) depicts the influence of permeability parameter ( $K$ ) on the pressure rise versus mean flow rate distributions. From this figure, we discern that an increase in the permeability parameter initially depresses the pressure difference; however, with subsequent increase in volumetric flow rate the pattern is strongly reversed with a significant upsurge in pressure difference during peristaltic pumping. Permeability is a key characteristic of porous media. This parameter characterizes the hydraulic transmissivity of the porous medium. It does not however relate to the porosity of the medium which is connected to the relative volume of voids to the volume of solids. Permeability features in the linear Darcian impedance term in the reduced momentum equation (8.21), namely the term  $-(1/K) \partial^2 \psi / \partial y^2$  and this is associated with the retarding effect of the porous solar wafer fibers. Darcy's law is generally valid for Reynolds numbers less than 10 i.e. it is

applicable for viscous-dominated pumping dynamics as opposed to inertially-dominated transport (this requires a Forchheimer-extended Darcy model to simulate second or higher order drag effects and is presently being considered as an extension to the current work to extend the operational range to higher Reynolds numbers). With increasing permeability, the regime solid fibers progressively decrease. This results in effective enhancement in pressure differences across the channel length i.e. a boost in  $\Delta p$ . This behavior is sustained for the majority of positive volumetric flow rates. The initial depletion in pressure rise is more associated with the entry length hydrodynamics and negative flow rates (back flow) and a threshold volumetric flow rate is necessary to enforce the dominant effect of permeability as elucidated in detail by (Wang, et al., 2004) and also earlier by (Al-Nimr & Alkam, 1998) for different solar cell and pump configurations i.e. the permeability effect is independent of conduit geometry and is controlled by the nature of the wafer material. The presence of a low permeability porous medium (solar wafer) i.e.  $K=0.1$  generally damps the pressure difference generated in the pump whereas higher permeability i.e.  $K=0.3$  induces the opposite effect. It is also pertinent to note that the permeabilities studied are high i.e. the medium is sparsely packed which obviates the possibility of compressibility effects, consolidation effects or compaction phenomena, as further highlighted by (Ren, et al., 2017). Fig. 8.2(d) presents the impact of thermal radiation flux on pressure rise versus mean flow rate profiles. It is remarked that there is a strong presence of positive pumping ( $\Theta > 0$  and  $\Delta p > 0$ ) when  $Rn = 0$  as compared with  $Rn > 0$ . Thermal radiation is the most significant contribution from solar heat loading (Hottel & Sarofim, 1967). The parameter  $Rn$  arises in the augmented energy equation (8.19) i. e. in the term  $Rn \partial^2 \theta / \partial y^2$ . Rosseland's model assumes radiative equilibrium and that the nanofluid has gray properties which are popular in solar pump designs. Furthermore, Rosseland's model assumes that the intensity is the black-body intensity at the nanofluid temperature and since it



is generally confined to incompressible flows it is particularly appropriate for low speed transport characteristic of porous media hydromagnetic pumping. The parameter  $R_n$  embodies the relative contribution of conduction heat transfer to thermal radiation transfer. It is variously known in thermal physics as the Stark number and Rosseland-Boltzmann number [1]. Large  $R_n$  values imply small radiation contribution and small  $R_n$  values correspond to high radiative flux. As  $R_n \rightarrow 0$ , thermal radiation flux contribution vanishes and the dominant mode of heat transfer is thermal conduction. Hence with smaller  $R_n$  values, thermal radiation is stronger than thermal conduction (the contribution is only equal for both modes of heat transfer when  $R_n = 1$ ). Thermal radiation supplements the fluid thermal conductivity via the energy equation and serves to increase temperatures, simultaneously reducing momentum transfer which serves to decrease pressure difference at positive flow rates (the converse effect is induced at negative flow rates). The influence of radiative flux on velocity, temperature and nano-particle volume fraction distributions is described in due course. The variation in pressure rise for different values of heat source/sink parameter ( $\beta$ ) is illustrated in Fig. 8.2(e). It is evident that pressure rise is assisted with an increase in heat source (generation) parameter in all the peristaltic pumping regions. The maximum peristaltic pumping is achieved when  $\beta > 0$  as compared with the least efficient pumping attained with  $\beta = 0$ . Generally, the presence of heat generation (mimicking for example thermal hot spot zones in solar pumps) strongly elevates temperatures (see fig 8.4a). This also assists in momentum development and manifests in pressure difference depletion. The influence is maintained at both negative and positive flow rates i.e. whether correct pumping or reverse flow is present. The observations are consistent with the findings of (Tien & Vafai, 1989). The heat source effect is also particularly relevant to ground-heat source solar pumps (Romero & González-Aguilar, 2017). It works effectively to energize the pumping fluid and aids in increasing thermal pumping efficiency. Figs. 8.2(f) display the

influence of the species buoyancy force (simulated via local nanoparticle i.e., solutal Grashof number  $Br$ ) on the pressure rise ( $\Delta p$ ) versus mean flow rate ( $\Theta$ ).  $Br$  arises in the species buoyancy term in the reduced momentum eqn. (8.21) i. e.  $Br\sigma$  and this term couples the momentum field with the nano-particle species concentration field described by eqn. (8.20). It represents the relative magnitude of the species buoyancy force to the viscous hydrodynamic force in the channel. When  $Br \rightarrow 0$  species (solutal) buoyancy effects vanish. Thermal Grashof number ( $Gr$ ) is prescribed a value of 2 implying the thermal buoyancy force is double the magnitude of the viscous hydrodynamic force. Pressure rise is considerably elevated with increasing solutal Grashof number  $Br$ . This applies at both negative and positive flow rates and in the pumping region ( $\Delta p > 0$ ), the augmented pumping region ( $\Delta p < 0$ ), and the free pumping region ( $\Delta p = 0$ ). Pressure rise is clearly suppressed with absence of species buoyancy forces indicating that the presence of nano-particles is beneficial to solar peristaltic pump performance. Nano-particle solutal buoyancy is shown therefore to be a critical characteristic which modifies the pump hydrodynamic regime. It is also judicious to mention that positive values of  $Br$  correspond to nano-particle transfer from the channel walls by natural species convection currents which implies a reduction in wall mass transfer rate (channel wall nano-particle concentration gradient).

### 8.3-2 Axial Velocity distribution

The effects of the principal flow parameters i. e. Hartmann magnetic number, thermal conduction-radiation parameter (Stark number), Prandtl number, permeability parameter, heat source parameter and Reynolds viscosity parameter on axial velocity distribution ( $u = u_0 + \alpha u_1$ ) are visualized in Fig. 8.3 (a-f) at the axial location  $x = 0.5$ . It is observed that the axial velocity distributions exhibit a parabolic nature in which the maximum/minimum

axial velocity appears at the core zone of the channel. However, there is a slight dis-symmetry which is a manifestation of the different amplitudes of left and right walls i.e.  $a, b$  as 0.3 and 0.2 respectively i.e. the profiles are either skewed to the left or to the right wall. The influence of Hartmann number ( $M$ ) on axial velocity distribution versus transverse coordinate is plotted in Fig. 8.3 (a). It is noticed that the performance of axial velocity near the channel walls and at the core part of the channel demonstrates a reflective symmetry approximately about the channel centre line ( $y = 0$ ). Axial velocity enhances with an increase in Hartmann number near the lower deformable channel wall. However, it reduces in the core region of the porous medium channel and all profiles merge towards the upper wall i.e. there is invariance in the magnetic field effect near the upper wall. The presence of magnetic field in the electrically conducting magnetized nanofluid, as explained earlier, mobilizes the Lorentz magnetic force. This acts to resist the channel flow in magnetic generator operations but accelerates the flow in magnetic pumping operations (as considered here). Fig. 8.3 (b) shows the effect of thermal radiation on axial velocity distribution. It is noticed that velocity is depressed in the lower channel half space i.e.  $y \in [-1.07, -0.2499]$  whereas it is enhanced in the upper channel half space, with increasing  $Rn$  i.e. with decreasing thermal radiative flux. Energization of the nanofluid with stronger solar radiative flux therefore decelerates the pumping flow. The Prandtl number effect on the axial velocity distribution is plotted in Fig. 8.3(c). It is apparent that the axial velocity is raised with an elevation in Prandtl number over the lower channel half-space range  $y \in [-1.07, -0.2386]$ ; however, in the upper channel half space range velocity is strongly decreased with increasing Prandtl number. The no-slip condition requires that the flow velocity at the surface of the channel walls is zero and that the nanofluid temperature is equal to the surface temperature. Prandtl number defines the relative rate of momentum diffusion to energy (heat) diffusion in the regime. For Prandtl number of unity, both heat and

momentum diffuse at the same rate. In the entry length zone of the magnetohydrodynamic solar pump channel, for Prandtl number below unity, the thermal boundary layer is thicker than the velocity boundary layer. The flow is also accelerated with increasing Prandtl number in the lower channel half space since this is closer to the entry length zone whereas the converse effect is induced in the upper channel half space. As elaborated in (Shahidian, et al., 2012) it is unfeasible to achieve a consistent acceleration or deceleration throughout the entire magnetohydrodynamic pump with purely an increase in Prandtl number. Fig. 8.3 (d) displays the axial velocity distribution for three different value of the permeability parameter ( $K = 0.1, 0.2$  and  $1$ ). It is viewed that the axial velocity is suppressed in the region  $y \in [-1.07, -0.2846]$ , whereas it is magnified in the region  $y \in [-0.2846, 0.64]$ . The switch-over for this behavior is located to the left of the channel centre line. Maximum axial flow is generated mid-way within the upper channel half space with maximum permeability i.e. minimal Darcian retarding force. Increasing permeability parameter results in depletion in resistance of the solid fibers to the percolating nanofluid. This accelerates the nanofluid pumping and increases the shearing effect at the channel walls leading to greater shearing stresses at these boundaries. As  $K \rightarrow \infty$  the porous matrix disappears and the regime becomes pure nanofluid. In the opposite limit as  $K \rightarrow 0$ , the medium permeability vanishes and the pump is completely filled with solid material preventing pumping operations. Many studies including (Vasiliev, et al., 2001) and (Ramesh, 2016) have confirmed that optimum solar and peristaltic pump performance and flow control is attainable with high but not excessive permeabilities. Fig. 8. 3 (e) shows the influence of the three different values of heat source parameter ( $\beta = 0, 0.5$  and  $1$ ) on the axial velocity distribution for the fixed values of other parameters. It is evident that with increasing heat source/sink parameter,  $\beta$ , the axial velocity field is depleted in the lower channel half space  $y \in [-1.07, -0.4046]$  where as it is enhanced in the

upper channel half space in the range  $y \in [-0.4046, 0.64]$ . The influence of the Reynolds viscosity ( $\alpha$ ) parameter on  $u$  is presented in Fig. 8.3(f). Axial velocity distribution ( $u$ ) reduces with the increase in Reynolds viscosity effect ( $\alpha$ ) in the lower channel half space (here the boost in viscosity inhibits strongly the entry flow in the solar pump channel duct) whereas the contrary behavior is computed in the upper channel half space (right hand side of the channel geometry). This trend is consistent with several studies on nanofluid non-Newtonian viscosity behavior, including (Choi & Eastman, 1995), and (Shahidian, et al., 2012) (Shahidian, et al., 2009). The latter investigation has confirmed experimentally that viscosity abnormally increases when an increase in volume concentration of nanoparticles is present and this leads to deceleration in flows earlier in micro-channels with subsequent acceleration.

### 8.3-3 Temperature and Nanoparticle volume fraction distributions

In Figs. 8.4 (a-d) the evolution of nanofluid temperature distribution ( $\theta$ ) and nanoparticle volume fraction ( $\sigma$ ) with respectively different values of *heat source parameter* ( $\beta$ ), *thermophoretic nanoscale parameter* ( $Nt$ ), *Prandtl number* ( $Pr$ ) and *conduction-radiation Stark number* ( $Rn$ ). A significant feature of the temperature distributions is the concave upward profile whereas a downward concave topology is exhibited by the nanoparticle volume fraction distributions. The heat source parameter influences on temperature and nanoparticle fraction distributions are presented in Fig. 8.4(a). It is evident that the temperature increases with enhancing the heat source parameter effects (since thermal energy is imparted to the nanofluid with heat source in the pump) whereas the nanoparticle volume fraction (i.e., nano-particle concentration magnitude) is clearly reduced with increasing the heat source parameter. The implication is that the heat generation effect only assists thermal distribution homogeneity in

the channel whereas it is counter-productive for the diffusion of nanoparticles. The temperature and nanoparticle volume fraction distributions for the various values of thermophoresis parameter ( $Nt$ ) are presented in Fig. 8.4 (b). Inspection of the graph reveals that the temperature distribution increases with an increase in the thermophoresis parameter. It also noticed from this figure that the nanoparticle volume fraction reduces with an increase in the thermophoresis parameter. Different nanoparticles types transport differently under the thermophoretic force which is associated with migration of nanoparticles from hot to cold surfaces. This is of great utility in solar magnetic nanofluid pumps [26-28] since via selection of specific nanoparticles, customized performance may be achieved. It is further of interest to consider the mechanism of thermal enhancement in nanofluids under solar radiative conditions. It is also noted that the Brownian motion parameter ( $Nb$ ) is fixed at 0.6. Since Brownian dynamics is also present, the nanofluid molecules are organized into an ordered layer at the nano-particle solid-liquid interface which results in thermal conductivity in that ordered layer being lower than thermal conductivity of the solid particles but larger than that of the base fluid. As earlier suggested by (Buongiorno, 2006), this interfacial layer is a solid-like structure, and it is referred to as nanolayer. This hypothetical nanometre size layer is considered as a thermal layer between the solid particle surface and the base fluid and to the current state of knowledge of nanofluid mechanics, this nanolayer is one of the most probable mechanisms producing the popular thermal conductivity enhancement. In fact, the existence of even a *thin nanolayer at relatively high Brownian motion parameter* values still may contribute markedly to the elevation in thermal conductivity of nanofluids, mainly when the particle diameter is smaller than 10 nm. In conjunction with thermophoresis, the extra energy transport of nanoparticles is due to result of Brownian motion. The relative motion between nanoparticles and base fluid molecules generates micro-convection which when summated over the entire body of the nanofluid results

in an effective boost in heat transfer i.e. temperatures. The present theoretical results confirm these observations. However, it is sincerely hoped that experimental solar engineering researchers will be motivated to verify actual performance in both laboratory models and scale-up processes to actual implementation of the current solar magnetic biomimetic nanofluid pump configuration. The influences of four different value of Prandtl number (i.e.,  $Pr = 1, 2, 3$  and 4) on temperature and nanoparticle volume fraction are computed in Figs. 8.4(c). It is found that elevation in Prandtl number leads to a strong enhancement in fluid temperature whereas it depletes the nanoparticle volume fraction. Generally, higher  $Pr$  nanofluids will have relatively low thermal conductivities which will suppress thermal conduction heat transfer from the wall and reduce thermal boundary layer thickness, resulting in higher nanofluid temperatures throughout the channel space. Smaller values of  $Pr$  are equivalent to increasing thermal conductivities, and therefore heat is able to diffuse away from the deformable pump walls more rapidly than for higher values of  $Pr$ . Hence in the case of smaller  $Pr$  the boundary layer is thicker and the rate of heat transfer to the wall is reduced. This has important implications in practical solar pump operations. In Fig. 8.4(d), we observe that with increasing thermal radiation (lower  $Rn$  values) there is a substantial elevation in fluid temperature. It is also noticed that the thermal radiation effect suppresses nanoparticle volume fraction magnitudes i.e. counter-acts diffusion of nano-particles, which has been confirmed in many experimental investigations including (Said, et al., 2013) and (Du & Tang, 2015).

### **8.3-4 Trapping phenomena**

A unique characteristic of the present solar pump design is the peristaltic wave feature achieved with distensible channel walls. This generates an intriguing phenomenon known as trapping, the formulation of an inside circulating bolus of nanofluid which migrates together with the wave at a fixed mean flow rate. In axisymmetric peristaltic flows, the positive motion

displacing fluid forward manifests in a torus shape. The bolus is trapped by the wave and therefore propagates forward with the same speed as that of the wave. However, in the current analysis, non-symmetric peristaltic pumping is studied owing to the difference in amplitudes of left and right walls i.e.  $a, b$  as 0.3 and 0.2 respectively. However, a single-phase difference of  $\pi/4$  between the left and right wall peristaltic waves is assumed. Although asymmetric peristaltic flows may generate reflux (or retrograde flux), that is, reversed motion of fluid in the opposite direction opposite to the net flow (i.e. in the negative  $x$ -direction) this has not been observed in the current work. The streamlines for different Reynolds viscosity parameter ( $\alpha$ ), heat source/sink parameter ( $\beta$ ) and Hartmann magnetic number ( $M$ ) for fixed values of other parameters are illustrated in Figs. 8.5-7.

Figs. 8.5(a-b) indicate that with increasing Reynolds number viscosity ( $\alpha$ ) the size of trapped bolus increases in amplitude in the right part (upper half space) of the channel and the reverse situation is generated in the left part (lower half space) of the channel wall. The impact of two different values for heat source parameter ( $\beta = 0$  and  $\beta = 0.5$ ) on trapping is shown in Fig. 8.6(a-b). One can notice that the size of the bolus increases in the vicinity of the right part of the channel with increasing heat source parameter. Fig. 8.7(a-b) clearly reveals that the size of tapped bolus increases with magnetic field effect i. e. as Hartmann number increases from the non-magnetic case ( $M = 0$ ) to the strongly magnetic case ( $M=1$ ) trapping is more potent in the channel regime.

### 8.3-5 Further Validation with Published Literature

Fig. 8.8 is explained to authenticate the results of proposed model without buoyance forces ( $Br = Gr = 0$ ), permeability parameter ( $K$ ) and Reynolds number viscosity parameter ( $\alpha$ )



with existing results (Srinivas & Kothandapani, 2008) in the asymmetric channel. It is perceived that the results of proposed model is significantly close to that described by Srinivas and Kothandapani (2008) across the entire width of the channel.

## 8.4 Concluding remarks

In this chapter an alternative solar collector design with magnetized nanoparticles has been studied. The influence of temperature-dependent viscosity, thermal radiation flux, nanoscale phenomena, heat generation, solutal (nanoparticle) buoyancy force and magnetic field on the two-dimensional flow, heat and species diffusion in this solar biomimetic (peristaltic) magnetohydrodynamic nanofluid pump containing a homogenous, isotropic porous medium. A modified (Buongiorno, 2006) nanofluid model is deployed which emphasizes thermophoretic body force and Brownian dynamic effects. To simulate solar thermal loading conditions the Rosseland radiative diffusion flux model is implemented and heat generation is included. Multiple amplitudes and phases are considered for the deformable channel walls. The moving boundary value problem is non-dimensionalised and perturbation solutions are derived for axial velocity, temperature and nanoparticle volume fraction. Validation is conducted with Maple numerical quadrature and volumetric flow rate, pressure difference and streamline distributions are also computed. The impact of Reynolds number viscosity ( $\alpha$ ), heat source/sink parameter ( $\beta$ ), Prandtl number ( $Pr$ ), Hartmann number ( $M$ ), thermal radiation ( $Rn$ ), permeability parameter ( $K$ ) and local nanoparticle Grashof number ( $Br$ ) on thermal and flow characteristics is visualized. The important findings of this chapter may be summarized as follows:

- The free pumping flux for a fluid with variable viscosity is greater than that for a fluid with constant viscosity.
- Greater peristaltic work has to be expended versus a greater pressure for a fluid with constant viscosity when compared with that fluid of variable viscosity.
- Pressure rise increases as the Reynolds viscosity of nanofluid and the heat generation effects are increased.
- Fluid axial velocity distribution is only enhanced with Reynolds viscosity increasing, in the inner core zone of pump channel, owing to the lesser impact of shear stress (wall friction) in the inner core.
- The nanoparticle fraction distribution exhibits the reverse behavior as compared with the temperature distribution under the influence of thermophoresis, Reynolds viscosity, Prandtl number and magnetohydrodynamic Hartmann number.
- With increasing Reynolds viscosity, the size of trapped bolus decreases in amplitude in the left section of the channel whereas the opposite behavior is observed in the right channel half space.
- Increasing radiation solar flux significantly heats the nanofluid whereas it inhibits nanoparticle diffusion in the regime.
- Increasing magnetic Hartmann number serves to reduce pressure differences in the pumping channel with a corresponding acceleration in the axial flow.
- Excellent accuracy, stability and convergence is achieved with both the perturbation solutions and MAPLE17 computations.
- Pressure difference is strongly boosted with increasing solutal Grashof number at both negative and positive flow rates and in all three solar peristaltic pumping regimes i.e.

the pumping region ( $\Delta p > 0$ ), the augmented pumping region ( $\Delta p < 0$ ), and the free pumping region ( $\Delta p = 0$ ).

- Solar thermal radiation flux energizes the nanofluid in the pump and elevates temperatures via the augmentation of the nanofluid thermal conductivity; however, increasing radiation flux acts to reduce pressure difference at positive flow rates (the reverse trend is computed at negative flow rates).
- The presence of a low permeability porous medium (solar wafer) is observed to strongly decelerate axial flow and suppress pressure difference generated in the pump whereas higher permeability manifests in flow acceleration and pressure difference elevation.
- At all values of Pressure rise in magnetohydrodynamic pumping is stifled with strong magnetic field whereas it is enhanced for electrically non-conducting nanofluids (i.e. when the external magnetic field in the pump circuit is switched off).

This chapter has presented a different nanoscale formulation (Buongiorno) to that in the previous chapters. Interesting features of the thermal characteristics have been identified for the first time. The current status of ANSYS FLUENT material physics does not permit multi-physical simulations of all the features included in the current model. Although more complex radiative models (e. g. Chandrasekhar discrete ordinates method- see chapter 7 for example, STS, P1 differential flux etc) are available in ANSYS FLUENT with the possibility of fluid-structure interaction (FSI) via coupling with ANSYS structural solvers, the magnetic nanofluid model cannot be analyzed presently with CFD codes. The numerical methodology elaborated herein has shown that alternative techniques are available for simulating more complex hybrid magnetic nanofluid solar peristaltic collectors which do feature Brownian motion and thermophoresis without the requirement for particle-based modelling (e. g. Lattice Boltzmann methods). Rosseland's model has provided a reasonable estimate of radiative effects from solar

heat flux loads; however, analysis has been confined to two-dimensional optically thick (dense) nanofluids. Future work could consider three-dimensional numerical simulations with ANSYS CFD software and in particular the effects of optical thickness and absorption coefficient which would allow a more precise evaluation of how much a given medium (nanofluid) interacts with thermal radiation. Radiative intensity falls by an exponential factor when optical thickness is unity. Physically optical thickness will be a function of the absorption coefficient, medium density and propagation distance in actual solar collectors whether rigid-walled or deformable. It may be advantageous to explore the P1 radiative flux model which although more computationally expensive predicts the actual influence of solar radiative flux more accurately than the Rosseland model and also is applicable to non-gray nanofluids although it may slightly over-predict radiative fluxes from localized heat sources or sinks. *Non-Darcy porous media* effects may also be examined which feature second order (quadratic) porous drag physics and can therefore extend the operational Reynolds number range for the current solar pump to higher values encroaching into the inertially-dominant range. Another important issue is the fact that while Buongiorno's model can analyze nanoparticle species diffusion (volume fraction) effects, Brownian dynamics and thermophoretic body force effects, and is clearly superior in this regard to the Tiwari-Das nanoparticle model employed in Chapters 3-7, it cannot however simulate the performance of specific nanoparticles e. g. Titanium dioxide, copper oxide, diamond etc. A possible remedy to this situation is the amalgamation of both Buongiorno's model with the Tiwari-Das model. Efforts in this direction have led to hybrid nanoscale models for nanofluids which furthermore have combined more than one nanoparticle type in the simulations and have also incorporated shape factors (spherical, ellipsoidal, brick shaped, nanotubes etc). Important progress in this regard has been led by my supervisor, Professor Anwar Bég and co-workers, lthough they have focused on electrokinetic applications

(Tripathi, et al., 2020) (Prakash, et al., 2020) and thus far have not explored solar collector systems. Finally, *supplementary electromagnetic phenomena* may also be examined in refinements of the present solar magnetic nanofluid peristaltic collector model, including Hall currents, Maxwell displacement currents, magnetic induction, Joule heating, oblique magnetic field (orientated at an angle to the longitudinal axis of the solar collector). All these aspects have been considered albeit separately (Prakash, et al., 2019) (Narla, et al., 2019) Finally, there is the possibility of utilizing nanoparticles for smart coatings on photovoltaic solar collectors, deploying tactic micro-organisms for hybrid solar fuel cells in combination with nanoparticles, studying hydrodynamic slip effects and in addition using Eringen micropolar rheological models for nanoparticle clustering aspects (spin effects of the nanoparticles) which I have also investigated but have not reported here in this PhD Thesis for brevity (Aneja, et al., 2020) (Nima, et al., 2020) (Mehmood, et al., 2020) (Mehmood, et al., 2018) (Bég, et al., 2020) (Bég, et al., 2019). These I hope to continue to explore for 3-dimensional direct absorber solar collector (DASC) nanofluid coating/hybrid nano-bio-microorganism design simulations (Kuharat, et al., 2021) (Kuharat, et al., 2020) in post-doctoral collaborations with my present supervisory team in the near future.

## **PUBLICATION NOTE**

A long version of this chapter was published in *J. Prakash, E.P. Siva, D Tripathi, S. Kuharat and O. Anwar Bég, Peristaltic pumping of magnetic nanofluids with thermal radiation and temperature-dependent viscosity effects: modelling a solar magneto-biomimetic nanopump, Renewable Energy, 133, 1308-1326 (2019).*

---

## Chapter 9 Conclusions, Recommendations and Future Research

### Directions

#### ABSTRACT

In this PhD a diverse spectrum of numerical simulations has been presented using ANSYS FLUENT CFD finite volume software (and for one case, MATLAB symbolic software with shooting quadrature) for *a variety of direct absorber solar collector geometries utilizing a wide range of metallic and non-metallic nanoparticles*. Both thermal buoyancy (natural convection) and forced convection scenarios have been addressed. Radiative heat transfer due to solar flux has also been simulated with 3 different approaches- Rosseland diffusion flux model, P1 Traugott differential and finally the Chandrasekhar discrete ordinates model (DOM). Although the Tiwari-Das volume fraction nanoscale model has been deployed for ANSYS FLUENT simulations, I have also utilized the Buongiorno nanoscale model for one nanofluid solar collector (pump) configuration (Chapter 8) in addition to considering magnetic properties of the nanoparticles. The superior thermal performance of base fluids doped with nanoparticles has been strongly confirmed and the simulations, where possible, have been compared with earlier experimental studies, showing good correlation. The benefits of nanoparticles include ease of deployment, avoidance of clogging and agglomeration and sustained performance in the field. The PhD has included 8 chapters, *6 of which (i.e. chapters 3-8) constitute novel contributions* and much of this research has been published in leading international journals and at international conferences. In this final chapter of the PhD a summary of the main findings is now given in particular with respect to *types of convection, nanoparticle types, solar collector geometry and radiative transfer model*. Later some directions are outlined for future work including non-Newtonian models, turbulence, solar day light tracking etc.

## 9.1 CONCLUSIONS

In this PhD, eight different metallic nanoparticles have been considered as aqueous nanofluids in a variety of configurations. These have shown different thermal enhancement features under different convection conditions and geometrical enclosures. The aspect ratio has also been addressed in some scenarios. The main conclusions drawn are summarized below:

### 9.1-1 Natural Convection and Inclination Effects

Chapters 3-7 show that nanofluids influence natural and forced convection in solar collectors. For a **natural convection**, it clearly shows that the increase in volume fraction enhances the heat transfer of the solar collector, as this increases fluid thermal conductivity. However, an increase in volume fraction can enhance heat transfer of the fluid up to a certain value after which subsequent increase in volume fraction has no tangible effect. **Rayleigh number** also has a big influence on heat transfer in natural convection, as increasing the Rayleigh number enhances the heat transfer of the fluid due to thermal buoyancy force effects. Chapter 3 shows the changes in the thermal flow characteristics with increasing Rayleigh number which manifest with the emergence of a dual structure in the circulation. Temperatures generally increase as the Rayleigh number becomes greater for the both the silver-water nanofluid case and titanium oxide water nanofluid case, although greater temperatures are computed in the former and slightly higher Nusselt numbers in the latter. In Chapter 4, simulations of nanofluid convection in the 2-D trapezoid and the 3-D prismatic solar collector also showed the same behaviour. However, in Chapter 5, various inclinations of the collector is were also investigated, which scales the gravity force and therefore modifies the thermal buoyancy force. With greater inclination of the enclosure, there is a progressive elevation in heat transfer from

the left hot face (heated wall) towards the opposite cold wall, and temperatures are elevated mainly in the upper left zone with a more extensive warming in the central zone.

### **9.1-2 Solar Collector Enclosure Geometrical Effects**

**Geometry** is a complex aspect which also influences the heat transfer in natural convection. This also involves the influence of the heating location of the geometry and boundary conditions. In this research three geometries (square, rectangle, and trapezoid) have been investigated in 2-Dimensions in chapter 3-4, and three geometries (annulus, cube, prism) have been investigated in 3-Dimensions in chapter 5 and 6. All studies suggested that the *high aspect ratio* (narrow geometry) improved the heat transfer relative to the *low aspect ratio* (wider geometry), where the aspect ratio is defined as the ratio of base length relative to height of the solar collector geometry. Chapter 3 showed that for high aspect ratio geometries, higher temperatures are generated in the enclosure and the hotter titanium oxide water nanofluid reaches deeper into the enclosure space. At lower aspect ratio (less than or equal to unity) geometries, dual thermal zones are generated in the upper and lower zones of the enclosure. A substantial deceleration in the titanium oxide water nanofluid flow is induced initially with a decrease in aspect ratio from 4 to 2; however, this pattern is reversed with subsequent decrease in aspect ratio (aspect ratio of 4/3, 1 and 0.5) and the flow is accelerated. The *singular symmetric cell structure* observed at higher aspect ratio is modified into a *non-symmetric laterally elongated structure* at low aspect ratios. For the trapezoid geometry mentioned in Chapter 4, it is apparent that a strong negative boundary inclination (wall slope of -10 degrees) acts as a heat sink which moves closer to the heat source, resulting in improved heat transfer to the walls of the cavity. Again, in Chapter 5, 3-D simulation results show that higher geometrical aspect ratios lead to improved heat transfer in the region with deeper penetration of warmer zones in the enclosure.



### 9.1-3 Forced Convection Effects

Chapters 3-4 investigated natural convection inside the solar collector in 2D and Chapter 5 in 3D, and both analyses provided excellent knowledge of the thermofluid characteristics of various metallic and non-metallic nanofluids in natural convection, as concluded previously. However, the 3-dimensional simulation for forced convection inside solar collectors has been found to be more representative of actual solar collector applications and provides a more dependable approach for comparing actual efficiencies of various nanofluids (metallic and non-metallic). Therefore, further research (ANSYS FLUENT simulations) has been conducted to elucidate the **forced convection** in direct absorption solar collectors in Chapters 6 and 7. Chapter 6 investigated forced convective heat transfer in a solar tube (annulus) type direct absorption solar collector. Chapter 7 simulated the forced convective heat transfer in a plate type direct absorption solar collector. From Chapters 6-7, the heat transfer efficiency of water based nanofluids can be listed in order of highly efficient to the least efficient for Silver, Graphite, Copper, Copper oxide, Titanium oxide, Aluminium, and pure water. It is concluded that overall *silver nanoparticles* provide consistently high thermal efficiency, although graphite is also very impressive and even other metallic nanofluids (copper, copper oxide, titanium oxide and aluminium) produce much better heat transfer performance compared with conventional base fluids (water) used in traditional direct absorber solar collectors.

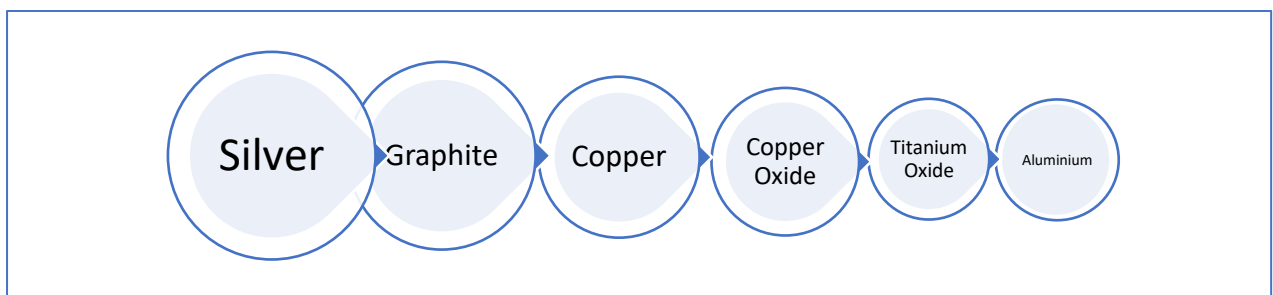


**Fig. 9.1 Metallic nanoparticles considered in PhD**

#### 9.1-4 Radiative Heat Transfer aspects

In this PhD thermal radiation heat transfer has been included in all the chapters; three different models have been used which are the Rosseland diffusion, P1 (Traugott) first order spherical harmonics model and the Chandrasekhar discrete ordinates model (DOM). All three models are all available in ANSYS FLUENT. The computations have generally shown that Rosseland's model provides a faster and quite reasonable estimate of radiative effects from solar heat flux loads; however, analysis has been confined to two-dimensional optically thick (dense) nanofluids. Rosseland's model does not need as much mesh density refinement or compilation times. Future work could consider three-dimensional numerical simulations with ANSYS CFD software and in particular the effects of optical thickness and absorption coefficient which would allow a more precise evaluation of how much a given medium (nanofluid) interacts with thermal radiation. Radiative intensity falls by an exponential factor when optical thickness is unity. Physically optical thickness will be a *function of the absorption coefficient*, medium density and propagation distance in actual solar collectors whether rigid-walled or deformable. The P1 radiative flux model provides more accurate estimates of radiative heat transfer flux but is significantly more computationally expensive. It more precisely predicts the actual influence of solar radiative flux which cannot be achieved with the Rosseland model; the P1 model is applicable to non-gray nanofluids although it may slightly over-predict radiative fluxes from localized heat sources or sinks. Chandrasekhar discrete ordinates method (DOM) is available for more robust simulation of non-gray fluids which allows wavelength-dependent optical properties of the working fluid to be included in radiative transfer analysis. The model spans the entire range of optical thicknesses, which provides a full range of capability for solar engineering simulation. It also allows the solution of *radiation at semi-transparent walls*, which is an extremely useful feature for DASCs as these types of collectors often feature a

glazing glass cover. However, the downside is that solving a problem with a fine angular discretization may be CPU-intensive and therefore more expensive.

ANSYS FLUENT while restricted to single phase nanoscale models does provide a very powerful methodology for studying different geometries, nanoparticles and convection and radiative scenarios. Of course, only *steady state and laminar* flows were investigated, and these could be extended to *transient behaviour* and *turbulent nanofluid dynamics* in the future. However, very interesting and feasible predictions of realistic nanofluid DASC flows for multiple scenarios have been successfully simulated with the ANSYS FLUENT CFD platform in this PhD and have provided a solid and validated base for future computational studies.

### **9.1-5 Magnetic metallic nanoparticles**

In the last chapter (chapter 8) an alternative solar collector design with magnetized nanoparticles has been studied. The influence of temperature-dependent viscosity, thermal radiation flux, nanoscale phenomena, heat generation, solutal (nanoparticle) buoyancy force and magnetic field on the two-dimensional flow, heat and species diffusion in this solar biomimetic (peristaltic) magnetohydrodynamic nanofluid pump containing a homogenous, isotropic porous medium has been simulated. The nanoparticle fraction distribution exhibits the *reverse behaviour as compared with the temperature distribution* under the influence of thermophoresis, Reynolds viscosity variation, Prandtl number and magnetohydrodynamic Hartmann number (ratio of Lorentz magnetic drag force to viscous hydrodynamic force). Solar thermal radiation flux energizes the nanofluid in the solar pump and elevates temperatures via the augmentation of the nanofluid thermal conductivity; however, increasing radiation flux acts to reduce pressure difference at positive flow rates (the reverse trend is computed at negative flow rates). The presence of a low permeability porous medium (solar wafer) is observed to

strongly decelerate axial flow and suppress pressure difference generated in the pump whereas higher permeability manifests in flow acceleration and pressure difference elevation. At all values of pressure rise in magnetohydrodynamic pumping is stifled with strong magnetic field whereas it is enhanced for electrically non-conducting nanofluids (i. e. when the external magnetic field in the pump circuit is switched off). Although the simulations were restricted to Darcian porous media (viscous dominated) and conducted in MATLAB symbolic software (not ANSYS FLUENT, since the latter does not permit Buongiorno nanoscale modelling), *non-Darcy porous media* effects may also be examined. The Darcy-Forchheimer-Brinkman model features second order (quadratic) porous drag physic and boundary vorticity and can therefore extend the operational Reynolds number range for the current solar pump to higher values encroaching into the inertially-dominant range. These aspects will be considered in future post-doctoral investigations.

### **9.1-6 Future pathways**

The present PhD has examined a number of aspects of nanofluid solar collector performance with different combinations of geometries (annular, trapezium, rectangular, prismatic etc.) and robust radiative transfer models. The main two nanoscale models available were also deployed i. e. Tiwari-Das (chapters 3,4,5,6,7) and Buongiorno (chapter 8). However as with any study not all phenomena could be examined. Generally Newtonian fluids only in the laminar regime. Here I have provided some important suggestions for future pathways which define some good directions for extending my PhD. Already I have started to examine non-Newtonian nanofluids, electrical nanofluids and hydrodynamic/thermal slip effects. These are just some of the areas which are now growing in 21<sup>st</sup> century solar energy engineering and in which computational fluid dynamics is critical.

### **9.1-7 Extension to Non-Newtonian nanofluid systems**

Many studies have verified that nanofluids exhibit strong non-Newtonian characteristics associated with the presence of nanoparticle clusters e. g. stress relaxation, normal stress differences, variation in the viscosity, non-linearity of creeping, threshold stress, shear thickening/thinning, temperature-dependent viscosity and memory fluid behavior. Many experimental and theoretical studies have supported this non-linear behavior of nanofluids. Suspension of nano-sized particles in conventional base fluid or base fluid itself contributes to a modification in the rheology and leads to non-Newtonian behavior of nanofluids under different shear rate conditions. (Tseng & Chen, 2003) have demonstrated the pseudoplastic nature of nanofluid (suspensions of nickel-terpineol) experimentally. The experimental study of (Lu, 2007) showed the shear thinning property of nanofluid with variation in rate of shear. (Phuoc & Massoudi, 2009) observed viscoplastic non-Newtonian behavior (yield stress) in nanofluids. An experimental justification has been given by (Chen, et al., 2009) relating to nanofluid dependence on temperature and concentration and this also constitutes a non-Newtonian property. To study thermo-fluid behaviour of real nanofluids, it is necessary to adopt robust 'non-Newtonian theory' in conjunction with an appropriate 'nanoscale fluid model'. Chemical engineers and polymer physicists have developed a wide range of comprehensive rheological fluid models e. g. integral, rate and differential type non-Newtonian models. These can be utilized also to elucidate the non-linear shear stress-strain behaviour in nanofluids. The viscoelastic third-grade fluid model is another thermodynamically rigorous formulation which belongs to the Reiner-Rivlin subclass of differential type of fluids, that are known to exhibit relationships between the stress history and deformation gradient. This model also simulates quite accurately the shear thickening (dilatant) & shear-thinning (pseudoplastic) features observed in nanofluid suspensions. It has been deployed by (Hiremath, et al., 2019) in

viscoelastic nanofluid coating flows. The second order Reiner-Rivlin model (viscoelastic) has been used in (Rana, et al., 2017). Cross, Sisko and Williamson viscoelastic rheological models have been considered in (Rao, et al., 2017), (Ali, et al., 2018) and (Nagendra, et al., 2017) respectively. Another branch of non-Newtonian models are micromorphic models introduced by Eringen in the 1960s. These can simulate the spin of nanoparticles and also larger parcels of fluids surrounding them (micro-elements) and are much more elegant than any other non-Newtonian model. They can easily be unified with the Buongiorno or Tiwari-Das nanoscale models. Another advantage of micromorphic models is that the classical Newtonian (Navier-Stokes) model can be retrieved when micromorphic effects are negated. Recent applications of micropolar nanofluid flows include (Latiff, et al., 2016), (Kumar, et al., 2019) and (Bég, et al., 2020). Couple stress (polar) fluids can also be used for rheological characteristics of nanofluids and have been examined by (Umavathi & Bég, 2020). Finally, power-law and exponential viscosity models (e.g. Reynolds model) also offer an alternative approach to simulate rheological behaviour of nanofluids and I have been explored these in solar coating (Prakash, et al., 2019) and solar pump (Mehmood, et al., 2018) flows (chapter 8). Other investigations include (Bég, et al., 2019). However, these models have thus far not been explored for 3-D solar nanofluid collectors and this is a very rich area in the future to explore.

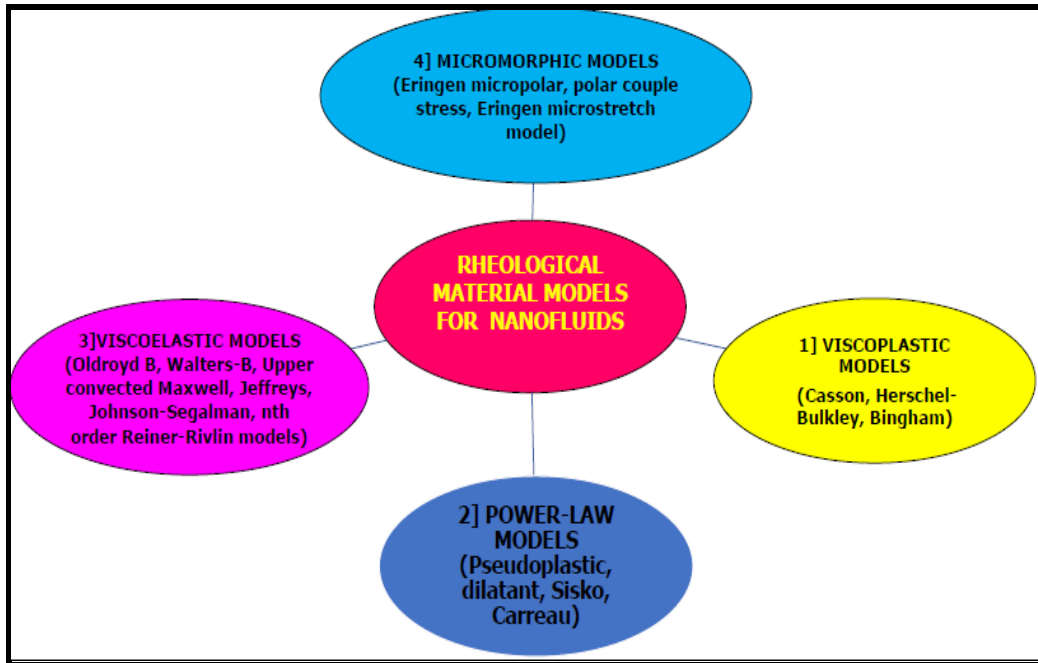


Figure 9.2 Range of robust non-Newtonian models available for nanofluids

### 9.1-8 Extension to bioconvection in solar nanofluid collectors

A further refinement is the incorporation of motile micro-organisms in direct absorber solar collector nanofluid systems. These feature different taxes e. g. chemotactic, gyrotactic, phototactic, magneto-tactic etc. which respond to different stimuli (chemical concentration, torque, light, magnetic field etc). Bioconvection occurs in these micro-organisms and they can be combined with nanoparticles to achieve improved stability and mass diffusion. During my PhD I also investigated several problems in nanofluid bioconvection although I only considered solar coatings for photovoltaic collectors (Nima, et al., 2020) (Aneja, et al., 2020). These studies all assumed that the nanofluid is dilute and no interaction between nanoparticles and micro-organisms occurs. However, no serious work has been reported of micro-organism doping of solar nanofluid collectors and this again offers a good pathway for ANSYS FLUENT 3-D simulations.

### **9.1-9 Extension to Include Turbulence Effects**

It is also noteworthy that all the simulations in this PhD have been restricted to laminar flows. In field solar collector operators, of course turbulence may also arise. Several investigators have examined turbulent nanofluid DASC flows. These include (Behroyan, 2015) on copper water nanofluids in forced convection in a tube and (Zhang, 2021)  $\text{Al}_2\text{O}_3\text{-CuO/water}$  nanofluid turbulent transport. Of course, many turbulence models are available in ANSYS FLUENT e.g., k-epsilon, LES, SST, K-omega etc. An important consideration is the much greater mesh densities needed for turbulent flows and also the requirement for better correlations of nanoparticle behaviour from experiments.

Extension to consider solar daylight tracking for different geographical locations by rotating solar panels to follow the sun across the sky, solar trackers can generate more power. These solar power plants can be damaged at high wind speeds. ANSYS has a facility for simulating real time solar daylight tracking, which Single-axis solar trackers that automatically rotate to follow the sun from east to west can generate 10 percent to 30 percent more power than stationary or “fixed tilt” solar panels. Certain wind conditions can cause a torsional instability that damages solar trackers.



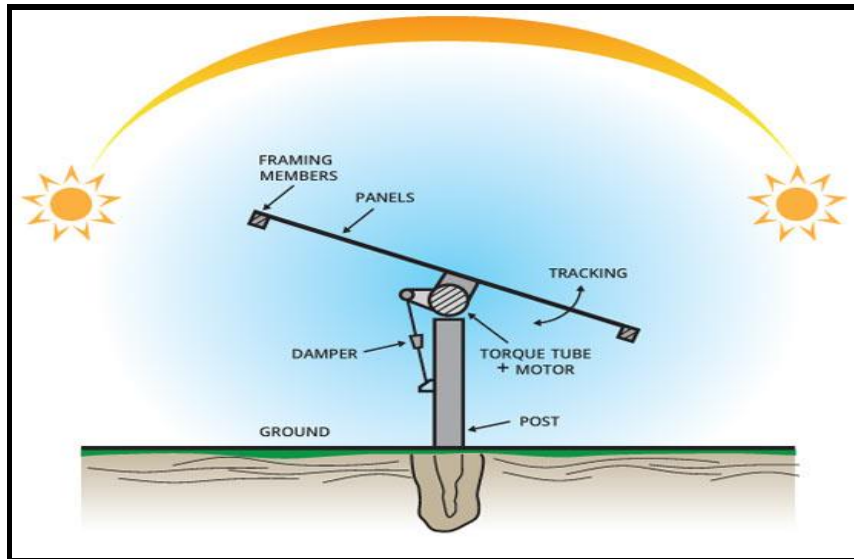
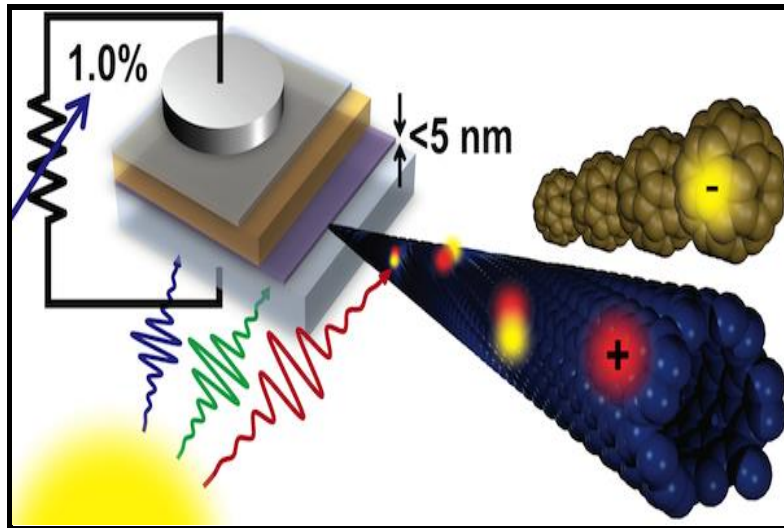


Figure 9.3 Solar daylight tracking

### 9.1-10 Extension to More Refined Nanopowder Coatings and Carbon Nanotube Coatings

Although in this PhD generally spherical nanoparticles – either metallic or carbon-based- have been considered, there are many other types of geometry available for nanoparticles. These include carbon nanotubes (CNTs), nano-shells (Mahbubul, 2018) and also different shape factors for metallic nanoparticles (bricks, ellipsoids, cylinders etc). Nanofluid transport with these approaches has been considered by a number of researchers e.g. (Akbar, et al., 2015) using elegant shape factor relations which permit different types of nanoparticles to be simulated and surface areas to be considered.



**Figure 9.4 CNT for nanofluid collectors-** courtesy MIT Energy Institute, USA.

The carbon nanotubes are allotropes of carbon in which the length to diameter ratio exceeds 1,000,000 to produce very high tensile strength, unique electrical properties, and a very efficient conductor of heat.

## REFERENCES

1. Abadshapoori, M. H. & Saidi, M. H., 2018. Lattice Boltzmann simulation of TiO<sub>2</sub>-water nanofluid in a curved boundary domain at high Rayleigh numbers. *Computers & Fluids*, Volume 168, pp. 159-169 .
2. Abid, M., Ratlamwala, T. & Atikol, U., 2016. Performance assessment of parabolic dish and parabolic trough solar thermal power plant using nanofluids and molten salts. *Int. J. Energy Res.* , Volume 40 , p. 550–563.
3. Abu-Nada, E. & Oztop, H., 2009. Effects of inclination angle on natural convection in enclosures filled with Cu–water nanofluid. *International Journal Heat Fluid Flow*, 30(4), pp. 669-678.
4. Ahmed, M. & Eslamian, M., 2015. Numerical simulation of natural convection of a nanofluid in an inclined heated enclosure using two-phase lattice Boltzmann method: accurate effects of thermophoresis and Brownian forces. *Nanoscale Research Letters*, Volume 10, pp. 296-307.
5. Akbar, N. S., Tripathi, D. & Bég, O. A., 2015. Modelling nanoparticle geometry effects on peristaltic pumping of medical magnetohydrodynamic nanofluids with heat transfer. *J. Mechanics in Medicine and Biology*, 16(2).
6. Akbar, N. S., Tripathi, D. & Bég, O. A., 2016. Modeling nanoparticle geometry effects on peristaltic pumping of medical magnetohydrodynamic nanofluids with heat transfer. *J. Mech. Med. Biol.* , Volume 16.
7. Akbarzadeh, P. & Fardi, A. H., 2018. Natural convection heat transfer in 2d and 3d trapezoidal enclosures filled with nanofluid. *Journal of Applied Mechanics and Technical Physics*, Volume 59, p. 292–302 .

8. Akbarzadeh, P. & Fardi, A. H., 2018. Natural convection heat transfer in 2d and 3d trapezoidal enclosures filled with nanofluid. *Journal of Applied Mechanics and Technical Physics*, Volume 59, p. 292–302.
9. Alashkar, A. & Gadalla, M., 2018. Performance analysis of an integrated solar-based power generation plant using nanofluids. *Int. J. Energy Res.* .
10. Ali, H. M. et al., 2015. Experimental investigation of convective heat transfer augmentation for car radiator using ZnO-water nanofluids. *Energy*, Volume 84, pp. 317-324.
11. Ali, N. et al., 2018. Computational study of unsteady non-Newtonian blood flow containing nano-particles in a tapered overlapping stenosed artery with heat and mass transfer. *NanoScience and Technology: An International Journal*, 9(3), p. 247–282.
12. Ali, N. et al., 2015. Unsteady non-Newtonian blood flow through a tapered overlapping stenosed catheterized vessel. *Mathematical Biosciences*, Volume 269, pp. 94-103.
13. Al-Nimr, M. & Alkam, M., 1998. A modified tubeless solar collector partially filled with porous substrate. *Renew. Energy*, Volume 13 , p. 165–173.
14. Alsaady, M. et al., 2018. An experimental investigation on the effect of ferrofluids on the efficiency of novel parabolic trough solar collector under laminar flow conditions.. *Heat Transf. Eng.* , Volume 118, pp. 742-751.
15. Al-Srayyih, B., 2019. Natural convection flow of a hybrid nanofluid in a square enclosure partially filled with a porous medium using a thermal non-equilibrium model. *Physics of Fluids*, Volume 31.
16. Aminossadati, S., Raisi, A. & Ghasemi, B., 2011. Effects of magnetic field on nanofluid forced convection in a partially heated microchannel. *Int J Nonlinear Mech*, Issue 46, pp. 1373-1382.

17. Amirsom, N. et al., 2019. Computation of melting dissipative magnetohydrodynamic nanofluid bioconvection with second order slip and variable thermophysical properties. *Applied Sciences (Applied Biosciences and Bioengineering section)*, Issue 9, pp. 1-22.
18. Aneja, M., Sharma, S., Kuharat, S. & Bég, O. A., 2020. Computation of electroconductive gyrotactic bioconvection under nonuniform magnetic field: Simulation of smart bio-nanopolymer coatings for solar energy. *Int. J. Modern Physics B*, p. 33.
19. Aneja, M., Sharma, S., Kuharat, S. & Bég, O. A., 2020. Computation of electroconductive gyrotactic bioconvection under nonuniform magnetic field: Simulation of smart bio-nanopolymer coatings for solar energy. *Int. J. Modern Physics B*, Volume 33.
20. ANSYS, Inc, 2018. *ANSYS FLUENT Theory Manual ver 19.1*, s.l.: s.n.
21. Arani, A., Ababaei, A., Sheikhzadeh, G. & Aghaei, A., 2017. Numerical simulation of double-diffusive mixed convection in an enclosure filled with nanofluid using Bejan's heatlines and masslines. *Alexandria Engineering Journal*, 57(3), pp. 1287-1300.
22. Azari, A., Kalbasi, M., Derakhshandeh, M. & Rahimi, M., 2013. An Experimental Study on Nanofluids Convective Heat Transfer Through a Straight Tube under Constant Heat Flux.. *Chinese Journal of Chemical Engineering*, 21(10), pp. 1082-1088.
23. Azari, A., Kalbasi, M. & Rahimi, M., 2014. CFD and experimental investigation on the heat transfer characteristics of alumina nanofluids under the laminar flow regime. *Brazilian Journal of Chemical Engineering*, 31(2), pp. 469-481.
24. Baek, S. et al., 2014. Au@Ag Core–Shell Nanocubes for Efficient Plasmonic Light Scattering Effect in Low Bandgap Organic Solar Cells. *ACS Nano* , 8(4), pp. 3302-3312.

25. Bait, O. & Si-Ameur, M., 2018. Enhanced heat and mass transfer in solar stills using nanofluids: A review.. *Solar Energy*, Volume 170, pp. 694-722.
26. Bait, O. & Si-Ameur, M., 2018. Enhanced heat and mass transfer in solar stills using nanofluids: A review.. *Solar Energy*, Volume 170, pp. 694-722..
27. Balakinab, B., Zhdaneev, O., Kosinska, A. & Kutsenko, K., 2019. Direct absorption solar collector with magnetic nanofluid: CFD model and parametric analysis. *Renewable Energy*, Volume 136, pp. 23-32.
28. Bardsgard, R., Kumzmenkov, D. M., Kosinski, P. & Balakin, B. V., 2020. Eulerian CFD model of direct absorption solar collector with nanofluid. *Journal of renewable and sustainable energy*, Issue 12.
29. Bég, O. A., 2018. Nonlinear multi-physical laminar nanofluid bioconvection flows: Models and computation. In: A. Sohail & Z. Li, eds. *Computational Approaches in Biomedical Nano-Engineering*. s.l.: Wiley, pp. 113-145 .
30. Bég, O. A. et al., 2016. Computational modeling of heat transfer in an annular porous medium solar energy absorber with the P1-radiative differential approximation. *J. Taiwan Inst. Chem. Eng.* , Volume 66, p. 258–268..
31. Bég, O. A. et al., 2020. Unsteady nonlinear magnetohydrodynamic micropolar transport phenomena with Hall and ion-slip current effects: numerical study. *Int. J. Applied Electromagnetics & Mechanics*, pp. 1-33 .
32. Bég, O. A. et al., 2020. Unsteady nonlinear magnetohydrodynamic micropolar transport phenomena with Hall and ion-slip current effects: numerical study. *Int. J. Applied Electromagnetics & Mechanics*, pp. 1-33 .

33. Bég, O. A. et al., 2018. Experimental study of improved rheology and lubricity of drilling fluids enhanced with nano-particles.. *Applied Nanoscience*, 8(5), pp. 1069-1090.
34. Bég, O. A., Islam, B., Shamshuddin, M. D. & Bég, T. A., 2019. Computational fluid dynamics analysis of moisture ingress in aircraft structural composite materials. *Arabian J. Science Engineering* .
35. Bég, O. A. et al., 2020. Computation of radiative heat transfer in solar direct absorber collector flows with robust numerical methods and multi-physical effects. In: K. S. Rawat, ed. *Understanding Thermal Radiation*. New York: Nova Science, pp. 200-310.
36. Bég, O. A. et al., 2019. Magnetic nano-polymer flow with magnetic induction and nanoparticle solid volume fraction effects: solar magnetic nano-polymer fabrication simulation. *Proc. IMechE-Part N: J Nanoengineering, Nanomaterials and Nano-systems*.
37. Bég, O. A. et al., 2019. Magnetic nano-polymer flow with magnetic induction and nanoparticle solid volume fraction effects: solar magnetic nano-polymer fabrication simulation. *Proc. IMechE-Part N: J Nanoengineering, Nanomaterials and Nano-systems* .
38. Bég, O. A. & Tripathi, D., 2011. Mathematica simulation of peristaltic pumping with double-diffusive convection in nanofluids: a bio-nano-engineering model. *Proc. Inst. Mech. Eng. Part N J. Nanoeng. Nanosyst.*, Volume 225, p. 99–114.
39. Bég, O. A., Uddin, M. J. & Rashidi, M. M. a. K. N., 2014. Double-diffusive radiative magnetic mixed convective slip flow with Biot and Richardson number effects. *J. Engineering Thermophysics*, 2(23), pp. 79-97 .

40. Bég, O., Basir, M., Uddin, M. & Ismail, A., 2017. Numerical study of slip effects on asymmetric bioconvective nanofluid flow in a porous microchannel with an expanding/contracting upper wall using Buongiorno's model. *J. Physics*, Issue 55, pp. 2048-2063 .
41. Bég, O., Khan, W. & Uddin, M., 2015. Multiple slip effects on unsteady magnetohydrodynamic nanofluid transport with heat generation/absorption effects in temperature dependent porous media. *J. Porous Media*, Issue 18, pp. 907-922.
42. Bég, O., Khan, W. & Uddin, M., 2016. Multiple slip and variable transport property effects on magneto-hydrodynamic dissipative thermo-solutal convection in porous media. *ASCE J. Aerospace Engineering* .
43. Bég, O. et al., 2019. Modeling magnetic nanopolymer flow with induction and nanoparticle solid volume fraction effects: Solar magnetic nanopolymer fabrication simulation. *Part N: Journal of Nanomaterials, Nanoengineering and Nanosystems*, 1(233), pp. 27-45..
44. Beg, O. et al., 2020. Computation of radiative-convective heat transfer in direct absorber solar collectors. In: *Understanding thermal radiation*. New York: Nova Science, pp. 300-409.
45. Bég, O., Uddin, M., Bég, T. & Gorla, R., 2016. Numerical simulation of self-similar thermal convection from a spinning cone in anisotropic porous medium. *J. Hydrodynamics Series B*, 2(28), pp. 184-194.
46. Bég, O. et al., 2019. Modelling mass transfer from a rotating cone in anisotropic porous media with Stefan blowing and Navier slip. *Indian J. Physics* .



47. Bég, O., Uddin, M. & Khan, W., 2015. Bioconvective non-Newtonian nanofluid transport in porous media containing micro-organisms in a moving free stream. *J. Mechanics Medicine Biology*, Issue 15.
48. Bég, O., Zubair, A., Kuharat, S. & Babaie, M., 2018. *CFD simulation of turbulent convective heat transfer in rectangular mini-channels for rocket cooling applications*. Istanbul, ICHTFM 2018: 20th International Conference on Heat Transfer and Fluid Mechanics WASET.
49. Behroyan, I., 2015. Turbulent forced convection of Cu–water nanofluid: CFD model comparison. *International Communications in Heat and Mass Transfer*, Volume 67, pp. 163-172.
50. Bellos, E., Said, Z. & Tzivanidis, C., 2018. The use of nanofluids in solar concentrating technologies: A comprehensive review. *Journal of Cleaner Production*, Volume 196, pp. 84-99.
51. Bhalla, V. & Tyagi, H., 2017. Solar energy harvesting by cobalt oxide nanoparticles, a nanofluid absorption based system. *Sustain. Energy Technol. Assess.* , Volume 24 .
52. Bhargava, R. et al., 2017. Finite element simulation of nonlinear convective heat and mass transfer in a micropolar fluid-filled enclosure with Rayleigh number effects. *Int. J. Applied Computational Mathematics*, 2(3), p. 1347–1379 .
53. Bhatti, M. M., Zeeshan, A. & Ellahi, R., 2016. Endoscope analysis on peristaltic blood flow of Sisko fluid with Titanium magneto-nanoparticles. *Comput. Biol. Med.* , Volume 78, p. 29–41.
54. Bouhaleb, M. & Abbassi, H., 2014. Natural convection of nanofluids in enclosures with low aspect ratios. *International Journal of Hydrogen Energy*, 39(27), pp. 15275-15286.

55. Bozorgan, N. & Shafahi, M., 2015. Performance evaluation of nanofluids in solar energy: a review of the recent literature. *Micro and Nano Systems Letters*, 3(1).
56. Braga, E. J. & de Lemos, M. J. S., 2009. Laminar and turbulent free convection in a composite enclosure. *Int. J. Heat Mass Transfer*, Volume 52, pp. 588-596.
57. Branson, B. T. et al., 2013. Nanodiamond nanofluids for enhanced thermal conductivity. *ACS Nano*, 7(4), pp. 3183-3189 .
58. Bretado de los Rios, M., Rivera-Solorio, C. & García-Cuéllar, A., 2018. Thermal performance of a parabolic trough linear collector using Al<sub>2</sub>O<sub>3</sub>/H<sub>2</sub>O nanofluids.. *Renewable Energy*, Volume 122, pp. 665-673.
59. Buongiorno, J., 2006. Convective transport in nanofluids. *ASME J. Heat Transfer*, Issue 128, pp. 240-250.
60. Campos, C. et al., 2019. Palza H. About the relevance of particle shape and graphene oxide on the behavior of direct absorption solar collectors using metal based nanofluids under different radiation intensities.. *Energy Conversion and Management*, Volume 181, pp. 247-257.
61. Chandrasekhar, S., 1960. *Radiative Transfer*. Oxford, New York: s.n.
62. Chang, H. et al., 2004. A study of magnetic field effect on nanofluid stability of CuO. *Materials Transactions*, 4(45), pp. 1375-1378.
63. Chatterjee, D., Kumar, S. G. & Mondala, B., 2014. Mixed convective transport in a lid-driven cavity containing a nanofluid and a rotating circular cylinder at the center. *International Communications in Heat and Mass Transfer*, Volume 56, pp. 71-78.
64. Chaudhari, K., Walke, P., Wankhede, U. & Shelke, R., 2015. An Experimental Investigation of a Nanofluid (Al<sub>2</sub>O<sub>3</sub> + H<sub>2</sub>O) Based Parabolic Trough Solar Collectors. *Br. J. Appl. Sci. Technol*, Volume 9, p. 551–557.

65. Chen, H., Ding, Y. & Lapkin, A., 2009. Rheological behaviour of nanofluids containing tube / rod-like nanoparticles. *Powder Technology*, Volume 194, p. 132–141.
66. Chiang, Y., Chieh, J. & Ho, C., 2012. The magnetic-nanofluid heat pipe with superior thermal properties through magnetic enhancement, *Nanoscale Res Lett* , 1(7), p. 322.
67. Chin, R.-M.et al., 2018. Preparation of highly dispersed and concentrated aqueous suspensions of nanodiamonds using novel diblock dispersants.. *Journal of Colloid and Interface Science*, Volume 520, pp. 119-126.
68. Choi, S. U. S. & Eastman, J. A., 1995. Enhancing thermal conductivity of fluids with nanoparticles. *San Francisco, ASME International Mechanical Engineering Congress and Exposition*.
69. Cingarapu, S., Singh, D., Timofeeva, E. V. & Moravek, M. R., 2014. Nanofluids with encapsulated tin nanoparticles for advanced heat transfer and thermal energy storage. *Int. J. Energy Res.* , Volume 38 , p. 51–59.
70. Cramer, K. & Pai, S., 1973. *Magnetofluid Dynamics for Engineers and Applied Physicists*. New York: McGraw-Hill Book Company.
71. Cristaldo, C., Bakuzis, A., De Bortoli, A. & Fachini, F., 2011. Extended numerical analysis for the magnetic nanofluid droplet heating and vaporization. *Rio de Janeiro, Brazil, Thermal Sciences and Engineering Workshop em Engenharia e Tecnologia Espaciais*.
72. Das, C., Wang, G. & Payne, F., 2013. Some practical applications of magnetohydrodynamic pumping. *Sens. Actuators Phys.*, Volume 201, p. 43–48.
73. Das, S. K., Choi, S. U. S., Yu, W. & Pradeep, T., 2007. *Nanofluids*. s.l.:Wiley Interscience.

74. Daud, H. A., Li, Q., Bég, O. A. & AbdulGhani, S., 2011. Numerical investigations of wall-bounded turbulence. *Proc. Institution of Mechanical Engineers-Part C: Journal of Mechanical Engineering Science*, Volume 225, pp. 1163-1174.
75. Daud, H. A., Li, Q., Bég, O. A. & AbdulGhani, S., 2012. Numerical investigation of film cooling effectiveness and heat transfer along a flat plate. *Int. J. Applied Math. Mechanics*, 8(17), pp. 17-33.
76. De Schepper, E., Van Passel, S. & Lizin, S., 2015. Economic benefits of combining clean energy technologies: the case of solar photovoltaics and battery electric vehicles. *Int. J. Energy Res.* , Volume 39 , p. 1109–1119.
77. Dehaj, M. & Mohiabadi, M., 2019. Experimental investigation of heat pipe solar collector using MgO nanofluids. *Solar Energy Materials and Solar Cells*, Volume 191, pp. 91-99.
78. Dobrolyubov, A. & Douchy, G., 2002. Peristaltic transport as the travelling deformation waves. *J. Theor. Biol.* , Volume 219, p. 55–61.
79. Duffie, J. A., Beckman, W. A. & Blair, N., 2017. *Solar Engineering of Thermal Processes, Photovoltaics and Wind*. 5 ed. USA: Wiley.
80. Duffie, J. & Beckman, W., 2013. *Solar Engineering of Thermal Processes*. 4 ed. New York: Wiley, .
81. Dugaria, S., Bortolato, M. & Del Col, D., 2018. Modelling of a direct absorption solar receiver using carbon based nanofluids under concentrated solar radiation. *Renewable Energy*, Volume 128, pp. 495-508.
82. Du, M. & Tang, G., 2015. Optical property of nanofluids with particle agglomeration. *Sol. Energy*, Volume 122, p. 864–872.

83. Du, P. et al., 2014. A theoretical study of the initiation, maintenance and termination of gastric slow wave re-entry. *Math. Med. Biol. J. IMA.* , Volume 32 , p. 405–423.
84. Eldabe, N., Ibashbeshy, M. & Elsai, E., 2013. Effect of magnetic field on flow and heat transfer over an unsteady stretching surface embedded in a porous medium filled with nanofluid. *Int J Energy Tech* , 5(6), pp. 1-8.
85. Esfandiary, M., Mehmandoust, B., Karimipour, A. & Pakravan, H., 2016. Natural convection of Al<sub>2</sub>O<sub>3</sub>–water nanofluid in an inclined enclosure with the effects of slip velocity mechanisms: Brownian motion and thermophoresis phenomenon. *International Journal of Thermal Sciences*, Volume 105, pp. 137-158.
86. Farhana, K. et al., 2018. *CFD modelling of different properties of nanofluids in header and riser tube of flat plate solar collector*. Pahang, Malaysia, IOP Conference Series: Materials Science and Engineering.
87. Farhana, K. et al., 2019. Improvement in the performance of solar collectors with nanofluids — A state-of-the-art review. *Nano-Structures & Nano-Objects*, Volume 18.
88. Fedele, L., Colla, L. & Bobbo, S., 2012. Viscosity and thermal conductivity measurements of water-based nanofluids containing titanium oxide nanoparticles. *International Journal of Refrigeration*, 5(35), pp. 1359-1366..
89. Ferdows, M., Khan, M., Alam, M. & Sun, S. M., 2012. MHD mixed convective boundary layer flow of a nanofluid through a porous medium due to an exponentially stretching sheet. *Math Prob Eng*, pp. 1-21.
90. Ferdows, M., Khan, M. & O.A., B., 2014. Numerical study of transient magnetohydrodynamic radiative free convection nanofluid flow from a stretching permeable surface. *Proc IMechE-Part E: J Proc Mech Eng*, Issue 228, pp. 181-196.
91. Ferziger, J., 2001. *Computational Methods for Fluid Dynamics*.. New York: Springer.

92. Fiveland, W. A., 1982. A Discrete Ordinates Method for Predicting Radiative Heat Transfer in Axisymmetric Enclosures. *ASME*.
93. Fiveland, W. A., 1984. Discrete-Ordinates Solutions of the Radiative Transport Equation for Rectangular Enclosures. *Journal of Heat Transfer*, Volume 106, pp. 699-706.
94. Fotukian, S. & Nasr, E. M., 2010. Experimental investigation of turbulent convective heat transfer of dilute Al<sub>2</sub>O<sub>3</sub>/water nanofluid inside a circular tube. *International Journal of Heat and Fluid Flow*, Volume 31, pp. 606-612.
95. Fusegi, T., Hyun, J. & Kuwahara, K., 1991. A numerical study of 3D natural convection in a cube: effects of the horizontal thermal boundary conditions. *Fluid Dynamics Research*, Volume 8, pp. 221-230.
96. Gertzos, K. P. & Caouris, Y. G., 2007. Experimental and computational study of the developed flow field in a flat plate integrated collector storage (ICS) solar device with recirculation. *Experimental Thermal and Fluid Science*, Volume 31, pp. 1133 - 1145.
97. Ghachem, K. et al., 2015. Numerical study of combined natural convection and radiation in three- dimensional solar thermal collector: focus on the inclination effect on heat transfer. *American Journal of Modern Energy*, 1(2), pp. 44-51.
98. Ghosh, S. K., Bég, O., Zueco, J. & Prasad, V., 2010. Transient hydromagnetic flow in a rotating channel permeated by an inclined magnetic field with magnetic induction and Maxwell displacement current effects. *ZAMP: J. Applied Mathematics and Physics*, Volume 61, p. 147–169.
99. Gimeno-Furio, A., Hernandez, L., Navarrete, N. & R., M., 2019. Characterisation study of a thermal oil-based carbon black solar nanofluid. *Renewable Energy*, Volume 140, pp. 493-500.

100. Godson, L., Raja, B., Lal, D. & Wongwises, S., 2010. Enhancement of heat transfer using nanofluids an overview.. *Renew. Sustain. Energy Rev.*, Volume 14, p. 629–641.
101. Gómez, M. A. et al., 2012. CFD simulation of a solar radiation absorber. *International Journal of Heat and Mass Transfer*, 57(1), pp. 231-240.
102. Gómez, M. et al., 2013. CFD simulation of a solar radiation absorber. *International Journal of Heat and Mass Transfer*, 1(57), pp. 231-240.
103. Gorji, T. & Ranjbar, A., 2017. Thermal and exergy optimization of a nanofluid-based direct absorption solar collector. *Renewable Energy*, Volume 106, pp. 274-287.
104. Hamad, M., 2011. Analytical solution of natural convection flow of a nanofluid over a linearly stretching sheet in the presence of magnetic field. *Int Commun Heat Mass Transfer*, Issue 38, pp. 487-492.
105. Hamad, M., Pop, I. & Ismail, A., 2011. Magnetic field effects on free convection flow of a nanofluid past a vertical semi-infinite flat plate. *Nonlinear Analysis: Real World Applications* , Issue 12, pp. 1338-1346.
106. Hatwar, A. & Kriplani, V., 2016. Experimental Study of Convective Heat Transfer in a Horizontal Tube Using Nanofluids. *International Journal of Advanced Engineering Research and Science*, 3(11), pp. 39-44.
107. Hayat, T., Rani, S., Alsaedi, A. & Rafiq, M., 2017. Radiative peristaltic flow of magneto nanofluid in a porous channel with thermal radiation. *Results Phys.*, Volume 7, p. 3396–3407.
108. Hiller, W. J. et al., 1992. Visualization of 3-d natural convection Flow Visualization VI. *Springer*, pp. 474-478.

109. Hiremath, A., Reddy, G. J. & Bég, O. A., 2019. Transient analysis of third-grade viscoelastic nanofluid flow external to a heated cylinder with buoyancy effects. *Arabian Journal for Science and Engineering*, Volume 44, p. 7875–7893.
110. Ho, C., Wei, L. & Li, Z., 2010. An experimental investigation of forced convective cooling performance of a microchannel heat sink with Al<sub>2</sub>O<sub>3</sub>/water nanofluid. *Applied Thermal Engineering*, Volume 30, pp. 96-103.
111. Ho, J. E., 2007. Characteristic study of MHD pump with channel in rectangular ducts. *J. Mar. Sci. Technol.* , Volume 15 , p. 315–321.
112. Hottel, H. & Sarofim, A., 1967. *Radiative Transfer*. New York: McGraw-Hill .
113. Howell, J. & Pinar Menguc, M., 2015. *Siegel R. Thermal Radiation Heat Transfer*. 6 ed. Florida: CRC Press.
114. Izadi, M. et al., 2018. Natural convection of a nanofluid between two eccentric cylinders saturated by porous material: Buongiorno's two phase model. *International Journal of Heat and Mass Transfer*, Volume 127, pp. 67-75.
115. Jang, S. P. & Choi, S., 2006. Cooling performance of a microchannel heat sink with nanofluids. *Applied Thermal Engineering*, Volume 26, pp. 2457-2463.
116. Jin, X. et al., 2019. Solar photothermal conversion characteristics of hybrid nanofluids: An experimental and numerical study. *Renewable Energy*, Volume 141, pp. 937-949.
117. Job, V. M., Gunakala, S. R., Rushi Kumar, B. & Sivaraj, R., 2017. Time-dependent hydromagnetic free convection nanofluid flows within a wavy trapezoidal enclosure. *Applied Thermal Engineering*, Volume 115, pp. 363-377.



118. Joo, D. & Lee, J., 2018. Numerical study on bubble behavior in magnetic nanofluid used for waste heat recovery power generation concept. *Int. J. Energy Res.* , Volume 42 , p. 520–531.
119. Jubran, B., Iweida, J. & Haimour, N., 1997. Experimental investigation of convective cells generated by side walls in solar ponds using various salts. *J. Sol. Energy Eng.* , Volume 119, p. 292–297.
120. Kadir, A. et al., 2019. Computational fluid dynamic and thermal stress analysis of coatings for high-temperature corrosion protection of aerospace gas turbine blade. *Heat Transfer*.
121. Kalogirou, S. A., 2013. *Solar Energy Engineering*. 2nd ed. USA.: Academic Press.
122. Kandasamy, R., Loganathan, P. & Arasu, P., 2011. Scaling group transformation for MHD boundary-layer flow of a nanofluid past a vertical stretching surface in the presence of suction/injection. *Nuc Eng Des* , Issue 241, pp. 2053-2059.
123. Karami, M., Bozorgi, M., Delfani, S. & Akhavan-Behabadi, M., 2018. Empirical correlations for heat transfer in a silver nanofluid-based direct absorption solar collector. *Sustainable Energy Technologies and Assessments*, Volume 28, pp. 14-21.
124. Kaushik, S., Verma, S. & Chandra, A., 1995. Solar-assisted Liquid Metal MHD power generation: A state of the Art Study. *Heat Recovery Syst. CHP.*, Volume 15, p. 675–689.
125. Kayhani, M. et al., 2012. Experimental analysis of turbulent convective heat transfer and pressure drop of Al<sub>2</sub>O<sub>3</sub>/water nanofluid in horizontal tube. *Micro and nano Letters*, 7(3), pp. 223-227.

126. Khalil, K. & Vafai, K., 2018. A review on the applications of nanofluids in solar energy field. *Renewable Energy*, Issue 123, pp. 398-406.
127. Khanafer, K. & Vafai, K., 2018. A review on the applications of nanofluids in solar energy field. *Renewable Energy*, Volume 123, pp. 398-406.
128. Khanafer, K. & Vafai, K., 2018. A review on the applications of nanofluids in solar energy field. *Renew. Energy.*, Volume 123, pp. 398-406.
129. Khatak, P., Jakhar, R. & Kumar, M., 2015. Enhancement in cooling of electronic components by nanofluids. *J. Inst. Eng. India Ser. C*, Volume 96, pp. 245-251.
130. Khullar, V. & Tyagi, H., 2010. *Applications of nanofluids as the working fluid in concentrating parabolic solar collectors*. Chennai, 37th National & 4th International Conferences on Fluid Mechanics & Fluid Power,.
131. Khullar, V. et al., 2013. *Solar Energy Harvesting Using Nanofluids-Based Concentrating Solar Collector*. Georgia, ASME 2012 Third International Conference on Micro/Nanoscale Heat and Mass Transfer, pp. 1003-1012.
132. Koo, J., 2004. *Computational nanofluid flow and heat transfer analyses applied to microsystems*. *Ph.D. Thesis*, NC State University: Raleigh.
133. Kosti, S., Das, M. K. & Saha, A. K., 2013. Buoyancy-driven flow and heat transfer in a nanofluid-filled enclosure. *Nanomaterials and Energy*, 4(2), pp. 200-211.
134. Kuharat, S., 2017. *Simulation of natural convection in enclosure-based spacecraft solar collector systems*, *MSc Dissertation*, Manchester: Department of Aeronautical and Mechanical Engineering, University of Salford.

135. Kuharat, S., 2019. *Numerical and experimental study of nanofluid-based solar collector systems, Year 2 Internal Evaluation Report*, Manchester: School of Science, Engineering and Environment (SEE), University of Salford.
136. Kuharat, S. & Bég, O. A., 2018. *Simulation of a nanofluid-based annular solar collector*. Istanbul, Turkey, ICHTFM 2018: 20th International Conference on Heat Transfer and Fluid Mechanics.
137. Kuharat, S. & Bég, O. A., 2019. Computational fluid dynamics simulation of a nanofluid-based annular solar collector with different metallic nanoparticles. *Heat and Mass Transfer Research Journal*, 23(1), pp. 1-23.
138. Kuharat, S. et al., 2020. CFD simulation of 3-D radiative convection in diamond/copper-water direct absorber solar collectors with daylight tracking. *AIAA J Thermophysics and Heat Transfer*.
139. Kuharat, S., Bég, O. A., Kadir, A. & Babaie, M., 2019. *Computational fluid dynamic simulation of a solar enclosure with radiative flux and different metallic nanoparticles*. Oxford, International Conference on Innovative Applied Energy (IAPE'19).
140. Kuharat, S., Bég, O. A., Kadir, A. & Shamshuddin, M., 2019. Computational study of heat transfer in solar collectors with different radiative flux models. *Heat Transfer Asian Research*, Volume 48, pp. 1002-1031.
141. Kuharat, S. et al., 2020. Computation of gold-water nanofluid natural convection in a three-dimensional tilted prismatic solar enclosure with aspect ratio and volume fraction effects. *Nanoscience and Technology- An International Journal*.
142. Kuharat, S. et al., 2021. Numerical study of buoyancy-driven convection in a trapezoidal solar enclosure with zinc and diamond nanoparticles. In: *Energy Systems and Nanotechnology*. s.l.:Springer-Germany.

143. Kumar, M., Reddy, G. J., Kumar, N. N. & Bég, O. A., 2019. Computational study of unsteady couple stress magnetic nanofluid flow from a stretching sheet with Ohmic dissipation. *Proc. IMechE-Part N: J Nanoengineering Nanomaterials and Nano-systems* .
144. Kumar, S., 2004. Natural convective heat transfer in trapezoidal enclosure of box-type solar cooker. *Renewable Energy*, Volume 29, pp. 211-222.
145. Kumar, S. et al., 2019. Nanodiamonds: Emerging face of future nanotechnology. *Carbon*, Volume 143, pp. 678-699.
146. Kumar, Y. R., Murthy, M. R. & Sreenadh, S., 2010. Unsteady peristaltic pumping in a finite length tube with permeable wall. *ASME J. Fluids Eng.* , Volume 132 .
147. Kundan Guide Lal, S. K., 2014. *An Experimental Investigation into the Performance of a Nanofluid Based Concentrating Parabolic Solar Collector (NCPSC)*, s.l.: Thapar institute.
148. Laria, K. et al., 2011. Combined heat transfer of radiation and natural convection in a square cavity containing participating gases. *International Journal of Heat and Mass Transfer*, 54(23–24), pp. 5087-5099.
149. Lataillade, A. et al., 2002. Monte Carlo Methods and sensitivity Estimations. *Journal of Quantitative Spect. and Rad. Transfer* , Volume 75, p. 529–538.
150. Latiff, N. A., Uddin, M. J. B. O. A., Izani, A. & Ismail, M., 2016. Unsteady forced bioconvection slip flow of a micropolar nanofluid from a stretching/ shrinking sheet. *Proc. IMECHE- Part N: J. Nanoengineering and Nanosystems*, 230(4), pp. 177-187.

151. Latiff, N., Uddin, M., Bég, O. & Ismail, A., 2016. Unsteady forced bioconvection slip flow of a micropolar nanofluid from a stretching/ shrinking sheet. *Proc. IMECHE- Part N: J. Nanoengineering and Nanosystems*, 4(230).
152. Leboucher, L., Boissonneau, P. & Villani, D., 1995. Channel shape optimization of electromagnetic pumps. *IEEE Trans. Magn.* , Volume 31, p. 2142–2145.
153. Lee, B., Park, K., Walsh, T. & Xu, L., 2012. Radiative heat transfer analysis in plasmonic nanofluids for direct solar thermal absorption. *J. Sol. Energy Eng.*, 134(2).
154. Lee, G. et al., 2012. Thermal conductivity enhancement of ZnO nanofluid using a one-step physical method. *Thermochim. Acta*, Volume 542, pp. 24-27.
155. Lee, S.-H. & PilJang, S., 2013. Extinction coefficient of aqueous nanofluids containing multi-walled carbon nanotubes. *International Journal of Heat and Mass Transfer*, Volume 67, pp. 930-935.
156. Lee, T., Lee, J. & Jeong, Y., 2013. Flow boiling critical heat flux characteristics of magnetic nanofluid at atmospheric pressure and low mass flux conditions. *Int J Heat Mass Transfer* , Issue 56, pp. 101-106.
157. Lim, S. & Choi, B., 2009. A study on the MHD (magnetohydrodynamic) micropump with side-walled electrodes. *J. Mech. Sci. Technol.* , Volume 23 , p. 739–749.
158. Liu, J., Z. Ye, Z. L., Fang, X. & Z.. Zhang, 2015. A combined numerical and experimental study on graphene/ionic liquid nanofluid based direct absorption solar collector. *Sol. Energy Mater. Sol. Cell.* , Volume 136.
159. Liu, X. et al., 2018. Volumetric solar steam generation enhanced by reduced graphene oxide nanofluid. *Appl. Energy* 220.

160. Li, Z., Yang, M. & Zhang, Y., 2016. Lattice Boltzmann method simulation of 3-D natural convection with double MRT model. *International Journal of Heat and Mass Transfer*, Volume 94, pp. 222-238.
161. Lu, K., 2007. Rheological behavior of carbon nanotube-alumina nanoparticle dispersion systems. *Powder Technology*, 177(3), pp. 154-161.
162. Maddah, H., Rezazadeh, M., Maghsoudi, M. & Kokhdan, S. N., 2013. The effect of silver and aluminium oxide nanoparticles on thermophysical properties of nanofluids. *Journal Nanostructure in Chemistry*, Volume 3.
163. Mahbubul, M., 2018. Carbon nanotube nanofluid in enhancing the efficiency of evacuated tube solar collector. *Renewable Energy*, Volume 121, pp. 36-44.
164. Mahmoodi, M. & Sebdani, S. M., 2012. Natural convection in a square cavity containing a nanofluid and an adiabatic square block at the center. *Superlattices and Microstructures*, 52(2), pp. 261-275.
165. Mallah, A., Kazi, S., Zubir, M. & Badarudin, A., 2018. Blended morphologies of plasmonic nanofluids for direct absorption applications. *Applied Energy*, Volume 229, pp. 505-521.
166. Mallinson, G. & De Vahl Davis, G., 1997. Three-dimensional natural convection in a box: a numerical study. *Journal Fluid Mechanics.*, Volume 83, pp. 1-31.
167. Mandviwalla, X. & Archer, R., 2008. The influence of slip boundary conditions on peristaltic pumping in a rectangular channel. *ASME J. Fluids Eng.*, Volume . 130 .
168. maplesoft, 2019. *maplesoft*. [Online] Available at: <https://maplesoft.com/> [Accessed 2019].

169. Marefati, M., Mehrpooya, M. & Shafii, M., 2018. Optical and thermal analysis of a parabolic trough solar collector for production of thermal energy in different climates in Iran with comparison between the conventional nanofluids. *J. Clean. Prod.*, Volume 175, p. 294–313.
170. Mashali, F. et al., 2019. Thermo-physical properties of diamond nanofluids: A review. *International Journal of Heat and Mass Transfer*, Volume 129, pp. 1123-1135.
171. Mashali, F., Languri, E. M., Davidson, J. & Kerns, D., 2020. Diamond nanofluids: microstructural analysis and heat transfer study. *Heat Transfer Engineering*, Volume 1, pp. 1-13.
172. Matino, F. & Maccari, A., 2015. Molten Salt Receivers Operated on Parabolic Trough Demo Plant and in Laboratory Conditions. *Energy Procedia*, Volume 69, pp. 481-486.
173. Mehmood, R. et al., 2018. Thermal slip in oblique radiative nano-polymer gel transport with temperature-dependent viscosity: solar collector nanomaterial coating manufacturing simulation.. *Arabian Journal Science and Engineering*.
174. Mehmood, R. et al., 2018. Thermal slip in oblique radiative nano-polymer gel transport with temperature-dependent viscosity: solar collector nanomaterial coating manufacturing simulation. *Arabian J. Science and Engineering*.
175. Mehmood, R. et al., 2019. Thermal slip in oblique radiative nano-polymer gel transport with temperature-dependent viscosity: solar collector nanomaterial coating manufacturing simulation. *Arabian Journal Science and Engineering*, 44(2), p. 1525–1541.

176. Mehmood, R., Tabassum, R., Kuharat, S. & Bég, O. A., 2020. Computation of magnetic field and homogeneous-heterogeneous chemical reaction effects on oblique stagnation point flow of variable viscosity micropolar Fe<sub>3</sub>O<sub>4</sub> electro-conductive nanofluids. *Microsystems Technologies* .
177. Mehrali, M., Ghatkesar, M. & Pecnik, R., 2018. Full-spectrum volumetric solar thermal conversion via graphene/silver hybrid plasmonic nanofluids. *Applied Energy*, Volume 224, pp. 103-115.
178. Menbari, A., Alemrajabi, A. & Rezaei, A., 2016. Heat transfer analysis and the effect of CuO/Water nanofluid on direct absorption concentrating solar collector.. *Appl. Thermal Eng.*, Volume 104, p. 176–183.
179. Minardi, J. & Chuang, H., 1975. Performance of a “black” liquid flat-plate solar collector. *Sol. Energy*, 17(3), pp. 179-183.
180. Moghadam, A. J., Farzane-Gord, M., Sajadi, M. & Zadeh, M. H., 2014. Effects of CuO/water nanofluid on the efficiency of a flat-plate solar collector. *Experimental Thermal and Fluid Science*, Volume 58, p. 9–14.
181. Moghadam, M., Edalatpour, M. & Solano, J., 2017. Numerical study on conjugated laminar mixed convection of alumina/water nanofluid flow, heat transfer, and entropy generation within a tube-on-sheet flat plate solar collector. *ASME J. Sol. Energy Eng.*, 139(4), pp. 694-722.
182. Moradi, H., Zandi, S. & Floryan, J., 2017. Algorithm for analysis of peristaltic annular flows. *Comput. Fluids* ., Volume 147 , p. 72–89.
183. Moreno, J., Casado, C. & Marugán, J., 2019. Improved discrete ordinate method for accurate simulation radiation transport using solar and LED light sources. *Chemical Engineering Science*, Volume 205, pp. 151-164.



184. Motlagh, S. & Soltanipour, H., 2017. Natural convection of Al<sub>2</sub>O<sub>3</sub>-water nanofluid in an inclined cavity using Buongiorno's two-phase model. *International Journal of Thermal Sciences*, Volume 111, pp. 310-320.
185. Nadeem, S. & Akbar, N. S., 2009. Effects of heat transfer on the peristaltic transport of MHD Newtonian fluid with variable viscosity: application of Adomian decomposition method. *Commun. Nonlinear Sci. Numer. Simul.* , Volume 14.
186. Nagarajan, P., Subramani, J., Suyambazhahan, S. & Sathyamurthy, R., 2014. Nanofluids for solar collector applications: A Review. *Energy Procedia*, Volume 61, pp. 2416-2434.
187. Nagendra, N. et al., 2017. Hydromagnetic non-Newtonian nanofluid transport phenomena past an isothermal vertical cone with partial slip: aerospace nanomaterial enrobing simulation. *Heat Transfer-Asian Research* .
188. Narla, V. K., Tripathi, D. & Bég, O. A., 2019. Analysis of entropy generation in biomimetic electro-osmotic nanofluid pumping through a curved channel with Joule dissipation. *Thermal Science and Engineering Progress* .
189. Nasrin, R., Parvin, S. & Alim, M., 2004. Heat transfer by nanofluids through a flat plate solar collector. *Procedia Engineering*, Issue 90, pp. 364-370.
190. Nasrin, R., Parvin, S. & Alim, M. A., 2014. Heat transfer by nanofluids through a flat plate solar collector. *Procedia Engineering*, Volume 90, pp. 364-370.
191. Natarajan, E., Basak, T. & Roy, S., 2008. Natural convection flows in a trapezoidal enclosure with uniform and non-uniform heating of bottom wall. *International Journal of Heat and Mass Transfer*, Volume 51, pp. 747-756 .
192. Ni, G. et al., 2015. Volumetric solar heating of nanofluids for direct vapor generation. *Nano Energy* , Volume 17.

193. Nima, N. I. et al., 2020. Biomathematical model for gyrotactic free-forced bioconvection with oxygen diffusion in near-wall transport within a porous medium fuel cell. *Int. J Biomathematics* .
194. Nima, N. I. et al., 2020. Biomathematical model for gyrotactic free-forced bioconvection with oxygen diffusion in near-wall transport within a porous medium fuel cell,. *Int. J Biomathematics* .
195. Ögüt, E. B., 2009. Natural convection of water-based nanofluids in an inclined enclosure with a heat source. *International Journal of Thermal Sciences*, 18(11), pp. 2063-2073.
196. Okonkwo, E. et al., 2018. Optimal Analysis of Entropy Generation and Heat Transfer in Parabolic Trough Collector Using Green-Synthesized TiO<sub>2</sub>/Water Nanofluids.. *Journal of Solar Energy Engineering.*, 141(3).
197. Oliveira, G. & Bandarra Filho, E. P., 2014. *Nanofluid as a coolant in automotive radiators.*. Orlando, 10th International Conference on Heat Transfer. Fluid Mechanics and Thermodynamics..
198. Otanicar, T. P. .. et al., 2010. Nanofluid-based direct absorption solar collector. *Journal of Renewable and Sustainable Energy*, 2(3).
199. Otanicar, T. et al., 2010. Nanofluidbased direct absorption solar collector. *J. Renew. Sustain. Energy* 2, Issue 2.
200. Otanicar, T. P. et al., 2010. Nanofluid-based direct absorption solar collector. *journal of renewable and sustainable energy*, Issue 2.
201. Owolabi, A. L., Al-Kayiem, H. H. & Baheta, A. T., 2017. Performance investigation on a thermal energy storage integrated solar collector system using nanofluid. *Int. J. Energy Res.* 41 , p. 650–657.

202. Ozsoy, A. & Corumlu, V., 2018. Thermal performance of a thermosyphon heat pipe evacuated tube solar collector using silver-water nanofluid for commercial applications. *Renewable Energy*, Issue 122, pp. 26-34.
203. Padki, M. & Sherif, S., 1999. On a simple analytical model for solar chimneys. *Int. J. Energy Res.* , Volume 23 , p. 345–349.
204. Pal, A. & Brasseur, J. G., 2002. The mechanical advantage of local longitudinal shortening on peristaltic transport. *ASME J. Biomech. Eng.* , Volume 124 , p. 94–100.
205. Paul, T. & Morshed, A. K. J., 2013. Nanoparticle Enhanced Ionic Liquids (NEILS) as Working Fluid for the Next Generation Solar Collector. *Procedia Engineering*, Volume 56, pp. 631-636.
206. Petela, K., Manfrida, G. & Szlek, A., 2017. Advantages of variable driving temperature in solar absorption chiller. *Renew. Energy*, Volume 114 , p. 716–724.
207. Phuoc, T. X. & Massoudi, M., 2009. Experimental observations of the effects of shear rates and particle concentration on the viscosity of Fe<sub>2</sub>O<sub>3</sub>–deionized water nanofluids. *International Journal of Thermal Sciences*, Volume 48, pp. 1294-1301.
208. Pop, E., Varshney, V. & Roy, A. K., 2012. Thermal properties of graphene: fundamentals and applications. *MRS Bull*, Volume 37.
209. Prabu, T. & Ajay, S. C., 2017. Improving heat transfer in hybrid solar systems using liquid metal alloys as a coolant. *ASME J Sol Energy Eng*, 6(139).
210. Prakash, J., Siva, E. P., Tripathi, D. & A., B. O., 2019. Thermal slip and radiative heat transfer effects on electro-osmotic magneto-nanoliquid peristaltic propulsion through a microchannel. *Heat Transfer-Asian Research* .

211. Prakash, J. et al., 2019. Peristaltic pumping of magnetic nanofluids with thermal radiation and temperature-dependent viscosity effects: modelling a solar magneto-biomimetic nanopump. *Renewable Energy*, Volume 133, pp. 1308-1326 .
212. Prakash, J. et al., 2019. Peristaltic pumping of magnetic nanofluids with thermal radiation and temperature-dependent viscosity effects: Modelling a solar magneto-biomimetic nanopump.. *Renewable Energy*., Volume 133, pp. 1308-1326.
213. Prakash, J., Tripathi, D. & Bég, O. A., 2020. Comparative study of hybrid nanofluid performance in microchannel slip flow induced by electroosmosis and peristalsis. *Applied Nanoscience*.
214. Qian, S. & Bau, H. H., 2009. Magneto-hydrodynamics based microfluidics. *Mech. Res. Commun.*, Volume 36, p. 10–21.
215. Qi, C., Yang, L. & Wang, G., 2017. Numerical study on convective heat transfer enhancement in horizontal rectangle enclosures filled with Ag-Ga nanofluid. *Nanoscale Research Letters*, Volume 12.
216. Radkar, R. N., Bhanvase, B. A., Barai, D. P. & Sonawane, S. H., 2019. Intensified convective heat transfer using ZnO nanofluids in heat exchanger with helical coiled geometry at constant wall temperature. *Materials Science for Energy Technologies*, 7(2), pp. 161-170.
217. RafiqulIslam, M., Shabani, B. & Rosengarten, G., 2016. Nanofluids to improve the performance of PEM fuel cell cooling systems: A theoretical approach. *Applied Energy*., Volume 178, pp. 660-671.
218. Ramesh, K., 2016. Influence of heat and mass transfer on peristaltic flow of a couple stress fluid through porous medium in the presence of inclined magnetic field in an inclined asymmetric channel. *J. Mol. Liq.* , Volume 219, p. 256–271.

219. Rana, P., Bhargava, R., Bég, O. A. & Kadir, A., 2017. Finite element analysis of viscoelastic nanofluid flow with energy dissipation and internal heat source/sink effects. *Int. J. Applied Computational Mathematics* , 3(2), p. 1421–1447.
220. Rana, P., Bhargava, R. & O.A., B., 2013. Finite element simulation of unsteady magneto-hydrodynamic transport phenomena on a stretching sheet in a rotating nanofluid. *IMechE- Part N: J Nanoengineering and Nanosystems*, 2(227), p. 77–100.
221. Rao, S. et al., 2017. Computational analysis of non-Newtonian boundary layer flow of nanofluid past a vertical plate with partial slip, Modelling. *Measurement and Control B* , 86(1), pp. 271-295.
222. Rarani, E., Etesami, N. & Esfahany, M., 2012. Influence of the uniform electric field on viscosity of magnetic nanofluid (Fe<sub>3</sub>O<sub>4</sub>-EG). *J Appl Phys* , Issue 112.
223. Rashidi, M. M. A. A. & Bég, O. A., 2012. Utilization of waste heat in combined power and ejector refrigeration for a solar energy source. *Int J Appl Math Mech*, Volume 8 , p. 1–16.
224. Rativa, D. & Gómez-Malagón, L. A., 2015. Solar radiation absorption of nanofluids containing metallic nanoellipsoids. *Solar Energy*, Volume 118, pp. 419-425.
225. Ravindran, S., 2017. *Nanofluids in Aerospace Engineering: Solar pumps, rocket propulsion and landing gear tribology* , Manchester, UK: MSc Dissertation, University of Salford.
226. Reddy, M., Mishra, M., Sreenadh, S. & Rao, A. R., 2005. Influence of lateral walls on peristaltic flow in a rectangular duct. *ASME J. Fluids Eng*, Volume 127 , p. 824–827.

227. Rehan, M. et al., 2018. Experimental performance analysis of low concentration ratio solar parabolic trough collectors with nanofluids in winter conditions. *Renew Energy*, Volume 118, p. 742–751..
228. Ren, Y. et al., 2017. Thermal performance characteristics of porous media receiver exposed to concentrated solar radiation. *J. Energy Eng.* , Volume 143.
229. Rightley, M. J., 1989. *Multi-dimensional discrete ordinates solutions to combined mode radiation heat transfer problems and their application to a free-falling particle, direct absorption solar receiver*, United States: Sandia National Lab.
230. Romero, M. & González-Aguilar, J., 2017. Next generation of liquid metal and other high-performance receiver designs for concentrating solar thermal (CST) central tower systems. *Adv. Conc. Sol. Therm. Res. Technol*, p. 129–154.
231. Roy, S. et al., 2015. Heat transfer performance of silver/water nanofluid in a solar flat-plate collector. *J. Thermal Engineering*, 1(2), pp. 104-112.
232. Saidur, R. et al., 2012. Evaluation of the effect of nanofluid-based absorbers on direct solar collector. *International Journal of Heat and Mass Transfer*, 55(21-22), pp. 5899-5907.
233. Said, Z., Saidur, R. & Rahim, N. A., 2014. Optical properties of metal oxides based nanofluids. *International Communications in Heat and Mass Transfer*, Volume 59, pp. 46-54.
234. Said, Z. et al., 2013. Radiative properties of nanofluids. *Int. Commun. Heat Mass Transf.* , Volume 46, p. 74–84.
235. Salata, O., 2004. Applications of nanoparticles in biology and medicine. *Nanobiotechnology*, Volume 3.

236. Saleh, R. et al., 2014. Titanium dioxide nanofluids for heat transfer applications. *Experimental Thermal and Fluid Science*, Issue 52, pp. 19-29.
237. Sani, E., Papi, N., Mercatelli, L. & Żyła, G., 2018. Graphite/diamond ethylene glycol-nanofluids for solar energy applications. *Renewable Energy*, Volume 126, pp. 692-698.
238. Satyamurthy, P., Venkatramani, N., Quraishi, A. & Mushtaq, A., 1999. Basic design of a prototype liquid metal magnetohydrodynamic power generator for solar and waste heat. *Energy Convers. Manag.* , Volume 40 , p. 913–935.
239. Schulz, R. et al., 2010. Functional rotation of the transporter Acrb: the essentials of peristaltic motion and subsequent substrate extrusion. *Biophys. J.* , Volume 98.
240. Sekhar, T., Prakash, R., Nandan, G. & Muthuraman, M., 2017. Performance enhancement of a renewable thermal energy collector using metallic oxide nanofluids. *Micro Nano Lett*, Volume 13, p. 248–251.
241. Shahidian, A. et al., 2009. Flow analysis of non-Newtonian blood in a magnetohydrodynamic pump. *IEEE Trans. Magn.* , Volume 45, p. 2667–2670.
242. Shahidian, A., Ghassemi, M. & Mohammadi, R., 2012. Effect of nanofluid properties on magnetohydrodynamic pump (MHD). *Adv. Mater. Res. Trans Tech Publ*, p. 663–669.
243. Shahi, M., Mahmoudi, A. H. & Raouf, A. H., 2011. Entropy generation due to natural convection cooling of a nanofluid. *International Communications in Heat and Mass Transfer*, 38(7), pp. 972-983.
244. Shah, T. & Ali, H., 2019. Applications of hybrid nanofluids in solar energy, practical limitations and challenges: A critical review. *Solar Energy*, Volume 183, pp. 173-203.

245. Shamsirgaran, R., Assadi, M. K., Al-Kayiem, H. & Korada, V., 2018. Energetic and Exergetic Performance of Solar Flat-Plate Collector Working with Cu Nanofluid. *J. Sol. Energy Eng.* .
246. Sharaf, O., Kyritsis, D. & Abu-Nada, E., 2018. Impact of nanofluids, radiation spectrum, and hydrodynamics on the performance of direct absorption solar collectors. *Energy Conversion and Management*, Volume 156, pp. 706-722.
247. Sharaf, O., Kyritsis, D., Al-Khateeb, A. & Abu-Nada, E., 2018. Effect of bottom surface optical boundary conditions on nanofluid-based DASC: Parametric study and optimization. *Solar Energy*, Volume 164, pp. 210-223.
248. Sharma, Y. N., Shivamalliah, M. M. & Karanth, V. K., 2013. *Three-dimensional CFD simulation of thermosyphon flow in an unglazed solar flat plate collector*. San Diego, ASME 2013 International Mechanical Engineering Congress and Exposition.
249. Sheikhzadeh, G. A. & Nikfar, M., 2013. Aspect ratio effects of an adiabatic rectangular obstacle on natural convection and entropy generation of a nanofluid in an enclosure. *J. Mechanical Science and Technology*, 27(11), pp. 3495-35.
250. Sheremet, M., Grosan, T. & Pop, I., 2015. Free convection in a square cavity filled with a porous medium saturated by nanofluid using Tiwari and Das' nanofluid model. *Transport in Porous Media*, 106(3), p. 595–610.
251. Shi, Y. et al., 2011. Effects of porous media on thermal and salt diffusion of solar pond. *Appl. Energy.* , Volume 88 , p. 2445–2453.
252. Shukla, N., Rana, P. & Beg, O., 2019. Unsteady MHD non-Newtonian (rheological) heattransfer nanofluids with entropy generation analysis. *Nonlinear Engineering* , Volume 8, p. 630–644.



253. Siva Reddy, E., Reddy, R. & Reddy, K., 2015. *Experimental Study on Thermal Efficiency of Parabolic Trough Collector (PTC) Using Al<sub>2</sub>O<sub>3</sub>/H<sub>2</sub>O Nanofluid*. Zurich Switzerland, Applied Mechanics and Materials Trans Tech Publ..
254. Slawinski, P. & Terry, B., 2014. An automated intestinal biomechanics simulator for expediting robotic capsule endoscope development. *J. Med. Devices.* , Volume 8.
255. Sokolik, I., 2008. Radiation Balance and Solar Radiation Spectrum. In: B. D. F. Steven Erik Jørgensen, ed. *Encyclopedia of Ecology*. s.l.:Academic Press, pp. 2951-2955.
256. Srinivas, S. & Kothandapani, M., 2008. Peristaltic transport in an asymmetric channel with heat transfer. *Int. J. Heat Mass Transf.* , Volume 35, pp. 514-522.
257. Srivastava, V., Tripathi, D. & Bég, O., 2016. Numerical study of oxygen diffusion from capillaries to tissues with external force effects. *J. Mechanics in Medicine and Biology*, 2(17).
258. Subramani, J., Nagarajan, P., Mahian, O. & Sathyamurthy, R., 2018. Efficiency and heat transfer improvements in a parabolic trough solar collector using TiO<sub>2</sub> nanofluids under turbulent flow regime. *Renew. Energy*, p. 19–31.
259. Subramani, J. et al., 2017. Experimental study on the thermal performance and heat transfer characteristics of solar parabolic trough collector using Al<sub>2</sub>O<sub>3</sub> nanofluids. *Environ. Prog. Sustain. Energy* , Volume 37.
260. Syam Sundar, L. et al., 2016. Nanodiamond-Fe<sub>3</sub>O<sub>4</sub> nanofluids: Preparation and measurement of viscosity, electrical and thermal conductivities. *International Communications in Heat and Mass Transfer*, Volume 73, pp. 62-74.

261. Sze, C. N. P., Hughes, B. R. & Bég, O. A., 2011. *Computational study of improving the efficiency of photovoltaic panels in the UAE*. Dubai, United Arab Emirates, ICFDT 2011-International Conference on Fluid Dynamics and Thermodynamics.
262. Tafarroj, M. M., Daneshazarian, R. & Kasaeian, A., 2019. CFD modeling and predicting the performance of direct absorption of nanofluids in trough collector. *Applied Thermal Engineering*, Volume 148, pp. 256-269.
263. Taylor, R. A. et al., 2011. Nanofluid optical property characterization: towards efficient direct absorption solar collectors. *Nanoscale research letters*, 225(6).
264. Taylor, R. P. P., Otanicar, T., Adrian, R. & Prasher, R., 2011. Nanofluid optical property characterization: towards efficient direct absorption solar collectors. *Nanoscale Res. Lett.* , Volume 6.
265. Tien, C. L. & Vafai, K., 1989. Convective and radiative heat transfer in porous media. *Adv. Appl. Mech. Elsevier*, p. 225–281.
266. Tiwari, A. K. & Kalamkar, V. R., 2018. Effects of total head and solar radiation on the performance of solar water pumping system. *Renew. Energy.* , Volume 118 , p. 919–927.
267. Tiwari, R. K. & Das, M. K., 2007. Heat transfer augmentation in a two-sided lid-driven differentially heated square cavity utilizing nanofluids. *International Journal of Heat and Mass Transfer*, Volume 50, p. 2002–2018.
268. Tripathi, D. & Bég, O., 2012. A study of unsteady physiological magneto-fluid flow and heat transfer through a finite length channel by peristaltic pumping. *Proc. Inst. Mech. Eng. Part H. J Eng. Medicine*, Issue 226, p. 631–644.

269. Tripathi, D. & Bég, O. A., 2012. A study of unsteady physiological magneto-fluid flow and heat transfer through a finite length channel by peristaltic pumping. *Proc. Inst. Mech. Eng. Part H. J Eng. Medicine.* , Volume 226, p. 631–644.
270. Tripathi, D., Jhorar, R., Bég, O. A. & Kadir, A., 2017. Electro-magneto-hydrodynamic peristaltic pumping of couple stress biofluids through a complex wavy micro-channel. *J. Mol. Liq.* , Volume 236, p. 358–367.
271. Tripathi, D., Prakash, J. & Bég, O. A., 2020. Peristaltic pumping of hybrid nanofluids through an asymmetric microchannel in the presence of electromagnetic fields. *ASME J. Thermal Science and Engineering Applications* .
272. Tripathi, D., Yadav, A. & Bég, O., 2017. Electro-kinetically driven peristaltic transport of viscoelastic physiological fluids through a finite length capillary: mathematical modelling. *Mathematical Biosciences*, Issue 283, pp. 155-168 .
273. Trodi, A. & Benhamza, M., 2017. Particle shape and aspect ratio effect of Al<sub>2</sub>O<sub>3</sub>–water nanofluid on natural convective heat transfer enhancement in differentially heated square enclosures. *Chemical Engineering Communications*, 204(2), pp. 158-167.
274. Tseng, W. J. & Chen, C., 2003. Effect of polymeric dispersant on rheological behavior of nickel/terpineol suspensions. *Materials Science and Engineering*.
275. Tsui, Y. Y., Guo, D. C., Chen, S. H. & Lin, S. W., 2014. Pumping flow in a channel with a peristaltic wall. *ASME J. Fluids Eng.* , Volume 136 .
276. Tyagi, H., Phelan, P. & Prasher, R., 2009. Predicted efficiency of a low-temperature nanofluid-based direct absorption solar collector. *ASME J. Sol. Energy Eng.*, 131(4).

277. Tyler, T. et al., 2006. Thermal transport properties of diamond-based nanofluids and nanocomposites. *Diamond and Related Materials*, Volume 15, pp. 2078-2081.
278. Uddin, j., Alginahi, Y., Bég, O. & Kabir, M., 2016. Numerical solutions for nonlinear gyrotactic bioconvection in nanofluid saturated porous media with Stefan blowing and multiple slip effects. *Computers and Mathematics with Applications*, 10(72), pp. 2562-25.
279. Uddin, M., Bég, O., Ghose, P. & Ismael, A., 2016. Numerical study of non-Newtonian nanofluid transport in a porous medium with multiple convective boundary conditions and nonlinear thermal radiation effects. *Int. J. Num. Meth. Heat Fluid Flow*, 5(26).
280. Uddin, M., Bég, O. & Ismail, A., 2015. Radiative-convective nanofluid flow past a stretching/shrinking sheet with slip effects. *Thermophysics Heat Transfer*, 3(29), pp. 513-523.
281. Uddin, M., Bég, O. & Uddin, M., 2016. diffusion and nonlinear Energy conversion under conjugate conduction, magneto-convection, radiation over a non-linearly stretching sheet with slip and multiple convective boundary conditions. *Energy*, 2(115), pp. 1119-1129.
282. Uddin, M. J., Bég, O. A. & Amin, N., 2014. Hydromagnetic transport phenomena from a stretching or shrinking nonlinear nanomaterial sheet with Navier slip and convective heating: a model for bio-nano-materials processing. *J. Magnetism Magnetic Materials*, Issue 368, pp. 252-261.
283. Uddin, M. J., Khan, W., Ismail, A. M. & Bég, O. A., 2016. Computational study of three-dimensional stagnation point nanofluid bioconvection flow on a moving

- surface with anisotropic slip and thermal jump effect. *ASME J. Heat Transfer.* , Volume 138.
284. Uddin, M., Khan, W. & Bég, O., 2017. Bioconvection nanofluid slip flow past a wavy surface with applications in nano-biofuel cells *Chin. J. Physics*, Issue 55, pp. 2048-2063.
285. Uddin, M., Khan, W. & Ismail, A. B. O., 2016. Computational study of three-dimensional stagnation point nanofluid bioconvection flow on a moving surface with anisotropic slip and thermal jump effect. *ASME J. Heat Transfer*, Issue 138.
286. Umavathi, J. C. & Bég, O. A., 2020. Modelling the onset of thermosolutal convective instability in a non-Newtonian nanofluid-saturated porous medium layer. *Chinese J. Physics*, Volume 68, p. 147–167 .
287. Vasiliev, L., Mishkinis, D., Antukh, A. & Vasiliev Jr, L., 2001. Solar–gas solid sorption heat pump. *Appl. Therm. Eng.* , Volume 21 , p. 573–583.
288. Vasu, B. et al., 2019. Unsteady flow of a nanofluid over a sphere with nonlinear Boussinesq approximation. *Journal of Thermophysics and Heat Transfer*, 2(33), pp. 343-355.
289. Vasudeva Karanth, K. & Corneli, J. A. Q., 2017. CFD Analysis of a Flat Plate Solar Collector for Improvement in Thermal Performance with Geometric Treatment of Absorber. *Research India Publications*, Volume 12, pp. 4415-4421.
290. Vékás, L., 2004. Magnetic nanofluids properties and some applications. *Romanian J Phys*, 9(49).
291. Vetter, B., Fischer, S. & Drück, H., 2018. *CFD-based development, testing and optimization of flat plate collectors*. s.l., International Solar Energy Society.

292. Wang, L., Shi, B. & Chai, Z., 2018. Effects of temperature-dependent properties on natural convection of nanofluids in a partially heated cubic enclosure. *Applied Thermal Engineering*, Volume 128, pp. 204-213.
293. Wang, P. J., Chang, C. Y. & Chang, M. L., 2004. Simulation of two-dimensional fully developed laminar flow for a magneto-hydrodynamic (MHD) pump. *Biosens. Bioelectron*, Volume 20, p. 115–121.
294. Wang, P. et al., 2017. Thermo-Fluid Optimization of a Solar Porous Absorber With a Variable Pore Structure. *J. Sol. Energy Eng.* , Volume 139 .
295. Wang, X., He, Y., Chen, M. & Hu, Y., 2018. ZnO–Au composite hierarchical particles dispersed oil-based nanofluids for direct absorption solar collectors. *Solar Energy Materials and Solar Cells*, Volume 179, p. 185–93.
296. Wong, K., Bon, B., Vu, S. & Samed, S., 2007. *Study of nanofluid natural convection phenomena in rectangular enclosures*. Washington , ASME International Mechanical Engineering Congress and Exposition.
297. Xuan, Y. & Roetzel, W., 2000. Conceptions for heat transfer correlation of nanofluids. *International Journal of Heat and Mass Transfer*, 43(19), pp. 3701-3707.
298. Yu, Q., Xu, H. & Liao, S., 2018. Analysis of mixed convection flow in an inclined lid-driven enclosure with Buongiorno’s nanofluid model. *International Journal of Heat and Mass Transfer*, Volume 126, pp. 221-236.
299. Yu, W., Xie, H., Chen, L. & Li, Y., 2009. Investigation of thermal conductivity and viscosity of ethylene glycol based ZnO nanofluid. *Thermochim. Acta*, Volume 491, pp. 92-96..

300. Zayed, M. et al., 2019. Factors affecting the thermal performance of the flat plate solar collector using nanofluids: A review. *Solar Energy*, Volume 182, pp. 382-396.
301. Zeinali, H. S., Nasr, E. M. & Etemad, S., 2007. Experimental investigation of convective heat transfer of Al<sub>2</sub>O<sub>3</sub>/water nanofluid in circular tube. *International Journal of Heat and Fluid Flow*, 28(2), pp. 203-210.
302. Zeiny, A. et al., 2018. Solar evaporation via nanofluids: A comparative study. *Renewable Energy*, Volume 122, pp. 443-454.
303. Zhang, C., Zhang, Y., Lei, X. & Gao, W., 2017. Design and comparison of solar thermal oilfield steam production system plans. *J. Sol. Energy Eng*, Volume 139 .
304. Zhang, L., Ding, Y., Povey, M. & York, D., 2008. ZnO nanofluids – a potential antibacterial agent. *Prog. Nat. Sci.*, Volume 18, pp. 939-944.
305. Zhang, L. et al., 2007. Investigation into the antibacterial behaviour of suspensions of ZnO nanoparticles (ZnO nanofluids). *J. Nanoparticle Res*, Volume 9, pp. 479-489.
306. Zhang, S. e. a., 2021. Turbulent heat transfer and flow analysis of hybrid Al<sub>2</sub>O<sub>3</sub>-CuO/water nanofluid: An experiment and CFD simulation study. *Applied Thermal Engineering*, Volume 188.
307. Zhang, Y. et al., 2018. Enhancement of energy utilization using nanofluid in solar powered membrane distillation. *Chemosphere*, Volume 212, pp. 554-562.
308. Zhao, N., Wen, X. & Li, S., 2015. An Evaluation of the Application of Nanofluids in Intercooled Cycle Marine Gas Turbine Intercooler. *Journal of Engineering for Gas Turbines and Power*, 138(1).

309. Zheng, X., Xue, Q., Mittal, R. & Beilamowicz, S., 2010. A coupled sharp-interface immersed boundary-finite-element method for flow-structure interaction with application to human phonation. *ASME J. Biomech. Eng.* , Volume 132.



# Appendix

## Chapter 3

Nano-particle properties (titanium oxide copper, silver)

<i>TiO<sub>2</sub></i>		<i>Cu</i>		<i>Ag</i>	
<i>V<sub>np</sub></i>	1	<i>V<sub>np</sub></i>	1	<i>V<sub>np</sub></i>	1
<i>V<sub>f</sub></i>	100	<i>V<sub>f</sub></i>	100	<i>V<sub>f</sub></i>	100
<i>Φ</i>	0.01	<i>Φ</i>	0.01	<i>Φ</i>	0.01
<i>P<sub>f</sub></i>	997.1	<i>P<sub>f</sub></i>	997.1	<i>P<sub>f</sub></i>	997.1
<i>P<sub>s</sub></i>	4250	<i>P<sub>s</sub></i>	8933	<i>P<sub>s</sub></i>	10500
<i>P<sub>nf</sub></i>	1029.629	<i>P<sub>nf</sub></i>	1076.459	<i>P<sub>nf</sub></i>	1092.129
<i>C<sub>pf</sub></i>	4179	<i>C<sub>pf</sub></i>	4179	<i>C<sub>pf</sub></i>	4179
<i>C<sub>ps</sub></i>	686.2	<i>C<sub>ps</sub></i>	385	<i>C<sub>ps</sub></i>	235
<i>C<sub>pnf</sub></i>	4034.827682	<i>C<sub>pnf</sub></i>	3864.154734	<i>C<sub>pnf</sub></i>	3799.814025
<i>K<sub>s</sub></i>	8.9538	<i>K<sub>s</sub></i>	401	<i>K<sub>s</sub></i>	429
<i>K<sub>f</sub></i>	0.613	<i>K<sub>f</sub></i>	0.613	<i>K<sub>f</sub></i>	0.613
<i>K<sub>nf</sub></i>	0.617981786	<i>K<sub>nf</sub></i>	0.619041831	<i>K<sub>nf</sub></i>	0.619043619
<i>u<sub>f</sub></i>	1.08E-03	<i>u<sub>f</sub></i>	1.08E-03	<i>u<sub>f</sub></i>	1.08E-03
<i>u<sub>nf</sub></i>	0.001107275	<i>u<sub>nf</sub></i>	0.001107275	<i>u<sub>nf</sub></i>	0.001107275
<i>V<sub>nf</sub></i>	1.07541E-06	<i>V<sub>nf</sub></i>	1.02863E-06	<i>V<sub>nf</sub></i>	1.01387E-06

**Table 1:** Properties of Titanium Oxide, Copper and Silver nano-particles at volume fraction

(*Φ*) = 0.01 i.e. 1%



## COMPUTATIONAL FLUID DYNAMIC SIMULATION OF A SOLAR ENCLOSURE WITH RADIATIVE FLUX AND DIFFERENT METALLIC NANO-PARTICLES

Miloš Števelin Kuharac<sup>1</sup>, Dr. O. Anwar Bag<sup>1</sup>, Mr. Ali Kadiri<sup>1</sup> and Dr. Meisam Sabale<sup>2</sup>  
<sup>1</sup>Aerospatial and Mechanical Engineering, University of Salford, Manchester, M6 6PU, UK  
<sup>2</sup>Automotive & Autonomous Vehicle Technology (AAVT), University of Salford, Manchester, M6 6PU, UK



### ABSTRACT

Nanofluids are currently being explored extensively in solar energy engineering to achieve improved performance in direct thermal absorption systems [1]. Nanofluids achieve significant enhancement in the heat transfer performance (i.e. thermal efficiency) attributed by these developments in nanotechnology. In this paper we present recent simulations of steady-state radiative natural convection in a solar collector enclosure [2]. Two-dimensional, steady-state, incompressible laminar Newtonian viscous convection-radiative heat transfer in a rectangular solar collector enclosure geometry is modeled with ANSYS FLUENT finite volume code (version 19.5). The enclosure has two adiabatic walls, one hot (solar receiving) and one cooler wall. The Three-Dos volume fraction nanofluid model [3] is used and three different nanoparticles are studied (Copper [Cu], Silver [Ag] and Titanium Oxide [TiO<sub>2</sub>] in water base fluid). The solar radiative heat transfer is simulated in the ANSYS software, with the coupled P1 flux model and the Rosseland model. The influence of geometrical aspect ratio (AR) and solid volume fraction for nanofluids is also studied and a wider range is considered than in other studies. These conductive convective conditions in the area of solar nanofluid collectors show these aspects are considered collectively inter-dependence links are considered. Radiation with polished stainless steel from the finiture is included for the copper-water nanofluid case. The P1 model is shown to more accurately predict the actual influence of solar radiative flux on thermal fluid behaviour compared with Rosseland radiative model. With increasing Rayleigh number (natural convection) (i.e. buoyancy effect), significant modification in the thermal flow characteristics is induced with emergence of different vortex regions. With increasing aspect ratio (order less relative to height of the solar collector geometry) there is a greater thermal convection pattern around the entire geometry, higher temperatures and the extension of the cold upper zone associated with lower aspect ratio. Titanium Oxide nano-particles achieve higher temperatures and a greater local heat flux at the hot wall; thermal performance can be optimized with careful selection of aspect ratio and nanoparticles and this is very beneficial to solar collector designers. The modeling approach can be extended in future to consider fully three-dimensional situations and conductive effects.

### MATHEMATICAL MODEL

Laminar, steady-state, incompressible flow is considered with forced convective heat transfer. The nanofluid is the absorber fluid and the Three-Dos nano-particle volume fraction model is deployed [3]. The fluid model equations are the following form:

**Continuity (mass conservation) (2-D continuity):**

$$\frac{\partial u}{\partial x} + \frac{\partial v}{\partial y} = 0$$

**and  $\rho$  effective molecular concentration:**

$$\left[ \frac{\partial}{\partial x} + \frac{\partial}{\partial y} \right] = -\frac{\partial}{\partial x} + \frac{\partial}{\partial y} + \frac{\partial}{\partial x} + \frac{\partial}{\partial y}$$

$$\left[ \frac{\partial}{\partial x} + \frac{\partial}{\partial y} \right] = -\frac{\partial}{\partial x} + \frac{\partial}{\partial y} + \frac{\partial}{\partial x} + \frac{\partial}{\partial y} - \rho(1 - \beta(T - T_0))$$

**Energy conservation:**

$$\frac{\partial}{\partial x} + \frac{\partial}{\partial y} = \rho_0 \left( \frac{\partial}{\partial x} + \frac{\partial}{\partial y} \right) - Q_{rad}$$

The Three-Dos model allows different concentrations (volume fractions) and types of metallic nanoparticles to be studied. Nanofluid properties can be calculated from the following form:

$\rho = \rho_0(1 - \phi) + \rho_p \phi$  (mass fraction)

$\beta = \frac{\beta_p \phi}{\rho_0(1 - \phi) + \rho_p \phi}$  (volume fraction)

$\mu = \mu_0(1 - \phi)^{-2.5}$  (dynamic viscosity)

$k = k_0(1 - \phi)^{-1}$  (thermal conductivity)

The key flow dimensional parameters which may be computed in the post-processing in ANSYS FLUENT [4] are:

**Rayleigh number:**  $Ra = \frac{g \beta \Delta T L^3}{\nu \alpha}$

**Nusselt number:**  $Nu = \frac{h L}{k_f}$

Here  $g$  is gravity,  $\beta$  is coefficient of thermal expansion,  $\Delta T$  is thermal affinity,  $L$  is coordinate,  $\alpha$  is convection coefficient,  $L$  is height of the enclosure,  $\nu$  is kinematic heat flux rate.

**ANSYS FLUENT Boundary condition and radiative model**

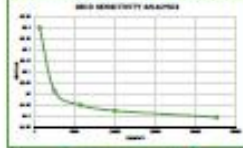
- Left wall: Constant temperature,  $T = 300\text{K}$ .
- Right wall: Constant temperature,  $T = 300\text{K}$ .
- Top and bottom walls: Adiabatic.
- Radiative heat transfer is also incorporated using the ANSYS P1 model and Rosseland radiative model.



Figure 1: Enclosure geometry

### ANSYS FLUENT CFD METHOD

Structures are modeled in ANSYS software with the SIMPLE algorithm available with the pressure-based solver appropriate for incompressible flows. Quadratic (Qu2) elements have been used in the modeling process. (The square enclosure case is shown,  $AR = 1$ ) in Fig. 1. Grid elements are commonly used in a simple geometry to reduce simulation time. Fig. 2 illustrates the grid sensitivity analysis which shows that the structure attains mesh-independent convergence with 75,000 elements.



### VALIDATION

To validate the results obtained from the ANSYS Model for natural convection inside a 2-D enclosure filled with copper-water nanofluid, with a Rayleigh number of  $10^7$ , a comparison is conducted with the earlier study of Abu-Nada & Dahab [5] for an aspect ratio of 1 (square enclosure) as shown in Fig. 2(a-c). The CFD simulation, using ANSYS FLUENT achieves close correlation with the results in [5] as testified by the very close similarity in stream line and isotherm contour patterns. Other test cases were also conducted to further confirm confidence in the ANSYS FLUENT model. Close confidence was established in the simulations it is possible to progress with simplicity in the geometry, buoyancy, radiated type and radiative effects.

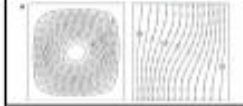


Figure 2: Comparison of results with Abu-Nada & Dahab [5] for an aspect ratio of 1 (square enclosure)

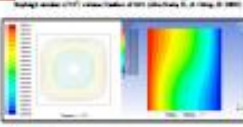


Figure 3: ANSYS FLUENT simulation results for a square enclosure filled with copper-water nanofluid

### RESULTS

#### COMPARISON BETWEEN RADIATIVE FLUX MODELS

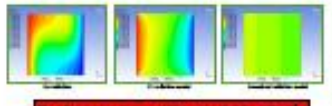


Figure 4: Comparison of velocity profiles for different radiative flux models

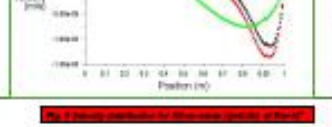


Figure 5: Comparison of Nusselt number profiles for different radiative flux models

#### COMPARISON OF HEAT TRANSFER RATES FOR DIFFERENT NANO-PARTICLES

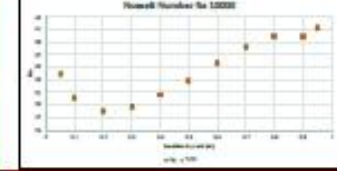


Figure 6: Comparison of Nusselt number profiles for different nanoparticles

#### COMPARISON OF ASPECT RATIO EFFECT FOR TITANIUM OXIDE-WATER

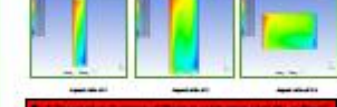


Figure 7: Comparison of aspect ratio effect for Titanium Oxide-water

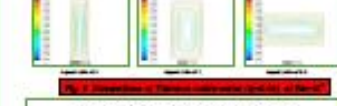


Figure 8: Comparison of aspect ratio effect for Titanium Oxide-water

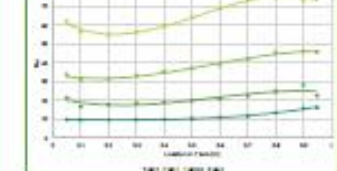


Figure 9: Comparison of aspect ratio effect for Titanium Oxide-water

### CONCLUSIONS

- Results of selected simulations have been presented in Figs. 2-9.
- Simulations show that the Rosseland model provides a temperature field (Figure 4) very different from that obtained without radiation. For the very optimal enclosure in this effect, the temperature field predicted by the Rosseland model is not completely realistic. The P1 differential radiative model produces a more homogeneous thermal effect adjacent to the hot wall and enables better flow to penetrate more evenly through the nanofluid enclosure, whereas the Rosseland model provides a layered temperature enhancement only to the top left corner.
- The P1 model yields the control velocity profiles across the enclosure surface in the energy equation, which is proportional to the absorption coefficient,  $\kappa_0$  used. The Rosseland model uses an effective conductivity to account for radiation, and yields the wrong temperature field, which in turn results in an inaccurate velocity field.
- Deviation in the velocity profile are compared for the three cases of the Rosseland model, P1 model and radiation model. The P1 velocity profile accurately simulate the presence of a constant boundary layer along the hot and cold walls. These compare with other studies in the literature [5].
- Higher Nusselt numbers (Fig. 5) are achieved for the Titanium Oxide water nanofluid compared with Silver-water profiles are much closer to those obtained from nanofluid which is attributable to the higher thermal conductivity of the former.
- With increasing aspect ratio (AR = ratio of height of enclosure to width of enclosure) there is significant expansion in the thermal fluid zones at the upper and lower zones of the enclosure (Fig. 7). A more homogeneous temperature distribution is achieved at lower aspect ratio.
- At Rayleigh number,  $Re = 10^7$  the structure of streamlines suggest that the flow pattern is characterized by single cell circulation for all three aspect ratios considered (AR = 1, AR = 2, AR = 3). Fig. 8. For AR = 2.0 the circulation is a single flow at the other aspect ratios. However at higher aspect ratio, the streamlines distribution are more symmetrical than at the lowest AR value where the asymmetric is observed and a narrower streamer in the circulation which is found towards the left wall end of the solar enclosure. While streamlines a distinctive clarity (Rayleigh [5]).
- Closest the walllines are compressed towards the hot wall and the cold ceiling and middle of the enclosure is occupied by narrow fluid at higher aspect ratios. Due to this effect, the single cell is expanded in both vertical and horizontal directions at higher aspect ratio with lesser deviation in the flow. This expansion results in boundary layer formation. Nusselt number at the left hot wall is maximised at low aspect ratio (AR = 1.0) and minimised at high aspect ratio (AR = 3) indicating that smaller and wider solar enclosures achieve significantly better heat transfer rates than taller and narrower enclosures.
- The present simulation provide a good benchmark for experimental studies and may also be generalised for other metallic nanoparticles (gold, zinc and silver) and extended to the convective case. These aspects are currently under consideration [7, 8].

### Contact

Miloš Števelin Kuharac MSc & Dr. O. Anwar Bag, SMAIAA Department of Aeronautical and Mechanical Engineering, University of Salford, Newton Building, The Crescent, Manchester, M6 6PU, UK.  
 Email: S.kuharac@salford.ac.uk & O.A.bag@salford.ac.uk



### REFERENCES

1. O. Anwar Bag et al., A review of the applications of nanofluids in solar energy, *Int. J. Heat Mass Transfer*, 57, 382-394 (2014).
2. S. Subramani, An Investigation of Nanofluid Solar Collectors with Different Geometries using CFD Simulation, *Final PhD Thesis Assessment Report, Aeronautical and Mechanical Engineering Department, University of Salford, Manchester, UK, November* (2016).
3. R.C. Tiew and M.R. Das, Heat transfer augmentation in a horizontal 60-degree differentially heated square cavity utilizing nanofluids, *Int. J. Heat Mass Transfer*, 50, 2020-2036 (2007).
4. R. Abu-Nada and M.P. Dahab, Effect of inclination angle on natural convection in enclosures filled with Cu-water nanofluid, *Int. J. Heat and Mass Transf.* 30 (1) 189-179 (2008).
5. ANSYS FLUENT Systems, ANSYS FLUENT Theory Manual, ver 18.2, Philadelphia, USA (2019).
6. O. A. Sheddad et al., M.F. 7006: Aspect ratio effects of an adiabatic rectangular enclosure on natural convection and entropy generation of a nanofluid in an enclosure, *J. Mechanical Science and Technology*, 37 (11) 4458-55 (2019).
7. M. Khatami et al., Pressure effect of gold nanoparticles in organic solar cells, *Solar Energy*, 138, 23-31 (2016).
8. S. Subramani and O. Anwar Bag, Investigation of aspect ratio effects on grid, titanium oxide, silver and zinc metallic-nano-particle water based solar collectors with CFD, *Int. J. Energy Research* (2019), in preparation.



## Computation of Metallic Nanofluid Natural Convection in a Two-Dimensional Solar Enclosure with Radiative Heat Transfer, Aspect Ratio and Volume Fraction Effects

Sireetorn Kuharat<sup>1</sup> · O. Anwar Bég<sup>1</sup> · Ali Kadir<sup>1</sup> · B. Vasu<sup>2</sup>

Received: 20 January 2019 / Accepted: 29 May 2020  
© King Fahd University of Petroleum & Minerals 2020

### Abstract

As a model of nanofluid direct absorber solar collectors (nano-DASCs), the present article describes recent numerical simulations of steady-state nanofluid natural convection in a two-dimensional enclosure. Incompressible laminar Newtonian viscous flow is considered with radiative heat transfer. The ANSYS FLUENT finite volume code (version 19.1) is employed. The enclosure has two adiabatic walls, one hot (solar receiving) and one colder wall. The Tiwari–Das volume fraction nanofluid model is used and three different nanoparticles are studied (Copper (Cu), Silver (Ag) and Titanium Oxide (TiO<sub>2</sub>)) with water as the base fluid. The solar radiative heat transfer is simulated with the P1 flux and Rosseland diffusion models. The influence of geometrical aspect ratio and solid volume fraction for nanofluids is also studied and a wider range is considered than in other studies. Mesh independence tests are conducted. Validation with published studies from the literature is included for the copper–water nanofluid case. The P1 model is shown to more accurately predict the actual influence of solar radiative flux on thermal fluid behaviour compared with Rosseland radiative model. With increasing Rayleigh number (natural convection, i.e. buoyancy effect), significant modification in the thermal flow characteristics is induced with emergence of a dual structure to the circulation. With increasing aspect ratio (wider base relative to height of the solar collector geometry), there is a greater thermal convection pattern around the whole geometry, higher temperatures and the elimination of the cold upper zone associated with lower aspect ratio. Titanium Oxide nanoparticles achieve slightly higher Nusselt number at the hot wall compared with Silver nanoparticles. Thermal performance can be optimized with careful selection of aspect ratio and nanoparticles and this is very beneficial to solar collector designers.

**Keywords** Nanofluid · Solar enclosure · Convection radiation · Vortex · Aspect ratio

### Abbreviations

AR	Aspect ratio of enclosure
$c$	ANSYS linear-anisotropic phase function coefficient
$C_p$	Specific heat capacity of the base fluid (J/Kg.K)
$C_{p, \text{nf}}$	Nanofluid specific heat (J/Kg.K)
$g$	Gravitational acceleration (m/s <sup>2</sup> )
$h$	Convective heat transfer coefficient (W/m <sup>2</sup> K)
$k_f$	Base fluid thermal conductivity (W/mK)
$k_{\text{nf}}$	Nanofluid thermal conductivity (W/mK)
$k_s$	Nanoparticle thermal conductivity (W/mK)
$L$	Height of the enclosure (m)
$n$	Refractive index of the nanofluid
$Nu$	Nusselt number (-)
$Q_{\text{rad}}$	Radiative flux term (W/m <sup>2</sup> )
$q''_{\text{wCFD}}$	ANSYS FLUENT heat flux term (W/m <sup>2</sup> )
Ra	Rayleigh number (-)
$T$	Temperature (K)

B. Vasu  
bvasu@mmnit.ac.in

Sireetorn Kuharat  
S.Kuharat@edu.salford.ac.uk

O. Anwar Bég  
O.A.Beg@salford.ac.uk; gortoab@gmail.com

Ali Kadir  
A.Kadir@salford.ac.uk

<sup>1</sup> Aeronautical & Mechanical Engineering Department, School of Computing, Science and Engineering, Newton Building, University of Salford, Manchester M54WT, UK

<sup>2</sup> Department of Mathematics, Motilal Nehru National Institute of Technology Allahabad, Prayagraj, Uttar Pradesh 211004, India

Published online: 10 June 2020



Springer



## Chapter 4

a. Nanofluids properties (diamond and zinc)

Diamond nano- water based fluid			Zinc nano-water based fluid		
Volume fraction	0.02	Units	Volume fraction	0.02	Units
Density	1047.358	kg/m <sup>3</sup>	Density	1119.158	kg/m <sup>3</sup>
Thermal expansions (B)	0.0001959 72	1/K	Thermal expansion (B)	0.000187	1/K
Specific Heat (C <sub>pnf</sub> )	3932.9416 13	J/kg.K	Specific Heat (C <sub>pnf</sub> )	3698.221	J/kg.K
Thermal conductivity (K <sub>nf</sub> )	0.6250092 94	W/m.K	Thermal conductivity (K <sub>nf</sub> )	0.624828	W/m.K
Dynamic viscosity (U <sub>nf</sub> )	0.0011357 38	kg/m.s	Dynamic viscosity (U <sub>nf</sub> )	0.001136	kg/m.s
Pr	7.1467593 31		Pr	6.72218	
Volume fraction	0.04		Volume fraction	0.04	
Density	1097.616	kg/m <sup>3</sup>	Density	1241.216	kg/m <sup>3</sup>
Thermal expansion (B)	0.0001832 28	1/K	Thermal expansion (B)	0.000169	1/K
Specific Heat (C <sub>pnf</sub> )	3709.4164 3	J/kg.K	Specific Heat (C <sub>pnf</sub> )	3311.999	J/kg.K
Thermal conductivity (K <sub>nf</sub> )	0.6365570 81	W/m.K	Thermal conductivity (K <sub>nf</sub> )	0.636209	W/m.K
Dynamic viscosity (U <sub>nf</sub> )	0.0011958 18	kg/m.s	Dynamic viscosity (U <sub>nf</sub> )	0.001196	kg/m.s
Pr	6.9684065 11		Pr	6.225232	
Volume fraction	0.06		Volume fraction	0.06	
Density	1147.874	kg/m <sup>3</sup>	Density	1363.274	kg/m <sup>3</sup>
Thermal expansion (B)	0.0001716	1/K	Thermal expansion (B)	0.000154	1/K
Specific Heat (C <sub>pnf</sub> )	3505.4646 99	J/kg.K	Specific Heat (C <sub>pnf</sub> )	2994.936	J/kg.K
Thermal conductivity (K <sub>nf</sub> )	0.6476694 63	W/m.K	Thermal conductivity (K <sub>nf</sub> )	0.647167	W/m.K
Dynamic viscosity (U <sub>nf</sub> )	0.0012604 44	kg/m.s	Dynamic viscosity (U <sub>nf</sub> )	0.00126	kg/m.s
Pr	6.8220652 09		Pr	5.83304	

**Proc. IMechE- Part N: Journal of Nanomaterials, Nanoengineering and Nanosystems.**

ISSN: 2397-7914; Online ISSN: 2397-7922. Publisher- Sage

In press, January 2021

**FINITE VOLUME NUMERICAL ANALYSIS OF DIAMOND AND ZINC NANOPARTICLES PERFORMANCE IN A WATER-BASED TRAPEZIUM DIRECT ABSORBER SOLAR COLLECTOR WITH BUOYANCY EFFECTS**

Sireetorn Kuharat<sup>1</sup>, O. Anwar Bég<sup>1</sup>, Ali Kadir<sup>1</sup>

<sup>1</sup>Aeronautical & Mechanical Engineering Department, School of Computing, Science and Engineering, Newton Building, University of Salford, Manchester, M54WT, UK.

Emails- [O.A.Beg@salford.ac.uk](mailto:O.A.Beg@salford.ac.uk) ; [S.Kuharat@edu.salford.ac.uk](mailto:S.Kuharat@edu.salford.ac.uk) ; [a.kadir@salford.ac.uk](mailto:a.kadir@salford.ac.uk) ;

\*Corresponding author

**ABSTRACT**

In recent years many nanomaterials have been deployed in solar energy systems. These include both carbon-based (e.g. silicates, diamond, carbon nanotubes) and metallic nanoparticles (gold, silver, copper, tin, zinc etc). By combining these nanoparticles with water base fluids, to create nanofluids, improved performance can be achieved in direct absorber solar collector (DASC) systems. In the current work, motivated by these developments, a finite volume code (ANSYS FLUENT ver 19.1) is employed to simulate the relative performance of both carbon-based (i.e. diamond) and metal-based (i.e. zinc) nanoparticles in a trapezium geometry. The Tiwari-Das formulation is implemented to compute viscosity, thermal conductivity and heat capacity properties for diamond-water and zinc-water nanofluids at different volume fractions. Steady state nanofluid buoyancy-driven incompressible laminar Newtonian convection is examined. The SIMPLE solver is deployed, and residual iterations utilized for convergence monitoring. Mesh independence is included. Verification with the penalty finite element computations of Natarajan *et al.* (*Int. J. of Heat and Mass Transfer*, 51:747-756, 2008) for the case of a Newtonian viscous fluid (zero volume fraction) is also conducted and excellent correlation achieved. Isotherm, streamline and local Nusselt number plots are presented for different volume fractions, sloping wall inclinations (both negative and positive slopes are considered) and Rayleigh numbers. Vortex structure and thermal distributions are shown to be modified considerably with these parameters. Overall diamond achieves higher heat transfer rates while more stable velocity distributions are produced with zinc nanoparticles. These trends are amplified at higher volume fractions. The present computations may be further generalized to the three-dimensional case although this requires significantly greater mesh densities and compilation times.

**KEY WORDS:** *Nanoparticles; diamond; zinc; direct absorber solar collectors (DASCs), finite volume method; ANSYS FLUENT; free convection; Rayleigh number; trapezoidal enclosure; volume fraction, Tiwari-Das model.*

**NOTATION**

$AR$	aspect ratio of enclosure
$C_p$	specific heat capacity of the base fluid ( $J/Kg.K$ )
$C_{pmf}$	nanofluid specific heat ( $J/Kg.K$ )
$g$	gravitational acceleration ( $m/s^2$ )
$h$	convective heat transfer coefficient ( $W/m^2K$ )

## Chapter 5

Property	Value	Units
Grashof number (Ra/Pr)	$2.45 \times 10^4$	–
Rayleigh number (Ra)	$10^5$	–
Gold density ( $\rho_p$ )	1912.245	kg/m <sup>3</sup>
Gold thermal expansion ( $\beta$ )	$1.11 \times 10^{-4}$	1/K
Height of enclosure (L)	0.5	m
Water kinematic viscosity ( $\nu$ )	6.42E-07	m <sup>2</sup> /s
Water thermal diffusivity ( $\alpha_m$ )	1.57355E-07	m <sup>2</sup> /s
Gravity (g)	9.81	m/s <sup>2</sup>
Temperature difference ( $\Delta T$ )	10	K
Nanofluid Specific Heat ( $C_{p_{nf}}$ )	2133.684154	J/kg.K
Nanofluid thermal conductivity ( $K_{nf}$ )	0.642029776	W/m.K
Nanofluid dynamic viscosity ( $\mu_{nf}$ )	0.001227536	kg/m.s
Prandtl number (Pr)	4.079521928	–

**Table 1:** Thermophysical and hydrodynamic properties of gold nano-particles and gold-water nanofluid

Tilt angle ( $\alpha$ )	Surface Heat Flux $Q$ (W/m <sup>2</sup> )
0	83.872254
10	80.130418
30	70.722287
45	60.323023
60	47.4667

**Table 2.** Heat flux computed on hot wall for *gold-water nanofluid*, with  $\phi = 5\%$ ,  $AR = 2$  and  $Ra = 10^5$  for inclination ( $\alpha$ ) = 60 degrees.

Volume Fraction ( $\phi$ )	Surface Heat Flux $Q$ (W/m <sup>2</sup> )
0.02	69.212486
0.05	70.722287
0.08	72.398288
0.11	73.886681
0.14	75.408061

**Table 3.** Heat flux computed on hot wall for *gold-water nanofluid*, with  $\alpha = 30$  degrees  $AR = 2$  and  $Ra = 10^5$  for different gold nano-particle volume fractions ( $\phi$ ).

Aspect ratio (AR)	Surface Heat Flux $Q$ (W/m <sup>2</sup> )
1	56.805868
2	70.722287
4	74.055584

**Table 4.** Heat flux computed on hot wall for *gold-water nanofluid*, with  $\alpha = 30$  degrees,  $Ra = 10^6$  and gold volume fraction ( $\phi$ ) = 5% for various aspect ratios (AR). The three-dimensional gold prism nanofluid model study was submitted to *Nanoscience and Technology Journal* in August 2019 and will also be presented next year in *July 2020 at Eurotherm Conference in Portugal*

# COMPUTATION OF GOLD-WATER NANOFUID NATURAL CONVECTION IN A THREE-DIMENSIONAL TILTED PRISMATIC SOLAR ENCLOSURE WITH ASPECT RATIO AND VOLUME FRACTION EFFECTS

Miss Sireetorn Kuharat and Dr. D. Anwar Beg  
University of Salford, Manchester, UK.

## ABSTRACT

Nanofluids are increasingly being employed in numerous energy applications owing to their impressive thermal enhancement properties. Motivated by these developments in the current study we present three volume fraction simulations of natural convection in an inclined three-dimensional (3D) prismatic glass enclosure solar collector (3D-SC) employing gold-water nanofluid. Boundary conditions (impenetrable bottom, isothermal vertical base, adiabatic top, adiabatic side and rear walls) and one solid wall with all the remaining walls are adiabatic. ANSYS FLUENT computational fluid dynamics software is employed. The Three-Phase volume fraction nanofluid model is utilized to simulate nanofluid effects and allows a systematic exploration of volume fraction effects. The effects of thermal buoyancy (Rayleigh number), prismatic aspect ratio and enclosure tilt angle on isotherms and temperature contours distribution are presented with extensive visualization in both two and three dimensions. Grid-independence tests are included. Tabulation with published studies from the literature is also included. A significant modification in terms of pressure and temperature distribution is observed with volume fraction, Rayleigh number, aspect ratio and tilt angle. Grid-independence test is relatively low volume fraction are observed. Relative numerical improvement in low nanofluid concentration.

## MATHEMATICAL MODEL

The 3D model of base enclosure in the solar nanofluid collector are designed in ANSYS FLUENT [6]. The geometric configuration is illustrated in Fig. 1. The fundamental equations for steady state, incompressible laminar flow and thermal convection are the three-dimensional three-dimensional Navier-Stokes equations and energy equation, which is a Cartesian coordinate system, take the following form:

$$\rho \left( \frac{\partial u}{\partial t} + u \frac{\partial u}{\partial x} + v \frac{\partial u}{\partial y} + w \frac{\partial u}{\partial z} \right) = -\frac{\partial p}{\partial x} + \mu \left( \nabla^2 u \right) + \rho \beta g_x \theta \quad (1)$$

$$\rho \left( \frac{\partial v}{\partial t} + u \frac{\partial v}{\partial x} + v \frac{\partial v}{\partial y} + w \frac{\partial v}{\partial z} \right) = -\frac{\partial p}{\partial y} + \mu \left( \nabla^2 v \right) + \rho \beta g_y \theta \quad (2)$$

$$\rho \left( \frac{\partial w}{\partial t} + u \frac{\partial w}{\partial x} + v \frac{\partial w}{\partial y} + w \frac{\partial w}{\partial z} \right) = -\frac{\partial p}{\partial z} + \mu \left( \nabla^2 w \right) + \rho \beta g_z \theta \quad (3)$$

$$\rho c_p \left( \frac{\partial \theta}{\partial t} + u \frac{\partial \theta}{\partial x} + v \frac{\partial \theta}{\partial y} + w \frac{\partial \theta}{\partial z} \right) = k \nabla^2 \theta \quad (4)$$

Three-Phase model allows different concentrations (volume fraction) and types of nanofluid nanoparticles. Three nanofluid properties are calculated from below equation:

$$\rho = \phi \rho_p + (1 - \phi) \rho_f \quad (5)$$

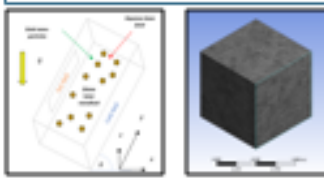
$$c_p = \phi c_{p,p} + (1 - \phi) c_{p,f} \quad (6)$$

$$k = \phi k_p + (1 - \phi) k_f \quad (7)$$

The key dimensionless parameters which employed are local Rayleigh number (Ra) and the average Nusselt number on the hot wall (Nu).

$$Ra = \frac{g \beta \Delta T D^3}{\nu \alpha} \quad (8)$$

$$Nu = \frac{h D}{k_f} \quad (9)$$



## GRID STUDY & VALIDATION

An extensive mesh testing procedure was conducted to guarantee a grid-independent solution. The grid independence test has been performed on a tilted enclosure (in aspect ratio = 1) with Ra = 10^6 (volume fraction = 0.02) in 3D grid comparison by volume. The results of the mesh variation are shown in Fig. 2. It is evident that the simulation results are grid-independent convergence with approximately 45,000 Tetrahedron elements (Fig. 2). From Fig. 2, it shows that the non-dimensional temperature along the horizontal coordinate in the TG-0.4 confirms that the present results are close to the benchmark results. Furthermore, it also confirms that the grid resolution of the simulation is fine enough to obtain the independent results.



Fig. 2. Grid-independence test of 3D-SC solar collector.

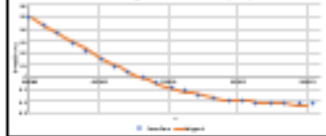


Fig. 3. The non-dimensional temperature along the horizontal coordinate for Ra = 10^6, 10^7, 10^8.

## RESULT AND DISCUSSION

### TILT EFFECT

Fig. 4 shows the influence of the Rayleigh number on the 3D-SC solar collector. Initially, there is an intensification in temperature contours only on the left hot wall with higher Rayleigh number. This is modified as a function of time in the upper left corner of the enclosure with an increase in Rayleigh number from 10^6 to 10^8. This trend continues to prevail with further increases in Rayleigh number up to 10^8. However, at very high Rayleigh number of 10^8 the temperature distribution achieved is much more homogeneous. Significantly more balanced thermal diffusion through the enclosure is observed achieved with very strong thermal buoyancy effect and there is a connection in the preferential hot zone on the hot wall for this scenario.



Fig. 4. Higher Rayleigh number 3D-SC solar collector.

### VOLUME FRACTION EFFECT

Fig. 5 shows the influence of the Rayleigh number on the 3D-SC solar collector. The presence of nanoparticles modifies the convection and enhances thermal diffusion away from the wall. This reduces the thermal enhancement. Similar findings have been reported by numerous authors including Tahir et al. [2], Tahir et al. [3], Balade et al. [4] and Shariq et al. [5] for both water-based and oil-based nanoparticles although they did not mention the case of gold.

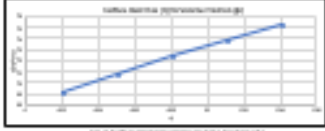


Fig. 5. Effect of volume fraction on 3D-SC solar collector.

### ASPECT RATIO EFFECT

Fig. 6 shows the influence of the Rayleigh number on the 3D-SC solar collector. Initially, there is an intensification in temperature contours only on the left hot wall with higher Rayleigh number. This is modified as a function of time in the upper left corner of the enclosure with an increase in Rayleigh number from 10^6 to 10^8. This trend continues to prevail with further increases in Rayleigh number up to 10^8. However, at very high Rayleigh number of 10^8 the temperature distribution achieved is much more homogeneous. Significantly more balanced thermal diffusion through the enclosure is observed achieved with very strong thermal buoyancy effect and there is a connection in the preferential hot zone on the hot wall for this scenario.



Fig. 6. Higher Rayleigh number 3D-SC solar collector.

### CONCLUSIONS

- Higher aspect ratio leads to improved heat transfer in the enclosure with larger penetration of warmer zones in the enclosure.
- Increasing Rayleigh number (thermal buoyancy force relative to viscous hydrodynamic force), there is an intensification in heat transfer from the left hot wall through the enclosure space and much more homogeneous temperature distribution are eventually obtained.
- With increasing nanoparticles volume fraction, heat transfer more effectively into the enclosure from the hot wall and temperature magnitude are enhanced.
- With greater inclination of the enclosure there is a progressive alteration in heat transfer from the left hot wall (hot wall) towards the upper left wall, and temperature are shared mainly in the upper left zone with a more extensive cooling in the central zone.
- Heat flux is dramatically increased with greater nanoparticles volume fraction and aspect ratio whereas it is supplemented with greater inclination of the enclosure.

### References

1. Ghosh, S. and Ghosh, S. Simulation of a nanofluid-based solar collector. *ASME J. Sol. Energy Eng.* 129, 1-11 (2007).
2. Tahir, M., Ghosh, S., and Ghosh, S. Numerical simulation of a nanofluid-based solar collector. *Applied Thermal Engineering*, 108, 104-110 (2016).
3. Tahir, M., Ghosh, S., and Ghosh, S. Numerical simulation of a nanofluid-based solar collector. *International Journal of Thermal Sciences*, 41, 1271-1280 (2012).
4. Balade, S., Ghosh, S., and Ghosh, S. Numerical simulation of a nanofluid-based solar collector. *International Journal of Thermal Sciences*, 41, 1271-1280 (2012).
5. Shariq, A., Ghosh, S., and Ghosh, S. Numerical simulation of a nanofluid-based solar collector. *International Journal of Thermal Sciences*, 41, 1271-1280 (2012).
6. ANSYS FLUENT, *ANSYS Inc., Canonsburg, PA* (2015).

**Contact**  
Miss Sireetorn Kuharat, Dr. D. Anwar Beg  
Email: S.Kuharat@salford.ac.uk & D.A.Beg@salford.ac.uk  
University of Salford  
Department of Aeronautics and Mechanical Engineering, Newton Building,  
The Crescent, Manchester M6 6PU, UK.

## COMPUTATION OF GOLD–WATER NANOFLUID NATURAL CONVECTION IN A THREE-DIMENSIONAL TILTED PRISMATIC SOLAR ENCLOSURE WITH ASPECT RATIO AND VOLUME FRACTION EFFECTS

Sireetorn Kuharat,<sup>1</sup> O. Anwar Bég,<sup>1</sup> Ali Kadir,<sup>1</sup> B. Vasu,<sup>2,\*</sup>  
Tasveer A. Bég,<sup>3</sup> & W.S. Jouri<sup>1</sup>

<sup>1</sup>*Multi-Physical Engineering Sciences Group, Aeronautical and Mechanical Engineering Department, School of Science, Engineering and Environment (SÉE), Newton Building, University of Salford, Manchester, M54WT, UK*

<sup>2</sup>*Department of Mathematics, Motilal Nehru National Institute of Technology Allahabad, Prayagraj, Uttar Pradesh- 211004, India*

<sup>3</sup>*Renewable Energy/Computational Mechanics, Israfil House, Dickenson Rd., Manchester, M13, UK*

\*Address all correspondence to: B. Vasu, Department of Mathematics, Motilal Nehru National Institute of Technology Allahabad, Prayagraj, Uttar Pradesh- 211004, India, E-mail: bvasu@mnnit.ac.in

*Original Manuscript Submitted: 6/16/2019; Final Draft Received: 11/13/2019*

*Nanofluids are increasingly being deployed in numerous energy applications owing to their impressive thermal enhancement properties. Motivated by these developments in the current study we present finite volume numerical simulations of natural convection in an inclined three-dimensional prismatic direct absorber solar collector (DASC) containing gold–water nanofluid. Steady-state, incompressible laminar Newtonian viscous flow is assumed. The enclosure has two adiabatic walls, one hot (solar receiving) and one colder wall. ANSYS FLUENT software (version 19.1) is employed. The Tiwari–Das volume fraction nanofluid model is utilized to simulate nanoscale effects and allows a systematic exploration of volume fraction effects. The effects of thermal buoyancy (Rayleigh number), geometric aspect ratio, and enclosure tilt angle on isotherm and temperature contour distributions are presented with extensive visualization in three dimensions. Grid-independence tests are included. Validation with published studies from the literature is also conducted. A significant modification in vortex structure and temperature distribution is computed with volume fraction, Rayleigh number, aspect ratio, and tilt angle. Heat flux and average Nusselt number results are also included. Gold nanoparticles even at relatively low volume fractions are observed to achieve substantial improvement in heat transfer characteristics.*

**KEY WORDS:** *gold nanoparticles, prismatic direct absorber solar collector, inclination, dilute aqueous nanofluid, finite volume method, thermal buoyancy, isotherms, streamlines, aspect ratio, volume fraction, thermal conductivity, Nusselt number*



# Chapter 6

CuO		Al2O3		TiO2		Cu		Ag	
Vnp	1	Vnp	1	Vnp	1	Vnp	1	Vnp	1
Vf	100	Vf	100	Vf	100	Vf	100	Vf	100
Φ	0.01	Φ	0.01	Φ	0.01	Φ	0.01	Φ	0.01
Pf	997.1	Pf	997.1	Pf	997.1	Pf	997.1	Pf	997.1
Ps	6500	Ps	3970	Ps	4250	Ps	8933	Ps	10500
Pnf	1052.129	Pnf	1026.829	Pnf	1029.629	Pnf	1076.459	Pnf	1092.129
Cpf	4179	Cpf	4179	Cpf	4179	Cpf	4179	Cpf	4179
Cps	535.6	Cps	765	Cps	686.2	Cps	385	Cps	235
Cpnf	3953.912582	Cpnf	4047.005481	Cpnf	4034.8276816	Cpnf	3864.1547342	Cpnf	3799.8140247
Ks	20	Ks	40	Ks	8.9538	Ks	401	Ks	429
Kf	0.613	Kf	0.613	Kf	0.613	Kf	0.613	Kf	0.613
Knf	0.6185482274	Knf	0.6188011308	Knf	0.6179817858	Knf	0.6190418312	Knf	0.6190436195
uf	1.08E-03	uf	1.08E-03	uf	1.08E-03	uf	1.08E-03	uf	1.08E-03
unf	0.0011072746	unf	0.0011072746	unf	0.0011072746	unf	0.0011072746	unf	0.0011072746
Vnf	1.052413E-006	Vnf	1.078344E-006	Vnf	1.075411E-006	Vnf	1.028627E-006	Vnf	1.013868E-006
Bs	1.80E-05	Bs	8.50E-06	Bs	9.00E-06	Bs	1.67E-05	Bs	1.86E-05
Bf	2.10E-04	Bf	2.10E-04	Bf	2.10E-04	Bf	2.10E-04	Bf	2.10E-04
Bnf	0.0001981383	Bnf	0.0002022095	Bnf	0.0002017033	Bnf	0.000193959	Bnf	0.0001915983

CuO		Al2O3		TiO2		Cu		Ag	
Vnp	4	Vnp	4	Vnp	4	Vnp	4	Vnp	4
Vf	100	Vf	100	Vf	100	Vf	100	Vf	100
Φ	0.04	Φ	0.04	Φ	0.04	Φ	0.04	Φ	0.04
Pf	997.1	Pf	997.1	Pf	997.1	Pf	997.1	Pf	997.1
Ps	6500	Ps	3970	Ps	4250	Ps	8933	Ps	10500
Pnf	1217.216	Pnf	1116.016	Pnf	1127.216	Pnf	1314.536	Pnf	1377.216
Cpf	4179	Cpf	4179	Cpf	4179	Cpf	4179	Cpf	4179
Cps	535.6	Cps	765	Cps	686.2	Cps	385	Cps	235
Cpnf	3400.7617908	Cpnf	3693.2155668	Cpnf	3652.2367177	Cpnf	3147.706768	Cpnf	2976.2257075
Ks	20	Ks	40	Ks	8.9538	Ks	401	Ks	429
Kf	0.613	Kf	0.613	Kf	0.613	Kf	0.613	Kf	0.613
Knf	0.6346062392	Knf	0.6355639216	Knf	0.6324528691	Knf	0.6364732558	Knf	0.6364800038
uf	1.08E-03	uf	1.08E-03	uf	1.08E-03	uf	1.08E-03	uf	1.08E-03
unf	0.0011958184	unf	0.0011958184	unf	0.0011958184	unf	0.0011958184	unf	0.0011958184
Vnf	9.824209E-007	Vnf	1.071507E-006	Vnf	1.060860E-006	Vnf	9.096886E-007	Vnf	8.682868E-007
Bs		Bs		Bs	9.00E-06	Bs	1.67E-05	Bs	1.86E-05
Bf	2.10E-04	Bf	2.10E-04	Bf	2.10E-04	Bf	2.10E-04	Bf	2.10E-04
Bnf		Bnf	0.0001801187	Bnf	0.0001796864	Bnf	0.0001574568	Bnf	0.0001516301

CuO		Al2O3		TiO2		Cu		Ag	
Vnp	8	Vnp	8	Vnp	8	Vnp	8	Vnp	8
Vf	100	Vf	100	Vf	100	Vf	100	Vf	100
Φ	0.08	Φ	0.08	Φ	0.08	Φ	0.08	Φ	0.08
Pf	997.1	Pf	997.1	Pf	997.1	Pf	997.1	Pf	997.1
Ps	6500	Ps	3970	Ps	4250	Ps	8933	Ps	10500
Pnf	1437.332	Pnf	1234.932	Pnf	1257.332	Pnf	1631.972	Pnf	1757.332
Cpf	4179	Cpf	4179	Cpf	4179	Cpf	4179	Cpf	4179
Cps	535.6	Cps	765	Cps	686.2	Cps	385	Cps	235
Cpnf	2860.8856047	Cpnf	3300.9869596	Cpnf	3234.4984682	Cpnf	2517.6086526	Cpnf	2293.7785393
Ks	20	Ks	40	Ks	8.9538	Ks	401	Ks	429
Kf	0.613	Kf	0.613	Kf	0.613	Kf	0.613	Kf	0.613
Knf	0.6547412368	Knf	0.6565257052	Knf	0.6507090826	Knf	0.6582151152	Knf	0.658227634
uf	1.08E-03	uf	1.08E-03	uf	1.08E-03	uf	1.08E-03	uf	1.08E-03
unf	0.0013300677	unf	0.0013300677	unf	0.0013300677	unf	0.0013300677	unf	0.0013300677
Vnf	9.253727E-007	Vnf	0.000001077	Vnf	1.057849E-006	Vnf	0.000000815	Vnf	7.568676E-007
Bs		Bs		Bs	9.00E-06	Bs	1.67E-05	Bs	1.86E-05
Bf	2.10E-04	Bf	2.10E-04	Bf	2.10E-04	Bf	2.10E-04	Bf	2.10E-04
Bnf		Bnf	0.0001559922	Bnf	0.0001556468	Bnf	0.000125354	Bnf	0.0001185113

# SIMULATION OF A NANOFLUID-BASED ANNULAR SOLAR COLLECTOR

Miss Sireetorn Kuharat and Dr. O. Anwar Bég  
 University of Salford, Manchester, UK.

## Abstract

A numerical study of convective heat transfer in an annular pipe solar collector system (Fig. 1) is conducted. The inner tube contains pure water and the annular region contains nanofluid. Three-dimensional steady-state incompressible laminar flow comprising water-based nanofluid containing a variety of metallic nanoparticles (copper oxide, aluminium oxide and titanium oxide nanoparticles) is examined. The Tiwari-Das model is deployed for which thermal conductivity, specific heat capacity and viscosity of the nanofluid suspensions is evaluated as a function of solid nano-particle volume fraction. Radiative heat transfer is also incorporated using the ANSYS solar flux and Rosseland radiative models. The ANSYS FLUENT finite volume code (version 18.1) is employed to simulate the thermo-fluid characteristics. Mesh-independence tests are conducted. The influence of volume fraction on temperature, velocity, pressure contours is computed and visualized. Copper oxide nanofluid is observed to achieve the best temperature enhancement. Temperature contours at cross-sections of the annulus are also computed.



Fig. 1: Geometrical and physical model for annular nanofluid solar collector

## MATHEMATICAL MODEL

The three-dimensional models of heat and fluid flow in the solar collector tube are designed in ANSYS FLUENT computational fluid dynamics software. Laminar, steady-state, incompressible flow is considered with forced convective heat transfer. The annular nanofluid is the absorber fluid and the Tiwari-Das nano-particle volume fraction model is deployed [1]. The fundamental equations for steady viscous, incompressible laminar flow are the three-dimensional time-independent Navier-Stokes equations, which in a Cartesian coordinate system, take the following form:

**D'Alembert mass conservation (3-D continuity)**

$$\frac{\partial u}{\partial x} + \frac{\partial v}{\partial y} + \frac{\partial w}{\partial z} = 0$$

**x-direction momentum conservation**

$$\rho \left[ u \frac{\partial u}{\partial x} + v \frac{\partial u}{\partial y} + w \frac{\partial u}{\partial z} \right] = \rho F_x - \frac{\partial p}{\partial x} + \mu \left[ \frac{\partial^2 u}{\partial x^2} + \frac{\partial^2 u}{\partial y^2} + \frac{\partial^2 u}{\partial z^2} \right]$$

**The same in y and z direction**

**The appropriate energy conservation equation is:**

$$u \frac{\partial T}{\partial x} + v \frac{\partial T}{\partial y} + w \frac{\partial T}{\partial z} = \alpha_{eff} \left( \frac{\partial^2 T}{\partial x^2} + \frac{\partial^2 T}{\partial y^2} + \frac{\partial^2 T}{\partial z^2} \right) + Q_{rad}$$

**Tiwari-Das model** allows different concentrations (volume fraction) and types of metallic nanoparticles. Where nano fluid properties can be calculated from the following equation:

$$\phi = \frac{V_{np}}{V_f}, \mu_{nf} = \frac{\mu_b}{(1-\phi)^{2.5}}, \rho_{nf} = (1-\phi)\rho_f + \phi\rho_s,$$

$$C_{p,nf} = \frac{(1-\phi)(C_{p,f}) + \phi(C_{p,s})}{\rho_{nf}}, k_{nf} = \frac{k_s + 2k_f - 2\phi(k_f - k_s)}{k_f + 2k_f - \phi(k_f - k_s)}$$

Here  $\phi$ =volume fraction,  $V_{np}$ =nano particles volume and  $V_f$ =volume of fluid,  $\mu_b$ = dynamic viscosity of nanofluid (kg/m.s),  $\mu_s$ = dynamic viscosity of base fluid,  $\rho_{nf}$ =nanofluid density,  $\rho_f$ =base fluid density,  $\rho_s$ =nanoparticle density,  $C_{p,nf}$ =nanofluid specific heat,  $k_{nf}$ =nanofluid thermal conductivity,  $k_f$ = fluid thermal conductivity and  $k_s$ = nanoparticle thermal conductivity.

**ANSYS FLUENT Boundary condition and radiation model**

**At the inlet:** Volume flow rate inlet of 0.002 kg/s

**At the outlet:** Zero pressure outlet from one face.

**Heat flux:** Heat is added as the sun radiation intensity of 877 W/m<sup>2</sup>. In ANSYS FLUENT physics, gravity is set as 9.81 m/s<sup>2</sup>.

Radiative heat transfer is also incorporated using the ANSYS solar load model and Rosseland radiative models. The ANSYS FLUENT finite volume code [2] is employed to simulate the thermo-fluid characteristics.

## ANSYS FLUENT CFD Method

Fig. 2 shows the ANSYS methodology employed for the CFD simulations (SIMPLE). Fig. 3a shows the ANSYS FLUENT full hex element mesh and Fig. 3b shows the mesh cross-section used.

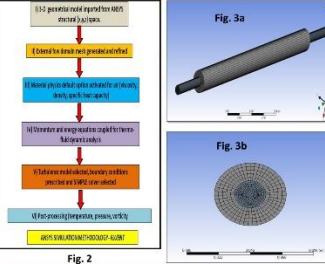


Fig. 2

## Grid Study

Fig. 4 shows the grid sensitivity analysis. The largest elements used in case one can be considered as a coarse mesh with 103068 elements. On increasing the number of elements by 100000 (case two), the graph shows a variation indicating that the simulation is not convergent. The next part of the grid dependent study covers cases three, four and five. Upon observation of cases four (325951 elements) and five (448836 elements), these cases utilize a fine mesh, where the difference between the two values are infinitesimal and hence considered negligible. This shows that the simulation is convergent at case four with 448836 elements. This grid-independence study provides an appropriate grid size (case four) which is subsequently adopted for all further simulations and is of sufficient quality to guarantee mesh-independent and converged results i.e. the most accurate results possible with the minimum number of elements.

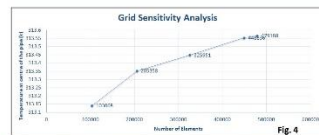
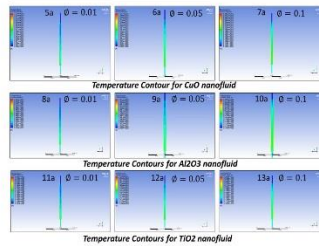


Fig. 4

## Results & Discussion

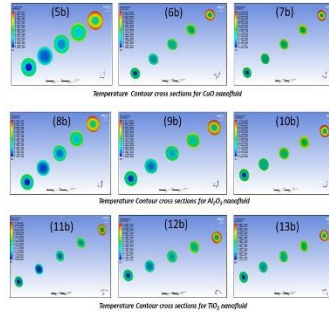
5a, 5b and 7a show a significant modification in temperature distributions as volume fraction is enhanced from  $\phi = 0.01$ , to  $\phi = 0.05$  and finally  $\phi = 0.1$ . There is progressive heating from the base upwards of the annular region with increasing volume fraction. The blue zones are progressively eliminated, and green zones (higher temperature) extend further towards the upper adiabatic end. Red (maximum temperature zones) begin to appear at the highest volume fraction (Fig. 7a). The increase in concentration of metallic nanoparticles clearly enhances thermal conductivity of the nanofluid in the annular region and this intensifies thermal diffusion and heat transfer (Figs. 11a, 12a, 13a) The temperature magnitudes exceed those computed at the same values of volume fraction for Aluminium oxide (Figs. 8a, 9a, 10a) but are substantially lower than those obtained for Copper oxide (Figs. 6a, 7a, 8a). This confirms the superior performance of Copper oxide in achieving thermal enhancement in the solar annular collector.



Temperature Contours for TiO2 nanofluid



Temperature Contours for TiO2 nanofluid



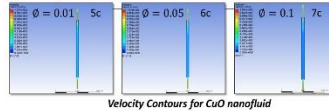
Temperature Contour cross sections for CuO nanofluid

Temperature Contour cross sections for Al2O3 nanofluid

Temperature Contour cross sections for TiO2 nanofluid

Fig. 11b, 12b and 13b (temperature cross-section slice views) also show that temperatures are markedly enhanced with increasing volume fraction of titanium oxide nano-particles, as we progress from the lower end of the annular region to the upper end. Stronger red (high temperature) and yellow zones (quite high temperature) appear to grow considerably. The magnitudes achieved are larger than those for the Aluminium oxide cases (Figs. 8b, 9b and 10b). However, they are still somewhat less than those attained for the Copper oxide cases (Figs. 5b, 6b and 7b). Apparently therefore higher nano-particle concentrations (volume fractions) of Copper oxide attain the best thermal performance since the best absorption of solar thermal energy is achieved. Intensified thermal convection currents are generated for this case. Titanium oxide is the next best option, whereas Aluminium oxide is the least successful option. These findings are important since they generalize previous studies in which a single metallic nano-particle was examined e.g. Copper oxide by Moghadam et al. [3] or two metallic nanofluids (silver oxide and aluminium oxide) by Maddah et al. [4].

Figs. 6c, 6c and 7c illustrate the evolution in velocity through the annular space. A less tangible influence is computed with increasing volume fraction. In all cases high velocity zones arise at the inlet and outlet with slower zones in the interim sections. The primary influence on velocity is via the viscosity modification in the Tiwari-Das model. Although there is a slight intensification in velocity i.e. flow acceleration at the highest volume fraction (Fig. 7c), this is only identified in the extremity zones of the annular geometry.



Velocity Contours for CuO nanofluid

## Conclusions

- (i) Copper oxide nanofluid is observed to achieve the best temperature enhancement. Temperature contours at cross-sections of the annulus are also computed.
- (ii) Titanium Oxide achieves higher temperatures than Aluminium Oxide but significantly lower temperatures than Copper Oxide.
- (iii) Temperature cross-sections exhibit significant enhancement in magnitudes with volume fraction for all three metallic nanoparticles, although the best performance again is with Copper Oxide.
- (iv) There is flow acceleration for the Copper oxide case at the highest volume fraction although it is confined to the extremity zones of the annular geometry (inlet and outlet).
- (v) Velocities are initially increased with volume fraction for the Aluminium Oxide case but subsequently with maximum volume fraction they are reduced.
- (vi) Pressures are also reduced somewhat with increasing volume fraction for the Copper oxide case and not altered significantly for either Titanium Oxide or Aluminium Oxide cases.

## References

1. Tiwari RK, Das MK, Heat transfer augmentation in a two-sided lid-driven differentially heated square cavity utilizing nanofluids. *Int J Heat Mass Transfer*, 50, 2002–2018 (2007).
2. ANSYS FLUENT Theory Manual, ver 18.1, Swanson Analysis Systems, Pennsylvania, USA (2018).
3. A. J. Moghadam, M. Farzane-Gord, M. Sajadi and M. Hoseny Zadeh, Effects of CuO/water nanofluid on the efficiency of a flat-plate solar collector, *Experimental Thermal and Fluid Science*, 58, 9–14 (2014).
4. H. Maddah, M. Rezaeadeh, M. Maghsoudi, and S. Nasiri Kokhdan, The effect of silver and aluminium oxide nanoparticles on thermophysical properties of nanofluids, *J. Nanostructure in Chemistry*, 3, article 28, 6 pages (2013).

## Contact



Miss Sireetorn Kuharat MSc & Dr. O. Anwar Bég  
 University of Salford  
 Department of Aeronautical and Mechanical Engineering  
 Newton Building, The Crescent, Manchester, M5 4WT, UK.  
 Email: S.Kuharat@edu.salford.ac.uk & O.A.Beg@salford.ac.uk

## Computational Fluid Dynamics Simulation of a Nanofluid-Based Annular Solar Collector with Different Metallic Nano-Particles

Sireetorn Kuharat and O. Anwar Bég\*

*Aeronautical & Mechanical Engineering Department, School of Computing, Science and Engineering, Newton Building, University of Salford, Manchester, M6 4WT, UK*

### Abstract

A numerical study of convective heat transfer in an annular pipe solar collector system is conducted. The inner tube contains pure water and the annular region contains nanofluid. Three-dimensional steady-state incompressible laminar flow comprising water-based nanofluid containing a variety of metallic nano-particles (copper oxide, aluminium oxide and titanium oxide nano-particles) is examined. The Tiwari-Das model is deployed for which thermal conductivity, specific heat capacity and viscosity of the nanofluid suspensions is evaluated as a function of solid nano-particle volume fraction. Radiative heat transfer is also incorporated using the ANSYS solar flux and Rosseland radiative models. The ANSYS FLUENT finite volume code (version 18.1) is employed to simulate the thermo-fluid characteristics. Mesh-independence tests are conducted. The influence of volume fraction on temperature, velocity, pressure contours is computed and visualized. Copper oxide nanofluid is observed to achieve the best temperature enhancement. Temperature contours at cross-sections of the annulus are also computed.

**Keywords:** *Thermal convection; nanofluid; annulus; ANSYS FLUENT; finite volume; metallic nano-particles; Temperature contours; Velocity; Pressure; Solar collector.*

### Nomenclature

$C_p$	specific heat capacity	$\nabla T$	temperature gradient
$k$	thermal conductivity	$\mu$	dynamic viscosity of base fluid
$k_r$	radiative conductivity	$\mu_{nf}$	dynamic viscosity of nanofluid
$n$	refractive index	$\rho$	density
$Q_c$	thermal conduction flux	$\phi$	volume fraction
$Q_{rad}$	radiative flux term	$C_{p,nf}$	nanofluid specific heat
$T$	denotes temperature	$\rho_f$	base fluid density
$V_f$	volume of fluid	$\rho_{nf}$	nanofluid density
$V_{sp}$	nano particles volume	$\rho_s$	nanoparticle density

### 1. Introduction

Motivated by cleaner and more sustainable energy resources in the 21<sup>st</sup> century, engineers have intensified efforts in studying and developing more efficient renewable energy designs. While many different options exist, solar energy remains the most promising owing to the vast quantities of heat received daily in many parts of the world. The current energy utilization globally is a fraction of the total solar radiation reaching the earth as noted by Kalogirou [1]. Solar collector design continues to undergo refinements and is being implemented on large scales in many continents. A wide spectrum of solar collectors has been implemented of which solar thermal absorption collectors (including concentrated solar power plants) are the most popular and absorb solar radiation directly via heating a working fluid which then drives a turbine connected to electrical generator units. These are the most widely deployed in commercial and domestic applications and include parabolic troughs, solar flat plate panels,

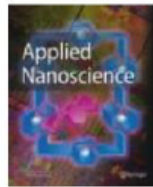
\* Corresponding Author  
Submitted: August 2, 2018

Accepted: June 22, 2019

## Chapter 7

Ag		Graphite		Cu		CuO	
Vnp	0.004	Vnp	0.004	Vnp	0.004	Vnp	0.004
Vf	100	Vf	100	Vf	100	Vf	100
$\Phi$	0.00004	$\Phi$	0.00004	$\Phi$	0.00004	$\Phi$	0.00004
Pf	997.1	Pf	997.1	Pf	997.1	Pf	997.1
Ps	10500	Ps	1300	Ps	8933	Ps	6500
Pnf	997.4801	Pnf	997.1121	Pnf	997.4174	Pnf	997.3201
Cpf	4179	Cpf	4179	Cpf	4179	Cpf	4179
Cps	235	Cps	717	Cps	385	Cps	535.6
Cpnf	4177.339	Cpnf	4178.819	Cpnf	4177.641	Cpnf	4178.05
Ks	429	Ks	25	Ks	401	Ks	20
Kf	0.613	Kf	0.613	Kf	0.613	Kf	0.613
Knf	0.613024	Knf	0.613023	Knf	0.613024	Knf	0.613022
uf	1.08E-03	uf	0.00108	uf	1.08E-03	uf	1.08E-03
unf	0.00108	unf	0.00108	unf	0.00108	unf	0.00108
Vnf	1.08E-06	Vnf	1.08E-06	Vnf	1.08E-06	Vnf	1.08E-06
Bs	1.86E-05	Bs	1.2E-06	Bs	1.67E-05	Bs	1.80E-05
Bf	2.10E-04	Bf	0.00021	Bf	2.10E-04	Bf	2.10E-04
Bnf	0.00021	Bnf	0.00021	Bnf	0.00021	Bnf	0.00021





***SUBMITTED FEBRUARY 20<sup>TH</sup> 2021 (UNDER REVIEW)***

**NUMERICAL SIMULATION OF FORCED CONVECTION-RADIATION TRANSFER IN A FLAT PLATE PRISMATIC 3-D SOLAR COLLECTOR WITH INLET/OUTLET CONDITIONS, METALLIC/CARBON NANOPARTICLES AND THE CHANDRASEKHAR DISCRETE ORDINATES METHOD**

*Sireetorn Kuharat<sup>1</sup>, O. Anwar Bég<sup>1\*</sup>, Ali Kadir<sup>1</sup>*

*<sup>1</sup>Aeronautical & Mechanical Engineering Department, School of Computing, Science and Engineering, Newton Building, University of Salford, Manchester, M64WT, UK.*

*Emails- [O.A.Beg@salford.ac.uk](mailto:O.A.Beg@salford.ac.uk) ; [S.Kuharat@edu.salford.ac.uk](mailto:S.Kuharat@edu.salford.ac.uk) ; [a.kadir@salford.ac.uk](mailto:a.kadir@salford.ac.uk) :*

*\*Corresponding author*

**Abstract**

It has been demonstrated in many studies that nanofluids provide significant thermal enhancement in a variety of direct absorber solar collectors i.e., prismatic, trapezoidal, annular etc. A range of metallic nanoparticles (copper, titanium oxide, aluminium oxide, zinc, silver diamond) and different volume fractions have been explored. However, other thermal solar collectors in the current market have different features such as conventional surface absorption-based solar collectors, which use a *black surface or spectrally selective surface* to absorb solar irradiance and heat the heat transfer fluids (HTF). In these systems the efficiency depends on the absorber capturing solar energy and how effectively heat is transferred to the working fluid. Heat transfer in surface absorption-based solar collectors mostly relies on thermal conductivity of nanofluids, flow rate (forced convection) and temperature gradient (radiation). In this presentation, the flat plate solar collector geometry with inlet and outlet features (for controlling flow rates) is examined. Three different metallic (copper, copper oxide, silver) and one non-metallic (Graphite) nanoparticles are simulated in a 3-dimensional solar collector geometry. Forced convection is considered i. e. thermal buoyancy effect (neglected), and therefore Reynolds and Prandtl numbers and volume fraction are the critical control parameters. The Tiwari-Das nanoscale model is deployed in ANSYS FLUENT. To cater for variable optical properties of nanofluids, a more advanced radiative approximation model is deployed, namely the Chandrasekhar discrete ordinates method (DOM). Extensive visualization of different geometric and nanoscale effects is included. The relative performance of the different metallic and non-metallic nanoparticles on thermal efficiency e. g. local Nusselt number at the enclosure (collector) boundaries is also described. Interesting thermofluid characteristics are computed and it is identified that specific volume fractions of different metallic and non-metallic nanoparticles under carefully selected flow rates produce optimum heat transfer performance.

**Key words:** *DASCs, solar energy, nanofluids, graphite, silver, copper, Nusselt number, CFD, flat plate solar collector, mesh independence, Discrete ordinates model.*

*“UNDERSTANDING THERMAL RADIATION”, NOVA SCIENCE, NEW YORK, USA. EDITOR: DR.K.S.RAWAT. IN PRESS - DECEMBER 2019.*



**CHAPTER 1: COMPUTATION OF RADIATIVE-  
CONVECTIVE HEAT TRANSFER IN DIRECT  
ABSORBER SOLAR COLLECTORS**

***O. Anwar Bég\****

*Aeronautical and Mechanical Engineering, University of Salford, Manchester,  
England.*

***Sireetorn Kuharat***

*Aeronautical and Mechanical Engineering, University of Salford, Manchester,  
England.*

***Ali Kadir***

*Aeronautical and Mechanical Engineering, University of Salford, Manchester,  
England.*

---

**ABSTRACT**

---

Solar energy is an important application of thermal radiation heat transfer. To simulate radiative transfer, generally the integro-differential radiative transfer equation (RTE) has to be solved. However, this is very challenging

---

\* Corresponding Author address

Email: *O.A.Beg@salford.ac.uk*

## Chapter 8

### *Perturbation solutions*

Although in most previous studies of fluid mechanical problems for the sake of simplicity of the analysis, fluid viscosity has been taken to be constant, in many real MHD solar pump flows the viscosity is a function of temperature. Keeping this in mind, here we deploy a temperature-dependent fluid viscosity which is modelled as a linear function of temperature. Thus, for the analysis, we adopt Reynolds' model of viscosity as:

$$\mu(\theta) = 1 - \alpha\theta \quad \text{for} \quad \alpha \ll 1. \quad (8.29)$$

Applying Eqn. (8.29) to Eqn. (8.21), we obtain:

$$0 = (1 - \alpha\theta) \frac{\partial^4 \psi}{\partial y^4} - 2\alpha \frac{\partial \theta}{\partial y} \frac{\partial^3 \psi}{\partial y^3} - \left( \alpha \frac{\partial^2 \theta}{\partial y^2} + N^2 \right) \frac{\partial^2 \psi}{\partial y^2} + Gr \frac{\partial \theta}{\partial y} + Br \frac{\partial \sigma}{\partial y}, \quad (8.30)$$

The case for a nanofluid with constant viscosity can be retrieved as a special case of the present investigation when we assume  $\alpha = 0$ . Eqn. (8.30) is a highly nonlinear partial differential equation, and it is not possible to derive exact solutions. However, we may deploy a perturbation method in terms of  $\alpha$  (viscosity parameter), by expanding  $\psi$  and  $F$  in the following forms:

$$\psi = \psi_0 + \alpha\psi_1 + o(\psi_2), \quad (8.31)$$

$$F = F_0 + \alpha F_1 + o(F_2). \quad (8.32)$$

Inserting the above expressions into Eqn. (8.30) and boundary conditions Eqn. (8.26), the following systems emerge:

#### **8.3.1. For the system of order ( $\alpha^0$ )**

$$\frac{\partial^4 \psi_0}{\partial y^4} - N^2 \frac{\partial^2 \psi_0}{\partial y^2} + Gr \frac{\partial \theta}{\partial y} + Br \frac{\partial \sigma}{\partial y} = 0, \quad (8.33)$$

$$\psi_0 = \frac{q_0}{2}, \quad \frac{\partial \psi_0}{\partial y} = -1 \quad \text{at} \quad y = h_1, \quad (8.34a)$$

$$\psi_0 = -\frac{q_0}{2}, \quad \frac{\partial \psi_0}{\partial y} = -1 \quad \text{at} \quad y = h_2. \quad (8.34b)$$

#### **8.3.2. For the system of order ( $\alpha^1$ )**

$$\frac{\partial^4 \psi_1}{\partial y^4} - \theta \frac{\partial^4 \psi_0}{\partial y^4} - 2 \frac{\partial \theta}{\partial y} \frac{\partial^3 \psi_0}{\partial y^3} - \frac{\partial^2 \theta}{\partial y^2} \frac{\partial^2 \psi_0}{\partial y^2} - N^2 \frac{\partial^2 \psi_1}{\partial y^2} = 0, \quad (8.35)$$

$$\psi_1 = \frac{q_1}{2}, \quad \frac{\partial \psi_1}{\partial y} = 0 \quad \text{at} \quad y = h_1, \quad (8.36a)$$

$$\psi_1 = -\frac{q_1}{2}, \quad \frac{\partial \psi_1}{\partial y} = 0 \quad \text{at} \quad y = h_2. \quad (8.36b)$$

#### **8.3.3. Solution for system of order ( $\alpha^0$ )**

Solution of Eqn. (8.33) subject to boundary conditions Eqn. (8.34a & 8.34b) can be derived as:

$$\psi_0(y) = c_5 + c_6 e^{-Ny} + L_{10} y^2 - \frac{c_8 y}{N^2} + L_{11} e^{-A_1 y} + c_7 e^{Ny}. \quad (8.37)$$

### 8.3.4. Solution for system of order ( $\alpha^1$ )

Using Eqn. (8.37) into Eqn. (8.35) and invoking the boundary conditions (8.36 a & b), we arrive at:

$$\begin{aligned} \psi_1(y) = & c_9 + c_{10} e^{-Ny} + c_{11} e^{Ny} - \frac{c_{12} y}{N^2} + L_1 e^{-A_1 y} + L_2 + L_3 e^{-2A_1 y} + L_4 y e^{-A_1 y} + L_5 e^{-Ny} \\ & + L_6 e^{Ny} + L_7 y e^{Ny} + L_8 e^{-(A_1+N)y} + L_9 e^{-(A_1-N)y} \end{aligned} \quad (8.38)$$

The stream function of the nanofluid is given by the expression:

$$\psi = \psi_0 + \alpha \psi_1 + o(\psi_2),$$

$$\begin{aligned} \psi(y) = & c_5 + c_6 e^{-Ny} + L_{10} y^2 - \frac{c_8 y}{N^2} + L_{11} e^{-A_1 y} + c_7 e^{Ny} \\ & + \alpha \left( c_9 + c_{10} e^{-Ny} + c_{11} e^{Ny} - \frac{c_{12} y}{N^2} + L_1 e^{-A_1 y} + L_2 + L_3 e^{-2A_1 y} + L_4 y e^{-A_1 y} \right. \\ & \left. + L_5 e^{-Ny} + L_6 e^{Ny} + L_7 y e^{Ny} + L_8 e^{-(A_1+N)y} + L_9 e^{-(A_1-N)y} \right). \end{aligned} \quad (8.39)$$

Axial velocity can also be derived as:

$$\begin{aligned} u(y) = & 2L_{10} y - \frac{c_8}{N^2} - A_1 L_{11} e^{-A_1 y} - c_6 N e^{-Ny} + c_7 N e^{Ny} \\ & + \alpha \left( (L_7 + L_7 N y + c_{11} N + L_6 N) e^{Ny} - \frac{c_{12}}{N^2} + L_4 e^{-A_1 y} - (c_{10} + L_5) N e^{-Ny} \right. \\ & \left. - L_8 (N + A_1) e^{-(N+A_1)y} + L_9 (N - A_1) e^{(N-A_1)y} - 2L_3 A_1 e^{-2A_1 y} \right. \\ & \left. - (L_4 y + L_1) A_1 e^{-A_1 y} \right). \end{aligned} \quad (8.40)$$

All the coefficients featured in the above closed-form solutions, are presented below:

$$c_1 = \left( \frac{Nb + Nt}{Nb(h_1 - h_2)} \right), c_2 = -c_1 h_2, \xi = \left( \frac{1 + Rn Pr}{Pr} \right), A_1 = \frac{c_1 Nb}{\xi}, A_2 = \frac{\beta}{\xi}, A_3 = \frac{A_1 + A_2 (h_1 - h_2)}{A_1 (e^{-A_1 h_2} - e^{-A_1 h_1})}, \quad (8.41)$$

$$A_4 = \frac{(A_1 e^{-A_1 h_2} + A_2 h_1 e^{-A_1 h_2} - A_2 h_2 e^{-A_1 h_1})}{A_1 (e^{-A_1 h_1} - e^{-A_1 h_2})}, A_5 = \frac{(Nb + A_3 Nt (e^{-A_1 h_1} - e^{-A_1 h_2}))}{Nb(h_1 - h_2)}, A_6 = \frac{A_3 Nt}{Nb}, \quad (8.42)$$

$$A_7 = \frac{(Nb h_2 - A_3 Nt h_1 e^{-A_1 h_2} + A_3 Nt h_2 e^{-A_1 h_1})}{Nb(h_1 - h_2)}, A_8 = \frac{Gr A_2}{A_1 - Br A_5}, A_9 = -\frac{Br A_1 A_6}{Gr A_1 A_3}, \quad (8.43)$$

$$L_{10} = -\frac{A_8}{2N^2}, L_{11} = (A_1^4 - N^2 A_1^2), \quad (8.44)$$

$$D_1 = N^3 Nb^2 c_1 \xi^5 (h_1 - h_2) (4 \cosh(N(h_1 - h_2)) - 2N h_1 \sinh(N(h_1 - h_2)) + 2N h_2 \sinh(N(h_1 - h_2)) - 4), \quad (8.45)$$



$$D_2 = 4N^3Nb^2c_1\xi^5 \left( 2\cosh(N(h_1 - h_2)) - Nh_1 \sinh(N(h_1 - h_2)) + Nh_2 \sinh(N(h_1 - h_2)) - 2 \right), \quad (8.46)$$

$$D_3 = 2N^2Nb^7c_1^4(h_1 - h_2) + 2N^3Nb^6c_1^5(h_1 - h_2) - 2N^4Nb^5c_1^4(\xi^2 - \xi^3)(h_1 - h_2), \quad (8.47)$$

$$D_4 = 8N^2Nb^2c_1\xi^5(h_1 - h_2) + 4BrNt\beta\xi^5(h_1^2 - h_2^2) + 4BrNb^2c_1\xi^5(h_1 + h_2) - 4GrNb\beta\xi^5(h_1^2 - h_2^2), \quad (8.48)$$

$$D_5 = 2Nb^2c_1\xi^5(h_1 - h_2)(4\cosh(N(h_1 - h_2)) - 2Nh_1 \sinh(N(h_1 - h_2)) + 2Nh_2 \sinh(N(h_1 - h_2)) - 4), \quad (8.49)$$

$$\begin{aligned} c_5 = & -(2N^3Nb^2c_1(h_1^2 - h_2^2) + BrNNbNtc_1(h_1^2 - h_2^2) + BrNNt\beta h_1 h_2(h_1 - h_2) - GrNNb\beta h_1 h_2(h_1 - h_2) \\ & - (2BrNt\beta(h_1^2 + h_2^2) - 2BrNbc_1(h_1^2 - h_2^2) + 2GrNb\beta(h_1^2 + h_2^2) - 2BrNbNtc_1(h_1 - h_2) \\ & + 4(BrNt - GrNb)\beta h_1 h_2 - q_0N^4Nb^2c_1(h_1^2 - h_2^2) + BrN^2Nt\beta(h_1^3 + h_2^3) - GrN^2Nb\beta h_1 h_2(h_1^2 + h_2^2) \\ & - 2BrN^2Nt\beta h_1^2 h_2^2 - BrN^2Nb^2c_1 h_1 h_2(h_1 - h_2) + 2GrN^2Nb\beta h_1^2 h_2^2 \\ & - BrN^2NbNtc_1 h_1 h_2(h_1 - h_2)) \sinh(N(h_1 - h_2)) + BrNNt\beta(h_1^3 - h_2^3) - GrNNb\beta(h_1^3 - h_2^3) \\ & + BrN Nbc_1(h_1^2 - h_2^2) + (BrNNt\beta(h_1^3 - h_2^3) - 2N^3Nb^2c_1(h_1^2 - h_2^2) - GrNNb\beta(h_1^3 - h_2^3) \\ & + BrNNb^2c_1(h_1^2 - h_2^2) + BrNNbNc_1(h_1^2 - h_2^2) + 5BrNNt\beta h_1 h_2(h_1 - h_2) - 4BrMNb^2c_1 h_1 h_2 \\ & - 5GrN Nb\beta h_1 h_2(h_1 - h_2) - 4BrNNbNtc_1 h_1 h_2) \cosh(N(h_1 - h_2)) / D_1 \\ & - \xi^2 \left( (2N^5Nb^5c_1^4(h_1^2 - h_2^2) - 2N^5Nb^5c_1^4 h_1 h_2) (e^{-A_1 h_1} - e^{-A_1 h_2}) \right. \\ & + (N^5Nb^5c_1^4 h_2(h_2 - h_1) - N^5Nb^5c_1^4 h_2(h_2 - h_1)) (e^{N(h_1 - h_2) - A_1 h_1} - e^{-N(h_1 - h_2) - A_1 h_1}) \\ & + (N^5Nb^5c_1^4 h_1(h_2 - h_1) - N^5Nb^5c_1^4 h_2(h_2 - h_1)) (e^{N(h_1 - h_2) - A_1 h_2} - e^{-N(h_1 - h_2) - A_1 h_2}) \\ & \left. - (2N^3Nb^7c_1^6(h_1^2 - h_2^2) - 2N^3Nb^7c_1^6 h_1 h_2) (e^{-A_1 h_1} - e^{-A_1 h_2}) \right) / D_1 \\ & - \xi \left( (2N^3Nb^3c_1^5(h_1 - h_2)) (e^{-A_1 h_1} - e^{-A_1 h_2}) \right. \\ & + (N^4Nb^6c_1^5 h_2(h_2 - h_1) + N^3Nb^2c_1^5(h_2 - h_1) + N^3Nb^7c_1^6 h_2(h_2 - h_1) + N^2Nb^7c_1^6(h_2 - h_1)) \\ & \left. (e^{N(h_1 - h_2) - A_1 h_1} - e^{-N(h_1 - h_2) - A_1 h_1}) \right. \\ & + (N^4Nb^5c_1^5 h_1(h_1 - h_2) - N^3Nb^6c_1^5(h_1 - h_2) + N^3Nb^7c_1^6 h_1(h_1 - h_2) - N^2Nb^7c_1^6(h_1 - h_2)) \\ & \left. (e^{N(h_1 - h_2) - A_1 h_2} - e^{-N(h_1 - h_2) - A_1 h_2}) \right) / D_1 + \xi^3 \left( (2N^5Nb^4c_1^3(h_1 - h_2)) (e^{-A_1 h_1} - e^{-A_1 h_2}) \right. \\ & + (N^6Nb^4c_1^3 h_2(h_2 - h_1) + N^5Nb^4c_1^3(h_2 - h_1)) (e^{N(h_1 - h_2) - A_1 h_1} - e^{-N(h_1 - h_2) - A_1 h_1}) \\ & \left. + (N^6Nb^4c_1^3 h_1(h_1 - h_2) - N^5Nb^4c_1^3(h_1 - h_2)) (e^{N(h_1 - h_2) - A_1 h_2} - e^{-N(h_1 - h_2) - A_1 h_2}) \right) / D_1, \quad (8.50) \end{aligned}$$

$$\begin{aligned}
c_6 = & (2N^4 Nb^5 c_1^4 \xi^2 + 2N^5 Nb^4 c_1^3 \xi^3 - 2N^3 Nb^6 c_1^5 \xi - 2N^2 Nb^7 c_1^6) (e^{Nh_1 - Ah_1} + e^{Nh_2 - Ah_2}) \\
& + (2N^2 Nb^7 c_1^6 + 2N^3 Nb^7 c_1^6 (h_2 - h_1) + 2N^3 Nb^6 c_1^5 \xi + 2N^4 Nb^5 c_1^4 \xi^2 - 2N^4 Nb^4 c_1^3 \xi^3 \\
& + 2N^5 Nb^5 c_1^4 \xi^2 (h_1 - h_2)) (e^{Nh_1 - Ah_2} + e^{Nh_2 - Ah_1}) + 2BrNNt\beta h_1 h_2 \xi^5 \\
& + (2BrNb^2 c_1 \xi^5 + 2BrNt\beta (h_1 - h_2) \xi^5 - 2GrNb\beta (h_1 - h_2) \xi^5 + 2q_0 M^3 Nb^2 c_1 \xi^2 \\
& + 2N^3 Nb^2 c_1 \xi^5 (h_1 - h_2) + 2BrNbNtc_1 \xi^5) (e^{Nh_1} - e^{Nh_2}) \\
& + (BrNNb^2 c_1 (h_2 - h_1) \xi^5 + GrNNb\beta \xi^5 (h_1^2 - h_2^2) - BrNNbNtc_1 \beta \xi^5 (h_1 - h_2) \\
& - 2GrNNb\beta h_1 h_2 \xi^5 - BrNNt\beta \xi^5 (h_1^2 - h_2^2)) (e^{Nh_1} + e^{Nh_2}) / D_2, \tag{8.51}
\end{aligned}$$

$$\begin{aligned}
c_7 = & (2N^4 Nb^5 c_1^4 \xi^2 + 2N^5 Nb^4 c_1^3 \xi^3 - 2N^3 Nb^6 c_1^5 \xi - 2N^2 Nb^7 c_1^6) (e^{-Nh_1 - Ah_1} + e^{-Nh_2 - Ah_2}) \\
& + (2N^2 Nb^7 c_1^6 + 2N^3 Nb^7 c_1^6 (h_2 - h_1) + 2N^3 Nb^6 c_1^5 \xi + 2N^4 Nb^5 c_1^4 \xi^2 - 2N^4 Nb^4 c_1^3 \xi^3 \\
& + 2N^5 Nb^5 c_1^4 \xi^2 (h_1 - h_2)) (e^{-Nh_1 - Ah_2} + e^{-Nh_2 - Ah_1}) \\
& + (2BrNb^2 c_1 \xi^5 + 2BrNt\beta (h_1 - h_2) \xi^5 - 2GrNb\beta (h_1 - h_2) \xi^5 + 2q_0 N^3 Nb^2 c_1 \xi^2 \\
& + 2N^3 Nb^2 c_1 \xi^5 (h_1 - h_2) + 2BrNbNtc_1 \xi^5) (e^{-Nh_1} - e^{-Nh_2}) + (BrN Nb^2 c_1 (h_2 - h_1) \xi^5 \\
& + GrN Nb\beta \xi^5 (h_1^2 - h_2^2) - BrN NbNtc_1 \beta \xi^5 (h_1 - h_2) + 2BrNNt\beta h_1 h_2 \xi^5 \\
& - 2GrMNb\beta h_1 h_2 \xi^5 - BrMN_t \beta \xi^5 (h_1^2 - h_2^2)) (e^{-Mh_1} + e^{-Mh_2}) / D_2, \tag{8.52}
\end{aligned}$$

$$\begin{aligned}
c_8 = & (D_3 (e^{Nh_1 - Nh_2 - Ah_1} + e^{-Nh_1 + Nh_2 - Ah_1} + e^{Nh_1 - Nh_2 - Ah_2} + e^{-Nh_1 + Nh_2 - Ah_2}) \\
& - (4N^2 Nb^7 c_1^6 (h_1 - h_2) - 2N^4 Nb^5 c_1^4 \xi^2 (h_1 - h_2)) (e^{-Ah_1} + e^{-Ah_2}) \\
& + D_4 - D_4 (\cosh(N(h_1 - h_2))) \\
& + (2BrNNt\beta \xi^5 (h_1^3 + h_2^3) - 2GrNNb\beta \xi^5 (h_1^3 + h_2^3) + 2BrNNb^2 c_1 \beta \xi^5 (h_1^2 - h_2^2) \\
& - 4q_0 N^3 Nb^2 c_1 \xi^5 (h_1 - h_2) - 4BrNbNtc_1 \xi^5 (h_1 + h_2) + 2BrNNbNtc_1 \xi^5 (h_1^2 - h_2^2) \\
& - 2BrNNtNb\beta h_1 h_2 \xi^5 (h_1 + h_2) + 2GrNNb\beta h_1 h_2 \xi^5 (h_1 + h_2)) \sinh(N((h_1 - h_2))) / D_5, \tag{8.53}
\end{aligned}$$

$$B_1 = 2A_1^2 A_2 L_{11} - A_1^2 A_2 L_{11} - A_1^4 A_4 L_{11} - 2A_1 A_3 L_{10}, B_2 = -\frac{2A_2 L_{10}}{A_1}, B_3 = 3A_1^4 A_3 L_{11} - A_1^3 A_3 L_{11} \tag{8.54}$$

$$B_4 = -A_1^3 A_2 L_{11}, B_5 = \frac{2A_2 c_6 N^3}{A_1} - \frac{A_2 c_6 N^2}{A_1} - \frac{A_2 c_6 N^4}{A_1}, B_6 = -\frac{2A_2 c_7 N^3}{A_1} - \frac{A_2 c_7 N^2}{A_1} - A_4 c_6 N^4, \tag{8.55}$$

$$B_7 = -\frac{A_2 c_7 N^4}{A_1}, B_8 = -A_1 A_3 c_6 N^2 + 2A_1 A_3 c_6 N^3 + A_3 c_6 N^4, B_9 = -A_1 A_3 c_7 N^2 - 2A_1 A_3 c_7 N^3 + A_3 c_6 N^4 \tag{8.56}$$

$$Z_1 = A_1^4 - N^2 A_1^2, Z_2 = A_1^3, Z_3 = A_1^2 - N^2, Z_4 = Z_2 Z_3, Z_5 = 4B_4 (A_1^2 - 2N^2), \tag{8.57}$$

$$L_1 = \frac{B_1}{Z_1} + \frac{Z_5}{Z_4}, L_2 = -\frac{B_2}{2N^2}, Z_6 = 16A_1^4 - 4N^2 A_1^2, L_3 = \frac{B_3}{Z_6}, L_4 = \frac{B_4}{Z_1}, L_5 = -\frac{B_5}{2N^3}, \tag{8.58}$$

$$L_6 = \frac{B_6}{2N^3} + \frac{5B_7}{N^4}, L_7 = -\frac{B_7}{4N^3}, Z_7 = (A_1 + N)^4, Z_8 = (A_1 + N)^2, Z_9 = Z_8 N^2, \quad (8.59)$$

$$Z_{10} = Z_7 - Z_9, L_8 = \frac{B_8}{Z_{10}}, Z_{11} = (A_1 - N)^4, Z_{12} = (A_1 - N)^2, Z_{13} = Z_{12} N^2, \quad (8.60)$$

$$Z_{14} = Z_{11} - Z_{13}, L_9 = \frac{B_9}{Z_{14}}, \quad (8.61)$$

$$D_6 = N\xi(4\cosh(Nh_1 - Nh_2) - 2N(h_1 - h_2)\sinh(Nh_1 - Nh_2) - 4), \quad (8.62)$$

$$D_7 = 2\xi(2\cosh(Mh_1 - Mh_2) - M(h_1 - h_2)\sinh(Mh_1 - Mh_2) - 2), \quad (8.63)$$

$$\begin{aligned}
c_9 = & \left( 2L_9 Nbc_1 - 4L_9 N\xi + 4L_9 N^2 h_1 \xi - 2L_9 NNbh_1 c_1 \right) \left( e^{Nh_1 - A_1 h_2} + e^{Nh_2 - A_1 h_1} \right) \\
& - \left( 2L_8 Nbc_1 + 4L_8 N\xi + 4L_8 N^2 h_2 \xi + 2L_8 NNbh_2 c_1 \right) \left( e^{Nh_2 - A_1 h_1} + e^{-Nh_1 - A_1 h_2} \right) \\
& + \left( 2L_3 Nbc_1 - 2L_3 N\xi + 2L_3 N^2 h_1 \xi - 4L_3 NNbh_1 c_1 \right) \left( e^{Nh_1 - Nh_2 - 2A_1 h_2} \right) \\
& - \left( 4L_3 Nbc_1 + 2L_3 N\xi + 2L_3 N^2 h_1 \xi + 4L_3 NNbh_1 c_1 \right) \left( e^{Nh_1 - Nh_2 - 2A_1 h_1} + e^{Nh_2 - Nh_1 - 2A_1 h_2} \right) \\
& + \left( 4L_3 Nbc_1 - 2L_3 N\xi + 2L_3 N^2 h_2 \xi + 4L_3 NNbh_2 c_1 \right) \left( e^{Nh_2 - Nh_1 - 2A_1 h_1} \right) \\
& - \left( 4L_7 \xi N^2 h_1^2 - 4L_7 h_2 N^2 \xi - 2L_7 Nh_1 \xi + 4L_7 Nh_2 \xi + 2L_7 \xi \right) e^{Nh_1} \\
& - \left( 4L_7 \xi N^2 h_2^2 - 4L_7 h_1 N^2 \xi - 2L_7 Nh_2 \xi + 4L_7 Nh_1 \xi + 2L_7 \xi \right) e^{Nh_2} \\
& + \left( 4L_4 NNbc_1 h_1^2 + 4L_1 h_1 NNbc_1 + 4L_1 N\xi \right) e^{-A_1 h_1} \\
& + \left( 4L_4 NNbc_1 h_2^2 + 4L_1 h_2 NNbc_1 + 4L_1 N\xi \right) e^{-A_1 h_2} \\
& + \left( 2L_8 Nbc_1 - 2L_8 NNbh_2 c_1 \right) \left( e^{2Nh_2 - 2Nh_1 - A_1 h_1} + e^{2Nh_1 - 2Nh_2 - A_1 h_2} \right) \\
& - \left( 2L_9 Nbc_1 + 2L_9 NNbh_2 c_1 \right) \left( e^{2Nh_1 - 2Nh_2 - A_1 h_1} + e^{2Nh_2 - 2Nh_1 - A_1 h_2} \right) \\
& + \left( 4L_8 N\xi + 4L_8 N^2 h_1 \xi + 4L_8 NNbc_1 h_1 \right) \left( e^{-Nh_1 - A_1 h_1} \right) \\
& + \left( 4L_9 N\xi - 4L_9 N^2 h_1 \xi + 4L_9 NNbc_1 h_1 \right) \left( e^{Nh_1 - A_1 h_1} \right) \\
& + \left( 4L_8 N\xi + 4L_8 N^2 h_2 \xi + 4L_8 NNbc_1 h_2 \right) \left( e^{-Nh_2 - A_1 h_2} \right) \\
& + \left( 4L_9 N\xi - 4L_9 N^2 h_2 \xi + 4L_9 NNbc_1 h_2 \right) \left( e^{Nh_2 - A_1 h_2} \right) \\
& + \left( 2L_7 \xi + 2L_7 Nh_1 \right) \left( e^{2Nh_2 - Nh_1} \right) + \left( 2L_7 \xi + 2L_7 Nh_2 \right) \left( e^{2Nh_1 - Nh_2} \right) \\
& - \left( \begin{array}{l} 2L_1 Nbc_1 - 2L_4 N\xi + 2L_1 N^2 h_2 \xi + 2L_4 Nbh_1 c_1 - 2L_4 Nh_1 \xi \\ -2L_4 Nh_2 \xi + 2L_1 NNbh_2 c_1 + 2L_4 N^2 h_1 h_2 \xi + 2L_4 NNbh_1 h_2 \xi \end{array} \right) \left( e^{Nh_1 - Nh_2 - A_1 h_1} \right) \\
& - \left( \begin{array}{l} 2L_4 \xi - 2L_1 Nbc_1 + 2L_1 N\xi - 2L_1 N^2 h_2 \xi \\ +2L_4 Nbc_1 h_1 + 2L_4 Nh_1 \xi - 2L_4 Nh_2 \xi + 2L_1 NNbc_1 h_2 \\ -2L_4 N^2 h_1 h_2 \xi + 2L_4 NNbc_1 h_1 h_2 \end{array} \right) \left( e^{Nh_2 - Nh_1 - A_1 h_1} \right) \\
& - \left( \begin{array}{l} 2L_4 \xi - 2L_1 Nbc_1 + 2L_1 M\xi - 2L_1 N^2 h_1 \xi \\ -2L_4 Nbc_1 h_1 - 2L_4 Nh_1 \xi + 2L_4 Nh_2 \xi + 2L_1 NNbc_1 h_1 \\ -2L_4 N^2 h_1 h_2 \xi + 2L_4 NNbc_1 h_1 h_2 \end{array} \right) \left( e^{Nh_1 - Nh_2 - A_1 h_2} \right) \\
& - \left( \begin{array}{l} 2L_1 Nbc_1 - 2L_4 \xi + 2L_1 N\xi + 2L_1 N^2 h_1 \xi + 2L_4 Nbh_2 c_1 \\ -2L_4 Nh_1 \xi + 2L_4 Nh_2 \xi + 2L_1 NNbc_1 h_1 + 2L_4 N^2 h_1 h_2 \xi + 2L_4 NNbc_1 h_1 h_2 \end{array} \right) \left( e^{Nh_2 - Nh_1 - A_1 h_1} \right) \\
& + \left( 4L_3 N\xi + 8L_3 NNbc_1 h_1 \right) e^{-2A_1 h_1} + \left( 4L_3 N\xi + 8L_3 NNbc_1 h_2 \right) e^{-2A_1 h_2} \\
& + 8L_2 N\xi (1 - \cosh(Nh_1 - Nh_2)) + 2q_1 N^2 (h_1 - h_2) \xi + 4L_2 N^2 h_1 \xi \sinh(Nh_1 - Nh_2),
\end{aligned} \tag{8.64}$$

$$\begin{aligned}
c_{10} = & -\left(L_8 Nbc_1 + 2L_8 N\xi + L_8 N^2 h_1 \xi - L_8 N^2 h_2 \xi + L_8 NNb(h_1 - h_2)c_1\right)\left(e^{Nh_2 - Nh_1 - A_1 h_1}\right) \\
& -\left(L_8 Nbc_1 + 2L_8 N\xi\right)\left(e^{-A_1 h_2} + e^{-A_1 h_1}\right) \\
& +\left(L_8 Nbc_1 + 2L_8 N\xi + L_8 N^2 h_1 \xi - L_8 N^2 h_2 \xi + L_8 NNb(h_1 - h_2)c_1\right)\left(e^{Nh_2 - Nh_1 - A_1 h_1} + e^{Nh_1 - Nh_2 - A_1 h_2}\right) \\
& -\left(L_1 Nbc_1 - L_4 \xi + L_1 N\xi + L_4 Nbc_1 h_1 + L_4 Nh_1 \xi\right)\left(e^{Nh_1 - A_1 h_1}\right) \\
& -\left(L_1 Nbc_1 - L_4 \xi + L_1 N\xi + L_4 Nbc_1 h_2 + L_4 Nh_2 \xi\right)\left(e^{Nh_2 - A_1 h_2}\right) \\
& +\left(L_1 Nbc_1 - L_4 \xi + L_1 N\xi + L_4 Nbc_1 h_1 + L_4 Nh_2 \xi\right) \\
& +\left(L_1 NNb c_1 (h_1 - h_2) + L_4 NNb c_1 h_1 (h_1 - h_2)\right)\left(e^{Nh_2 - A_1 h_1}\right) \\
& +\left(L_1 Nbc_1 - L_4 \xi + L_1 N\xi + L_4 Nbc_1 h_2 + L_4 Nh_1 \xi\right) \\
& +\left(-L_1 NNb c_1 (h_1 - h_2) + L_4 NNb c_1 h_2 (h_1 - h_2)\right)\left(e^{Nh_1 - A_1 h_2}\right) \\
& -\left(L_7 \xi N^2 h_1^2 + h_2^2 - 2L_7 h_1 h_2 N^2 \xi + 2L_7 \xi\right)\left(e^{Nh_1} + e^{Nh_2}\right) \\
& -\left(2L_3 Nbc_1 + L_3 N\xi\right)\left(e^{Nh_1 - 2A_1 h_1} + e^{Nh_2 - 2A_1 h_2}\right) \\
& +\left(2L_3 Nbc_1 + L_3 N\xi + 2L_3 NNb c_1 h_1 - 2L_3 NNb c_1 h_2\right)\left(e^{Nh_1 - 2A_1 h_2} + e^{Nh_2 - 2A_1 h_1}\right) \\
& +\left(L_9 Nbc_1 - L_9 N^2 h_1 \xi + L_9 N^2 h_2 \xi + L_9 NNb c_1 (h_1 - h_2)\right)\left(e^{Nh_1 + Nh_2 - A_1 h_1}\right) \\
& +\left(L_9 Nbc_1 + L_9 N^2 h_1 \xi - L_9 N^2 h_2 \xi - L_9 NNb c_1 (h_1 - h_2)\right)\left(e^{Nh_1 + Nh_2 - A_1 h_2}\right) \\
& +\left(L_7 \xi\right)\left(e^{2Nh_1} + e^{2Nh_2}\right) + 4L_5 N\xi \cosh(Nh_1 - Nh_2) \\
& -L_9 Nbc_1 \left(e^{Nh_1 - A_1 h_1} + e^{2Nh_2 - A_1 h_2}\right) + q_1 N\xi \left(e^{Nh_1} - e^{Nh_2}\right) \\
& -2L_5 N^2 (h_1 - h_2)\xi \sinh(N(h_1 - h_2)) - 4L_5 N\xi / D_6,
\end{aligned} \tag{8.65}$$

$$\begin{aligned}
c_{11} = & \left(2L_9 N - L_9 N^2 (h_1 - h_2)\right)\left(e^{Nh_1 - Nh_2 - A_1 h_1} - e^{Nh_2 - Nh_1 - A_1 h_2}\right) \\
& -L_8 N^2 (h_1 - h_2)\left(e^{-Nh_1 - Nh_2 - A_1 h_1} - e^{-Nh_1 - Nh_2 - A_1 h_2}\right) + \left(L_4 + L_1 N + L_4 Nh_1 + L_1 N_b c_1\right)\left(e^{-Nh_1 - A_1 h_1} - e^{-Nh_1 - A_1 h_2}\right) \\
& -\left(L_4 + L_1 N + L_4 Nh_2 - L_1 Nbc_1 - 2L_3 Nbc_1\right)\left(e^{-Nh_2 - A_1 h_1} - e^{-Nh_2 - A_1 h_2}\right) - 2L_7 \cosh(N(h_1 - h_2)) + 4L_6 N + 2L_7 \\
& +\left(L_3 N + 2L_3 Nbc_1\right)\left(e^{-Nh_1 - 2A_1 h_1} - e^{-Nh_1 - 2A_1 h_2}\right) + 2L_7 N (h_1 + h_2) - q_1 N \left(e^{-Nh_1} - e^{-Nh_2}\right) \\
& +\left(2L_9 N - 2L_9 Nbc_1\right)\left(e^{-A_1 h_1} + e^{-A_1 h_2}\right) - 4L_6 N \cosh(Nh_1 - Nh_2) \\
& +\left(L_7 N^2 (h_1^2 - h_2^2)\right)\left(e^{Nh_1 - Nh_2} - e^{Nh_2 - Nh_1}\right) - 2L_7 N (h_1 + h_2) \cosh(Nh_1 - Nh_2) \\
& +2L_6 N^2 (h_1 - h_2) \sinh(Nh_1 - Nh_2) - 2L_7 N^2 h_1 h_2 \cosh(Nh_1 - Nh_2) \\
& +\left(L_8 Nbc_1\right)\left(e^{-2Nh_1 - A_1 h_1} + e^{-2Nh_2 - 2A_1 h_2}\right) - \left(L_8 Nbc_1\right)\left(e^{-Nh_1 - Nh_2 - A_1 h_1}\right) - L_9 Nbc_1 \left(e^{Mh_1 - Mh_2 - A_1 h_1}\right) \\
& +\left(L_4 Nbc_1 (h_1 - h_2)\right)\left(e^{-Nh_1 - A_1 h_1} - e^{-Nh_2 - A_1 h_1}\right) \\
& -\left(L_1 NNb c_1 (h_1 - h_2)\right)\left(e^{-Nh_1 - A_1 h_2} - e^{-Nh_2 - A_1 h_1}\right) - \left(2L_3 NNb c_1 (h_1 - h_2)\right)\left(e^{-Nh_1 - 2A_1 h_2} - e^{-Nh_2 - 2A_1 h_1}\right) \\
& +\left(L_8 NNb c_1 (h_1 - h_2)\right)\left(e^{-Nh_1 - Mh_2 - 2A_1 h_1} - e^{-Nh_2 - 2A_1 h_2}\right) \\
& +\left(L_9 NNb c_1 (h_1 - h_2)\right)\left(e^{Nh_1 - Nh_2 - 2A_1 h_1} - e^{Nh_2 - 2A_1 h_2}\right) \\
& +\left(L_4 NNb c_1 h_1^2 - h_1 h_2\right)\left(e^{-Nh_2 - A_1 h_1}\right) + \left(L_4 MN_b c_1 h_2^2 - h_1 h_2\right)\left(e^{-Mh_1 - A_1 h_2}\right) / D_6,
\end{aligned} \tag{8.66}$$

$$\begin{aligned}
c_{12} = & -\left(L_7\xi + 2L_7N(h_1 - h_2)\xi\right)N^2e^{Nh_1} + \left(L_7\xi - 2L_7N(h_1 + h_2)\xi\right)e^{Nh_2} \\
& + \left(L_1Nbc_1 - L_4\xi + L_1N\xi + L_4Nbc_1h_1 + L_4Nh_1\xi\right)e^{Nh_1 - Nh_2 - A_1h_1} \\
& - \left(L_4\xi - L_1Nbc_1 + L_1N\xi - L_4Nbc_1h_1 + L_4Nh_1\xi\right)e^{Nh_2 - Nh_1 - A_1h_1} \\
& + \left(L_1Nbc_1 - L_4\xi + L_1N\xi + L_4Nbc_1h_2 + L_4Nh_2\xi\right)e^{Nh_2 - Nh_1 - A_1h_2} \\
& - \left(L_4\xi - L_1Nbc_1 + L_1N\xi - L_4Nbc_1h_2 + L_4Nh_2\xi\right)e^{Nh_1 - Nh_2 - A_1h_2} \\
& + \left(2L_8Nbc_1 + 2L_8N\xi\right)\left(e^{-Nh_1 - A_1h_2} + e^{-Nh_2 - A_1h_1}\right) + \left(2L_9Nbc_1 - 2L_9N\xi\right)\left(e^{Nh_1 - A_1h_2} + e^{Nh_2 - A_1h_1}\right) \\
& - \left(2L_8Nbc_1 + 2L_8N\xi\right)\left(e^{-Nh_1 - A_1h_1} + e^{-Nh_2 - A_1h_2}\right) - \left(2L_9Nbc_1 - 2L_9N\xi\right)\left(e^{Nh_1 - A_1h_1} + e^{Nh_2 - A_1h_2}\right) \\
& - \left(2L_1Nbc_1 - 2L_4\xi + 2L_4Nbc_1h_1\right)e^{-A_1h_1} - \left(2L_1Nbc_1 - 2L_4\xi + 2L_4Nbc_1h_2\right)e^{-A_1h_2} \\
& + \left(2L_3Nbc_1 + L_3N\xi\right)\left(e^{Nh_1 - Nh_2 - 2A_1h_1} + e^{Nh_2 - Nh_1 - 2A_1h_2}\right) \\
& + \left(2L_3Nbc_1 - L_3N\xi\right)\left(e^{Nh_2 - Nh_1 - 2A_1h_1} + e^{Nh_1 - Nh_2 - 2A_1h_2}\right) \\
& - L_7\xi\left(e^{2Nh_2 - Nh_1} + e^{2Nh_1 - Nh_2}\right) - 4L_3Nbc_1\left(e^{-2A_1h_1} + e^{-2A_1h_2}\right) \\
& - 2c_1N\xi\sinh(Nh_1 - Nh_2) + L_8Nbc_1\left(e^{Nh_2 - 2Nh_1 - A_1h_1} + e^{Nh_1 - 2Nh_2 - A_1h_2}\right) \\
& + L_9Nbc_1\left(e^{2Nh_1 - Nh_1 - A_1h_1} + e^{2Nh_2 - Nh_1 - A_1h_2}\right) / D_7,
\end{aligned} \tag{8.67}$$